UNIVERSITÀ DEGLI STUDI DI MILANO

DOTTORATO DI RICERCA IN SCIENZE DELLA TERRA

Ciclo XXXV

DIPARTIMENTO DI SCIENZE DELLA TERRA

Crystal chemistry and physical-chemical behavior of REE-bearing phosphates and arsenates: the case study of Mt. Cervandone

GEO09

Francesco Pagliaro

Tutor: Prof. Paolo Lotti

Co-tutor: Dr. Alessandro Guastoni

PhD Coordinator: Prof. Maria Iole Spalla

Academic Year 2022/2023

Abstract

The crystal chemistry, crystal structure and behavior at non-ambient conditions of natural Rare Earth Elements-bearing phosphates [monazite-(Ce), nominally $Ce(PO_4)$, and xenotime-(Y), nominally $Y(PO_4)$] and arsenates [gasparite-(Ce), nominally $Ce(AsO_4)$, and chernovite-(Y), nominally $Y(AsO_4)$], from the hydrothermal quartz-bearing fissures outcropping at Mt. Cervandone (Lepontine Alps, Piedmont, Italy), have been investigated. The chemical and structural characterization, performed via electron microprobe analysis, Raman spectroscopy and single-crystal X-ray diffraction, showed that the zircon-type minerals chernovite-(Y) and xenotime-(Y) share a very similar (Y,HREE) composition and the same can be stated for the LREE content of the two monazite-type minerals [gasparite-(Ce) and monazite-(Ce)]. An almost complete solid solution has been found between xenotime-(Y) and chernovite-(Y), while a wide miscibility gap has been observed within the monazite series minerals of Mt. Cervandone. Moreover, both the unit-cell and the REE-coordination polyhedral volumes are strongly controlled by the cationic population at the *T*-site: an increase in As not only expands the volume of the TO_4 tetrahedron, but even that of the REE-polyhedron, irrespective of the *A*-site population. An exception is provided by the relative abundance of Th and Ca at the *A*-site, which was found to expand the coordination polyhedron and unit-cell volumes irrespective of the *T*-site composition.

The comparative analysis of the thermo-elastic behavior of selected samples has been conducted by *in situ* high-*P*, high-*T* and combined H*P*–H*T* X-ray diffraction experiments using both single-crystals and polycrystalline samples at synchrotron or conventional lab facilities. The compressional behavior of the investigated minerals is compatible with the literature data on the synthetic endmember counterparts. The two zircon-type minerals undergo different phase transitions under compression, while the monazite-type minerals experience a change in the compressional behavior, likely induced by the increase in coordination number of the REE-bearing polyhedron. The thermal expansion behavior of monazite-(Ce) and xenotime-(Y) confirm the literature data available, while the studied chernovite-(Y) is significantly less expandable than the synthetic counterparts described in the literature. The phosphates were found to be less compressible, but more expandable than the isostructural arsenates. The structural analysis at non-ambient conditions has been carried out on the basis of the refined structure models, allowing the description of the deformation mechanisms accommodating the bulk compression or expansion at the atomic scale. Both are mainly accommodated by the $REEO_x$ coordination polyhedra, while the tetrahedra behave as a quasi-rigid units. In conclusion, all the experimental data confirm the central role played by the *T*-site in controlling the structural deformation and, in turn, the bulk thermal expansion and compression.

Index

Chapter 1

1 Rare Earth Elements

1.1 Definition, history and critical issues

According to the red book of the International Union of Pure and Applied Chemistry (IUPAC, Connelly et al. 2005), the Rare Earth Elements (REE) consist of a group of 17 elements, comprising the lanthanoids (also named lanthanides, La-Lu series and generally represented with the symbol **Ln**), Y and Sc, all characterized by similar chemical properties and geochemical behavior. In the Periodic System of Elements (Figure 1.1) lanthanoids are reported with their classical, separated "footnote" position, due to the successful 18-groups layout designed by Deming (1923). On the other hand, the placement of lanthanoids into the Periodic System was a major issue among physicist and chemists in the 19th century and the La-Lu series found its own place rather recently (*e.g.*, Laing 2005). The discovery of the REE started out in 1794, with the isolating of Y_2O_3 from gadolinite-(Y), [$Y_2FeBe_2Si_2O_{10}$] by Johan Gadolin, a Finnish chemist and mineralogist (Gadolin 1794; Weeks 1932; Gupta and Krishnamurthy 2005; Royal Society of Chemistry 2022). The yttrium oxide was named *yttria*, after the Swedish site of Ytterby, where the mineral came from. Few years later, in 1803, the first REE to be isolated as a metal was Ce by Jöns Jacob Berzelius and Wilhelm Hisinger. During the 19th and the early 20th centuries, almost all the REE were isolated. Lutetium and promethium were discovered more than one century later the discovery of yttrium: lutetium was isolated only in 1907, independently by Carl Auer, baron von Welsbach, and Charles James (Weeks 1932; Royal Society of Chemistry 2022), while promethium was discovered in 1947, as a decay product of europium and uranium (Marinsky et al. 1947). Further information see Weeks (1932), Royal Society of Chemistry (2022), Voncken (2016), Cleve (1879) de Marignac (1878), Nilson (1879a,b), Gupta and Krishnamurthy (2005).

As outlined by several authors (*e.g.*, Voncken 2016; Gambogi 2017), the name "Rare Earth" is misleading. In the first place, these elements are not related to the alkaline earth metals: the term

"earth" comes from a literal translation of the French term *terre*, or from the German *erde*, commonly used to define metal oxides. Indeed, most of the REE, at first, were obtained in form of oxides, believed to be element themselves until the beginning of 19th century. Furthermore, the REE are neither rare. The appellative "rare" comes from the old belief that these elements were actually rare. The deposits of REE-minerals are rather scarce and, despite most of the REE in the continental crust are as common as some base metals (for instance Cu and Pb, Figure 1.2), there are no geological processes capable to enrich those metals in the rock at more than few point percent (*e.g.*, Hoshino et al. 2016). In the 19th century, at the time of their first discoveries, only few deposits were known to host REE-bearing minerals. In this context, the Ytterby and the Bastnäs mines played a paramount role. The Ytterby mine, in Resarö island, belonging to the Proterozoic Baltic belt, has been exploited since the 14th century to produce quartz and feldspar for the ceramic industry (*e.g.*, Sjöberg et al. 2017). The majority of the REE has been isolated for the first time from gadolinite specimens found at the Ytterby mine. Yttrium, ytterbium, terbium, and erbium are named after Ytterby mine. Gadolinium, holmium, thulium, scandium, lutetium, have been isolated for the first time starting from Ytterby's minerals. On the other hand, lanthanum, cerium, praseodymium and neodymium have been isolated from the mineral cerite-(Ce) [$(Ce,La,Ca)_9(Mg,Fe^{3+})(SiO_4)_3(SiO_3OH)_4(OH)_3$] found in the Bastnäs mine, in the Paleoproterozoic Fennoscandian Shield (Skinnskatteberg District, Sweden) (*e.g.*, Jonsson et al. 2014).

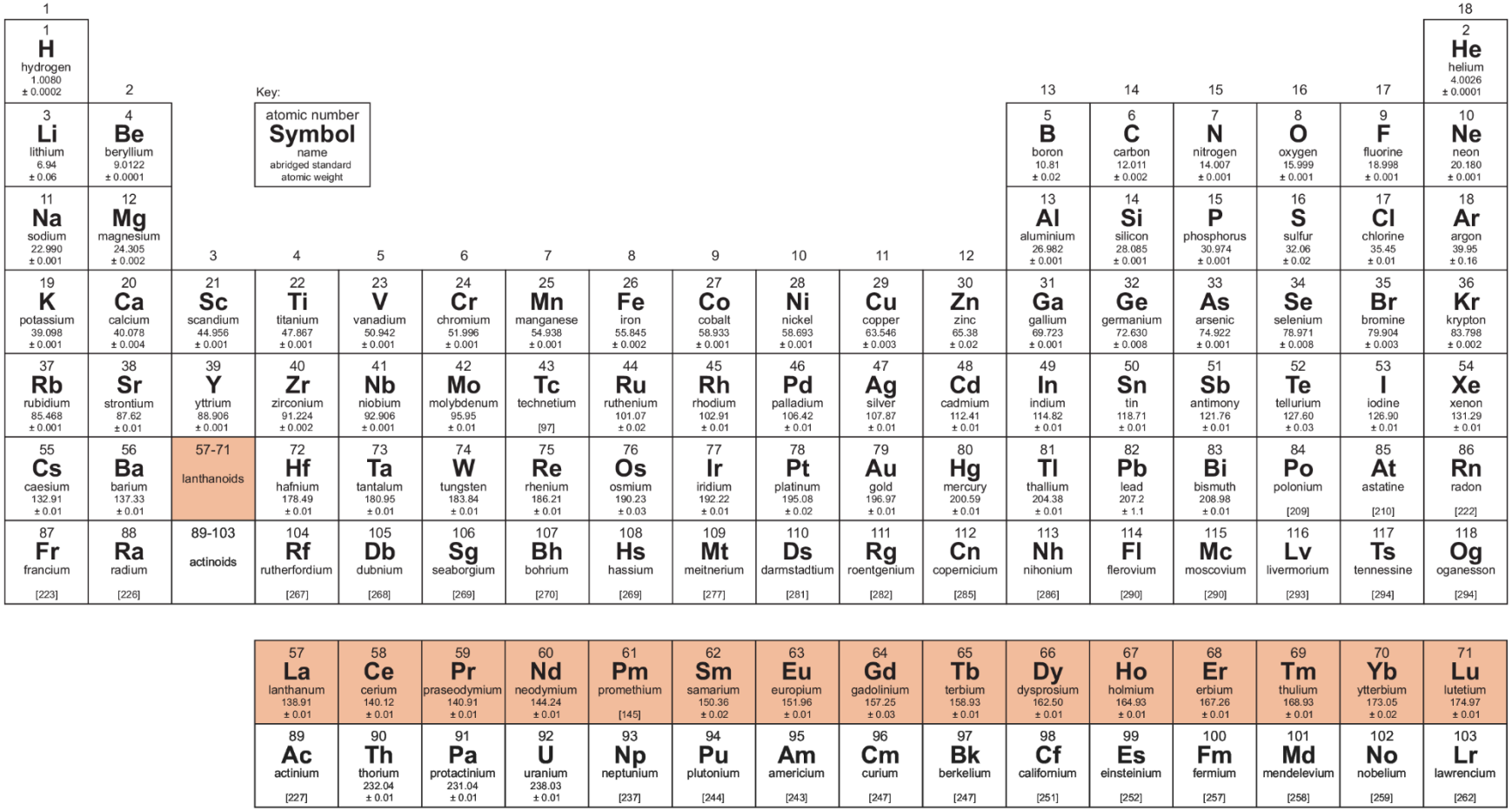

Figure 1.1: Periodic Table of the elements issued by IUPAC (2022). In red are highlighted the lanthanoids (Ln)

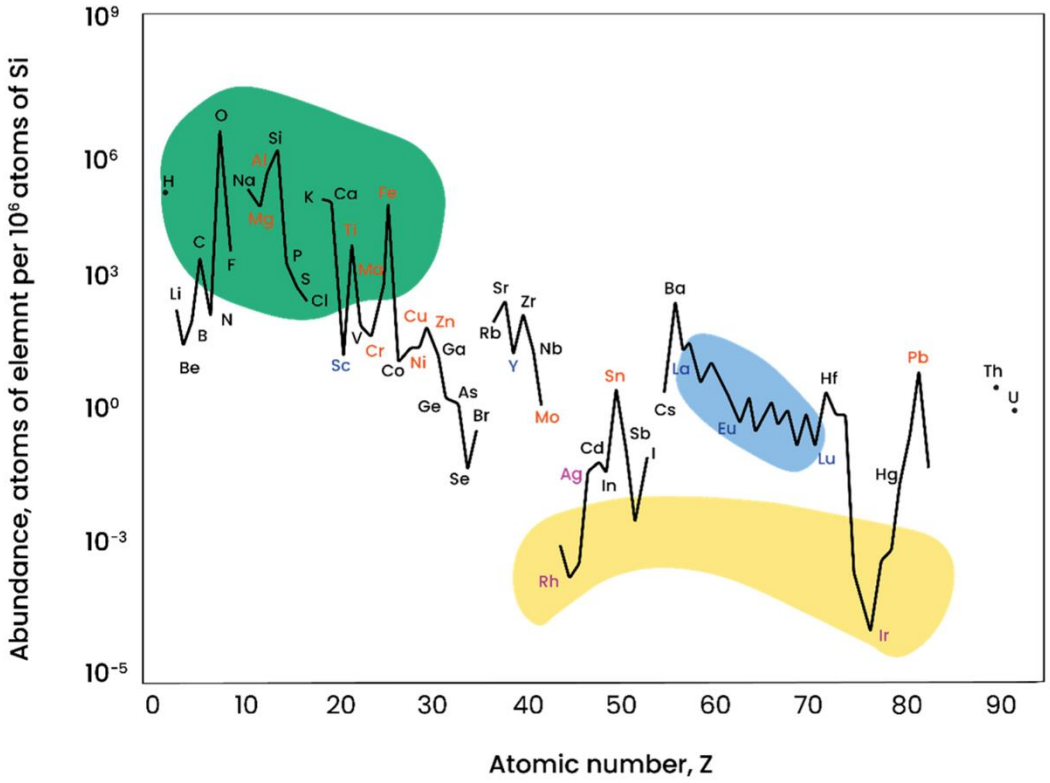

Figure 1.2: Element abundance of elements up to uranium. The green field highlights the rock-forming elements, the yellow one highlights the rarest metal, while the blue field highlights the lanthanoids (after Kim et al. 2018).

The electronic configuration of REE plays a dominant role in the peculiar properties that make those elements such good candidates for several magnetic and optical applications. In the first place, the lanthanoid (atomic number Z ranging between Z=57 and Z=70) are featured with 4*f*-orbitals, except for La or Lu: whether La or Lu should be assigned to the 5*d* -block is still under debate (Jensen 2015; Scerri 2021). The electronic configuration of lanthanoids is rather complex and can be summarized as the electronic configuration of the noble gas Xe plus partially or completely filled 4*f*, 5*d* and 6*s* orbitals: (Xe) $4f^{1\text{-}14}\ 5d^{0\text{-}1}\ 6s^2$ (Table 1.1).

Table 1.1: Electronic valence configuration of REE, atomic and ionic radii after Shannon et al. (1970). Arbitrarily, La has been considered among the 5d-block, while Lu has been assigned to the 4f-block.

Rare Earth Element	Electronic configuration	Crystal radius (Å)	Ionic radius (Å)
Scandium (Sc)	(Ar) $3d^1\ 4s^2$	1.01	0.87
Yttrium (Y)	(Kr) $4d^1\ 5s^2$	1.159	1.019
Lanthanum (La)	(Xe) $5d^1\ 6s^2$	1.30	1.16
Cerium (Ce)	(Xe) $4f^1\ 5d^1\ 6s^2$	1.283	1.143
Praseodymium (Pr)	(Xe) $4f^3\ 6s^2$	1.266	1.126
Neodymium (Nd)	(Xe) $4f^4\ 6s^2$	1.249	1.109
Promethium (Pm)	(Xe) $4f^5\ 6s^2$	1.233	1.093
Samarium (Sm)	(Xe) $4f^6\ 6s^2$	1.219	1.079
Europium (Eu)	(Xe) $4f^7\ 6s^2$	1.206	1.066
Gadolinium (Gd)	(Xe) $4f^7\ 5d^1\ 6s^2$	1.193	1.053
Terbium (Tb)	(Xe) $4f^9\ 6s^2$	1.180	1.040
Dysprosium (Dy)	(Xe) $4f^{10}\ 6s^2$	1.167	1.027
Holmium (Ho)	(Xe) $4f^{11}\ 6s^2$	1.155	1.015
Erbium (Er)	(Xe) $4f^{12}\ 6s^2$	1.144	1.004
Thulium (Tm)	(Xe) $4f^{13}\ 6s^2$	1.134	0.994
Ytterbium (Yb)	(Xe) $4f^{14}\ 6s^2$	1.125	0.985
Lutetium (Lu)	(Xe) $4f^{14}\ 5d^1\ 6s^2$	1.117	0.977

For lanthanoids in general, REE are trivalent, due to the loss of a $4f$ electron and two $6s^2$ electrons. In addition, in geological environments, Ce and Eu can also form Ce^{4+} and Eu^{2+} cations. In these cases, the occurrence of this alternative valence states is due to a higher stability of completely-filled and half-filled electronic configurations: [(Xe) $4f^0\ 5d^0\ 6s^0$] for Ce^{4+} and [(Xe) $4f^7\ 6s^0$] for Eu^{2+}. Moreover, the occurrence of unpaired electrons in $4f$ orbitals is coupled with magnetic and optical properties shown by those elements, while the lack of such a configuration in Y, La and Lu reflects in the absence of the aforementioned peculiar features. Eventually, the lanthanoids (as most of the element do) are well known to undergo to a decrease in atomic radii moving within the period from La to Lu (lanthanoid contraction) and this property influences several of the features discussed below.

Rare Earth Elements are conventionally split into two major groups, the Light REE (LREE) and Heavy REE (HREE), based on their atomic number and ionic size. Unfortunately, this system has led

to several misunderstanding, since several authors provided a different threshold to separate the two groups (Zepf 2013). In order to set a clear threshold, based on objective basis, the U.S. Geological Survey (2011) has provided an elegant classification system, based on the electronic configuration of the 4*f* electron shell (see Table 1.1): LREE (Ce-Gd) are characterized by exclusively unpaired 4*f* electrons, whereas HREE (Tb-Lu) show at least a couple of paired electrons in the 4*f* shell; in addition, Y was included as one of the HREE (U.S. Geological Survey 2011), being its atomic radius intermediate between those of Ho and Er, while Sc is not included in any of the two groups, although it is worth to mention that the smaller ionic radius of Sc makes it to behave as one of the HREE.

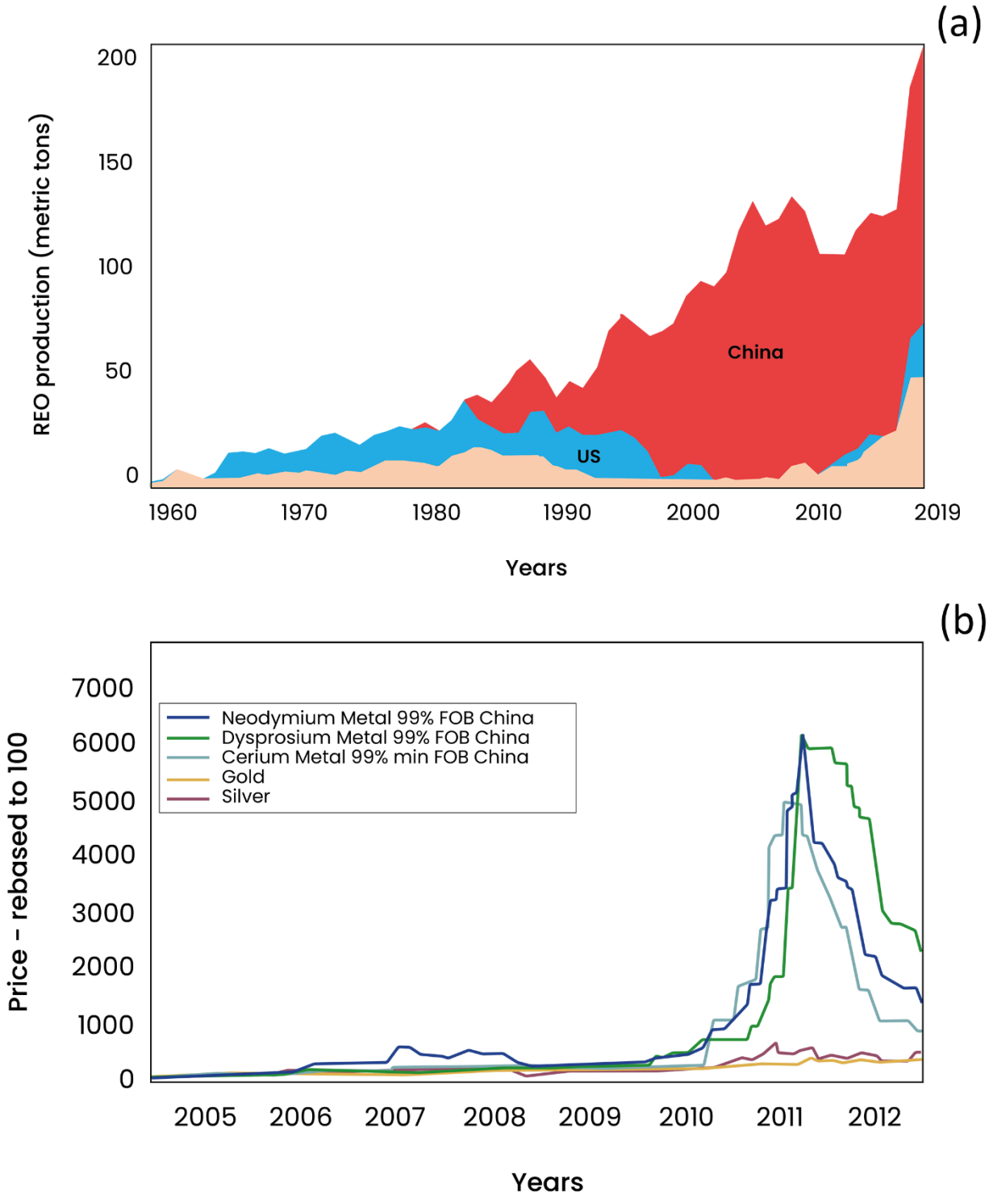

Figure 1.3: **(a)** REE production through time, divided by major country producer (China, USA and others) (sources: USGS and US bureau of mines); **(b)** prices of some REE, through time, compared to the ones of gold and silver, showing the significant price rising due to the REE crisis (source: Thomson Reuters datastream).

1.2 Applications, global market and REE crisis

The first economic income from REE took place in the 1880s, from the production of the Welsbach incandescent lamp, made of zirconium, lanthanum and yttrium (*e.g.*, Swift et al. 2014). Since then, REE market has flourished (Figure 1.3a). Rare Earth Elements are indisputably fundamental materials for several economic sectors, mostly connected with high-tech industry and the so-called "green" energy, and their market has experienced strong increase within the last three decades (*e.g.*, Blengini et al. 2020). Due to the REE peculiar spectroscopic, magnetic and catalytic properties, those metals represent irreplaceable raw materials (*e.g.*, Izzat et al. 2014). The applications of REE are bound to several modern technologies, like, but not limited to, permanent magnets, battery alloys, catalyst for petroleum and automotive sectors, glass additives, polishing and phosphors in monitors (Goonan 2011; Du and Graedel 2013; U.S. Geological Survey 2021; Gambogi 2017; http://metalpedia.asianmetal.com/metal/rare_earth/application.shtml). So far, the most complete report about the REE end of use has been provided by Goonan (2011), Balaram (2019) and within the framework of the USGS reports. The main end of uses sectors are discussed below.

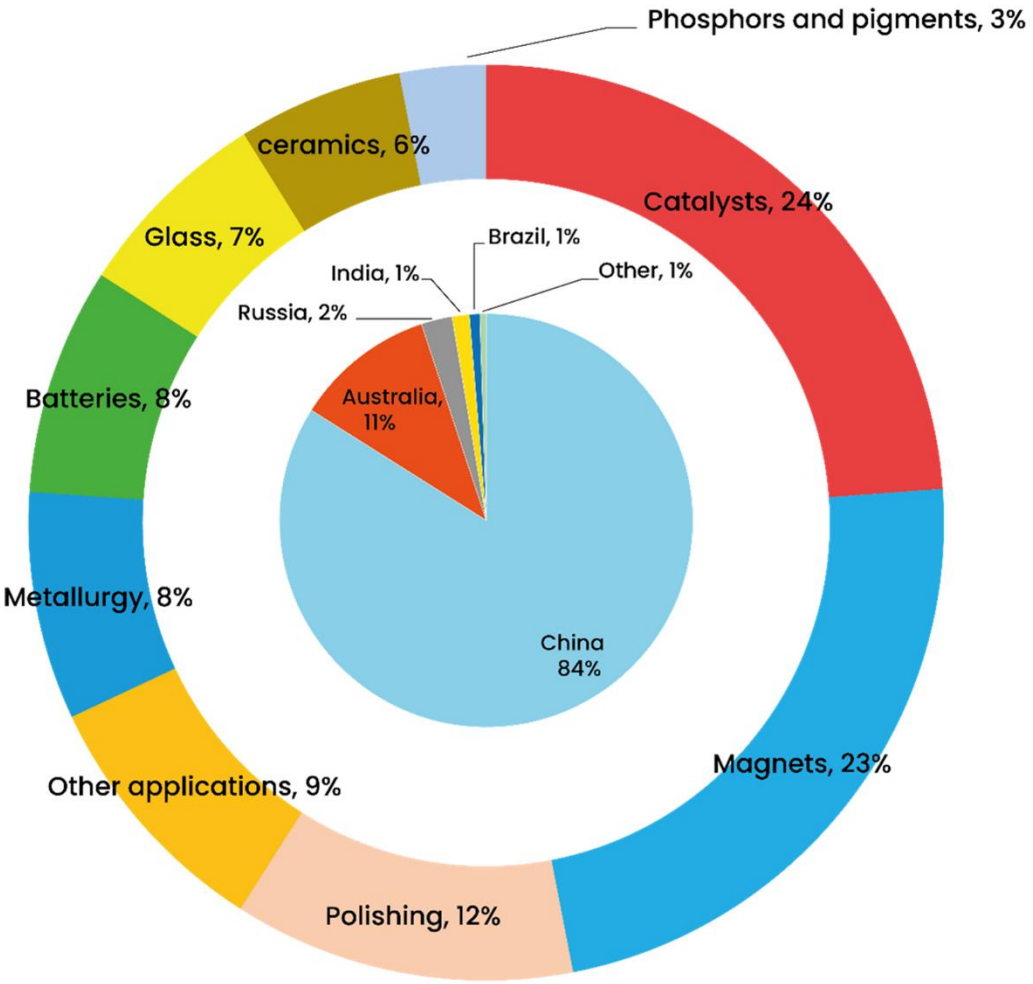

Figure 1.4: major industrial sectors and country production of REE after Zhou et al. (2017).

1.2.1 Catalysts in fluid cracking processes

Nowadays, fluid cracking catalysis (or fluid catalytic cracking, FCC) is one of the major industrial sectors that uses REE oxides and, in the USA, the most important. Fluid catalytic cracking constitutes a part of petroleum refining in which the heavier hydrocarbons decompose into a lighter and more valuable hydrocarbons. Since the early 1960s, zeolitic compounds (Y-type zeolites) were introduced as catalysts in FCC, marking a turning point in the gasoline industry. The occurrence of structural voids and acid Brønsted sites within the Y-zeolites result in a high active surface and, consequently, in a more efficient production (*e.g.*, Kharat et al. 2013). In order to improve the amount of acid Brønsted sites, the Y-zeolites were de-aluminized, with the bottleneck that the stability field of the zeolite itself was drastically reduced. The usage of REE in FCC, with the aim to improve the stability,

efficiency and life of the zeolitic catalysts, started out in the ’60s, shortly after the introduction of Y-type catalyst. Several studies demonstrated that both the stability field of the Y-zeolite and the amount of acid Brønsted sites improve for the presence of REE (*e.g.*, Akah 2017; Doronim et al. 2014). These zeolitic catalysts are doped with REE (mostly a La_2O_3 (66 wt. %), CeO_2 (32 wt. %), Nd_2O_3 (0.8 wt. %) and Pr_6O_{11} (0.6% wt. %) according to Goonan (2011)), resulting in a bulk amount of REE oxides ranging between 1.5 and 5.0 wt. % (Sousa-Aguiar at al. 2013).

1.2.2 Catalysts in automotive convertors

Catalytic convertors are devices devoted to the removal of engine exhaust gases. Rare Earth Elements are currently applied in different types of catalytic convertors, like three-way type, capable to get rid of the most important pollutants (*i.e.*, CO, HC, N oxides) in gasoline vehicles, as well as diesel catalytic convertors, with the additional purpose to remove particulate matter (PM), a significant pollutant from diesel vehicles. Cerium oxide CeO_2 is the most important compound used in all the used catalytic convertors, but La_2O_3 and Nd_2O_3 are also used. In three-way catalytic convertors, the active part is constituted by a platinoid metal (usually Pt, Pd or Rh), whereas a solid solution of CeO_2 and ZrO_2 act as promoters (*e.g.*, Wang et al. 202).

The overall catalysts sector (automotive convertors and FCC) is the second most important REE market after permanent magnets production (see below), whereas in the USA it accounts for ~62 wt. % of the total REE oxides production (Gambogi 2017).

1.2.3 Glass and optical industry

Rare Earth Elements oxides are commonly used in glass industry, with the aim to alter the absorbing properties, the refractive index, or the color of the material. The fluoride LaF_3 is one of the most important compounds in Zr-Ba-La-Al-Na fluoride glass, which is, so far, the most stable and spread fluoride glass for optical fiber production. The presence of LnF_3 as an additive promote the glass stability (*e.g.*, Tanabe 2015; Lucas 1985). Yttrium oxide, as other HREE, is used to strengthen the silica glasses, whereas La_2O_3 and Gd_2O_3 are raw materials to produce high-refractive index low-chromatic dispersion glasses (*e.g.*, Tanabe 2015).

Pertaining to Y, Gd, Nd and Er, another fortunate, large application is the production of garnet-structured $Y_3Al_5O_{12}$ (YAG), $Gd_3Ge_5O_{12}$ (GGG), in which REE act as dopant, as well as main components. Several branches of medicine, military sector (for target designators), distance and temperature sensing, industrial cutting, photochemistry and photoluminescence provide examples of YAG and GGG applications (USGS 2022; Hendrick 2004). Neodymium, as well as other REE, is the

most common dopant, used to modify the emission properties of the YAG lasers (*e.g.*, Anscombe 2002).

1.2.4 Polishing

Eventually, the fine polishing properties shown by the REE oxide powder, used in precision optical glass, touch-screen devices, light-crystal display (LCD) monitors and ceramics, is also worth to mention (*e.g.*, Wu et al. 2021). The polishing powder can have a rather variable chemical composition, usually dominated by the most common CeO_2, since purity is not a fundamental feature in polishing. For unknown reasons, the polishing achieved with the REE oxide powder, give to the surfaces a superior smooth surface (Wu et al. 2021; Tanabe 2015).

Polishing do not represent a marginal activity, being alone the third-class worldwide REE market, according to the USGS Mineral Yearbook (Gambogi 2017).

1.2.5 Permanent magnets

Usage of REE within permanent magnets has been developed since the 1980s. Permanent magnets constitute a paramount application of REE and are currently used to produce motors and generators, used in hard disks, wind turbines and electric cars (*e.g.*, Dent 2012). They are divided into two main categories: Sm–Co magnets and Nd–Fe–B magnets. The first is fundamental in electronics, while the latter is a key point of the effect of REE in the green economy sector (*e.g.*, Stegen 2015). Samarium–cobalt magnets are largely used in electronics, due to their high performance under high temperature conditions, coupled with a rather brittle behavior that make them unsuitable for motors and large magnets. On the other hand, Nd–Fe–B, are used for large-scale generators, like wind turbines and other kinds of electricity generators (*e.g.*, Stegen 2015).

As outlined by Gambogi (2017) and Goonan (2011), permanent magnets represent the main end of use of REE, accounting for the majority of the Dy, Nd, Pr and Gd consuption: in 2008, production of Nd–Fe–B magnets accounted for almost 100 wt. % of consumption of Dy_2O_3 (1 310 tons), 76 wt. % of consumption of Nd_2O_3 (18 200 tons), 70 wt. % of consumption of Pr_2O_3 (6 140 tons), 69 wt. % of the consumption of Gd_2O_3 (525 tons), and 11 wt. % of consumption of Tb_2O_3 (53 tons).

1.2.6 Ceramics

The application of ceramic materials with peculiar optical and absorption properties have already been discussed among glasses (as USGS does), while the ceramics discussed in this section are characterized by their electric or insulation features and mostly used in electric circuits.

In this context, REE are used as dopants within dielectric of multilayer ceramic capacitors (MLCC), an irreplaceable component of electric circuits in automotive, aerospace, defense, entertainment,

medical and telecommunication electronics applications (*e.g.*, Alam et al. 2012). The MLCC are composite materials, made by alternation of a metal and a ceramic. As ceramic material perovskites are often used and barium titanite [$BaTiO_3$] powder, doped with REE, is commonly used, due to its excellent dielectric properties. Another important application of REE-doped ceramics is the construction Y-stabilized ZrO_2 (YSZ) for oxygen sensors in combustion engines (*e.g.*, Dimitrov et al. 2007). Yttrium, praseodymium, neodymium and lanthanum oxides are the most used REE uses for this purpose (Goonan 2011).

1.2.7 Phosphors

Phosphors are materials capable to emit light corresponding to a specific wavelength when exposed to an incident radiation of a higher frequency. The light-emitting phenomenon is a cold process bound to electronic transitions from an exited condition to the ground state and the wavelength is function of the chemical composition of the phosphors material (*e.g.*, Lucas 2015). Phosphors are made by an inert, crystalline host-matrix and a dopant, active component, usually made of transition metals or REE and their luminescent properties are connected to the electronic configuration of *4f* and *5d* shells. Among REE, the most widely used active cations (usually less than 10 wt. % of the overall compound weight) are Ce^{3+}, Tb^{3+}, Eu^{3+}/Eu^{2+}, Gd^{3+}, Yb^{3+}, Dy^{3+}, Sm^{3+}, Tm^{3+}, Er^{3+} and Nd^{3+} (Gupta et al. 2021; Tripathi et al. 2018). It is worth to mention that the most used REE in phosphors, Y (and La, widely used in phosphors as well), behaves as a completely inactive ion due to its empty or complete electronic configuration (Lucas 2015). Indeed, the wide utilization of Y and La in phosphors is merely tied to their atomic radii, essential to stabilize a suitable host matrix to embody the active ions (*i.e.*, the other REE). Nowadays, several host matrixes are applied in phosphors, including La and Y oxides, aluminates, phosphates, silicates, vanadates and titanates, often including Ba^{2+}, Sr^{2+}, and Ca^{2+} replacing the active REE. The main application of phosphors is the production of white-light emitting diodes (WLED or simply LED), a paramount component of LED monitors; moreover, phosphors are also used for the emissive coating in fluorescent lamps, also an important part of liquid crystal display (LCD) backlight monitors (*e.g.*, Innocenzi et al. 2018).

In 2008, phosphors were responsible for almost all the consumption of europium oxide, 89 wt. % of Tb_2O_3, over than 50 wt. % of Y_2O_3 and 21 wt. % of Gd_2O_3 (Goonan 2011).

1.2.8 Alloys and battery alloys

Rare Earth Elements also represent an important raw material used to produce alloys, as additives in battery components and construction materials that requires high-corrosion resistance. Rare Earth Elements are widely used for improving the corrosion-resistant properties, as well as mechanical strength and fire resistance, of Al, Fe, Ti and Mg alloys (*e.g.*, Zhang et al. 2019; Azzeddine et al.

2020). Cerium is the most used REE with this purpose, followed by lanthanum, neodymium, and praseodymium (Goonan 2011). REE are also used as dopants in several types of batteries and energy-storage devices. Among the others, REE are used in lithium/sodium and lithium-sulfur batteries, supercapacitor, nickel-zinc and cerium-redox-flow batteries with rather different purposes, ranging from protection of the electrodes to enhancer of their properties, as well as electrolytes component (Zhao et al. 2019). Cerium, neodymium lanthanum, and praseodymium oxides are those mainly used for this purpose (Goonan 2011).

Table 1.2: end of use applications of REE (Weng et al. 2015).

Rare Earth Element	Common end of use
Sc	Alloys in aerospace engineering, lighting
Y	Lasers, superconductors, microwave filters, lighting
La	Optics, batteries, catalysis
Ce	Chemical applications, colouring, catalysis
Pr	Magnets, lighting, optics
Nd	Magnets, lighting, lasers, optics
Pm	Limited use due to radioactivity, used in paint and atomic batteries; very rare in nature
Sm	Magnets, lasers, masers
Eu	Lasers, colour TV, lighting, medical applications
Gd	Magnets, glassware, lasers, X-ray generation, computer applications, medical applications
Tb	Lasers, lighting
Dy	Magnets, lasers
Ho	Lasers
Er	Lasers, steelmaking
Tm	X-ray generation
Yb	Lasers, chemical industry applications
Lu	Medical applications, chemical industry applications

As mentioned above, the REE market experienced a strong growth in the last three decades, that have seen the extraction of REE rising from 64 kt in 1994 to over than 270 kt tons in 2020 (Blengini et al. 2020). Between 1990s and 2007, the rising of REE usage has seen a rather slow growth rate and

China was the most important producer, but most of the mined REE were exported. Indeed, the mining exploitation of REE has been largely concentrating in China (U.S. Geological Survey, 2021) and their commodities export policy changed significantly in the last decade, introducing export quotas and taxes. The introduction of export quotas and taxes in 2009-2011 followed a change in China's economy, after China itself became not only a significant REE producer, but an important consumer as well (Massari and Roberti 2013; Mancheri 2015). Tied to the increasing demand for these metals and the peculiar, odd worldwide distribution of REE resources, all the REE have been classified as "critical raw materials" (CRM) by both the United States of America and the European Union (van Gosen et al. 2017; Wall 2014; Nassar et al. 2015; Massari and Ruberti 2013; Li et al. 2020). The changing of the China's export policies has highly influenced the price fluctuation of REE, which underwent to two distinct phases (Massari and Roberti 2013): the first, between the 1990s and 2007 is characterized by a slight decrease in REE prices due to an uprise in REE production; afterwards, when China's domestic consumption became significant, the prices had undergone a continuous growth, which reached the peak at the end of the 2010s. During the REE-crisis, between 2009 and 2011 (Figure 1.3b), the REE prices showed an abrupt growth (*e.g.*, Labruto et al. 2013; Chen and Zheng 2019), which determined, outside China, an average increase of 3041% for Sm_2O_3 and over than 2000% for both La_2O_3 and cerium oxide. In 2015 China removed the export quotas and tariffs and the REE prices showed a quick decrease. Since 2015, the REE prices are still growing but at a more stable trend (*e.g.*, Barakos et al. 2015; Guyonnet et al. 2018).

To cope with the REE-crisis, within the last few years, a new impulse in geological survey and exploitation of REE resources started and it is esteemed that over than 200 REE survey projects have been funded in 2011, for example (Chen 2011). As a result, although still led by China, nowadays the production of REE is much more diversified among different countries. Compared to ten years ago, according to the USGS Mineral Commodity Summaries reports (USGS 2022; USGS 2012 and USGS 1996) the Chinese mine production of REE shifted from 97 % of the global production (corresponding to 130 kt in 2011) to 61 % (corresponding to 168 kt in 2021). The REE mine production has seen the entrance of new significant players: in the first place, the REE production of the USA, rose to 16 % (corresponding to 43 kt in 2021, compared to the <1 % in 2011), Myanmar (12 %, corresponding to 26 kt in 2021, compared to the <1 % in 2011) and Australia (8 %, corresponding to 22 kt in 2021, compared to the <1 % in 2011). It is interesting to note that in the 1990s the REE mine production was rather even: China and the USA were still the main players, but their respective production in 1994 was 31 kt (48 %) and 21 kt (31 %), according to the USGS (1996). Other important present REE producers are Thailand, Madagascar, India and Russia. The most recent USGS Mineral Commodity Summary report (2022) underlines that the major REE resources are located in China (44

Mt) Vietnam (22 Mt), Brazil (22 Mt) and Russia (22 Mt) (followed by India, Australia, USA and Greenland). Eventually, it is worth mentioning that USA became the second world producer by exploiting a significant fraction of the available reserves (mostly connected to the world-class deposit of Mt. Pass, California), which changed from 13 Mt (in 1994) to 1.8 Mt (in 2021).

1.2.9 Rare Earth Elements recycling

Within the last decade, in the framework of the hot topics of circular economy and REE crisis, rising attention and efforts have been given to REE recycling. So far, most of the REE commodities production is bound to mine products and a rather small amount of REE is recycled from exhaust devices and industrial wastes. In most of the circumstances, due to the types of the REE end products (*i.e.*, complex, composites materials, the recycling is rather difficult). Magnets used in wind turbines are rather easily recyclable materials and their recycling could represent a clever way to compensate the undersupplied metals (despite the long-life of magnets in wind turbines makes their recycling presently rather small). Besides the obvious advantages of recycling, the recycling of turbine magnets balances the REE product available on the market, that mostly craves for Nd and Dy, which are rather scarce. Indeed, due to geological factors, Ce and La are the most produced of the REE commodities. So far, most of the recycled REE come from the magnets, battery alloys, fluorescent lamps (*e.g.*, Binnemans et al. 2013; Jowitt et al. 2018). According to Binnemans et al. (2013) the more optimist scenario predicted for the recycling of REE in 2020 could account for 10 kt of metal (the current mine production of REE oxides is ~270 kt). Thus, the REE commerce strongly rely on mine production, which will reasonably remain the major REE-source for the next decade.

1.3 Geology of REE and REE ore deposits

Due to their similar atomic size and charge, all the REE are characterized by a similar geochemical behavior. The partition coefficient, D_i, defined as the ratio between the concentrations (X) of a given trace element i among two phases at equilibrium (α and β, in this case; for an ease of clarity, a solid and a liquid phase), is defined by the formula $D_i = X_i^{\alpha}/X_i^{\beta}$. The D_i provides a useful tool to understand the geochemical behavior of REE among a solid and a liquid phase. The partition coefficient D_i is controlled by a plenty of factors, as temperature, pressure and oxygen fugacity. However, D_{REE} for most of the rock-forming minerals enlightens their general incompatible nature, being preferentially segregated into melt phases and late crystallization products (*e.g.*, Lipin and McKay 2018; Kennedy et al. 1993; Mysen and Virgo 1980; Irving 1978; Nandedkar et al. 2016; Randive et al. 2014; Rollinson 1993). In addition, the influence of ionic radii in REE partitioning has been enlightened since the 1960s (Onuma et al. 1968): in most of the minerals (with some exceptions

as plagioclase, among major igneous rock-forming minerals) as suggested by Figure 1.5, HREE behave as more compatible elements, due to their smaller ionic radii. In particular, garnets are well known to have a rather high D_{HREE} (*i.e.*, a strong affinity for HREE). In geochemistry, the La/Lu (or LREE/HREE) is a fairly common tool to evaluate the LREE abundance and the source of a magma. In rocks crystallized from primitive magmas, if further processes have not occurred, in general, the higher the La/Lu ratio, the smaller the fusion of the parent source.

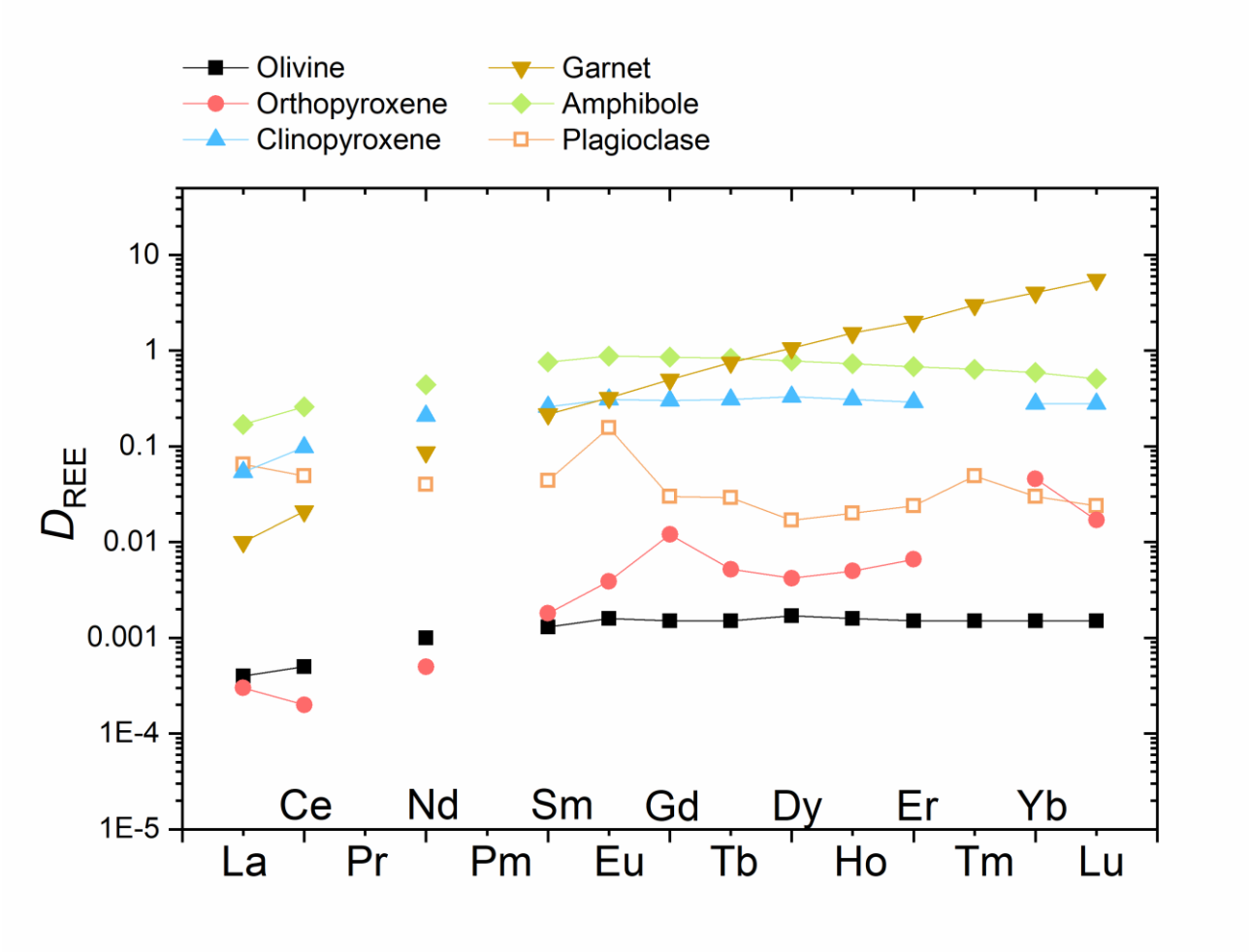

Figure 1.5: partitioning coefficients of the La-Lu series elements for several rock forming minerals. Data from Geochemical Earth Reference Model (GERM database) (Staudigel et al. 1998).

The distribution of REE within the Earth is a rather complex issue, controlled by several factors, including the partition coefficient, the nature of the geological processes and fluids, as well as the history and the composition of the source reservoirs. Hoshino et al. (2016) put together data about REE abundances from several sources, including C1 chondrite, primitive mantle, oceanic crust, lower, middle and upper continental crust, as well as the average REE composition of continental crust. The data are reported in Table 1.3. In the first place, due to their incompatible nature, REE are

largely segregated within the Upper Continental crust, which represent a wide reservoir with a relatively high REE content of few hundred ppm, on average. The mantle is rather enriched in REE with respect to the C1 chondrite, due to the segregation of the siderophile elements into the Earth core, while the La/Lu and LREE/HREE are almost identical in the two reservoirs. Thus, no preferential LREE or HREE partitioning occurs during mantle formation processes. In addition, either the total REE content, La/Lu and LREE/HREE increase from Oceanic crust to Upper continental crust. It is interesting to note that Lower and Middle crust are more enriched in Eu with respect to the Upper crust. This phenomenon is the so-called Eu anomaly, caused by the early crystallization of plagioclase, characterized by a high D_{Eu}.

Table 1.3: chemical composition of REE in several reservoir after Hoshino et al. (2016). Data from Lodders and Fegley (1998), Lyubetskaya and Korenaga, (2007), White and Klein (2013) and Rudnick and Gao (2003).

	CI Chondrite	Primitive Mantle	Oceanic Crust	Lower Continental crust	Middle Continental crust	Upper Continental crust	Average Continental crust
La (ppm)	0.235	0.508	2.13	8	24	31	20
Ce (ppm)	0.62	1.34	5.81	20	53	63	43
Pr (ppm)	0.094	0.203	0.94	2.4	5.8	7.1	4.9
Nd (ppm)	0.46	0.994	4.9	11	25	27	20
Sm (ppm)	0.15	0.324	1.7	2.8	4.6	4.7	3.9
Eu (ppm)	0.057	0.123	0.62	1.1	1.4	1	1.1
Gd (ppm)	0.20	0.432	2.25	3.1	4	4	3.7
Tb (ppm)	0.037	0.08	0.43	0.5	0.7	0.7	0.6
Dy (ppm)	0.25	0.54	2.84	3.1	3.8	3.9	3.6
Ho (ppm)	0.056	0.121	0.63	0.7	0.82	0.83	0.77
Er (ppm)	0.16	0.346	1.85	1.9	2.3	2.3	2.1
Tm (ppm)	0.025	0.054	0.28	0.24	0.32	0.3	0.28
Yb (ppm)	0.16	0.346	1.85	1.5	2.2	2	1.9
Lu (ppm)	0.025	0.054	0.28	0.25	0.4	0.31	0.3
Y (ppm)	1.56	3.37	18.1	16	20	21	19
Sc (ppm)	5.90	12.70	36.2	31	19	14	21.9
LREE (ppm)	1.56	3.37	15.48	44.20	112.40	132.80	91.80
HREE (Y excluded) (ppm)	0.91	1.97	10.41	11.29	14.54	14.34	13.25
Total (ppm)	9.99	21.54	80.81	104	167	183	147
La/Lu	9.4	9.4	7.6	32	60	100	66.7
LREE/HREE	1.71	1.71	1.49	3.91	7.73	9.26	6.93

In order to draw an overview of REE enrichment in different geological environments, MORB (Middle Ocean Ridge Basalts), OIB (Ocean Island Basalts), continental drift and collision are discussed below (Figure 1.6). An average chemical composition of MORB is reported as the Oceanic crust column within Table 1.3. In such a geological context, the rocks are rather depleted in REE, following the same pattern as the depleted mantle source. The shallow mantle has been depleted in REE and incompatible elements in general by successive extraction of melts. In particular, a strong depletion in LREE occurs within shallow residual mantle, while a relative HREE enrichment occurs.

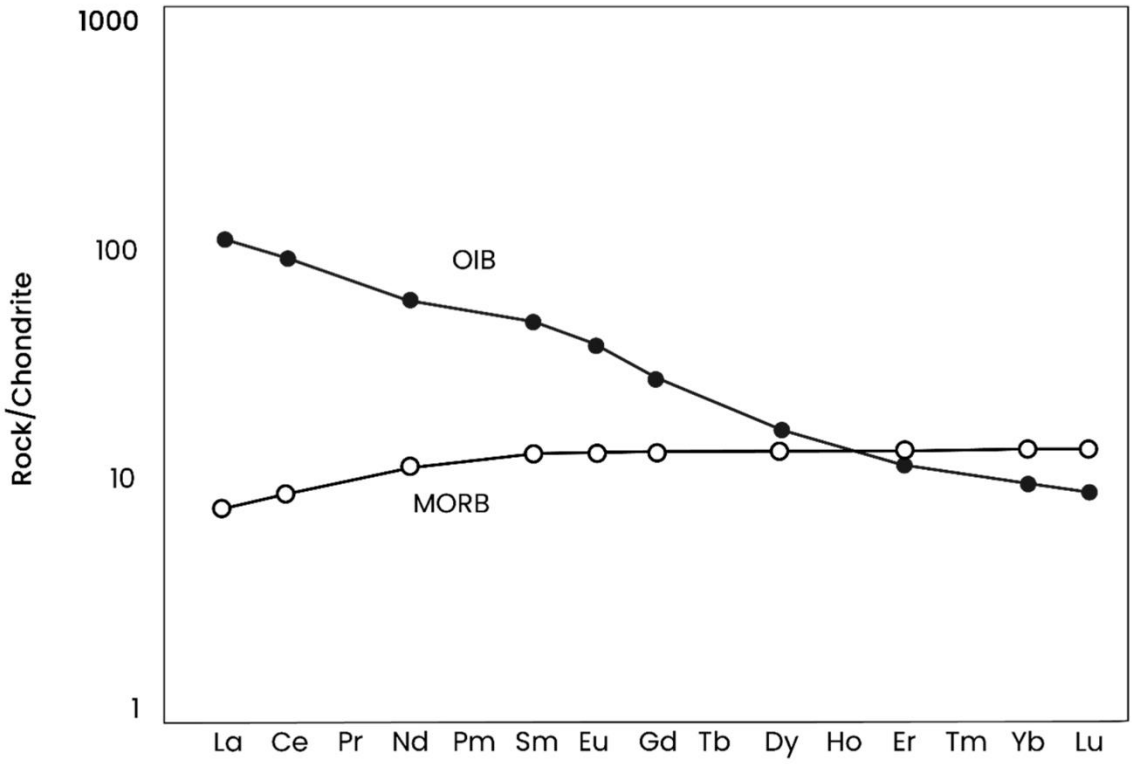

Figure 1.6: rock/chondrite abundance of lanthanoids within OIB and MORB (after Rollinson 1993).

The continental drift associated magmatism is characterized by the occurrence of alkali basalts, kimberlites and carbonatites. Most of the nowadays exploited REE resources are someway bound to alkaline rocks, which have a unique geochemical signature. Kimberlites and alkaline-rich basalts are among the most REE-enriched igneous rocks (Cullers and Graf 1984), following the carbonatitic magmas, the most relevant REE-source (Haskin et al. 1996; Loubet et al. 1972). Carbonatites, kimberlites and alkaline-rich basalts can exceed few thousands of ppm of REE and are well-known to have a rather high La/Lu ratio (La/Lu=15-216 in kimberlites, La/Lu=7-240 in carbonatites, La/Lu=2.7-262 in alkaline-rich basalts), suggesting a deep origin of the magma and rather small amount of melt produced (Cullers and Graf 1984).

The role of hydrothermal fluids in REE-enrichment has been highlighted by a plentitude of authors, in both pegmatite formation and secondary processes (*e.g.*, Andersson 2019; Cheng et al. 2018; Migdisov et al. 2019). At first, REE were believed to be rather immobile in hydrothermal systems, due to their low concentrations within those fluids (van Middlesworth and Wood 1998). Secondary hydrothermal alteration, within the past decade, has been pointed as one of the main processes

responsible for enrichment of REE up to ore-grade concentration (*e.g.*, Migdisov and Williams-Jones 2014; Williams-Jones et al. 2012). Usually, in hydrous solutions, REE^{3+} cations form complex ions, bounding to anions like F^-, SO_4^{2-}, CO_3^{2-}, PO_4^{3-}, OH^- and seldom Cl^-. The stability of the complex ion of REE increase with temperature. On average, the REE content of acid rocks is strongly variable, likely controlled by the partitioning of few REE-bearing accessory minerals (Rollinson 1993). Among the REE-enriched rocks, it is worth to mention some pegmatites associated with F-rich granites, marked by a significant REE-signature. In this context, the occurrence of a separate, salt melt phase that segregates Li, F, H_2O and REE can lead to REE-enriched hydrothermal, economic source of REE (Shchekinaa et al. 2020). In case of granitic Cl-rich melts, the behavior is rather different: REE have a strong preference for the silicate fluids with respect the separate Cl-enriched hydrous fluid phase, while an increase in either Cl^- concentration and temperature leads to an increase of the soluble REE^{3+} cation (Samson and Wood 2005).

Several factors contribute to REE ore formation. Bulk enrichment in REE, on one side, represents a fundamental feature, whereas a proper mineralogical assemblage is likely the most important aspect to consider in the REE exploiting. Although several REE minerals are currently exploited, the world market mostly rely on few REE-bearing minerals: the carbonate bastnäsite-(Ce) (nominally $Ce(CO_3)F$), the two phosphates monazite-(Ce) (nominally $CePO_4$) and xenotime-(Y), (nominally YPO_4) and REE-enriched clays. Other important minerals are allanite-(Ce) and synchysite-(Ce), despite it is worth to highlight that bastnäsite-(Ce) monazite-(Ce), xenotime-(Y) and clay minerals account for most of worldwide production (*e.g.*, Dushyantha et al. 2020). Within the last century, the main source of REE has changed.

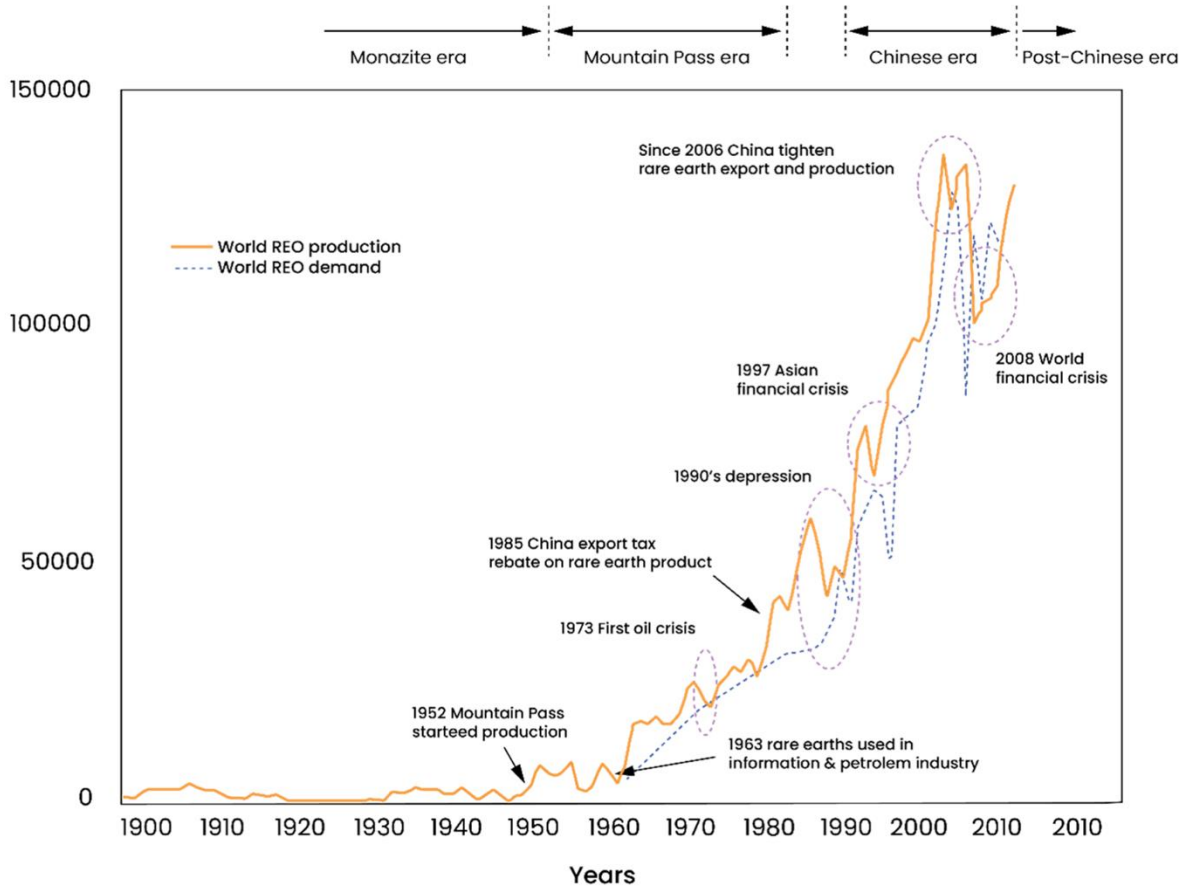

Figure 1.7: REE oxide production through time, showing the most relevant periods of REE mines cultivation.

At the beginning of the 20th century, REE were obtained from monazite recovered from placers deposits and then extracted as byproduct of Th used as nuclear fuel. Until the middle of the 1950s, with the rising interest in U over Th, carbonatites became much more important for REE production, while the interest for monazite-(Ce) decreased (Figure 1.7). As a result, bastnäsite-(Ce), easier to process and Th-poor became more valuable than monazite-(Ce). Between the 1960s and the middle 1980s, the carbonatitic Mt. Pass mine was the major REE reserve and afterwards China joined the REE market, gaining the main role already discussed in section 1.2 (*e.g.*, Naumov 2008). After the late 1990s, the role of ion-adsorption clays enriched in REE has gained rising importance, becoming the current main HREE resource. Several authors provided different classification systems of the REE-enriched deposits. In the present project, the classification provided by Hoshino et al. (2016) has been adopted. As mentioned above, the majority of REE resources are hosted in carbonatites, also characterized by the easiest exploitable mineral association. Other important sources for REE are

absorption-clay deposits, peralkaline/alkaline igneous rock, iron oxide deposits and placers (Balaram 2019).

1.3.1 Carbonatites deposits

Carbonatites are igneous rocks, usually volcanic, containing more than 50 modal % of carbonates and less than 20 wt. % of SiO_2 (Streckeisen 1980; Le Maitre 2002). These rocks form exclusively in extensional geological environments and are commonly associated with other alkaline rocks, as alkaline basalts and seldom kimberlites, whereas their occurrence as isolated batholites and dykes has also been described (*e.g.*, Yang and Woolley 2006). Through geological time, carbonatites are known to occur since Archean to present, with a higher occurrence in Mesozoic. Carbonatites derive from a deep mantle, high alkaline and evolved magma, while most of the ore enrichment processes are supposed to be hydrothermal and caused by fluids evolved from the magma itself (except for Mt. Pass in the USA). Bastnäsite-(Ce), synchysite-(Ce), monazite-(Ce) and apatite constitute the common REE-mineral association. In addition, weathering can increase the ore grade, as well as changing the mineralogical association (*e.g.*, Wang et al. 2020; Hoshino et al. 2016). As mentioned above, in this context, the rocks are generally enriched in LREE over HREE. In general, bastnäsite-(Ce) deposits are the preferred mineralization, due to their relatively high grade (~4 wt. % of REE oxydes) and straightforward REE-extraction. On the other hand, apatite ores contain lower amount of ~1 wt. % of REEO, but are relatively enriched in the more valuable HREE (*e.g.*, Hoshino et al. 2016). As reported in Table 1.4, among the ten largest REE deposits, eight are classified as carbonatites or as weathered carbonatites (Wang et al. 2020). Among the others, Bayan Obo, Mt. Pass and Mt. Weld deposits are characterized by large reserves, exceeding 10 Mt.

Table 1.4: Major exploitable REE deposits in the world in 2020 (Wang et al. 2020).

Country	Deposit	Deposit-type
China	Bayan Obo (REE-Nb-Fe)	Carbonatite
China	Maoniuping (REE)	Carbonatite
China	HREE-enriched deposits in southern China	Weathered crust elution
Brazil	Araxá Catalão (REE)	Weathered carbonatite
Brazil	Mrro do Ferro (Th-REE)	Carbonatite
Australia	Mount Weld (REE)	Weathered carbonatite
USA	Mountain Pass (REE)	Carbonatite
Russia	Tomtor (REE)	Weathered carbonatite
Russia	Lovozero (REE-Nb)	Alkaline igneous rock
India	Amba Dongar (REE)	Carbonatite
Vietnam	Mau Sai (REE)	Carbonatite
Burundi	Gakara (REE)	Carbonatite
Malawi	Kangankunde (REE)	Carbonatite
South Africa	Palabora (REE)	Carbonatite
South Africa	Steenkampskraal (REE-Th-Cu)	Alkaline igneous rock
Turkey	Aksu Diamas (REE)	Placer
Greenland	Tanbreez (REE)	Alkaline igneous rock
Sweden	Norra Kärr (REE)	Alkaline igneous rock

1.3.2 Residual deposits and absorption clays

Residual deposits currently represent a rather important REE resource, in particular for the rarer HREE, whereas LREE-enriched deposits are also known. These deposits from after meteoric weathering from any kind of REE deposit, like carbonatites, as well as from parent granitoid rocks without a significant pristine enrichment in REE. Among these weathering products, the absorption clays are a rather newly discovered source of REE, with the discovery of the so-called "701" mine in southern Jiangxi province in 1969 (*e.g.*, Li et al. 2017). Ion adsorption clays deposits are known to occur exclusively in few places, mostly within the provinces of South China, while other deposits occur in Brazil and Madagascar. The process is well known to drive to the formation of the world class deposits of Al, lateritic Ni and kaolinite. Rare Earth Elements are highly insoluble in meteoric water: consequently, they are preferentially concentrated within the residual phases (*e.g.*, Li et al. 2017). The REE mostly concentrated in the interlay of clay minerals, namely kaolinite and halloysite, mostly in form of complex ions $REE(OH)_2^-$. These deposits are characterized by a variable tonnage, in general higher than 1 Mt. The cutoff grade for ion-adsorption clay deposits is rather low, since the

REE extraction does not require any complex procedure. According to Ding and Deng (2013) the ion-adsorption clays can be exploited if the HREE oxides exceed ~0.06 wt. %, whereas the LREE oxides must be higher than ~0.08 wt. %. Ion adsorption clay deposits account for ~80 wt. % of HREE worldwide production (*e.g.*, Borst et al. 2020). Rising attention has been given to the REE content of residual rocks like bauxite, which form in the same geological environment. Mondillo et al. (2019) found a REE content that may suffice to turn REE into a byproduct of Al in bauxites.

1.3.3 Placers

Placers are sedimentary deposits formed by selective deposition and concentration of heavy minerals in the so-called "energetic traps". The deposition is mechanically driven by stream or wind, capable to concentrate in shores, rivers, dunes, as well as offshore areas. In general, the "traps" are represented by slopes in fluvial environment, while the action of waves, wind and tides is responsible for the deposition in shores and offshore settings. The sediments are usually made by silt and sand and the ore minerals must be capable to withstand meteoric weathering conditions. Monazite-(Ce) and xenotime-(Y) are the most common REE ore minerals in this context, due to their unusual high density of ~5 g/cm^3 for either monazite-(Ce) and xenotime-(Y). The average heavy mineral content ranges from 2 to 10 wt. %, while the average tonnage is in general above 10 Mt (*e.g.*, Sengupta and Van Gosen, 2016). Usually, the mineralization is poorly consolidated, which makes the cultivation of the rock much less expensive. In addition, these deposits can represent a more valuable resource, due to the possible accumulation of REE-bearing minerals along with other economic phases, as gold, rutile and zircons. In placers, REE are mainly extracted as a byproduct than as the main commodity (*e.g.*, Papadopoulos et al. 2019) The placers occur, among the others, along the coast of India, Australia, Brazil and China.

1.3.4 Alkaline, peralkaline rocks and association with NYF pegmatites

The REE deposits associated with alkaline/peralkaline rocks are in general low grades, with a REEO content lower than 2 wt.% and tonnage lower than 10 Mt (*e.g.*, Dostal 2017). Consequently, the importance of these rocks for REE extraction nowadays is limited as byproducts of other elements, as in the Russian Lovozero mine in Kola Peninsula, where Nb is the main element extracted. On the other hand, in the framework of the current project, a major attention is dedicated to this specific deposit type, being the Mt. Cervandone mineralization associated with alkaline pegmatites within metagranitoids. Alkaline refers to rock characterized by a significant enrichment in Na_2O and K_2O that can lead to the crystallization of feldspathoids, as well as alkali-bearing pyroxenes and amphiboles. The term peralkaline has been introduced to classify a highly variable family of alkaline felsic rocks, characterized by a $Na_2O+K_2O>Al_2O_3$ and $[(Na_2O+K_2O+CaO)/Al_2O_3]>1]$. The alkaline

family embodies granites, nepheline syenites, alkaline granites, alkaline volcanic rocks deposits and pegmatites in general associated with the late stages of magma, evolved from alkaline basalts. In particular, peralkaline granites and nepheline sienites contain rather high amount of REE, Nb, Zr, Ta, actinides and halogens. Deposits associated with peralkaline rocks usually contain significant amount of the more valuable HREE. The age of alkaline/peralkaline deposits ranges from Paleoproterozoic to Mesozoic, with a remarkable peak in Mesoproterozoic. As occur in carbonatites, several authors (*e.g.*, Dostal et al. 2014; Dostal 2017; Andersson 2019) suggested that the REE-enrichment is believed to be associated with late hydrothermal fluids, formed in advanced stages of crystallization. In this context, REE-bearing minerals are carbonates, phosphates, silicates and oxides.

Pegmatites are often associated with alkaline/peralkaline rocks, although it is worth to mention that pegmatites are not necessarily associated with them and can form from a wide range of granitoid rocks. Rare Earth Element-enriched pegmatites, according to the classical definition, are classified into the two major LCT (lithium, cesium, tantalum) and NYF (niobium, yttrium, fluorine), families, in relation to their geochemical signature (Černý 1991a,b; Ercit et al. 2005; Černý and Ercit 2005; Simmons and Webber 2008). These pegmatites form under low pressure (~2-4 kbar) and temperature conditions (from greenschist to amphibolite facies, corresponding to ~650-500° C). **LCT** pegmatites are generally related to peraluminous [$Na_2O+K_2O+CaO<Al_2O_3$] granites, formed by melting of sedimentary material, and characterized by an enrichment in Li, Rb, Cs, Be, Sn, Ta, Nb (Ta>Nb) (*e.g.* Goodenough et al. 2019). On the other side, **NYF** pegmatites show Nb>Ta, Ti, REE, Sc, Zr, U, Th, F enrichment. The REE content is rather variable and the parent magma can range from metaluminous [$Na_2O+K_2O+CaO>Al_2O_3$] to peralkaline [$(Na_2O+K_2O+CaO)/Al_2O_3<1$] granites (*e.g,*. Goodenough et al. 2019). NYF mineralization are supposed to form after the exsolution of a high-F saline fluid capable to mobilize elements and fix them into disseminated skarn and veins. In general, due to complex mineralogy, low grade and small tonnage, these rocks do not allow any REE profitable extraction, although subsequent weathering can lead to a significant enrichment in rare metals (*e.g.*, Chakhmouradian and Zaitsev 2012).

1.3.5 Kiruna-type Iron-Oxide-Apatite (IOA) deposits

These deposits are named after the Swedish Kiruna-type deposit, discovered in the early 1900. In the first place, the IOA are one of the most important sources of Fe, with a mineralogical composition dominated by magnetite, apatite and actinolite. The ore is always bound to intermediate-felsic magmatism and can occur in several forms, including banded, massive, breccia, pegmatitic types (*e.g.*, Yan and Liu 2022). The geological processes responsible for their formation are still unclear (Hoshino et al. 2016) and possibly relates to a segregation of an immiscible Fe-enriched fluids, as

well as to a direct hydrothermal deposition of Fe oxides (Naslund et al. 2002; Nold et al. 2013). In this context, apatite can contain over than 7000 ppm of REE, and if associated with other REE-bearing minerals, as monazite-(Ce), xenotime-(Y) and allanite-(Ce), the REEO content can jump over 10 wt. %. These deposits are known to occur in Sweden, USA, Canada, Chile and Iran and are not currently exploited to produce REE.

Chapter 2

2 Geological background

The present study focuses on several mineral samples from hydrothermal fissures outcropping at the Mt Cervandone (Lepontine Alps), in Piemonte, Italy. From the geographical point of view, the area of interest is in the Verbano-Cusio-Ossola province, within the natural park "Parco dell'Alpe Veglia e dell'Alpe Devero". The Mt. Cervandone represents the ridge between the Italian Devero valley and the adjacent Binn valley in Switzerland (*Canton du Valais*). The official geological maps of the Cervandone area are still based on the field work carried out in the early 1910s on the Domodossola and the Val Formazza quadrants of the "*Carta geologica alla scala 1:100.000*" (Italian geologic map to the scale 1:100.000). A more recent description of the geological setting in the Mt. Cervandone area has been provided by the works of Bigioggiero et al. (2007), Steck (2008; 2013; 2015; 2019), dal Piaz (1975) and by the geological-structural map 1:10.000, released by the "*Piano Regolatore Generale Comunale*" of the Baceno municipality (2003). The first geological studies within the Mt. Cervandone zone have been carried out at the beginning of the 1990s, in the framework of the first Alpine studies, corroborated by the impulse given by the perforation of the Simplon tunnel. The Simplon railway tunnel, which excavation ended in 1905, still provides an irreplaceable tool to uncover the nappe structure of the interest area, passing right below the "Parco dell'Alpe Veglia e dell'Alpe Devero" (Milnes et al. 1973). The Cervandone area is located within the Penninic domain of the Cerntral Alps and, more specifically, within the Lower Penninic units, discussed in the following section. A simplified geological sketch is reported in Figure 2.1.

2.1 Structure of the nappe system in the Lepontine dome

There is common agreement about the origin of Penninic Units of the Alps, which are believed to represent the rather complex domain made by slices of the ancient Alpine Tethys (Valais Ocean, Piedmont-Ligurian Ocean and the microcontinent named Briançonnais terrain), as well as

metamorphosed subducted European margin rocks (*e.g.*, Schmid et al. 2004). The Penninic domain is furtherly divided into three major subdomains, known as the lower, the middle and the upper Penninic domains. The Lower Penninc units, cropping out in the Central Alps, consist of two domal complexes: the Simplon (or Tosa) Culmination, to the West (the area in which this study is focused on), and the Ticino culmination, to the East. These two domes compose together the regional structure known as Lepontine dome. The two complexes are parted each other by the major north–south striking structural line, the so-called Maggia Steep Zone. For the purposes of the current project, the Lepontine dome is the area of interest, therefore the following discussion is focused on its internal structure. The Lepontine dome is embodied between two major tectonic lines: the Rhône-Simplon line (hereafter simply Simplon line), a southwestward dipping normal fault, to the West, and the northward dipping Canavese line (a part of the Insubric line), to the South. The Simplon fault marks the tectonic contact between the Lower Penninic units (footwall) and Upper Penninic units (hanging wall) to the west, while the Canavese line puts in contact the Penninic units with the Southalpine unit of the Ivrea-Verbano zone. In addition, the Centovalli fault line represents the shear zone that puts in connection the Simplon and Canavese lines. The Canavese and the Simplon lines, during Oligocene and Pliocene-Miocene respectively, are believed to be responsible for the dextral movement and rather quick uplift o the Lepontine dome. (Hurford 1986; Merle et al. 1989; Hunziker et al. 1992; Keller et al. 2005). The Lepontine dome consists in an Alpine high-pressure metamorphosed unit, overprinted by Tertiary amphibolite facies metamorphism. The Lepontine dome has formed because of the shortening and underthrusting related to the continental collision, coupled with orogen-parallel extension (Ratschbacher et al. 1989; 1991). After the subduction and associated high-pressure metamorphism of the Austroalpine units of the Sesia-Lanzo zone, in the early stages of Alpine orogenesis [75–65 Ma (*e.g.* Regis et al. 2014)], the underthrusting of the Penninic nappe system under the Austroalpine units started in Eocene, at about 42 My ago. During this stage, collision and the subsequent thickening of the crust drove to a Barrovian-style metamorphism, with temperature exceeding 500°C (Burg and Gerya 2005; Herwartz et al. 2011; Boston et al. 2017). The peak of the metamorphism was reached between 30 and 19 My from south to north (Schärer et al. 1996), while the uplift of the dome, whit its consequent cooling, started around 30 My (Hurford,1986; Steck and Hunziker 1994).

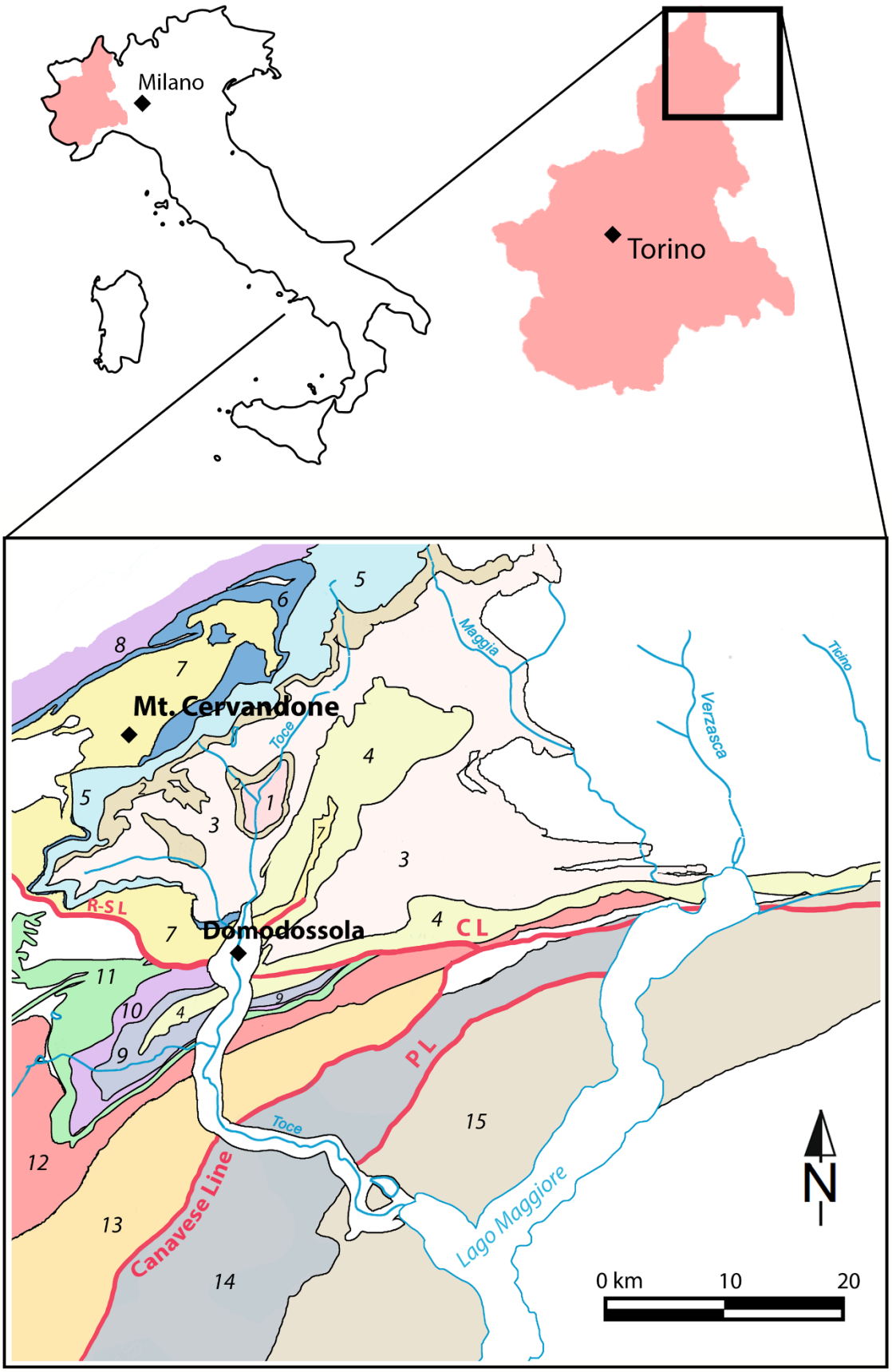
Milano
Torino
Mt. Cervandone
Domodossola
Toce
Maggia
Verzasca
Ticino
R-S L
C L
P L
Canavese Line
Lago Maggiore
N
0 km
10
20
1
2
3
4
5
6
7
8
9
10
11
12
13
14
15

Figure 2.1: Detail of the central Alps modified after Steck et al. (2015), Steck et al. (2019), showing the location of Mt. Cervandone. CL: Centovalli line, R-SL: Simplon Line, PL: Pogallo Line; (1) Verampio Unit, (2) Teggiolo unit, (3) Antigorio nappes, (4) Adula underthrust, (5) Lebendun unit, (6) Devero calchschists, (7) Mt. Leone nappe, (8) Valais units, (9) Ruginenta nappe, (10) Camughera unit, (11) Antrona ophiolitic unit, (12) Mt. Rosa nappe, (13) Sesia zone, (14) Ivrea-Verbano zone (15) Strona-Ceneri zone.

The nappes of Mt. Leone, Lebendun, Antigorio and Verampio are the major tectonic units, within the Simplon Culmination (Castiglioni 1958; Maxelon and Mancktelow 2005; Berger and Mercolli 2006; Dal Piaz 2010; Steck et al. 2013; Schmid et al. 2004). In addition, even though they are not a component of the Lepontine dome, the Moncucco and Camughera Units, as well as the Monte Rosa nappe are continuous with the Lepontine Units system. The nappe structure composing the Lepontine dome has been described in detail by several authors and its succession, with a focus on the western part pertaining the Ossola valley, is discussed below, from the deepest to the shallowest, according to Steck et al. (2013) and Steck et al. (2015). For further details, see Figure 2.1.

2.1.1 The Verampio Unit

The Verampio Unit, also called the "level zero" represents the core of the Simplon dome and the deepest Penninic unit. Its mineral assemblage is made by 40 modal % of quartz, an equal amount of plagioclase and microcline and, eventually, green biotite (Hunziker 1966). The granites intruded a Paleozoic metasedimentary level known as Baceno schists, with a likely argillaceous to arenaceous protolith (Escher et al. 1993). The age of those metagranites has been determined by U–Pb zircon data, which enlightens a Permian age of the intrusion (*e.g.*, Castiglioni 1958; Steck et al. 2013; dal Piaz 2001).

2.1.2 The Antigorio Unit

The Antigorio Unit mostly consists in a fold, rather thick nappe, mainly composed by the leucocratic Antigorio orthogneiss (Schmidt and Preiswerk 1908a; Milnes 1964). Major variations within the gneiss relate to the amount of biotite. A rather basic orthogneiss, as well as amphibolite, have also been described, especially in the eastern part of the unit (Hunziker 1966). In addition, the presence of aplitic veins and micaschist is rather diffuse. The protoliths of the orthogneisses in the Toce and Devero valley are mainly made by three distinct, granitoid intrusions: the Antigorio tonalite, the dominant Antigorio granodiorite and the Antigorio granite. The protoliths have been dated by Bergomi et al. (2007) and are all Permian, while the amphibolite metamorphism is Tertiary. Moreover, the southern part of the Antigorio Unit is composed by the so-called "Pioda di Crana gneiss" (Steck et al. 2013), a fine-grained granite gneiss, dated 301 ± 4 Ma old (Bergomi et al. 2007).

2.1.3 The Teggiolo Unit

The Teggiolo Unit is composed by quartzite, metapelite, dolomites, calc-schists and marbles, derived from several sedimentary cycles deposited from the Triassic to Eocene. The autochthone sedimentary cover, now overprinted by Tertiary amphibolite facies metamorphism, overlays the Antigorio and Verampio units (*e.g.*, Steck 2013; 2019; Spring et al. 1992).

2.1.4 The Adula underthrust (the Mergoscia and Cima Lunga units, and the Bosco–Bombogno–Isorno–Orselina zone)

The Adula suture zone is made by two major units: the Mergoscia–Cima Lunga units and the Bosco–Bombogno–Isorno–Orselina zone. The eclogitic Mergoscia and Cima Lunga units share a rather similar lithology as the Bosco–Bombogno–Isorno–Orselina zone, characterized by amphibolite facies, Oligocene metamorphism. The Mergoscia and Cima Lunga unit crops out to the East of the Zicher anticline axis and shows sporadic relicts of eclogitic facies, then overprinted by amphibolite regional metamorphism. The lithological composition of the two units is rather complex, comprehending several oceanic crust rocks (ultramafites, metagabbros, amphibolites and calc-schists), as well as orthogneiss and micaschist. The occurrence of oceanic rocks suggests the presence of a former Cretaceous–Paleogene basin, between the European Antigorio and Monte Leone nappe domains (Berger et al. 2005; Steck et al. 2013).

2.1.5 The Osbarino and Valgrande units

The connected Osbarino and the Valgrande units are well foliated, gneissic rocks with granitic composition. According to Schmidt and Preiswerk (1905), the Valgrande unit represents the basement of the autochthone Lebendun Unit (see below), while Steck (2013) proposed an allochthone origin of Lebendun Unit.

2.1.6 The Lebendun Unit

The Lebendun Unit consists by metasedimentary rocks, mostly metaconglomerates, micaschists, calc-schists and meta-arenites, known as "*scisti bruni*" (Burckhardt 1942; Joos 1969). Traditionally, this area is attributed to the European continental margin and is mostly characterized by terrigenous sedimentation, which took place from Early to Late Jurassic (*e.g.*, Spring et al. 1992).

2.1.7 The Mt. Leone Nappe (Mt. Leone-Arbola)

The Mt. Leone Nappe crops out in the footwall and hanging wall with respect to the Simplon line. The Mt. Leone Nappe in the Isorno Valley is made by fine to medium grained biotite–K-feldspar–oligoclase gneiss, metamorphosed from Permian granitoids protolith. Locally, as in the upper parts of the units, including the Mt. Cervandone area, serpentinites are also described [such units are known as Cervandone-Geisspfad complex, reported by Gerlach (1882)] (Wieland 1966; Burri et al. 1994).

After Steck (2008) the Moncucco (Bearth 1957) has become obsolete and divided into two distinct units: a lower part, composed by granites, now attributed to the Mt. Leone Nappe, and an upper part which composes the new so-called Ruginenta unit (Steck et al. 2014). From a palaeogeographical point of view, the Monte Leone unit is attributed to the European continent, to the North of the Valais basin (Steck et al. 1999, 2001). Bigioggero et al. (1981) defined the Permian age of 271 ± 4.8 Ma (Rb–Sr) in the former Moncucco (now part of the Mt. Leone Nappe) in two micas K-feldspar–oligoclase-gneiss.

2.1.8 The Valais Units

The Valais underthrust, overlaying the Mt. Leone Nappe, consists of metasedimentary (calc-schists) cropping out to the north of the Mt. Leone and Lebendun units. The interpretation given by Bagnoud et al. (1998) is that these rocks represent the metamorphosed sediments, deposited between Cretaceous and Palaeogene of the Valais basin. Among the oceanic units madding up the Valais Units, it is worth to mention the Geisspfad ultramafic complex (Pelletier et al. 2008), made by serpentinites, occurring within the Mt. Cervandone area.

2.1.9 The Ruginenta nappe

The Ruginenta nappe has been defined by Steck (2008) and is made by Carboniferous metasedimentary (sandstones, slates and metaconglomerates), followed by Permo-Triassic phengitic quartzites and Triassic dolostones.

2.2 Geology of the rocks occurring in the Mt. Cervandone area

The Mt. Cervandone (known as *Scherbadung* or *Cherbadung* in the Swiss) is one of the most renowned REE deposits of the Alps, known among both collectors and scientists for its unusual and changing nature of the REE- and As-bearing mineralogical species. In order to avoid misunderstanding, it is worth mentioning that mineral cultivation has never been conducted at Mt. Cervandone, although, mineral specimens have been extracted since the first half of 1900, for collecting and, secondly, scientific purposes, within the area between Pizzo Bandiera, della Rossa Glacier and Wanni Glacier (Bianchi 1920). Unfortunately, despite the huge number of studies focused on the Mt. Cervandone area, most of them relate to the mineralogy of unusual specimens and very little efforts have been dedicated to unveil its geological features. A brief outline of the Mt. Cervandone is reported below.

The Mt. Cervandone massif encloses, from the deepest to the shallowest, the stacking of the following units: Devero calcschist, Mt. Leone gneiss, Geisspfad ultramafic complex and, eventually, the Berisal gneiss and micaschist. For the purposes of the present work, the Mt. Leone gneiss represents the most

important formation. The REE-minerals are hosted within Alpine fissures (*e.g.*, Graeser and Albertini 1995), closely related to pegmatitic dykes, presumably of Alpine age, even though data about their age are missing (Guastoni et al. 2006). These dykes, tens of cm thick, intrude the fine-grained two-mica leucocratic gneisses of Mt. Leone (Dal Piaz 1975), and extend for hundreds of meters, being concordant with the gneiss schistosity. The dykes show a strong pegmatitic texture and a strong NYF (niobium-yttrium-fluorine) chemical signature (Guastoni et al. 2006; Černý 1991a,b; Ercit et al. 2005; Černý and Ercit 2005), which reflects into the formation of Be-As-Nb-REE minerals. Locally, the pegmatitic dykes are interrupted by discordant, subvertical quartz veins, mainly composed by vitreous and smoky quartz and green muscovite. These quartz veins commonly contain open Alpine-type fissures, which host several REE-bearing accessory minerals, including, among the others, cafarsite, synchysite-(Ce), chernovite-(Y), gasparite-(Ce), xenotime-(Y), monazite-(Ce). During the Lepontine dome uplift, the circulation of hydrothermal fluids within the pegmatitic dykes, strongly enriched in arsenic, led to the mobilization REE, Nb, Ta, Th and U. Subsequently, the circulating hydrothermal fluids led to the formation of the aforementioned quartz veins with the concomitant precipitation of As-, P- and REE-enriched minerals (Guastoni et al. 2006; Gatta et al. 2018).

2.2.1 Mineralogy and anomalous content of arsenic and REE

As mentioned above, the enrichment in REE and As are two of the major features among the Mt. Cervandone mineralization. The enrichment in As has been object of studies by Graeser and Roggiani (1976), Hettmann et al. (2014), Guastoni et al. (2006). According to Graeser and Roggiani (1976), which still provides the most comprehensive overview on the Mt. Cervandone mineralization, three stages can be drawn to explain the mineral association within the selected area.

I group: A primitive sulphide orebody, of pre-Alpine (Hercynian) age, according to Graeser and Roggiani (1976), mainly enriched in sulfosalts and sulphides, commonly altered to copper carbonates;

II group: Fissure minerals, formed during the late stages (exhumation) of the metamorphism in the Lepontine dome (20-30 My), mainly represented by fissure oxides, silicates and some of the phosphates;

III group: Fissure minerals, connected to the alteration of the of the *Group I* Cu-As sulphides, and comprehending the arsenates, arsenites and some of the phosphates.

Arsenic often occurs within arsenates and arsenites, mostly represented by cafarsite [$Ca_8(Ti,Fe,Mn)_{6-7}(AsO_3)_{12}\cdot 4H_2O$], fetiasite [$(Fe,Ti)_3O_2(As_2O_5)$], chernovite-(Y) [$Y,HREE(AsO_4)$], cervandonite-(Ce) [$(Ce,Nd,La)(Fe,Ti,Al)_3O_2(Si_2O_7)_{1-x+y}(AsO_3)_{1+x-y}(OH)_{3x-3y}$], asbecasite [$Ca_3(Ti,Sn)As_6Si_2Be_2O_{20}$], gasparite-(Ce) [$Ce,LREE(AsO_4)$]; paraniite-(Y) [$Ca_2Y(AsO_4)(WO_4)_2$] (Demartin and Gramaccioli

2008; Gatta et al. 2018; Graeser and Roggiani 1976; Graeser 1966; Graeser et al. 1994; Graeser and Schwander 1987; Demartin et al. 1994, Armbruster et al. 1988). The enrichment in As is also witnessed by the occurrence of significant amount of this element within nominally As-free minerals, like β-fergusonite and a rather high As-content within monazites-(Ce) and xenotimes-(Y) (Guastoni et al. 2003). In addition, the occurrence of Cu, associated with As within the *I group* minerals, has been observed in Cu-enriched chlorites (Graeser and Roggiani 1976).

In this context, fahlore, (the solid solution between tennantite and tetrahedrite), in this case enriched in tennantite component $[Cu_6[Cu_4(Fe,Zn)_2]As_4S_{13}]$ (belonging to the Graeser and Roggiani (1976) *I group*) seems to play a remarkable role in the As-mobilization (Guastoni et al. 2006; Hettmann et al. 2014; Graeser and Roggiani 1976). Tennantite occurs within quartz veins along with mica, and sulphides (arsenopyrite, bournonite, bismuthinite, chalcopyrite, and molybdenite), often rimmed by alteration carbonates, like azurite, chrysocolla and malachite, tyrolite and amorphous As-Bi-Cu earthy phase (Graeser 1998; Guastoni et al. 2006). The chemical composition of tennantite has been object of several studies carried out by Graeser (1965), Graeser and Roggiani (1976) and Hettmann et al. (2014): the composition of fahlore shows up to 85 mol % of pure Cu-As-tennantite component, with rather small amount of Sb, Zn and Ag, while the abundance of Bi and Fe are relatively high. Moreover, Hettmann et al. (2014) highlighted how the Tl isotope composition of Mt. Cervandone is close to that of porphyry copper deposits, corroborating a probable magmatic origin of the *I group* minerals as firstly suggested by Graeser and Roggiani (1976). In addition, the breakdown of *I group* minerals is proposed to represent a likely source of metals within the near sulphide Legenbach mine, on the Swiss flank of Mt. Cervandone (Graeser 1975). In the surroundings of Alpe Veglia, the occurrence of As-enriched springs has been reported since Graeser and Roggiani (1976), indicating that the mobilization of As is still active.

To the best of our knowledge, there are only few studies (Guastoni et al. 2006; Guastoni et al. 2013) concerning the REE-source in Mt. Cervandone. It is known that the origin of REE-minerals is connected to the NYF pegmatites: within the pegmatites, the REE-bearing minerals are much more abundant, with respect to the quartz fissures in the Mt. Ceravdone zone. In the latter case, the occurrence of REE-bearing minerals is rather sporadic (Guastoni et al. 2006). Either during and after the Alpine event (corresponding to the *II* and *III group* of Graeser and Roggiani 1976) fluids percolation within the pegmatites led to the decomposition of primary REE-bearing minerals. The most common REE-bearing accessory minerals are allanite-(Ce), aeschynite-(Y), agardite-(Y), niobianatase, cervandonite-(Ce), chernovite-(Y), crichtonite-senaite group minerals, β-fergusonite-(Y), fluorite, gadolinite-(Y), monazite-(Ce), paraniite-(Y), niobian-rutile, synchysite-(Ce), and

xenotime-(Y) (Graeser and Stalder 1976; Albertini 1991; Graeser and Albertini 1995; Guastoni et al. 2010). The most likely REE-source is allanite-(Ce) (Alessandro Guastoni, personal communication). The allanite-(Ce) specimens from Mt. Cervandone pegmatitic dykes are centimetric in size and their chemical composition has been studied by Gatta et al. (2021), which unveiled its enrichment in LREE. Moreover, allanites can undergo a complete dissolution, leaving centimetric allanite-shaped voids, often filled by monazite-(Ce) and synchyste-(Ce) (Alessandro Guastoni, personal communication). Within the Mt. Cervandoene complex, the occurrence of unusual REE-enriched minerals and fluids led to the crystallization of rather rare REE-decomposition minerals. Among these, low temperature oxalates, as deveroite-(Ce) (nominally $Ce_2(C_2O_4)_3 \cdot 10H_2O$), forms as decomposition rims around cervandonite-(Ce) in rock cavities permeated by meteoric water (Guastoni et al. 2013). Unfortunately, within the Mt. Cervandone area, no studies about the actinides content have been carried out and thus are not discussed here.

2.2.2 Fissure formation in the Lepontine dome

The formation of the Alpine fissures within the specific case of Mt. Cervandone context has never been studied, although several studies (Bergemann et al. 2020; Mullis et al. 1994; Mullis 1996; Rauchenstein-Martinek et al. 2016; Weisenberger et al. 2012; Gnos et al. 2021) about similar structures have been carried out in the Lepontine dome, in the area surrounding the Mt. Cervandone. There is a general agreement that quartz fissures in the Lepontine dome formed after the metamorphic peak, as a result of the extensional regime active within the brittle zone.

Within the Lepontine dome, the modal composition of the fissures is always dominated by quartz, followed by a variable mineralogy composed of a plentitude of minerals, formed either at the same time of quartz, precipitated by meteoric water or somewhat in between. It is worth to mention that the mineral association does not represent a paragenesis. According to Bergemann et al. (2020) the crystallization process within an Alpine fissure is discontinuous and complex, caused by the succession of several events under non-equilibrium conditions. Indeed, the disequilibrium conditions are also enlightened by the rather variable pattern of the fluid inclusions contained in quartz, which show a rather step-wise growth, instead of a continuous one. Moreover, patchy grains of monazites-(Ce) have been found within the quartz clefts, because of dissolution-precipitation reactions that took place during the crystallization of the vein minerals (Bergemann et al. 2020; Janots et al. 2012). During each fluid impulse, the new forming minerals are believed to be in equilibrium with the surrounding fluids. Different fluid impulses come from several sources, including decomposition of hydrated phases during prograde metamorphism, meteoric water, as from the country rock. Considering the Lepontine dome, the prograde decomposition of minerals represents an unlikely

source of fluids, since the clefts are connected to extension and uplifting of the dome and, consequently, to a retrograde dynamic.

The fluid temperature has been esteemed by Mullis et al. (1994) by means of microthermometry. A temperature below 450° C has been found. As mentioned above, the complete opening of the fissure is supposed to occur in a rather shallow zone, above the ductile to brittle transition zone. Assuming a temperature between 420° C and 450° C, Mullis (1996) esteemed, for the Alpine fissures of the Gotthard and Aar massif an opening of the fissures between 13 to 17 km. Eventually, dating of the monazites-(Ce) occurring within the Lepontine dome veins has been reported by Bergemann et al. (2020). The resulting ages are quite compatible with the exhumation of the Lepontine dome itself, between 15 and 5 My (Bergemann et al. 2020).

Chapter 3

3 Minerals under study and the structure of ATO_4 compounds

The nomenclature ATO_4 (MXO_4, ABO_4, ABX_4 and AXO_4 are also used) is a general term used in the literature to define ternary, inorganic compounds, usually oxides (Vorres 1962). Within ATO_4, *A* and *T* represent two cations, not necessarily different, that can combine with oxygen (and seldom with other anions) in several structural topologies, including, but not limited to, scheelite, zircon, monazite, fergusonite, barite, quartz, cristobalite, wolframite and rutile topologies (Fukunga and Yamaoka 1979). In order to define which structural type is stable varying the radii of *A* and *T* in relation with oxygen's size, several studies have been conducted. An elegant way to describe the stable structure type, as a function of either the *A*, *T* and O ionic radii has been provided by Muller and Roy (1975), Fukunga and Yamaoka (1979), Bastide (1987) and is reported in Figure 3.1. The diagram (Figure 3.1) provides a tool to describe and predict the phase transitions among the ATO_4 compounds and is often referred to in literature as the Bastide diagram. Several versions of the diagram with slight variations of the two axes have been developed, whereas the most useful remains the one reported by Fukunga and Yamaoka (1979) (Figure 3.1): the two axes of the diagram are defined as $k = r_A/r_T$ and $t = (r_A + r_T)/2r_O$, being r_A, r_T and r_O the ionic radii of the *A*-cation, *T*-cation and O^{2-} respectively. Indeed, the relations among the ionic radii of the three atomic species determine which crystal structure is stable. Ionic radii provided by Shannon (1976) have been used. The coordination number of oxygen has been fixed at six, corresponding to an ionic radius of 1.40 Å. For all the other atomic species, the ionic radii have been used accordingly to the coordination number of the specific structural topology involved. As a result of the *k* and *t* axes used, for a given *T*-cation the corresponding ATO_4 compounds lie on a straight line which equation can be drawn as $k = (2r_O/r_T)t - 1$. The importance of the present diagram in describing non ambient conditions phenomena, and the relations among the different structures is discussed below in section 6.

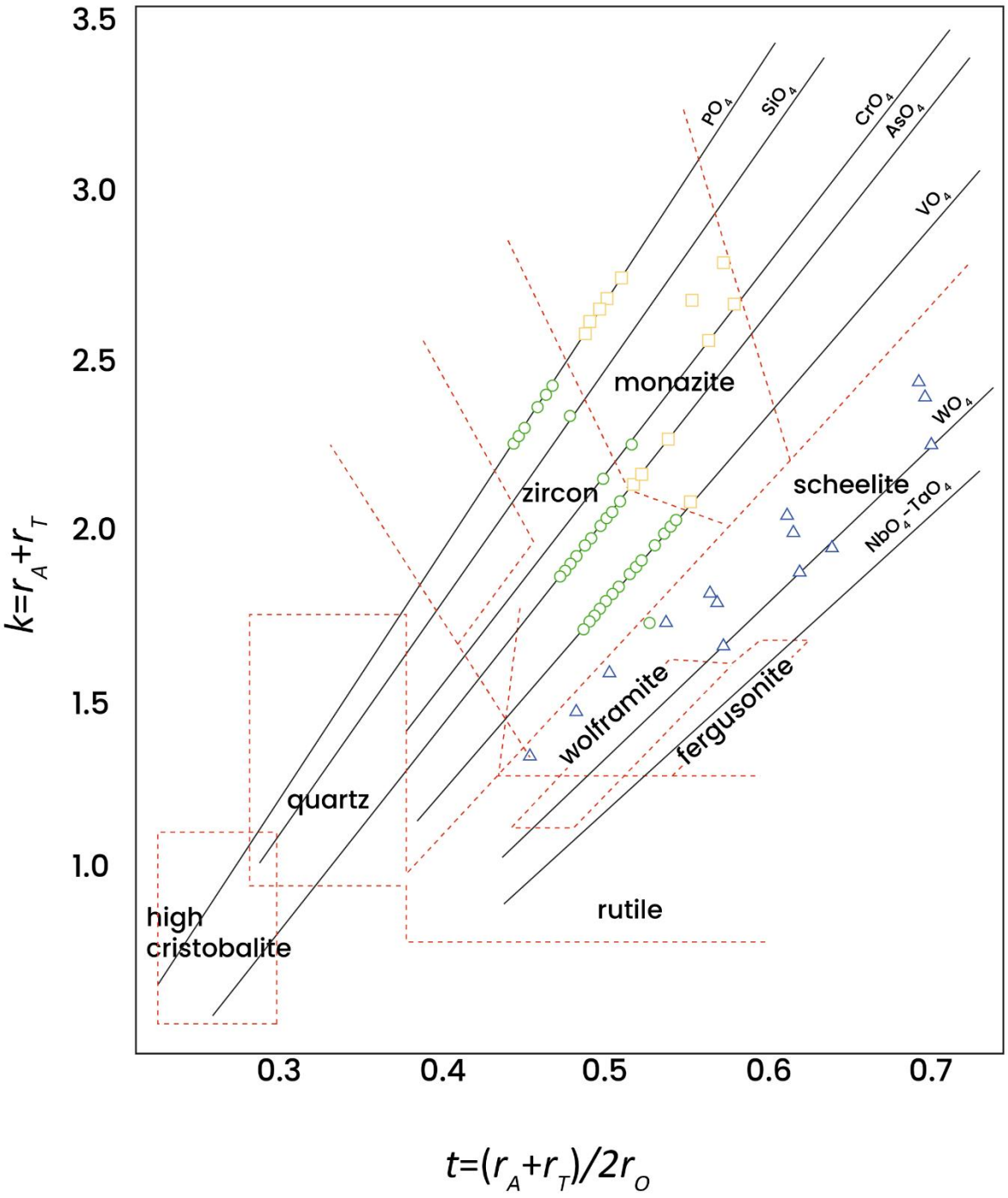

Figure 3.1: Bastide diagram (after Fukunaga and Yamaoka 1979) showing several fields pertaining to the ATO_4 family. The borders that divide a field from another is represented by a red dashed line. The continuous lines with a positive inclination represent the evolution of *t* and *k* for phosphates, silicates, chromates, arsenates, vanadates, wolframates and niobates-tantalates. The dots represent the *t* and *k* values of monazite-, zircon- or scheelite-type compounds.

The charge and rather large size assumed by the *A*-cation (*i.e.*, REE^{3+}, in this particular case) also restrict the chemical composition (and charge) of the possible *T*-site, which is limited to As, P, V, Cr

and Si. Thus, within the ATO_4 minerals object of the present study, *A* stands for REE, Ca, U and Th, whereas *T* stands for tetrahedrally-coordinated cations (As, P, V, as well as minor Si and Cr). Concerning the structural topologies, almost exclusive attention is dedicated to the zircon and monazite structures, shown by the four minerals object of this work: chernovite-(Y) [nominally $YAsO_4$], xenotime-(Y) [nominally YPO_4], gasparite-(Ce) [nominally $CeAsO_4$] and monazite-(Ce) [nominally $CePO_4$]. The crystal structure of these minerals has been object of a large number of studies and reviews (*e.g.*, Mooney 1948; Boatner 2002; Ni et al. 1995; Kolitsch and Holtstam 2004b; Clavier et al. 2011; Finch and Hanchar, 2003) and a detailed description of the monoclinic monazite-type structure and the tetragonal zircon-type (also known, but rarely reported as "xenotime-type") is discussed below, in section 3.1 and section 3.2.

As reported by several authors (Fukunga and Yamaoka 1979; Ushakov *et al.* 2001; Boatner *et al.* 2002; Kolitsch and Holtsam 2004a), whether the monazite or the zircon-type structure is stable within ATO_4 phosphates and arsenates depends on different factors. In the first place, as mentioned earlier, the atomic radii of either the *A*- and *T*-site cations play a paramount role. In addition, the synthesis conditions (*i.e.*, temperature, features of the precursor materials and pH of the solution) have been pointed as other important features that influence the stable polymorph. More specifically, a large size of the *A*-cation promotes the crystallization of the monazite topology over the zircon one; on the other hand, the larger is the *T*-site cation, the more stable is the zircon stricture across the REE-series. The relations among the stable polymorphs and the REE series is summarized in Figure 3.1 for phosphates, silicates, chromates, arsenates, vanadates, wolframates and niobates-tantalates. Within the REE-bearing phosphates, the larger and lighter REE ranging from La to Eu are preferentially hosted by the monazite-type structure, whereas the smaller and heavier REE, from Tb to Lu, as well as Y and Sc, best fit into the zircon-type structure (Mooney 1948; Boatner, 2002; Ni *et al.* 1995; Kolitsch and Holtstam, 2004b; Clavier *et al.* 2011). For synthetic Gd, Tb and Dy phosphates, the possible occurrence of two coexisting polymorphs is observed: they may crystallize in both monazite- and zircon-type structures likely in relation to synthesis conditions. A similar behavior has been reported for the $REEAsO_4$ series, although the threshold among the two structures is pulled to a smaller Z in the lanthanoid series: the monazite-type structure preferentially hosts the larger REE (from La to Nd), whereas the smaller REE (from Sm to Lu, as well as Y and Sc) are preferentially hosted by the tetragonal zircon-type crystal structure (*e.g.*, Ushakov *et al.* 2001; Boatner *et al.* 2002). Concerning the REE-bearing vanadates, the zircon-type topology is stable for all the $REEVO_4$, except for $LaVO_4$, although the synthesis conditions can lead to the crystallization of metastable $CeVO_4$,

$PrVO_4$, $NdVO_4$ with monazite-type topology and zircon-type $LaVO_4$ can be also obtained (*e.g.*, Bazuev et al. 1974; Ropp and Carroll 1973).

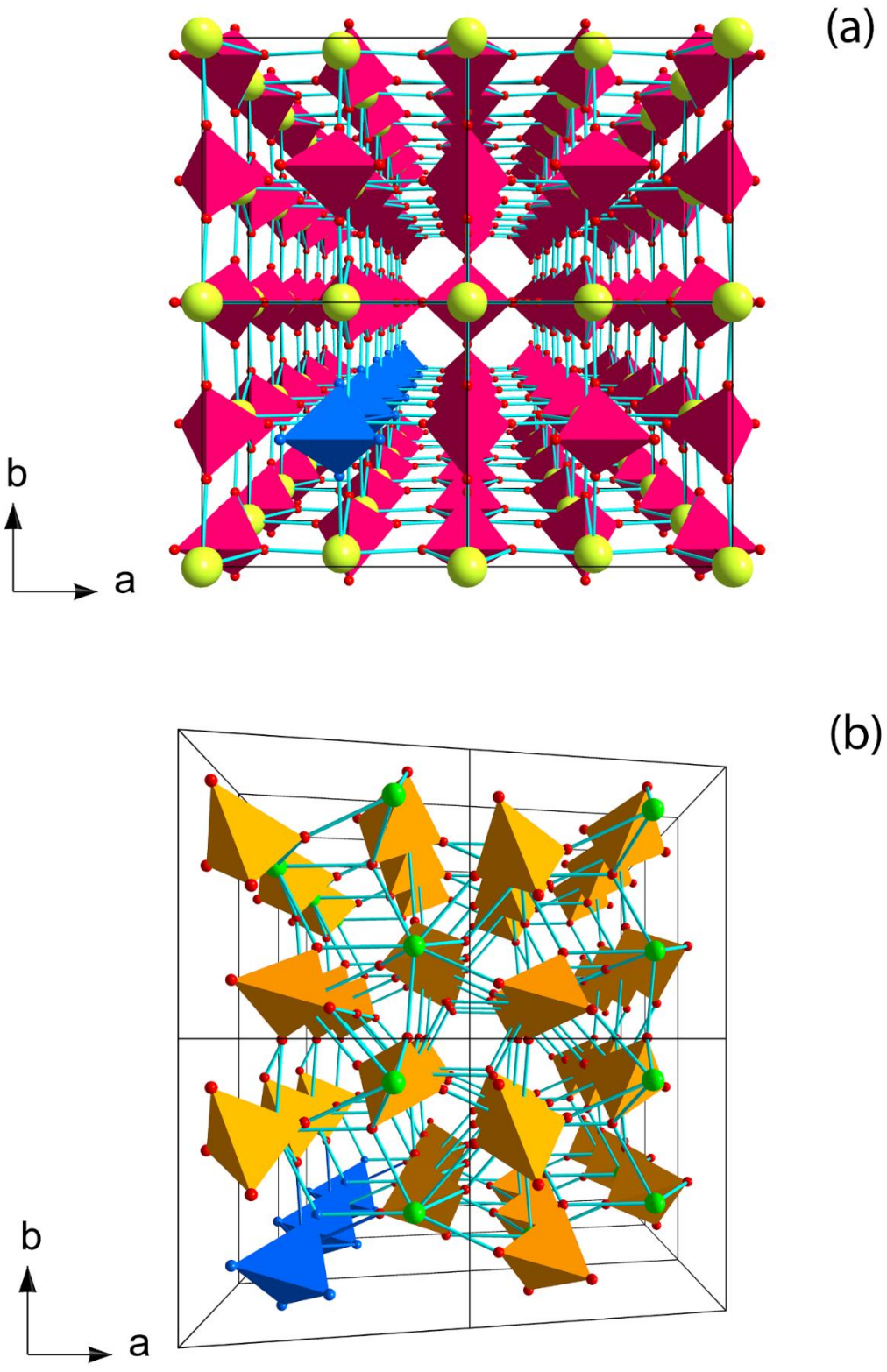

Figure 3.2: perspective view showing a comparison among the crystal structures of the zircon **(a)** and the monazite topology **(b)**, showing the configuration of the chain-units; only the *T*-site tetrahedra are shown (see section3.1 and 3.2 for further details).

3.1 Zircon-type structure topology

The first studies concerning the crystal structure of zircon date back to the early 20th century and were carried out independently by Vegard (1916, 1926), Binks (1926), Hessel (1926) and Wyckoff and Hendricks (1928), in the framework of the pioneering works about the silicate's structure determination, later gathered by Bragg (1929) in his *Atomic Arrangement in Silicates*. After the first studies on zircon, its structural topology has been described in several REE-bearing compounds, including xenotime-(Y) (Vegard 1927) and the synthetic counterpart of chernovite-(Y), $YAsO_4$ (Strada and Schwendimann 1934).

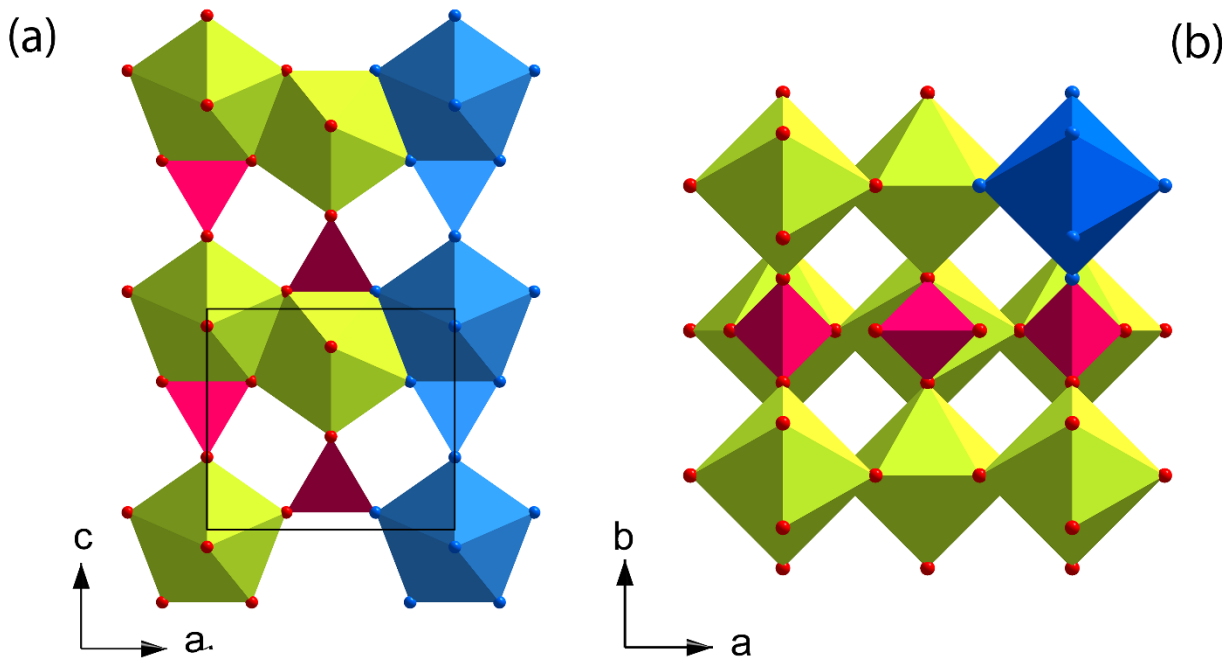

Figure 3.3: crystal structure of zircon topology viewed along the [010] **(a)** and [001] **(b)**.

The zircon-type topology is characterized by a highly symmetric tetragonal *I*-centered lattice (space group $I4_1/amd$). The tetragonal zircon-type is made by the infinite chains, developed along [001]. Those chain units are the result of the connection along the polyhedral edges, between the eightfold coordinated *A*-site dodecahedron (AO_8 or $REEO_8$) and the TO_4 tetrahedra (Figure 3.3). The AO_8 polyhedron displays two independent *A*-O atomic distances, whereas the TO_4 is an undistorted polyhedron defined by a single *T*-O bond distance. Each chain is in contact with 4 others in the (001) plane, by means of the connecting edges along a AO_8 units and the four surroundings. The structure is featured with interstitial linear voids, running along [001], large enough to host interstitial atom or small molecules (*e.g.*, Finch and Hanchar 2003). Due to the high symmetry space group ($I4_1/amd$)

the zircon structure shows only three independent atomic coordinates. The atomic coordinates of the *A*- and *T*-sited are placed in special, completely fixed positions, both characterized by a $\bar{4}2m$ symmetry. The oxygen atom also shows special position (*m*), being its *y* and *z* coordinates the sole refinable parameters.

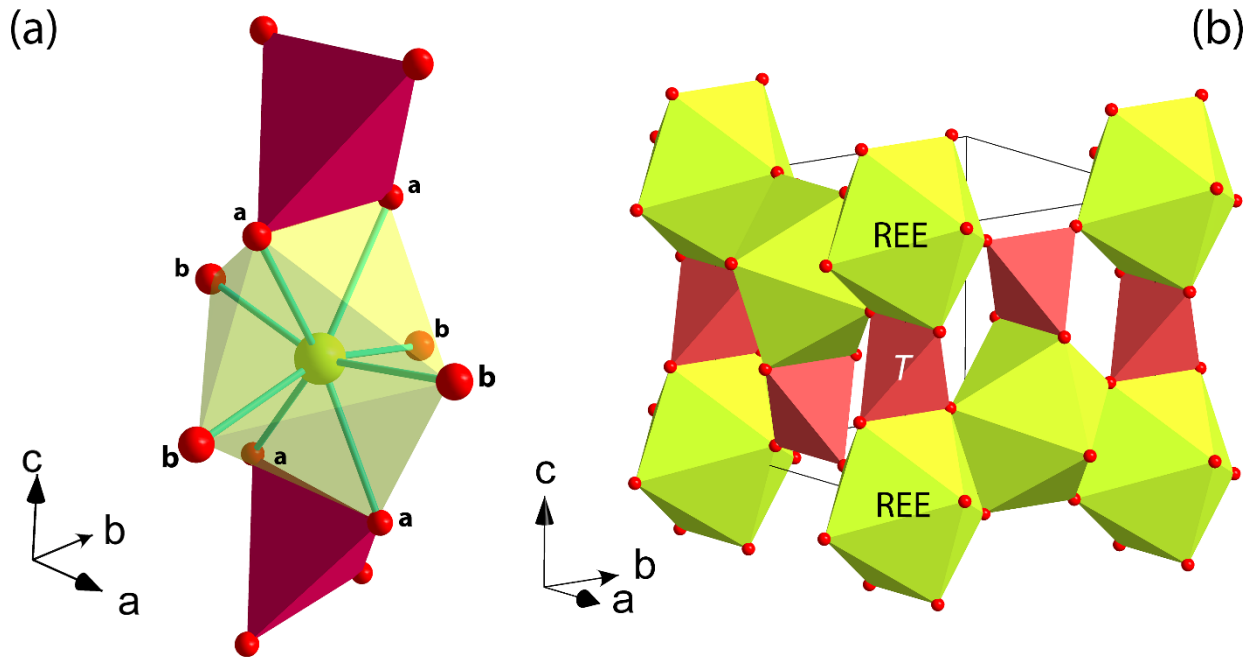

Figure 3.4: crystal stcruture of zircon, showing **(a)** the topology of the chain unit and bond distances configuration among the AO_8 polyhedron, and **(b)** the overall crystal structure.

3.1.1 Chernovite-(Y)

Chernovite-(Y), the zircon-type structured HREE-bearing arsenate, is a rare mineral, recovered in few localities. In principle, its crystal structure has been solved from the synthetic counterpart $YAsO_4$ by Strada and Schwendimann (1934). The unit-cell of chernovite-(Y) is reported in Table 3.1, along with the unit-cell parameters of its synthetic counterparts As a mineral, chernovite-(Y) was first described from the Nyarta-Sya-Yu River, Urals, and named after the Russian geologist Aleksandr Aleksandrovich Chernov (Goldin et al. 1967). In the meanwhile, chernovite-(Y) has been found also at the Mt. Cervandone mineral deposit, in form of a solid solution along with xenotime-(Y) (Graeser and Roggiani 1973). In addition, chernovite-(Y) can form a solid solution along with the isostructural vanadate wakefieldite-(Y) (nominally YVO_4) (*e.g.*, Bagiński et al. 2020). Chernovite-(Y) usually occurs as an accessory mineral in hydrothermal environments, commonly found as an alteration product of minerals within A-type granites and gneisses, altered by As-rich fluids (Breiter et al. 2009, Förster et al. 2011, Papoutsa and Pe-Piper, 2014; Li et al. 2019; Alekseev and Marin 2012) as well as

within reduction spots in slates (Kerbey 2013). In addition, microcrystalline $YAsO_4$, along with $LaAsO_4$ (*i.e.*, gasparite-(La)), were also detected within the Fe–Mn deposits of the Corsaglia Valley, Maritime Alps, Italy (Cabella et al. 1999). Also Mills et al. (2010), along with arsenoflorencite-(La), reported the occurrence of chernovite-(Y) in Mn-rich nodules from the Grubependity Lake cirque, Komi Republic, Urals. So far, chernovite-(Y) has no economic relevance. On the other side, its synthetic counterpart, $YAsO_4$, has been object of several publications, since it is a promising phosphors material, due to its capacity to host light emitting HREE, as Er, Dy, Ho (*e.g.*, Strzep et al. 2017).

Table 3.1: unit-cell parameters of several zircon-type arsenates.

	a (Å)	*c* (Å)	Volume (Å^3)	reference
Chernovite-(Y)				Strada and Schwendimann
	6.890	6.269	297.6	1934
$ScAsO_4$	6.7102(2)	6.1132(3)	275.26(1)	Schmidt et al. 2005
$YAsO_4$	7.070(6)	6.214(4)	310.61(2)	Errandonea et al. 2011
$SmAsO_4$	7.1857(4)	6.3906(4)	329.97(2)	Kang and Schleid 2005
$EuAsO_4$	7.1617(2)	6.3750(2)	326.97(2)	Golbs et al. 2009
				Choudhary and Choudhary
$GdAsO_4$	7.187(4)	6.400(5)	330.58(3)	1990
$TbAsO_4$	7.090	6.320	317.69(2)	Schäfer and Will 1979
$DyAsO_4$	7.073(3)	6.313(5)	315.82(2)	Choudhary and Yadav 1992
$HoAsO_4$	7.0499(3)	6.2928(3)	312.75(2)	Schmidt et al. 2005
$ErAsO_4$	7.0203(2)	6.2761(4)	309.315(12)	Swanson et al. 1964
$TmAsO_4$	6.9939(3)	6.2595(3)	306.18(1)	Swanson et al. 1964
$YbAsO_4$	6.9712(4)	6.2431 (4)	303.40(3)	Kang et al. 2005
$LuAsO_4$	6.949(2)	6.227(2)	300.69(15)	Lohmüller et al. 1973

3.1.2 Xenotime-(Y)

Xenotime-(Y), along with pretulite [$ScPO_4$] is the only natural zircon-structured phosphate. The name xenotime comes from the Greek for "foreign", *xenos*, and *time*, meaning "honor". Xenotime-(Y) is a rather common accessory mineral in granites, rhyolites, gneiss, pegmatites and their associated residual and placer deposits. Before the incoming of the ion absorption clays, xenotime-(Y) was the

most important HREE source and it is still among the major REE ore minerals. Several geological sites are known to provide xenotime-(Y) crystals where it is often extracted as byproduct of other commodities, like monazite-(Ce) and niobates. The unit-cell of xenotime-(Y) is reported in Table 3.2, along with the unit-cell parameters of its synthetic counterparts. The first description of the crystal structure of xenotime-(Y) dates back to the 1927 (Vegard 1927) and subsequent studies carried out by Strada and Schwendimann (1934) and Krstanović (1956) furnished a complete description of the structure.

Table 3.2: unit-cell parameters of several zircon-type phosphates.

	a (Å)	*c* (Å)	Volume (Å^3)	reference
Pretulite	6.5870(9)	5.809(1)	252.05(7)	Moëlo et al. 2002
Xenotime-(Y)	6.888(1)	6.030(1)	286.09(8)	Guastoni et al. 2012
$ScPO_4$	6.5768(2)	5.7938(3)	250.60(2)	Ushakov et al. 2001
YPO_4	6.8832(3)	6.0208(4)	285.25(2)	Ushakov et al. 2001
$TbPO_4$	6.9424(3)	6.0734(3)	292.71(2)	Ushakov et al. 2001
$DyPO_4$	6.9151(6)	6.0494(7)	289.27(3)	Ushakov et al. 2001
$HoPO_4$	6.8878(3)	6.0284(6)	285.99(2)	Ushakov et al. 2001
$ErPO_4$	6.8614(5)	6.0082(9)	282.85(2)	Ushakov et al. 2001
$TmPO_4$	6.8404(2)	5.9884(3)	280.20(2)	Ushakov et al. 2001
$YbPO_4$	6.8167(2)	5.9700(4)	277.41(3)	Ushakov et al. 2001
$LuPO_4$	6.7943(2)	5.9592(5)	275.09(3)	Ushakov et al. 2001

3.2 Monazite-type structure topology

Parrish (1939) within the first crystallography studies on monazites, identified its correct space group, as $P2_1/n$. The first description of the monazite-type structure has been reported by Mooney (1948), who investigated the La, Ce, Pr and Nd phosphates as part of the Manhattan project and described the REE atomic site in eightfold coordination. The crystal structure of monazite with the REE site in ninefold coordination has been proposed by Ueda (1953 1967), but with non-reliable average P-O bond lengths of ~1.6 Å. The structure has been later described correctly by Beall et al. (1981), Mullica et al. (1984) and Ni et al. (1995), whereas an exhaustive review of the monazite-structure topology has been carried out by Boatner (2002) and then by Clavier et al. (2011). The monazite-type structure is characterized by infinite chains running along the [001] direction (*c*-axis), composed by the alternation of the REE-coordination polyhedra and the *T*-hosting tetrahedra (Figure 3.5).

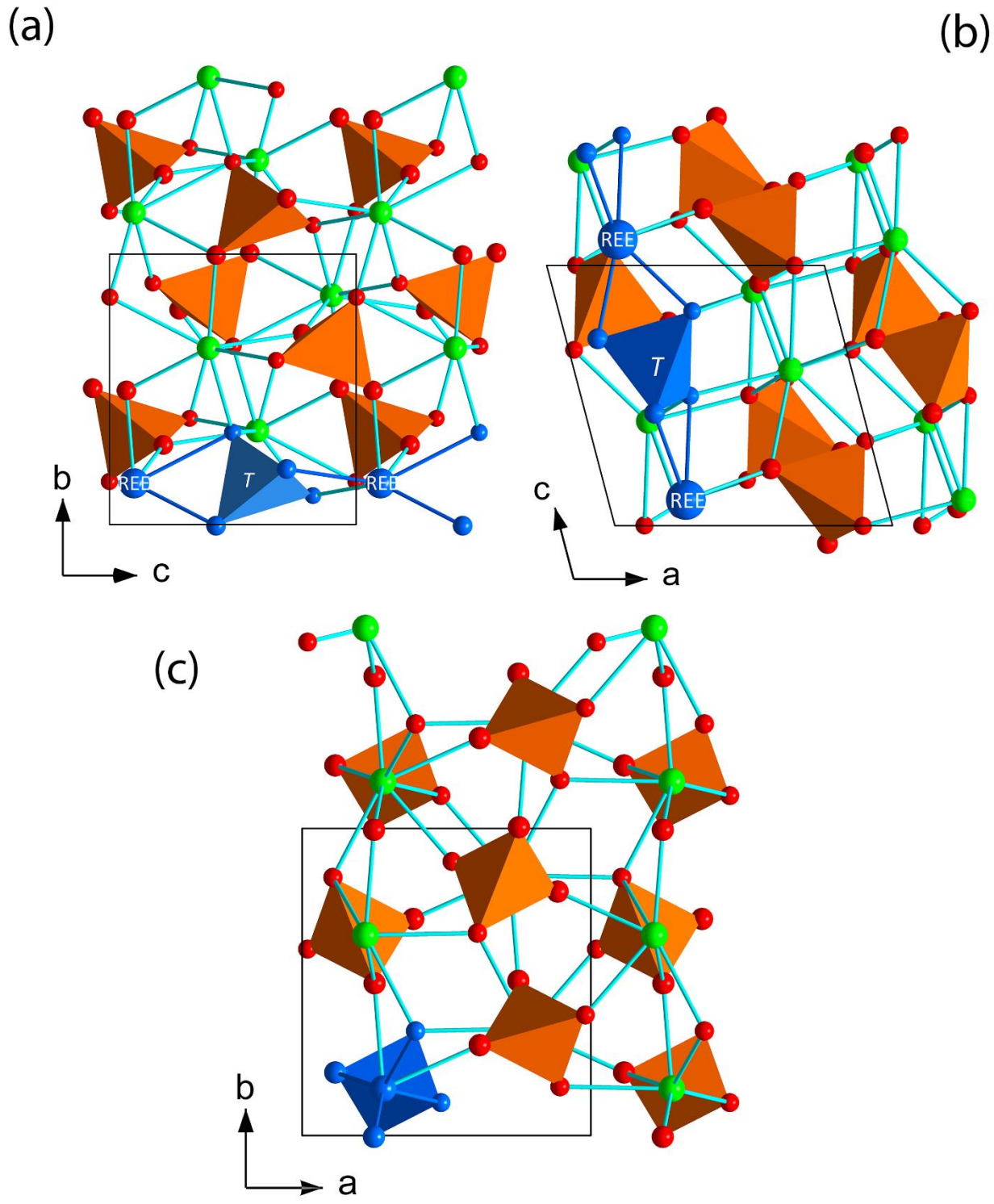

Figure 3.5: crystal structure of monazite, viewed from [100] **(a)**, [010] **(b)** and [001] **(c)**; in blue is highlighted a chain-unit.

The REE-polyhedron coordination environment is made by nine oxygen atoms ($REEO_9$). According to Mullica et al. (1984), the $REEO_9$ polyhedron can be described as an equatorial pentagon (sharing

vertices with five TO_4 tetrahedra of five adjacent chains in correspondence of the $O1_b$, $O2_b$, $O2_c$, $O3_b$ and $O4_b$ oxygen atoms), interpenetrated by a tetrahedron (made by the $O1_a$, $O2_a$, $O3_a$ and $O4_a$ oxygen atoms, see Figure 3.6), which is in contact, along the [001] direction, with two subsequent TO_4 tetrahedra, leading to the formation of the infinite chain units. According to the notation reported in Figure 3.6, the REE-$O2_a$ bond length is sharply longer than the other REE-O bonds, contributing to a significant distortion of the $REEO_9$ polyhedron (Clavier et al. 2011; Ni et al. 1995; Beall et al. 1981).

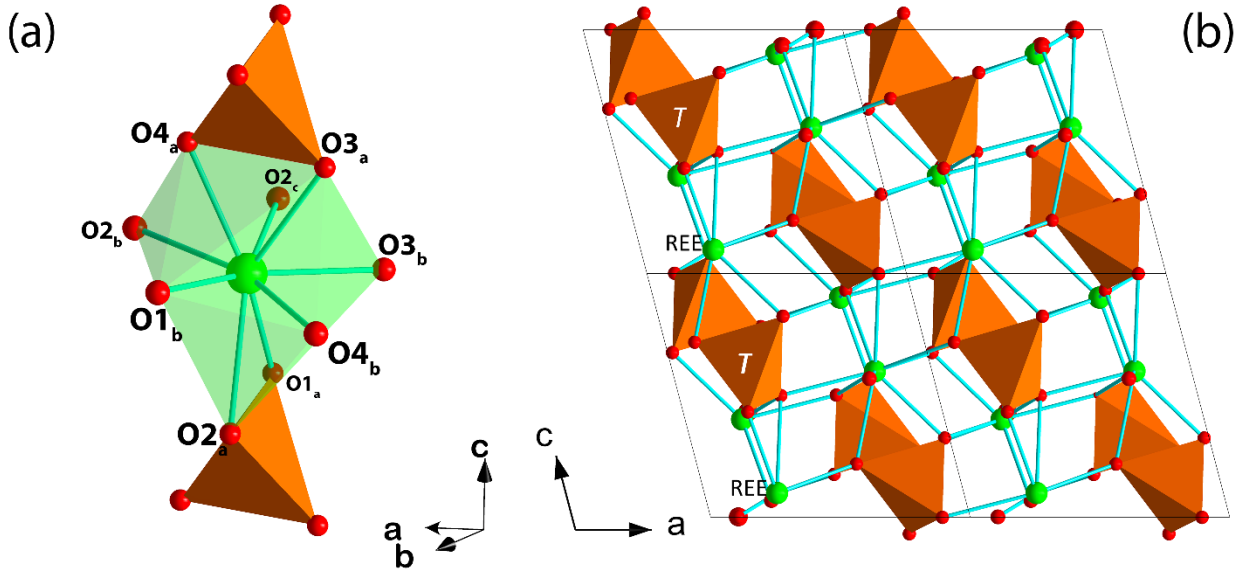

Figure 3.6: crystal structure of monazite, showing the architecture of the chain-unit and REE-coordination polyhedron **(a)**; overall structure of monazite **(b)**.

3.2.1 Gasparite-(Ce)

Gasparite-(Ce) is the natural arsenate with the monazite-type structure and, as the HREE-bearing arsenate chernovite-(Y), is a rare mineral. As chernovite-(Y), gasparite-(Ce), seems strongly linked to post-magmatic and metasedimentary environments, influenced by late hydrothermal processes. The monazite-type structure in REE-bearing arsenates had been firstly described from synthetic $CeAsO_4$ by Beall et al. (1981). Only after Graeser and Schwander (1987) it has been reported in a mineral, named gasparite-(Ce), after the local collector Giovanni Gaspari and occurring within the hydrothermal Alpine fissures of Mt. Cervandone (Italy) and adjacent Binn Valley (Switzerland). Occurrences of gasparite-(Ce) have been later also reported in: Tisovec-Rejkovo rhyolite, Slovakia (Ondrejka et al. 2007); Beryllium Virgin Claim, New Mexico, U.S.A. (Anthony et al. 2000); Kesebol Mn-Fe-Cu deposit, Västra Götaland, Sweden (Kolitsch et al. 2004a); Grubependity Lake cirque, Komi Republic, Russia (Mills et al. 2010); Artana, Apuane Alps, Italy (Mancini 2000). Recently, gasparite-(La), the La-dominant $REEAsO_4$, has been identified by Vereshchagin et al. (2019) within

the Alpine-fissures of the Wanni glacier, Binn Valley, Switzerland, as well as from the Mn ores of the Ushkatyn-III deposit, Central Kazakhstan. Despite the lack of structural data, microcrystalline $LaAsO_4$, very consistent with the chemical composition of gasparite-(La), has been described from the Ponte dei Gorrazzi Fe–Mn deposit in the Corsaglia Valley, Maritime Alps, Italy (Cabella et al. 1999). Moreover, a solid solution between monazite-(Ce) and gasparite-(Ce) has been recovered in Kesebol Mn–Fe–Cu deposit, Västra Götaland, Sweden (Kolitsch et al. 2004) and Tisovec-Rejkovo rhyolite, Slovakia (Ondrejka et al. 2007). In the case of the fissures of Mt. Cervandone, where the samples of the current study come from, gasparite-(Ce) has a low phosphorous content and occurs as an alteration product of the REE-bearing carbonate synchysite-(Ce), nominally $CaCe(CO_3)_2F$ (Graeser and Schwander 1987). Eventually, Table 3.3 shows the unit-cell parameters of several monazite-type arsenates.

Table 3.3: unit-cell parameters of several monazite-type arsenates.

	a (Å)	*b* (Å)	*c* (Å)	*β* (deg)	Volume (Å^3)	reference
Gasparite-(Ce)	6.929(3)	7.129(3)	6.697(3)	104.46(3)	320.3	Kolitsch et al. 2004
Gasparite-(La)	6.9576(4)	7.1668(4)	6.7155(4)	104.414(1)	324.3	Vereshchagin et al. 2019
$LaAsO_4$	7.0056(4)	7.2103(4)	6.7615(4)	104.507(4)	330.7	Kang and Schleid 2005
$CeAsO_4$	6.975(1)	7.177(1)	6.759(2)	104.69(1)	327.29(12)	Brahim et al. 2002
$PrAsO_4$	7.011(1)	7.125(1)	6.570(1)	104.3(3)	318.02(5)	Choudhary 1991
$NdAsO_4$	6.6852(3)	7.0885(5)	6.8935(4)	104.91(1)	315.67(3)	Schmidt et al. 2005

3.2.2 Monazite-(Ce)

Among all the minerals that this study is focused on, monazite-(Ce) is undoubtedly the most common and important from an economic perspective. The name of monazite-(Ce) come from the Greek *mona* "being alone", since has been firstly observed as lone crystals within the rock specimens. Monazite-(Ce) represents the most common form of monazite, whereas the natural La-, Nd- and Sm-dominant forms are fairly rare (Fleischer and Altschuler 1969; Rosenblum and Fleischer 1995; Long et al. 2012). Monazite-(Ce) is a rather common accessory mineral in different geological settings, including granites, aluminous metamorphic rocks (*e.g.*, amphibolites or medium- to high-grade metasedimentary rocks), carbonatites, pegmatites and hydrothermal veins (Cesborn 1989). Moreover, monazite-(Ce) is also a common detrital mineral in sedimentary placers and a newly formed phase during diagenesis (Sengupta and Van Gosen 2016; Čopjaková et al. 2011). Monazite-(Ce) is indeed

a possible source for Th and U (Salehuddin et al. 2021). The unit-cell parameters of monazite-(Ce) are reported in Table 3.4, along with the parameters of monazite-(Sm) and its synthetic pure endmember counterparts. For a complete table of the possible polymorphic compounds with the monazite-type structure, see Clavier et al. (2011).

Table 3.4: unit-cell parameters of several monazite-type phosphates.

	a (Å)	*b* (Å)	*c* (Å)	*β* (deg)	Volume (Å^3)	reference
Monazite-(Ce)	6.7640(5)	6.9850(4)	6.4500(3)	103.584(2)	296.22(3)	Zarman and Antao 2020
Monazite-(Sm)	6.7010(4)	6.9080(4)	6.4300(4)	103.817(3)	289.04(3)	Zarman and Antao 2020
$LaPO_4$	6.8391	7.0772	6.509	103.27	306.63	Konings et al. 2008
$CePO_4$	6.8035	7.0274	6.4761	103.46	301.12	Konings et al. 2008
$PrPO_4$	6.7623(5)	6.9785(5)	6.4304(4)	103.516(1)	295.05(4)	Horchani-Naifer and Férid 2009
$NdPO_4$	6.7392(9)	6.9621(6)	6.4053(6)	103.6(1)	292.1	Ushakov et al. 2001
$SmPO_4$	6.6891(3)	6.8958(3)	6.3770(6)	103.9(1)	285.5	Ushakov et al. 2001
$EuPO_4$	6.6660(7)	6.8684(6)	6.3486(8)	103.9(1)	282.2	Ushakov et al. 2001
$GdPO_4$	6.6543(15)	6.8542(11)	6.3415(13)	104.016(14)	280.6	Cherniak et al. 2004

data without uncertainties are reported as they are in the original publications.

3.3 State of art about chernovite-(Y), gasparite-(Ce), xenotime-(Y) and monazite-(Ce)

As mentioned above (section 3) the *A*- and *T*-site play a fundamental role in determining which structural type is stable. As reported by in Table 3.1, Table 3.2, Table 3.3 and Table 3.4, the unit-cell parameters of the four minerals under investigation and their synthetic analogues are strongly influenced by the lanthanoid contraction. In general, within all the four groups (*i.e.*, zircon-type arsenates, zircon-type phosphates, monazite-type arsenates and monazite-type phosphates), the unit-cell parameters decrease with the increase of the atomic number across the lanthanoid series. The small ionic radii of Y and Sc (*i.e.*, the smaller REE), reflects in the smallest unit-cell parameters among the zircon-type phosphates and arsenates. The relation between ionic radii of the *A*-site and the unit-cell has been highlighted in ATO_4 compounds since Graeser et al. (1973) and confirmed by all the different subsequent studies. The same relation can be also drawn for vanadates and silicates

(in the latters, being Si tetravalent instead of pentavalent, actinides replace lanthanoids, except for $CeSiO_4$). It is interesting to note that, even though data reported in Table 3.1, Table 3.2, Table 3.3 and Table 3.4, come from independent publications, the relations between the unit-cell axes are maintained, following the lanthanoid contraction. Therefore, the density follows an opposite trend, increasing along with the atomic number of the *A*-cation through the lanthanoid series. Taking into account the zircon-type ATO_4 compounds, the prediction of the unit-cell parameters varying the size (*i.e.*, atomic number) of the *A*-site cation is rather simple, as highlighted by Brik et al. (2015). In particular, the two crystallographic axes *a* and *c*, are a linear function of two empirical parameters defined as: (**1**) the sum of ionic radii of the *A*-cation and oxygen and (**2**) the difference of electronegativity among the *A*-cation and oxygen.

3.3.1 Isomorph substitutions in ATO_4 compounds and actinides

Both the monazite- and the zircon-type topology are well known to show isomorph solid solutions. Apart from the possible substitutions that may occur between P, As and V among the *T*-site of monazite- and the zircon-type structures, the occurrences of monovalent, bivalent and tetravalent cations within its *A*-site has been studied by several authors. The substitution of a trivalent cation (REE^{3+}) with a tetravalent cation (A^{4+}) is controlled by the following, alternative mechanisms:

$$A^{4+} + A^{2+} = 2REE^{3+} \quad (3.1)$$

$$A^{4+} + T^{4+} = REE^{3+} + T^{5+} \quad (3.2)$$

$$vacancy + 3A^{4+} = 4REE^{3+} \quad (3.3)$$

All these mechanisms are responsible for the occurrence of actinides within the zircon- or monazite-type structures. In geological environments the tetravalent cation A^{4+} is usually an actinide (Th and U are the most important), whereas Zr and Hf can also be present in significant amount. Calcium is the most important bivalent A^{2+} cation, although Sr, Mg and Fe may also be present in significant abundance. The equation 3.1 is also named cheralite or brabantite (nominally $CaTh(PO_4)_2$) substitution, and for extension, all the $A^{4+}A^{2+}(TO_4)_2$ compounds are named cheralites. Uranium can also occupy the A^{4+}-site, leading to the monazite-type structured $CaU(PO_4)_2$, which is not known to occur in nature (Keskar et al. 2019). Cheralites are endmember compounds featuring a monazite-type unit-cell: thus, the equation 3.1 is particularly important for monazites, while its importance for zircon-type compounds is rather limited.

Within the equation 3.2 the T^{4+} cation involved is usually Si and this substitution mechanism is called thorite or huttonite substitution, after the name of the two natural polymorphs of $ThSiO_4$: huttonite is the monazite-type, while thorite is the zircon-type mineral. A complete solid solution is known to occur among xenotime-(Y) and thorite, as well as among monazite-(Ce) and huttonite (Shelyug et al.

2021; Clavier et al. 2011; Mesbah et al. 2016). Equation 3.3, on the other side, is the only characterized by the occurrence of vacancies as charge-compensating mechanism. When the *T*-site is occupied by a pentavalent cation, as As and P, the REE*T*O_4 is electroneutral and characterized by no vacancies. On the other hand, if the *A*-site is occupied by a tetravalent cation, as a result, the occupancy of the *A*-site results reduced by $1/4$. The possible solid solutions are rather well known from several studies focused on either synthetic compounds or minerals. Immobilization of actinides in monazites is rather well-studied, being monazite a suitable waste form for actinides. In addition, monazite-(Ce) is pointed as one of the main resources of actinides (*e.g.*, Breiter and Förster 2021). Therefore, the solid solution among the monazites *sensu stricto* and the actinide-bearing *AT*O_4, according to the equation 3.1 and equation 3.2, have been object of a multitude of both experimental and theoretical studies.

The cheralite solid solidution has been studied by different authors and several synthesis techniques were developed (*e.g.*, Glorieux et al. 2009; Montel et al. 2006). According to the principles of cheralite substitution equation 3.1 synthesis experiments have been conducted, using La, Ce, Pr and Nd. Natural, complete solid solution monazite-(Ce)–cheralite has been found in the Podlesí Granite System, Czech Republic (Breiter and Förster 2021). For the best of our knowledge no studies have been carried out about the solid solution in the REEAsO_4–$Ca_{0.5}Th_{0.5}SiO_4$ system.

Unlike equation 3.1, equation 3.2 is important for explaining the presence of tetravalent cations within both monazite- and zircon-type compounds. In this case, the charge-compensating mechanism is the inclusion of tetravalent cations in the *T*-site, leading to an equal molar proportion of A^{4+} and T^{4+}. Among such solid solutions, Th is more common than U in monazite-type minerals. Huttonite-monazite-(Ce) solid solution occurring in nature has been described by several authors (Förster 1998; Della Ventura et al. 1996;). Within such solid solutions, the huttonite component is generally lower than 30 mol. % (*e.g.*, Della Ventura et al. 1996). However, Förster (1998) found an amount of ThO_2 exceeding 41.8 wt. % (corresponding to ~0.43 apfu of Th when the formula of the *AT*O_4 is calculated on the basis of 4 oxygen atoms), even though such an occurrence might be rather rare. Concerning synthesis products, a complete solid solution has been observed among $ThSiO_4$ and the two monazite-type compounds $LaPO_4$ and $CePO_4$ (Peiffert and Cuney 1999; Hikichi et al. 1978). Regarding the solid solution among synthetic $USiO_4$ and $LaPO_4$, an incomplete solubility of U has been identified, corresponding to ~0.13 apfu of U (Montel et al. 1999).

Few studies regarding the miscibility among zircon-type REE-bearing phosphates and Ac-bearing silicates have been carried out. In principle, Mesbah et al. (2016) and Shelyug et al. (2021) found, among $ErPO_4$ and $ThSiO_4$, a complete solid solution that can be produced through hydrothermal

synthesis. For the best of our knowledge, studies concerning the solid solution in the $USiO_4$-YPO_4 series have never been conducted. The solid solution system thorite–coffinite (*i.e.*, the zircon type $USiO_4$)–zircon–xenotime-(Y) has been studied by Förster (2006) within Variscan granites. In most cases, such solid solutions are hydrated minerals, likely metastable. In addition, Förster (2006) defined that the solid solution among xenotime-(Y) and Ac-bearing silicates (thorite and coffinite) is almost complete. Similarly, the solid solution among Ac-bearing silicates and zircon is complete, while the solid solution among xenotime-(Y) and zircon is also possible although it seems rather rare. Synthetic zircon-type arsenates doped with actinides have never been studied. On the other side, such a solid solution has been studied in minerals by Ondrejka et al. (2008) and are usually described as As-thorite or Th-chernovite-(Y). In detail, such solid solutions among chernovite-(Y) and thorite seems frequently stabilized by a certain amount of P within the *T*-site. Förster et al. (2011) found As-rich thorites with an As content up to 0.36 apfu in granitic cupola of Zinnwald, close to the Germany-Czech Republic border. The coffinite samples belonging to the same site are generally characterized by a lower As-content, when compared to thorite (lower than ~0.16 apfu). In addition, a certain amount of As in thorite has been described by Breiter et al. (2009) in the Hora Svaté Kateřiny granite, permeated by As-rich water. It is worth mentioning that the zircon from the same granite shows an As content always under ~0.1 apfu. The presence of a limited solid solution among zircon and chernovite-(Y) is probably related to smaller ionic radius of the *A*-site cation in zircon (ionic radius of Zr=0.98 Å), compared to Y (ionic radius of Y=1.159 Å), after Shannon et a. (1970).

Chapter 4

4 Experimental techniques

A brief outline about the experimental techniques used to carry out the present study is discussed in the current section. Particular attention in this devoted to unconventional experimental settings and to the devices used to allow non ambient temperature and pressure conditions.

4.1 Non-ambient studies in X-ray diffraction

Non ambient experiments can be ascribed to two different, major systems: *ex situ* and *in situ* and experiments. The first one is mostly applied to understand the phase associations at varying pressure and temperature conditions and it is based on the assumption that the retrograde reactions are avoided by a fast cooling (quenching) or removal of pressure. Occurrence of non-ambient polymorphs can be thus maintained even under ambient pressure and temperature. The latter finds its major application in describing the compressional and expansive behavior of minerals. In the context of the present study, the devices to allow high pressure and high temperature conditions are be coupled with an X-ray diffractometer, either in a conventional or synchrotron X-ray source experimental setup.

4.1.1 High pressure transmitting devices used in situ in X-ray diffraction

Several devices are used to achieve high-pressure conditions and a compete outline of such pressure devices is reported in Anbukumaran et al. (1994), Liebermann (2011) and Bassett (2009). Such devices are used to synthesize compounds stable under high-pressure or combined H*P*–H*T* conditions. In engineer, several elastic properties of solids are obtained by means of presses. The study of the atomic structural response of a material is often carried out by means of a pressure-transmitting device couple with any kind of spectroscopic device (*e.g.*, a diffractometer, a Raman-spectrometer *etc*.). In 1958, Vharlie Weir developed the first, primitive diamond anvil cell (DAC) marking a turning point in the structural studies of solid matter under high pressure. Van Valkenburg then developed the DAC, by adding the gasket and the pressure transmitting medium (Bassett 2009).

In a modern DAC, the sample, along with the pressure calibrant, is placed in the so-called pressure chamber, a cylindrical hole in a metal foil, placed between the culets of two diamond anvils. The two anvil culets define the top and the bottom surfaces of the pressure chamber. The hydrostatic conditions within the pressure chamber are allowed by the so-called pressure transmitting media. The increase of pressure is allowed by reducing the distance between the two diamond flat surfaces, resulting in a plastic deformation of the gasket in between. The pressure is thus transmitted to the pressure media and consequently to the sample and pressure calibrant. The main components of a DAC are briefly outlined in this section as following.

Backing plates

The backing plates constitute the support of the anvil diamonds and all the other DAC components. The first DAC specimens were characterized by backing plates made from Be, which is practically transparent to X-ray radiation. Such backing plates have the disadvantage that Be is toxic and also its mechanical strength drops significantly under high temperature conditions, with obvious disadvantages during combined H*T*–H*P* experiments. Nowadays, the backing plates are made of tungsten or boron carbide, with a high mechanical strength under high temperature. On the other hand, the support on the back of the diamond is limited if compared to the backing plates in Be.

Diamonds

Diamonds currently used in DACs are cut in the so-called Drukker standard design cut, which has been pointed as the most effective shape, due to its superior mechanical strength in the designed setting. The usage of diamonds as anvil material represented rather important turning point for several reasons. In the first place, diamonds are almost transparent to both X-ray and visible light, that lead to a rather easy sample preparation and analysis. Diamonds do not absorb the incident beam and their rather low scattering power (*e.g.*, Brown et al. 2006) scarcely affect the background signal during a spectroscopic measurement. In addition, diamond is the hardest known compound and has a rather low thermal expansion. Diamond anvils used for X-ray diffraction studies weights approximately ~0.2 grams, have a thickness between 1.5 and 2 mm and a culet size variable from 3 mm to 400 μm (Dunstan and Spain 1989; Miletich et al. 2000). The design of the diamond, as the size of the culets influences the maximum pressure reachable within the pressure chamber.

Gasket

The gasket is the metal foil that deforms plastically in between the diamond anvils, yielding to a hydrostatic pressure. The gasket prevents to diamonds to contact each other, hosts the pressure chamber and, eventually, plays a paramount role in transmitting the pressure to the pressure chamber

itself. The metal foil can be made by different materials including steel, rhenium and tungsten. The thickness of the gasket is few hundreds of microns thick (~200 μm-250 μm).

Before the high-pressure experiment, the gasket has to be pre-indented with the diamond anvil culets by closing the DAC before the drilling of the pressure chamber. The gasket is thus thinned to a thickness of few tens of microns. The pre-indentation has the aim to increase the maximum pressure achievable during the experiment. After the pre-indentation, the pressure chamber is drilled within the center of the pre-indented area. The pressure chamber is obtained by means of spark or mechanical erosion alternatively. The size of the drilled hole defines, along with the diamond design, the maximum pressure achieved during the experiment (Miletich et al. 2000).

Pressure transmitting fluids

As mentioned above in this section, pressure transmitting media are responsible to transmit the uniaxial stress, applied through the diamonds, to the sample and pressure calibrant in hydrostatic regime. The pressure, through the pressure transmitting medium is transmitted to both the sample and the pressure calibrant. The primitive DACs did not contain any pressure fluid, which lead to the transmission of non-hydrostatic stress conditions and, consequently, to unreliable compressibility values. In general, fluid materials are used, although the application of rather "soft" solid compounds, as NaCl, KCl and KBr has been applied (Miletich et al. 2000). Several fluids and solutions have been developed as pressure media. Fluid compounds exhibit hydrostatic behavior only in limited to a pressure range. Such a limit is different for different compounds and solutions and the hydrostatic limit for usual pressure transmitting media are reported in Table 4.1 after Takemura (2001) and Klotz et al. (2009a). Usually, pure liquids crystallize at low pressure and solutions are thus widely used. Ethanol-methanol 4:1 mixture and methanol-ethanol-water (*m.e.w.*) 16:3:1 are among the most commonly used pressure transmitting media. Moreover, under certain circumstances, as highlighted in Klotz et al. (2009b), the hydrostatic limit of pressure transmitting media can be pushed to higher pressure by heating.

Table 4.1: hydrostatic limits for several pressure transmitting media tested by Takemura (2001) and Klotz (2009). It is worth mentioning that neon hydrostatic limit is rather complex. After 15 GPa, neon shows the first signs of non-hydrostatic behavior, although the deviation from elasticity remains very small even at pressure exceeding 50 GPa.

Medium	Hydrostatic limit (GPa)
4:1 methanol-ethanol	9.8
16:3:1 methanol-etnaol-water	10.5
Anhydrous 2-prponol	4.2
Nitrogen	3.0
Silicon-oil viscosity 0.65 sSt	0.9
Silicon-oil viscosity 37 cSt	0.9
helium	50
argon	10
neon	>15

Pressure calibrant

The most widespread pressure calibrant are undoubtedly the ruby spheres. Ruby are Cr-doped α-Al_2O_3 spheres, which, under excitement with the proper incident radiation, emits light. The wavelength of such fluorescent emission is dependent on the pressure applied to the calibrant. The excited ruby spheres emitted two characteristic radiations, the so-called R_1 and R_2, corresponding to the wavelengths λ_1~694.2 nm and λ_2~692.8 nm. The wavelength of both R_1 and R_2 shift with pressure changing. A first determination of the relationship between the measured wavelength and pressure has been carried out by Barnett et al. (1973) and then Piermarini et al. (1975). Eventually, the semiempirical linear relation defined by Mao et al. (1986) has been described as:

$$P_{T0} = 1904\left[\left(\frac{R_i}{R_{i0}}\right)^B - 1\right]/B \qquad (4.1)$$

Where R_i defines the measured wavelength, R_{i0} stands for the measured wavelength under room pressure, while B stands for a coefficient dependent on the experiment conditions. In detail, B=7.665 in case of hydrostatic conditions and B=5 in non-hydrostatic conditions. Mao et al. (1986) determined for ruby fluorescence, a pressure uncertainty ranging between 0.05 GPa and 0.1 GPa.

Unfortunately, the main drawback in using ruby pressure calibrant is the dependance of the wavelength of the R_i radiations with temperature. Miletich et al. (2000) calculated that an increasing in temperature of 6 K causes a shift in wavelenght corresponding to a change in pressure ΔP=0.1 GPa. A suitable alternative internal standard that can be successfully applied in case of combined

H*P*–H*T* conditions is the known *P*-*V*-*T* EoS of the standard itself. By measuring the unit-cell volume of the internal standard through X-ray diffraction and determining temperature with an alternative method, defining the pressure is thus possible.

***P*-generating mechanisms**

In general, as mentioned above in this section, the pressure is increased when the distance among the two backing plates and, consequently, the diamonds are pushed closer. Two alternative mechanisms are generally used: 1) screw-bolts mechanism and 2) circular membrane. The first one consists in pushing together the backing plates by tightening screws. The screws are organized in pairs, in order to attain a homogeneous load. The membrane system, on the other side, provokes a relative movement of a backing plate close to the other, obtained by pushing air into the membrane itself. Such a system presents several advantages, including the possibility to control the compression by a remote system, a more homogeneous load, which determines faster experiments when compared to other *P*-generating mechanisms.

4.1.2 High temperature transmitting devices used in situ in X-ray diffraction

The first devices used to carry out high temperature *in situ* studies on crystalline compounds are dilatometers. Dilatometers are used, in general, to obtain the thermal expansion of a homogeneous polycrystalline or amorphous material (*e.g.*, ceramic materials). Diffractometric studies have been coupled with high temperature devices rather recently. The most common heater is represented by the gas blower device, although other methods involving laser heating may be used. In general, a gas blower consists in a furnace that expels the gas (in general N_2) that is heated by a coil

High-temperature single crystal X-ray diffraction experiments

In situ single crystal X-ray diffraction experiments reported in this study have been carried out by means of a Stoe diffractometer coupled with a nitrogen-flow gas blower furnace (Figure 4.1d). The sample, within this experimental setting, is a single crystal (the maximum size of the crystal ranges from ~15 μm to ~200 μm) or a powder material contained in a SiO_2 glass capillary. The heating system consists in a furnace which provides a constant flux of hot N_2 gas. The furnace operates between room temperature and the upper limit is ~800° C. The temperature is continuously measured by an online system, in order to control the heating system. The detector consists of a flat image plate detector. The temperature calibration had been previously conducted using the decomposition reactions of K_2SO_4 and K_2CrO_4 embodied into glass capillaries. Further details about the experimental setup and the calibration strategy are reported in Stoe and Cie (2004) and in Krüger and Breil (2008).

4.1.3 Combined H*P*–H*T* devices for in situ studies

Several methods have been developed in order to study the response of a sample when both temperature and pressure are increased. Among the others, the development of X-ray diffraction multi-anvil device has been carried out (*e.g.*, Le Godec et al. 2009). On the other hand, the most diffuse system is the application of a DAC modified for high-temperature measurement. The heating system can be provided by a resistor, which for Ohm effect or by laser heating. Furter details concerning the combined H*P*–H*T* device used in the present study are reported below, in section 4.2.2.

4.2 Synchrotron radiation facilities

Synchrotron radiation was firstly observed in 1947 at the General Electric synchrotron in the USA. Within the past three decades, synchrotron have become more and more important facilities in the study of material science, physics, chemistry, Earth science and biology, representing a desiderable alternative X-ray source to common X-ray tubes. Synchrotrons provide continuous, white radiation and the produced electromagnetic phenomenon is known as “synchrotron light”. Synchrotron radiation facilities are storage rings where electrons are forced in a circular motion due to the action of magnetic fields perpendicular (bending magnets) to direction of motion of the particles. The radiation is produced after the changing in trajectory (acceleration) of the electrons, travelling at a speed close to the speed of light, in the vacuum pipes (*e.g.*, Mobilio et al. 2016).

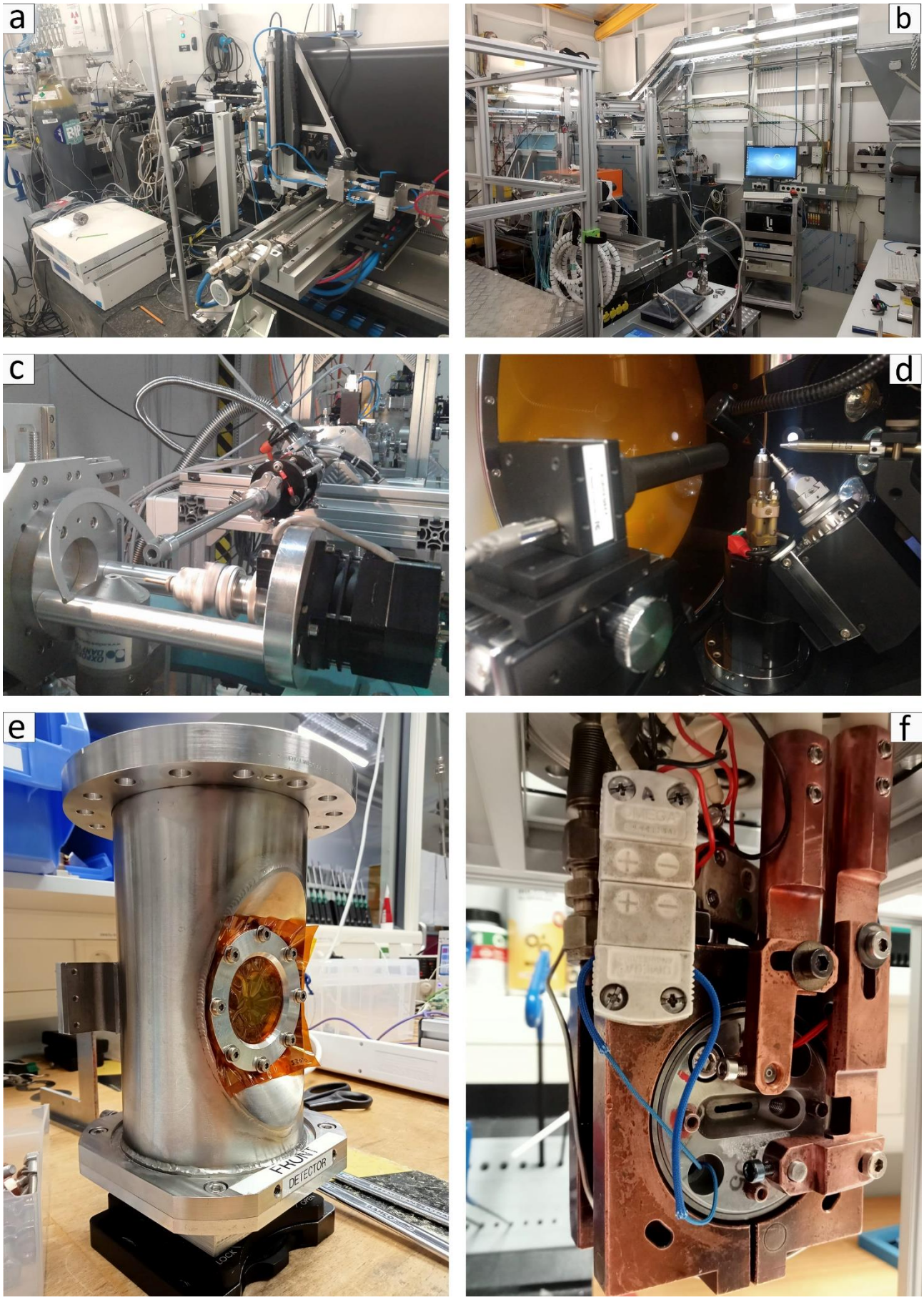
a
b
c
d
e
f
FRONT
DETECTOR

Figure 4.1: some of the devices and labs used in the present study; **(a)** experimental hutch of the ID15b beamline (ESRF); **(b)** experimental hutch of the p02.2 extreme conditions beamline (PETRA-III); **(c)** experimental hutch of the MCX beamline (Elettra sincrotorne Trieste); **(d)** Stoe diffractometer at the Institute of Minerlaogy and Petrology (Innsbruck); (e,f) details of the resistive DAC used in the present research.

The electrons enter the circular path after they are accelerated in a linear accelerator after their energy reaches millions of electron volts (MeV). Four different components control the flux of electrons: the wiggler, the undulator, the bending magnets and the RF cavities. The electrons make a polygonal path, made by several linear sectors (wigglers and undulators are placed in these sections) and the connection among those parts is achieved by the bending magnets. In the linear sectors, radio frequency (RF) cavities are installed to accelerate the particles and drive the emitted light to the experimental hutch. Wigglers and undulators are multipole magnets known as injection devices (ID) and are installed along the straight parts of the synchrotron. The ID affect the trajectory of the electron beam and also increase the brightness of the light emitted, although no change in the overall direction of the electron beam itself occurs. Among the main reasons for the success of synchrotron radiation facilities, the high intensity of the primary source, the continuous spectrum of the emitted radiation and the small cross section of the incident beam are worth of mention, along with an overall relatively cheap maintenance expenses. For further information concerning the synchrotron radiation facilities and synchrotron radiation, see the complete review issued by Mobilio et al. (2016).

4.2.1 European Synchrotron Radiation Facility (ESRF), Grenoble (France)

The ESRF has been constructed as the cooperation among 12 European countries (France, Germany, Italy, United Kingdom, Russia, Belgium, the Netherlands, Denmark, Finland, Norway, Sweden, Spain and Switzerland) and it has been operating since 1994. After its inauguration, in 1998, the ESRF was featured with 30 beamlines, then increased to 44 in 2017. Currently, the ESRF storage ring operates at about ~6 GeV and it is made by 32 straight sections; among the straight sections, 29 host IDs. Further information is reported in Haensel (1992) and on the ESRF website available at https://www.esrf.fr/cms/live/live/en/sites/www/home.html.

ID15 beamline

Most of the high-pressure experiments reported in the framework of this project have been carried out at the ID15 beamline. The ID15 beamline (the former ID09 beamline), is optimized for *in situ* single crystal high pressure experiments. The goniometer is mounted on a system of three translation stages, which allow an accurate and stable three-axis centering of the sample within the DAC. Centering the gasket hole and sample are performed by a series of scans of the pressure chamber in the plane perpendicular to the direction of the incident X-ray beam. Such scans are based on the

absorption of the incident beam by the sample and the gasket, which reduce the intensity of the primary beam itself, that is detected by a diode device. An usual data collection consists in a step-wise rotation along the ω-axis, the vertical axis perpendicular to the direction of the incident beam. The use of a membrane device as *P*-driven system is controlled from the control hutch. The diffraction signal is collected with a Dectris Eiger2 9M CdTe detector. The beamline is features with an incident beam of ~30 keV. Further information pertaining the experimental setup of the beamline is reported in detail by Merlini and Hanfland (2013). In section 7.4 are reported the main features of the experimental setup for ID15B beamline, along with other beamlines features relevant for the present study.

4.2.2 DESY-Petra III, Hamburg (Germany

The national, German synchrotron (Deutsches Elektronen-Synchrotron od DESY). has been operating since 1964 and has a quite complex history. Indeed, after the construction of the synchrotron, several storage rings accelerators have been used as light source (DESY, DORIS II, DORIS III, Petra III). Currently, the source of radiation is Petra III, a third-generation synchrotron, characterized by an energy of ~6 GeV (Haibel et al. 2008). Nowadays, Petra III is featured with 19 independent IDs and 30 experimental hutches capable to operate at the same time. Further details are reported in the issue by Balewski et al. (2004).

P02.2 extreme conditions beamline and combined H*P*–H*T* device

As the ID15B, the P02.2 extreme conditions beamline is optimized for high pressure and combined H*P*–H*T* single crystal measurements. The experimental setting for the conventional high pressure experiments is close to the setup reported above for ID15B and is thus not described in detail. The detector type, energy of the incident beam and other experimental details are reported in section 7.4. For a deep description of the beamline experimental setup, see Liermann et al. (2015).

In Figure 4.1, is reported the device used in the P02.2 extreme conditions beamline to achieve combined H*P*–H*T* experiments. A membrane system allows the increasing of pressure within the pressure chamber. Increasing of temperature is provided by the resistive heating system made by an electric circuit that heats the gasket and the diamonds by means of a graphite foil, which is the resistive component. In order to avoid contact between the heating system and the other conductive components, the entire electric circuit is coated with insulating materials. Two thermocouples, in contact with the two diamond anvils, control the temperature. The current intensity of the heating circuit is controlled and changed manually with a remote panel on the basis of the measurement of the thermocouples and the target temperature. In general, the two thermocouples measure slightly

different temperatures and such difference increases along with absolute temperature. The combined H*P*–H*T* is carried out assuming that the temperature within the pressure chamber is between the temperatures measured by the thermocouples. The main bottleneck of the system concerns the usual huge uncertainty of the temperature measured within the DAC, due to difference of the two independent temperature measurements, which can differ from several tens of K. In addition, the temperature influences the pressure within the pressure chamber and is thus rather complex, if not impossible, to perform isobaric high-temperature ramps. For further details about this experimental setup see section 7.4.

4.2.3 Elettra Sincrotrone Trieste, Basovizza (Italia)

As ESRF and Petra III, the Elettra synchrotron is a third generation synchrotron. The electrons are injected into the electron circuit by a linac, which provides electrons at ~2.4 GeV. It was completed in 1993 and currently hosts 26 beamlines, dedicated to X-ray diffraction, microscopy, tomography and spectroscopy. An outline of the Elettra synchrotron is reported in Lausi et al. (2015)

MCX beamline

The MCX beamline is optimized for *in situ* powder X-ray diffraction under either high or low temperature conditions. The energy of the incident beams ranges between ~6 keV to ~22 keV. The experimental setup, in Debye-Scherrer geometry, consists in a Huber 4 circle diffractometer in a full circle configuration. The samples are powdered materials, contained in a SiO_2 glass capillary and its centering is allowed by a three axes motors. During the data collection, to achieve a better statistic, the sample rotates along the φ-axis. The diffraction signals are collected with a high-count rate fast scintillator detector.

The non ambient conditions can be achieved by means of either a gas blower or a cryostat, which can be alternatively used to attain temperature between 100 K and 1273 K. In alternative, the heating can be achieved by means of a furnace, operating in a vacuum chamber. When the furnace is used, in place of the scintillator detector, a image plate detector is mounted. Further details about the MCX beamline are reported in Plaisier et al. (2017), Lausi et al. (2015).

Xpress beamline

The general setup of the Xpress beamline is similar to the one described above for the ID15B beamline. The detector model, and the energy of the incident X-ray beam are reported in section 7.4.

Chapter 5

5 Equation of State and modelling of physical behavior under non-ambient conditions

When a material undergoes to change in pressure and temperature, it undergoes to a change in volume as well. An equation of state (EoS) is any thermodynamic equation that puts in relation an intensive variable (*i.e.*, temperature and pressure) with volume. The perfect gas equation of state, for instance, issued in 1834 by Émile Clapeyron, combing the Boyle's and Charles's laws, represent a turning point in the description of the behavior of a gas in response to variations in response to temperature and pressure. The perfect gas equation is defined in its simplest form as $PV = nRT$ (5.1). In equation 5.1, *P*, *T* and *V* stand for pressure, temperature and volume respectively, *n* is the Avogadro number, while R is the universal gas constant [J/mol·K].

In case of solid-state materials, it is important to highlight that no overall-accepted EoS exists, although different empirical and semi-empirical equation have been drawn to model the volume variation in response to changing in pressure and temperature. It is worth to mention that, even though these parameters are often described as scalar units, they are dependent on directions and crystal anisotropy and thus they are tensorial properties.

5.1 High-pressure behavior

The relation among mechanical stress and strain within solids is historically defined by the linear theory of elasticity or Hooke's law. The Hooke's law represent a rather straightforward tool and it is in general applied to isotropic materials, characterized by equal properties in all the directions and in its simple, general form it states that:

$$\sigma = E\varepsilon \qquad (5.1)$$

where σ is the applied mechanical stress, ε is the deformation, while E stands for the elastic coefficient. The coefficient E in equation 5.1 has the units of [N/m^2], the same as stress, being deformation a unitless parameter. Another fortunate constitutive relation that can be described for isotropic materials is:

$$\begin{bmatrix} \varepsilon_{xx} \\ \varepsilon_{yy} \\ \varepsilon_{zz} \\ \varepsilon_{yz} \\ \varepsilon_{zx} \\ \varepsilon_{xy} \end{bmatrix} = \begin{bmatrix} \frac{1}{E} & -\frac{\nu}{E} & -\frac{\nu}{E} & 0 & 0 & 0 \\ -\frac{\nu}{E} & \frac{1}{E} & -\frac{\nu}{E} & 0 & 0 & 0 \\ -\frac{\nu}{E} & -\frac{\nu}{E} & \frac{1}{E} & 0 & 0 & 0 \\ 0 & 0 & 0 & \frac{1}{G} & 0 & 0 \\ 0 & 0 & 0 & 0 & \frac{1}{G} & 0 \\ 0 & 0 & 0 & 0 & 0 & \frac{1}{G} \end{bmatrix} \begin{bmatrix} \sigma_{xx} \\ \sigma_{yy} \\ \sigma_{zz} \\ \sigma_{yz} \\ \sigma_{zx} \\ \sigma_{xy} \end{bmatrix} \quad (5.2)$$

Where E is the Young's modulus, G is the shear modulus, while v is the Poisson's ratio often used in engineer. The Young's, shear and Poisson's modulus represent the compressive/tensile stiffness, the shear stiffness and the deformation perpendicular to the direction of loading, respectively.

The stress tensor can be described as the first derivative of the energy density function with respect to the strain tensor, according to equation:

$$\sigma_{ij} = \frac{\partial w}{\partial \varepsilon_{ij}} \quad (5.3)$$

Where w is the strain energy density function. The deformation of a crystalline, solid material under compression can be described in a much more complete way by the compliance and stiffness tensor according to the equations:

$$\sigma = C\varepsilon, \text{ or } \sigma_{ij} = C_{ijkl}\varepsilon_{kl}, \quad (5.4)$$

$$\varepsilon = S\sigma, \text{ or } \varepsilon_{kl} = S_{ijkl}\sigma_{ij}, \quad (5.5)$$

where C (C_{ijkl}) and S (S_{ijkl}) stand for the compliance and stiffness tensors. The stiffness tensor can be described as the inverse of the compliance tensor and *vice versa*. The number of independent components in elasticity tensor is 81, being both the stress and strain tensors two 3×3 matrixes. Due

to the symmetry of the stress tensor, the relation $C_{ijkl} = C_{jikl}$ is valid and the number of the independent component drops from 81 to 54. In the same way, the symmetry of the strain tensor, as well as the fact that the strain energy density function does not change if the *ij* and *kl* are inverted, resulting in a drop of the independent terms down to 21. Therefore, both stiffness and the compliance tensors can be described by two symmetric 6×6 matrixes, while stress and strain can be both described with a 6×1 matrixes as following:

$$\begin{bmatrix}\sigma_{11}\\ \sigma_{22}\\ \sigma_{33}\\ \sigma_{23}\\ \sigma_{31}\\ \sigma_{12}\end{bmatrix} = \begin{bmatrix}c_{1111} & c_{1122} & c_{1133} & c_{1123} & c_{1131} & c_{1112}\\ c_{2211} & c_{2222} & c_{2233} & c_{2223} & c_{2231} & c_{2212}\\ c_{3311} & c_{3322} & c_{3333} & c_{3323} & c_{3331} & c_{3312}\\ c_{2311} & c_{2322} & c_{2333} & c_{2323} & c_{2331} & c_{3312}\\ c_{3111} & c_{3122} & c_{3133} & c_{3123} & c_{3131} & c_{3112}\\ c_{1211} & c_{1222} & c_{1233} & c_{1223} & c_{1231} & c_{1212}\end{bmatrix}\begin{bmatrix}\varepsilon_{11}\\ \varepsilon_{22}\\ \varepsilon_{33}\\ 2\varepsilon_{23}\\ 2\varepsilon_{31}\\ 2\varepsilon_{12}\end{bmatrix} \quad (5.6)$$

and

$$\begin{bmatrix}\varepsilon_{11}\\ \varepsilon_{22}\\ \varepsilon_{33}\\ 2\varepsilon_{23}\\ 2\varepsilon_{31}\\ 2\varepsilon_{12}\end{bmatrix} = \begin{bmatrix}s_{1111} & s_{1122} & s_{1133} & 2s_{1123} & 2s_{1131} & 2s_{1112}\\ s_{2211} & s_{2222} & s_{2233} & 2s_{2223} & 2s_{2231} & 2s_{2212}\\ s_{3311} & s_{3322} & s_{3333} & 2s_{3323} & 2s_{3331} & 2s_{3312}\\ 2s_{2311} & 2s_{2322} & 2s_{2333} & 4s_{2323} & 4s_{2331} & 4s_{3312}\\ 2s_{3111} & 2s_{3122} & 2s_{3133} & 4s_{3123} & 4s_{3131} & 4s_{3112}\\ 2s_{1211} & 2s_{1222} & 2s_{1233} & 4s_{1223} & 4s_{1231} & 4s_{1212}\end{bmatrix}\begin{bmatrix}\sigma_{11}\\ \sigma_{22}\\ \sigma_{33}\\ \sigma_{23}\\ \sigma_{31}\\ \sigma_{12}\end{bmatrix}. \quad (5.7)$$

It is worth to mention that the independent terms that can be defined for the stiffness *C* (C_{ijkl}) and compliance tensors *S* (S_{ijkl}) are dependent on the crystal symmetry. For triclinic materials, 21 terms of the tensors can be defined, three can be defined for cubic crystalline materials, while only two independent terms are required to describe the behavior of non-crystalline isotropic materials. In order to ease the expression of both the compliance and stiffness tensors, the so-called Voight notation can be introduced. In Voight notation, the double indices are substituted by a single index running from 1-6, following the criteria: $s_{ijkl} = 1 \cdot s_{nm}$ if *m* and *n* are 1, 2, 3; $s_{ijkl} = \frac{1}{2} \cdot s_{nm}$ if *m* or *n* are 4, 5, 6; $s_{ijkl} = \frac{1}{4} \cdot s_{nm}$ if *m* or *n* are 4,5,6. Therefore, the stress and strain tensor, become respectively:

$$\sigma_{ij} = \begin{pmatrix}\sigma_{11} & \sigma_{12} & \sigma_{13}\\ \sigma_{21} & \sigma_{22} & \sigma_{23}\\ \sigma_{31} & \sigma_{32} & \sigma_{33}\end{pmatrix} \rightarrow \sigma = \begin{pmatrix}\sigma_1 & \sigma_6 & \sigma_5\\ \sigma_6 & \sigma_2 & \sigma_4\\ \sigma_5 & \sigma_4 & \sigma_3\end{pmatrix} \quad (5.8)$$

and

$$\varepsilon_{kl} = \begin{pmatrix} \varepsilon_{11} & \varepsilon_{12} & \varepsilon_{13} \\ \varepsilon_{21} & \varepsilon_{22} & \varepsilon_{23} \\ \varepsilon_{31} & \varepsilon_{32} & \varepsilon_{33} \end{pmatrix} \rightarrow \varepsilon = \begin{pmatrix} \varepsilon_1 & \frac{1}{2}\varepsilon_6 & \frac{1}{2}\varepsilon_5 \\ \frac{1}{2}\varepsilon_6 & \varepsilon_2 & \frac{1}{2}\varepsilon_4 \\ \frac{1}{2}\varepsilon_5 & \frac{1}{2}\varepsilon_4 & \varepsilon_3 \end{pmatrix}. \quad (5.9)$$

In addition, some scaling factors have been introduced for convenience. Thus, for instance, $\varepsilon_{23} = \frac{1}{2}\varepsilon_4$. Such a transformation yields to $\varepsilon_1 = s_{11}\sigma_1 + s_{16}\sigma_6 + s_{15}\sigma_5 + s_{14}\sigma_4 + s_{12}\sigma_2 + s_{13}\sigma_3$. In Voight notation, the stiffness and compliance tensors are thus defined as:

$$\begin{bmatrix} \sigma_1 \\ \sigma_2 \\ \sigma_3 \\ \sigma_4 \\ \sigma_5 \\ \sigma_6 \end{bmatrix} = \begin{bmatrix} c_{11} & c_{12} & c_{13} & c_{14} & c_{15} & c_{16} \\ c_{21} & c_{22} & c_{23} & c_{24} & c_{25} & c_{26} \\ c_{31} & c_{32} & c_{33} & c_{34} & c_{35} & c_{36} \\ c_{41} & c_{42} & c_{43} & c_{44} & c_{45} & c_{46} \\ c_{51} & c_{52} & c_{53} & c_{54} & c_{55} & c_{56} \\ c_{61} & c_{62} & c_{63} & c_{64} & c_{65} & c_{66} \end{bmatrix} \begin{bmatrix} \varepsilon_1 \\ \varepsilon_2 \\ \varepsilon_3 \\ \varepsilon_4 \\ \varepsilon_5 \\ \varepsilon_6 \end{bmatrix} \quad (5.10)$$

and

$$\begin{bmatrix} \varepsilon_1 \\ \varepsilon_2 \\ \varepsilon_3 \\ \varepsilon_4 \\ \varepsilon_5 \\ \varepsilon_6 \end{bmatrix} = \begin{bmatrix} s_{11} & s_{12} & s_{13} & s_{14} & s_{15} & s_{16} \\ s_{21} & s_{22} & s_{23} & s_{24} & s_{25} & s_{26} \\ s_{31} & s_{32} & s_{33} & s_{34} & s_{35} & s_{36} \\ s_{41} & s_{42} & s_{43} & s_{44} & s_{45} & s_{46} \\ s_{51} & s_{52} & s_{53} & s_{54} & s_{55} & s_{56} \\ s_{61} & s_{62} & s_{63} & s_{64} & s_{65} & s_{66} \end{bmatrix} \begin{bmatrix} \sigma_1 \\ \sigma_2 \\ \sigma_3 \\ \sigma_4 \\ \sigma_5 \\ \sigma_6 \end{bmatrix}. \quad (5.11)$$

The compliance tensor *S* can be divided into four major "quadrants" that are connected to specific relations among strain and stress. In detail, the four "quadrants" thus defined are:

$$S_{mn}^{A} = \begin{bmatrix} s_{11} & s_{12} & s_{13} & \cdots \\ s_{21} & s_{22} & s_{23} & \cdots \\ s_{31} & s_{32} & s_{33} & \cdots \\ \vdots & \vdots & \vdots & \ddots \end{bmatrix}; \quad (5.12)$$

$$S_{mn}^{B} = \begin{bmatrix} \ddots & \vdots & \vdots & \vdots \\ \cdots & s_{44} & s_{45} & s_{46} \\ \cdots & s_{54} & s_{55} & s_{56} \\ \cdots & s_{64} & s_{65} & s_{66} \end{bmatrix}; \quad (5.13)$$

$$S_{mn}^{C} = \begin{bmatrix} \cdots & s_{14} & s_{15} & s_{16} \\ \cdots & s_{24} & s_{25} & s_{26} \\ \cdots & s_{34} & s_{35} & s_{36} \\ \iddots & \vdots & \vdots & \vdots \end{bmatrix}; \quad (5.14)$$

$$S_{mn}^{D} = \begin{bmatrix} \vdots & \vdots & \vdots & \iddots \\ s_{41} & s_{42} & s_{43} & \cdots \\ s_{51} & s_{52} & s_{53} & \cdots \\ s_{61} & s_{62} & s_{63} & \cdots \end{bmatrix}. \qquad (5.15)$$

The S_{mn}^{A} upper left "quadrant" represents the part of the compliance matrix that describes the relationship between normal stress and normal strain; the lower right S_{mn}^{B} "quadrant" describes the relationship between shear stress and shear strain; on the other side, the two "diagonal" upper right and lower left "quadrants" (S_{mn}^{C} and S_{mn}^{D}) represent the relationship among normal stress and shear deformation and *vice versa*. Moreover, the stiffness and compliance tensor are related to the elastic coefficients and the Young's modulus, shear (rigidity) modulus and the Poisson's ratio mentioned above in this section. In detail in relation to the compliance tensor, the Young's modulus can be defined as $E = 1/s_{11}$, the Poisson's ratio can be described as $\nu = -s_{11}/s_{11}$, while the rigidity modulus is $\mathrm{G} = 1/s_{44}$. These three constitutive relations can be drawn only for isotropic bodies and the relation among them is given by:

$$G = E/2(1 + \nu). \qquad (5.16)$$

In case of isotropic compression, which is the peculiar strain compression condition important for the purpose of the present work, characterized by $\sigma_{ij} = 0$ when $i \neq j$ and $\sigma_1 = \sigma_2 = \sigma_3 = -\Delta P$, the strain tensor assumes the following form:

$$\sigma_{ij} = \begin{pmatrix} -\Delta P & 0 & 0 \\ 0 & -\Delta P & 0 \\ 0 & 0 & -\Delta P \end{pmatrix}. \qquad (5.17)$$

Consequently, the compliance (S_{mn}) tensors in Voight notation can be defined in the following simplified form:

$$\begin{bmatrix} \varepsilon_1 \\ \varepsilon_2 \\ \varepsilon_3 \\ \varepsilon_4 \\ \varepsilon_5 \\ \varepsilon_6 \end{bmatrix} = \begin{bmatrix} s_{11} & s_{12} & s_{13} & 0 & 0 & 0 \\ s_{21} & s_{22} & s_{23} & 0 & 0 & 0 \\ s_{31} & s_{32} & s_{33} & 0 & 0 & 0 \\ s_{41} & s_{42} & s_{43} & 0 & 0 & 0 \\ s_{51} & s_{52} & s_{53} & 0 & 0 & 0 \\ s_{61} & s_{62} & s_{63} & 0 & 0 & 0 \end{bmatrix} \begin{bmatrix} -\Delta P \\ -\Delta P \\ -\Delta P \\ 0 \\ 0 \\ 0 \end{bmatrix}. \qquad (5.18)$$

In case of crystalline compounds of orthorhombic symmetry or higher, only within the upper left "quadrant" the s_{mn} values are different from zero.

Under hydrostatic pressure conditions, the compressibility second-rank tensor β can be introduced, which describes the strain per unit pressure. The strain in a generic direction can be defined as $\varepsilon_1 = s_{11}\sigma_1 + s_{12}\sigma_2 + s_{13}\sigma_3 = -\Delta P(s_{11} + s_{12} + s_{13})$. Thus, $-\frac{\varepsilon_1}{\Delta P} = (s_{11} + s_{12} + s_{13})$, which yields to the classical definition of the compressibility as $\beta_1 = -\frac{1}{\Delta P}\frac{\Delta x_1}{x_1}$. Therefore, $\beta_1 = (s_{11} + s_{12} + s_{13}) = \beta_{11}$, while $\beta_6 = (s_{61} + s_{62} + s_{63}) = 2\beta_{21}$, due to the condition established by the Voight conditions. The general equation $\beta_i = s_{i1} + s_{i2} + s_{i3}$ is then defined and, and can be expressed as simple pressure and strain relation according to:

$$\beta_{ij} = \frac{\varepsilon_{ij}}{\Delta P} \qquad (5.19)$$

Compressibility has the units of the inverse of pressure [m^2/N]. It is in general more common to express the relationship among hydrostatic pressure and strain with the bulk modulus, which can be defined as the inverse of compressibility, according to the equation:

$$K = -\left(\frac{\partial P}{\partial V}\right)_T \rightarrow K = -\left(\frac{\partial P}{\partial V}\right)_T = \left(\frac{\Delta P}{\varepsilon_1 + \varepsilon_2 + \varepsilon_3}\right)_T \qquad (5.20)$$

The subscript *T* stands for its isothermal conditions. The bulk modulus has the dimensions of pressure, [N/m^2]. The bulk modulus can be defined in two different ways: the Reuss and Voight bulk moduli. The Reuss bulk modulus is defined as the bulk modulus calculated under homogeneous stress, while the Voight bulk modulus is calculated under homogeneous stress conditions. From a theoretical point of view, they are the same only for crystals belonging to the cubic crystal system. Within the present study, only the Reuss bulk modulus has been considered and it is therefore simply pointed as "bulk modulus" below, in the text. Moreover, from equation 5.20, one can determine that the bulk modulus can be derived from the combination of the linear compressibility along the three orthornormal directions of space. In addition, the bulk modulus depends on the applied stress (pressure) and its changing with pressure is described by its first and second derivative with respect pressure:

$$K_0 = -V_0\left(\frac{dP}{dV}\right)_{P=0} \rightarrow K'_0 = -\left(\frac{dK}{dP}\right)_{P=0} \rightarrow K''_0 = -\left(\frac{d^2K}{dP^2}\right)_{P=0} \qquad (5.21)$$

The bulk modulus can be directly derived from the X-ray diffraction experimental data, measuring the deformation of the crystal lattice coupled with hydrostatic pressure conditions. Several equations have been proposed to model the volumetric deformation under high pressure, each of them based on different assumptions (see Angel et al. 2014 for a review). Amongst them, the linear interpolation represents the simplest way to describe the compressional behavior of a compound and in general it

can be applied successfully only in relatively small temperature or pressure ranges, as well as for poor data sets. In the following section, the main EoS used to model the compression and expansion of the studied minerals are reported.

5.1.1 Murnaghan, Birch-Murnaghan EoS and evaluation of the *P-V* fit

The Murnaghan (1937) EoS defines a linear variation of bulk modulus with pressure according to the equation $K_{PT} = K_{OT} + K'_{OT}P$. Consequently, the relation between pressure and volume can be described by the two following equations:

$$\mathrm{V} = \mathrm{V_0}\left(1 + \frac{\mathrm{K'_{0T}P}}{\mathrm{K_{0T}}}\right)^{-1/\mathrm{K'}} \quad (5.22)$$

$$\mathrm{P} = \frac{\mathrm{K_{0T}}}{\mathrm{K'_{0T}}}\left[\left(\frac{\mathrm{V_0}}{\mathrm{V}}\right)^{\mathrm{K'}} - 1\right] \quad (5.23)$$

As pointed out by Freund and Ingalls (1989), the capability to express the Murnaghan EoS as simple function of both pressure and volume represents one of the bases for its success. In addition, the equation is characterized by $K''_{OT} = 0$ and it is accurate only for rather small compression (at volumetric deformation above $V/V_0 \sim 0.9$).

The "finite strain" Birch-Murnaghan EoS (BM-EoS) (Birch 1947) has become the most used EoS to model the compression of crystalline materials and it applied in the thermodynamic database of geologic importance (Holland and Powell 1998). The BM-EoS is an isothermal equation of state based on the assumption that the high-pressure strain energy of a solid can be expressed as a Taylor series in the Eulerian finite strain, defined as:

$$f_E = \left[(V_0/V)^{2/3} - 1\right]/2. \quad (5.24)$$

The BM-EoS allows to refine the isothermal bulk modulus (or compressibility coefficient) at ambient pressure conditions and its *P*-derivatives, obtained by means of a least-squared fitting refinement method. When truncated to the fourth order, the BM-EoS (BM4-EoS) is expressed as:

$$P = 3K_{0T}f_E(1 + 2f_E)^{5/2}\left[1 + \frac{3}{2}(K'_{OT} - 4)f_E + \frac{3}{2}\left(K'_{0T}K''_{0T} + (K'_{0T} - 4)(K'_{0T} - 3) + \frac{35}{9}\right)f_E^2\right]. \quad (5.25)$$

When truncated to the third order, the coefficient of f_E^2 becomes zero and the BM3-EoS results in a three-parameter EoS, that becomes, expressed as function of bulk modulus and its first derivative as:

$$\mathrm{K_{PT}} = \mathrm{K_{0T}}(1 + 2\mathrm{f_E})^{5/2}\left[1 + (3\mathrm{K'_{OT}} - 5)\mathrm{f_E} + \frac{27}{2}(\mathrm{K'_{0T}} - 4)\mathrm{f_E^2}\right] \quad (5.26)$$

and

$$\mathrm{K'_{PT}} = \frac{\mathrm{K_{0T}}}{\mathrm{K_{PT}}}(1 + 2\mathrm{f_E})^{5/2}\left[\mathrm{K'_{0T}} + \left(16\mathrm{K'_{OT}} - \frac{143}{3}\right)\mathrm{f_E} + \frac{81}{2}(\mathrm{K'_{0T}} - 4)\mathrm{f_E^2}\right]. \quad (5.27)$$

Within the BM3-EoS approximation, only V_0 and K_{P_0,T_0} and K'_{P_0,T_0} are refined. The value of K''_{0T} is fixed and given by the equation:

$$K''_{0T} = -\frac{1}{K_{0T}}\left[(3 - K'_{0T})(4 - K'_{0T}) + \frac{35}{9}\right]. \quad (5.28)$$

A further approximation is the truncation of the Taylor series down to the second order. When truncated to the second order (BM2-EoS) yields to $K''_{0T} = 4$ and the coefficient of f_E drops to zero. This yields to a two-parameters EoS, with only two refinable variables (V_0 and K_{P_0,T_0}). The BM2-EoS can be given by the following equation:

$$P = 3K_{P_0,T_0}\, fe\, (1 + 2fe)^{5/2}. \quad (5.29)$$

As the Murnaghan EoS, the BM-EoS is valid only for rather small compression, namely isotropic stress condition characterized by V/V_0>0.9.

The quality of the conduced fitting can be easily evaluated through the so-called f_e-F_e plot, which puts in relation the finite Eulerian strain (f_e) with the normalized pressure F_e (Angel et al. 2000). The normalized pressure is thus defined as following:

$$F_E = \frac{P}{3f_E(1 + 2f_E)^{5/2}} \quad (5.30)$$

And, consequently, the BM-EoS can be expressed as function of F_e as:

$$F_E = K_0 + \frac{3}{2}(K' - 4)f_E + \frac{3}{2}\left[K_0K'' + (K' - 4)(K' - 3) + \frac{35}{9}\right]f_E^2 \quad (5.31)$$

Equation 5.31 is a simple polynomial function of F_e in f_e. Plotting the experimental data, along with the BM-EoS resulted from the fitting, in a F_e-f_e field led to several features that can be used to describe the processed fitting. In principle, the intercept of the BM-EoS curve on the F_e axis represents the bulk modulus at ambient pressure conditions. In addition, the trend of the *fe-Fe* plot gives rather useful hints to define the order of truncation of the Taylor's series. In detail, a horizontal or sub-horizontal trend of the data suggests the application of a second-order truncation (BM2-EoS) of the Taylor's series. On the other side, a positive trend suggests a truncation on the third order (BM3-EoS), while a parabolic trend of the data lead to a fourth order truncation of the Taylor's series.

5.2 High-temperature behavior

The relation defined for the compressibility in section 5.1 can be also applied to a change in temperature ΔT, yielding to the thermal expansion tensor α_{ij}. The analogy among the compressibility and the thermal expansion can be expressed as following:

$$\varepsilon_{ij}^{Mechanical} = -\beta_{ij}\Delta P \rightarrow \varepsilon_{ij}^{Thermal} = \alpha_{ij}\Delta T. \quad (5.32)$$

In general, the thermal expansion coefficient α_{ij} is defined through the inverse relation that can be used for anisotropic materials:

$$\alpha_{ij} = \frac{1}{\varepsilon_{ij}}\left(\frac{\partial \varepsilon}{\partial T}\right)_P \quad (5.33)$$

The subscript P stands for isobaric conditions. The thermal expansion coefficient α_{ij} has the dimension [K^{-1}]. In general, the thermal expansion tensor α_{ij} is a symmetric second-rank 3×3 tensor:

$$\alpha_{ij} = \begin{pmatrix} \alpha_{11} & \alpha_{12} & \alpha_{13} \\ \alpha_{21} & \alpha_{22} & \alpha_{23} \\ \alpha_{31} & \alpha_{32} & \alpha_{33} \end{pmatrix}. \quad (5.34)$$

Thermal expansion is usually derived from experimental diffractometric data and, in the most general case, two independent sets of unit-cell parameters are obtained: one for the temperature T_1 and the other for the temperature T_2:

T_1: a_1, b_1, c_1, α_1, β_1, γ_1;

T_2: a_2, b_2, c_2, α_2, β_2, γ_2.

There are two different system to calculate the thermal expansion, known as the finite and the infinitesimal description of thermal expansion. According to the finite thermal expansion description, the terms of the thermal expansion tensor are expressed, for a triclinic crystal, as:

$$\alpha_{11} \approx \frac{1}{T_2 - T_1}\left(\frac{a_2 \sin\beta_2}{a_1 \sin\beta_1} - 1\right) \quad (5.35)$$

$$\alpha_{22} \approx \frac{1}{T_2 - T_1}\left(\frac{b_2 \sin\alpha_2 \sin\gamma_2^*}{b_1 \sin\alpha_1 \sin\gamma_1^*} - 1\right) \quad (5.36)$$

$$\alpha_{33} \approx \frac{1}{T_2 - T_1}\left(\frac{c_2}{c_1} - 1\right) \quad (5.37)$$

$$\alpha_{12} \approx \frac{1}{2(T_2 - T_1)}\left(\frac{a_2 \sin\beta_2 \cos\gamma_2^*}{a_1 \sin\beta_1 \sin\gamma_1^*} - \frac{b_2 \sin\alpha_2 \cos\gamma_2^*}{b_1 \sin\alpha_1 \sin\gamma_1^*}\right) \quad (5.38)$$

$$\alpha_{13} \approx \frac{1}{2(T_2 - T_1)}\left(\frac{a_2 \cos\beta_2}{a_1 \sin\beta_1} - \frac{c_2 \cos\beta_1}{c_1 \sin\beta_1}\right) \quad (5.39)$$

$$\alpha_{12} \approx \frac{1}{2(T_2 - T_1)}\left(\frac{a_2 \sin\beta_2 \cos\gamma_1^*}{a_1 \sin\beta_1 \sin\gamma_1^*} + \frac{b_2 \cos\alpha_2}{b_1 \sin\alpha_1 \sin\gamma_1^*} - \frac{c_2 \cos\alpha_1}{c_1 \sin\gamma_1^* \sin\alpha_1} - \frac{c_2 \cos\beta_1 \cos\gamma_1^*}{c_1 \sin\beta_1 \sin\gamma_1^*}\right) \quad (5.40)$$

Such a description of the terms of the thermal expansion tensor is given for an axis setting defined as: $e_3 // c$, $e_2 // b^*$ and $e_1 = e_2 \times e_3$, where e_i represent the general directions of the orthonormal system after Webber et al. (1998).

In the infinitesimal definition for the thermal expansion tensor, the temperature-induced deformation of the lattice parameters is given by continuous functions. In case of a triclinic crystal, after Paufler and Weber (1999), which describe the orthonormal system as $e_3 // c$, $e_2 // b^*$ and $e_1 = e_2 \times e_3$, the six independent terms of the thermal expansion tensor are expressed as:

$$\alpha_{11} \approx \frac{1}{a} \cdot \frac{da}{dT} + \frac{d\beta}{dT} \cdot \cot\beta \quad (5.41)$$

$$\alpha_{22} \approx \frac{1}{b} \cdot \frac{db}{dT} + \frac{d\alpha}{dT} \cdot \cot\alpha + \frac{d\gamma^*}{dT} \cdot \cot\gamma^* \quad (5.42)$$

$$\alpha_{33} \approx \frac{1}{c} \cdot \frac{dc}{dT} \quad (5.43)$$

$$\alpha_{12} \approx \frac{1}{2} \cdot \cot\gamma^* \cdot \left[\frac{1}{a} \cdot \frac{da}{dT} - \frac{1}{a} \cdot \frac{db}{dT} - \frac{d\alpha}{dT} \cdot \cot\alpha + \frac{d\beta}{dT} \cdot \cot\beta\right] + \frac{1}{2} \cdot \frac{d\gamma^*}{dT} \quad (5.44)$$

$$\alpha_{13} \approx \frac{1}{2} \cdot \left[\frac{1}{a} \cdot \frac{da}{dT} - \frac{1}{c} \cdot \frac{dc}{dT}\right] \cdot \cot\beta - \frac{1}{2} \cdot \frac{d\beta}{dT} \quad (5.45)$$

$$\alpha_{23} \approx \frac{1}{2} \cdot \left\{\left[\frac{1}{a} \cdot \frac{da}{dT} - \frac{1}{c} \cdot \frac{dc}{dT}\right] \cdot \cot\gamma^* \cdot \cot\beta + \left[\frac{1}{b} \cdot \frac{db}{dT} - \frac{1}{c} \cdot \frac{dc}{dT}\right] \cdot \frac{cot\alpha}{\sin\gamma^*} - \left[\frac{1}{\sin\gamma^*} \cdot \frac{d\alpha}{dT} + \frac{d\beta}{dT} \cdot \cot\beta\right]\right\} \quad (5.46)$$

In general, the thermal expansion coefficient α are defined for either a volumetric and linear deformation, according to the following equations 5.47 and 5.48:

$$\alpha_V = \frac{1}{V}\left(\frac{\partial V}{\partial T}\right)_P \quad (5.47)$$

$$\alpha_l = \frac{1}{l}\left(\frac{\partial l}{\partial T}\right)_P \quad (5.48)$$

The latter equation equations 5.48 is mostly used in engineer to describe the thermal expansion of a homogeneous elongated bar. The integration of the equation of volumetric expansion led to the volume variations under isobaric conditions:

$$V_{0T} = V_{00} exp \int_{T_{ref}}^{T} \alpha(T) dT \qquad (5.49)$$

where V_{00} is the volume at the reference temperature T_{ref}(often referred as T_0 in text and following equations) corresponding to *T*=298 K (room temperature). As discussed for pressure in the section 5.1, the interpolation of *T*-*V* data can be performed by means of several empirical and semiempirical equations, starting from different assumptions. In this section, the equations used in the present work to fit the *T*-*V* are discussed and these the polynomial interpolation and the Holland-Powell EoS.

The relation among the linear and the volumetric thermal expansion can be defined as:

$$\alpha_V = \frac{1}{3}(\alpha_{11} + \alpha_{22} + \alpha_{33}) \qquad (5.50)$$

It is worth to mention that the thermal expansion α_{l_i} along the l_i direction coincides with the three crystallographic axes only in symmetry higher than orthorhombic. The LTEC can be directly obtained from the X-ray diffraction data. Moreover, also the values of l_i are directly obtained from diffraction data for symmetry higher than orthorhombic.

5.2.1 Polynomial interpolation

The polynomial interpolation is a rather simple mathematical tool to describe any curve and it is fitted to the experimental data with a least-square minimum method. The equation can be described with the following equation:

$$l(T) = l_0 + l_1 \cdot T + l_2 \cdot T^2 + l_3 \cdot T^3 + \cdots + + l_n \cdot T^n \qquad (5.51)$$

Where *n* is the order of the polynomial function, *T* is the temperature, while $l(T)$ can represent either a volume or any linear cell parameter. The polynomial interpolation can be restricted to any order and any number of refinement coefficients may be defined. The l_n coefficients are the refined parameters of the fitting and, only in first approximation, they can relate to the actual thermal expansion. In detail, the l_1 can be considered as the angular coefficient of the thermal expansion curve, while l_0 coincides with the considered cell parameter at the reference temperature. According to this approximation,

both the volumetric and linear the thermal expansion coefficients can be calculated as: $\alpha_V = l_{1_V}/V_0$ and $\alpha_L = l_{1_L}/L_0$.

In general, polynomial curves with two, three or four terms as used. Especially in case of poor dataset and or rather thin investigated temperature range, the first order polynomial equation is often used. in this case, the interpolation curve is defined by a straight line according to equation: $\Delta L_i = L_i \alpha_{l_i} \Delta T$ and $\Delta V = V \alpha_V \Delta T$, for the general crystallographic direction and volume respectively.

5.2.2 Holland-Powell and modified Holland-Powell EoS

The Holland-Powell EoS provides a rather easy way to model the thermal expansion of minerals. In addition, the Holland-Powell EoS has been extensively used in the mineralogical thermodynamic database issued in 1998 by Holland and Powell (1998) and extend by following authors. Thus, applying the Holland and Powell EoS is of great importance for minerals. According to the model, the reference temperature is fixed at $T_{ref} = 298\,K$ and it assumes that the thermal expansion is constant under high temperatures. The model proposed by Holland and Powell (1998) represents an evolution of the equation proposed by Pawley et al. (1996) which was:

$$V_{0T} = V_{00}\left(1 + \alpha_0(T - T_{ref}) - 2\alpha_1\left(\sqrt{T} - \sqrt{T_{ref}}\right)\right) \qquad (5.52)$$

Pawley et al. (1996) also proposed a relationship among α_0 and α_1 expressed by $\alpha_1 = 10\alpha_0$, which yields to:

$$V_{0T} = V_{00}\left(1 + \alpha_0(T - T_{ref}) - 2(10\alpha_0)\left(\sqrt{T} - \sqrt{T_{ref}}\right)\right) \qquad (5.53)$$

The equation 5.53 has been furtherly undergone several modifications. The ultimate version reported, below, has been yielded in Holland and Powell (2011) and then in Angel et al. (2014):

$$V_{0T} = V_{00}\left(1 + \alpha_0(T - T_{ref}) - 2(10\alpha_0 + \alpha_1)\left(\sqrt{T} - \sqrt{T_{ref}}\right)\right). \qquad (5.54)$$

If the α_1 is fixed at zero ($\alpha_1 = 0$), then the equation 5.54 reported in Pawley et al. (1996) is obtained. The two refined parameters have the unit of measurement of α_0=[K^{-1}] α_1=[$K^{-1/2}$], while the orders of magnitude of the two refinable coefficients are α_0=10^{-5} K^{-1} and α_1=-10^{-4} $K^{-1/2}$. The two refined parameters, α_0 and α_1 do not correspond to the thermal expansion coefficient. Even at the reference temperature *T*=298 K, when the $\alpha_1 = 0$, the thermal expansion coefficient is till different from α_0. The Holland and Powell EoS cannot be used under low temperature conditions. Indeed, at temperature $T = \left(\frac{10\alpha_0 + \alpha_1}{\alpha_0}\right)^2$ the thermal expansion becomes negative and the expression ceases to have a reasonable physical meaning.

5.2.3 Linear Thermal Expansion Coefficient (LTEC)

Even though it does not represent an interpolation system, the linearized (or linear) thermal expansion coefficient (LTEC is used in the text, although in literature it is also often referred as CLTE or CTE) is a quite straightforward way to report *T*-*V* data and therefore represents a useful tool to compare the present data with literature ones. In detail, the LTEC expresses the thermal expansion of a three dimensional object as it is isotropic. It follows that an individual parameter is required to determine the thermal expansion at a specific temperature. Such an "average" thermal expansion results from the expression LTEC=$\alpha_V/3$. Alternatively, the following, equivalent equation can be used:

$$\text{LTEC}=(\alpha_{11}+\alpha_{22}+\alpha_{33})/3, \qquad (5.55)$$

where α_{11}, α_{22} and α_{33} are the axial thermal expansion along the three orthogonal directions of the space, corresponding to the normal component of the thermal expansion tensor.

5.3 Combined H*P*–H*T* EoS

The combined H*P*–H*T* EoS can be obtained by the combination of any isothermal and isobaric EoS. In addition, the modification of the thermal expansion with pressure ($\partial\alpha_{P0}/\partial P$) and a model to esteem the variation of bulk modulus with temperature ($\partial K_{0T}/\partial T$) are required to fully describe the behavior under combined H*P*–H*T* conditions. Anderson (1989) defined how *P* influences thermal expansion and the *T*-dependence of thermal expansion through the so-called thermodynamic identity:

$$\frac{\partial\alpha}{\partial P}=\frac{1}{K_{V(T)}^2}\left(\frac{\partial K_{V(T)}}{\partial T}\right)_P \qquad (5.56)$$

defines the impact of temperature in influencing the bulk modulus and *vice versa*. Then, as highlighted by Angel et al. (2014), if $\partial K_{0T}/\partial T=0$, consequently $\partial\alpha_{P0}/\partial P=0$ and the thermal expansion does not change with pressure. The most straightforward system to model the influence of temperature on compressibility is the linear, constant variation of bulk modulus with pressure. Such an assumption is reasonable only under high temperature experiments performed after Anderson (1995). On the other hand, assuming a constant $\partial K_{0T}/\partial T$ often lead to a negative thermal expansion coefficient at low pressure conditions (Helffrich and Connolly 2009).

From an experimental point of view, a quite simple system to model the *P*-*V*-*T* EoS for crystalline compounds is the performing of a set of *n* independent, compressional X-ray diffraction experiments, each of which conducted under different isothermal conditions. Therefore, a set of isothermal BM-EoS performed under high-temperature can be defined, providing the refinable variable V_{0T}, K_{0T} and K'_{0T} and their variation through temperature.

5.3.1 Modelling of the non-ambient behavior in three dimensions

A tensor surface is a continuous surface which represents the variation of any tensorial property with respect space. According to Neumann's principle, the physical properties of a crystalline material must respect the symmetry of the point group itself. In particular, the thermal, the thermal expansion and compressibility can be described by tensorial surfaces, which symmetry depend on the symmetry of the crystal. Such three dimensions representation are described according to an orthonormal axes system, which does not necessarily correspond to any of the crystallographic axes. The thermal expansion and the compressibility tensors are often represented through ellipsoidal surfaces, in case that none of the directions shows either negative thermal expansion or positive compression (expansion of a specific crystallographic direction with increasing hydrostatic pressure). Therefore, the thermal expansion or compression can be described with a three axes surface in triclinic, monoclinic and orthorhombic space group, while only two independent axes are allowed in trigonal, hexagonal and tetragonal point groups. For cubic crystals, both the changing of physical properties with crystallographic directions are described by a sphere.

Chapter 6

6 State of the art about zircon- and monazite-structures under non-ambient conditions

The ATO_4 compounds with either the zircon or monazite-type structure have been used or proposed for several usage, including the host of several nuclear wastes, magnetic materials, catalysts, phosphors, scintillators, solid state laser materials, ceramics, not to mention the usage for REE-extraction. Such economic usage opened the path to several studies, devoted to the understanding of the properties of these minerals, including their response to high pressure and high temperature conditions. In detail, the behavior of these compounds, focusing on their atomic structure deformation and stability field, is summarized below, in this section.

6.1 High pressure behavior of ATO_4 compounds

Within the past decades, several studies have been dedicated to the understanding of the stability field and the H*P* behavior of the REE*T*O_4, either using an experimental or theoretical approach. In Table S13.17 are gathered the bulk moduli of $REEPO_4$, $REEAsO_4$ and $REEVO_4$ compounds with the zircon- and the monazite-type topology. Concerning the H*P* response of REE*T*O_4 compounds, a general rule, highlighted by several authors and corroborated by both theoretical (Zhang et al. 2008; Li et al. 2009) and experimental studies (Lacomba-Perales et al. 2010, Zhang et al. 2008; Errandonea et al. 2011) is that, at a given structural type, the bulk modulus shifts towards lower values as the atomic radius of the *A*- and *T*-sites increase. In addition, Li et al. (2009) in a systematic, theoretical study carried out on REE*T*O_4 phosphates and arsenates, found out that the zircon-type structure is, on average, less compressible than the monazite-type structure, confirming the independent results reported in many previous studies (*e.g.*, Mogilewsky et al. 2006, Errandonea et al. 2005, Zhang et al. 2009), there is no general agreement on the bulk modulus of every single $REEPO_4$ compound, as different authors obtained results significantly different. In the following section, the H*P* behaviors of the two

structural topologies are discussed independently, with a particular attention dedicated to phosphates and arsenates.

6.1.1 Zircon-type topology under H*P*

The first studies about the H*P* behavior of zircon dates back to the beginning of 1950s, in an experimental study carried out by Ryshkewitch (1951). In the 1970s, several papers were published on *sensu stricto* zircon (Worlton 1972; Özkan et al. 1974; Sirdeshmukh and Subhadra 1975; Özkan 1976; Hazen and Finger 1979; Özkan and Jamieson 1979). The anisotropic compression was firstly described by Worlton (1972) and then confirmed by subsequent authors. The anisotropic compressional behavior is characterized by a crystallographic axis *a* (=*b*) being more compressible with respect the *c* crystallographic direction. Many other studies explored the compressional behavior and stability field of zircon and its synthetic counterpart, $ZrSiO_4$ (Ono et al. 2004a; Ono et al. 2004b; Ríos and Boffa-Ballaran 2003; Marqués et al. 2008; Dutta and Mandal 2012; Stangarone et al. 2019; Timms et al. 2017; Marqués et al. 2006; Knittle and Williams 1993; Scott et al. 2000; Van Westrenen et al. 2004; Crocombette and Ghaleb 1998; Binvignat et al. 2018) and the corresponding bulk moduli are reported in Table S13.17, in section 13. As one might note, the bulk moduli from Ríos and Boffa-Ballaran (2003), Özkan (1976) and Binvignat et al. (2018) are significantly lower than the others obtained for $ZrSiO_4$, either natural or synthetic. This is due to the metamict nature of those zircons, which elastic properties are strongly influenced by its damaged microstructure.

Among the compressional behavior of REE*T*O_4 compounds is also the elastic behavior of zircon-type REE-vanadates reported by several authors (Zhang et al. 2008; Mittal et al. 2008; Errandonea et al. 2009; Hirano et al. 2002; Chakoumakos et al. 1994; Duclos et al. 1989; Errandonea et al. 2011; Minykayev et al. 2010; Marqueno et al. 2019; Panchal et al. 2011; Yuan et al. 2015). Even though vanadates are not among the compounds under study in the present research, the understanding of their behavior provides a relevant tool to understand the variation in compressibility of zircon-structured minerals across the entire lanthanoid series in *AT*O_4. The trend described above is still respected in the complete Ln-series, being $LaVO_4$ and $LuVO_4$ the most and the least compressible REE-vanadates respectively: the decrease in compressibility is almost linear, as observed for phosphates and arsenates in the comparative study by Li et al. (2009). Among the zircon-type REE-bearing arsenates, only $YAsO_4$ has been investigated through *in situ* X-ray diffraction. The usage of compounds like Er-doped $YAsO_4$ as phosphors materials have led to several studies devoted to understand the impact of pressure in light-emitting properties (*e.g.*, Ledderboge et al. 2018; Strzep et al. 2017). Therefore, the high-pressure behavior of most of arsenates has been exclusively studied by

means of theoretical methods (*e.g.*, Li et al. 2009; Errandonea et al. 2005; Errandonea et al. 2011). In case of $EuPO_4$, $GdPO_4$ and $TmPO_4$ the compressibility has never been modelled, even by means of theoretical results. As for the *s.s.* zircon, and other zircon-type compounds, the anisotropic behavior has been described, with the *a* axis being more compressible than the *c* crystallographic direction. Synthetic zircon-type phosphates (*i.e.*, $ScPO_4$, YPO_4, $ErPO_4$, $TmPO_4$, $HoPO_4$, $YbPO_4$ and $LuPO_4$) have been experimentally studied under high pressure conditions (Errandonea et al. 2005, Zhang et al. 2009; Lacomba-Perales et al. 2010; Gomis et al. 2017; Zhang et al. 2008). Natural xenotime-(Y) has been studied under high pressure by Mogilewsky et al. (2006), while studies concerning natural pretulite-(Sc) have never been conducted. Experimental studies on zircon type $TbPO_4$ and $DyPO_4$ are missing. On the other hand, the relation among the bulk moduli and the chemical composition of the *A*-site respects the general trend described above, with a negative linear relation among the ionic radii (Table S13.17).

6.1.2 Monazite-type topology under H*P*

The high-pressure behavior of monazite-type phosphates has been object of numerous studies (Lacomba-Perales et al. 2010; Errandonea et al. 2018; Errandonea 2017; Feng et al. 2013; Riutz-Fortes et al. 2016; Heffernan et al. 2016; Huang et al. 2010; Li et al. 2009), while the literature available on arsenates is rather limited (Metzger et al. 2016, Li et al. 2009). A comprehensive review on the high-pressure behavior of monazite-type ATO_4 compounds has been carried out by Errandonea (2017). Experimental high-pressure studies of REE-bearing monazite-type phosphates (Lacomba-Perales et al. 2010; Errandonea et al. 2018; Feng et al. 2013; Ruitz-Fortes et al. 2016; Heffernan et al. 2016; Huang et al. 2010) slightly differs from the results of theoretical studies obtained by Li et al. (2009) and Muñoz et al. (2018). Lacomba-Perales et al. (2010) studied the compressional behavior of the REE-phosphates $LaPO_4$, $NdPO_4$, $EuPO_4$ and $GdPO_4$, all with the monazite structure, up to 30 GPa. Errandonea et al. (2018) studied the high-pressure behavior of La-, Ce- and Pr-bearing phosphates, by means of *ab initio* simulations, providing their bulk moduli by a Birch-Murnaghan Equation of state truncated to the third order (BM3-EoS; Birch 1947; Angel 2002): $K_{V0} = 1/\beta_V = -V\cdot(\partial P/\partial V)_T$ = 114.2(5) GPa ($K_V' = \partial K_{V0}/\partial P$ = 4.64(6)) for $LaPO_4$; K_{V0} = 117.3(3) GPa (K_V'=4.54(3)) for $CePO_4$ and K_{V0} = 120.2(6) GPa (K_V'=4.59(7)) for $PrPO_4$, respectively. Generally, what has been observed in synthetic REE-phosphates end members (Lacomba-Perales et al. 2010; Feng et al. 2013; Li et al. 2009; Errandonea 2017) is the already-mentioned rule: the bulk modulus increases (*i.e.*, the compressibility decreases) when the atomic radius of the REE-cation decreases, from $LaPO_4$ to $GdPO_4$. Whereas several studies have been dedicated to the compressional behavior of the monazite structure analogues, few of them explore the structural mechanisms responsible for the high-pressure bulk compression and deformation. Heffernan et al. (2016) studied the structural (at the atomic scale)

response of $GdPO_4$ under high-pressure conditions up to 7.06 GPa, refining a bulk modulus of 128.1(8) GPa (*vs*. 138.3 GPa reported by Muñoz et al. 2018). Either Heffernan et al. (2016), Errandonea et al. (2018) and Muñoz et al. (2018) point out the relevant role played by the compression of the $REEO_9$ polyhedron, whereas the PO_4 tetrahedra substantially act as rigid bodies. Heffernan et al. (2016) also show that the anisotropic behavior of $GdPO_4$ is mainly controlled by the variations of the O−Gd−P linkages, resulting from the distortion of the GdO_9 polyhedra. Rare Earth Elemets-arsenates with the monazite structure, have been studied by Metzger et al. (2016), and Stubican and Roy (1963), who found a monazite-to-scheelite *P*-induced phase transition in LREE arsenates ($LaAsO_4$, $CeAsO_4$, $PrAsO_4$ and $NdAsO_4$).

6.1.3 Pressure-induced phase transitions in ATO_4 compounds

The phase transitions and the stability field under compression of several structure types belonging to the huge group of the ATO_4 compounds have been object of investigation of several studies. In this light, a comprehensive understanding is given by the Bastide diagram (Figure 3.1). Under compression, in such a r_A/r_O *vs* r_T/r_O diagram, any ATO_4 compound follows a positive linear path and is thus possible to predict which phase transition occurs during compression. For the purposes of the current project, the zircon-to-scheelite, zircon-to-monazite, monazite-to-scheelite, monazite-to-postbarite, monazite-to-$BaWO_4$-II, scheelite-to-fergusonite-β and scheelite-to-$SrUO_4$ are analyzed in this section.

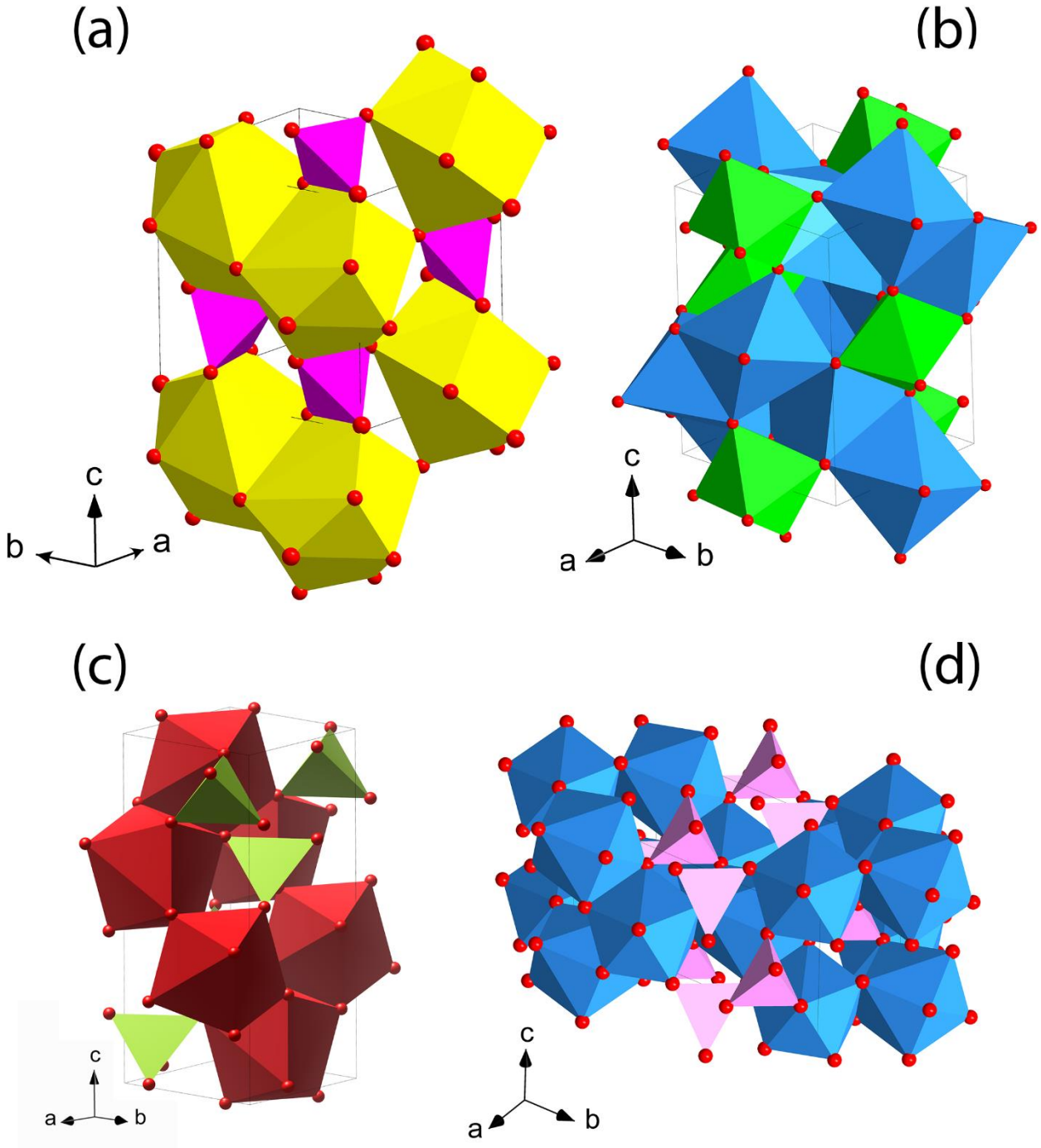

Figure 6.1: crystal strcuture of several ATO_4 compounds; **(a)** postbarite; **(b)** *fergusonite-β*; **(c)** scheelite; **(d)** $SrUO_4$.

Figure 3.2 and Figure 6.1 report the crystal structures of zircon, monazite, scheelite, postbarite, $SrUO_4$ and fergusonite-*β*. In first analysis, the most important relations, coupled with the increase of both

the r_A/r_O and r_T/r_O parameters, is the increase in the number of chemical bonds of the independent oxygen atoms. Indeed, in zircon, all the oxygen atoms share two bonds with the *A*-cation and a bond with the *T*-site cation, while in the monazite-topology, three of the four independent oxygens have three bonds (O1, O3 and O4) and one oxygen atom (the O2 atom) have four bonds (three *A*-O2 bonds and one *T*-O2 bond, according to the notation reported in Figure 3.6). In case of post-barite-type structure, the coordination number of the *A*-cation is 10 and all the oxygen atoms but one (the O1 atom) form four symmetry-independent bonds: in this case, the 3/4 of the oxygen atoms are bonded with *A*-site and *T*-site cations. For both the scheelite-type and the fergusonite-β-type structures, all the oxygen atoms form three bonds. In case of $SrUO_4$, the coordination of the *T*-atom rises to six and each oxygen atom forms 4 bonds. A similar behavior can be described for the $BaWO_4$-II structural topology, characterized by an increase in the coordination number of the *T*-site cation from 4 to 6. The main phase transitions occurring in monazites and zircons is discussed below. In discussing the stability fields of *AT*O_4 compounds under compression, it should be kept in mind that monazite can also form as a high-pressure product of *AT*O_4 compounds with zircon-type structure. This yields to a series of H*P*-monazite phases, as $REEVO_4$ and HREE-bearing phosphates, which conflict with the relations among structural type and ionic radius discussed elsewhere in the text, which were valid for ambient conditions.

Phase transitions involving the zircon-type compounds

In *s.s.* zircon, at pressure exceeding 12 GPa and temperature above 900° C, Reid and Ringwood (1969) observed a phase transition from zircon to a tetragonal scheelite-type structure (space group $I4_1/a$). Such a phase has been then observed by Glass et al. (2002) in natural upper Eocene impact-formed products in sediments in the continental slope off New Jersey and Barbados and then, the scheelite-type polymorph of zircon has been called reidite, after Reid, who firstly described the crystal structure (Reid and Ringwood 1969). The phase transition is coupled with an increase in density of ~9% and no change in the coordination number of neither the *A*-site nor the *T*-site cation (Glass et al. 2002). The phase transition to reidite is predicted to occur under shock conditions between 20 and 53 GPa, with an increase in reidite content along with pressure (Kusaba et al. 1985; and Fiske 1999). More recently, the zircon-to-scheelite (zircon-to-reidite) phase transition has been described by Knittle and Williams (1993), Scott et al. (2000), Van Westrenen et al. (2004), Ono et al. (2004b), Stangarone et al. (2019), while a review on the $ZrSiO_4$ phase transition is reported in Mihailova et al. (2019). Knittle and Williams (1993) and Scott et al. (2000) found the phase transition at ~23 GPa, while Van Westrenen et al. (2004) found the zircon-to-scheelite phase transition at 19.7 GPa. In addition, the bulk modulus of the scheelite-type zircon has been modelled by several authors by

means of a BM2-EoS (Ono et al. 2004b; Scott et al. 2000; Marqués et al. 2006), obtaining higher values with respect the low-pressure polymorph and ranging from 259 to 392(9) GPa (see Table S13.17).

The scheelite-type structure, as mentioned above in this section can also form as a H*P*-product of monazite, yielding to a series of ATO_4 polymorphs, as zircon → monazite → scheelite. Whether a direct zircon→scheelite or a zircon→monazite→scheelite occur depends on the reciprocal relations among the ionic radii of the three atoms involved, as summarized in the empiric Bastide diagram (Figure 3.1 an). In detail, a large *T*-cation promotes a direct zircon-to-scheelite phase transition, while a small *T*-cation cation favors an intermediate monazite-type polymorph. Concerning the *A*-site cation, the larger it is, the more likely is to have a monazite polymorph over the scheelite one, which stability field is "pushed" to higher pressure. This relation is particularly clear in case of $REEVO_4$ compounds: in REE-bearing zircon-type vanadates, the *A*-cation can be any of the lanthanoids and the role played by the *A*-site cation can be easily defined. All the $REEVO_4$ with a REE atom larger than Nd (La-Nd) are characterized by a zircon-to-monazite phase transition; when, on the other side, the REE cation's size ranges between Eu to Lu, the zircon-to-scheelite phase transition occurs.

All the studied zircon-type ATO_4 silicates shows a zircon-to-scheelite phase transition. The direct xenotime-to-scheelite phase transition has been described for $YAsO_4$ (~8 GPa) and $YCrO_4$ (~4.2 GPa) (Errandonea et al. 2011), YVO_4 (above ~7.5 GPa) (Manjón et al. 2010; Wang et al. 2004; Jayaraman et al. 1987). *Ex situ* H*P* and H*T* experiments, carried out by Stubican and Roy (1963), reveal that Sm-Lu $REEAsO_4$ and Pr-Lu $REEVO_4$ undergo to a direct zircon-to-scheelite phase transition. In a combined *P*–*T* field, $CeVO_4$ studied by Range et al. (1990), clearly displays an intermediate monazite-type structure polymorph, whereas under the simple compression, the structure displays a direct xenotime-to-scheelite phase transition. As previously cited, after the first zircon-to-monazite phase transition, ATO_4 compounds can experience a monazite-to-scheelite phase transition, as predicted to happen in YPO_4 at pressure exceeding ~30 GPa (Zhang et al. 2009). A comprehensive description of the zircon-to-monazite phase transition in phosphates is reported in Hay et al. (2013), suggesting a possible, metastable intermediate term with an anhydrite-type structure between the zircon and the monazite-type polymorphs. In case of $YAsO_4$, after the scheelite-type polymorph, a second *P*-induced phase transition is predicted to occur at pressure exceeding 32 GPa. The so-called $YAsO_4$-III polymorph defined by *ab initio* simulations, is predicted to have a tetragonal $SrUO_4$-type structure and has never been experimentally observed (Errandonea et al. 2011). Moreover, after the stabilization of the scheelite-type polymorph, a further H*P*-β-fergusonite phase can form in ATO_4

compounds, leading to zircon→scheelite→*β*-fergusonite series. This complete series has been observed in REE-bearing vanadates and it occurs at pressure above 20 GPa.

Phase transitions involving the monazite-type compounds

In monazites, three major phase transitions have been described: the monazite-to-postbarite, the monazite-to-scheelite and the monazite-to-$BaWO_4$-II phase transitions (in literature the last one may occur as monazite-to-$PbWO_4$-III, although this term is misleading and there is no actual reason to that). The relations among monazite and its H*P*-polymorphs again depend upon the reciprocal relations among the *A*, *T* and oxygen ionic radii as shown in the Bastide diagram. The monazite-to-postbarite phase transition has been described in $REEPO_4$ and $REEVO_4$. In general, the pressure stability field of the monazite-structured phosphates increases to higher pressures from $LaPO_4$ to $GdPO_4$. For $LaPO_4$, a phase transition at a pressure exceeding 27.1 GPa to a post-barite-type structure ($P2_12_12_1$ space group) occurs and the same phase transition is predicted to occur at 35 and 45 GPa for $NdPO_4$ and $GdPO_4$, respectively (Lacomba-Perales et al. 2010; Riutz-Fortes et al. 2016; Errandonea 2017). Such a phase transition has been described in monazite-type $CeVO_4$ at 14.7 GPa (*vs* 27.1 GPa in $LaPO_4$) suggesting that the monazite-postbarite boundary is pushed at higher pressure as the ionic radius of the *T*-site reduces (Errandonea et al. 2011). On the other hand, monazite-type $LaVO_4$, $PrVO_4$ and $NdVO_4$, under high-pressure, undergo a phase transition to a monoclinic $BaWO_4$-II-type structure (Errandonea et al. 2016, Panchal et al. 2017, Marqueño et al. 2021). Such a phase transition is shifted at higher pressure as the ionic radius of the *A*-site reduces and, interestingly, it is not coupled with a change in the space group (which remains $P2_1/n$), while the unit-cell volume doubles (Z=8). Eventually, the monazite-to-scheelite has been described for YPO_4 and several other REE-free compounds, as $SrCrO_4$ and $CaSeO_4$ (Gleissner et al. 2016; Crichton et al. 2012).

6.2 High temperature behavior of ATO_4 compounds

As mentioned above, due to their capability for hosting actinides and other possible fission products, either monazite and zircon structures have been proposed as nuclear waste disposal forms (Ewing and Wang 2002; Montel et al. 2006; Wang and Liang 2012; Schlenz et al. 2013; Orlova and Ojovan 2019). In this light, several studies have been dedicated to the investigation of the H*T* stability and other temperature-related properties of the REE-bearing phosphates. There is general agreement within the authors that the thermal expansion coefficient of the REETO_4 shows a clear chemical-dependent trend: the thermal expansivity increases along with the ionic radii of the *A*-cation, while it reduces if the radius of the *T*-site increases (Zhang et al. 2008; Li et al. 2009; Perrière et al. 2007;

Subbarao et al. 1990). In comparing the two structural types, Li et al. (2009) found out that the monazite topology is, in general more expandable than the zircon-type structure. Unfortunately, as for the compressibility, several studies, show rather different results and it is complex to compare datasets from different studies. In addition, as discussed in section 5.2, several equations are used to model the high temperature behavior, much more than those used to model the compressional one. In order to overcome this bias, the linear thermal expansion coefficient (LTEC) has been used as a sort of standard to describe the thermal behavior of the compounds under investigation. Even considering the LTEC may not accurately model the thermal behavior of ATO_4 compounds. Therefore, both considering a proper temperature range and using the same EoS method are important features for obtaining comparable results. In addition, the experimental setting used has also a strong influence on the results.

6.2.1 High-temperature behavior of zircon-type compounds

Due to its low thermal conductivity and thermal expansion, zircon is an interesting ceramic material (*e.g.*, Kaiser et al. 2008). In this light, several studies, dedicated to $ZrSiO_4$ thermal expansion and thermal stability have been carried out (Pavlik and Holland 2001; Ono et al. 2004; Kaiser et al. 2008; Mursic et al. 2002). Early literature studies on $ZrSiO_4$ are rather conflicting. Incongruent, congruent melting and solid-state decomposition of $ZrSiO_4$ have been proposed to explain the reactions occurring under high-temperature conditions in zircon-type compounds (Butterman and Foster 1967). Although after the 1960s solid state dissociation has been identified as the decomposition mechanism in $ZrSiO_4$, few uncertainties remain about the temperature of decomposition of $ZrSiO_4$, between a lowest value of 1285° C (Pavlik and Holland 2001) and a maximum of 2550° C (Washburn and Libman 1920). Mursic et al. (1992) identified a displacive phase transition of metamict *s.s.* zircon at 826° C K and a decomposition in ZrO_2 and SiO_2 at temperature exceeding 1476° C. In general, most of the authors identified a decomposition temperature between 1550° C and 1700° C (Kaiser et al. 2008).

The high-temperature stability field of zircon-type phosphates has been investigated by Han et al. (2020), Hikichi et al. (1998) in comparative studies. All the zircon-type phosphates are stable at least at temperatures exceeding 1400° C (Han et al. 2020), and the melting point of REE-bearing phosphates YPO_4 and $ErPO_4$ are 1995(20)° C and 1896(20)° C, respectively, while the thermal stability of $YbPO_4$ is about 2020° C (Garvichev et al. 2013; Bondar et al. 1976). In general, according to Ushakov et al. (2001), $LuPO_4$ is predicted to be the least refractory among the $LnPO_4$ with a zircon-type structure and the melting point is predicted to decrease along with the ionic radius of the *A*-site. Unfortunately, the decomposition temperatures obtained independently by Garvichev et al. (2013),

Bondar et al. (1976) and Hikichi et al. (1998) are quite scattered. Along the zircon-type arsenate series, the melting point of pure $LuAsO_4$ (2000° C) has been determined by Angapova and Serebrennikov (1973).

If, on one side, the zircon-type compounds stability field is often labeled as "very high", without further investigations, on the other hand, the thermal expansion is a rather well studied feature, with a large number of publications about (Schopper et al. 1972; Kahle et al. 1970; Hikichi et al. 1997; Hikichi et al. 1998; Morgan and Marshall 1995; Patwe et al. 2009; Taylor 1986; Subbarao et al. 1990; Sallese 1986; Bayer 1972; Austin 1931; Subbarao et al. 1968; Worlton et al. 1972; Reddy et al. 1985; Reddy et al. 1981; Zhao et al. 2004; Skanthakumar et al. 1995; Reddy et al. 1988; Reddy et al. 1995; Asuvathraman et al. 2014; Zhang et al. 2008; Li et al. 2009). *S.s.* zircon is characterized by a rather low thermal expansion coefficient, ranging between $2.6 \cdot 10^{-6}$ K^{-1} and $5.5 \cdot 10^{-6}$ K^{-1}. As mentioned above, although LTEC represents a rather raw system for describing the high-temperature behavior of compounds, it has been pointed out as the simplest and widespread tool to describe the behavior of zircon-type minerals. As underlined by Reddy and Murthy (1988), the ratio *a*/*c* depends on the relations between the atomic species involved and becomes higher as the difference among the *A*-cation and the *T*-cation ionic radii becomes larger. Table S13.18 reports the LTEC of REE-bearing phosphates, arsenates and vanadates and zircon-type silicates and chromates. As discussed above for high-pressure conditions, an important contribute has been provided by the comparative works carried out by Li et al. (2009) and Zhang et al. (2008) on theoretical models (Table S13.18).

Li et al. (2009) and Zhang et al. (2008) provided the LTEC of most of the phosphates, arsenates and vanadates, building a solid base in understanding the behavior of zircon-type compounds through the lanthanoid series. Comparative theoretical studies show that LTEC increases with the increase of the ionic radii of the *A*-site cation in phosphates, arsenates and vanadates. In addition, Li et al. (2009) pointed out the influence of the *T*-site cation in LTEC. In general, the LTEC becomes higher as the ionic radii of the *T*-site become smaller, although experimental studies do not always confirm this trend (see Table S13.18). Indeed, there is not a significant agreement among theoretical and experimental results (Table S13.18): conversely to theoretical studies, experimental data comparison among phosphates and arsenates show a thermal expansion slightly higher for arsenates; on the other hand, the general trend resulting in comparing YVO_4 and $YAsO_4$ under high temperature confirm that arsenates are slightly more expansible than vanadates, the latters characterized by a larger *T*-site cation (Reddy et al. 1988). In addition, Schopper and Urban (1972) obtained a slightly higher LTEC for $YAsO_4$ compared to YPO_4. Kahle et al. (1970), found out a similar thermal expansion for $YAsO_4$ and YPO_4.

Eventually, it is important to point out that the thermal expansions obtained from different authors may differ significantly: excluding dilatometry results, on *s.s.* zircon (Sallese 1986) the LTECs ranges between $3.8 \cdot 10^{-6}$ K^{-1} and $5.5 \cdot 10^{-6}$ K^{-1}, with a difference of ~30 % (Worlton et al. 1972; Subbarao 1968). In YPO_4, experimentally determined LTEC ranges from a maximum of $6.27 \cdot 10^{-6}$ K^{-1} (Kahle et al. 1970) to a minimum of $5.5 \cdot 10^{-6}$ K^{-1} (Sallese 1986). In $YAsO_4$, the thermal expansion coefficients obtained are more consistent and values range between $6.23 \cdot 10^{-6}$ K^{-1} and $6.57 \cdot 10^{-6}$ K^{-1} (Kahle et al. 1970). The LTEC of YVO_4, also ranges significantly from a minimum of $4.47 \cdot 10^{-6}$ K^{-1} (Reddy and Murthy 1983) to $6.70 \cdot 10^{-6}$ K^{-1} (Kahle et al. 1970).

6.2.2 High-temperature behavior of monazite-type compounds

As pointed out in section 3.2, monazites are interesting compounds proposed for both nuclear waste storage and ceramic materials (*i.e.*, Heuser et al. 2014; Schlenz et al. 2013; Brandt et al. 2014). Therefore, the melting point and thermal expansion of monazite-type phosphates have been widely investigated. The melting point of pure endmember monazite phosphates ($LaPO_4$, $CePO_4$, $NdPO_4$, $SmPO_4$), as well as a natural monazite, have been firstly studied by Hikichi et al. (1998). Hikichi et al. (1998) found out that the monazite structure displays a clear composition-dependent thermal stability field, decreasing along with the ionic radii from 2072°C ($LaPO_4$) to 1916° C ($SmPO_4$). The melting temperature of monazite-type $LaAsO_4$ was investigated by Angapova and Serebrennikov (1973), which determined a decomposition temperature of 1830° C. Unlike zircon-type compounds there is no disagreement concerning the decomposition mechanism active under high temperature in monazites and only congruent melting has been proposed.

On the other hand, there is significant disagreement in describing the relationship between LTEC and ionic radii in ATO_4 compounds defined by different authors in comparative investigations, as already discussed for zircon-type compounds (Table S13.18). The influence of chemical composition over thermal expansion in REE-bearing phosphates and arsenates was investigated by Li et al. (2009) by density functions calculations. Li et al. (2009) defined, as for the zircon-type compounds, that the LTEC in REE-bearing monazites increases with the increase of the ionic radii of the *A*-site (decrease in atomic number of the *A*-site). Such a result is confirmed by Hikichi et al. (1997) in a comparative study pertaining to $CePO_4$, $NdPO_4$ and $SmPO_4$. Dilatometric studies (Perrière et al. 2007; Thust et al. 2015) do not confirm such a behavior: indeed, they found that the thermal expansion of ceramic $REEPO_4$ decreases almost linearly with ionic radii of the *A*-site (increase in atomic number of the *A*-site). Thust et al. (2015) studied the $La_{1-x}Er_xPO_4$ system under high temperature conditions and the LTEC increases along with the increase of Er content. In order to clarify this bias, clearly influenced by the technique used, Thust et al. (2018) compared the thermal expansion obtained with the two

alternative methods (*i.e.*, dilatometry and *in situ* X-ray diffraction) for a $LaPO_4$-$PrPO_4$ solid solution. Thust et al. (2018) found that the two techniques actually show opposite trends: in dilatometry, a larger *A*-site cation yields to a lower thermal expansion. Such a different behavior is due to the density-dependance of the LTEC obtained with dilatometry that cannot be observed when thermal expansion is studied by means of X-ray diffraction. Eventually, as discussed for zircon-type compounds and high-pressure behavior, also the refined/calculated LTEC in monazites for a given compound can vary significantly (Table S13.18). The LTEC in $CePO_4$, for instance, ranges from $7.71 \cdot 10^{-6}$ K^{-1} (Li et al. 2009) and $9.91 \cdot 10^{-6}$ K^{-1} (Asuvathraman et al. 2014).

6.3 Combined H*P*–H*T* studies on *AT*O_4

In conclusion, the combined H*P*–H*T* behavior of *AT*O_4 compounds has been rather poorly studied (Ehlers et al. 2022; Range et al. 1990; Metzger et al. 2016; Reid and Ringwood 1969; Mogilevsky 2007). Unlike most of the studies discussed in this section, the H*P*–H*T* are often dedicated to unveiling the phase relations rather than the structural behavior of *AT*O_4 compounds. It is worth to mention that, in case of *s.s.* zircon, the stability field at varying both temperature and pressure has been accurately drawn in several dedicated studies (*e.g.*, Butterman and Foster 1967; Timms et al. 2017). On the other side, studies pertaining to the H*P*–H*T* behavior of REE*T*O_4 phosphates and, specially, the much rarer arsenates are rather scarce if compared to $ZrSiO_4$. Among the other topics, the solid solution among monazite-type and zircon-type phosphates in order to define an effective thermobarometer has been studied by Mogilevsky (2007), Heinrich et al. (1997), Gratz and Heinrich (1997, 1998), Andrehs and Heinrich (1998) Mogilevsky et al. (2006). Mogilevsky (2007), using the data collected by other authors (Heinrich et al. 1997; Gratz and Heinrich 1997, 1998; Andrehs and Heinrich 1998; Mogilevsky et al. 2006) studied the miscibility among monazite-(Ce) and zircon-type phosphates by means of their synthetic counterparts in the systems $LaPO_4$–YPO_4 and $CePO_4$–YPO_4. It has been defined that, under the most favorable conditions (*i.e.*, *T*=1600 K and room pressure), in $LaPO_4$ more than 40 mol % of the *A*-site can be replaced by Y, while ~1.7 mol % of La can fit into YPO_4. In addition, with increasing pressure, the xenotime solubility in monazite also increases. In general, the solubility of HREE in monazite can increase significantly (from 15% to 40%) with a pressure increase from room conditions to 1.5 GPa (Mogilevsky 2007). Eventually, in phosphates and vanadates the role of combined H*P*–H*T* has been investigated. In a combined *P*–*T* field, tetragonal zircon-type $CeVO_4$ studied by Range et al. (1990), clearly displays an intermediate monazite-type structure polymorph, whereas under the simple compression, the structure displays a direct xenotime-to-scheelite phase transition. By direct heating, on the contrary, the $CeVO_4$ undergoes a xenotime-to-monazite phase transition at ~1300°C. Concerning the monazite-type arsenates, Metzger et al. (2016)

achieve the monazite-to-scheelite phase transition by means of H*P*–H*T* synthesis (*P*=11 GPa and temperature ranging from 1100° C to 1300° C) in a Walker-type multi anvil device. The synthesis of scheelite-type arsenates was successfully achieved and the crystal structure of the scheelite-type H*P*-arsenate polymorphs were then described.

Chapter 7

7 Materials and methods

Fourteen rock specimens, pertaining to different Alpine quartz-bearing fissures, have been selected from several private collections. All these samples crop out at Mt. Cervandone and contain REE-bearing arsenates and phosphates. The samples have been provided by the personal collection of the Italian collector Enzo Sartori and collected within the Mt. Cervandone area between 2000 and 2020. They were first observed under a stereomicroscope, with the aim to identify their mineralogical assemblage, which was later confirmed by single-crystal X-ray diffraction. In Table 7.1 is reported the mineral association within each rock sample, coupled with a specific label for the REE-bearing minerals. Fifteen REE-bearing phosphate and arsenate crystals have been selected and extracted from the fourteen rock specimens under study (see Table 7.1), and then characterized by means of electron probe microanalysis in wavelength dispersion mode (EPMA-WDS), single-crystal X-ray diffraction, Raman spectroscopy and non-ambient X-ray diffraction studies.

Table 7.1: Mineralogical assemblage of each sample from the quartz Alpine-fissures of Mt. Cervandone (quartz is ubiquitous and not reported in the Table), identified by single-crystal X-ray diffraction, except for the $ThSiO_4$ grains).

Quartz-fissure sample	REE-minerals	REE-bearing sample name	Associated accessory minerals
M-C1	monazite-(Ce)	Mon1	muscovite, magnetite, rutile, hematite
M-C2	monazite-(Ce)	Mon2	muscovite, magnetite, rutile, hematite, clinochlore
M-C3	gasparite-(Ce)	Gasp3	muscovite, magnetite, clinochlore
M-C4	gasparite-(Ce)	Gasp4	muscovite, magnetite, clinochlore
M-C6	chernovite-(Y)	Ch6	muscovite, magnetite
M-C7	chernovite-(Y)	Ch7	titanite, muscovite, magnetite
M-C8	chernovite-(Y)	Ch8	muscovite, magnetite, rutile, tourmaline
M-C9	chernovite-(Y)	Ch9	muscovite
M-C10	chernovite-(Y)	Ch10	muscovite, magnetite
M-C11	chernovite-(Y)–xenotime(Y) s.s.	Ch11	muscovite, magnetite, rutile, hematite, $ThSiO_4$ (thorite or huttonite)
M-C12	chernovite-(Y)	Ch12	muscovite
M-C13	chernovite-(Y)	Ch13	muscovite, clinochlore
M-C14	xenotime-(Y), monazite-(Ce)	Xen14, Mon14	muscovite, magnetite, rutile, hematite, $ThSiO_4$ (thorite or huttonite)
M-C16	chernovite-(Y)	Ch16	magnetite, plagioclase

7.1 Chemical analysis and chemical maps

The chemical composition of the investigated REE-bearing phosphates and arsenates was determined using a JEOL JXA-8200 electron microprobe at the Earth Sciences Dept. of the University of Milano (ESD-MI), operating in wavelength dispersive mode (WDS) with a focused beam (~5 μm in

diameter), an acceleration voltage of 20 kV, and a beam current of 20 nA. The counting time was set to 30 s for peaks and 10 s for the background, respectively. Correction for matrix effects was applied using the *PhiRhoZ* method, as implemented in the JEOL suite of programs. The following natural and synthetic standards (with spectral lines) were used: grossular (Ca*K*α, Si*K*α), nickeline (As*K*α), synthetic YPO_4 (Y*L*α, P*K*α), synthetic Ln(PO_4) set (La*L*α, Ce*L*α, Pr*L*α, Nd*L*α, Sm*L*α, Eu*L*α, Gd*L*α, Tb*L*α, Dy*L*α, Ho*L*α, Er*L*α, Tm*L*α, Yb*L*α, Lu*L*α), synthetic UO_2 (U*M*β), synthetic ThO_2 (Th*M*α) and galena (Pb*M*α). Backscattered (BSE) images were acquired (Figure 8.3), as well as EDS compositional maps for the Ch11 sample, concerning the concentration of As, Ce, Sm and Th (see section 9.1). The average chemical composition for all the samples (excluding the more heterogeneous Ch13 and Ch16 specimens) is reported in Table 8.1. The chemical composition, expressed as oxide wt% and *atoms per formula unit* (apfu), pertaining to all the points of analysis, is reported in section 13 (Table S13.1- Table S13.15). Chemical maps, pertaining to the sample Ch11 have been collected for the following elements: As, Sm, Ce and Th.

7.2 Raman spectroscopy

Unoriented micro-Raman spectroscopy analysis of gasparite-(Ce) has been carried out, at room conditions, at the Earth Science Department "A. Desio" of the University of Milano, using a Horiba LabRam HR Evolution micro-Raman spectrometer, equipped with an Nd-YAG 532 nm/100 mW, a Peltier-cooled charge-coupled device (CCD) detector, an Olympus microscope having 100× objectives and Ultra Low Frequency (ULF) filters. In addition, the 10% laser power filter used yields to an esteemed power of 6 mW on the sample surface. The spectra were collected with the *Labspec* software in the region between 30 to 1200 cm^{-1} and in the range 3200-4000 cm^{-1}, both with a step size of 1.8 cm^{-1} and 20 s of acquisition time. Peak analysis has been conducted using the *OriginPro* suite (OriginLab Corporation 2019).

7.3 Single crystal X-ray diffraction and structure refinement protocol

The ambient conditions single-crystal X-ray diffraction experiments were performed at the ESD-MI using a Rigaku XtaLAB Synergy-S diffractometer, equipped with a HyPix-6000HE HPC area detector and a PhotonJet-S Mo-*K*α (λ=0.71073 Å) microsource, operating at 50 kV and 1 mA. Each data collection was performed using a sample-to-detector distance of 62 mm and a step-scan width of 0.5°. The crystal size of all the samples investigated and the exposure times are reported in Table 7.2. For all the collected datasets, indexing of the diffraction peaks, unit-cell refinement and intensity data reduction were performed using the *CrysAlisPro* software (Rigaku Oxford Diffraction 2019).

Table 7.2: Selected data collections parameters pertaining to the single-crystal X-ray diffraction performed under ambient conditions.

Sample	Exposure time per frame (s)	Crystal size (μm·μm·μm)
Mon1	0.5	200·100·100
Mon2	3	80·80·70
Gasp3	170	10·10·5
Gasp4	60	20·20·10
Ch6	15	50·30·30
Ch7	20	50·50·30
Ch8	60	40·30·30
Ch9	10	20·20·15
Ch10	20	40·30·20
Ch11	10	20·20·15
Ch12	60	20·20·10
Ch13	60	20·20·10
Xen14	16	20·20·15
Mon14	2	50·50·50
Ch16	30	30·30·20

7.4 High-pressure single-crystal X-ray diffraction

7.4.1 High-pressure single-crystal X-ray diffraction and structure refinement protocol

In situ high-pressure single-crystal synchrotron X-ray diffraction experiments have been conducted at two different synchrotron beamlines: the P02.2 extreme condition beamline at Desy Petra III facilities (Hamburg, Germany) and the ID15b beamline at the European Synchrotron Radiation Facility, ESRF (Grenoble, France). Single crystals of REE-bearing minerals have been used. Details about the single-crystal X-ray diffraction experiments are summarized in Table 7.3. A parallel monochromatic incident X-ray beam was used. For each *P*-point, the collection strategy consisted in a step-wise ω-scan, with a step-width of 0.5°. The pressure increase was controlled through a remote, automated pressure-driven system. X-ray diffraction patterns were collected with a flat-panel detector (for details, see Table 7.3). Further details concerning the beamline setup are reported in Merlini and Hanfland (2013) for the ID15b beamline, while an accurate description of the P02.2 extreme conditions beamline is discussed in Rothkirch et al. (2013), Liermann et al (2015) and Bykova et al.

(2019). For all the experiments, REE-bearing minerals crystals were loaded in a membrane-driven diamond anvil cell (DAC), equipped with Boehler-Almax designed diamonds/seats. Metallic foils (steel or rhenium) were pre-indented to ca. 70 μm and then drilled by spark-erosion to obtain *P*-chambers. Ruby spheres were adopted as pressure calibrants (pressure uncertainty ±0.05 GPa; Mao et al. 1986; Chervin et al. 2001). Indexing of the X-ray diffraction peaks, unit-cell refinements and intensity data reductions were performed using the *CrysAlisPro* package (Rigaku Oxford Diffraction 2018). Absorption effects, due to the DAC components, were corrected using the semi-empirical ABSPACK routine, implemented in *CrysAlisPro*.

Table 7.3: details about the H*P* X-ray diffraction experiments.

Ramp name	Technique	Wavelenght (Å)	Sample to detector distance	*P*-transmitting media	Detector type	Exp. time	Synchrotron line
Ch10-P_A	SCXRD	0.40997	179.22	*m.e.w.*	Eiger2 9M CdTe	0.2	ID15b, ESRF
Ch10-P_B	SCXRD	0.40997	199.21	helium	Eiger2 9M CdTe	0.5	ID15b, ESRF
Ch13-P_C	PXRD	0.4830	370.72	*m.e.w.*	Perkin Elmer XRD1621	15 (total)	P02.2, Petra III
Xen14-P_D	SCXRD	0.29060	373.01	neon	Perkin Elmer XRD1621	1	P02.2, Petra III
Xen14-P_E	SCXRD	0.41029	179.19	helium	Eiger2 9M CdTe	0.5	ID15b, ESRF
Gasp3-P_F	SCXRD	0.41046	260.32	*m.e.w.*	Eiger2 9M CdTe	0.5	ID15b, ESRF
Gasp3-P_G	SCXRD	0.41046	260.32	helium	Eiger2 9M CdTe	0.2	ID15b, ESRF
Mon14-P_H	SCXRD	0.29060	373.01	neon	Perkin Elmer XRD1621	1	P02.2, Petra III

7.4.2 High-pressure powder X-ray diffraction

The high-pressure powder diffraction experiments have been performed at the P02.2 extreme condition beamline at Desy Petra III facilities (Hamburg, Germany), with a wavelength of λ =0.483 Å (25 keV) and a Debye-Scherrer geometry. The sample, several grains of the chernovite-(Y), belonging to the Ch13 sample, have been grinded to powder in an agata mortar to a proper size. Then, the sample, has been loaded into a DAC, equipped with Boehler-Almax designed diamonds of 400 μm culet size). Further detail about the beamline and the experimental procedure are reported in section 7.4.1 above.

The data collection strategy consists in a 30° rotation along ω, for an exposure time of The X-ray diffraction signals captured by the flat panel detector have been finalized and integrated by means of

the *Dioptas* software (Prescher and Prakapenka 2015), in order to remove the background noise due to DAC components and extract the *2θ*-intensity pattern for each experimental point. The model refined according to the protocol described in section 7.3 for the Ch13 sample was used as starting model. For each P_{step}, Rietveld refinements were performed over the entire measured profile using the *GSAS-II* software: the unit-cell parameters, crystallite size, individual scale factor and profile parameters have been modeled. Moreover, the background signal has been interpolated through a Chebychev polynomial function, with 4 to 15 terms.

7.5 High-temperature X-ray diffraction

7.5.1 High-temperature single-crystal X-ray diffraction

The high temerpature single-crystal X-ray diffraction data have been collected at the Department of Mineralogy and Petrology of the University of Innsbruck. The data collection has been conducted using a Stoe IPDS II diffractometer systems with a Heatstream H*T* device, which provides a continuous hot N_2 flux and the diffraction pattern has been collected using an image plate detector. The primary X-ray beam consist in Mo-anode, *K*α X-ray tube, operating at 50 kV and 40 mA. A plane graphite monochromator and a pinhole drove the beam to the sample, set at 100 mm from an image-plate detector. The temperature calibration had been previously conducted using the decomposition reactions of K_2SO_4 and K_2CrO_4, embodied into glass capillaries. Further details about the experimental setup and the calibration strategy are reported in Stoe and Cie (2004). The samples, a monazite-(Ce) (170×100×70 μm in size) and a xenotime-(Y) (220×150×100 μm in size) crystals have been inserted into 0.1 mm SiO_2 glass capillaries. For both the samples the data collection consists in a ω-axis rotation, between -180° and +180°, with a step size of 1° (see Table 7.4 for details). Further details about the experimental setting are reported in Krüger and Breil (2008). Further details about the experiments are reported in Table 7.4. The *WinXpose* software (Stoe and Cie 2008) has been used to treat the H*T* data. The indexed cell parameters were always compatible with either the unit-cells of chernovite-(Y), xenotime-(Y) or monazite-(Ce).

Table 7.4: scheme of the collected X-ray diffraction H*T*-ramps.

Ramp name	*Wavelenght (Å)*	*Exp. time*	*T*-range (° C)	Technique
Ch10-T_I	0.71359	5.5	106-780	SCXRD
Ch10-T_L	0.71359	60.0	106-780	SCXRD
Ch13-T_M	0.7293	-	30-1000	PXRD
Xen14-T_N	0.71359	2.0	30-780	SCXRD
Mon14-T_O	0.71359	2.0	30-780	SCXRD

7.5.2 High-temperature powder X-ray diffraction

The high-temperature powder diffraction experiments have been performed at the MCX beamline at the Elettra synchrotron (Basovizza, Trieste Italy), with a wavelength of λ =0.7293 Å (17 keV) and a Debye-Scherrer setting. The sample, several grains of the chernovite-(Y), Ch13 sample, has been grinded to powder in an agate mortar and then loaded in quartz capillary (0.3 mm as outer diameter). For each experimental point, the data collection strategy consisted in a 2θ-scan between 8° and 60°. A step size of 0.008° has been applied and an equivalent counting time for 1 s/step has been used. During the data collection, the sample spins at a rate of 1000 rotation per minute along the φ-axis. The heating of the sample was allowed by an air blower, which operates between the room temperature and 1000° C. Further details concerning the experimental setting are reported in Rebuffi et al. (2014) and Lausi et al. (2015). For each T_{step}, a Rietveld refinement was performed over the entire measured profile using the *GSAS-II* software (Toby and Von Dreele 2013). The unit-cell parameters, crystallite size, overall scale factor, zero shift have been modeled along with the profile paramenters. Moreover, the background signal has been interpolated through a Chebychev polynomial function, with 7 to 20 terms. The structural refinements have also been conducted, starting from the structural model defined for the Ch13 sample by Pagliaro et al. (2022). The structural refinements have been performed by keeping the occupancies and the atomic displacement parameters (ADP) fixed. Atomic coordinates have been kept identical for atoms occupying the same atomic site.

7.6 Combined *in situ* H*P*–H*T* single-crystal X-ray diffraction

Two combined, isothermal H*P*–H*T* single-crystal X-ray diffraction ramps have been collected on both chernovite-(Y) and monazite-(Ce) (see Table 7.5). Resistive heated DACs (Figure 4.1), equipped with Boehler-Almax diamonds (400 μm culet size) have been used as devices to increase both temperature and pressure. The data collection strategies consisted in a step ω-scan in the range ±30°, with a step-size of 0.5°. The sample, along with gold, used as pressure calibrant, was loaded in a pressure chamber, consisting in a hole pierced in a rhenium foil pre-indented to 60 μm. The sample heating was allowed by a resistive graphite sheet placed beneath the diamonds. Two Pt:Pt–Rh thermocouples, connected to the graphite resistor, were used to check the temperature of the ongoing experiments and change the resistor current in order to achieve the target temperature. Further information related to the experiments are listed into Table 7.5, while more details related to the experimental setup are reported by Liermann et al. (2015), Comboni et al. (2018), Méndez et al.

(2020). Pressure determination has been conducted according to the *P–T–V* equation of state of gold, after Fei et al. (2004; 2007).

Table 7.5: scheme of the collected single crystal X-ray diffraction *HP–HT-ramps.*

Ramp name	*Wavelenght (Å)*	Nominal *T* (° C)	Detector type	Sample to detector distance	Exp. time	*P*-transmitting media
Ch10-PT_{250}	0.29050	250	Perkin Elmer XRD1621	400.19	0.5	Silicon oil
Ch10-PT_{500}	0.29050	500	Perkin Elmer XRD1621	400.19	0.5	Silicon oil
Mon14-PT_{250}	0.29060	250	Perkin Elmer XRD1621	368.33	0.5	Silicon oil
Mon14-PT_{500}	0.29060	540	Perkin Elmer XRD1621	368.33	0.5	Silicon oil

7.7 Structure refinements

All the structure refinements were performed using the Jana2006 software (Petříček et al. 2014), starting from the models reported by Strada and Schwendimann (1934) for chernovite-(Y), Ni et al. (1995) for xenotime-(Y), Kolitsch and Holtsman (2004a) for gasparite-(Ce) and Ni et al. (1995) for The site occupancy factors of the *A* (REE-bearing) and tetrahedral sites were fixed according to the average chemical composition obtained from EPMA-WDS analysis for each crystal sample (Table 8.1), leaving out the elements with a low concentration (below 0.02 apfu) and assuming a full occupancy for both the sites. For the Ch11 and Ch13 samples, characterized by a significant chemical variability the same strategy has been followed, but the relative occupancies of the different chemical species have been varied (keeping the consistency with the measured chemical data) in order to obtain the best figures of merit of the structure refinements. Each structure refinement was performed adopting anisotropic displacement parameters (ADP). Considering the structure refinement for the high-pressure and high-temperature ramps a slightly different refinement protocol has been applied. In this case, it has been observed that the best figure of merit was obtained when the minor elements were excluded from the structure modelling. In this light, a cutoff for all the elements below 0.03 *atoms per formula unit* (apfu) has been applied. Moreover, in case of gasparite-(Ce), Ca was also excluded from the refinements, as this led to better figures of merit. For all the refinements based on *in situ* high-pressure diffraction data, in order to reduce the number of refined variables, the atomic displacement parameters (ADP) were refined as isotropic. All the refinements converged with no significant correlations among the refined variables. Some statistical parameters pertaining to the refinements are reported in Table 7.6.

Table 7.6: Selected statistical parameters pertaining to the single-crystal X-ray diffraction data collections and structure refinements of this study.

Sample	R_{int}	R_1 (obs)	R_1 (all)	wR_1 (obs)	Observed reflections $I > 3\sigma(I)$	Unique reflections	Refined param.	Isotropic Extinction refined
Mon1	0.0532	0.0276	0.0317	0.0344	1351	1515	55	no
Mon2	0.0353	0.0257	0.0299	0.0299	1314	1515	55	no
Gasp3	0.0544	0.0398	0.0726	0.0409	1032	1582	55	no
Gasp4	0.0939	0.0473	0.0750	0.0487	831	1088	56	yes
Ch6	0.0270	0.0161	0.0188	0.0205	190	219	12	yes
Ch7	0.0382	0.0361	0.0497	0.0829	159	219	11	no
Ch8	0.0531	0.0351	0.0426	0.0364	108	135	11	no
Ch9	0.0299	0.0229	0.0297	0.0270	119	151	11	no
Ch10	0.0546	0.0444	0.0511	0.0502	180	218	11	no
Ch11	0.0591	0.0371	0.0553	0.0454	151	214	11	no
Ch12	0.0109	0.0142	0.0153	0.0286	110	115	11	no
Ch13	0.0374	0.0330	0.0698	0.0373	132	223	11	no
Xen14	0.0282	0.0214	0.0260	0.0270	127	142	11	no
Mon14	0.0494	0.0194	0.0235	0.0228	917	1029	55	no
Ch16	0.0492	0.0439	0.0567	0.0530	88	107	11	no

Chapter 8

8 Results

8.1 Mineral association and habit of the REE-bearing minerals

Chernovite-(Y) occurs as idiomorphic bipyramidal or prismatic crystals, as well as micrometric aggregates (Figure 8.1). Bipyramidal crystals represent the most common form: they were identified within the samples Ch6, Ch7, Ch8, Ch9, Ch10 (Figure 8.1a), Ch12 (Figure 3.5, Figure 8.1c) and Ch13. Xenotime-(Y), has a bipyramidal habit as well (Figure 8.1f). Chernovite-(Y) forms idiomorphic crystals as Ch11 (Figure 8.1b) and Ch12 (Figure 8.1) or Ch13 and Ch16, ranging from 40 μm to 2 mm in size (Figure 8.1d,e).

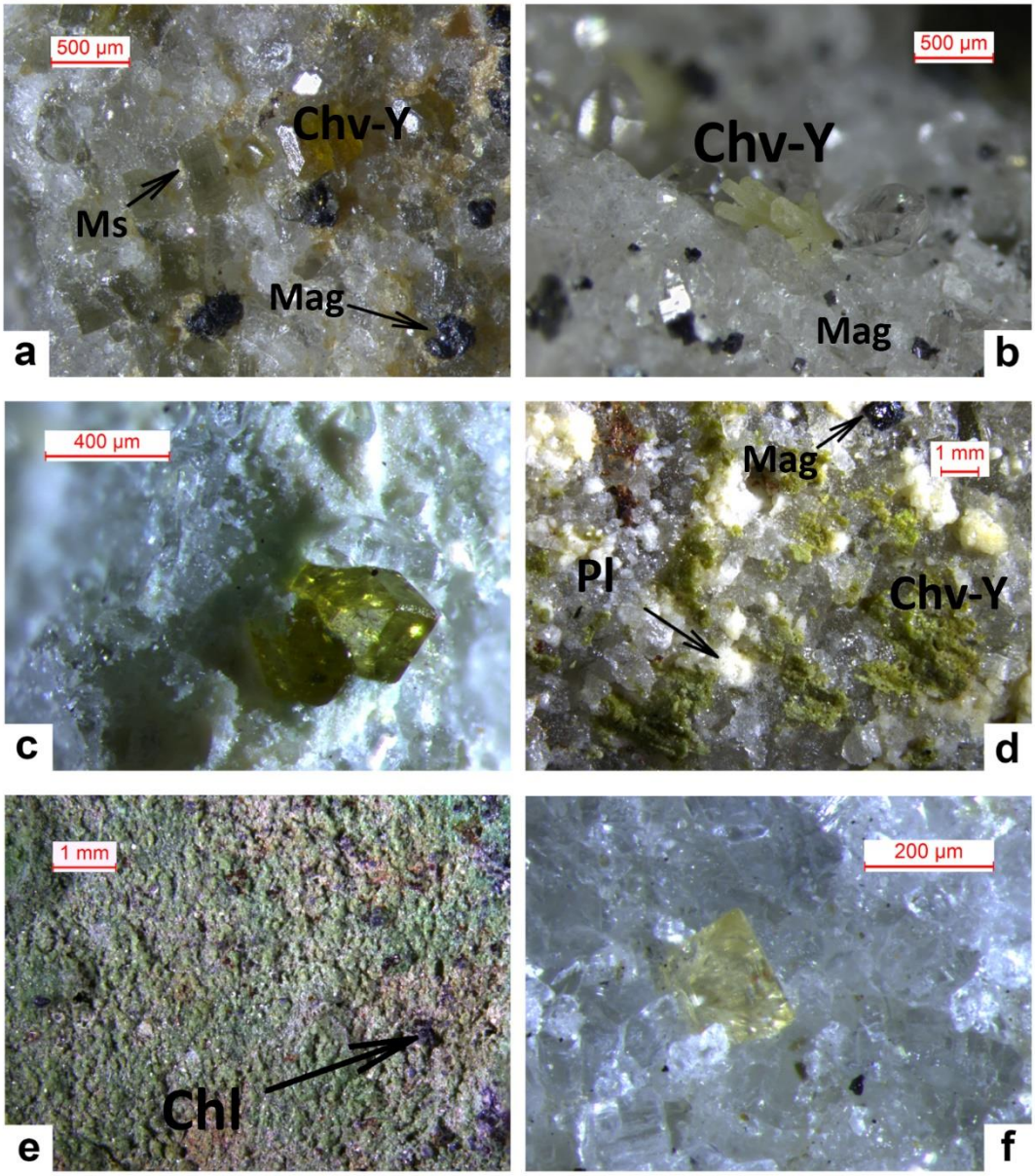

Figure 8.1: Photographs of selected samples from the Alpine quartz fissures of Mt. Cervandone bearing REE-phosphates and -arsenates: **(a)** yellow Ch10 chernovite-(Y) sample with magnetite and muscovite on quartz; **(b)** prismatic Ch11 chernovite-(Y) sample with magnetite grains on quartz; **(c)** yellow Ch12 chernovite-(Y) sample on quartz; **(d)** greenish microcrystals of Ch16 chernovite-(Y) sample, with plagioclase and magnetite, on quartz; **(e)** M-C13 orthogneiss lined with several Ch13 chernovite-(Y) microcrystals and few grains of clinochlore; **(f)** bipyramidal crystal of Xen14 xenotime-(Y) on quartz (see also Table 7.1). [Chv-Y: chernovite-(Y); Mag: magnetite; Ms: muscovite; Pl: plagioclase; Chl: clinochlore. Warr 2021].

Among the chernovites-(Y), only the Ch11 sample (Figure 8.2b) shows a prismatic habit. The three monazite-(Ce) samples are euhedral and vitreous orangish aggregates (or millimetric crystals) (Figure 8.2a), coupled with anhedral aggregates in Mon2 and Mon14. The samples of gasparite-(Ce) are characterized by brownish to green crystals (3 to 20 µm in diameter, Figure 8.2b) clustered in

aggregates. Both the samples of gasparite-(Ce) under investigation were formed by replacement of barrel shape crystals of synchysite-(Ce).

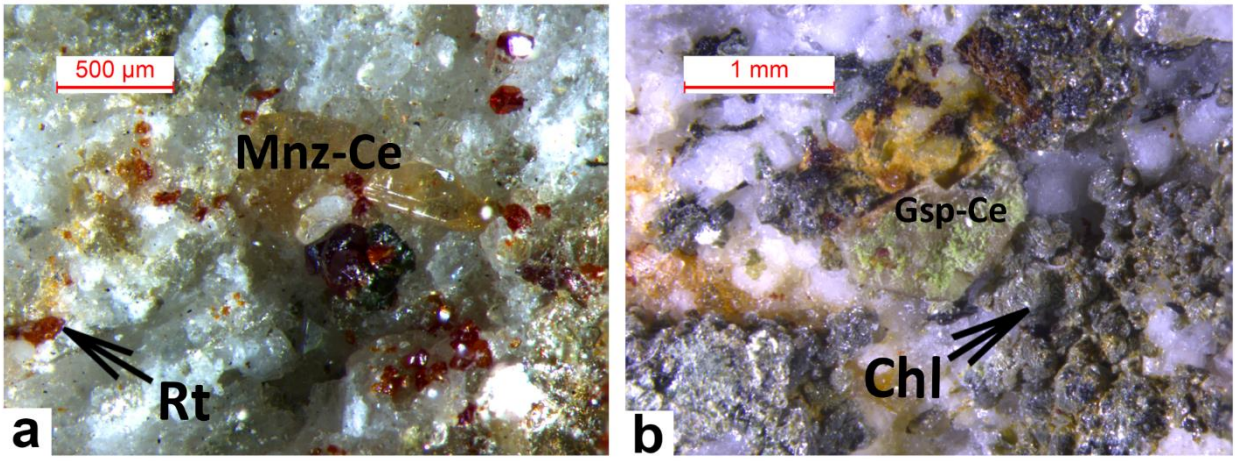

Figure 8.2: Photographs of two samples of the gasparite-(Ce)–monazite-(Ce) series: (**a)** Mon2 monazite-(Ce) sample, with rutile (red); **(b)** greenish, barrel-shape Gasp4 gasparite-(Ce) sample, pseudomorph after synchysite-(Ce), with clinochlore grains, on quartz. [Rt: rutile; Mnz-Ce: monazite-(Ce); Gsp-Ce: gasparite-(Ce); Chl: clinochlore. Warr 2021].

8.2 Chemical composition by EPMA-WDS analysis

Table 8.1 reports the average chemical composition of the samples Mon1, Mon2, Gasp3, Gasp4, Ch6, Ch7, Ch8, Ch9, Ch10, Ch11, Ch12, Xen14 and Mon14, while in Table S13.12 and Table S13.15 are reported the results from each point analysis of the chemically heterogeneous samples, Ch13 and Ch16 (Table S13.1- Table S13.15 report the chemical analysis of each point of analysis). For the sample Ch11, the average chemical compositions of four domains, identified from EPMA compositional maps (see Figure 8.3), are reported in Table 8.1, labeled as $Ch11_a$ $Ch11_b$, $Ch11_c$ and $Ch11_d$.

Figure 8.3: BSE images of selected samples under investigation: **(a)** quasi-homogeneous crystal of Ch10, containing a brighter $ThSiO_4$-enriched level; **(b)** crystal of Mon2 monazite-(Ce) sample, showing brighter domains characterized by a higher Th-content; **(c)** chemically-homogeneous and fractured Xen14 xenotime-(Y) sample, containing $ThSiO_4$ grains (indicated by the yellow arrow); **(d)** highly zoned Ch11 sample, with $ThSiO_4$ grains indicated by the yellow arrow; **(e)** Gasp3 gasparite-(Ce) sample, made by several microcrystals (~10 µm size); **(f)** highly-zoned Ch16 chernovite-(Y) sample, containing P-enriched darker patchy domains and brighter As-enriched domains, separated by lobate interface.

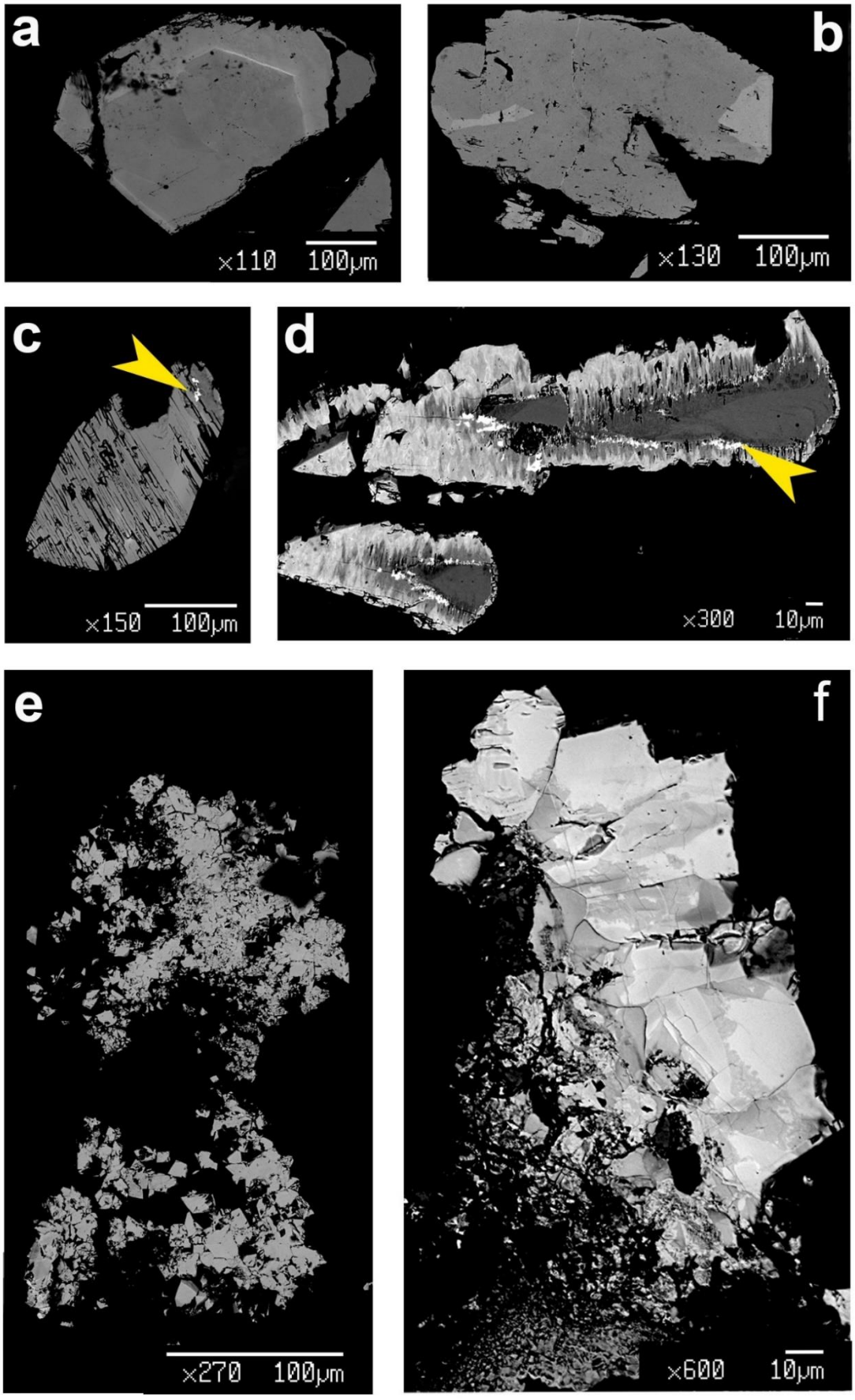
a
×110 100μm
b
×130 100μm
c
×150 100μm
d
×300 10μm
e
×270 100μm
f
×600 10μm

Table 8.1: Average chemical composition (expressed in oxide wt % and in atoms per formula unit (apfu) calculated on the basis of 4 oxygen atoms) of all the samples under investigation (except for the heterogeneous Ch13 and Ch16 specimens, the composition.

	Mon1		Mon2		Gasp3		Gasp4		Ch6		Ch7	
As_2O_5	0.15	(0.09-0.23)	2.26	(1.40-3.14)	38.61	(36.38-40.59)	41.39	(38.45-42.97)	33.41	(30.14-35.61)	37.10	(32.82-39.44)
P_2O_5	28.64	(28.33-29.00)	27.77	(26.69-28.62)	0.83	(0.25-3.01)	0.13	(0-0.61)	7.81	(2.17-10.1)	5.29	(4.01-8.87)
SiO_2	0.21	(0.05-0.37)	0.24	(0.09-0.59)	1.72	(1.21-2.39)	1.48	(0.58-3.11)	0.65	(0.39-3.17)	0.76	(0.29-1.08)
V_2O_5	b.d.l.		b.d.l.		b.d.l.		b.d.l.		0.01	(0-0.07)	0.02	(0-0.10)
CaO	1.40	(0.88-1.65)	0.68	(0.20-1.22)	1.46	(1.22-1.79)	1.92	(1.64-2.26)	0.02	(0-0.06)	0.01	(0-0.03)
Y_2O_3	0.90	(0.65-1.12)	0.52	(0.43-0.67)	0.01	(0-0.07)	0.05	(0-0.19)	33.97	(25.38-35.05)	35.87	(35.11-37.17)
La_2O_3	13.24	(12.12-14.76)	13.08	(12.39-14.53)	11.38	(10.74-12.16)	12.86	(10.89-14.43)	0.04	(0-0.22)	0.05	(0-0.16)
Ce_2O_3	29.88	(28.77-31.23)	31.31	(29.13-32.61)	28.3	(27.08-31.19)	26.86	(24.56-27.95)	0.13	(0.01-0.37)	0.12	(0-0.20)
Pr_2O_3	3.28	(2.79-3.45)	3.70	(3.10-4.03)	2.98	(2.68-3.38)	2.56	(1.92-2.82)	0.04	(0-0.17)	b.d.l.	
Nd_2O_3	12.93	(12.15-14.36)	13.70	(12.72-15.03)	11.63	(10.26-12.75)	9.40	(8.03-10.2)	0.58	(0.38-2.20)	0.25	(0.07-0.35)
Sm_2O_3	2.51	(2.07-3.21)	2.51	(2.28-2.81)	1.43	(0.90-1.84)	1.22	(0.91-1.48)	0.96	(0.73-2.36)	0.43	(0.22-0.61)
Eu_2O_3	b.d.l.		b.d.l.		b.d.l.		b.d.l.		b.d.l.		b.d.l.	
Gd_2O_3	1.88	(1.33-2.33)	1.48	(1.17-1.93)	0.38	(0.04-0.62)	0.62	(0.31-0.97)	2.58	(2.10-4.52)	1.58	(1.38-1.85)
Tb_2O_3	b.d.l.		b.d.l.		b.d.l.		b.d.l.		0.59	(0.31-0.77)	0.46	(0.29-0.62)
Dy_2O_3	0.39	(0.18-0.70)	0.30	(0.11-0.49)	0.03	(0-0.13)	0.04	(0-0.22)	4.86	(4.45-5.36)	4.07	(3.68-4.41)
Ho_2O_3	0.45	(0.21-0.75)	0.32	(0.01-0.54)	b.d.l.		0.03	(0-0.16)	2.39	(2.11-3.05)	1.87	(1.57-2.28)
Er_2O_3	0.02	(0-0.10)	b.d.l.		0.03	(0-0.13)	0.03	(0-0.23)	3.38	(2.23-3.85)	3.36	(3.20-3.72)
Tm_2O_3	0.08	(0-0.30)	0.04	(0-0.32)	0.03	(0-0.15)	0.01	(0-0.13)	0.42	(0.11-0.62)	0.36	(0.18-0.53)
Yb_2O_3	0.01	(0-0.08)	0.01	(0-0.06)	0.04	(0-0.16)	0.04	(0-0.22)	2.91	(1.73-3.20)	2.94	(2.56-3.25)
Lu_2O_3	0.15	(0.02-0.46)	0.10	(0-0.34)	0.04	(0-0.14)	0.05	(0-0.16)	1.21	(0.82-1.54)	0.99	(0.74-1.33)
PbO	0.02	(0-0.12)	0.01	(0-0.05)	0.02	(0-0.09)	0.05	(0-0.21)	0.19	(0-0.37)	0.29	(0.13-0.40)
ThO_2	3.10	(1.47-4.52)	2.32	(0.90-5.30)	0.90	(0.13-2.23)	1.96	(0-9.13)	2.51	(1.72-10.8)	0.78	(0.33-0.99)
UO_2	0.05	(0-0.20)	0.13	(0.00-0.23)	b.d.l.		0.06	(0-0.26)	0.91	(0.60-1.96)	3.39	(2.08-4.04)
Tot.	99.39		100.6		99.91		100.87		99.76		100.10	
As	0.003		0.047		0.913		0.964		0.698		0.777	
P	0.968		0.933		0.031		0.005		0.264		0.179	
Si	0.008		0.009		0.078		0.066		0.026		0.030	
V	/		/		/		/		/		/	
Ca	0.060		0.029		0.071		0.092		0.001		0	
Y	0.019		0.011		/		0.001		0.723		0.765	
La	0.195		0.191		0.189		0.211		/		/	
Ce	0.436		0.455		0.468		0.438		0.002		0.001	

Pr	0.047	0.053	0.049	0.041	0	/
Nd	0.184	0.194	0.188	0.149	0.008	0.003
Sm	0.034	0.034	0.022	0.019	0.013	0.005
Eu	/	/	/	/	/	
Gd	0.024	0.019	0.005	0.009	0.042	0.042
Tb	/	/	/	/	0.007	0.006
Dy	0.005	0.003	/	0.001	0.062	0.052
Ho	0.005	0.004	/	/	0.030	0.023
Er	/	/	/	/	0.022	0.007
Tm	0.001	/	/	/	0.005	0.004
Yb	/	/	0.001	0.001	0.035	0.035
Lu	0.002	0.001	0.001	0.001	0.014	0.012
Pb	/	/	/	/	0.002	0.003
Th	0.028	0.021	0.009	0.019	0.022	0.007
U	.698	0.001	/	/	0.008	0.030

b.d.l.: below the detection limit

	Ch8		Ch9		Ch10		$Ch11_a$		$Ch11_b$		$Ch11_c$	
As_2O_5	36.12	(34.22-37.14)	36.26	(34.38-38.83)	36.11	(34.77-36.91)	21.53	(19.55-22.21)	23.27	(21.75-23.39)	38.7	(36.5-41.6)
P_2O_5	5.41	(4.63-7.14)	5.64	(3.94-7.27)	5.41	(3.93-6.86)	18.73	(17.24-19.10)	15.81	(14.62-16.05)	2.79	(1.17-4.45)
SiO_2	0.67	(0.43-0.76)	0.62	(0.16-0.81)	0.82	(0.45-1.59)	0.11	(0.04-0.17)	0.87	(0.83-0.86)	1.01	(0.43-1.50)
V_2O_5	0.01	(0-0.04)	0.01	(0-0.03)	0.01	(0-0.05)	0.02	(0.00-0.04)	b.d.l.		b.d.l.	
CaO	b.d.l.		0.01	(0-0.05)	0.01	(0-0.03)	0.02	(0-0.04)	0.01	(0.00-0.02)	0.06	(0.02-0.12)
Y_2O_3	34.30	(33.67-35.22)	34.31	(33.70-35.01)	33.10	(29.91-35.38)	39.24	(38.03-38.10)	36.94	(35.59-36.07)	28.60	(26.5-31.3)
La_2O_3	0.03	(0-0.10)	0.06	(0-0.14)	0.01	(0-0.05)	0.01	(0-0.02)	b.d.l.		0.12	(0.04-0.24)
Ce_2O_3	0.09	(0-0.19)	0.14	(0-0.28)	0.13	(0.01-0.25)	0.03	(0-0.07)	0.10	(0.10-0.10)	1.24	(0.64-2.34)
Pr_2O_3	0.02	(0-0.12)	0.05	(0-0.14)	0.04	(0-0.09)	0.03	(0-0.06)	0.03	(0-0.06)	0.28	(0.00-0.63)
Nd_2O_3	0.37	(0.09-0.54)	0.37	(0.19-0.53)	0.37	(0.03-0.65)	0.36	(0.30-0.39)	0.40	(0.35-0.42)	2.75	(1.38-4.13)
Sm_2O_3	0.86	(0.65-0.97)	0.72	(0.34-0.93)	0.73	(0.55-1.06)	0.74	(0.68-0.75)	0.56	(0.41-0.68)	1.79	(1.37-2.14)
Eu_2O_3	b.d.l.		b.d.l.		b.d.l.		b.d.l.		b.d.l.		b.d.l.	
Gd_2O_3	2.98	(2.64-3.35)	2.92	(1.82-3.45)	2.30	(1.73-3.07)	2.11	(1.99-2.11)	1.98	(1.89-1.94)	3.24	(2.82-3.57)
Tb_2O_3	0.58	(0.49-0.68)	0.66	(0.52-0.85)	0.55	(0.39-0.60)	0.50	(0.35-0.62)	0.47	(0.38-0.52)	0.53	(0.47-0.60)
Dy_2O_3	5.27	(4.79-5.59)	4.96	(4.23-5.27)	5.10	(4.39-5.58)	5.18	(4.92-5.13)	5.31	(5.11-5.19)	4.47	(4.19-4.85)
Ho_2O_3	2.68	(2.55-2.91)	2.64	(2.24-2.77)	2.39	(2.09-2.78)	2.33	(2.09-2.43)	2.31	(2.19-2.29)	2.6	(2.55-2.63)
Er_2O_3	3.04	(2.72-3.19)	3.11	(2.89-3.42)	3.51	(2.98-4.24)	4.22	(4.01-4.18)	3.83	(3.69-3.75)	2.91	(2.63-3.40)
Tm_2O_3	0.46	(0.24-0.72)	0.44	(0.38-0.61)	0.48	(0.27-0.83)	0.67	(0.52-0.78)	0.33	(0.30-0.34)	0.5	(0.42-0.57)
Yb_2O_3	2.37	(1.69-3.22)	2.40	(1.76-3.31)	3.38	(1.87-5.07)	4.34	(4.16-4.26)	3.79	(3.48-3.87)	2.72	(2.34-3.20)
Lu_2O_3	1.26	(1.05-1.50)	1.14	(0.87-1.39)	1.29	(1.01-1.73)	1.42	(1.36-1.38)	1.43	(1.28-1.49)	0.96	(0.78-1.18)
PbO	0.24	(0.18-0.31)	0.22	(0.06-0.47)	0.26	(0.19-0.31)	0.27	(0.25-0.28)	0.28	(0.24-0.29)	0.21	(0.18-0.23)
ThO_2	3.12	(2.07-3.39)	2.72	(0.89-4.23)	2.40	(0.78-4.94)	0.68	(0.53-0.79)	2.80	(2.58-2.85)	2.78	(1.10-4.23)
UO_2	0.37	(0.28-0.58)	0.76	(0.11-3.79)	1.90	(1.26-2.32)	0.02	(0.00-0.04)	1.24	(0.95-1.45)	1.56	(1.04-2.07)
Tot.	100.39		100.3		100.41		99.58		98.87		100.01	
As	0.764		0.764		0.766		0.408		0.455		0.850	
P	0.185		0.192		0.185		0.575		0.500		0.098	
Si	0.027		0.025		0.033		0.004		0.032		0.042	
V	/		/		/		/		/		/	
Ca	/		/		/		/		/		0.003	
Y	0.739		0.736		0.714		0.757		0.735		0.638	
La	/		/		/		/		/		0.002	
Ce	0.001		0.002		0.001		/		0.001		0.019	
Pr	/		/		/		/		/		0.004	
Nd	0.005		0.005		0.005		0.004		0.005		0.042	

Sm	0.012	0.010	0.010	0.009	0.007	0.026
Eu	/	/	/	/	/	0.000
Gd	0.038	0.039	0.044	0.025	0.024	0.045
Tb	0.007	0.008	0.007	0.006	0.005	0.007
Dy	0.068	0.064	0.066	0.060	0.064	0.060
Ho	0.034	0.033	0.030	0.026	0.027	0.035
Er	0.028	0.039	0.022	0.048	0.045	0.038
Tm	0.005	0.005	0.006	0.007	0.003	0.007
Yb	0.029	0.029	0.042	0.048	0.043	0.035
Lu	0.015	0.013	0.015	0.015	0.016	0.012
Pb	0.002	0.002	0.002	0.002	0.002	0.002
Th	0.028	0.024	0.022	0.005	0.023	0.026
U	0.003	0.006	0.017	/	0.010	0.015

b.d.l.: below the detection limit

	$Ch11_d$		Ch12		Xen14		Mon14	
As_2O_5	44.23	(43.35-43.35)	38.71	(37.68-40.50)	5.49	(3.45-6.81)	1.95	(1.36-2.84)
P_2O_5	0.27	(0.26-0.27)	4.73	(3.55-5.49)	28.7	(25.99-31.00)	27.71	(26.60-
SiO_2	0.03	(0.02-0.05)	0.11	(0.02-0.16)	0.34	(0-0.81)	0.24	(0.02-0.69)
V_2O_5	b.d.l.		0.02	(0-0.06)	b.d.l.		b.d.l.	
CaO	0.11	(0.10-0.12)	0.01	(0-0.04)	0.01	(0-0.06)	1.19	(0.54-1.59)
Y_2O_3	21.44	(20.05-22.83)	34.84	(34.23-35.51)	39.44	(37.11-41.55)	0.54	(0.39-0.62)
La_2O_3	0.62	(0.52-0.73)	0.05	(0-0.13)	0.03	(0-0.12)	14.18	(12.31-
Ce_2O_3	3.67	(3.47-3.87)	0.11	(0.01-0.21)	0.07	(0-0.20)	30.84	(28.41-
Pr_2O_3	1.04	(0.84-1.24)	0.02	(0-0.09)	0.03	(0-0.18)	3.46	(3.09-3.93)
Nd_2O_3	9.91	(8.99-10.82)	0.51	(0.26-0.78)	0.26	(0.08-0.48)	12.88	(12.21-
Sm_2O_3	5.01	(4.85-5.18)	0.79	(0.52-1.23)	0.73	(0.43-1.04)	2.20	(1.86-2.45)
Eu_2O_3	b.d.l.		b.d.l.		b.d.l.		b.d.l.	
Gd_2O_3	5.36	(5.09-5.64)	2.92	(2.52-3.31)	3.84	(2.95-5.03)	1.41	(1.04-2.06)
Tb_2O_3	0.58	(0.57-0.60)	0.78	(0.65-0.97)	0.87	(0.68-1.07)	b.d.l.	
Dy_2O_3	3.05	(2.96-3.14)	5.62	(5.10-6.18)	6.23	(5.36-6.70)	0.27	(0.13-0.43)
Ho_2O_3	2.75	(2.70-2.81)	2.70	(2.25-2.95)	3.27	(2.65-4.14)	0.25	(0.10-0.44)
Er_2O_3	0.97	(0.82-1.12)	2.97	(2.58-3.38)	3.55	(3.13-4.13)	0.03	(0-0.22)
Tm_2O_3	0.47	(0.44-0.51)	0.34	(0.27-0.54)	0.46	(0-0.68)	0.07	(0-0.21)
Yb_2O_3	0.87	(0.83-0.91)	2.11	(1.74-2.43)	3.08	(2.34-3.71)	0.04	(0-0.39)
Lu_2O_3	0.51	(0.49-0.53)	1.23	(0.99-1.54)	1.56	(1.07-1.95)	0.07	(0-0.24)
PbO	0.00	(0-0)	0.23	(0.18-0.29)	0.25	(0.04-0.47)	0.03	(0-0.20)
ThO_2	0.03	(0-0.06)	0.38	(0.21-0.66)	1.89	(0.31-3.87)	2.55	(0.57-5.70)
UO_2	0.04	(0-0.08)	0.78	(0.60-0.99)	0.40	(0.01-0.74)	0.05	(0-0.17)
Tot.	100.97		100.08		100.62		100.05	
As	0.988		0.817		0.102		0.040	
P	0.010		0.161		0.861		0.934	
Si	0.001		0.004		0.012		0.009	
V	/		/		/		/	
Ca	0.005		/		/		0.051	
Y	0.487		0.748		0.744		0.011	
La	0.010		/		/		0.208	
Ce	0.058		0.001		/		0.449	
Pr	0.016		/		/		0.050	
Nd	0.151		0.007		0.003		0.183	

Sm	0.074	0.011	0.008	0.030
Eu	/	/	/	/
Gd	0.076	0.037	0.039	0.018
Tb	0.008	0.01	0.010	/
Dy	0.042	0.073	0.071	0.003
Ho	0.037	0.034	0.036	0.003
Er	0.013	0.003	0.015	/
Tm	0.006	0.004	0.005	/
Yb	0.011	0.026	0.033	/
Lu	0.007	0.015	0.016	/
Pb	/	0.002	0.002	/
Th	/	0.003	0.015	0.023
U	/	0.007	0.003	/

b.d.l.: below the detection limit

8.3 Unit-cell parameters and structure of the studied ATO_4 minerals

The unit-cell parameters of the fifteen mineral specimens, obtained from the single crystal X-ray diffraction patterns are reported in Table 8.2. Moreover, some relevant structural parameters, considered of paramount importance to fully describe the crystal structure of ATO_4 minerals are reported in Table 8.3.

Table 8.2: Unit-cell parameters of all the samples under investigation.

Sample	Mineral	*a* (Å)	*b* (Å)	*c* (Å)	β (°)	*V* (Å^3)
Ch6	Chernovite-(Y)	7.0030(2)	7.0030(2)	6.2117(3)		304.63(2)
Ch7	Chernovite-(Y)	7.0056(3)	7.0056(3)	6.2307(6)		305.79(3)
Ch8	Chernovite-(Y)	7.0216(3)	7.0216(3)	6.2455(3)		307.92(3)
Ch9	Chernovite-(Y)	7.0176(3)	7.0176(3)	6.2343(4)		307.02(3)
Ch10	Chernovite-(Y)	7.0321(2)	7.0321(2)	6.2552(2)		309.32(2)
Ch11	Chernovite-(Y)–xenotime-(Y) s.s.	6.9591(4)	6.9591(4)	6.1386(7)		297.29(4)
Ch12	Chernovite-(Y)	7.0351(2)	7.0351(2)	6.2630(3)		309.97(2)
Ch13	Chernovite-(Y)	7.0540(3)	7.0540(3)	6.2882(4)		312.89(3)
Ch16	Chernovite-(Y)	7.0648(10)	7.0648(10)	6.2860(12)		313.75(9)
Xen14	Xenotime-(Y)	6.9008(3)	6.9008(3)	6.0447(4)		287.86(3)
Gasp4	Gasparite-(Ce)	6.9259(3)	7.1201(3)	6.7137(3)	104.752(5)	320.16(2)
Gasp3	Gasparite-(Ce)	6.9274(3)	7.1273(3)	6.7118(3)	104.668(3)	320.59(2)
Mon1	Monazite-(Ce)	6.77986(11)	7.00460(12)	6.4587(1)	103.526(2)	298.219(8)
Mon2	Monazite-(Ce)	6.7924(2)	7.0173(2)	6.4735(2)	103.519(3)	300.01(2)
Mon14	Monazite-(Ce)	6.78910(14)	7.01221(12)	6.47346(13)	103.595(2)	299.55(1)

Table 8.3: *A*-O and *T*-O bond distances (in Å), volumes of *A*- and *T*-coordination polyhedra (in Å^3) and distortion index (DI, calculated using the routine implemented in the software Vesta 3, Momma and Izumi 2011), based on the structure refinements conducted on all the samples.

Sample	*A*–O1	*A*–O1'	*A*–O2	*A*–O2'	*A*–O2''	*A*–O3	*A*–O3'	*A*–O4	*A*–O4'	*T*–O1	*T*–O2	*T*–O3	*T*–O4	$V(AO_{8,9})$	$V(TO_4)$	*DI(A)*	*DI(T)*
Mon1	2.525(4)	2.452(4)	2.783(4)	2.557(3)	2.642(4)	2.577(3)	2.464(3)	2.519(3)	2.441(3)	1.525(3)	1.546(4)	1.534(3)	1.536(4)	32.29(3)	1.844(10)	0.031	0.004
Mon2	2.510(3)	2.465(3)	2.789(3)	2.559(3)	2.643(2)	2.583(2)	2.469(3)	2.521(2)	2.460(2)	1.536(3)	1.556(3)	1.546(2)	1.523(3)	32.44(2)	1.859(5)	0.031	0.007
Mon14	2.519(3)	2.456(3)	2.791(3)	2.556(3)	2.639(3)	2.581(3)	2.461(3)	2.516(3)	2.449(3)	1.535(2)	1.557(3)	1.549(3)	1.536(4)	32.31(2)	1.875(7)	0.031	0.005
Gasp3	2.550(5)	2.463(5)	2.931(5)	2.532(5)	2.603(5)	2.605(6)	2.435(5)	2.550(5)	2.463(5)	1.668(5)	1.676(5)	1.675(5)	1.660(6)	32.75(6)	2.350(14)	0.037	0.003
Gasp4	2.553(8)	2.449(8)	2.924(7)	2.527(7)	2.618(9)	2.618(9)	2.440(8)	2.546(7)	2.460(7)	1.678(7)	1.660(7)	1.674(7)	1.668(8)	32.80(9)	2.35(1)	0.038	0.004
Ch6	2.4089(13)	2.3019(12)								1.6363(13)				23.45(2)	2.205(5)	0.022	
Ch7	2.414(3)	2.298(3)								1.644(3)				23.46(5)	2.237(14)	0.025	
Ch8	2.419(4)	2.297(4)								1.655(4)				23.51(6)	2.28(2)	0.024	
Ch9	2.410(4)	2.302(3)								1.650(3)				23.46(3)	2.255(11)	0.022	
Ch10	2.419(4)	2.306(3)								1.653(3)				23.66(3)	2.271(8)	0.023	
Ch11	2.401(5)	2.298(5)								1.603(5)				23.27(4)	2.084(10)	0.022	
Ch12	2.416(2)	2.301(3)								1.663(3)				23.55(2)	2.309(4)	0.024	
Ch13	2.424(4)	2.305(5)								1.673(2)				23.71(4)	2.304(11)	0.025	
Ch16	2.422(8)	2.308(9)								1.675(9)				23.73(9)	2.36(2)	0.024	
Xen14	2.389(3)	2.308(3)								1.545(3)				23.22(3)	1.875(7)	0.017	

8.4 Raman Spectroscopy

The Raman spectra of chernovite-(Y), xenotime-(Y), gasparite-(Ce) and monazite-(Ce) have been collected at ambient conditions. The attribution of the signals is reported in section 9.4.

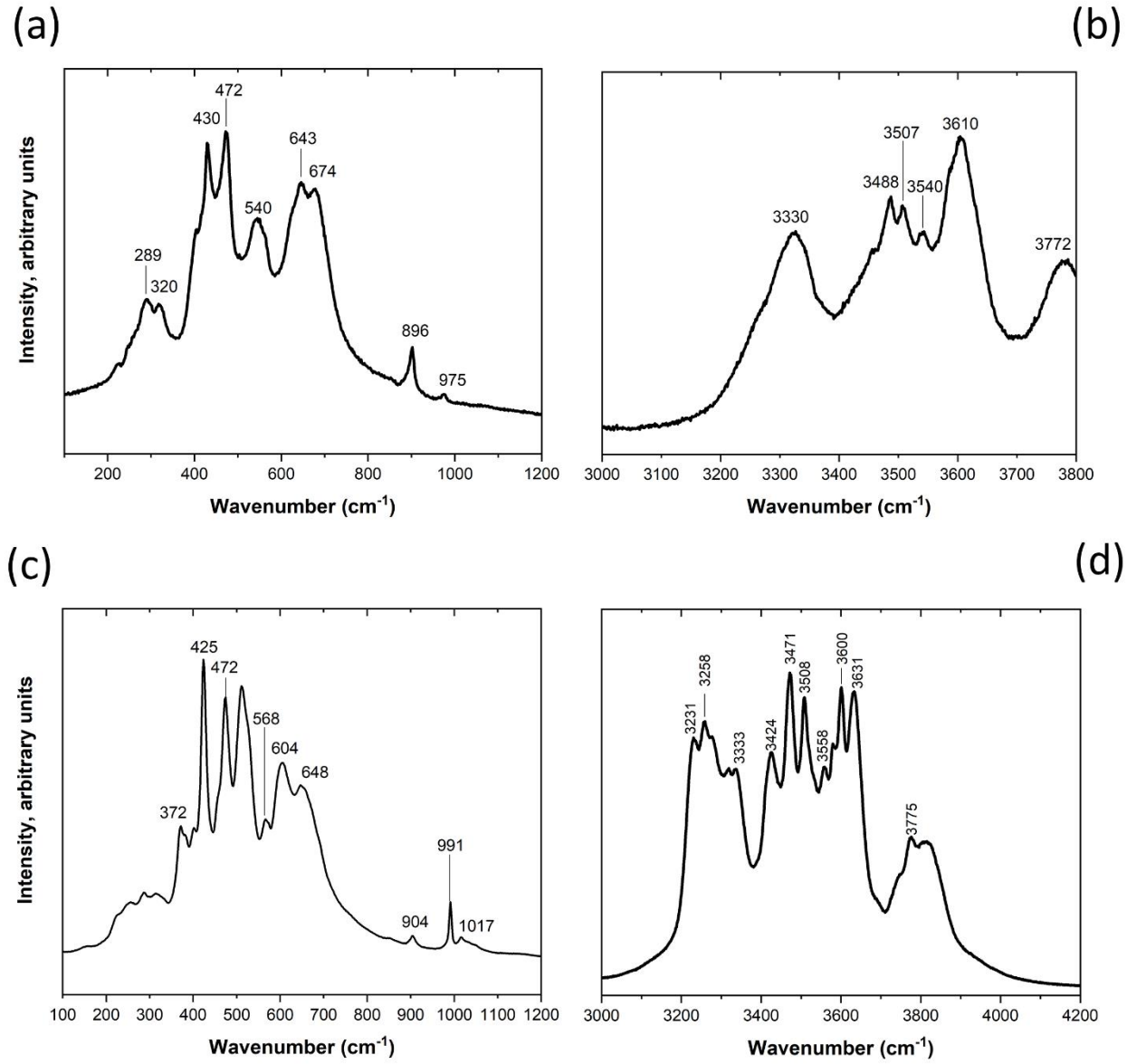

Figure 8.4: details of the Raman spectra showing the 100-200 cm^{-1} region of chernovite-(Y) **(a)**; the 3000-4200 cm^{-1} vibration region of chernovite-(Y) **(b)**; the 200-1200 cm^{-1} vibration region of xenotime-(Y) **(c)** and the 3000-4200 cm^{-1} vibration region of xenotime-(Y) **(d)**. See section 9.4.1 for a complete list of the peaks and their assignments.

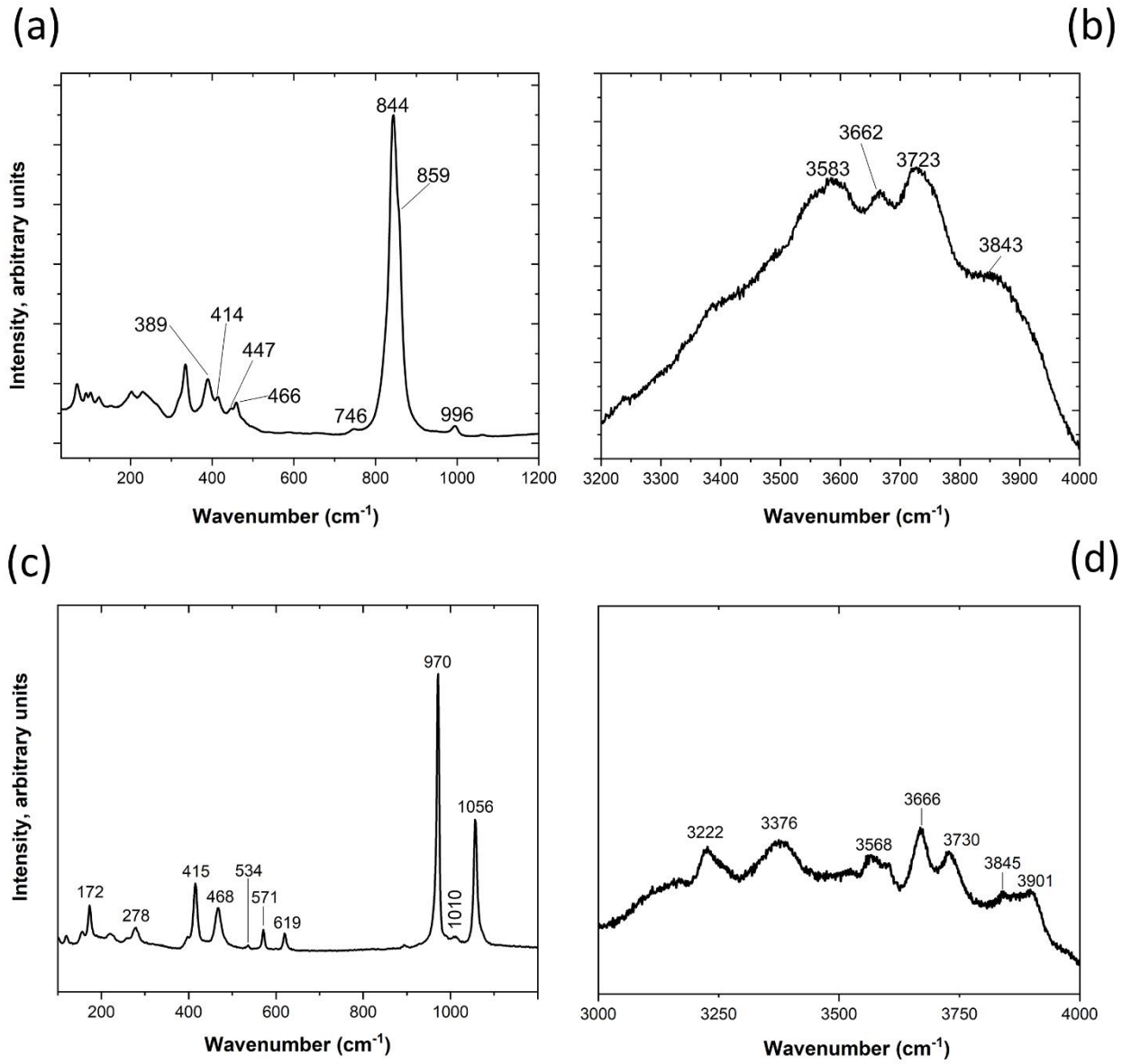

Figure 8.5: Raman spectra of gasparite-(Ce) in the range 30-1200 cm^{-1} **(a)** and in the region (3200-4000 cm^{-1}) **(b)**. See section 9.4.2 for a complete list of the peaks and their assignments.

8.5 High-pressure ramps

Eight different room temperature, H*P* ramps have been performed. The corresponding used technique, facilities and *P*-transmitting media are reported in Table 7.3. The evolution with pressure of the unit-cell parameters is reported in Table 8.4, Table 8.5, Table 8.6, Table 8.7 and Table 8.8. The refined bulk moduli are reported in Table 8.9. For gasparite-(Ce) and monazite-(Ce), in the whole *P*-range investigated, the unit-cell remains compatible with the monazite-type topology. The two zircon-

type minerals, on the other side, undergo a phase transition. Chernovite-(Y), at pressure higher than ~10 GPa is no longer stable, while, at pressure exceeding ~17 GPa, xenotime-(Y) undergoes a phase transition towards a monazite-type topology.

Table 8.4: Unit-cell parameters of chernovite-(Y) at different pressures based on the *m.e.w.* (Ch10-P_A) and He (Ch10-P_B) single crystal X-ray diffraction P-ramps collected on the Ch10 samples.

P (GPa)	a (Å)	c (Å)	V (Å^3)
m.e.w. ramp (Ch10-P_A)			
0.0001	7.03170(12)	6.26060(13)	309.50(2)
0.35	7.0232(2)	6.2549(2)	308.50(2)
1.07	7.0096(2)	6.2503(2)	307.100(14)
2.10	6.9882(2)	6.2411(2)	304.780(14)
2.99	6.97362(10)	6.2340(2)	303.160(11)
4.25	6.9531(2)	6.2252(2)	300.960(14)
4.95	6.9418(2)	6.2203(2)	299.70(2)
5.99	6.9230(2)	6.2102(2)	297.630(13)
7.32	6.9020(10)	6.1989(2)	295.290(10)
8.17	6.89010(10)	6.1926(2)	293.970(11)
9.03	6.8734(2)	6.1829(2)	292.100(13)
He ramp (Ch10-P_B)			
0.0001	7.0380(3)	6.2670(3)	310.40(2)
0.16	7.0350(3)	6.2660(3)	310.10(2)
0.62	7.0250(3)	6.2620(3)	309.00(2)
1.17	7.0150(3)	6.2590(3)	308.00(2)
2.00	6.9970(3)	6.2490(3)	305.90(2)
3.07	6.9760(3)	6.2390(3)	303.60(2)
4.54	6.9490(3)	6.2270(3)	300.60(2)
5.63	6.9330(3)	6.2200(3)	298.90(2)
6.43	6.9190(3)	6.2120(3)	297.30(2)
7.20	6.9040(3)	6.2030(3)	295.60(2)
7.79	6.8939(3)	6.2011(3)	294.70(2)
8.86	6.8780(3)	6.1900(3)	292.80(2)
10.16	6.8600(3)	6.1800(3)	290.80(2)
10.71	6.8500(3)	6.1740(3)	289.60(2)

Table 8.5: Unit-cell parameters of chernovite-(Y) at different pressures based on the *m.e.w* powder X-ray diffraction *P*-ramp collected on the Ch13 sample (Ch13-P_C).

P (GPa)	*a* (Å)	*c* (Å)	*V* (Å^3)
0.0001	7.0780(4)	6.3095(7)	316.09(4)
0.69	7.0675(4)	6.3034(6)	314.86(4)
0.96	7.0577(4)	6.2956(7)	313.59(4)
1.24	7.0473(4)	6.2958(4)	312.68(4)
1.52	7.0502(4)	6.2935(7)	312.82(4)
1.80	7.0380(4)	6.2881(4)	311.47(3)
2.54	7.0273(5)	6.2857(5)	310.40(4)
2.76	7.0193(5)	6.2907(8)	309.94(4)
3.25	7.0088(4)	6.2795(7)	308.47(4)
3.63	7.0033(4)	6.2769(8)	307.86(4)
3.82	6.9946(5)	6.2740(7)	306.95(4)
4.06	6.9952(4)	6.2589(6)	306.27(4)
4.20	6.9867(6)	6.2631(9)	305.73(6)
4.62	6.9825(4)	6.2674(4)	305.57(3)
4.87	6.9763(6)	6.2613(9)	304.73(5)
5.11	6.9708(6)	6.2611(7)	304.24(5)
5.25	6.9663(6)	6.2565(9)	303.62(5)
5.76	6.9588(6)	6.2513(7)	302.72(5)
6.05	6.9539(6)	6.2475(7)	302.10(5)
6.19	6.9515(4)	6.2516(4)	302.09(4)
6.34	6.9497(5)	6.2467(8)	301.71(4)
6.62	6.9432(5)	6.2481(5)	301.21(4)
6.91	6.9384(5)	6.2452(4)	300.66(3)
7.18	6.9358(5)	6.2448(6)	300.41(4)
7.48	6.9259(5)	6.2409(4)	299.37(4)
7.66	6.9276(4)	6.2355(6)	299.25(3)
7.92	6.9253(4)	6.2352(9)	299.04(4)
8.20	6.9130(3)	6.2325(4)	297.84(3)
4.40*	6.9884(6)	6.2594(8)	305.69(5)
3.40*	7.0051(5)	6.2800(8)	308.17(4)
2.31*	7.0324(5)	6.2843(7)	310.79(4)
1.97*	7.0369(4)	6.2897(5)	311.46(4)
0.43*	7.0709(5)	6.3040(6)	315.19(4)

*: P_{steps} collected under decompression conditions.

Table 8.6: Unit-cell parameters of xenotime-(Y) at different pressures based on the Ne and He single crystal X-ray diffraction *P*-ramps.

P (GPa)	*a* (Å)	*b* (Å)	*c* (Å)	*β* (°)	*V* (Å^3)
Ne ramp (Xen14-P_D)					
0.0001	6.9117(2)		6.04500(13)		288.78(5)
0.47	6.8963(5)		6.0475(3)		287.62(3)
1.28	6.8778(4)		6.0417(2)		285.8(2)
3.17	6.8425(4)		6.0271(2)		282.19(2)
4.84	6.8161(4)		6.0159(3)		279.49(3)
8.47	6.7577(4)		5.9875(2)		273.43(2)
9.98	6.7400(4)		5.9791(3)		271.62(2)
10.66	6.7308(4)		5.9761(2)		270.74(2)
11.42	6.7216(4)		5.9689(3)		269.55(9)
11.92	6.7171(2)		5.9675(2)		268.98(7)
12.64	6.7047(5)		5.9597(3)		267.91(3)
14.39	6.6813(7)		5.9519(5)		265.69(5)
15.46	6.6652(7)		5.9378(5)		263.78(5)
16.22	6.6583(6)		5.9361(4)		263.17(4)
17.53	6.631(2)		5.9315(7)		260.8(10)
He ramp (Xen14-P_E)					
0.22	6.9176(3)		6.06443(2)		290.10(2)
0.57	6.9108(2)		6.06115(2)		289.40(2)
1.23	6.8970(3)		6.05689(14)		288.110(13)
2.00	6.8808(2)		6.05013(13)		286.440(13)
2.83	6.8652(2)		6.04373(15)		284.840(15)
3.8	6.8500(2)		6.03679(13)		283.250(13)
4.99	6.8293(2)		6.0279(2)		281.140(13)
5.84	6.8159(2)		6.0220(2)		279.760(15)
6.53	6.8043(2)		6.01610(14)		278.530(12)
7.40	6.7924(2)		6.01014(14)		277.280(12)
8.26	6.7800(2)		6.00442(14)		276.010(12)
8.74	6.7731(2)		6.00066(13)		275.280(12)
9.88	6.7549(2)		5.9907(2)		274.040(12)
10.73	6.7455(2)		5.9859(2)		272.360(12)
11.73	6.7356(2)		5.98180(13)		271.380(12)
12.69	6.7219(2)		5.97431(15)		269.90(2)
13.71	6.7073(2)		5.9658(2)		268.390(14)
14.83	6.6924(2)		5.9552(2)		266.720(14)
15.72	6.6814(2)		5.9494(2)		265.580(14)
16.74	6.6677(2)		5.9424(2)		264.180(14)
17.95[§]	6.368(9)	6.5558(12)	6.1322(14)	103.67(6)	248.0(4)
18.79[§]	6.343(7)	6.5530(11)	6.1430(12)	103.56(5)	248.0(3)
19.97[§]	6.303(8)	6.5333(12)	6.1177(13)	103.37(6)	245.0(3)
20.55[§]	6.347(8)	6.5219(12)	6.1138(13)	103.45(6)	246.0(3)
21.41[§]	6.300(7)	6.5158(10)	6.1101(11)	103.39(5)	244.0(3)
22.39[§]	6.2980(10)	6.5008(12)	6.0999(14)	103.37(7)	243.0(4)
23.31[§]	6.2900(13)	6.489(2)	6.0975(13)	103.39(8)	242.0(5)
24.48[§]	6.2780(10)	6.489(2)	6.085(2)	103.30(7)	241.0(4)
25.51[§]	6.252(9)	6.4890(13)	6.0869(15)	103.03(6)	240.0(4)
26.63[§]	6.241(8)	6.4656(13)	6.0716(14)	103.09(6)	238.0(3)

27.68[§]	6.234(1)	6.4639(14)	6.0749(15)	103.02(7)	238.0(4)
28.74[§]	6.213(9)	6.4451(13)	6.0591(13)	102.91(6)	236.0(3)
30.38[§]	6.219(9)	6.4574(12)	6.0699(12)	102.91(6)	237.0(4)
19.30[§*]	6.3610(11)	6.548(2)	6.134(2)	103.66(8)	248.0(4)
15.28[§*]	6.384(9)	6.5873(11)	6.1723(2)	103.76(7)	252.0(3)
11.03[§*]	6.441(8)	6.6278(7)	6.1977(13)	103.90(6)	256.0(3)
6.15[§*]	6.505(7)	6.6923(7)	6.2462(12)	104.01(5)	263.0(3)
1.32[*]	6.9360(7)		6.1090(6)		293.80(5)
0.0001[*]	6.9204(4)		6.0638(3)		292.10(5)

[*]: P_{steps} data collected under decompression conditions; [§]: P_{steps} data pertaining to the H*P*-polymorph of xenotime-(Y).

Table 8.7: Unit-cell parameters of gasparite-(Ce) at different pressures based on the *m.e.w.* and He single crystal X-ray diffraction *P*-ramps.

P (GPa)	*a* (Å)	*b* (Å)	*c* (Å)	*β* (°)	*V* (Å^3)
m.e.w. ramp (Gasp3-P_F)					
0.0001	6.9593(9)	7.1596(4)	6.7433(3)	104.680(2)	325.02(5)
0.07	6.9500(5)	7.1450(3)	6.7350(2)	104.646(6)	323.58(5)
0.16	6.9451(4)	7.1416(4)	6.7340(3)	104.657(7)	323.14(5)
0.35	6.9412(6)	7.1345(3)	6.7295(3)	104.677(7)	322.38(5)
0.61	6.9343(7)	7.1288(3)	6.7245(3)	104.653(8)	321.60(5)
0.93	6.9270(6)	7.1238(4)	6.7192(3)	104.616(7)	320.84(5)
1.40	6.9144(6)	7.1126(4)	6.7105(3)	104.590(8)	319.38(5)
1.71	6.9072(7)	7.1070(4)	6.7046(3)	104.565(8)	318.55(5)
2.30	6.8945(6)	7.0956(3)	6.6946(3)	104.532(7)	317.03(5)
3.20	6.8759(6)	7.0754(3)	6.6797(3)	104.487(7)	314.63(5)
4.03	6.8562(5)	7.0601(3)	6.6641(2)	104.417(6)	312.42(5)
4.99	6.8365(5)	7.0422(3)	6.6484(3)	104.359(6)	310.08(5)
5.38	6.8295(5)	7.0343(3)	6.6421(2)	104.337(6)	309.15(5)
6.28	6.8125(5)	7.0192(3)	6.6289(3)	104.284(7)	307.18(5)
7.35	6.7914(5)	7.0008(3)	6.6129(3)	104.217(5)	304.79(5)
7.90	6.7818(6)	6.9897(3)	6.6042(3)	104.203(7)	303.49(5)
8.30	6.7739(6)	6.9834(3)	6.5981(3)	104.169(7)	302.63(5)
8.90	6.7616(5)	6.9728(3)	6.5891(2)	104.124(6)	301.27(5)
9.31	6.7537(6)	6.9651(3)	6.5821(3)	104.097(7)	300.30(5)
He ramp (Gasp3-P_G)					
0.26	6.9241(5)	7.1201(3)	6.7096(4)	104.651(5)	320.03(3)
1.26	6.9026(4)	7.0989(3)	6.6924(2)	104.628(2)	316.41(2)
2.41	6.8774(5)	7.0757(3)	6.6723(2)	104.509(5)	314.35(3)
3.63	6.8502(5)	7.0509(3)	6.6509(2)	104.439(5)	311.09(3)
4.84	6.8244(3)	7.0247(2)	6.6292(1)	104.369(3)	307.86(2)
6.12	6.7984(3)	7.0004(2)	6.6083(1)	104.308(3)	304.74(2)
7.41	6.7749(4)	6.9777(3)	6.5893(2)	104.232(4)	301.94(2)
8.68	6.7515(5)	6.9579(3)	6.5710(2)	104.160(4)	299.30(3)
9.67	6.7319(4)	6.9406(3)	6.5582(1)	104.086(4)	297.20(2)
10.65	6.7143(4)	6.9254(3)	6.5447(1)	104.024(4)	295.25(2)
11.15	6.7072(4)	6.9189(3)	6.5388(1)	103.988(4)	294.45(2)
11.58	6.7031(8)	6.9133(6)	6.5367(3)	103.967(4)	293.96(5)
12.32	6.6920(9)	6.9004(8)	6.5273(4)	103.94(1)	292.54(5)
13.14	6.6717(2)	6.8873(9)	6.5181(3)	103.843(4)	290.81(4)

13.72	6.6550(3)	6.8865(2)	6.5013(3)	103.832(4)	289.31(8)
15.22	6.6372(3)	6.8554(2)	6.4914(4)	103.740(6)	286.84(3)
16.39	6.6130(2)	6.8392(2)	6.4730(3)	103.561(5)	284.60(2)
17.22	6.5883(9)	6.8196(5)	6.460(1)	103.44(2)	282.27(6)
18.04	6.577(1)	6.8082(8)	6.458(1)	103.38(2)	281.34(9)
18.68	6.566(1)	6.7980(7)	6.454(2)	103.33(2)	280.33(8)
19.35	6.552(1)	6.7849(7)	6.451(1)	103.26(2)	279.11(8)
20.12	6.5149(6)	6.7544(4)	6.4355(8)	103.14(1)	275.77(5)
21.05	6.4885(6)	6.7355(3)	6.4263(1)	102.92(1)	273.74(5)
21.89	6.4563(7)	6.7068(3)	6.413(1)	102.74(2)	271.84(5)
22.76	6.4308(9)	6.6865(4)	6.404(1)	102.00(2)	269.00(7)

Table 8.8: Unit-cell parameters of monazite-(Ce) at different pressures based on the neon single crystal X-ray diffraction P-ramp data collected on the Mon2 sample (Mon2-P_H).

P (GPa)	*a* (Å)	*b* (Å)	*c* (Å)	*β* (°)	*V* (Å^3)
0.0001	6.7878(5)	7.0034(13)	6.4691(3)	103.554(6)	298.90(6)
0.77(5)	6.7685(9)	6.987(2)	6.4602(4)	103.422(9)	297.20(10)
1.98(5)	6.7466(4)	6.9784(8)	6.4473(2)	103.391(5)	295.20(4)
2.73(5)	6.7173(4)	6.9572(10)	6.4298(2)	103.299(5)	292.40(5)
3.99(5)	6.6927(5)	6.9391(14)	6.4139(3)	103.186(7)	290.00(6)
4.99(5)	6.6815(5)	6.9271(13)	6.4073(3)	103.113(7)	288.90(6)
6.35(5)	6.6487(4)	6.9018(10)	6.3894(2)	103.002(5)	285.80(5)
7.56(5)	6.6331(4)	6.8854(9)	6.3836(2)	102.930(5)	284.10(4)
9.38(5)	6.5895(5)	6.8555(12)	6.3531(3)	102.720(6)	279.90(5)
9.98(5)	6.5786(5)	6.8482(11)	6.3488(3)	102.709(6)	280.10(5)
12.86(5)	6.5196(5)	6.8006(13)	6.3075(3)	102.383(7)	273.10(6)
14.08(5)	6.5059(4)	6.7862(12)	6.2988(3)	102.317(6)	271.60(5)
15.45(5)	6.4910(6)	6.7791(2)	6.2907(4)	102.274(9)	270.40(7)
16.67(5)	6.4737(7)	6.7630(2)	6.2777(4)	102.208(10)	268.60(8)
18.36(5)	6.4480(8)	6.7510(2)	6.2630(5)	102.063(11)	266.60(9)
19.42(5)	6.4113(9)	6.7360(3)	6.2394(5)	101.788(13)	263.70(11)
21.50(5)	6.3866(11)	6.7080(3)	6.2177(7)	101.58(2)	260.90(12)
23.50(5)	6.3529(13)	6.6690(4)	6.2039(6)	101.28(2)	257.0(2)

The *P*-*V* data for all the studied minerals have been fitted with a Birch-Murnaghan EoS, with the aim to refine the corresponding bulk moduli (K_{P_0,T_0}), the unit-cell volume at atmospheric pressure (V_0) and the first derivative of the bulk modulus (*K*'). For the two monazite-type minerals, a change in compressional behavior has been observed at ~15 GPa and ~18 GPa for gasparite-(Ce) and monazite-(Ce) respectively. Moreover, whenever two *P*-*V* datasets are available [*i.e.*, in case of chernovite-(Y), xenotime-(Y) and gasparite-(Ce)], the refinement of the bulk moduli has been conducted by considering both the ramps (volumes normalized to ambient-conditions values). Further details about the modelling of the H*P*-behavior are discussed in section 9.5.1, for chernovite-(Y), in section 9.7.1, for xenotime-(Y), in section 9.6.1 for gasparite-(Ce) and in section 9.8.1 for monazite-(Ce). In Table

8.9 are reported the bulk moduli of all the ATO_4 minerals under study, while in Table 8.10 are reported the refined axial bulk moduli of the zircon-type minerals.

Table 8.9: refined bulk moduli, compressibilities, first derivative bulk modulus (K'=4 fixed for the BM2-EoS) and unit-cell volumes for all the ATO_4 minerals. Ch10-$P_{A,B}$, Xen14-$P_{D,E}$ and Gasp3-$P_{F,G}$ refer to the combination of the data pertaining to the two available P-ramps for chernovite-(Y), xenotime-(Y) and gasparite-(Ce) respectively.

	BM3-EoS				BM2-EoS		
	K_{P_0,T_0} (GPa)	β_V (GPa^{-1})	K'	V_0 (Å^3)	K_{P_0,T_0} (GPa)	β_V (GPa^{-1})	V_0 (Å^3)
Ch10-P_A	-	-	-	-	142(2)	0.00704(9)	309.37(11)
Ch10-P_B	136(2)	0.0074(1)	4.0(5)	310.43(3)	135.5(5)	0.00738(1)	310.43(3)
Ch10-$P_{A,B}$	136(2)	0.0074(1)	3.9(4)	309.96(3)	135.6(4)	0.00738(1)	309.97(2)
Ch13-P_C	125(3)	0.0080(1)	3.8(9)	316.16(9)	123.8(9)	0.00808(7)	316.17(7)
Xen14-P_D	142(4)	0.0070(3)	4.4(7)	288.63(14)	145.1(1.2)	0.00689(5)	288.59(13)
Xen14-P_E	148(4)	0.0068(2)	4.0(5)	290.37(16)	148.0(1.1)	0.00676(5)	290.36(1.1)
Xen14-$P_{D,E}$	148(4)	0.0068(2)	3.9(5)	289.5(2)	146.9(1.1)	0.00681(5)	289.5(2)
Gasp3-P_F	108.6(1.2)	0.00923(9)	4.0(4)	320.60(2)	108.5(3)	0.00926(3)	320.60(2)
Gasp3-P_G	109(4)	0.0092(3)	4.3(6)	320.6(3)	105.2(1.0)	0.00951(9)	320.7(2)
Gasp3-$P_{F,G}$	108.3(1.0)	0.00923(8)	4.2(2)	320.59(3)	109.4(3)	0.00914(3)	320.58(3)
Mon14-P_H	-	-	-	-	121(3)	0.0083(2)	299.3(4)

Table 8.10: axial moduli of zircon-type compounds under investigation.

	[100]		[001]	
	K_{P_0,T_0} (GPa)	L_0 (Å)	K_{P_0,T_0} (GPa)	L_0 (Å)
Ch10-P_A	353(3)	7.0302(8)	696(15)	6.2601(10)
Ch10-P_B	336.6(18)	7.0379(5)	659(8)	6.2682(6)
Ch13-P_C	306(3)	7.0793(7)	621(17)	6.3092(12)
Xen14-P_D	344(3)	6.9109(10)	763(13)	6.0516(11)
Xen14-P_E	365(3)	6.9181(10)	726(8)	6.0675(8)

Eventually, the evolution of several significant structural parameters (*i.e.*, *A*-O bonds, *T*-O bonds, *A*-coordination polyhedral and *T*-coordination polyhedral volumes) with pressure has been determined, based on the refined structure models, by using the *VESTA* software (Momma and Izumi 2011). The corresponding values are reported in Table 8.11, Table 8.12, Table 8.13, Table 8.15, Table 8.16, Table 8.17, Table 8.25, Table 8.26, Table 8.27, Table 8.28.

Table 8.11: *A*-O and *T*-O bond distances (in Å) evolution at high pressure based on the structure refinements from the chernovite-(Y) high-pressure data.

P (GPa)	V_{REEO_8}(Å^3)	V_{AsO_4}(Å^3)	REE-O_a	REE-O_b	As-O
0.0001	23.56(3)	2.31(2)	2.416(3)	2.303(3)	1.665(3)
0.16	23.46(3)	2.34(2)	2.419(4)	2.294(5)	1.670(4)
0.62	23.32(3)	2.34(2)	2.415(4)	2.289(4)	1.672(4)
1.17	23.32(3)	2.31(2)	2.412(4)	2.291(5)	1.665(4)
2.00	23.14(3)	2.31(2)	2.411(4)	2.281(4)	1.664(4)
3.07	22.97(3)	2.29(2)	2.408(3)	2.273(4)	1.660(4)
4.54	22.70(3)	2.28(2)	2.401(3)	2.263(4)	1.658(4)
5.63	22.56(3)	2.28(2)	2.402(3)	2.254(3)	1.657(3)
6.43	22.39(3)	2.28(2)	2.397(3)	2.247(3)	1.657(3)
7.20	22.23(3)	2.27(2)	2.391(4)	2.242(4)	1.655(4)
7.79	22.20(3)	2.26(2)	2.392(4)	2.239(4)	1.652(4)
8.86	22.01(3)	2.26(2)	2.388(3)	2.231(4)	1.652(4)
10.16	21.82(3)	2.25(2)	2.382(4)	2.223(4)	1.650(4)
10.71	21.76(3)	2.24(2)	2.382(4)	2.220(5)	1.648(4)

Table 8.12: *A*-O and *T*-O bond distances (in Å) evolution at high pressure based on the structure refinements from the *m.e.w.* ramp (Gasp3-P_F) of gasparite-(Ce).

P (GPa)	REE-O1$_a$	REE-O1$_b$	REE-O2$_a$	REE-O2$_b$	REE-O2$_c$	REE-O3$_a$	REE-O3$_b$	REE-O4$_a$	REE-O4$_b$	As-O1	As-O2	As-O3	As-O4
0.0001	2.568(12)	2.47(1)	2.94(1)	2.607(14)	2.55(1)	2.600(14)	2.460(12)	2.561(11)	2.482(14)	1.687(11)	1.687(11)	1.66(1)	1.67(2)
0.07	2.564(12)	2.465(11)	2.933(12)	2.60(2)	2.541(11)	2.600(14)	2.458(12)	2.560(12)	2.48(2)	1.674(13)	1.686(11)	1.668(11)	1.65(2)
0.16	2.53(1)	2.490(9)	2.94(1)	2.600(13)	2.538(9)	2.583(11)	2.46(1)	2.564(9)	2.449(11)	1.678(11)	1.681(9)	1.661(9)	1.661(9)
0.35	2.537(9)	2.491(9)	2.923(8)	2.598(11)	2.538(8)	2.595(11)	2.443(9)	2.559(9)	2.47(1)	1.677(9)	1.690(8)	1.665(8)	1.666(11)
0.61	2.54(1)	2.492(9)	2.93(1)	2.602(13)	2.539(9)	2.597(12)	2.45(1)	2.566(9)	2.447(11)	1.67(1)	1.682(9)	1.652(9)	1.676(12)
0.93	2.531(9)	2.486(8)	2.929(9)	2.599(12)	2.532(13)	2.593(12)	2.45(1)	2.55(1)	2.453(11)	1.68(1)	1.683(9)	1.655(8)	1.669(13)
1.40	2.53(1)	2.482(9)	2.92(1)	2.587(14)	2.535(9)	2.595(12)	2.45(1)	2.541(9)	2.451(11)	1.670(11)	1.680(9)	1.652(9)	1.679(13)
1.71	2.53(1)	2.481(9)	2.920(11)	2.590(14)	2.53(1)	2.599(12)	2.44(1)	2.55(1)	2.445(12)	1.672(12)	1.682(9)	1.649(9)	1.672(14)
2.30	2.52(1)	2.459(9)	2.894(11)	2.591(14)	2.52(1)	2.611(12)	2.44(1)	2.54(1)	2.453(12)	1.666(12)	1.684(9)	1.652(9)	1.659(14)
3.20	2.52(1)	2.451(9)	2.89(1)	2.582(14)	2.510(9)	2.601(12)	2.44(1)	2.530(9)	2.435(11)	1.662(11)	1.680(9)	1.648(9)	1.669(13)
4.03	2.51(1)	2.441(9)	2.86(1)	2.573(13)	2.507(9)	2.618(12)	2.44(1)	2.52(1)	2.435(12)	1.681(11)	1.66(1)	1.674(9)	1.668(14)
4.99	2.53(1)	2.426(9)	2.87(1)	2.570(13)	2.476(9)	2.604(12)	2.45(1)	2.51(1)	2.425(12)	1.678(11)	1.662(9)	1.677(9)	1.651(13)
5.38	2.51(1)	2.438(9)	2.87(1)	2.566(14)	2.474(9)	2.596(12)	2.45(1)	2.51(1)	2.419(12)	1.691(11)	1.668(1)	1.652(9)	1.663(13)
6.28	2.510(12)	2.41(11)	2.866(12)	2.57(2)	2.468(11)	2.606(14)	2.443(12)	2.51(1)	2.407(13)	1.685(14)	1.662(11)	1.656(11)	1.68(2)
7.35	2.490(9)	2.424(8)	2.855(9)	2.554(13)	2.464(8)	2.617(12)	2.44(1)	2.496(9)	2.408(12)	1.68(1)	1.67(1)	1.653(8)	1.663(13)
7.90	2.495(9)	2.412(8)	2.839(11)	2.542(13)	2.458(8)	2.617(12)	2.43(1)	2.493(9)	2.411(11)	1.651(12)	1.582(11)	1.57(1)	1.614(2)
8.30	2.489(11)	2.425(9)	2.84(1)	2.555(14)	2.44(1)	2.625(14)	2.436(11)	2.490(11)	2.396(13)	1.681(11)	1.660(11)	1.65(1)	1.65(2)
8.90	2.484(9)	2.407(8)	2.825(9)	2.539(13)	2.454(8)	2.609(12)	2.45(1)	2.482(9)	2.399(11)	1.67(1)	1.66(1)	1.659(8)	1.656(13)
9.31	2.500(11)	2.38(1)	2.83(1)	2.530(14)	2.45(1)	2.65(2)	2.433(12)	2.483(11)	2.396(14)	1.687(11)	1.67(12)	1.66(1)	1.65(2)

Table 8.13: Volumes of *A*- and *T*-coordination polyhedra (in Å^3) and significant bond angles (°) calculated using the routine implemented in the software Vesta 3 (Momma and Izumi 2011), based on the structure refinements from the *m.e.w.* ramp (Gasp3-P_F) of gasparite-(Ce).

P (GPa)	V_{REEO_9}(Å^3)	V_{AsO_4}(Å^3)	REE-O4-REE (I)	REE-O2-REE (I)	REE-O1-REE (II)	REE-O2-REE (II)	REE-O3-REE (III)	REE-O2-REE (IV)	REE-As-REE
0.0001	33.17(3)	2.386(7)	122.1(5)	105.3(4)	112.7(3)	99.5(2)	113.6(4)	116.2(4)	174.29(8)
0.07	33.02(3)	2.371(7)	122.1(8)	105.3(7)	112.7(6)	99.5(5)	113.6(5)	116.2(6)	174.30(8)
0.16	33.12(4)	2.387(8)	123.0(6)	105.1(5)	112.8(5)	99.2(4)	114.0(4)	116.1(4)	174.36(8)
0.35	32.79(3)	2.367(7)	122.2(7)	105.6(5)	112.4(5)	99.6(4)	114.3(5)	116.1(5)	174.30(8)
0.61	32.89(4)	2.355(7)	122.7(6)	105.2(5)	112.1(5)	99.1(4)	114.1(4)	115.7(4)	174.33(8)
0.93	32.53(4)	2.362(6)	123.1(6)	105.2(5)	112.3(4)	99.2(4)	114.1(4)	116.0(4)	174.30(8)
1.40	32.55(4)	2.354(6)	123.1(6)	105.5(5)	112.2(5)	99.0(4)	114.0(4)	116.0(4)	174.26(8)
1.71	32.51(4)	2.349(7)	123.0(6)	105.3(5)	112.0(5)	99.0(4)	114.2(5)	115.9(5)	174.28(8)
2.30	32.25(4)	2.353(4)	122.6(6)	105.8(5)	112.4(4)	99.6(4)	113.7(4)	116.0(4)	174.22(8)
3.20	31.96(4)	2.350(7)	123.3(6)	106.0(5)	112.0(4)	99.4(4)	113.9(4)	116.1(4)	174.16(8)
4.03	31.69(4)	2.345(6)	123.0(6)	106.6(5)	112.2(5)	99.5(4)	113.6(4)	116.0(4)	174.07(8)
4.99	31.44(4)	2.357(5)	123.7(6)	106.1(5)	111.1(5)	99.5(4)	113.8(5)	116.7(5)	174.10(8)
5.38	31.35(4)	2.346(8)	123.7(6)	106.2(5)	110.9(5)	99.4(4)	114.1(5)	116.7(5)	174.09(8)
6.28	31.25(4)	2.340(4)	123.9(6)	105.7(7)	111.5(6)	99.1(5)	113.6(4)	116.3(6)	174.02(8)
7.35	31.04(4)	2.313(3)	123.9(5)	106.1(5)	110.0(3)	98.9(4)	113.4(3)	116.6(4)	173.99(5)
7.90	30.79(4)	2.315(5)	123.6(6)	106.7(4)	110.9(3)	99.2(3)	113.5(3)	116.9(4)	173.98(5)
8.30	30.84(4)	2.308(6)	124.2(4)	106.1(4)	110.4(3)	99.2(3)	113.1(4)	116.9(4)	174.01(6)
8.90	30.56(4)	2.307(4)	124.1(4)	106.9(3)	110.7(3)	99.1(3)	113.3(3)	116.8(3)	174.03(8)
9.31	30.50(4)	2.337(4)	124.0(7)	106.9(5)	110.8(5)	99.0(4)	112.4(5)	117.1(5)	173.94(8)

Table 8.14: bond distances of xenotime-(Y) and its H*P* polymorph xenotime-(Y)-II.

P (GPa)	REE-$O1_a$	REE-$O1_b$	REE-$O2_a$	REE-$O2_b$	REE-$O2_c$	REE-$O3_a$	REE-$O3_b$	REE-$O3_c$	REE-$O4_a$	REE-$O4_b$	P-O1	P-O2	P-O3	P-O4
0.22	2.311(3)	2.388(3)									1.555(3)			
0.57	2.310(5)	2.388(4)									1.552(4)			
1.23	2.302(3)	2.385(3)									1.554(3)			
2.00	2.297(3)	2.384(3)									1.550(3)			
2.83	2.289(4)	2.380(4)									1.550(4)			
3.80	2.283(4)	2.378(3)									1.548(4)			
4.99	2.273(3)	2.376(3)									1.547(3)			
5.84	2.265(4)	2.375(3)									1.547(4)			
6.53	2.261(4)	2.371(3)									1.545(4)			
7.40	2.251(5)	2.371(4)									1.548(4)			
8.26	2.245(6)	2.370(5)									1.548(5)			
8.74	2.244(3)	2.367(3)									1.545(3)			
9.88	2.245(4)	2.360(3)									1.536(4)			
10.73	2.237(4)	2.362(3)									1.537(4)			
11.73	2.228(4)	2.359(3)									1.542(4)			
12.69	2.220(4)	2.358(4)									1.542(4)			
13.71	2.218(6)	2.352(5)									1.538(5)			
14.83	2.211(5)	2.351(4)									1.534(5)			
15.72	2.208(5)	2.345(4)									1.533(5)			
16.74	2.200(5)	2.345(4)									1.533(5)			
17.95	2.36(3)	2.23(3)	2.71(4)	2.54(10)	2.25(5)	2.33(6)	2.29(6)	3.10(6)	2.46(6)	2.37(3)	1.53(3)	1.64(5)	1.40(6)	1.46(7)
18.79	2.38(3)	2.26(2)	2.689(19)	2.47(5)	2.26(3)	2.45(5)	2.32(4)	2.92(5)	2.34(3)	2.20(5)	1.55(3)	1.56(3)	1.56(4)	1.56(5)
19.97	2.34(3)	2.27(2)	2.68(3)	2.49(7)	2.22(3)	2.46(6)	2.28(5)	2.86(5)	2.34(2)	2.23(5)	1.54(2)	1.54(4)	1.60(5)	1.51(5)
20.55	2.39(5)	2.26(4)	2.72(4)	2.40(9)	2.26(5)	2.39(7)	2.33(8)	3.02(8)	2.34(3)	2.23(7)	1.51(4)	1.56(6)	1.49(6)	1.56(8)
21.41	2.33(3)	2.26(2)	2.70(3)	2.46(6)	2.24(3)	2.45(5)	2.33(5)	2.86(5)	2.31(3)	2.24(6)	1.52(2)	1.54(4)	1.56(5)	1.51(6)
22.39	2.315(16)	2.278(14)	2.678(19)	2.34(5)	2.32(3)	2.38(4)	2.34(3)	2.93(4)	2.329(14)	2.27(4)	1.523(14)	1.54(3)	1.49(3)	1.49(4)
23.31	2.36(3)	2.24(3)	2.68(3)	2.54(8)	2.21(4)	2.44(6)	2.26(5)	2.88(6)	2.33(3)	2.17(5)	1.56(3)	1.50(4)	1.59(5)	1.54(5)
24.48	2.31(3)	2.25(2)	2.66(3)	2.34(5)	2.29(3)	2.42(5)	2.36(5)	2.86(6)	2.28(3)	2.23(6)	1.52(2)	1.58(4)	1.47(5)	1.56(6)
25.51	2.32(3)	2.27(2)	2.666(19)	2.42(6)	2.23(3)	2.38(5)	2.32(5)	2.91(5)	2.33(2)	2.22(4)	1.52(2)	1.56(4)	1.52(4)	1.51(5)

26.63	2.36(3)	2.22(3)	2.65(3)	2.29(4)	2.26(7)	2.41(7)	2.40(7)	2.86(8)	2.27(3)	2.30(7)	1.53(3)	1.64(5)	1.40(6)	1.46(7)
27.68	2.31(3)	2.24(2)	2.66(3)	2.35(7)	2.26(3)	2.42(5)	2.29(5)	2.86(5)	2.30(2)	2.30(6)	1.52(2)	1.56(4)	1.50(5)	1.46(6)
28.74	2.29(3)	2.23(2)	2.65(3)	2.34(6)	2.27(3)	2.43(5)	2.27(5)	2.82(5)	2.30(2)	2.27(6)	1.54(2)	1.54(4)	1.52(5)	1.47(6)
30.38	2.33(3)	2.22(2)	2.646(19)	2.28(6)	2.28(3)	2.43(6)	2.29(6)	2.83(6)	2.31(2)	2.26(6)	1.54(3)	1.60(4)	1.52(5)	1.48(6)

Table 8.15:relevant structural parameters of xenotime-(Y) and its high-pressure polymorph xenotime-(Y)-II.

P (GPa)	V_{REEO_X}(Å^3)	V_{PO_4}(Å^3)	REE-O4-REE (I)	REE-O2-REE (I)	REE-O1-REE (II)	REE-O2-REE (II)	REE-O3-REE (III)	REE-O2-REE (IV)	REE-As-REE
0.22	23.28(1)	1.908(7)							
0.57	23.26(1)	1.898(7)							
1.23	23.09(1)	1.902(7)							
2.00	22.98(1)	1.889(7)							
2.83	22.81(1)	1.890(7)							
3.80	22.68(1)	1.881(7)							
4.99	22.48(1)	1.878(7)							
5.84	22.35(1)	1.878(7)							
6.53	22.23(1)	1.874(7)							
7.40	22.07(1)	1.885(7)							
8.26	21.95(1)	1.884(7)							
8.74	21.91(1)	1.873(7)							
9.88	21.82(1)	1.84(7)							
10.73	21.73(1)	1.845(7)							
11.73	21.55(1)	1.861(7)							
12.69	21.41(1)	1.862(7)							
13.71	21.30(1)	1.846(7)							
14.83	21.18(1)	1.836(7)							
15.72	21.06(1)	1.829(7)							
16.74	20.93(1)	1.831(7)							
17.95	26.3(4)	1.5(3)	114(3)	101(3)	110(1)	99(2)	118(1)	114(3)	175.9(5)
18.79	25.9(4)	1.9(2)	126(2)	104(2)	108(1)	98(1)	113(1)	115(2)	176(1)

19.97	25.7(4)	1.8(2)	125(2)	102(2)	108(1)	99(1)	113(1)	114(2)	174.5(5)
20.55	25.6(4)	1.8(3)	125(3)	104(3)	107(2)	97(2)	115(1)	117(3)	173.7(1.1)
21.41	25.7(4)	1.8(2)	125(2)	103(2)	109(1)	98(1)	113(1)	114(2)	175.3(7)
22.39	25.3(4)	1.7(3)	122(1)	106(1)	108(1)	96(1)	114(1)	117(1)	173.0(5)
23.31	25.5(4)	1.8(2)	126(2)	101(3)	108(1)	98(1)	113(3)	114(1)	175.3(7)
24.48	24.8(4)	1.8(3)	126(3)	107(2)	109(1)	96(1)	112(1)	117(1)	173.2(6)
25.51	25.0(4)	1.8(2)	124(2)	105(2)	107(1)	98(1)	115(1)	116(2)	173.2(5)
26.63	24.9(4)	1.7(3)	123(3)	109(2)	107(1)	96(1)	111(1)	119(2)	174.3(8)
27.68	24.8(4)	1.7(2)	122(2)	106(2)	108(1)	96(1)	114(1)	117(2)	173.2(7)
28.74	24.5(4)	1.7(2)	122(2)	107(2)	108(1)	96(1)	114(1)	117(2)	173.1(7)
30.38	24.4(4)	1.8(2)	123(2)	109(2)	107(1)	96(1)	114(1)	119(2)	173.7(3)

Table 8.16: High-pressure evolution of the nine independent REE-O bond distances of monazite-(Ce).

P (GPa)	REE-O1$_a$	REE-O1$_b$	REE-O2$_a$	REE-O2$_b$	REE-O2$_c$	REE-O3$_a$	REE-O3$_b$	REE-O3$_c$	REE-O4$_a$	REE-O4$_b$
0.0001	2.519(6)	2.440(8)	2.788(6)	2.563(7)	2.637(6)	2.581(6)	2.469(8)	3.175(7)	2.515(5)	2.464(6)
1.98	2.508(6)	2.436(7)	2.773(6)	2.535(7)	2.623(6)	2.581(6)	2.456(7)	3.144(6)	2.503(4)	2.444(6)
2.73	2.491(5)	2.430(7)	2.766(5)	2.527(6)	2.608(5)	2.580(5)	2.456(6)	3.122(5)	2.503(4)	2.441(4)
3.99	2.490(5)	2.424(6)	2.754(4)	2.515(5)	2.598(4)	2.579(4)	2.463(6)	3.091(5)	2.496(4)	2.432(4)
4.99	2.484(4)	2.417(5)	2.753(4)	2.512(5)	2.588(4)	2.580(4)	2.450(5)	3.085(5)	2.491(4)	2.428(4)
6.35	2.479(4)	2.404(5)	2.738(4)	2.500(5)	2.578(4)	2.581(4)	2.448(5)	3.054(5)	2.483(4)	2.417(4)
7.56	2.480(6)	2.396(7)	2.737(5)	2.500(6)	2.566(6)	2.579(6)	2.444(7)	3.040(6)	2.477(4)	2.409(5)
9.38	2.451(5)	2.394(7)	2.731(5)	2.467(6)	2.549(5)	2.576(5)	2.449(6)	2.992(6)	2.470(4)	2.395(5)
9.98	2.469(12)	2.367(14)	2.76(2)	2.43(2)	2.523(13)	2.58(2)	2.46(2)	2.97(2)	2.456(11)	2.394(12)
12.86	2.438(5)	2.369(7)	2.708(5)	2.438(6)	2.523(5)	2.568(5)	2.437(6)	2.933(6)	2.452(4)	2.368(5)
14.08	2.436(5)	2.359(7)	2.705(5)	2.429(6)	2.518(5)	2.566(5)	2.442(6)	2.917(5)	2.438(4)	2.366(4)
15.45	2.430(6)	2.365(7)	2.698(5)	2.429(6)	2.510(5)	2.566(5)	2.434(6)	2.910(6)	2.438(4)	2.359(5)
16.67	2.425(6)	2.358(7)	2.694(5)	2.417(6)	2.503(6)	2.565(5)	2.433(6)	2.890(6)	2.429(4)	2.353(5)
18.36	2.424(6)	2.343(8)	2.689(6)	2.406(7)	2.498(5)	2.561(5)	2.437(7)	2.896(6)	2.417(5)	2.355(5)
19.42	2.417(9)	2.329(12)	2.690(8)	2.388(10)	2.481(9)	2.554(7)	2.424(9)	2.841(8)	2.418(6)	2.344(7)
21.50	2.397(8)	2.357(11)	2.679(8)	2.388(9)	2.469(7)	2.555(7)	2.417(9)	2.818(8)	2.403(6)	2.343(7)

23.50	2.413(13)	2.34(2)	2.680(11)	2.371(13)	2.455(11)	2.542(10)	2.418(12)	2.791(12)	2.397(8)	2.331(9)

Table 8.17: Volumes of *A*- and *T*-coordination polyhedra (in Å^3) and relevant bond angles (°), calculated using the routine implemented in the software Vesta 3 (Momma and Izumi 2011), based on the structure refinements from the *HP ramp* of monazite-(Ce).

P (GPa)	V_{REEO_9}(Å^3)	V_{PO_4}(Å^3)	REE-O4-REE (I)	REE-O2-REE (I)	REE-O1-REE (II)	REE-O2-REE (II)	REE-O3-REE (III)	REE-O2-REE (IV)	REE-P-REE
0.0001	32.33(3)	1.85(1)	119.3(3)	104.7(3)	110.5(3)	99.1(2)	110.6(3)	113.6(3)	174.71(5)
1.98	31.82(3)	1.86(1)	119.9(2)	105.0(3)	109.9(3)	99.3(2)	111.0(3)	113.7(3)	174.46(5)
2.73	31.53(3)	1.84(1)	119.5(2)	105.2(2)	109.9(2)	99.0(1)	110.8(2)	113.7(2)	174.36(4)
3.99	31.33(3)	1.82(1)	119.7(2)	105.2(2)	109.5(2)	99.1(1)	110.6(2)	113.8(2)	174.23(4)
4.99	31.13(3)	1.84(1)	119.8(1.)	105.7(2)	109.3(1)	98.8(1)	111.1(2)	113.9(2)	174.16(4)
6.35	30.73(3)	1.82(1)	120.1(2)	105.9(2)	109.0(1)	98.7(1)	111.0(2)	113.7(2)	174.06(5)
7.56	30.63(3)	1.82(1)	120.4(2)	106.1(2)	108.8(2)	98.3(1)	111.2(3)	113.6(3)	174.05(5)
9.38	30.13(3)	1.81(1)	120.5(2)	106.2(2)	108.6(2)	98.3(1)	110.9(2)	114.2(2)	173.87(4)
9.98	29.83(3)	1.87(1)	120.9(5)	105.8(8)	108.6(5)	98.1(5)	110.5(6)	116.3(8)	173.75(10)
12.86	29.33(3)	1.81(1)	121.3(2)	106.8(2)	107.7(2)	97.8(1)	111.4(2)	114.2(3)	173.65(5)
14.08	29.23(3)	1.81(1)	121.6(2)	106.8(2)	107.6(2)	97.7(1)	111.2(2)	114.3(3)	173.60(5)
15.45	29.03(3)	1.80(1)	121.7(2)	107.0(2)	107.2(2)	97.5(1)	111.5(2)	114.1(3)	173.58(5)
16.67	28.83(3)	1.80(1)	121.9(2)	107.1(2)	107.0(2)	97.4(1)	111.5(2)	114.1(3)	173.55(5)
18.36	28.63(3)	1.79(1)	122.0(3)	107.1(3)	106.9(3)	97.3(2)	111.4(3)	114.2(3)	173.45(5)
19.42	28.20(3)	1.81(1)	122.1(3)	107.3(4)	106.7(4)	97.0(3)	112.0(3)	114.5(4)	173.43(5)
21.50	28.10(3)	1.76(1)	122.4(3)	107.7(3)	105.4(4)	94.6(3)	112.1(3)	114.2(4)	173.29(2)
23.50	27.80(3)	1.76(1)	123.0(4)	108.0(5)	104.1(5)	95.6(4)	112.7(5)	114.1(6)	173.13(2)

Table 8.18: bulk moduli of REE coordination polyhedron and *T*-site tetrahedron for the ATO_4 minerals under study.

	REE polyhedron		*TO_4*	
	K_{P_0,T_0} (GPa)	V_0 (Å^3)	K_{P_0,T_0} (GPa)	V_0 (Å^3)
Ch10-P_A	120(12)	23.53(9)	262(56)	2.319(10)
Xen14-P_D	126(4)	23.18(4)	299(62)	1.900(9)
Xen14-II-P_D	87(26)	30.4(1.2)	\	\
Gasp3-P_F	99(3)	33.02(4)	\	\
Mon14-P_H	110(4)	32.45(8)	395(130)	1.863(12)

8.6 High-temperature ramps

Five different ambient pressure, H*T* ramps have been collected. In Table 8.19, Table 8.20, Table 8.21 and Table 8.22 are reported the unit-cell parameters at varying temperature. The corresponding refined thermal expansion parameters are reported in Table 8.23 and Table 8.24.

Table 8.19: Unit-cell parameters of chernovite-(Y) at different temperatures based on the two single crystal X-ray diffraction *T*-ramps collected on the Ch10 samples.

T (° C)	*a* (Å)	*c* (Å)	*V* (Å^3)
Ch10-T_I			
30	7.020(2)	6.2441(2)	307.71(12)
106	7.022(2)	6.2457(14)	307.93(11)
182	7.0236(14)	6.2502(13)	308.32(11)
258	7.0256(14)	6.2529(13)	308.63(11)
334	7.027(2)	6.2560(14)	308.87(11)
410	7.028(2)	6.2588(13)	309.16(11)
486	7.031(2)	6.2633(13)	309.59(11)
562	7.0333(14)	6.2661(13)	309.96(11)
638	7.033(2)	6.2692(14)	310.12(12)
714	7.036(2)	6.2737(14)	310.54(11)
790	7.038(2)	6.278(2)	310.94(12)
Ch10-T_L			
106	7.0187(14)	6.2385(11)	307.32(4)
182	7.0200(14)	6.2407(11)	307.54(4)
258	7.0220(14)	6.2433(11)	307.84(4)
334	7.0230(14)	6.2478(12)	308.15(4)
410	7.0265(14)	6.2491(12)	308.52(4)
486	7.0294(14)	6.2515(12)	308.90(4)
562	7.031(2)	6.254(12)	309.14(4)
638	7.033(2)	6.2583(12)	309.52(4)
714	7.035(2)	6.2632(12)	309.98(4)
790	7.037(2)	6.2669(12)	310.29(4)

Table 8.20: Unit-cell parameters of chernovite-(Y) at different temperatures based on the powder X-ray diffraction *T*-ramp collected on the Ch13 sample.

T (° C)	*a* (Å)	*c* (Å)	*V* (Å^3)
30	7.0518(3)	6.2901(3)	313.08(2)
100	7.0545(3)	6.2916(3)	313.27(2)
200	7.0571(3)	6.2953(3)	313.52(2)
300	7.0581(3)	6.3001(3)	313.85(2)
400	7.0606(3)	6.3037(3)	314.26(2)
500	7.0644(3)	6.3052(3)	314.66(2)
600	7.0665(3)	6.3095(3)	315.07(2)
700	7.0700(3)	6.3113(3)	315.48(2)
800	7.0702(3)	6.3184(3)	315.85(2)
900	7.0738(3)	6.3194(3)	316.22(2)
1000	7.0766(3)	6.3225(3)	316.62(2)

Table 8.21: Unit-cell parameters of xenotime-(Y) at different temperatures based on the single crystal X-ray diffraction *T*-ramp collected on the Xen14 sample.

T (° C)	*a* (Å)	*c* (Å)	*V* (Å^3)
30	6.8970(9)	6.0553(8)	288.04(5)
106	6.8993(9)	6.0585(8)	288.38(5)
182	6.9014(9)	6.0608(8)	288.67(5)
258	6.9044(9)	6.0629(8)	289.02(5)
334	6.9066(9)	6.0656(8)	289.33(5)
410	6.9087(9)	6.0698(8)	289.71(5)
486	6.9124(9)	6.0728(8)	290.16(5)
562	6.9155(9)	6.0759(8)	290.57(5)
638	6.9191(9)	6.0791(8)	291.03(5)
714	6.9227(9)	6.0821(8)	291.47(5)
790	6.9265(9)	6.0870(8)	292.03(5)

Table 8.22: Unit-cell parameters of monazite-(Ce) at different temperatures based on the single crystal X-ray diffraction *T*-ramp collected on the Mon14 sample.

T (° C)	*a* (Å)	*b* (Å)	*c* (Å)	*β* (°)	*V* (Å^3)
30	6.7795(5)	7.0058(5)	6.4543(5)	103.551(6)	298.02(4)
106	6.7835(5)	7.0089(5)	6.4572(5)	103.534(6)	298.48(4)
182	6.7867(5)	7.0124(5)	6.4621(5)	103.535(5)	299.00(4)
258	6.7926(5)	7.0159(5)	6.4676(5)	103.544(6)	299.65(4)
334	6.7970(5)	7.0200(5)	6.4734(5)	103.537(6)	300.30(4)
410	6.8029(5)	7.0236(5)	6.4793(5)	103.535(6)	300.99(4)
486	6.8076(5)	7.0278(5)	6.4842(5)	103.552(6)	301.58(4)
562	6.8139(5)	7.0325(5)	6.4912(5)	103.551(6)	302.39(4)
638	6.8184(5)	7.0351(5)	6.4961(5)	103.577(6)	302.92(4)
714	6.8245(5)	7.0406(5)	6.5034(5)	103.560(6)	303.77(4)
790	6.8313(5)	7.0454(5)	6.5105(5)	103.565(6)	304.60(4)

The unit-cell volume thermal expansion of the ATO_4 minerals has been modelled with three different equations: a modified Holland-Powell EoS, a 1st order polynomial (straight light) equation and a 2nd order polynomial equation. The corresponding refined parameters are gathered in Table 8.23 and Table 8.24.

Table 8.23: thermal expansion parameters refined from the Holland-Powell EoS. The thermal expansion coefficient (α_V) calculated at room temperature (298 K) based on the Holland-Powell EoS is also reported.

	α_V ($\times 10^{-6}$ K^{-1})	a_0 ($\times 10^{-5}$ K^{-1})	a_1 ($\times 10^{-4}$ K$^{-1/2}$)	V_0 (Å^3)
Ch10-T_I	9.7(1)	2.33(3)	0	307.02(3)
Ch10-T_L	9.5(3)	2.27(8)	0	307.75(6)
Ch13-T_M	8.0(1)	1.90(2)	0	313.06(2)
Xen14-T_N	9.6(1.2)	3.5(3)	0.8(4)	288.07(4)
Mon14-T_O	19.9(1.3)	4.9(3)	0.2(4)	297.97(5)

Table 8.24: refined parameters of the 1st and 2nd order polynomial fits. The first order polynomial fit, corresponding to the average thermal expansion, has also been expressed as LTEC.

	2nd order polynomial fit			1st order polynomial fit		
	l_1	l_2	V_0 (Å^3)	α_V ($\times 10^{-6}$ K^{-1})	LTEC ($\times 10^{-6}$ K^{-1})	V_0 (Å^3)
Ch10-T_I	$11.09 \cdot 10^{-6}$	$1.1499 \cdot 10^{-6}$	306.92	14.45	4.81	306.74
Ch10-T_L	$12.30 \cdot 10^{-6}$	$5.4318 \cdot 10^{-7}$	307.7	13.75	4.58	307.52
Ch13-T_M	$10.06 \cdot 10^{-6}$	$5.780 \cdot 10^{-7}$	312.94	11.95	3.98	312.84
Xen14-T_N	$11.95 \cdot 10^{-6}$	$2.0927 \cdot 10^{-6}$	289.97	18.01	6.00	287.73
Mon14-T_O	$22.59 \cdot 10^{-6}$	$2.3851 \cdot 10^{-6}$	297.77	29.18	9.73	297.50

Eventually, the evolution with temperature of several significant structural parameters (*i.e.*, *A*-O bonds, *T*-O bonds, *A*-coordination polyhedral and *T*-coordination polyhedral volumes) has been determined from the refined structure models, by means of the tools implemented in the *VESTA* software (Momma and Izumi 2011). The corresponding values are reported in Table 8.25, Table 8.26, Table 8.27 and Table 8.28. In Table 8.29 are reported the refined thermal expansion parameters of the REE-coordination polyhedra of chernovite-(Y), xenotime-(Y) and monazite-(Y).

Table 8.25: selected structural parameters of chernovite-(Y) under high temperature.

T (° C)	V_{REEO_8}(Å^3)	V_{AsO_4}(Å^3)	REE-O_a (Å)	REE-O_b (Å)	P-O (Å)
106	23.51(3)	2.305(8)	2.283(14)	2.437(13)	1.658(14)
182	23.52(3)	2.307(8)	2.283(14)	2.438(13)	1.658(14)
258	23.58(3)	2.275(8)	2.296(10)	2.426(11)	1.652(10)
334	23.67(5)	2.35(2)	2.26(3)	2.48(2)	1.67(3)
410	23.70(3)	2.283(8)	2.295(12)	2.434(12)	1.654(12)
486	23.78(3)	2.278(8)	2.295(14)	2.443(13)	1.651(14)
562	23.72(3)	2.348(8)	2.288(15)	2.418(13)	1.672(14)
638	23.80(4)	2.27(2)	2.30(3)	2.44(2)	1.65(3)
714	23.80(3)	2.311(8)	2.290(15)	2.451(18)	1.66(2)
790	23.92(3)	2.253(8)	2.309(12)	2.435(11)	1.647(12)

Table 8.26: selected structural parameters of xenotime-(Y) under high temperature.

T (° C)	V_{REEO_8}(Å^3)	V_{PO_4}(Å^3)	REE-O_a (Å)	REE-O_b (Å)	P-O (Å)
30	23.04(5)	1.911(6)	2.383(3)	2.301(3)	1.555(3)
106	23.05(5)	1.919(6)	2.385(3)	2.300(3)	1.558(3)
182	23.15(5)	1.904(6)	2.387(3)	2.303(3)	1.555(3)
258	23.16(5)	1.912(6)	2.389(3)	2.303(3)	1.556(3)
334	23.22(5)	1.903(6)	2.386(3)	2.308(3)	1.554(3)
410	23.24(5)	1.908(6)	2.390(3)	2.307(3)	1.555(3)
486	23.27(5)	1.899(6)	2.390(3)	2.310(3)	1.553(3)
562	23.37(5)	1.900(6)	2.393(3)	2.313(3)	1.553(3)
638	23.41(5)	1.900(6)	2.393(3)	2.315(3)	1.553(3)
714	23.41(5)	1.910(6)	2.394(3)	2.315(3)	1.556(3)
790	23.49(5)	1.915(6)	2.400(3)	2.314(3)	1.557(3)

Table 8.27: *A*-O and *T*-O bond distances (in Å) evolution at high temperature based on the structure refinements from monazite-(Ce).

T (° C)	REE-$O1_a$	REE-$O1_b$	REE-$O2_a$	REE-$O2_b$	REE-$O2_c$	REE-$O3_a$	REE-$O3_b$	REE-$O4_a$	REE-$O4_b$	P-O1	P-O2	P-O3	P-O4
30	2.523(3)	2.451(3)	2.784(3)	2.556(3)	2.648(3)	2.583(3)	2.466(3)	2.512(3)	2.444(3)	1.528(3)	1.540(3)	1.532(3)	1.535(3)
106	2.525(4)	2.452(4)	2.785(3)	2.558(3)	2.650(4)	2.585(3)	2.467(3)	2.515(3)	2.446(4)	1.528(4)	1.539(4)	1.532(3)	1.534(4)
182	2.525(3)	2.457(3)	2.786(3)	2.557(3)	2.657(3)	2.590(3)	2.468(3)	2.520(3)	2.441(3)	1.524(4)	1.541(4)	1.531(3)	1.539(4)
258	2.529(3)	2.457(3)	2.786(3)	2.563(3)	2.656(4)	2.591(3)	2.475(3)	2.520(3)	2.446(3)	1.523(4)	1.542(4)	1.529(3)	1.538(4)
334	2.531(3)	2.458(3)	2.786(3)	2.566(3)	2.662(3)	2.601(3)	2.471(3)	2.525(3)	2.449(3)	1.523(4)	1.541(4)	1.531(3)	1.533(4)
410	2.536(4)	2.457(3)	2.791(3)	2.564(3)	2.665(4)	2.600(3)	2.476(3)	2.527(3)	2.452(3)	1.524(4)	1.545(4)	1.532(3)	1.534(4)
486	2.537(4)	2.461(3)	2.790(3)	2.571(3)	2.666(4)	2.607(3)	2.473(3)	2.529(4)	2.453(3)	1.523(4)	1.541(3)	1.535(3)	1.536(4)
562	2.532(4)	2.466(3)	2.787(3)	2.572(3)	2.674(4)	2.611(4)	2.477(3)	2.534(3)	2.456(3)	1.523(4)	1.541(3)	1.538(3)	1.533(4)
638	2.539(4)	2.463(3)	2.791(3)	2.578(3)	2.673(4)	2.609(4)	2.483(3)	2.532(3)	2.458(3)	1.524(4)	1.542(3)	1.533(4)	1.537(4)
714	2.542(4)	2.469(3)	2.790(3)	2.583(3)	2.676(4)	2.613(3)	2.484(3)	2.538(3)	2.460(3)	1.520(3)	1.541(3)	1.535(3)	1.537(4)
790	2.544(4)	2.472(3)	2.789(3)	2.587(3)	2.679(3)	2.614(3)	2.487(3)	2.545(3)	2.460(3)	1.520(4)	1.543(4)	1.535(3)	1.536(4)

Table 8.28: Volumes of *A*- and *T*-coordination polyhedra (in $Å^3$) and significant bond angles (°) calculated using the routine implemented in the software Vesta 3 (Momma and Izumi 2011), based on the structure refinements of monazite-(Ce).

T (° C)	V_{REEO_9}	V_{PO_4}	REE-O4-REE (I)	REE-O2-REE (I)	REE-O1-REE (II)	REE-O2-REE (II)	REE-O3-REE (III)	REE-O2-REE (IV)	REE-P-REE
30	32.34(9)	1.83(5)	119.87(12)	104.31(12)	109.93(13)	99.31(10)	110.46(10)	113.25(13)	174.59(5)
106	32.41(9)	1.83(5)	119.82(14)	104.33(12)	109.93(13)	99.31(10)	110.41(10)	113.25(10)	174.60(5)
182	32.49(9)	1.84(5)	119.87(12)	104.16(12)	109.86(13)	99.42(10)	110.31(10)	113.27(10)	174.59(5)
258	32.58(9)	1.83(5)	119.81(12)	104.26(12)	109.84(13)	99.36(10)	110.18(10)	113.29(10)	174.66(5)
334	32.70(9)	1.83(5)	119.62(12)	104.19(12)	109.87(13)	99.37(10)	110.09(10)	113.24(10)	174.72(5)
410	32.77(9)	1.84(5)	119.56(12)	104.11(12)	109.85(13)	99.41(10)	110.12(10)	113.38(10)	174.73(4)
486	32.86(9)	1.84(5)	119.55(14)	104.13(12)	109.84(13)	99.35(10)	110.07(10)	113.27(10)	174.72(4)
562	32.95(9)	1.84(5)	119.36114)	104.14(12)	110.10(13)	99.54(10)	109.94(12)	113.22(10)	174.78(4)
638	33.02(9)	1.84(5)	119.44(14)	104.10(12)	109.95(13)	99.40(10)	109.91(12)	113.26(10)	174.76(4)
714	33.14(9)	1.83(5)	119.34(12)	104.20(12)	109.85(11)	99.41(10)	109.87(10)	113.23(10)	174.76(4)
790	33.23(9)	1.83(5)	119.22(14)	104.27(12)	109.84(13)	99.49(10)	109.88(13)	113.24(10)	174.79(4)

Table 8.29: Refined thermal expansion parameters of the REE coordination polyhedra in chernovite-(Y), xenotime-(Y) and monazite-(Ce) based on modified Holland-Powell EoS fits.

	α_{REEO_X} ($\times 10^{-6}$ K^{-1})	a_0 ($\times 10^{-5}$ K^{-1})	a_1 ($\times 10^{-4}$ K$^{-1/2}$)	V_0 (Å^3)
Ch10-T_L	16(3)	3.8(7)	0 (fixed)	23.49(4)
Xen14-T_N	18(2)	4.2(5)	0 (fixed)	23.03(4)
Mon14-T_O	25(2)	6.0(5)	0 (fixed)	32.36(4)

8.7 Combined H*P*–H*T* data

Four combined H*P*–H*T* ramps have been collected on chernovite-(Y) and monazite-(Ce). Table 8.30 and Table 8.31 report the unit-cell parameters at varying both the pressure and temperature.

Table 8.30: Unit-cell parameters of chernovite-(Y) at different temperatures and pressures based on two single crystal X-ray diffraction ramps collected under combined H*P*–H*T* conditions on the Ch10 sample.

P (GPa)	*T* (° C)	*a* (Å)	*c* (Å)	*V* (Å^3)
Ch10-PT_{250}				
1.0(1)*	21	6.9949(2)	6.2312(2)	304.88(2)
2.1(1)*	97	6.9817(3)	6.2271(4)	303.53(2)
3.4(1)	259	6.9572(2)	6.2201(3)	301.06(2)
4.1(1)	259	6.9475(3)	6.2152(4)	299.99(3)
4.8(1)	251	6.9294(5)	6.2050(6)	297.94(4)
5.8(1)	249	6.9107(6)	6.1952(9)	295.86(6)
7.1(1)	249	6.8848(8)	6.1820(10)	293.02(7)
7.6(1)	249	6.8722(8)	6.1795(10)	291.84(7)
8.8(1)	247	6.8512(9)	6.1694(10)	289.58(7)
9.6(1)	246	6.8322(8)	6.1620(11)	287.63(7)
10.7(1)	246	6.8283(9)	6.1570(11)	287.07(7)
12.1(1)	247	6.8189(8)	6.1476(9)	285.84(6)
13.3(1)	247	6.8072(7)	6.1253(8)	283.83(6)
Ch10-PT_{500}				
1.1(1)*	22	7.0002(3)	6.2317(3)	305.37(2)
3.0(1)*	169	6.9684(7)	6.2274(6)	302.39(5)
3.9(1)*	348	6.9548(2)	6.2207(2)	300.89(2)
4.1(1)	499	6.9526(3)	6.2217(2)	300.74(2)
4.4(1)	498	6.9460(4)	6.2162(3)	299.91(3)
5.2(1)	503	6.9319(4)	6.2080(3)	298.30(3)
6.5(1)	505	6.9142(7)	6.2050(6)	296.63(5)
7.4(1)	504	6.9026(1)	6.1990(8)	295.35(7)
8.4(1)	499	6.8846(4)	6.1928(5)	293.52(3)
9.6(1)	499	6.8746(4)	6.1876(5)	292.42(3)
10.6(1)	499	6.8520(12)	6.1601(12)	289.21(9)

*: P_{steps} not belonging to the isothermal section of the *P*–*T*-ramp.

Table 8.31: Unit-cell parameters of monazite-(Ce) at different temperatures and pressures based on two single crystal X-ray diffraction ramps collected under combined H*P*–H*T* conditions on the Mon14 sample.

P (GPa)	*T* (° C)	*a* (Å)	*b* (Å)	*c* (Å)	*β* (°)	*V* (Å^3)
Mon14-*PT*$_{250}$						
0.2(1)*	25	6.803(5)	6.9983(2)	6.4529(7)	103.37(3)	298.8(2)
0.2(1)*	75	6.804(5)	6.9956(2)	6.4518(8)	103.35(4)	298.7(2)
0.8(1)*	150	6.794(6)	6.9948(2)	6.4544(10)	103.34(4)	298.4(3)
1.6(1)	250	6.779(9)	6.9912(4)	6.4544(14)	103.35(7)	297.6(2)
3.4(1)	250	6.724(4)	6.9517(14)	6.4298(6)	103.33(3)	292.4(2)
4.4(1)	250	6.734(6)	6.9334(2)	6.4072(8)	103.33(4)	291.0(2)
6.0(1)	250	6.723(9)	6.8861(4)	6.3664(13)	103.11(6)	287.0(4)
7.6(1)	250	6.707(13)	6.8507(4)	6.343(2)	102.9(9)	284.0(5)
8.8(1)	250	6.62(2)	6.8599(7)	6.358(2)	103.02(12)	281.2(6)
10.0(1)	250	6.56(4)	6.859(2)	6.380(6)	102.9(3)	279(1)
12.6(1)	250	6.52(5)	6.843(2)	6.373(8)	102.4(4)	278(1)
Mon14-*PT*$_{500}$						
0.6(1)*	25	6.794(2)	7.0157(2)	6.4362(4)	103.45(2)	298.36(9)
1.4(1)*	100	6.795(4)	6.9991(2)	6.4453(6)	103.39(3)	298.2(2)
3.2(1)*	250	6.736(6)	6.9626(3)	6.4300(10)	103.11(4)	293.7(3)
4.6(1)*	400	6.699(4)	6.9474(2)	6.4284(6)	103.05(3)	291.4(2)
6.0(1)	540	6.681(5)	6.9128(3)	6.3997(7)	102.92(3)	288.0(2)
6.8(1)	540	6.690(8)	6.8935(4)	6.3850(11)	102.86(5)	287.0(3)
7.8(1)	540	6.643(4)	6.8920(2)	6.3858(6)	102.62(3)	285.3(2)
8.6(1)	540	6.646(5)	6.8758(2)	6.3592(8)	102.67(4)	283.5(1)
10.6(1)	540	6.626(4)	6.8543(2)	6.3149(6)	102.57(3)	279.9(2)
11.4(1)	540	6.614(3)	6.8430(2)	6.2996(5)	102.58(2)	278.2(1)
12.4(1)	540	6.591(4)	6.8364(2)	6.2938(5)	102.59(2)	276.7(2)
14.4(1)	540	6.579(6)	6.8105(3)	6.2657(8)	102.52(4)	274.0(3)
16.0(1)	540	6.567(10)	6.7756(5)	6.2378(13)	102.42(7)	271.0(4)
18.0(1)	540	6.524(11)	6.7561(6)	6.237(15)	102.59(7)	268.2(5)
20.0(1)	540	6.494(13)	6.7413(8)	6.2376(2)	102.45(9)	266.6(5)
21.8(1)	540	6.49(2)	6.7254(13)	6.227(3)	102.0(2)	265.7(8)

*: P_{steps} not belonging to the isothermal section of the *P*–*T*-ramp.

P–*T*–*V* equations of state, combining a 2nd order Birch-Murnaghan EoS, a modified Holland-Powell EoS and using a linear $\partial K/\partial T$ description to model the thermal dependance of the bulk modulus, have been fitted to the experimental H*P* (ambient-*T*), H*T* (ambient-*P*) and H*P*–H*T* data. The unit-cell volumes of all the independent ramps (Ch10-*PT*$_{250}$, Ch10-*PT*$_{500}$, Ch10-T_I, Ch10-P_A, Ch10-P_B for chernovite-(Y); Mon14-*PT*$_{250}$, Mon14-*PT*$_{500}$, Mon14-T_O, Mon14-P_H for monazite-(Ce)), have been normalized to the respective ambient conditions values. The data collected at pressure exceeding ~9.6 GPa in chernovite-(Y) have been excluded from the modelling of the *P*–*T*–*V* behavior (see section 9.5.3 for details). In monazite-(Ce), the data collected at pressure exceeding ~10 GPa (Mon14-*PT*$_{500}$) and ~18 GPa (Mon14-*PT*$_{250}$) have been excluded from the refinement *P*–*T*–*V* EoS (see section 9.8.3 for details). Table 8.32 reports the refined parameters for chernovite-(Y) and monazite-(Ce).

Table 8.32: refined *P–T–V* EoS parameters based on all the experimental data collected on the Ch10 and Mon14 samples respectively.

	Chernovite-(Y)	Monazite-(Ce)
$K_{P,T}$ (GPa)	132 (3)	124(1)
β_V (GPa^{-1})	0.0076(1)	0.00806(9)
V_0 (Å^3)	297.26(8)	299.53(2)
α_V (×10^{-6} K^{-1})	9.8(1.5)	19.9(5)
a_0 (×10^{-5} K^{-1})	2.4(4)	4.76(12)
dK/dT_P	-0.034(13)	-0.050(4)

Eventually, the evolution of several significant structural parameters (*i.e.*, *A*-O bonds, *T*-O bonds, *A*-coordination polyhedral and *T*-coordination polyhedral volumes), at varying both the temperature and pressure, has been determined from the refined structure models, by means of the tools implemented in the *VESTA* software (Momma and Izumi 2011). The corresponding values are reported in Table 8.33, Table 8.34 and Table 8.35.

Table 8.33: volume of the YO_8 polyhedron in chernovite-(Y) under combined H*P*–H*T* conditions.

P (GPa)	*T* (° C)	YO_8 (Å^3)
Ch10-PT_{250}		
3.4(1)	259	23.00(1)
4.1(1)	259	22.85(1)
4.8(1)	251	22.67(1)
5.8(1)	249	22.44(1)
7.1(1)	249	22.21(1)
7.6(1)	249	22.16(1)
8.8(1)	247	21.96(1)
9.6(1)	246	21.80(1)
Ch10-PT_{500}		
4.1(1)	499	23.01(1)
4.4(1)	498	22.97(1)
5.2(1)	503	22.76(1)
6.5(1)	505	22.72(1)
7.4(1)	504	22.88(1)
8.4(1)	499	22.39(1)
9.6(1)	499	22.28(1)

Table 8.34: relevant interatomic distances of monazite from the refined models based on selected data collected at combined *HP–HT* conditions.

P (GPa)	REE-O1$_a$	REE-O1$_b$	REE-O2$_a$	REE-O2$_b$	REE-O2$_c$	REE-O3$_a$	REE-O3$_b$	REE-O3$_c$	REE-O4$_a$	REE-O4$_b$
Mon14-*PT*$_{250}$										
1.6	2.50(1)	2.45(1)	2.76(1)	2.62(9)	2.560(9)	2.600(7)	2.47(1)	2.530(14)	2.467(14)	3.130(12)
3.4	2.50(1)	2.45(1)	2.76(1)	2.62(8)	2.560(9)	2.620(7)	2.47(1)	2.537(9)	2.463(14)	3.130(12)
4.4	2.48(1)	2.42(1)	2.76(1)	2.57(1)	2.530(9)	2.581(7)	2.469(8)	2.496(9)	2.437(14)	3.104(12)
6.0	2.46(1)	2.41(1)	2.75(9)	2.60(1)	2.510(9)	2.524(7)	2.51(8)	2.474(8)	2.450(14)	3.164(12)
7.6	2.46(1)	2.40(1)	2.74(8)	2.52(1)	2.514(8)	2.571(7)	2.473(8)	2.476(14)	2.454(14)	3.053(12)
8.8	2.46(1)	2.40(1)	2.75(1)	2.51(1)	2.49(1)	2.573(7)	2.463(8)	2.462(8)	2.414(14)	3.021(12)
10.0	2.44(1)	2.39(1)	2.73(1)	2.55(1)	2.46(1)	2.58(1)	2.41(8)	2.497(7)	2.318(14)	2.990(9)
12.6	2.43(1)	2.39(1)	2.74(1)	2.50(1)	2.48(1)	2.59(1)	2.44(8)	2.498(14)	2.290(14)	2.952(9)
Mon14-*PT*$_{500}$										
6.0	2.477(4)	2.420(4)	2.752(4)	2.580(2)	2.512(3)	2.579(3)	2.488(2)	2.491(2)	2.427(3)	3.067(4)
6.8	2.477(4)	2.409(4)	2.744(3)	2.600(3)	2.494(3)	2.592(4)	2.490(4)	2.486(2)	2.429(4)	3.051(5)
7.8	2.477(4)	2.406(4)	2.761(4)	2.547(3)	2.504(4)	2.591(4)	2.472(4)	2.486(2)	2.410(4)	3.019(5)
8.6	2.479(5)	2.407(5)	2.757(4)	2.540(3)	2.495(4)	2.600(4)	2.454(4)	2.497(2)	2.350(4)	2.990(5)
10.6	2.454(4)	2.396(4)	2.723(4)	2.550(3)	2.482(5)	2.580(5)	2.464(5)	2.465(4)	2.389(4)	2.983(6)
11.4	2.447(4)	2.392(4)	2.715(4)	2.538(3)	2.479(6)	2.571(5)	2.465(6)	2.452(3)	2.401(4)	2.981(6)
12.4	2.443(3)	2.385(3)	2.697(4)	2.553(4)	2.462(5)	2.572(5)	2.459(5)	2.446(4)	2.388(4)	2.971(7)
14.4	2.444(3)	2.384(3)	2.704(4)	2.538(4)	2.464(5)	2.580(5)	2.460(5)	2.443(4)	2.394(5)	2.956(7)
16.0	2.423(4)	2.362(4)	2.685(4)	2.525(4)	2.442(5)	2.569(5)	2.441(5)	2.429(4)	2.369(5)	2.920(8)
18.0	2.420(4)	2.355(4)	2.678(4)	2.514(5)	2.424(5)	2.569(5)	2.444(5)	2.418(4)	2.362(5)	2.908(8)
20.0	2.417(4)	2.354(4)	2.682(4)	2.490(3)	2.421(5)	2.588(5)	2.411(5)	2.414(4)	2.362(5)	2.866(9)
21.8	2.414(4)	2.343(4)	2.692(4)	2.510(3)	2.405(5)	2.590(5)	2.414(5)	2.410(2)	2.360(5)	2.859(7)

Table 8.35: selected structural parameters of monazite from the refined models based on selected data collected under combined H*P*–H*T* conditions.

P (GPa)	V_{REEO_9}(Å^3)	V_{PO_4}(Å^3)	REE-O4-REE (I) [°]	REE-O2-REE (I) [°]	REE-O1-REE (II) [°]	REE-O2-REE (II) [°]	REE-O3-REE (III) [°]	REE-O2-REE (IV) [°]	REE-P-REE [°]
Mon14-PT_{250}									
1.6	32.2(1)	1.84(7)	119.1(9)	105.8(8)	109.9(4)	98.8(5)	114.0(6)	110.3(5)	174.9(3)
3.4	31.5(1)	1.85(7)	120.2(4)	105.5(4)	109.0(4)	98.5(3)	114.3(3)	110.6(2)	174.5(2)
4.4	31.4(1)	1.83(7)	119.6(5)	105.9(4)	109.4(2)	98.3(3)	114.8(3)	110.9(3)	174.3(2)
6	31.2(1)	1.73(7)	119.7(9)	105.1(8)	109.1(4)	97.9(6)	114.4(7)	110.9(5)	173.9(3)
7.6	30.6(1)	1.77(7)	119.2(9)	108.0(10)	108.4(4)	96.8(5)	116.2(8)	111.0(4)	173.7(3)
8.8	30.3(1)	1.78(7)	120.0(7)	106.5(6)	108.0(3)	97.3(3)	115.0(5)	111.0(3)	173.6(3)
10	29.8(1)	1.92(7)	122.3(11)	105.9(12)	108.8(5)	98.3(6)	114.0(10)	111.9(6)	173.3(4)
12.6	29.6(1)	1.88(7)	124(2)	107(2)	108.0(6)	96.8(9)	113.5(14)	111.2(8)	173.4(5)
Mon14-PT_{500}									
6	31.24(6)	1.79(2)	120.0(7)	105.8(6)	108.9(3)	98.3(3)	114.1(5)	110.4(3)	174.3(2)
6.8	31.22(6)	1.78(2)	120.1(7)	105.5(6)	108.6(3)	98.4(3)	113.9(5)	110.2(3)	173.9(2)
7.8	30.85(6)	1.82(3)	120.7(5)	106.4(4)	108.4(2)	97.5(3)	114.7(4)	110.4(2)	174.0(2)
8.6	30.58(6)	1.87(3)	122.2(9)	106.3(9)	107.9(4)	97.4(5)	115.3(8)	110.5(4)	173.5(3)
10.6	30.25(6)	1.81(4)	121.2(5)	106.6(4)	108.1(2)	97.8(2)	114.6(4)	110.9(2)	174.0(2)
11.4	30.06(6)	1.79(3)	120.8(4)	106.8(4)	108.0(2)	97.7(2)	114.7(3)	111.2(2)	173.9(1)
12.4	29.84(6)	1.79(5)	121.1(5)	106.6(4)	108.0(2)	98.3(2)	114.2(3)	111.1(8)	173.8(1)
14.4	29.85(6)	1.80(4)	120.9(4)	106.7(4)	107.7(2)	97.8(3)	114.4(3)	111.6(2)	173.7(1)
16	29.19(6)	1.80(2)	121.6(5)	107.0(4)	107.3(2)	97.4(2)	114.5(3)	112.0(2)	173.6(1)
18	28.94(6)	1.77(4)	121.3(5)	106.7(4)	106.0(2)	97.4(2)	114.1(4)	112.1(2)	173.6(2)
20	28.74(6)	1.79(3)	121.3(7)	107.1(6)	106.4(3)	98.8(3)	114.1(5)	112.5(3)	173.6(2)
21.8	28.73(6)	1.79(3)	122.0(9)	106.8(8)	106.1(4)	96.3(4)	112.6(4)	113.9(7)	173.1(3)

Chapter 9

9 Discussion

9.1 Chemical composition of REE-bearing phosphates and arsenates

The results discussed in this section have already been published by Pagliaro et al. (2022a) in the following manuscript: Crystal chemistry and miscibility of chernovite-(Y), xenotime-(Y), gasparite-(Ce) and monazite-(Ce) from Mt. Cervandone, Western Alps, Italy, Mineralogical Magazine, 86, 150-167. Thorium is the most variable element within all the points of analysis for both zircon- and monazite-type minerals. The enrichment of Th within the REE*T*O$_4$ compounds is controlled by two potential substitution mechanisms:

$$(Th,U)^{4+} + Ca^{2+} = 2REE^{3+} \quad (9.1)$$

$$(Th,U)^{4+} + Si^{4+} = REE^{3+} + (P,As)^{5+} \quad (9.2)$$

respectively known as cheralite (equation 9.1) and thorite substitution mechanisms (equation 9.2). In Figure 9.1a, all the data are reported in a P/(P+As+Si) *vs.* Y diagram, which clearly allows to distinguish between the four minerals under investigation, arranged in four distinct domains. The Y-poor side of the diagram contains the chemical data from the monazite-(Ce) and gasparite-(Ce) crystals, respectively enriched in P and As. Data from chernovite-(Y) and xenotime-(Y) lie on the Y-enriched side of the diagram, and are characterized by a highly variable P and As fraction, resulting in an almost complete solid solution along the join chernovite-(Y)−xenotime-(Y) (as also shown by the chemical compositions of samples Ch11 and Ch16, showing results with equal fractions of As and P). On the contrary, the composition of gasparite-(Ce) and monazite-(Ce) crystals is closer to the ideal endmembers, and only a partial solution is observed. Monazite-(Ce) and gasparite-(Ce) are characterized by a poor Y content, coupled with an enrichment in LREE elements, with Ce (on average, 0.46(2) apfu) as the most common cation, followed by La (0.20(2) apfu) and Nd (0.17(2) apfu). The *A*-site of the chernovite-(Y)–xenotime-(Y) series is characterized by a relatively constant composition, where Y is always the dominant cation (ranging from a maximum of 0.78 apfu to a

minimum of 0.46 apfu), followed, on average, by Dy, Er, Gd, Yb and Ho. When the Y content is lower than ~0.6 apfu, Th or LREE become relevant *A*-site occupying cations. The fraction of LREE in chernovite-(Y) and xenotime-(Y) is generally low (see the section 7.1 for further details), reaching its maximal values in a few data points of analysis of Ch11. The REE pattern for all the samples under investigation is reported in Figure 9.2, normalized to the REE concentration of the Carbonaceous Chondrite C1, after Wasson and Kallemeyn (1988). For all the points, the abundance of Eu is always lower than the detection limit. As mentioned above, the tetragonal structure of chernovite-(Y) and xenotime-(Y) has a strong preference for Y and, in general, the smaller HREE: this pattern is reflected by the positive slope reported in Figure 9.2b.

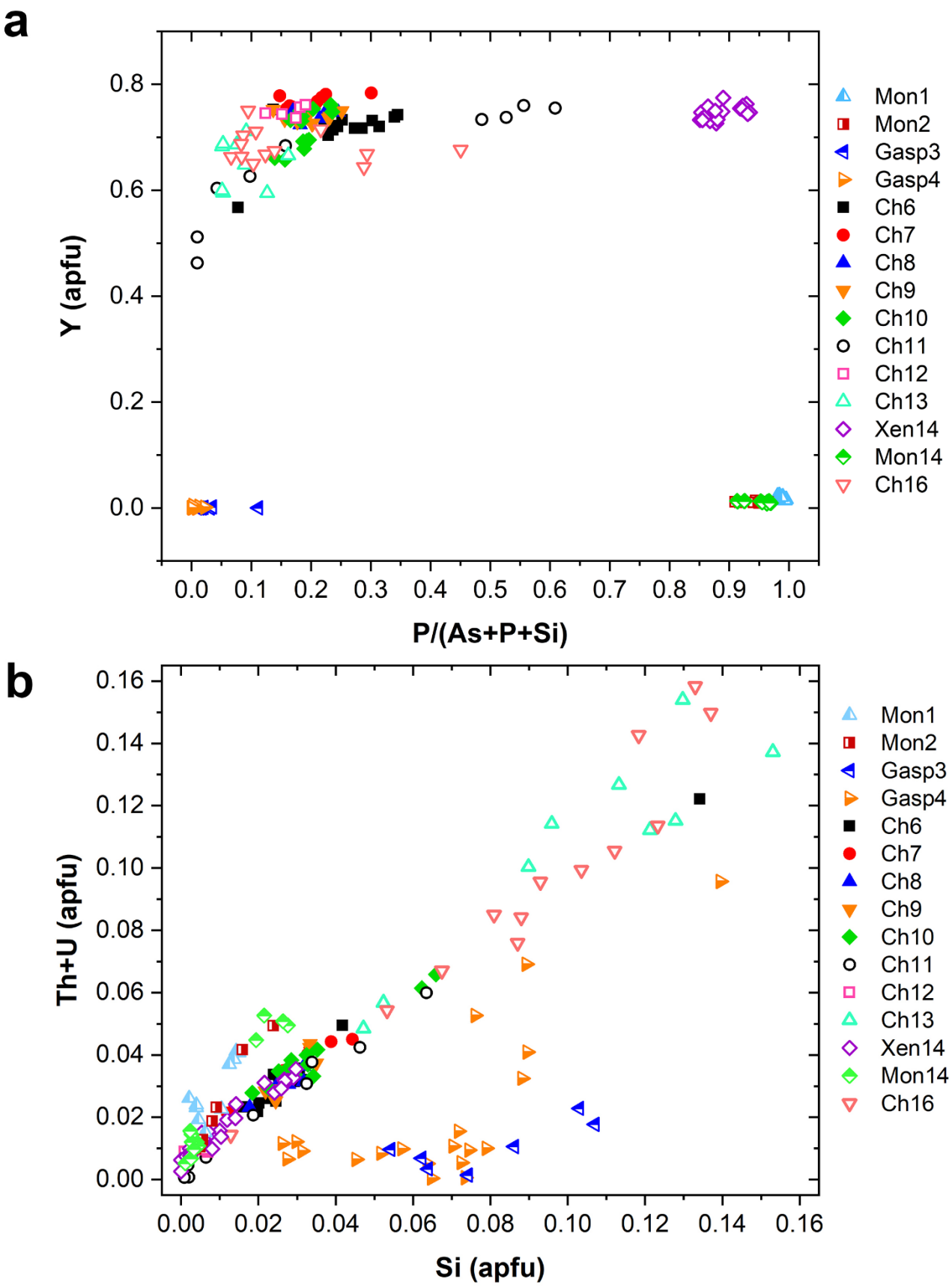

Figure 9.1: **(a)** P/(P+As+Si) vs. Y diagram and **(b)** Si *vs.* Th+U (in apfu) for all the samples under investigation.

Conversely, in the gasparite-(Ce)–monazite-(Ce) series, the LREE enrichment is responsible for the negative slope in Figure 9.2. It is worthwhile to point out that the relatively high Gd content, shown by the three monazites under investigation, has been already described in alpine-fissures minerals related to the circulation of hydrothermal fluids, as in the case of Mt. Cervandone (Demartin et al. 1991; Della Ventura et al. 1996). Due to their low content (<0.002 apfu), Er-Lu elements are not reported in Figure 9.2a. In addition, the Carbonaceous Chondrite C1 REE-normalized diagram reported in Figure 9.2b shows that there is a positive anomaly in the Ho and Lu concentrations in chernovite-(Y) and xenotime-(Y) from Mt. Cervandone. Literature data (Ondrejka et al. 2007; Förster et al. 2011; Papoutsa and Pe-Piper 2014), reporting the Ho and Lu contents in chernovites-(Y) and xenotimes-(Y), reveal that the maximum Ho_2O_3 content detected in chernovite-(Y) is 2.44 wt % (Papoutsa and Pe-Piper 2014), slightly lower than the highest average content of the samples of this study (Table 8.1), whereas Förster et al. (2011) reported the maximum content in Lu_2O_3 (1.29 wt %) very close to that of the samples of this study (Table 8.1). Although a correction protocol for REE interferences has been applied to the experimental chemical data of this study, we cannot unambiguously exclude that the observed anomalies may be slightly affected to the adopted experimental strategy. However, the previous findings reported in the literature (*e.g.*, Ondrejka et al. 2007; Förster et al. 2011; Papoutsa and Pe-Piper 2014) corroborate the results of this study.

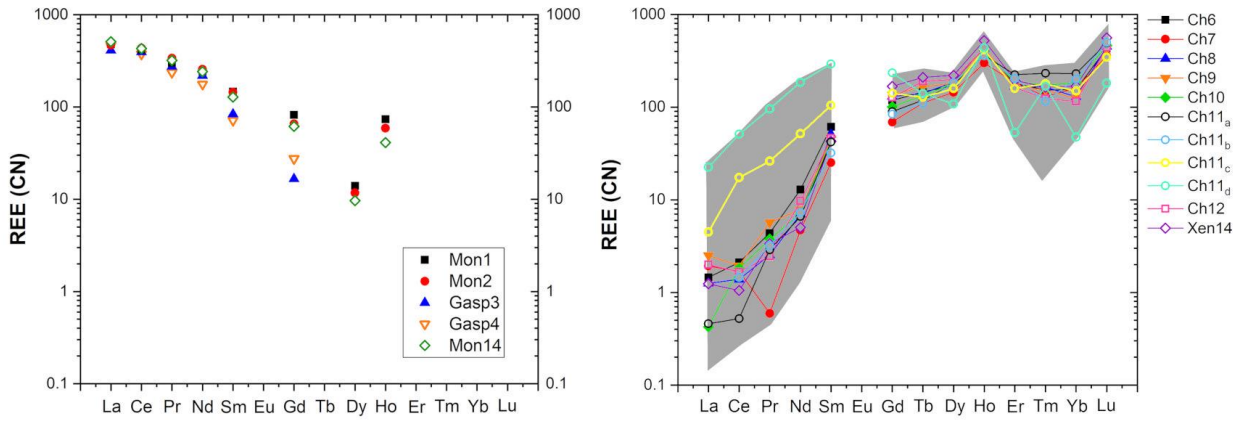

Figure 9.2: Average composition of REE (normalized to the CN-1 chondrite, after Wasson and Kallemeyn (1988)) of all the samples of the gasparite-(Ce)–monazite-(Ce) series **(a)** and of the chernovite-(Y)–xenotime-(Y) series **(b)**. The grey belt in **(b)** represents the range of the lanthanides composition for all the points of analysis of the chernovite-(Y)-xenotime-(Y) series. For the sample Ch11 in **(b)** are reported four distinct chemical compositions referring to the core ($Ch11_a$), the interface ($Ch11_b$), the Th-rich rim zone ($Ch11_c$) and the LREE-enriched outer rim zone ($Ch11_d$) (see section 8.2, Table 8.1, Figure 8.3 for further details). (Element with concentration < 0.002 apfu are not shown).

9.1.1 Chemical composition of the chernovite-(Y)–xenotime-(Y) series

Although the trivalent cations are always dominant within the *A*-site of the tetragonal series, some data points from the samples Ch6, Ch10, Ch11, Ch13 and Ch16 show a relatively large amount of Th. The thorite substitution mechanism (equation 9.2) likely occurs in the chernovite-(Y)–xenotime-(Y) series under investigation, as suggested by the strong positive linear correlation between Si and the Th+U fraction (Figure 9.1). For a better representation of the crystal-chemistry of the mineral samples of this study, the (tetragonal) 2-component system chernovite-(Y)–xenotime-(Y) could be replaced by a 3-component solid solution between the endmembers chernovite-(Y), xenotime-(Y) and $ThSiO_4$ (Figure 9.3). From Figure 9.3, as well as in the P/(P+As+Si) *vs.* Y diagram (Figure 9.1a), even in the more P-depleted samples (*i.e.*, Ch6, Ch7, Ch8, Ch9, Ch10, Ch12), the concentration of this element is relatively high, with an average of 20(3) mol % of xenotime-(Y) component, coupled with a very small $ThSiO_4$ fraction (on average 3(1) mol %). Conversely, the xenotime-(Y) sample Xen14 shows a chemical composition (Table 8.1) much closer to the ideal endmember, being As usually low, corresponding to an average chernovite-(Y) component between 7.0 mol % and 12.9 mol %. Between the chernovite-(Y)–xenotime-(Y) edge and the $ThSiO_4$ corner, the samples investigated show that a wide miscibility gap occurs (Figure 9.3). The most Th-enriched analyses on the chernovite-(Y)-xenotime-(Y) edge belong to Ch13 and Ch16 (Figure 9.3), which are also characterized by a highly altered texture (Figure 8.3) and variable composition. In these cases, the major chemical variations concern a strong Th-enrichment, reflected by a $ThSiO_4$ component ranging from 4.7 mol % to 15.3 mol % for Ch13, and between 1.3 mol % and 12.3 % for Ch16. The relatively large fraction of the $ThSiO_4$ component may be responsible for the greenish color observed only in these samples (Figure 8.1d,e) and their damaged appearance, likely due to metamictization (Figure 8.3). Moreover, these samples are also characterized by a larger fraction of CaO (up to 1.93 wt %, in Ch16, *vs.* an average 0.1(3) wt % for the other chernovite-(Y) samples), suggesting the occurrence also of the cheralite substitution mechanism (equation 9.1). In addition, Ch16 reveals the presence of P-enriched domains, with a maximum xenotime-(Y) component of 45.10 mol % (Figure 9.3). The P- and the As-enriched domains, respectively, are linked by an irregular lobate interface, as shown in Figure 8.3f.

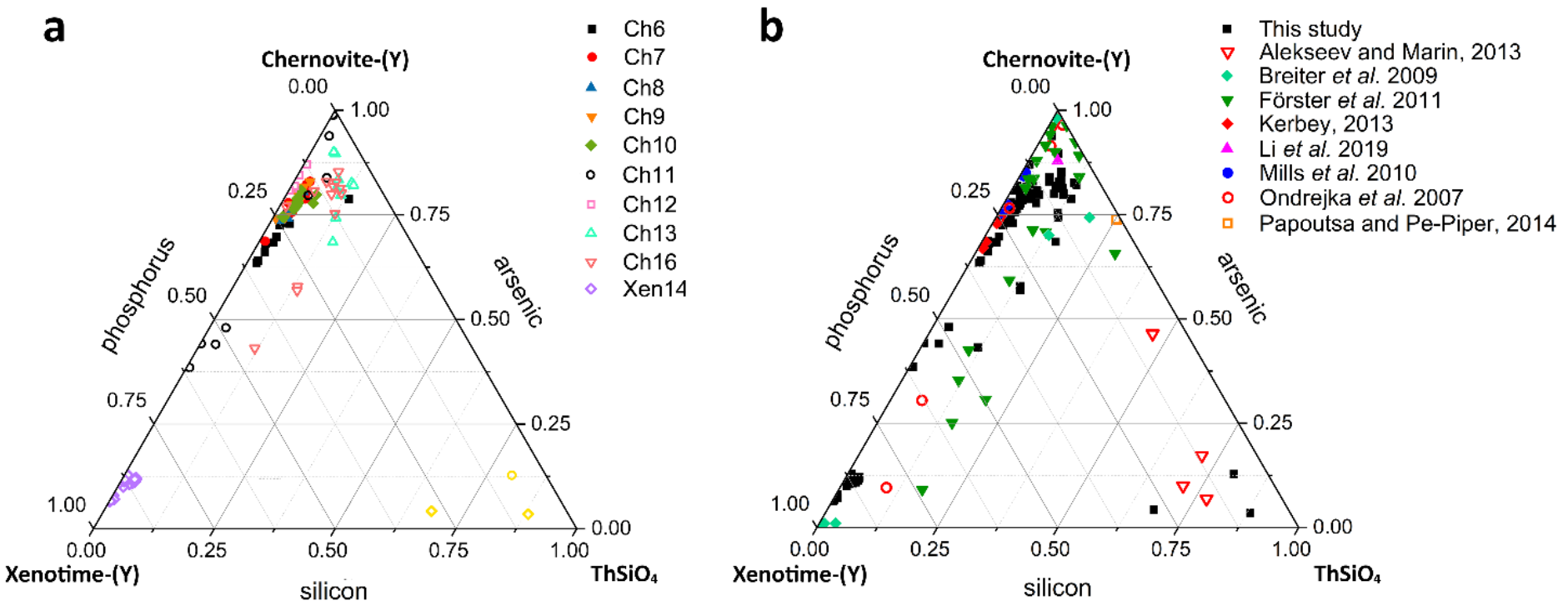

Figure 9.3: **(a)** Triangular chernovite-(Y)–xenotime-(Y)–$ThSiO_4$ compositional diagram, based on the As–P–Si relative abundance, containing all the points of chemical analysis performed on the zircon-type tetragonal minerals. The three points closer to the $ThSiO_4$ corner represent the $ThSiO_4$ grains found within the Ch11 and Xen14 samples (see also Figure 8.3). **(b)** The same diagram showing the chemical data from this and previously published studies on minerals of the chernovite-(Y)-xenotime-(Y) series.

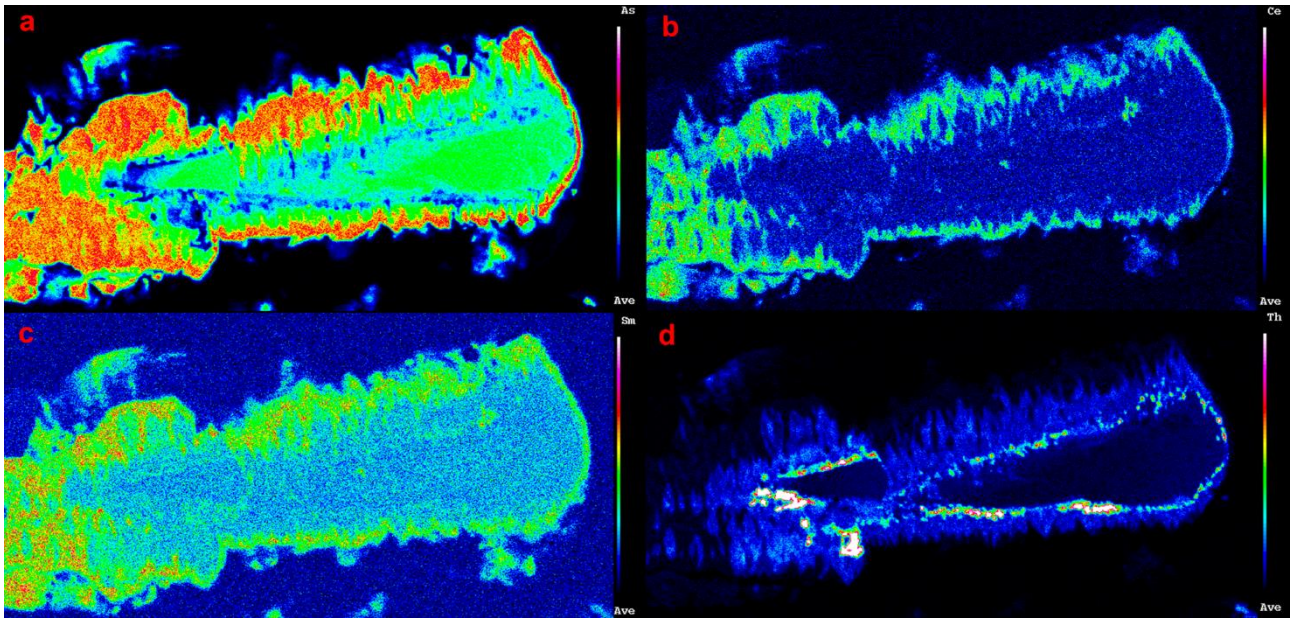

Figure 9.4: Compositional maps for the Ch11 chernovite-(Y) sample, showing the fraction of As **(a)**, Ce **(b)**, Sm **(c)** and Th **(d)**.

As mentioned above, the Ch11 sample (Figure 9.4) shows a clear core-to-rim zonation, which is characterized by a P-enriched core and an As- and LREE-enriched rim. EPMA X-ray compositional maps for the Ch11 sample (Figure 9.1), showing the fraction of As (Figure 9.4a), Ce (Figure 9.4b), Sm (Figure 9.4c) and Th (Figure 9.4d), allow a subdivision into five domains: 1) a *quasi*-homogeneous core ($Ch11_a$; d), characterized by an intermediate composition between chernovite-(Y) and xenotime-(Y), with a slight predominance of the latter (up to 60.86 mol % of xenotime-(Y) component) as reported in Table 8.1; 2) a segment enriched in $ThSiO_4$ (thorite or huttonite) inclusions in form of grains (~1-5 μm in size), clearly visible in Figure 8.3; 3) an interface zone [$Ch11_b$; characterized by an almost equal amount of P and As (xenotime-(Y) molar abundance reaches 52.68 mol %, slightly lower than the inner, darker core], as well as an enrichment in Th; 4) a chernovite-(Y) domain ($Ch11_c$), with high HREE and Th; 5) a relatively Th-poor outer domain ($Ch11_d$), characterized by an enrichment in LREE, as shown by the increase in Ce and Sm fractions towards the rim (Figure 9.4b and Figure 9.4c), coupled with the highest As content (Figure 9.4a). The contact between $Ch11_b$ and $Ch11_c$, as well as between $Ch11_c$ and $Ch11_d$, is marked by a discontinuous flame-like interface. The most As-enriched points of the EPMA-WDS analysis (up to 98.82 mol % of $(REE)AsO_4$ component) refers to the $Ch11_d$ domain and show also the highest LREE and lowest Th concentration within the chernovite-(Y)–xenotime-(Y)–$ThSiO_4$ solid solution: Y is still the most abundant *A* cation (0.487 apfu), but depleted with respect to the inner portions and the other

chernovite-(Y) samples (ca. 0.6-0.8 apfu; Table 8.1), whereas Nd is the second most abundant *A* cation, and significant fractions of Sm, Ce and Pr are also shown, up to 10.80 wt % for Nd_2O_3 (0.167 apfu *vs*. less than 0.01 apfu in the other chernovites), 5.18 wt % for Sm_2O_3 (0.077 apfu *vs.* < 0.015 apfu), 3.87 wt % for Ce_2O_3 (0.061 apfu *vs.* < 0.003 apfu) and 1.23 wt % for Pr_2O_3 (0.019 apfu *vs.* substantially absent in other chernovites). Overall, a comparative analysis of the *A*-site composition of the investigated chernovite-(Y) and xenotime-(Y) crystals does not reveal a preferential partitioning of Y and the other HREE among the investigated zircon-type tetragonal arsenates and phosphates (Figure 9.2a and Table 8.1). However, the chemical heterogeneity and altered texture of some selected investigated samples (*e.g*., Ch11, Ch13, Ch16) suggests a complex interplay with chemically variable hydrothermal fluids, which may have led to local chemical dissolutions of P-enriched chernovites-(Y) and precipitation of $ThSiO_4$ crystals. The identification of these crystals as thorite (isostructural with zircon) or huttonite (isostructural with monazite) is not straightforward. The phase stability relationships between the two $ThSiO_4$ polymorphs have been widely discussed by several authors (Harlov et al. 2007; Mazeina et al. 2005; Seydoux and Montel 1997), reporting that huttonite is stable at higher *T* and *P* with respect to thorite. However, the presence of REE at the *A*-site, according to Speer (1982), may enlarge the stability field of huttonite to lower temperatures. Harlov et al. (2007) found out that the crystallization of metastable huttonite at the expenses of monazite-(Ce) crystals can take place at 400° C (and 500 MPa), in the thorite field, as also reported by Guastoni et al. (2016) for pegmatitic monazites of the Central Alps. In this light, given the difficulty to tell apart thorite and huttonite by means of EPMA analyses (Harlov et al. 2002; Harlov and Föster 2002) and the lack of information on the (*P*,*T*) conditions of the hydrothermal fluids of Mt. Cervandone, it is impossible to unambiguously identify which polymorph of $ThSiO_4$ is associated to the zircon-type and monazite-type REE*T*O_4 minerals of this study.

The sample Ch11 shows the presence of a reaction contact. In this case, a Th-rich layer, *i.e.* $Ch11_b$ (see Figure 9.4), represents the reactional crown around the more chemically homogeneous $Ch11_a$. The few $ThSiO_4$ grain inclusions show a chemical composition closely related to the surrounding: $ThSiO_4$ shows an As-enrichment over P, when in contact with the chernovite-(Y)–xenotime-(Y) solid solution (Ch11) and an evident P-enrichment when included in the Xen14 grains (Table S13.13). The three points of analysis falling into the $ThSiO_4$ field (Figure 9.3) are characterized by a REE-pattern (Figure 9.5) in which, considering only the lanthanoids, the HREE slightly prevail over the LREE. This pattern likely reflects the chemical composition of the hydrothermal fluids, which may have been affected and, in turn, modified in response of several processes.

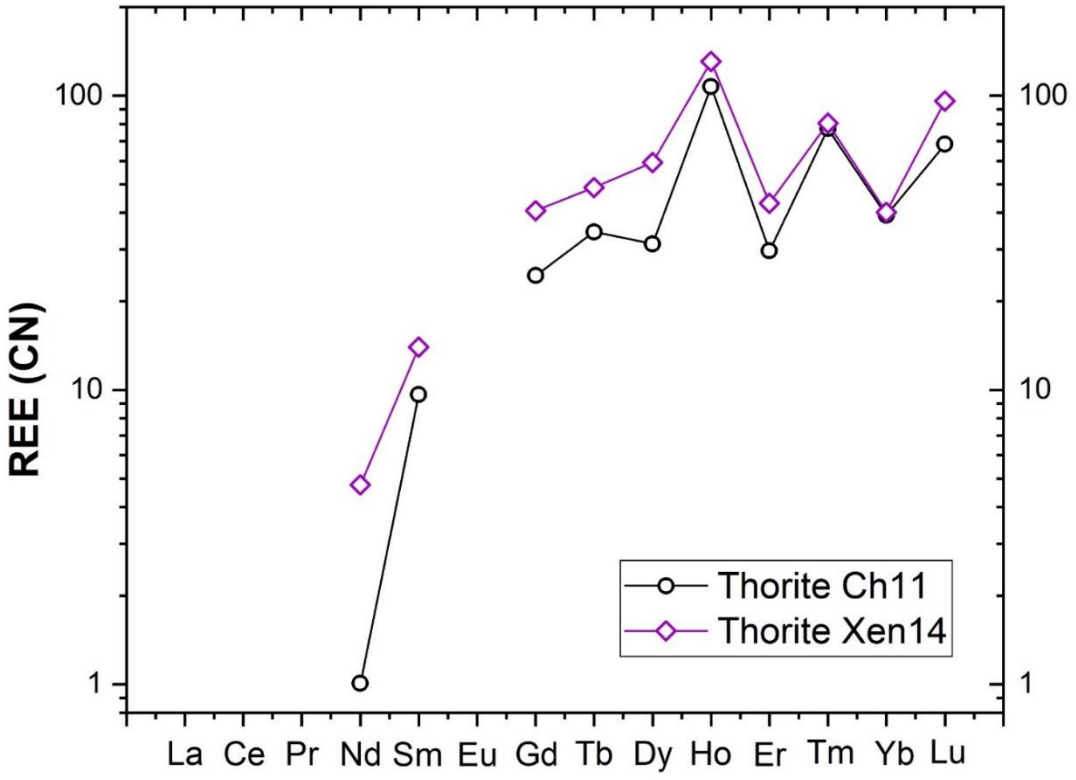

Figure 9.5: Average concentration of REE [normalized to the CN-1 chondrite, after Wasson and Kallemeyn (1988)] in the $ThSiO_4$ grains included into Ch11 and Xen14 samples.

These may include, but are not limited to, the destabilization of REE-enriched minerals as, for example, allanite and gadolinite, as well as a different partitioning of the different REE's as trace elements in nominally REE-free minerals. The paramount role of water in stabilizing the actinides and Ln orthosilicates has been suggested by several authors (*e.g.*, Johan and Johan 2005; Strzelecki et al. 2021) and the hydroxilized nature of the $ThSiO_4$ grain inclusions could explain the poor closure of their EPMA point analyses. Moreover, Mesbah et al. (2016) identified a complete solid solution between the zircon-type $ErPO_4$ and thorite, synthesized under hydrothermal conditions (250°C). However, in the natural samples here investigated a very sharp contact (Figure 8.3 and Figure 9.4) has been observed between the $ThSiO_4$ grains and the surrounding phosphates and arsenates.

9.1.2 Chemical features of the gasparite-(Ce)–monazite-(Ce) series

All the gasparite-(Ce) and monazite-(Ce) samples show a rather similar composition of the ninefold-coordinated *A*-site and the main differences concern in particular the abundance of Y and Ca. A relatively high amount of Y (Y_2O_3 on average, 0.7(2) wt %) is shown by the three monazite-(Ce) samples investigated, especially by the Mon1 sample (Y_2O_3 up to 1.12 wt %), whereas this element

is almost absent in the two gasparite-(Ce) samples (Y_2O_3<0.13 wt %). Unlike monazite-(Ce), gasparite-(Ce) shows a higher content and more uniform distribution of Ca (CaO 1.8(2) wt %, *vs* 1.1(4) wt % for monazite-(Ce)). Also in the gasparite-(Ce)–monazite-(Ce) series, Th has been found as the most variable element and, in addition, gasparite-(Ce) incorporates the highest fraction of Si among the investigated REE minerals (see Table 8.1). In this case, a further charge-compensating mechanism should be involved, to fully explain the anomalous amount of Ca and Si, not compensated by Th+U. The presence of monovalent anions, such as OH^-, F^- or Cl^-, in place of O^{2-}, may compensate the presence of Si and Ca, according to the following equation:

$$2(OH,F,Cl)^- + Ca^{2+} + Si^{4+} = 2O^{2-} + REE^{3+} + (P,As)^{5+} \quad (9.3)$$

According to equation 9.3, if just OH^- is taken into account, the corresponding amount of H_2O necessary to compensate the charge defect is, on average, ~0.45 wt % for both Gasp3 and Gasp4. Instead, for all the samples of monazite-(Ce), the combination of equation 9.1 and equation 9.2 fully satisfy the pattern shown in Figure 9.1b. The P and As contents in the arsenate and phosphate samples, respectively, are always low, as reflected by an average of 1.2(6) mol % of the phosphate component in gasparite-(Ce) and a maximum 6.60 mol % of the arsenate component in monazite-(Ce).

9.2 Chemical composition in relation with literature

The composition of chernovite-(Y) from the Binn Valley, reported by Graeser et al. (1973), shows a P and As content very close to that reported in Table 8.1 for our investigated samples, resulting in a As/(As+P) = 0.76 and 0.84, respectively. A comparison with published chemical analyses of chernovite-(Y) and xenotime-(Y) occurring in different localities (Ondrejka et al. 2007; Förster et al. 2011; Breiter et al. 2009; Li et al. 2019; Alekseev and Marin 2013; Kerbey 2013; Mills et al. 2010; Papoutsa and Pe-Piper 2014) shows that the zircon-type phosphates and arsenates here investigated selectively host HREE, with a very low LREE content. In Figure 9.6, the HREE *vs.* LREE content of several xenotimes-(Y) and chernovites-(Y) from different geological environments is reported, including crystals from hydrothermally-altered A-type granites, rhyolites, pegmatites (Ondrejka et al. 2007; Breiter et al. 2009; Li et al. 2019; Papoutsa and Pe-Piper 2014; Förster et al. 2011) and Mn nodules contained in metasedimentary rocks (Mills et al. 2010).

From Figure 9.6, the majority of the chernovite-(Y)–xenotime-(Y) samples from Mt. Cervandone are mostly enriched in HREE, and only in the outer domains of Ch11 ($Ch11_c$ and $Ch11_d$) the fraction of LREE is high (reaching a maximum of ~0.39 *apfu* in $Ch11_d$), where the LREE-enrichment is also shown by the compositional maps (Figure 9.4c,d; Table 8.1). Therefore, a few points of analysis from this study, and those reported by Ondrejka et al. (2007) and Förster et al. (2011), confirm that, within

the *A*-site of the series chernovite-(Y)–xenotime-(Y), a relatively large fraction of LREE (up to 0.48 *apfu*) may be hosted, despite being a fairly rare occurrence. As reported in Figure 8b, evidences of a complex solid solution between the end-members chernovite-(Y), xenotime-(Y) and $ThSiO_4$, according to equation 9.2, were already reported by several authors (Ondrejka and Uher 2008; Breiter et al. 2009; Förster et al. 2011; Förster 2006; Alekseev and Marin 2013). Chemical data reported by Ondrejka et al. (2007) and Förster et al. (2011), in particular, show a *T*-site range composition very close to that reported in the present study. In addition, the heavily altered crystals of Ch13 and Ch16 share similar features with the hydrated chernovites-(Y) and xenotimes-(Y) crystals described by Förster (2006) and Förster et al. (2011), including a similar Th-content (up to 18.4 wt % of ThO_2), as well as the variable composition, ranging between 9-84 mol % of chernovite-(Y) and 0-70 mol % of xenotime-(Y) component.

The barrel shaped morphology of gasparite-(Ce), pseudomorph after synchysite-(Ce), has been underlined by Graeser and Schwander (1987), and can be observed also for the sample Gasp4 (Figure 8.2b). As an alteration product of synchysite-(Ce), gasparite-(Ce) shows rather different chemical features with respect to the three other investigated species crystallized from the hydrothermal fluids. In particular, a comparison with the isostructural monazite-(Ce) points out a Ca-enrichment and a depletion in Y, likely inherited from the parental REE-carbonate. This study, as the previous one conducted at Mt. Cervandone by Graeser and Schwander (1987), reports rather straight compositions, very close to the ideal ones, resulting in a very limited solid solution along the join gasparite-(Ce)−monazite-(Ce). Since solid solutions among gasparite-(Ce) and monazite-(Ce) have been described by Ondrejka et al. (2007) and Kolitsch and Holtsman (2004a), respectively with As/(As+P) = 0.57-0.64 and 0.89-0.93, the wide miscibility gap observed in this study within the monazite-type series is a local feature of the Mt. Cervandone deposit, possibly related to the formation of gasparite-(Ce) after synchysite-(Ce). Conversely, the gasparite-(La), which occurs in the close Binn Valley (Vereshchagin et al. 2019), the Swiss flank of Mt. Cervandone, is characterized by a more phosphatian composition with As/(As+P+Si+S)=0.80.

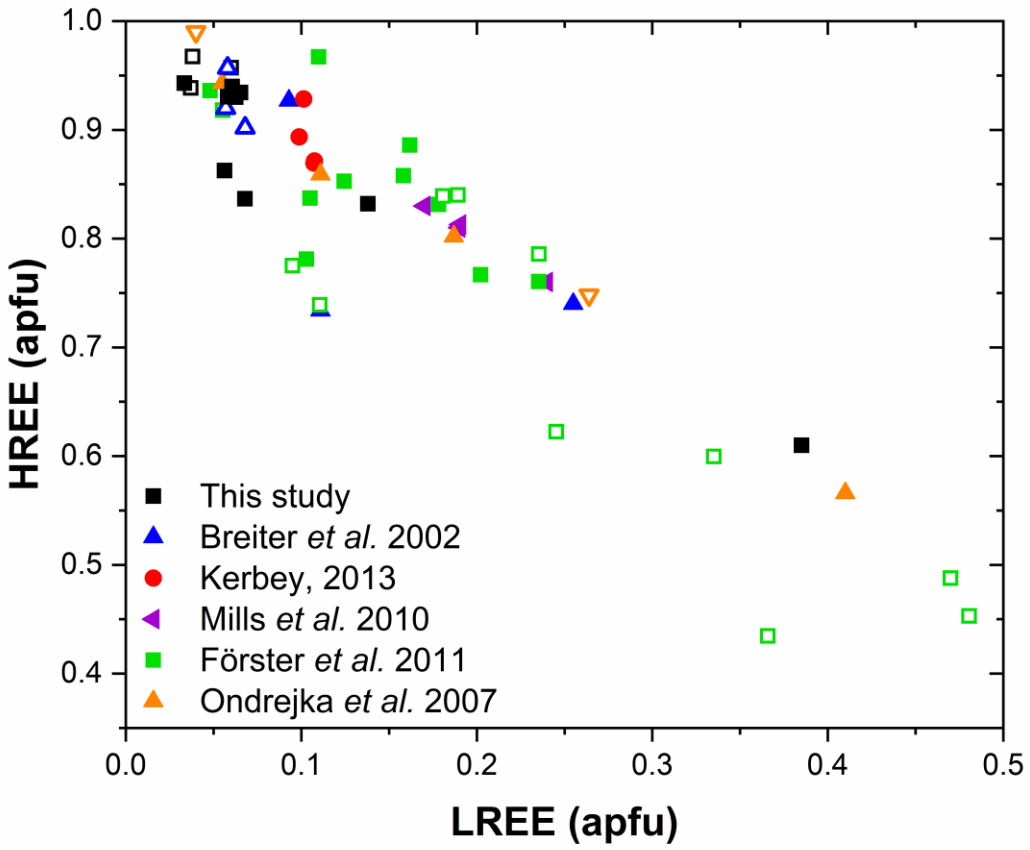

Figure 9.6: LREE vs. HREE diagram for all the chernovite-(Y)–xenotime-(Y) samples of this study, and for chernovites-(Y) (filled symbols), xenotime-(Y) and their solid solutions (void symbols) based on the data from Breiter et al. (2009), Ondrejka et al. (2007), Mills et al. (2010), Förster et al. (2011) and Kerbey (2013).

9.3 Crystal chemistry of minerals and the central role of the *T*-site

As previously discussed, the tetragonal minerals chernovite-(Y), xenotime-(Y) and thorite are isostructural. Considering the chernovite-(Y)–xenotime-(Y) side of the triangular compositional diagram (Figure 9.3a), the unit-cell volume of the investigated minerals gradually decreases from chernovite-(Y) to xenotime-(Y), as shown by Figure 9.7a, which reports the evolution of unit-cell *V* *vs*. the As fraction. Similarly, Figure 9.7b shows the evolution as a function of As of the tetrahedron volume, as calculated using the tools implemented in the software Vesta 3 (Momma and Izumi 2011). Concerning the sample Ch11, the unit-cell and structural data, when compared to those of the other chernovite-(Y) samples (see Table 8.3), suggest that the investigated single-crystal (20×20×15 μm^3) belongs to the P-enriched core portion (Ch11$_a$). This assignment is also corroborated by the BSE map shown Figure 9.4d, which suggests that the core portion is the only able to provide a sufficiently large

single crystal. For these reasons, data pertaining to the sample Ch11 have been plotted in Figure 9.7 assuming the average composition of the core portion reported in Table 8.1. Excluding the most Th-enriched samples, all the investigated chernovites-(Y) and xenotimes-(Y) share an almost identical composition of the REE-bearing *A*-polyhedral site (Table S13.1- Table S13.15), dominated by HREE, which cannot be responsible for the observed variations in the unit-cell and *A*-polyhedron volumes (Figure 9.7a; Table 8.3). Conversely, the cationic population of the *T*-site affects the volumes of the tetrahedra, with larger values almost linearly correlated with an increase in As and a decrease in P (Figure 9.7b). Figure 9.7c and Figure 9.7d show that a strong correlation exists between the tetrahedron volume, on one side, and the unit-cell and *A*-polyhedron volumes, on the other side, suggesting that the unit-cell volume within this series is significantly controlled by the tetrahedrally-coordinated cations. This is not surprising if we consider the bonding topology of the zircon-type structure, in which any (REE)-polyhedron is surrounded by 6 tetrahedra and, in turn, each tetrahedron share two edges with two adjacent (REE)-polyhedra. As a result, the volumes of the two building units (*i.e.*, polyhedron and tetrahedron) are mutually interconnected. Thus, when the *T*-site is mostly occupied by the smaller phosphorous, the (REE)-bearing polyhedron adapts with a smaller volume which, in turn, affects also the unit-cell volume; conversely, the opposite trend is observed with an enrichment in arsenic.

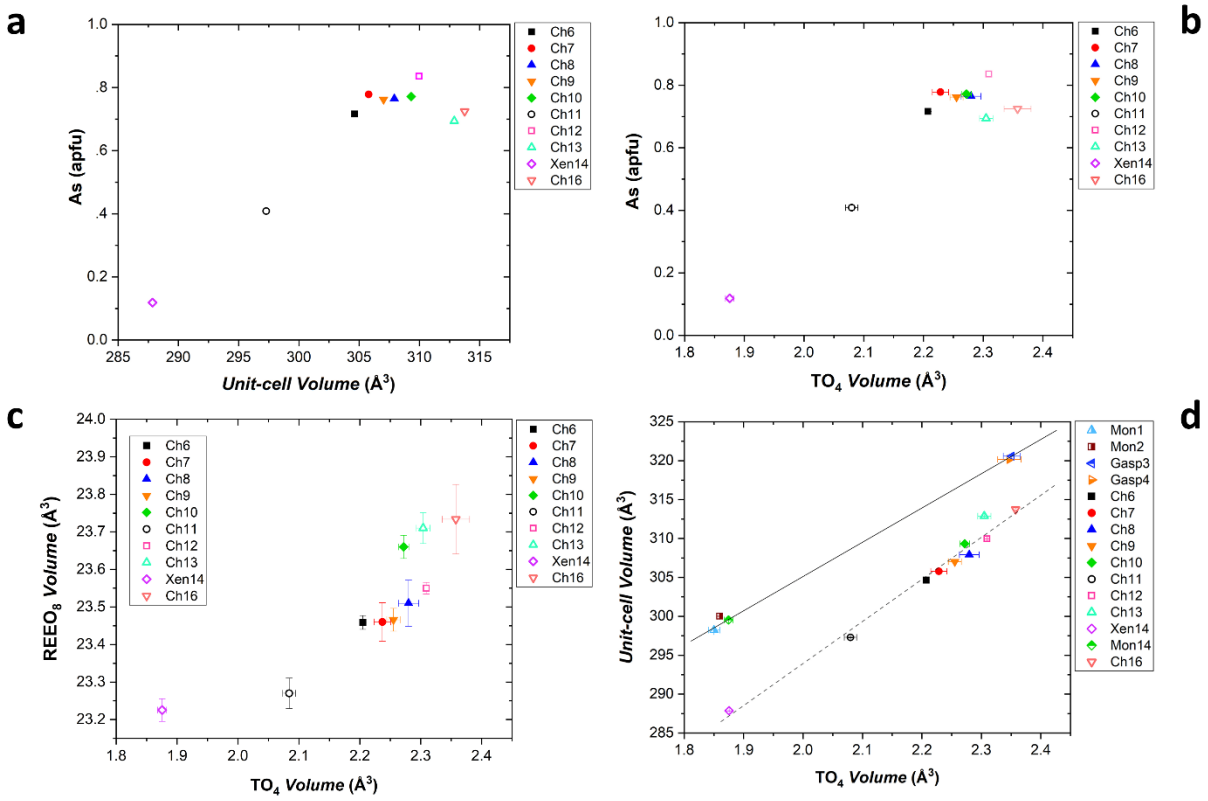

Figure 9.7: Unit-cell volume *vs.* As fraction (in apfu) **(a)**, volume of the *T*O$_4$ tetrahedron *vs.* As fraction (in apfu) **(b)** and volume of the *T*O$_4$ tetrahedron vs. volume of the (REE)-bearing *A*-polyhedron **(c)** for the samples pertaining to the chernovite-(Y)–xenotime-(Y) series. Volume of the *T*O$_4$ tetrahedron *vs.* unit-cell volume **(d)** for all the samples investigated.

A clear deviation from the previously described trends is represented by the Ch13 and Ch16 samples, which show appreciably larger unit-cell volumes, respectively of 312.89(3) Å^3 and 313.75(9) Å^3 (Figure 9.7a). This misalignment is likely related to the enrichment in Th and Ca at the *A*-site, being these elements characterized by larger ionic radii with respect to the HREE (Shannon 1976), which induce an expansion of the *A*-polyhedron and, in turn, of the unit-cell volume. A similar behavior to that described above for the (tetragonal) chernovite-(Y)-xenotime-(Y) series is also shown by the (monoclinic) gasparite-(Ce) and monazite-(Ce). However, in this case, the distribution of the chemical compositions in two clusters close to the ideal endmembers prevents a robust extrapolation along the whole series (Figure 9.7d).

A correlation among the volumes of (P,As)-tetrahedra and the *A*-site polyhedra is also shown by the synthetic RE*T*O$_4$ compounds, which structural models are reported in the International Crystal Structure Database. A comparative analysis of the structural parameters of synthetic REE-bearing phosphates [YPO$_4$, LaPO$_4$, CePO$_4$, NdPO$_4$, TbPO$_4$, HoPO$_4$, DyPO$_4$, YbPO$_4$ and LuPO$_4$ (Ni et al. 1995)) and their As-dominant endmembers (YAsO$_4$ (Ledderboge et al. 2018), LaAsO$_4$ (Kang and

Schleid 2005), $CeAsO_4$ (Brahim et al. 2002), $NdAsO_4$ (Schmidt et al. 2005), $TbAsO_4$ (Long and Stager 1977), $HoAsO_4$ (Schmidt et al. 2005), $DyAsO_4$ (Long and Stager 1977), $YbAsO_4$ (Kang et al. 2005) and $LuAsO_4$ (Lohmüller et al. 1973)] has been carried out. Given the same elemental composition of the REE-bearing *A*-site, the volume of its coordination polyhedron is different in phosphates and arsenates, being always lower in phosphates, pointing out the dominant role played by the TO_4 structural units (V_{TO4}~2.4 Å^3 for AsO_4 and ~1.8 Å^3 for PO_4) in controlling most of the structural features of the REETO_4 compounds. Selected structural parameters of synthetic REETO_4 compounds are reported in Table S13.16.

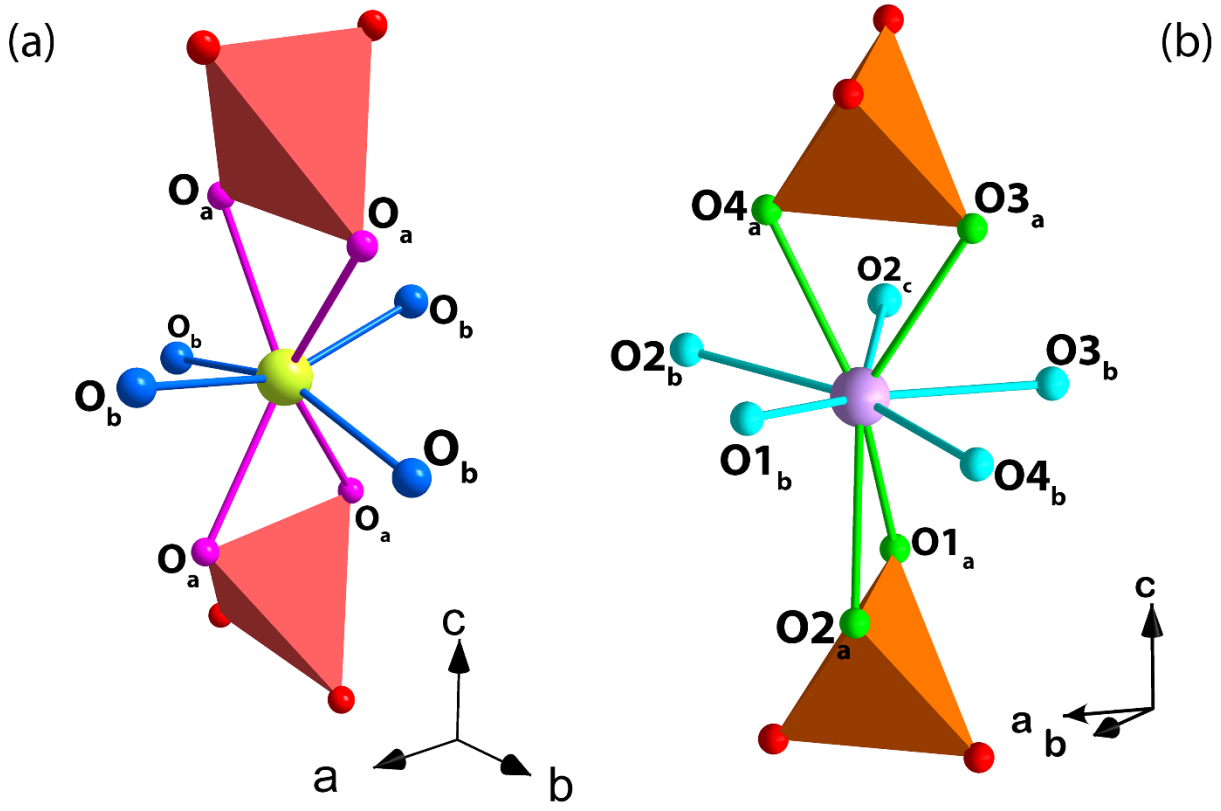

Figure 9.8: crystal structure of zircon **(a)** and monazite (b) showing the configuration of the *A*-site coordination sphere in the two structural topologies and the bond distances names reported in *Table 8.3*. In **(b)** the sky blue REE-O bonds are the ones of the equatorial pentagon.

In addition, based on all the structure refinements, the *A*-polyhedron distortion index (Baur 1974) has been calculated using the tools implemented in Vesta 3 (Momma and Izumi 2011). The *A*-polyhedron distortion index (*DI*), following Baur (1974), is based on the measured *A*-O distances (Figure 9.8), *i.e.* *DI*(*A*-O), and is expressed as: $DI(A-O) = \frac{1}{8}(\sum_{l=1}^{8}|AO_l - AO_{av}|)/AO_{av}$ (9.4) for the tetragonal series and $DI(A-O) = \frac{1}{9}(\sum_{l=1}^{9}|AO_l - AO_{av}|)/AO_{av}$ (9.5) for the monoclinic series, reported in

Table 8.3 (where AO_{av} is the average *A*-O interatomic distance). The analysis of the calculated distortion index values (Table 8.3) shows that the increase in As (and decrease in P) leads to an increase in the distortion of the (REE)-site coordination polyhedra in both the tetragonal and monoclinic series.

9.4 Raman spectroscopy

9.4.1 Raman spectroscopy of zircon-type minerals

According to Nipko et al. (1997), Miller et al. (1968), Mooney and Toma (1967) and Barros et al. (2010), the zircon-type structure allows 12 independent Raman active vibration modes. The vibration modes of the zircon-type topology can be defined as following:

$$\Gamma = 2A_{1g} + B_{2g} + 5E_g \qquad (9.6)$$

Five of these vibration modes, those pertaining to the internal motion of the TO_4 are defined as internal vibrations: $\Gamma_{int} = 2A_{1g} + B_{2g} + 2B_{1g} + 2E_g$. The vibrations associated to the motion of the tetrahedron within the unit-cell are the so-called external vibrations: $\Gamma_{int} = 2B_{1g} + 3E_g$.

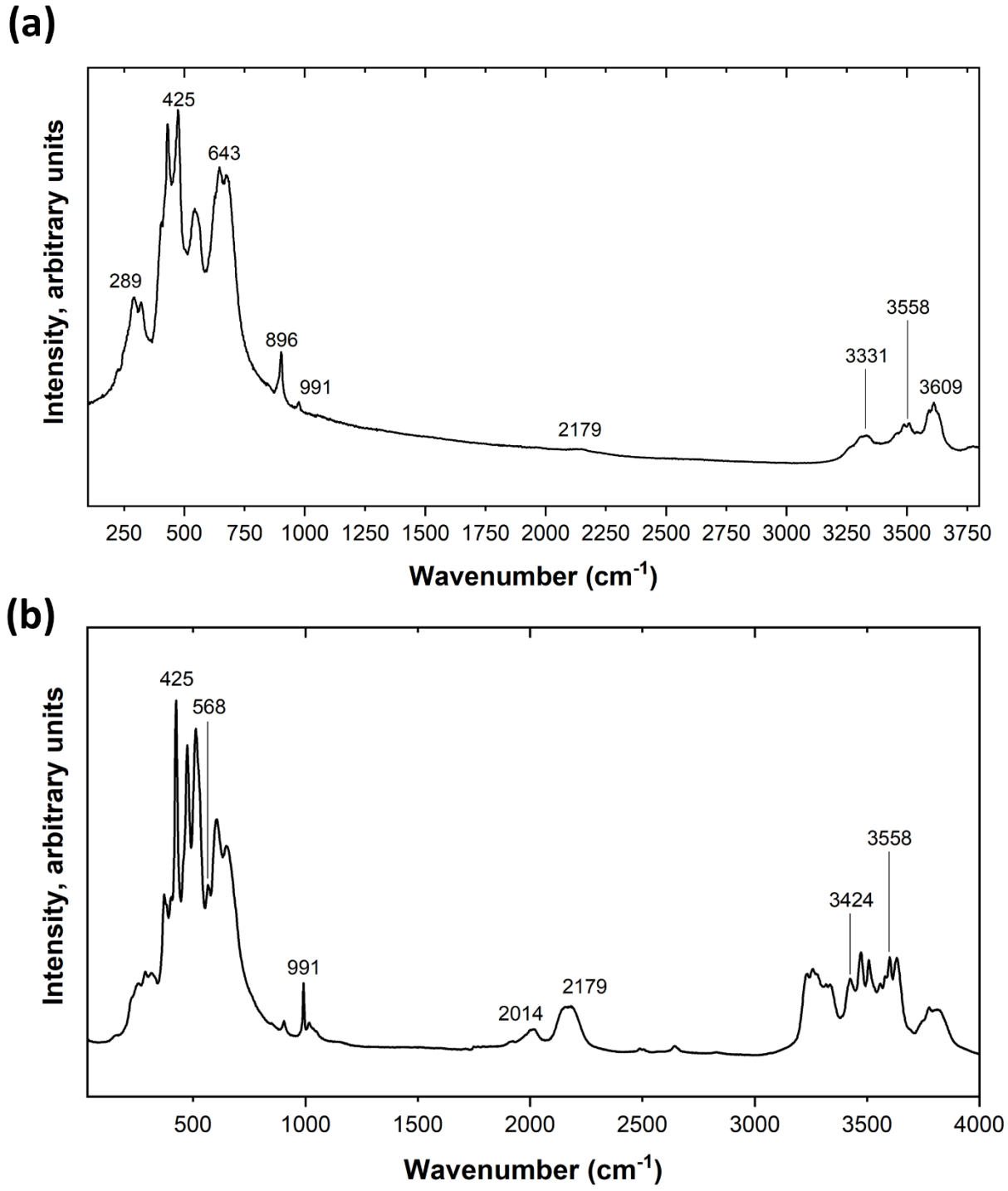

Figure 9.9: full Raman spectra of **(a)** chernovite-(Y) and **(b)** xenotime-(Y). See Table 9.1, Table 9.2 and Table 9.3 for a complete list of the peaks and their assignments.

Table 9.1: Raman spectral signatures of chernovite-(Y) and other zircon-type arsenates.

Raman shift (cm^{-1})						
Chernovite-(Y)[a§]	Chernovite-(Y)[b§]	$YAsO_4$[c]	$YAsO_4$[c§]	$YAsO_4$:Sm doped (100:1)[d]	$YAsO_4$[d]	Assignment
975 vw	–	–	–	–	–	A_{1g} ν_1 (PO_4)
896 s	888.8	888	882	882	882	A_{1g} ν_1 (AsO_4)
–	881.5	880	878	872	878	B_{1g} ν_3 (AsO_4)
842 vw	835.1	835	830	830	830	E_g ν_3 (AsO_4)
674 m	–	–	–	–	–	H_2O Libration
643 m	–	–	–	–	–	B_{1g} ν_4 (PO_4)
540 s	–	–	–	–	–	–
472 s	483.4	–	481	500	481	B_{1g} ν_4 (AsO_4)
430 s	–	–	–	431	–	E_g ν_4 (AsO_4)
–	–	–	393	394	393	A_{1g} ν_2 (AsO_4)
320 m	–	–	–	–	–	–
289 m	–	–	–	270	–	E_g
–	–	–	255	242	255	E_g
225 sh	233.4	234	234	235	234	B_{1g}
–	–	–	–	207	–	–
–	170.7	177	175	174	175	E_g
–	–	–	–	150	–	E_g
–	130.4	–	130	110	130	B_{1g}

[a]: This study; [b]: Errandonea et al. (2011); [c]: Pradhan et al. (1987); [d]: Pradhan and Choudhary (1989); [§]: single crystal data.

Table 9.2: Raman spectral signatures of several zircon-type arsenates, after Barros et al. (2010).

Raman shift (cm^{-1})									
$SmAsO_4$	$EuAsO_4$	$GdAsO_4$	$TbAsO_4$	$DyAsO_4$	$HoAsO_4$	$TmAsO_4$	$YbAsO_4$	$LuAsO_4$	Assignment
879	882	887	888	893	895	900	903	905	A_{1g} ν_1 (AsO_4)
863	859	875	877	882	887	893	897	905	B_{1g} ν_3 (AsO_4)
821	825	831	832	836	839	844	847	850	E_g ν_3 (AsO_4)
489	494	498	500	504	507	513	516	520	B_{1g} ν_4 (AsO_4)
429	456	435	435	438	437	–	443	442	E_g ν_4 (AsO_4)
401	404	408	407	408	407	408	410	410	A_{1g} ν_2 (AsO_4)
237	238	239	237	236	236	235	234	234	B_{1g}
250	238	242	244	246	247	249	247	249	E_g
159	161	160	158	159	159	159	158	158	E_g
131	132	133	131	133	131	129	128	128	B_{1g}

[e]: Barros et al. (2010).

Table 9.3: Raman spectral signatures of xenotime-(Y) and other zircon-type phosphates.

Raman shift (cm^{-1})							
Xenotime-(Y)[a§]	$GdPO_4$[b]	YPO_4[c]	YPO_4[d§]	YPO_4[e]	YPO_4[f]	$HoPO_4$[g]	Assignment
	1057	1056	1058	1057	1058	1057	B_{1g} ν_3 (PO_4)
1050 vw	1046	1023	1026	1025	1027	1021	E_g ν_3 (PO_4)
1017 vw	1013	–	–	–	–	–	
991 s	991	999	1001	999	1001	1000	A_{1g} ν_1 (PO_4)
	984	–	–	–	–	–	
904 w	–	–	–	–	–	–	A_{1g} ν_1 (AsO_4)
648 m	646	657	659	656	660	655	B_{1g} ν_4 (PO_4)
604 s	–	–	–	–	–	–	–
–	586	578	581	579	581	578	E_g ν_4 (PO_4)
568 w	–	–	–	–	–	–	–
513 s	–	–	–	–	–	–	–
472	481	480	485	482	484	485	A_{1g} ν_2 (PO_4)
425 s	–	–	–	–	–	–	E_g ν_4 (AsO_4)
401 w	–	–	–	–	–	–	A_{1g} ν_2 (AsO_4)
383 sh	–	–	–	–	–	–	
372 m	364	–	–	–	–	–	B_{1g}
–	346	–	–	–	–	–	
–	332	329	331	330	332	–	B_{2g}
287 vw	–	296	299	298	299	296	E_g
–	–	–	–	–	–	–	B_{1g}
155 vw	–	154	155	157	157	139	E_g

[a]: This study; [b]: Clavier et al. (2018); [c]: Yahaiaoui et al. (2017); [d]: Giarola et al. (2017); [e]: Zhang et al. (2009); [f]: Begun et al. (1981); [g]: Tossell (1975); [§]: single crystal data.

Figure 9.9 and Figure 8.4 show the obtained Raman spectra of the two zircon-type minerals. The peaks attribution for chernovite-(Y) and xenotime-(Y) are reported in Table 9.1, Table 9.2 and Table 9.3 respectively, along with a comparison of literature data. Both the Raman spectra of the two zircon-type minerals show a rather high background, due to the combined photoluminescence (PL effect) of Ho, Sm and Er atoms, excited by the 532 nm laser, as described by Lenz et al. (2015). The emission bands of Er and, secondly, Ho, are compatible with the vibration bands observed at 540 cm^{-1} and 566 cm^{-1} in chernovite-(Y) and xenotime-(Y) respectively, as defined by Lenz et al. (2015) and Assefa et al. (2004). The obtained results agree with the EPMA-WDS analysis discussed in section 9.1. Among the two minerals, xenotime-(Y) shows a rather sharp signal of the REE elements: the PL wavelengths of Sm have been identified (at 2014 cm^{-1} and 2179 cm^{-1}). Moreover, the PL Ho and Sm signals occur in the range 3000-4000 cm^{-1}. Also in this case, the xenotime-(Y) Raman spectrum shows more clearly the REE signals. The 3508 cm^{-1} peak has been identified in both chernovite-(Y) and xenotime-(Y), in agreement with the PL band of Sm (Muthulakshmi et al. 2020) Therefore, the hydroxyl region shows a rather significant interference of the REE species belonging to the REETO_4 minerals and swap of the REE PL signals for the OH^- vibration bands is possible, as stated by McCubbin et al. (2010) and Lenz et al. (2015). On the other hand, several peaks of the 3200-4000 cm^{-1} region of xenotime-(Y) (*i.e.*, 3424 cm^{-1}, 3558 cm^{-1}) match the OH^- vibration bands determined in natural zircons by Nasdala et al. (2001). Conversely, chernovite-(Y) does not show any prominent peak compatible with the OH^- vibration modes. It is not therefore impossible to state whether there is OH^- in place of oxygen within the structure of chernovite-(Y) or not.

Few studies have been devoted to the vibration spectra of zircon-type $REEAsO_4$ (Pradhan et al. 1987; Pradhan and Choudhary 1989; Barros et al. 2010; Errandonea et al. 2011). Among the previous studies on the Raman spectra of REE arsenates, only Errandonea et al. (2011) studied natural samples of chernovite-(Y). Errandonea et al. (2011) did not highlight any significant difference among the spectra collected on synthetic samples by previous authors, neither considering powder or single crystal samples. On the other side, the present research, as reported in Table 9.2, highlights some differences with respect to the literature data. The main difference is the occurrence of some additional Raman vibration bands, attributed to the vibration modes of the PO_4 unit, based on the Raman spectra collected on $REEPO_4$ (*e.g.*, Clavier et al. 2018; Yahaiaoui et al. 2017).

Figure 8.4 shows the Raman spectrum of xenotime-(Y). The Raman literature results of $REEPO_4$ are gathered in Table 9.3 and, in general, the Raman spectroscopic data obtained on $REEPO_4$ are mutually consistent. The major difference among the present study and the literature data of xenotime-(Y)

concerns the occurrence of some expected Raman peaks attributed to the vibration bands of AsO_4 (see the chemical composition of xenotime-(Y) in section 9.1.1 for further details).

9.4.2 Micro-Raman spectroscopy of monazite-type minerals

Figure 8.5 shows the experimental micro-Raman spectra of gasparite-(Ce) and monazite-(Ce) respectively. The Raman bands of the investigated gasparite-(Ce) and monazite-(Ce) are reported in Table 9.4 and Table 9.5, along with a comparison with the Raman spectra of other monazite-type compounds reported in literature. In case of gasparite-(Ce), the spectroscopic lines in the range 800-900 cm^{-1} are attributed to the stretching vibrations ν_1 and ν_3 of the AsO_4 tetrahedron, while in the range 350-500 cm^{-1} lie the bending vibrational bands ν_2 and ν_4 of the AsO_4 tetrahedron. Bands located at 746 cm^{-1} and 996 cm^{-1}, respectively, are consistent with the vibrational bands of the SiO_4 units, compatible with the relatively high silica content observed in natural gasparite-(Ce) from Mt. Cervandone. Spectral lines below 340 cm^{-1} are attributed to lattice vibrations and exhibit a good correspondence with data reported by Vereshchagin et al. (2019). In case of monazite-(Ce), the obtained Raman spectra is rather consistent with those determined by previous authors on $CePO_4$ compounds (Table 9.5). In addition, the vibration band occurring at 895 cm^{-1} is compatible with the $\nu_1(SiO_4)$ vibration mode of huttonite (*i.e.*, monazite-structured $ThSiO_4$) after Jin and Soderholm (2015).

In the so-called hydroxyl region, between 3200 cm^{-1} and 4000 cm^{-1}, the occurrence of some slight peaks has been observed for both the monazite-type minerals (Figure 8.5). Conversely to the zircon-structured REE*T*O_4 minerals chernovite-(Y) and xenotime-(Y), the background baseline of both monazite-(Ce) and gasparite-(Ce) Raman spectra suggests that no noticeable PL emission phenomena occur. In this light, the presence of slightly intense peaks in the range 3200-4000 cm^{-1} has been attributed to the OH^- groups for both the monazite-type minerals. The partial replacement of oxygen atoms by hydroxyl groups may explain some features of the chemical data of gasparite-(Ce), characterized by a slight charge defect, for to the combined presence of Ca^{2+} within the *A*-site (in place of REE^{3+}) and Si^{4+} within the tetrahedral *T*-site (in place of As^{5+}), apparently not counterbalanced. This might be explained by equation 9.3, which is further supported by the present Raman spectrum of gasparite-(Ce).

Table 9.4: Raman spectral signatures of gasparite-(Ce) and other monazite-type arsenates.

Raman shift (cm^{-1})							
Gasparite-(Ce)[a]	Gasparite-(La) Ushkatyn-III[b]	Gasparite-(La) Wanni glacier[b]	$LaAsO_4$[c]	$CeAsO_4$[c]	$PrAsO_4$[c]	$NdAsO_4$[c]	Assignment
996 vw	–	–	–	–	–	–	ν_3 (SiO_4)
–	–	–	872 sh	874 w	876 vw	875 sh	ν_3 (AsO_4)
844 vst	843 sh	848 sh	845 st	846 st	848 st	852 st	
–	–	–	–	–	–	830 w	
–	822 m	826 sh	827 m	827 m	828 m	817 w	
–		812 sh	798 vw	810 vw	800 vw	800 vw	
858 sh	860 vs	864 vs	861 vst	863 st	865 vst	868 vst	ν_1 (AsO_4)
746 vw	–	–	–	–	–	–	ν_1 (SiO_4)
–	–	951 w	–	–	–	–	ν_1 (PO_4)
466 w	–	462 w	461 w	466 vst	–	–	ν_4 (AsO_4)
447 vw	452 w		440 sh	–	451 vst	446 vw	
414 w	422 w	421 m	418 st	421 w	–	422 w	
–	364 vw	367 w	367 w	368 vw	–	367 w	
–			350 vw	340 w	–	–	
389 st	379 st	395 st	392 m	395 m	391 w	398 w	ν_2 (AsO_4)
334 m	334 vw	337 w	336 w	330 sh	320 w	339 vw	Lattice vibrations
–	320 w	–	322 w		320 w	305 vw	
–	264 vw	267 vw	–	–	–	–	
230 w	–	–	–	–	–	–	
203 w	203 m	203 vw	–	–	–	–	
–	190 vw	190 vw	–	–	–	–	

151 vw	153 vw	155 w	–	–	–	–
–	138 vw	139 vw	–	–	–	–
123 w	126 vw	125 w	–	–	–	–
102 w	104 vw	107 w	–	–	–	–
92 vw	92 vw	94 vw	–	–	–	–
70 m	–	–	–	–	–	–

Table 9.5: Raman spectral signatures of monazite-(Ce) and other monazite-type phosphates.

Raman shift (cm^{-1})				
Monazite-(Ce)[a]	$CePO_4$[a]	$CePO_4$[a]	$GdPO_4$[c]	Assignment
			1092	–
1071 sh	1072	1072	1071	ν_3 (PO_4)
1056 vs	1057	1055	1042	ν_3 (PO_4)
	1027	1025		ν_1 (PO_4)
1010 vw				
	994		1004	ν_1 (PO_4)
970 vs	972	969	987	ν_1 (PO_4)
895 vw				ν_1 (SiO_4)
619 m	621	618	632	ν_4 (PO_4)
		588	598	ν_4 (PO_4)
571 m	573	569	577	ν_4 (PO_4)
534 vw		535	539	ν_4 (PO_4)
468 m	469	466	476	ν_2 (PO_4)
			428	
415 s	416	413	–	Lattice vibrations
399 sh	398	396	404	

278 w	274	272	
262			
220 vw	221	220	
172 m	173	172	
156 w	155	152	
	131	127	ν_2 (AsO_4)
120 w	122		Lattice vibrations
	102		
	89		

Bouddouch et al. (2021); Lalla et al. (2021); Clavier et al. (2013).

9.5 Behavior of chernovite-(Y) at non-ambient conditions

9.5.1 High-pressure behavior of chernovite-(Y)

Elastic properties of chernovite-(Y) under compression

Figure 9.10 and Table 8.4 show the compressional behavior of the unit-cell of chernovite-(Y) in the two conducted isothermal ramps (*i.e.*, Ch10-P_A and Ch10-P_B), from which it emerges that the structure of chernovite-(Y) is not stable at pressure exceeding ~10 GPa. In detail, from both the isothermal ramps, chernovite-(Y) undergoes a phase transition in the ranges 10.70-11.28 GPa and 10.19-10.54 GPa, respectively. This phase transition is a single crystal to polycrystals transformation, as Figure 9.11 shows. The X-ray diffraction peaks of chernovite-(Y) are replaced by the discontinuous X-ray diffraction rings of chernovite's H*P* polymorph. The latters are compatible with the unit-cell of the scheelite-type polymorph defined by Errandonea et al. (2011) for $YAsO_4$.

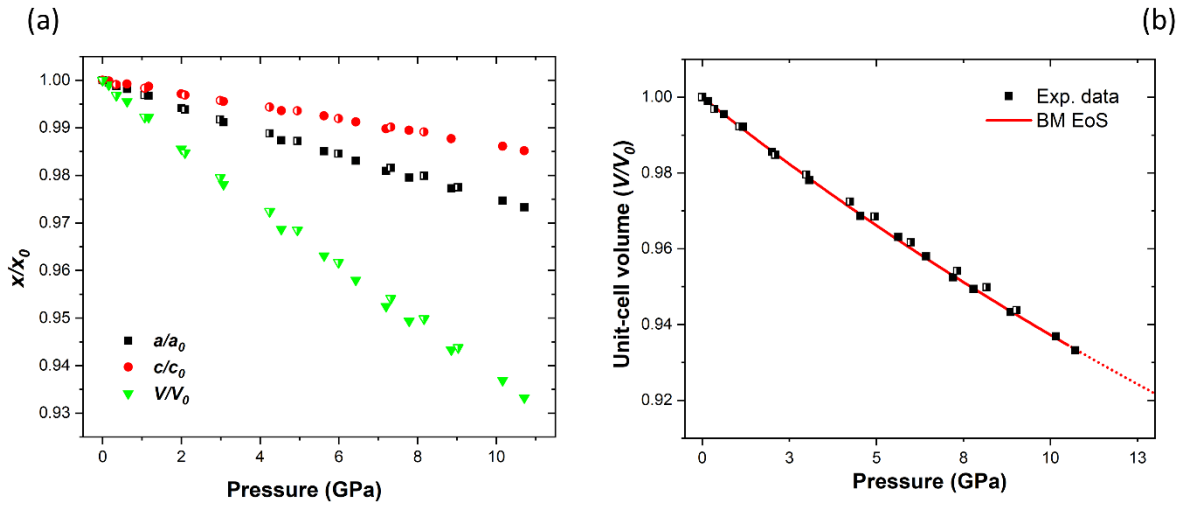

Figure 9.10: High-pressure evolution of **(a)** unit-cell parameters normalized to ambient-conditions values and **(b)** the experimental unit-cell volume normalized to ambient conditions of chernovite-(Y). The red line represents the fitted BM3-EoS, while the dotted red line line is an extension of the BM3-EoS at pressures exceeding the stability field of chernovite-(Y). Filled dots pertain to Ch10-P_B data, while half-filled dots refer to the Ch10-P_A data.

Errandonea et al. (2011) reported that this phase transition starts at 8 GPa and it is complete at pressure exceeding 12 GPa. The observed pressure-range is probably due to kinetic of the phase transition itself and it reasonably starts to happen at a pressure of 8 GPa in case of powdered samples. The zircon-to-scheelite phase transition occurs at different pressures in different compounds (Errandonea et al. 2011). In general, in X-ray powder diffraction experiments, rather than a specific pressure value,

a pressure range for the zircon-to-scheelite phase transition is defined. This pressure range defines the region between the first occurrence of the X-ray diffraction peaks belonging to the scheelite-type polymorph and the disappearance of those belonging to the zircon-type phase. For the purposes of the present work, the pressure corresponding to the occurrence of the first scheelite-polymorph X-ray diffraction peaks has been used and it is hereafter labeled as $P_{Z\text{-}S}$ (pressure of zircon-to-scheelite phase transition). Unfortunately, among the REE-bearing arsenates, only $YAsO_4$ has been investigated and there are no other data on zircon-type REE-bearing arsenates. Errandonea et al. (2011) defined the relations among $P_{Z\text{-}S}$ and the *T*-site cation ionic radius, by comparing the compressional behavior of $YAsO_4$, $YCrO_4$, $YMoO_4$ and YVO_4: the phase transition is pushed at higher pressure as the ionic radius of the *T*-cation is reduced (only $YCrO_4$ does not adhere to this trend, due to magnetic interference that can reduce the $P_{Z\text{-}S}$, as proposed by Long et al. (2006)). On the other hand, relations among the *A*-site cation and the $P_{Z\text{-}S}$ have only been defined in comparative studies by Errandonea et al. (2009) and Zhang et al. (2008). Errandonea et al. (2009) defined the $P_{Z\text{-}S}$ for $EuVO_4$ ($P_{Z\text{-}S}$=7.8 GPa) and $LuVO_4$ ($P_{Z\text{-}S}$=8.9 GPa), while Zhang et al. (2008) studied the $P_{Z\text{-}S}$ in $YbPO_4$ ($P_{Z\text{-}S}$=19.4 GPa) and $LuPO_4$ ($P_{Z\text{-}S}$=22.4 GPa). In both the cases, the $P_{Z\text{-}S}$ is higher in Lu*T*O_4 compounds. Therefore, it is reasonable to state that the $P_{Z\text{-}S}$ is pushed to higher pressures when the ionic radii of both the *A*-site and *T*-site are reduced.

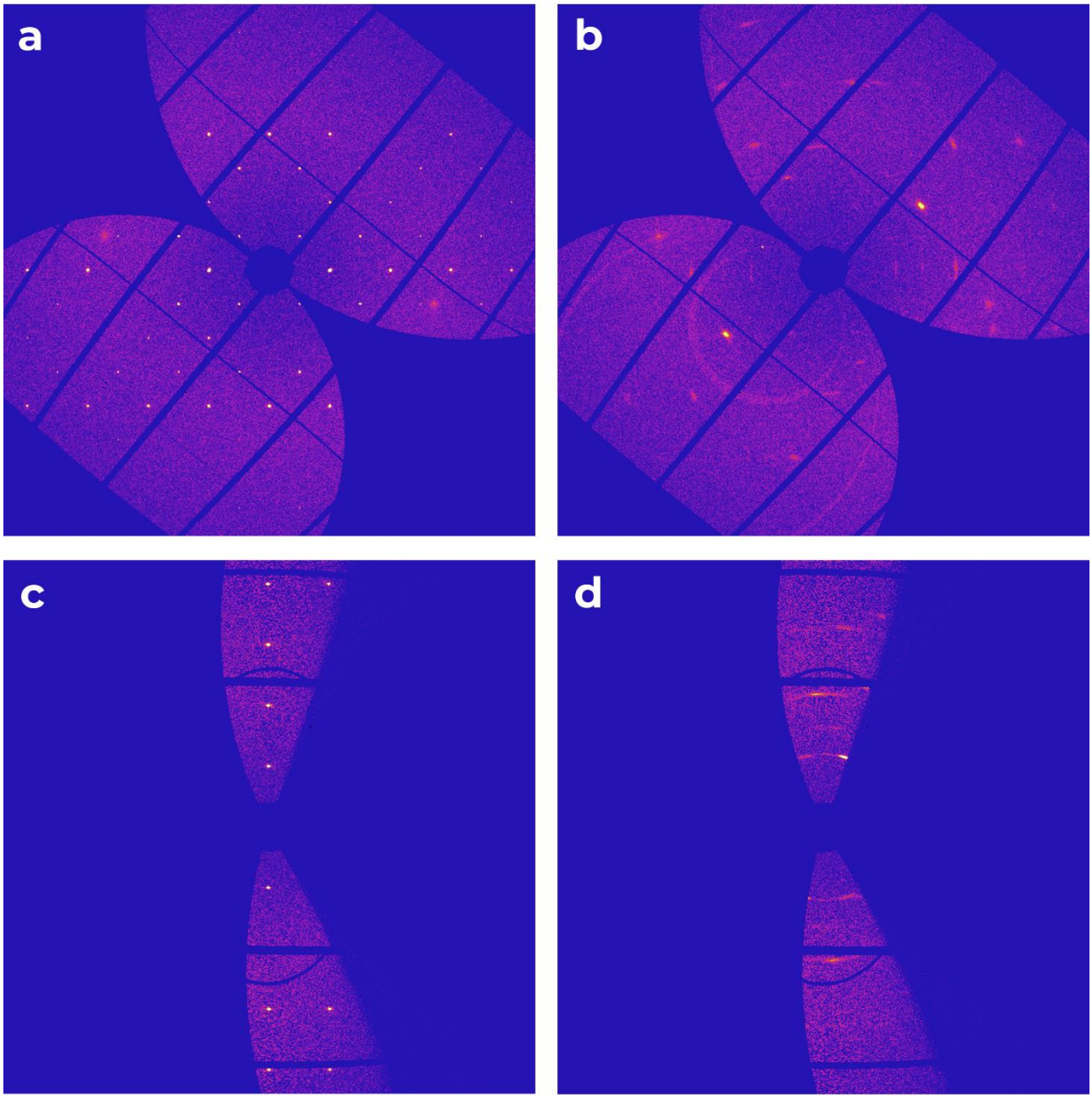

Figure 9.11: reconstructed sections of the reciprocal lattice of chernovite-(Y), showing the effect of the zircon-to-scheelite phase transition in the XRD data of the Ch10-P_A experiment; **(a)** (0*kl*)* lattice section at 6.43 GPa; **(b)** (0*kl*)* lattice section at 11.28 GPa; **(c)** (*hk*0)* lattice section at 6.43 GPa; **(d)** (*hk*0)* lattice section at at 11.28 GPa.

The powder investigated by Errandonea et al. (2011) is a natural sample of chernovite-(Y) from the Sierra County, New Mexico, USA. Although its natural origin, Erranodonea et al. (2011) do not provide a complete chemical analysis (only 0.6 wt % of P and 0.8 wt % of La are reported): the chemical composition can be summarized as $Y_{0.980}La_{0.013}(As_{0.982}P_{0.044}O_4)$, which is really close to the

ideal formula. On the basis of the chemical composition of the *A*-site, the weighted (*i.e.*, taking into account the different elemental composition and the ratio among the different elementals species) ionic and crystal radius of the *A*-site were calculated after Shannon et al. (1970). The resulting calculated ionic radii of the *A*-site are only slightly larger compared to the endmember $YAsO_4$: 1.161 Å in place of 1.159 Å (Y^{VIII} crystal radius) and 1.021 Å in place of 1.019 Å (Y^{VIII} ionic radius), according to Shannon et al. (1970). On the other hand, the chernovite-(Y) Ch10 samples studied in the present research is characterized by slightly larger weighted ionic radii (Shannon et al. 1970), corresponding to 1.164 Å (Y^{VIII} crystal radius) and 1.023 Å (Y^{VIII} ionic radius). The amount of P in our sample is ~4 times larger in Ch10 with respect to the powder investigated by Errandonea et al. (2011): such a difference might lead to a slight increase in the $P_{Z\text{-}S}$ as apparently observed in the data of this study.

The compression of chernovite-(Y) is characterized by an anisotropic behavior, with the [001] direction being the least compressible and [100] the most compressible directions, as reported in Figure 9.10. The same behavior has been defined by Errandonea et al. (2011). Errandonea et al. (2005; 2011) and Li et al. (2009) refined the bulk compressibility based on both experimental and theoretical methods (see Table S13.17). The bulk moduli refined in the present study are consistent with those reported in the literature. As reported in Table 8.9, the BM2-EoS's (K'=4), refined from both the independent ramps, yield the following refined bulk moduli: K_{P_0,T_0}=142(2) GPa (Ch10-P_A) and K_{P_0,T_0}=135.5(5) Gpa (Ch10-P_B). In addition, a Birch-Murnaghan EoS fit based on normalized unit-cell volumes from both the ramps (*i.e.*, merging together the two ramps data) has been performed. The corresponding bulk modulus, refined with the BM3-EoS is K_{P_0,T_0}=136(2) Gpa, with K'=3.9(4) (see Table 8.9). Therefore, the slightly larger weighted ionic radius of the *A*-site in the chernovites-(Y) here studied apparently does not affect the bulk modulus of $YasO_4$ and neither does the ~0.16 apfu of P in the *T*-site. In addition, the linear compressibility along the two axes has been determined for both the ramps. The two linear bulk moduli refined with a BM2-EoS (K'=4) for the [100] and [001] directions respectively are: K_{a,T_0}=117(1) GPa, a_0=7.0302(8) Å and K_{c,T_0}=232(5) GPa, c_0=6.2601(10) Å for the Ch10-P_A; K_{a,T_0}=112.3(6) GPa, a_0=7.0379(5) Å and K_{c,T_0}=220(3) GPa, c_0=6.2682(6) Å for the Ch10-P_B.

Structure deformation mechanisms at atomic scale in chernovite-(Y) under compression

It has been observed that, among the two ramps, structure refinements from the Ch10-P_B data provide the best figure of merit in terms of *P*-coverage and clarity of compressional trends. The following discussion is thus focused on the structure refinements from this ramp. With respect to monazite-type

compounds, the zircon-type topology is even more straightforward and only three independent atomic coordinates can be refined (see section 3.1 for further information). The significant smaller linear compressibility (higher linear modulus) along [001] is due to the crystal structure of zircon-type compounds, characterized by an exceptional rigidity along the structural chain-units (parallel to the *c*-axis). Moreover, the compressional behavior of the two independent REE-O bond distances (Y-O_a and Y-O_b) has been described. As Figure 9.12a,b shows, the Y-O_b is more compressible than the Y-O_a, confirming that the structure is stiffer along the chain units [001]. The Y-O_a bonds, indeed, are those responsible for the connections among the AsO_4 and YO_8 polyhedra along the [001] direction. In addition, the compression of the $REEO_8$ coordination polyhedron (hereafter YO_8) plays a paramount role in controlling the overall compression of chernovite-(Y). A good approximation of the role played by YO_8 in the compressional behavior can be given by its bulk modulus. The YO_8 coordination polyhedron volume variation with pressure has been fitted by a BM2-EoS, yielding to a K_{YO_8}=120(12) GPa (*K'*=4; V_0=23.53(9) $Å^3$). With the same approach, the *V*-*P* data of the tetrahedral AsO_4 units were fitted by a BM2-EoS and a bulk modulus of K_{AsO_4}=262(56) GPa (*K'*=4; V_0=2.32(1) $Å^3$) has been refined. The results of the conducted *P*-*V* fits and a comparison of the compressibilities of the two structural units (YO_8 and AsO_4) are reported in Figure 9.12 along with the bulk compression of the unit-cell volume. In conclusion, the bulk compression of chernovite-(Y) is mostly controlled by the compression of the "softer" YO_8-units, while the AsO_4 tetrahedra behave as much less compressible structural bodies.

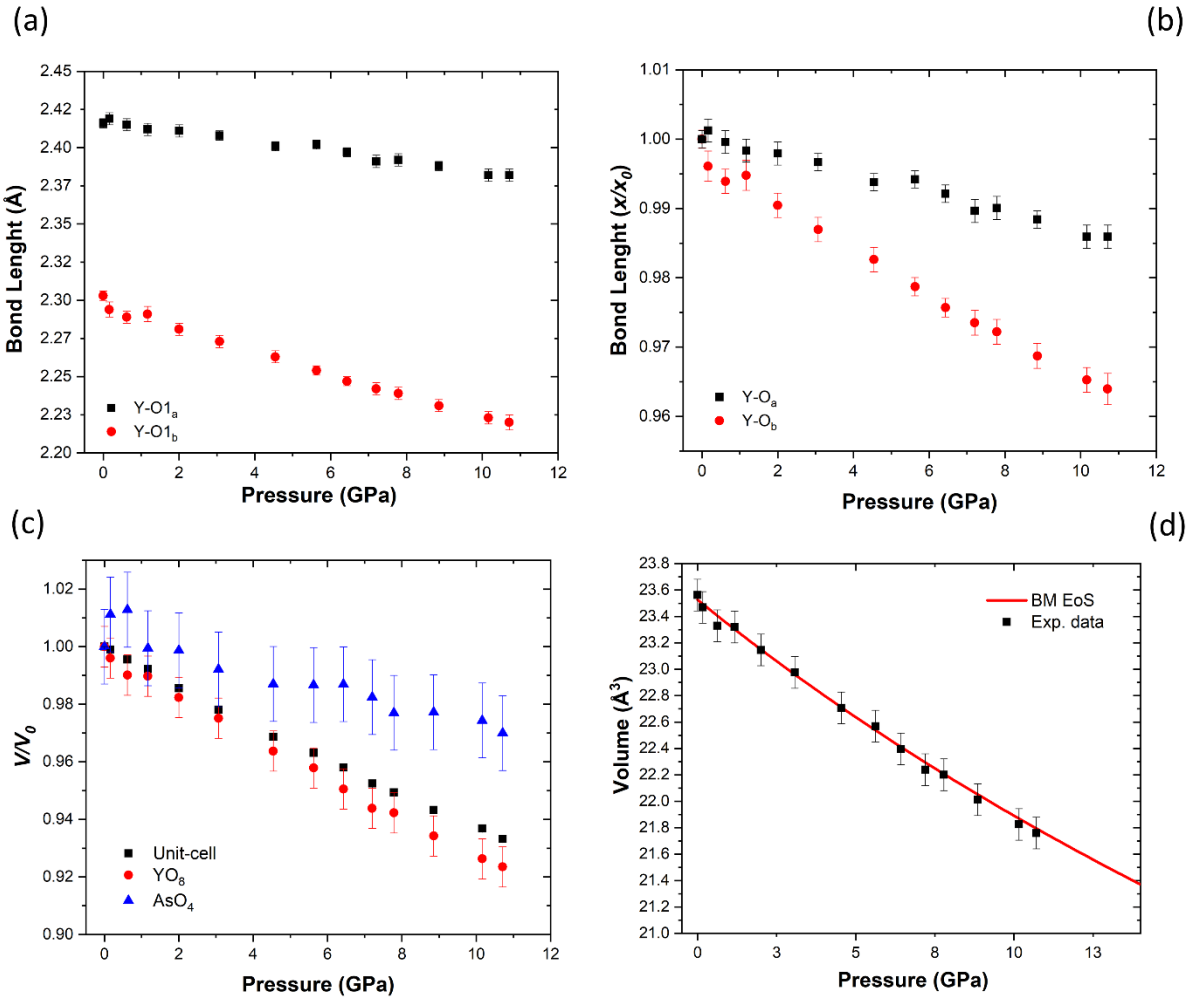

Figure 9.12: evolution as a function of pressure of the absolute **(a)** and normalized (to ambient conditions) values **(b)**, pertaining to the two independent Y-O bond distances; **(c)** *P-V* diagram (normalized to ambient-conditions values) showing the compressional evolution of the unit-cell, YO_8 and AsO_4 polyhedral volumes; **(d)** High-pressure evolution of the YO_8 coordination polyhedron volume of chernovite-(Y). The red line represents the fitted BM3-EoS.

High-pressure behavior of Th-enriched Ch13 sample (Ch13-P_C ramp)

Unlike all the other high-pressure experiments carried out in the present research, the compressional behavior of the Ch13 sample has been investigated by means of powder X-ray diffraction experiments. Due to the quality of the data, no structural refinement has been conducted and only a limited comparison among Th-enriched and Th-poor chernovite-(Y) under compression is discussed in this section. The unit-cell of chernovite-(Y) is indexable within the full pressure range under investigation and the evolution, with pressure, of the unit-cell parameters is shown in Figure 9.13.

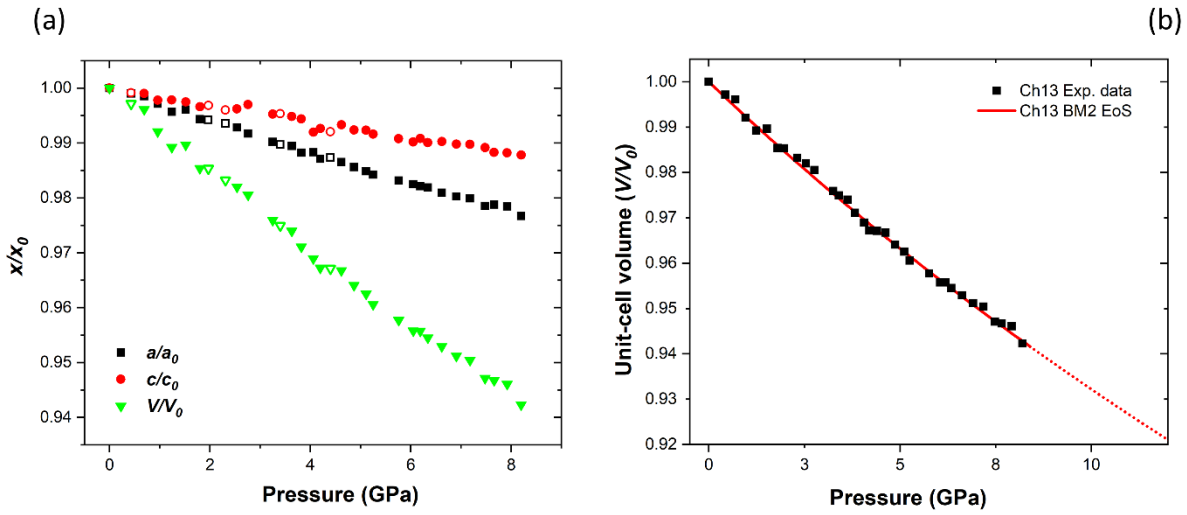

Figure 9.13: High-pressure evolution of **(a)** normalized unit-cell parameters and **(b)** experimental unit-cell volume of chernovite-(Y) (Ch13-P_C). The red line represents the fitted BM2-EoS, while the dotted red line line is an extension of the BM2-EoS at pressures exceeding the available data.

The experimental *P*-*V* data have been fitted with both a BM3-EoS and a BM2-EoS, yielding the following, consistent bulk moduli: K_{P_0,T_0}=123.8(9) GPa (*K'*=4; V_0=316.17(7) Å^3) and K_{P_0,T_0}=125(3) GPa (*K'*=3.8(9); V_0=316.16(9) Å^3). The axial bulk moduli have been refined with a linear BM2-EoS (*K'*=4): K_{a,T_0}=102(1) GPa, a_0=7.0793(7) Å and K_{c,T_0}=207(6) GPa, c_0=6.3092(12) Å. Compared to the Ch10 sample (Figure 9.14), which chemical composition is closer to the endmember chernovite-(Y) (Figure 9.3), the Th-enriched sample Ch13 is slightly more compressible.

(a)

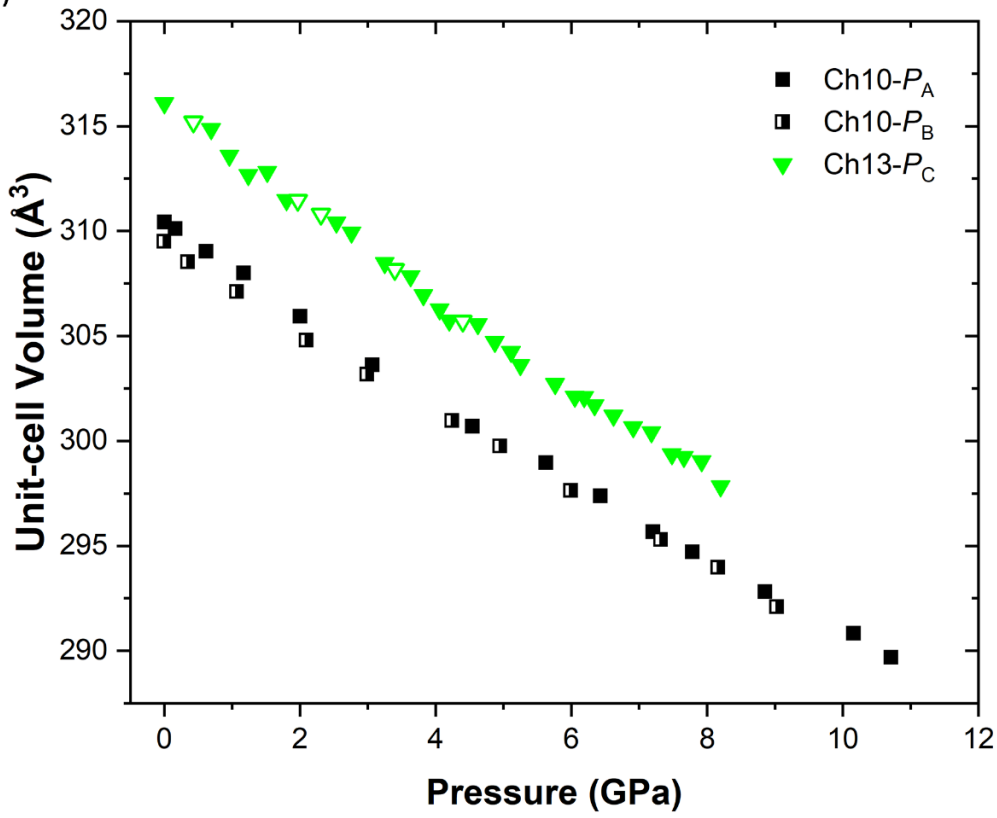
Ch10-P_A
Ch10-P_B
Ch13-P_C
Unit-cell Volume (Å^3)
Pressure (GPa)
320
315
310
305
300
295
290
0
2
4
6
8
10
12

(b)

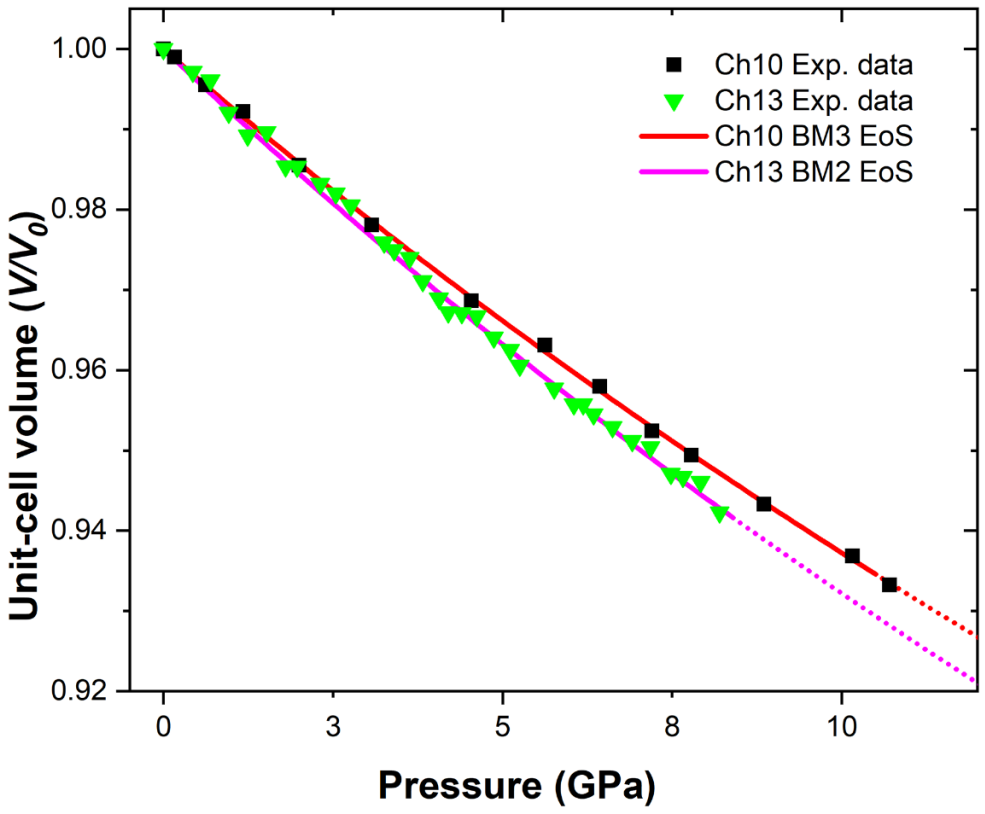
Ch10 Exp. data
Ch13 Exp. data
Ch10 BM3 EoS
Ch13 BM2 EoS
Unit-cell volume (V/V_0)
Pressure (GPa)
1.00
0.98
0.96
0.94
0.92
0
3
5
8
10

Figure 9.14: evolution, with pressure, of the unit-cell volume of chernovite; **(a)** absolute values of the unit-cell volumes based on the Ch10-P_A, Ch10-P_B and Ch13-P_C isothermal ramps, showing the close compressional behavior of the two ramps pertaining to the Ch10 sample and the slightly larger unit-cell volume and compressibility of the Ch13 sample; **(b)** unit-cell volumes of chernovite-(Y) [Ch10-P_B (black dots) and Ch13-P_C (green dots)] as a function of pressure (normalized to atmospheric pressure unit-cell volume). The red and the purple lines represent the fitted BM-EoS, while the dotted lines are an extension of the BM-EoS at pressures exceeding the available compressional data (see text for further details).

As discussed in section 9.3, the Ch13 sample is characterized by larger *T*-site tetrahedron, unit-cell volume and *A*-site polyhedron, when compared to other chernovites-(Y) studied in the current project. The average ionic radius of *A*-site in the Ch13 sample has been calculated after Shannon et al. (1970), following the chemical analysis reported in Table 8.1. The weighted average ionic radius of the *A*-site in the Ch13 chernovite-(Y) (1.178 Å, crystal radius) is intermediate between those of Tb^{VIII} and Dy^{VIII}, but the bulk modulus is significantly lower to the values predicted by Li et al. (2009) for $TbAsO_4$ and $DyAsO_4$. To the best of our knowledge, no data about the compressional behavior of thorite or its synthetic counterpart, $ThSiO_4$, are currently available. On the other side, as pointed out in several comparative studies (*e.g.*, Li et al. 2009), the bulk modulus decreases as the ionic radius of the *A*-site increases. Therefore, the difference among the ionic radii of Ch13 and Ch10 (1.197 Å *vs* 1.164 Å), due to the occurrence of a significant amount of Ca and Th within the *A*-site, might result in a decreasing in bulk modulus. As described by several authors (Ríos and Boffa-Ballaran 2003; Özkan 1976; Özkan and Jamieson 1979; Binvignat et al. 2018), metamictization in zircon has an impact on its physical properties, as compressibility and thermal expansion, among the others. For instance, Özkan (1976), in describing the effects of metamictization in zircons found out that the bulk modulus can drop significantly, from more than 200 GPa to less than 135 GPa. Indeed, as discussed in section 9.1.1, the pictures reported in Figure 8.3 show clear traces of metamictization in the Ch13 grains. The metamictization is thus considered as a possible reasonable point to explain the slightly larger compressibility of the Ch13 sample. However, a full understanding of the phenomena responsible for the observed compressional behavior could be carried out only with the availability of structural data of the thorian chernovite-(Y), that are missing in this study.

9.5.2 High-temperature behavior of chernovite-(Y)

Thermoelastic properties of chernovite-(Y)

Two single-crystal high-temperature X-ray diffraction ramps have been performed on chernovite-(Y) samples (Ch10-T_I and Ch10-T_L), while a third ramp has been performed by means of powder diffraction on the Ch13 sample (Ch13-T_M) (for further details, see Table 8.5). Figure 9.15 shows the

thermal evolution of the unit-cell parameters of chernovite-(Y) based on the Ch10-T_I and Ch13-T_M ramps, while in Figure 9.16 the evolution with temperature of the unit-cell volumes from the three ramps is compared. The volume thermal expansion of chernovite-(Y), based on the three ramps, has been modelled by two polynomial equations (second and first (*i.e.*, linear) polynomials), Holland-Powell EoS, as well as with the average linearized thermal expansion (LTEC).

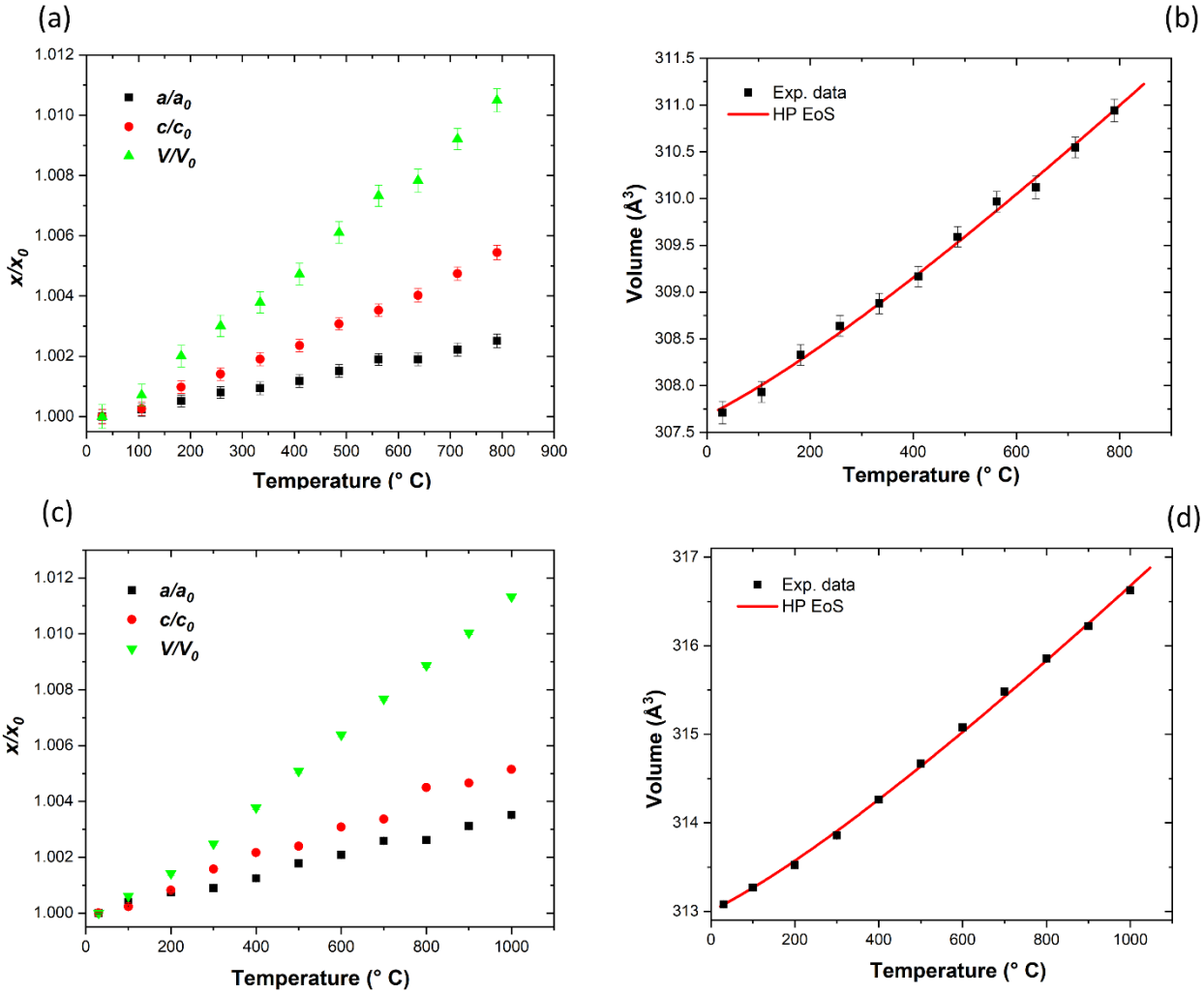

Figure 9.15: High-temperature evolution of **(a)** the unit-cell parameters (normalized to ambient conditions values) and **(b)** unit-cell volume of chernovite-(Y) based on the Ch10-T_I ramp; High-temperature evolution of **(c)** the unit-cell parameters (normalized to ambient conditions values) and **(d)** unit-cell volume of chernovite-(Y) based on the Ch13-T_M ramp. The red lines represent the fitted Holland-Powell EoS (it is worth to highlight that HP, in this case refers to the Holland Powell equation of state and it is not related to high-pressure, although the acronym is the same, by chance).

The corresponding refined parameters are reported in Table 8.25. The results from the two ramps pertaining to the sample Ch10 are mutually consistent, while the room temperature thermal expansion

coefficient of the Ch13 sample is significantly lower (α_{Ch10}=9.5(3)·10^{-6} K^{-1} *vs* α_{Ch13}=8.0(1)·10^{-6} K^{-1}). The thermal expansion coefficients, modelled with the Holland-Powell EoS, increase with temperature in the whole *T*-range studied: for the Ch13 sample, the thermal expansion coefficients range from $\alpha_{Ch13}^{300\,K}$=8.0(1)·10^{-6} K^{-1} at 300 K to $\alpha_{Ch13}^{1250\,K}$=13.5(1)·10^{-6} K^{-1} at 1250 K; for the Ch10 sample, the thermal expansion coefficient ranges from $\alpha_{Ch13}^{300\,K}$=9.5(3)·10^{-6} K^{-1} at 300 K to $\alpha_{Ch13}^{1050\,K}$=15.5(5)·10^{-6} K^{-1} at 1050 K. From all the ramps, the *average* thermal expansion coefficients (the first-order polynomial (linear) thermal expansion or the LTEC) are rather consistent with the Holland-Powell ones. Since chernovite-(Y) belongs to the tetragonal crystal system, the axial thermal expansions correspond to the maximum and minimum thermal expansion directions. The expansivity of the unit-cell axes has been modelled by means of a first and second order equations using the *TEV* software (Table 8.24). For all the studied ramps, the [001] is the most expandable direction based on both the single crystal and powder data (Figure 9.15). Table S13.18 shows the comparative behavior between the chernovite-(Y) samples investigated in the present research and $YAsO_4$ investigated by previous authors (Kahle 1970; Schopper 1972; Reddy et al. 1988; Li et al. 2009).

(a)

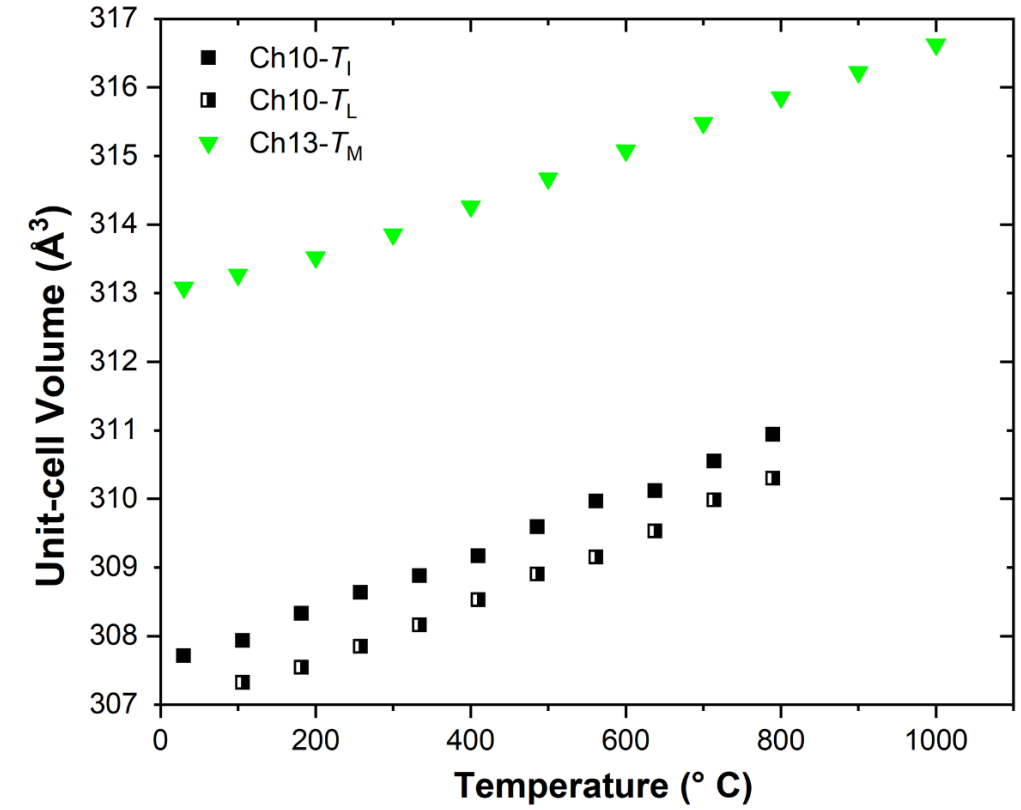
Ch10-T_I
Ch10-T_L
Ch13-T_M
Unit-cell Volume (Å^3)
Temperature (° C)
317
316
315
314
313
312
311
310
309
308
307
0
200
400
600
800
1000

(b)

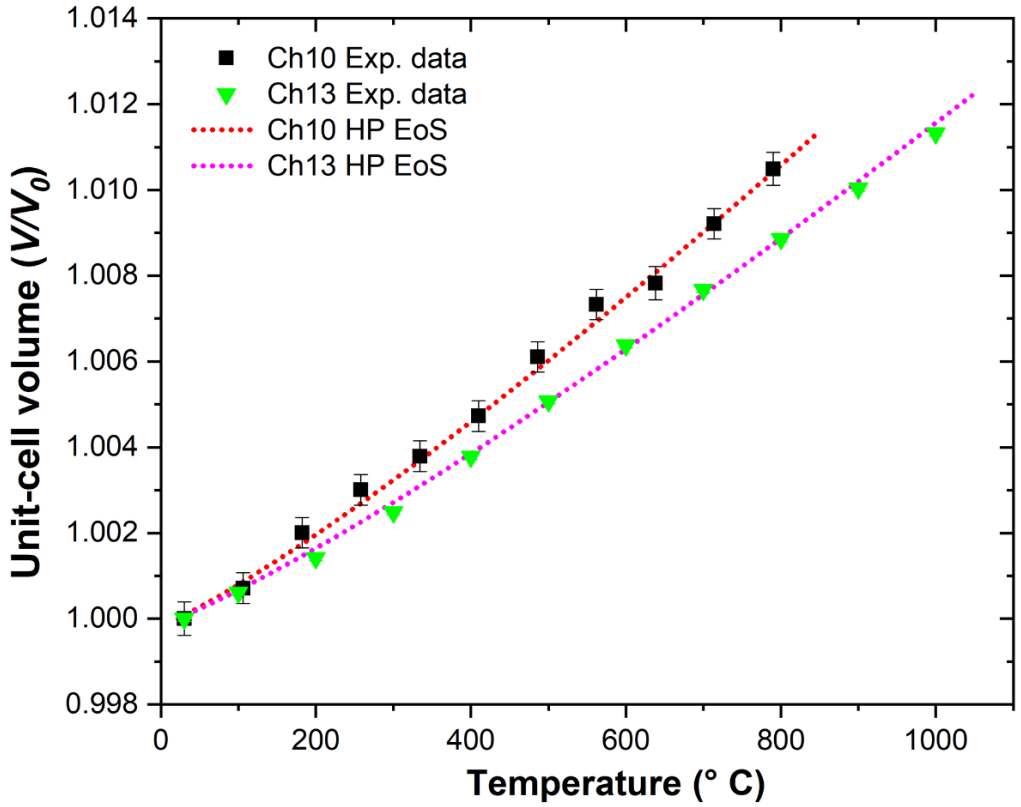
Ch10 Exp. data
Ch13 Exp. data
Ch10 HP EoS
Ch13 HP EoS
Unit-cell volume (V/V_0)
Temperature (° C)
1.014
1.012
1.010
1.008
1.006
1.004
1.002
1.000
0.998
0
200
400
600
800
1000

Figure 9.16: evolution, with temperature, of the unit-cell volume of chernovite; **(a)** absolute values of the unit-cell volumes of the Ch10 sample based on the Ch10-T_I and Ch10-T_L ramps and of the Ch13 sample based on the Ch13-T_M ramp; **(b)** unit-cell volumes of chernovite-(Y) based on the ramps Ch10-T_I (black dots) and Ch13-T_M (green dots) as a function of temperature (normalized to room temperature values). The red and the purple dotted lines represent the fitted Holland-Powell-EoS.

The thermal expansivities modelled in the present study are significantly lower compared to those reported in Table S13.18 for synthetic $YAsO_4$. Indeed, a comparison of the LTEC from the Ch10-T_I ramp ($LTEC_{Ch10}=4.58\cdot10^{-6}$ K^{-1}) with the literature data ($LTEC=6.23\cdot10^{-6}$-$6.61\cdot10^{-6}$ K^{-1}) shows a remarkable gap (Kahle 1970; Schopper 1972; Reddy et al. 1988; Li et al. 2009). Based on these data, it is not possible to determine unambiguously the reasons for the significant gap observed between the thermal expansivity of the investigated chernovite-(Y) and that reported in the literature for synthetic $YAsO_4$. Unfortunately, none of the authors (Kahle 1970; Schopper 1972; Reddy et al. 1988) reported the unit-cell volumes or axes evolution as a function of pressure and it is thus not possible to reanalyze the literature data. On the other hand, it is worth to mention that similar, small thermal expansivities occur in several zircon-type compounds, including many silicates (*e.g.*, $ZrSiO_4$ and $ThSiO_4$), studied by Sallese (1986), Bayer (1972), Austin (1931), Subbarao (1968), Worlton et al. (1972) (see Table S13.18). The slightly smaller thermal expansivity shown by the Ch13 sample can be easily related to the significant amount of ThO_2 within the sample itself, that enlarges significantly the average ionic radius of the *A*-site, as already discussed in section 9.5.1 for the bulk moduli difference among Ch10 and Ch13.

Chernovite-(Y) structural behavior at high temperature

As anticipated above in this section, only the Ch10-T_L ramp provides data that allow structural refinements and *T*-related trends robust enough to discuss the structure deformation mechanisms. Among all the considered structural parameters, the volume of the YO_8 coordination polyhedron, as discussed for the compressional behavior in section 9.5.1, seems to play a significant role in the thermal expansion of chernovite-(Y). The volume of the coordination polyhedra has been calculated from the refined structural models by means of the tools available in the *VESTA* software (Momma and Izumi 2011). Figure 9.17c reports the expansional behavior of the unit-cell and of the YO_8 polyhedron volumes. The expansion of the polyhedron has been modelled with the modified Holland-Powell EoS yielding to following bulk thermal expansion coefficient at ambient conditions: $\alpha_{YO_8}=16(3)\cdot10^{-6}$ K^{-1}. The corresponding refined parameters are reported in Table 8.29. The thermal expansion of the Y coordination polyhedron is significantly larger compared to that of the unit-cell ($\alpha_{YO_8}=16(3)\cdot10^{-6}$ K^{-1} *vs* $\alpha_{cell}=9.5(3)\cdot10^{-6}$ K^{-1}), as shown in the comparative normalized diagram

(Figure 9.17c). On the other side, the AsO_4 coordination tetrahedron does not show any clear *T*-related trend and is thus not shown in Figure 9.17c. Eventually, the *T*-evolution of the Y-O bonds does not show any significant difference among the Y-O_a and the Y-O_b (Figure 9.17a).

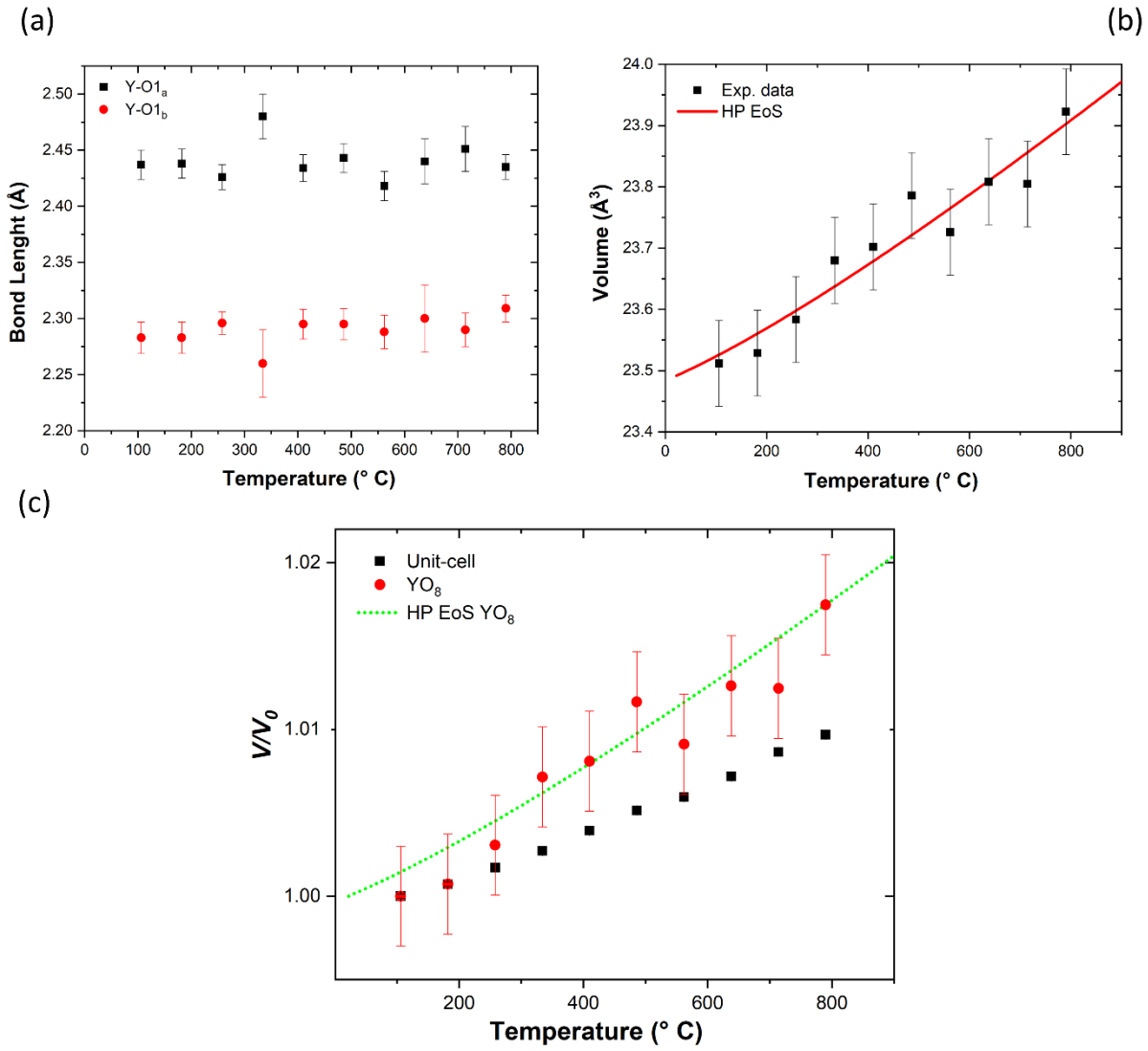

Figure 9.17: **(a)** evolution, with temperature, of the absolute Y-O bond distances, showing the similar thermal expansion behavior of the two bonds; **(b)** *T*-*V* diagram of the YO_8 polyhedral volume, with the fitted H*T*-EoS in red; **(c)** comparative diagram showing the high-temperature evolution of the unit-cell and YO_8 volumes, with a significant higher thermal expansion of the latter. The dotted green line represents the fitted H*T*-EoS (HP stands for Holland-Powell EoS)

9.5.3 Combined H*P*–H*T* behavior of chernovite-(Y)

Compressional behavior of chernovite-(Y) under combined H*P*–H*T* conditions

The unit-cell volume compressional behavior of chernovite-(Y) in the three different isothermal ramps is reported in Table 8.30. It has been observed that, conversely to the room temperature H*P*

ramps collected on chernovite-(Y) (Ch10-P_A and Ch10-P_B), the high-temperature compressional ramps (Ch10-PT_{250} and Ch10-PT_{500}) do not show the occurrence of any abrupt phase transition. Indeed, in place of a phase transition, the H*P*–H*T* data of chernovite-(Y) show a progressive amorphization of the structure, as shown in Figure 9.18 and Figure 9.19. At pressure exceeding 9.6 GPa, a change in the compressional behavior of chernovite-(Y) occurs in both the Ch10-PT_{250} and Ch10-PT_{500} ramps.

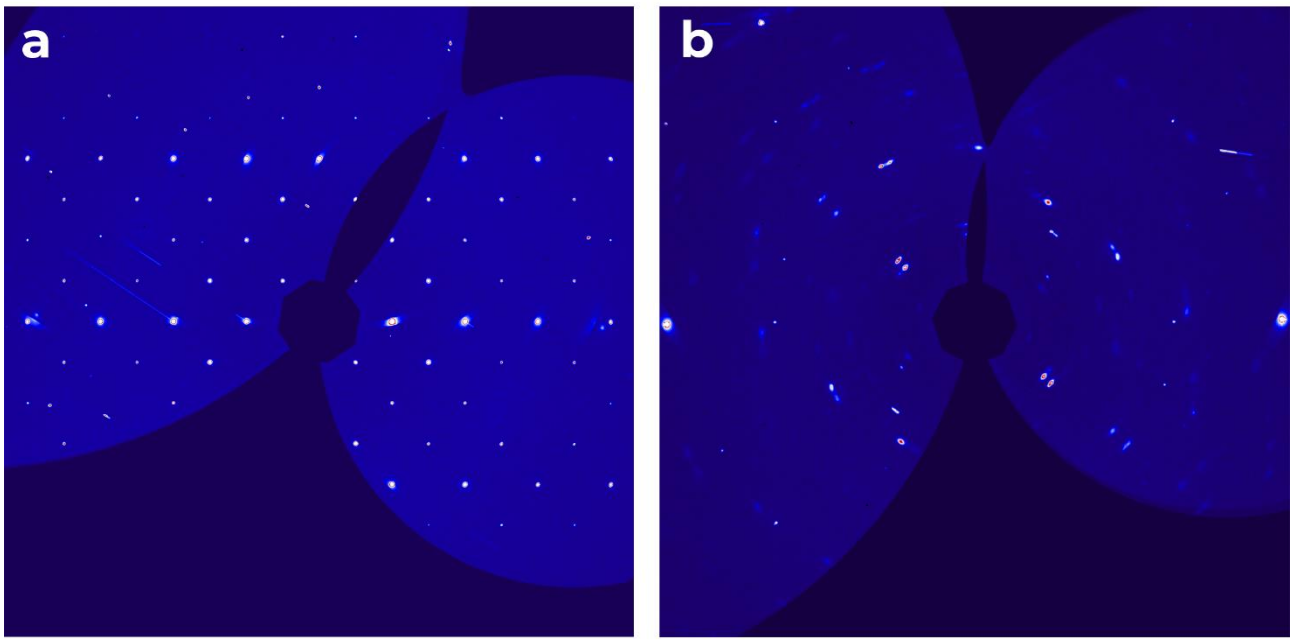

Figure 9.18: reconstruction of the (0*kl*)* reciprocal lattice section of chernovite-(Y), showing the X-ray diffraction peaks before **(a)** and after **(b)** ~9.6 GPa, based on the data of the Ch10-PT_{250} ramp.

As also shown by the compressional ramps at ambient temperature (Ch10-P_A and Ch10-P_B), the [001] axis is the less compressible direction even in the two combined H*P*–H*T* ramps.

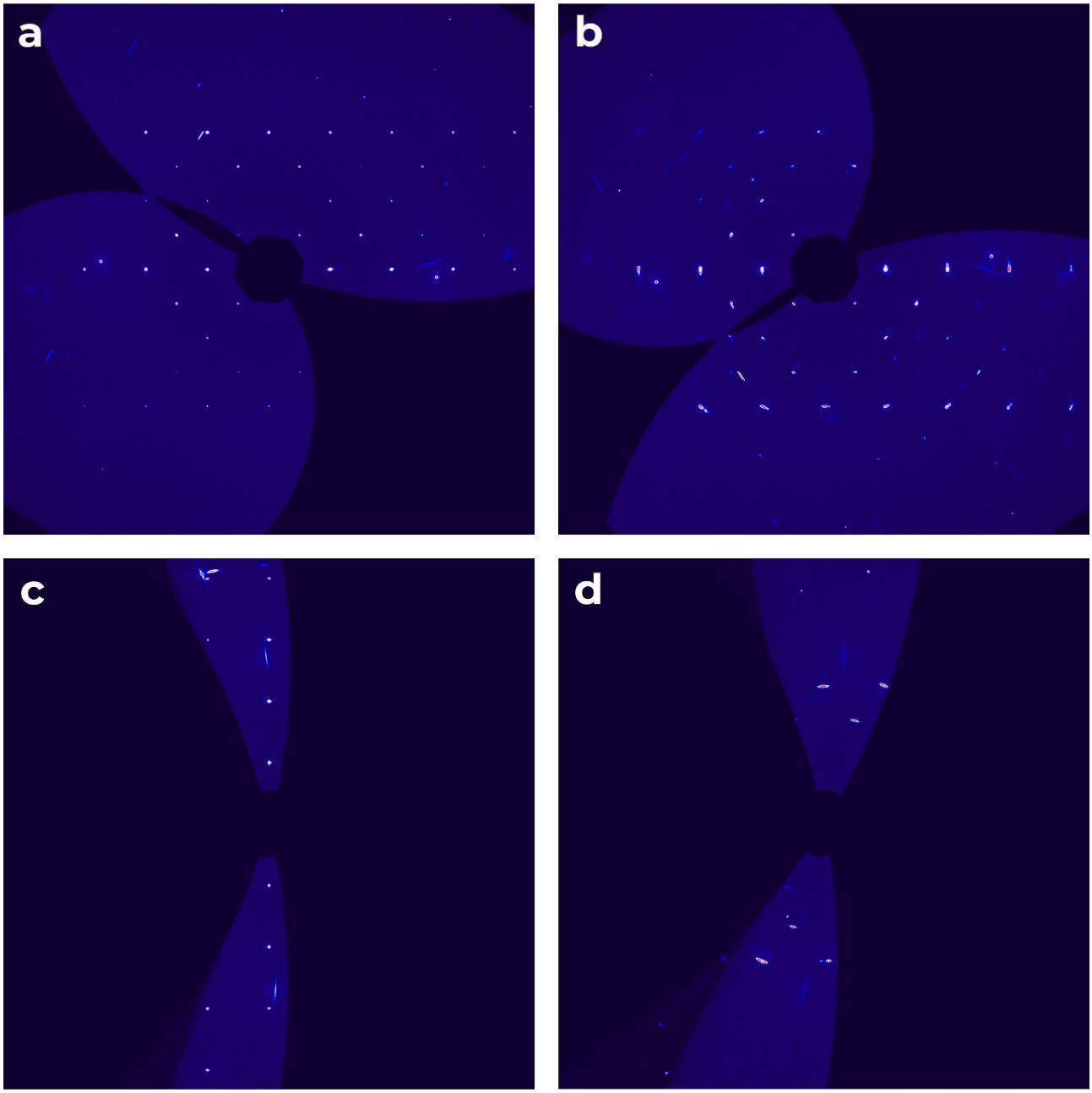

Figure 9.19: reconstructed reciprocal lattice sections of chernovite-(Y), showing the X-ray diffraction peaks before (a,c) and after (b,d) ~9.6 GPa, based on the data of the Ch10-PT_{500} ramp. The reconstructed reciprocal lattice sections are (0*kl*)* (a,b) and (*hk*0)* (c,d).

The refined *P*–*T*–*V* elastic parameters (see Table 8.32) are rather similar to the elastic parameters refined in the individual H*P*- and H*T*-ramps of chernovite-(Y), respectively (see Table 8.9 and Table 8.23). The temperature derivative of the bulk modulus for non-metamict zircon has been determined by Özkan (1978) and it is dK/dT_P=-0.021. In the present study, the dK/dT_P=-0.034(13) is rather close to the one determined for zircon.

Structural behavior of chernovite-(Y) under combined H*T*–H*P* conditions

The structural behavior of chernovite-(Y) at 250° C and 500° C has been described from the structural refinements based on the H*T*–H*P* ramps. The compressional behavior of some relevant structural parameters is reported in Table 8.33. In the first place, the compressional behavior of the YO_8 coordination polyhedron is considered (see Table 8.33). In both the ramps, the YO_8 polyhedron is more compressible compared to the unit-cell volume. The AsO_4 tetrahedron, on the other hand, it is rather rigid, as already observed from the other compressional and thermal data previously discussed. Overall, the structure refinements based on the H*P*–H*T* data have allowed to describe the same mechanisms already described from the room *T* H*P*-data.

9.6 Behavior of gasparite-(Ce) at non-ambient conditions

9.6.1 High-pressure behavior of gasparite-(Ce)

The results described and discussed in this chapter have already been published by Pagliaro et al. (2022b) in the following manuscript: High-pressure behavior of gasparite-(Ce) (nominally $CeAsO_4$), a monazite-type arsenate, Physics and Chemistry of Minerals, 49.

Elastic properties of gasparite-(Ce) under compression

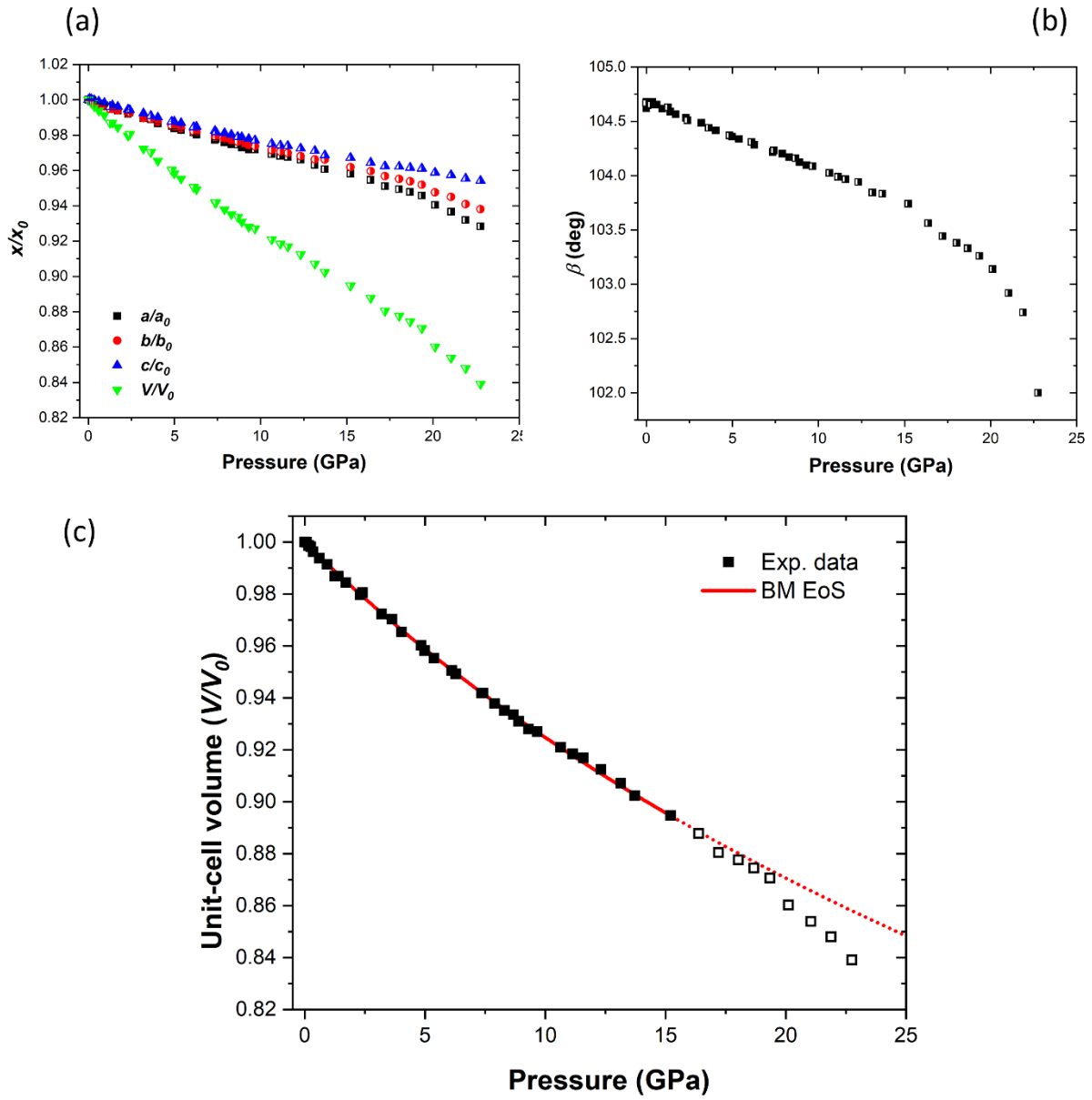

Figure 9.20: (a) high-pressure evolution of the experimental unit-cell parameters of gasparite-(Ce) normalized to their ambient-conditions values; **(b)** high-pressure evolution of the β monoclinic angle, showing the kinking at ~15 GPa; **(c)** high-pressure evolution of the experimental unit-cell volume of gasparite-(Ce) normalized to the ambient-conditions value. The void symbols represent the experimental data collected at pressure exceeding the change in compressional behavior; the half-filled dots reported in **(a)** and **(b)** refer to the Gasp3-P_G dataset the red line represents the fitted BM2-EoS, while the dotted red line line is an extension of the BM2-EoS at pressures exceeding the change in compressional behavior (see text for further details).

Figure 9.20 shows the compressional behavior of the unit-cell parameters of gasparite-(Ce). Gasparite-(Ce) is characterized by an anisotropic compressional behavior, with a lower compressibility along [001], a maximum shortening along [100], whereas [010] displays an intermediate compressibility (Figure 9.20a). At a first approximation, gasparite-(Ce) shows a similar compressional behavior with the other ATO_4 compounds sharing a monazite-type structure

(Errandonea 2017). The monoclinic β angle linearly decreases with pressure up to ~15 GPa, as shown in Figure 9.20b. Although still linear, at pressures exceeding ~15 GPa, the monoclinic angle decreases more pronouncedly, reaching 102.91(1)° at 21.05 GPa (Figure 9.20b). Above ~15 GPa an increase of unit-cell volume compression can also be observed. The compressional behavior of gasparite-(Ce) has been modeled with both a second-order Birch-Murnaghan Equation of State (BM2-EoS) and a third-order Birch-Murnaghan Equation of State (BM3-EoS) (Birch 1934; Angel 2000), using the *Eos_Fit7c_GUI* software (Angel et al. 2014; Gonzalez-Platas et al. 2016), based on both the *m.e.w.* and helium ramps unit-cell data (normalized to corresponding ambient-*P* values). The experimental data collected at pressures exceeding 15.22 GPa have not been taken into account, due to the observed change in the compressional behavior (Figure 9.20b,c). The fit of the BM-EoS to the experimental data yielded the following refined parameters: K_{P_0,T_0}=109.4(3) GPa (β_V=0.00914(3) GPa^{-1}) and V_0=320.58(3) Å^3 for the BM2-EoS, K_{P_0,T_0}=108.3(10) GPa (β_V=0.00923(9) GPa^{-1}), K'=4.2(2) and V_0=320.59(3) Å^3 for the BM3-EoS. The calculated BM2-EoS curve is reported in Figure 9.20c along with the experimental normalized unit-cell volumes.

An analysis of the finite Eulerian strain (*fe) vs.* the normalized pressure (*Fe*) plot (see Angel (2000) for further details) suggests that the refined BM2-EoS curve properly describes the elastic compressional behavior of gasparite-(Ce). Given the monoclinic symmetry of gasparite-(Ce), the compressibility of the unit-cell axes does not allow a comprehensive description of the elastic anisotropy, due to the variation of the β angle as a function of pressure. Therefore, the finite Eulerian unit-strain tensor has been calculated based on the data from the helium ramp, between atmospheric pressure and 15.22 GPa, using the software *Win_Strain* (Angel 2011). The average compressibility values along the axes of the strain ellipsoid (with $\varepsilon_1>\varepsilon_2>\varepsilon_3$) are: ε_1=0.00303(1) GPa^{-1}, ε_2=0.002546(9) GPa^{-1}, ε_3=0.001711(8) GPa^{-1}, leading to the following anisotropic scheme $\varepsilon_1:\varepsilon_2:\varepsilon_3$=1.77:1.49:1. The following matrix describes the geometric relations between the crystallographic axes and the strain ellipsoid orientation (where *X*//*a** and *Y*//*b*):

$$\begin{pmatrix}\varepsilon_1\\ \varepsilon_2\\ \varepsilon_3\end{pmatrix} \angle \begin{pmatrix}23.7(2)^\circ & 90^\circ & 127.4(2)^\circ\\ 90^\circ & 180^\circ & 90^\circ\\ 113.7(2)^\circ & 90^\circ & 142.6(2)^\circ\end{pmatrix} \cdot \begin{pmatrix}a\\ b\\ c\end{pmatrix}$$

The matrix shows that the both the directions of maximum and minimum compressibility lay in the (010) plane.

As previously described, the monazite-type structure of gasparite-(Ce) undergoes a change in the compressional behavior, responsible for the significant deviation in the *β,V vs. P* trends after 15.22 GPa. It is worth to underline that a similar behavior of the *β,V vs. P* trends was also described by

Huang et al. (2010) and Errandonea et al. (2018) for powder synthetic samples of $CePO_4$ and $LaPO_4$ at about 10 and 15 GPa, respectively. Errandonea et al. (2018) interpreted this phenomenon as a consequence of the non-hydrostatic conditions determined by inter-grains interaction. A careful analysis of the systematic extinction conditions in the experimental single crystal diffraction patterns of this study suggests that no change in symmetry occurs coupled with the change in compressibility. In this case, as the experiment was conducted using a single crystal compressed in helium, we can exclude that the observed change in the compressional behavior may be ascribed to non-hydrostatic conditions, generated by grain-to-grain compression. As previously discussed, no experimental data about the elastic properties of the monazite-type arsenates have ever been obtained. The bulk modulus of gasparite-(Ce) (K_{P_0,T_0}=109.4 GPa) is lower than the theoretical bulk moduli determined by Li et al. (2009) for both $LaAsO_4$ and $CeAsO_4$ (K_{P_0,T_0}=124.5 GPa and K_{P_0,T_0}=125.1 GPa, respectively). On the other hand, it is worth to mention that also the theoretical bulk moduli obtained by Li et al. (2009) for monazite-type phosphates usually overestimate the experimental ones. Moreover, since different bulk moduli have been refined or calculated for $CePO_4$, ranging from 109(1) to 122 GPa (Errandonea et al. 2017; 2018; Huang et al. 2010), it is not straightforward to provide a comparison between gasparite-(Ce) and the large family of synthetic monazite-type $REEPO_4$, also in the light of the multi-elemental composition of the *A*-site of the investigated natural sample. Considering the most recent and complete data, provided by Errandonea et al. (2018) on $CePO_4$ (K_{P_0,T_0}=117.3(5) GPa, K'=4.54(3) refined with a BM3-EoS), the high-pressure compressibility of gasparite-(Ce) is slightly higher. This difference could be ascribed to the complex composition of the REE-bearing site in gasparite-(Ce) or to the presence of arsenic in place of phosphorous within the tetrahedral site, or by a combination of the two factors. Several authors (Li at al. 2009; Errandonea et al. 2011) pointed out that, at a given composition of the REE-cation, the arsenates are always more compressible than the phosphates counterparts, due to the larger compressibility of the AsO_4 with respect the PO_4 tetrahedron. In addition, as pointed out by Pagliaro et al. (2022a), the *T*-site of arsenates and phosphates has a strong influence on the whole structural features and, in particular, on the volume of both the REE-coordination polyhedron and unit-cell. Thus, the REE-polyhedron in monazite-(Ce) is smaller, if compared to the REE-polyhedron in gasparite-(Ce), despite a very similar population of the REE-site. In this light, being the PO_4 tetrahedra less compressible than the AsO_4 ones, the smaller REE-polyhedron of phosphates is reasonably also less compressible than the larger REE polyhedron of arsenates.

Interestingly, the bulk modulus of gasparite-(Ce) is intermediate between those of synthetic $REEPO_4$ and $LaVO_4$ (K_{P_0,T_0}=95(5) GPa; Errandonea et al. 2016): the volume of AsO_4 is, indeed, intermediate

between those of the PO_4 and VO_4 tetrahedra ($LaVO_4$ is the only endmember vanadate crystallizing with the monazite-type structure, if synthesized under high-temperature conditions, according to Bashir and Khan (2006), Rice and Robinson (1976), Aldred (1984), Baran and Aymonino (1971)).

High-pressure structure deformation in gasparite-(Ce)

The analysis of the structural deformation mechanisms, acting at the atomic scale, is mainly based on the experimental data from the Gasp3-P_F dataset (*m.e.w.* ramp) Indeed, most of the analysis of the refined structural models from the He ramp revealed a scattering of the *P*-induced evolution of relevant structural parameters. Figure 9.21d, Table 8.16 and Table 8.17 show the high-pressure volume evolution for both the CeO_9 and the AsO_4 coordination polyhedra. A second order Birch-Murnaghan EoS (K'=4), fitted to the *P*-*V* data of the CeO_9 polyhedron leads, to a refined bulk modulus of K_{CeO_9}=99(3) GPa (β_{CeO_9}=0.0101(9) GPa^{-1}; V_0=33.02(4) $Å^3$). The AsO_4 tetrahedron clearly shows a discontinuity in the compressional behavior, with a significant compression until 2.30 GPa, followed by a stiffening that makes this structural unit substantially uncompressible between 2.30 and 9.31 GPa, preventing a modelling of its elastic behavior by an EoS. As the bulk compressibility of gasparite-(Ce) (β_V=0.00923(9) GPa^{-1}) is lower with respect to the compressibility of the CeO_9 coordination polyhedron (β_{CeO_9}=0.0101(9) GPa^{-1}), it follows that the latter plays a key role in accommodating the unit-cell volume compression.

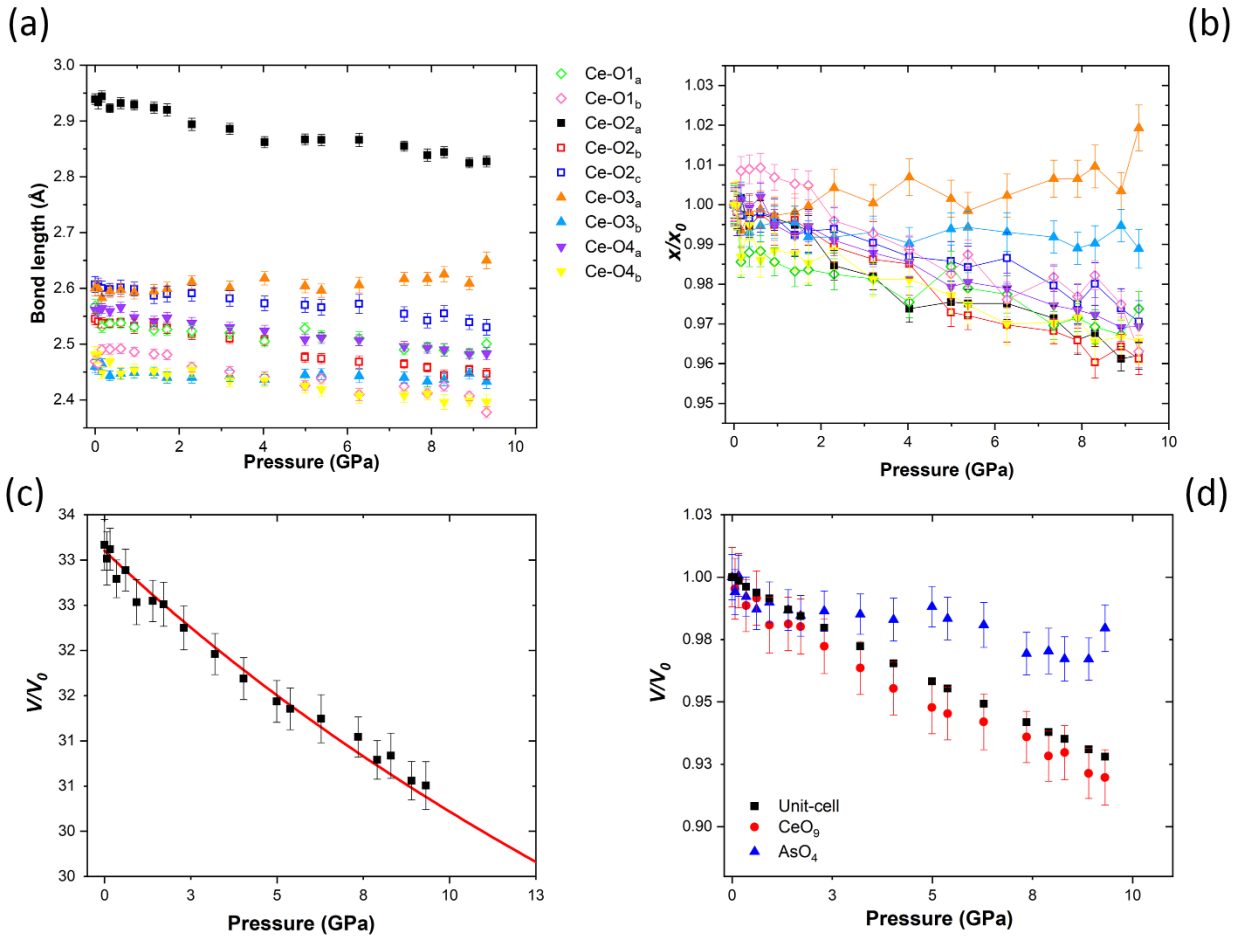

Figure 9.21: High-pressure evolution of the absolute **(a)** and normalized (to ambient conditions) values **(b)** of the nine independent Ce-O bond distances; **(c)** compressional behavior of the CeO_9 coordination polyhedron in gasparite-(Ce) where the red line represents the fitted BM2-EoS; **(d)** *P-V* diagram (normalized to ambient-conditions values) showing the compressional evolution of the unit-cell, CeO_9 and AsO_4 polyhedra volumes.

As reported in Figure 9.21a,b and Table 8.16, the analysis of the high-pressure behavior of the Ce-O bond distances shows that the CeO_9 polyhedron is characterized by a clear anisotropic behavior. The two Ce-O bond distances involving the O3 atoms are the less compressible with the Ce-$O3_a$ bond distance even showing an expansion with the pressure increase. According to the notation reported in Figure 3.6, the Ce-$O3_a$ bond distances, along with Ce-$O2_a$ and Ce-$O4_a$, represents the connection between the CeO_9 polyhedron and the AsO_4 tetrahedra along the *c* axis. The expansion of the Ce-$O3_a$ bond distance coupled with the contraction along the Ce-$O1_a$ bond leads to a tilting of the AsO_4 tetrahedra, with a slight closure of the Ce-As-Ce interatomic angle (Figure 9.22a, Figure 9.23d, Table 8.17).

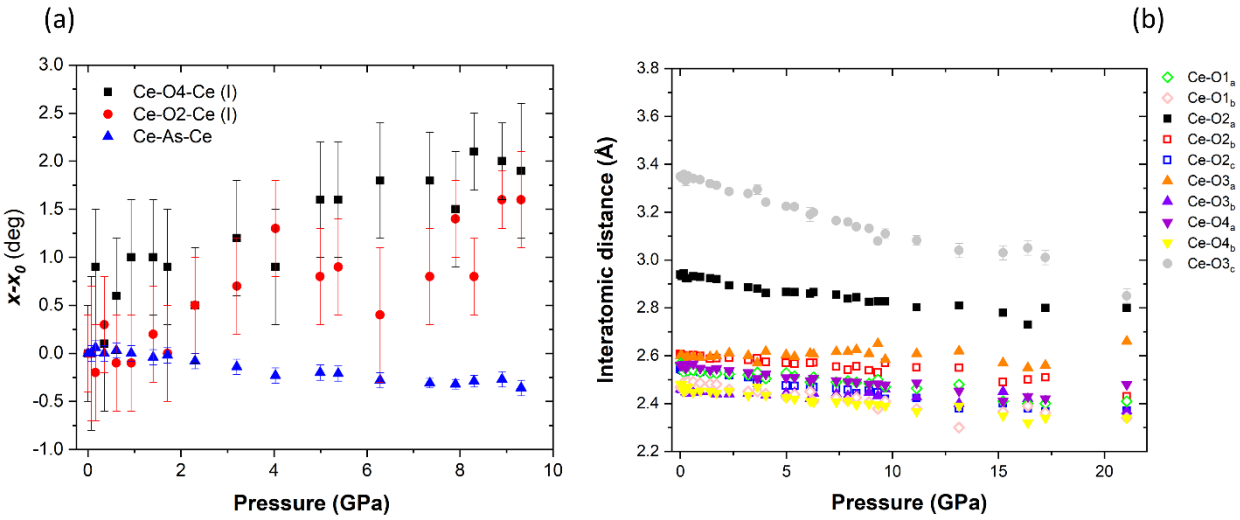

Figure 9.22: high-pressure evolution of **(a)** relevant interatomic angles and **(b)** of the ten Ce-O interatomic distances, showing that the Ce-$O3_c$ is rather more compressible than the others.

Therefore, we can conclude that the major mechanism responsible for the contraction along the *c* crystallographic direction is the bulk compression of the CeO_9 polyhedron, whereas a slight tilting of the AsO_4 polyhedron tends to accommodate this linear contraction.

.

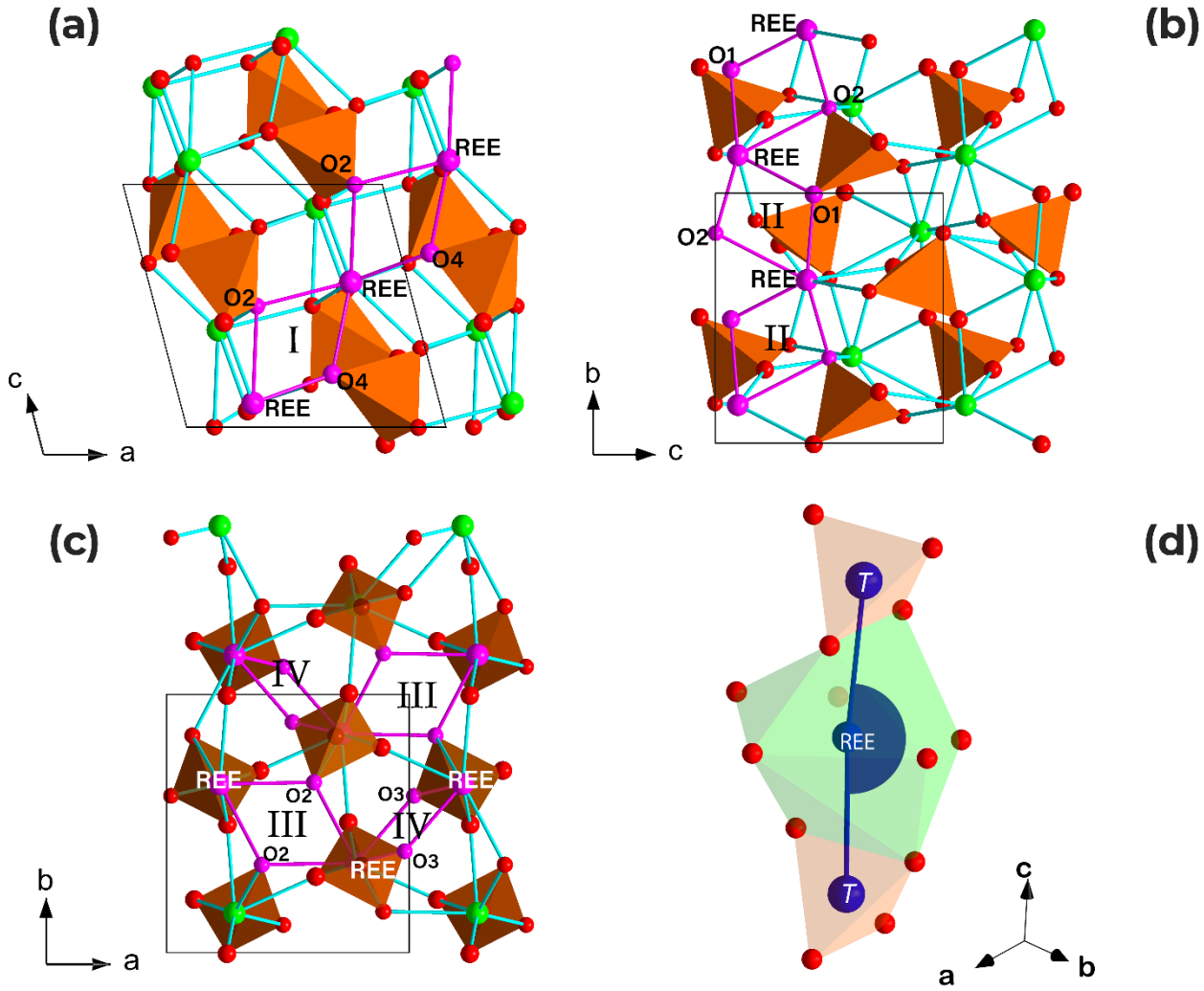

Figure 9.23: Representation of the monazite-type crystal structure, showing the seven bond angles considered for the structural description of gasparite-(Ce) and the other monazite-type minerals under investigation; four independent lozenge-like units in purple (a, b and c); **(d)** *T*-REE-*T* bond angles (equivalent to the REE-*T*-REE bond angles) describing the linearity along the [001] direction (see text for further details).

In addition, the evolution with pressure of the Ce-$O3_c$ interatomic distance, as it is defined in Figure 9.24b, has been investigated. As shown in the normalized diagram in Figure 9.22b, the Ce-$O3_c$ interatomic distance is significantly more compressible compared to any other Ce-O bond distance in the coordination sphere of the REE-site and it shows a similar and rather significant compressional trend both in the Gasp3-P_F and Gasp3-P_G ramps. Between 13.72 and 17.22 GPa, the shortening of the Ce-$O3_c$ undergoes a saturation before showing an abrupt compression above ~17 GPa, reaching the minimum value of 2.85(3) Å at 21.05 GPa. As the $O3_c$ oxygen (as defined in Fig. 8a) does not belong to the coordination sphere of the REE-site at ambient conditions, we can conclude that, at *ca.*

15 GPa, the $REEO_9$ coordination polyhedron in gasparite-(Ce) experiences an increase in its coordination number from CN=9 to CN=10. This structural mechanism is likely responsible for the change in the compressional behavior shown in Figure 9.20 and previously discussed. A more detailed discussion on this point is given later in section 9.8.1, where the high-pressure behavior of the investigated monazite-(Ce) sample will be discussed.

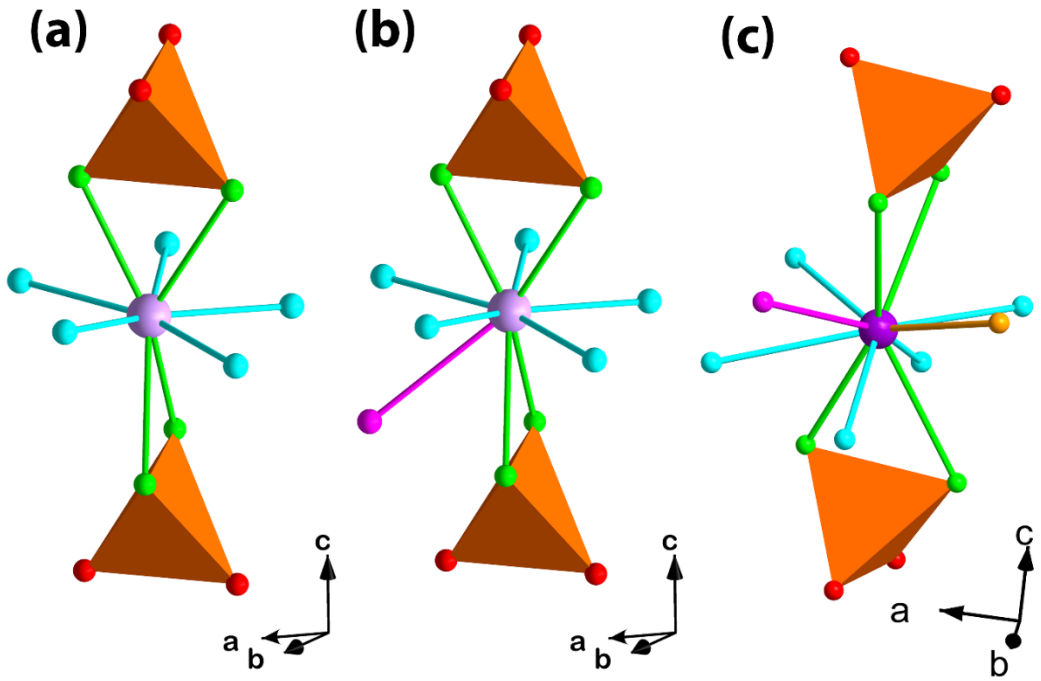

Figure 9.24: Crystal structure of a monazite-type (a,b) and postbarite-type **(c)** compound in the surrounding of the REE-bearing *A*-site (in purple): in green the REE-Ox_a (the four REE-O chain-connecting bonds in the monazite-type compounds); in sky blue the REE-$O1_b$, REE-$O2_b$, REE-$O2_c$, REE-$O3_b$, REE-$O4_b$ (the five REE-O distances making up the equatorial pentagon in the monazite-type compounds); in violet (b,c) it is reported the tenth REE-$O3_c$ interatomic distance; in orange **(c)** the eleventh REE-$O4_c$ bond distance of the postbarite-type structure (see the text for further details).

For a comprehensive understanding of the deformation mechanisms occurring in gasparite-(Ce) at high pressure and to explain the anisotropic behavior described by the finite-strain tensor analysis, it is essential to introduce the Ce-Ox-Ce angles (Figure 9.23a,b,c, Table 8.17) which represent the lozenge-like connection between adjacent chains. Huang et al. (2010) already studied the importance of such structural units in describing the distortion of the REE-coordination polyhedron, although a comprehensive description of their impact was not provided. Six independent angular units, defining 4 independent lozenge-like connections (Ce-O4-Ce–Ce-O2-Ce I); Ce-O1-Ce–Ce-O2-Ce (II), Ce-O2-Ce–Ce-O2-Ce(III); Ce-O3-Ce–Ce-O3-Ce (IV)) can be described as reported in Figure 9.23a,b,c and Table 8.17. The only mechanism significantly contributing to the anisotropic compression involves

the lozenge-like unit I, defined by the couple of interatomic angles Ce-O2-Ce and Ce-O4-Ce. These lozenge-like units define a slightly sinusoidal chain system running along the [101] direction, as reported in Figure 9.23a. The opening of these two angles in response to the pressure increase, as shown in Figure 9.22a, leads to a stretching of the chain. This deformation mechanism, coupled with the slight shortening of the Ce-As-Ce (Figure 9.22a) chains running along the [001], provides the rationale for the anisotropic scheme defined by the finite-strain Eulerian tensor.

9.7 Behavior of xenotime-(Y) at non-ambient conditions

9.7.1 High-pressure behavior of xenotime-(Y)

Elastic properties and phase transition of xenotime-(Y) under compression

Two compressional ramps have been performed for xenotime-(Y) under high pressure conditions: Xen14-P_D and Xen14-P_E (Table 8.6). At pressure above 17 GPa the structure of xenotime-(Y) is no longer stable and undergoes a reversible single-crystal to single-crystal phase transition characterized by a significant hysteresis (Figure 9.25). The diffraction pattern of the H*P* polymorph (xenotime-(Y)-II) is compatible with the unit-cell of the monazite-type structure. The phase transition is associated to a consistent drop of the unit-cell volume, with an increase in density around ~6 %. Such a phase transition is known to occur in other, synthetic *AT*O_4 phosphates (YPO_4 (Zhang et al. 2009; Lacomba-Perales et al. 2010), $GdPO_4$, $DyPO_4$ (Musselman et al. 2017), $ErPO_4$ (Lacomba-Perales et al. 2010), $TmPO_4$ (López-Solano et al. 2010; Tatsi et al. 2008) and solid solutions within the $SmPO_4$-$TbPO_4$ system (Heuser et al. 2018). The pressure of the zircon-to-monazite phase transition in xenotime-(Y) is consistent with those determined for YPO_4 (16.3-23.5 GPa, Zhang et al. 2009, Lacomba-Perales et al. 2010). In addition, the zircon-to-monazite phase transition is known to occur in several REE*T*O_4 vanadates, as $CeVO_4$ (Errandonea et al. 2011; Panchal et al. 2011), $PrVO_4$ (Marqueño et al. 2021), and $NdVO_4$ (Errandonea et al. 2011). According to the Bastide diagram (Fukunga and Yamaoka 1979; Bastide 1987), and the following studies on the compressional behavior of phosphates and vanadates, the pressure of the zircon-to-monazite phase transition, hereafter $P_{Z\text{-}M}$, is shifted at higher pressures whit a decrease of the ionic radius of the *A*-site cation. Although the zircon-to-monazite phase transition is often reported in literature as a non-reversible transformation, in the present study we observed a reversible, retrograde single-crystal to single-crystal transition in decompression (Figure 9.25), even though with a significant hysteresis, being the monazite-to-zircon phase transition occurring between 6.3 and 1.3 GPa..

The bulk moduli refined by the BM3-EoS fits of the two ramps of xenotime-(Y) are rather consistent (Figure 9.25c,d): K_{P_0,T_0}=142(4) GPa (β_V=0.0070(7) GPa^{-1}; *K'*=4.4(7); V_0=288.63(14) Å^3) and K_{P_0,T_0}=148(4) GPa (β_V = 0.0068(7) GPa^{-1}; *K'*=4.0(5); V_0=290.4(2) Å^3) respectively. Moreover, xenotime-(Y) is characterized by an anisotropic behavior, being the [001] direction less compressible compared to the [100] direction (Figure 9.25a). The two linear bulk moduli refined with a BM2-EoS (*K'*=4) for the [100] and [001] directions respectively are: K_{a,T_0}=122(1) GPa, a_0=6.9109(10) Å and K_{c,T_0}=242(3) GPa, c_0=6.0675(8) Å based on the Xen14-P_D dataset and K_{a,T_0}=115(1) GPa, a_0=6.9181(10) Å and K_{c,T_0}=254(3) GPa, c_0=6.0516(11) Å based on the Xen14-P_E dataset.

Concerning the compressional behavior of the high-pressure polymorph, *i.e.* xenotime-(Y)-II, the *V-P* data have been modelled by a BM2-EoS, while its finite-strain Eulerian tensor analysis has been performed with the *Win_strain* software, between 17.75 and 28.54 GPa, yielding a description of the anisotropic compression defined by the following matrix:

$$\begin{pmatrix}\varepsilon_1\\ \varepsilon_2\\ \varepsilon_3\end{pmatrix} \measuredangle \begin{pmatrix}17(3)^\circ & 90^\circ & 120(3)^\circ\\ 90^\circ & 180^\circ & 90^\circ\\ 107(3)^\circ & 90^\circ & 150(3)^\circ\end{pmatrix} \cdot \begin{pmatrix}a\\ b\\ c\end{pmatrix}$$

The analysis of the compressional strain tensor provides the mean compressibility values along the axes of the strain ellipsoid (with $\varepsilon_1>\varepsilon_2>\varepsilon_3$): ε_1=0.0024(2) GPa^{-1}, ε_2=0.00158(3) GPa^{-1}, ε_3=0.00067(8) GPa^{-1}, with an anisotrpic scheme $\varepsilon_1 : \varepsilon_2 : \varepsilon_3$ = 3.58 : 2.36 : 1. The BM2-EoS fit of the xenotime-(Y)-II *V-P* data yields: K_{P_0,T_0}=146(5) GPa (β_V = 0.0068(9) GPa^{-1}; V_0=274.7(9) Å^3).

It is worth to mention that the bulk modulus of xenotime-(Y) is consistent with the ones reported for YPO_4 by several authors (Table S13.17). Apart from Zhang et al. (2009), who reported rather high values, the bulk moduli reported in literature ranges from a minimum of 132 GPa and a maximum of 165.5 GPa. On the other hand, the compressional behavior modelled for xenotime-(Y)-II provides a bulk modulus significantly lower than the others refined for YPO_4-II (206 GPa and 266 GPa; Zhang et al. 2009; Lacomba-Perales et al. 2010). If the data collected in the decompression regime (*i.e.*, *P*=19.30, 15.38, 11.03 and 6.15 GPa) are excluded from EoSfit, the BM2-EoS bulk modulus of xenotime-(y)-II does not change significantly (K_{P_0,T_0}=139(13) GPa; β_V=0.007(1) GPa^{-1}; V_0=276(3) Å^3). However, conversely to the data here discussed, the bulk modulus refined by Zhang et al. (2009) and Lacomba-Perales et al. (2010) rely on a tiny amount of data. Therefore, we consider the EoS fit of this study more reliable.

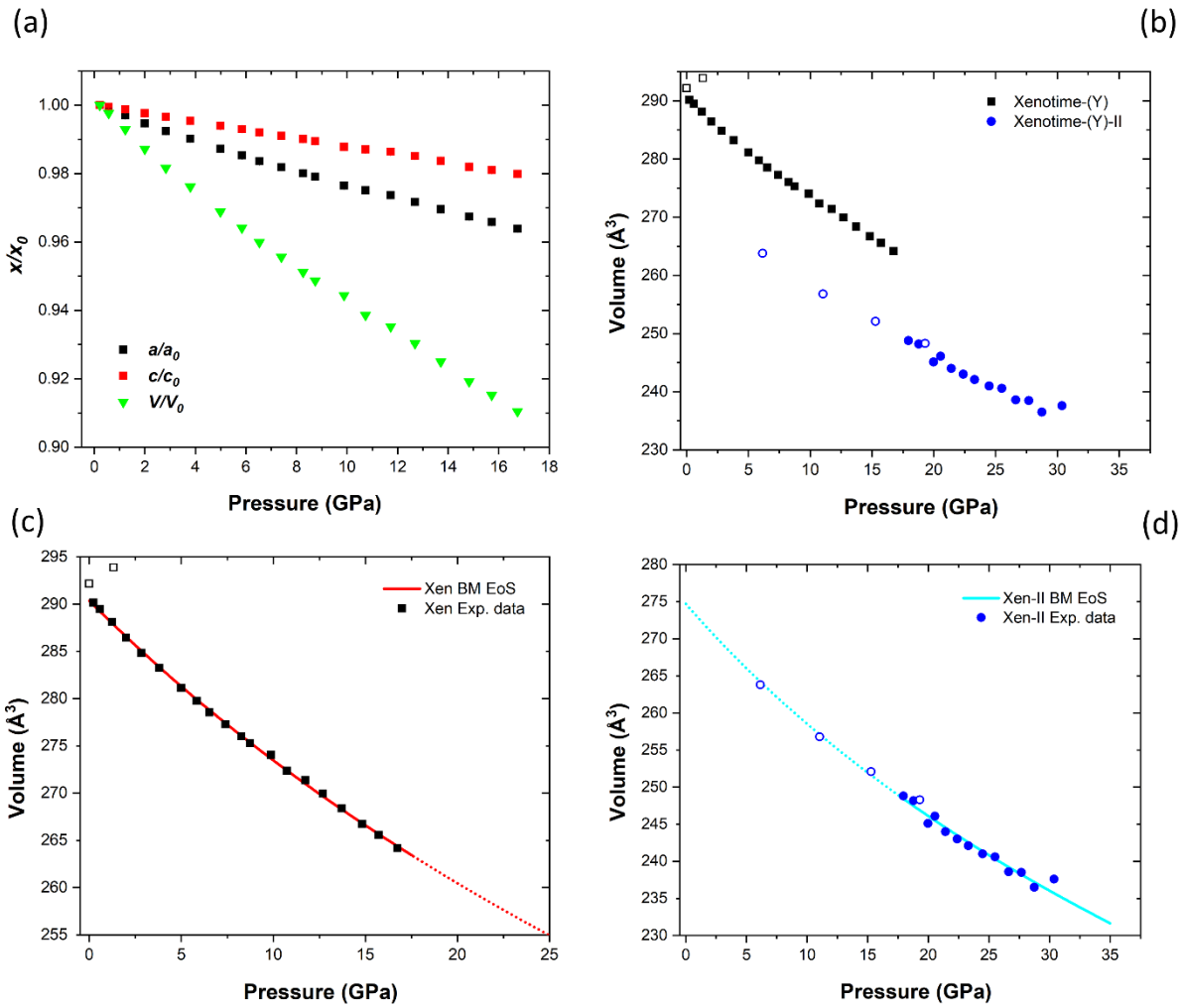

Figure 9.25: evolution as a function of pressure of the **(a)** normalized (to ambient conditions values) unit-cell parameters of xenotime-(Y) (Xen-P_D ramp data); **(b)** unit-cell volume of xenotime-(Y) and xenotime-(Y)-II; high-pressure evolution of the experimental unit-cell volume of xenotime-(Y) **(c)** and xenotime-(Y)-II **(d)**; the red and sky blue lines are the BM-EoS fits of xenotime-(Y) and xenotime-(Y)-II *P*-*V* data respectively. The void dots represent the experimental data collected under decompression while the dotted lines are an extension of the BM-EoS at pressures exceeding stability field of the two phases (see text for further details).

Deformation mechanisms at atomic scale in xenotime-(Y) and xenotime-(Y)-(II)

In the first place, when the zircon-type structure undergoes to a phase transition to a monazite-type, the coordination number of the *A*-site increases from eight to nine. As mentioned above, in xenotime-(Y), the anisotropic compression reported in Figure 9.25a clearly displays a lower compressibility of the [001] axis, the chain-development direction, whereas [100] is characterized by a much more significant contraction. As discussed for chernovite-(Y) in section 9.5.1, the deformation mechanisms accommodating at the atomic scale the bulk compression of xenotime-(Y), could be easily explained by a minor deformation of the chain-units parallel to the **c** axis, while in the (001) plane the structure

has more degrees of freedom and is, therefore, comparatively easier to deform. The evolution of the two independent Y-O bond lengths (*i.e.*, Y-O_a and Y-O_b, which can be defined as the intrachain and the interchain connecting bonds, respectively, as can be seen in Figure 3.4), shows that the Y-O_a is significantly less compressible compared to the Y-O_b. Therefore, the compression of the interatomic bond distances confirms that the REE-coordination polyhedron is more compressible in the (001) plane rather than in the orthogonal direction (*i.e.*, [001], parallel to the *c*-axis).

As already described in section 9.5.1 and section 9.6.1, the *A*-site plays a paramount role, since most of the H*P* compression is accommodated by the contraction of the REE coordination polyhedron itself in both monazite and zircon-type topologies. Considering the data from the structure refinements based on the Xen14-P_D ramp, the compressional evolutions of the volumes of the YO_8 and of the TO_4 coordination polyhedra in xenotime-(Y) have been fitted with a BM2-EoS, yielding a bulk modulus of K_{YO_4}=126(4) GPa (V_0=23.18(4) Å^3) and K_{PO_4}=299(62) GPa (V_0=1.900(9) Å^3) respectively. The bulk modulus of the YO_8 polyhderon is slightly lower compared to that of the unit-cell volume, suggesting that the bulk compressibility is mostly accommodated by the compression of the Y- and HREE-coordination polyhedron.

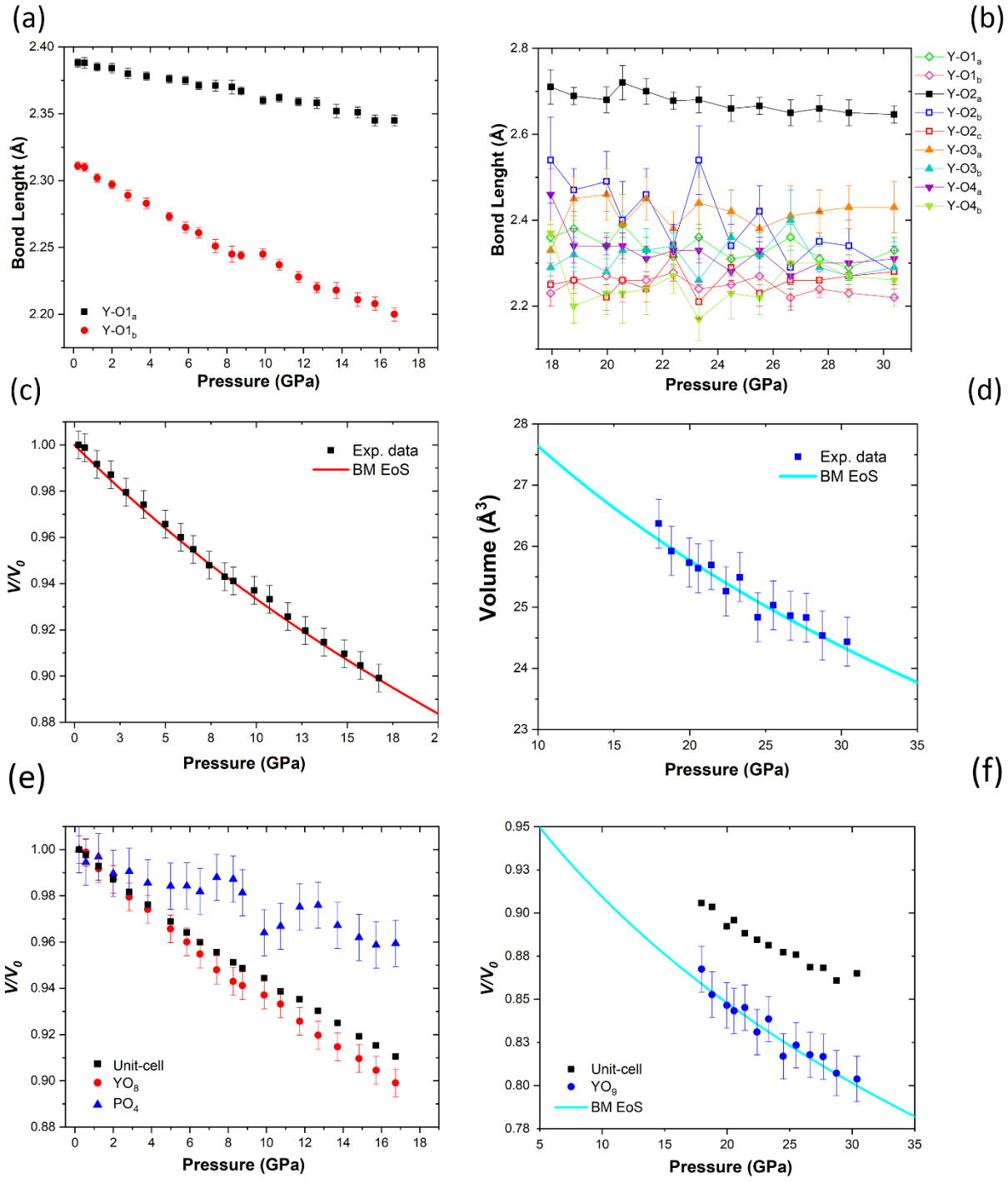

Figure 9.26: evolution as function of pressure of the independent Y-O bond distances pertaining to xenotime-(Y) **(a)** and xenotime-(Y)-II **(b)**; high-pressure evolution of the REE-coordination polyhedron volumes of xenotime-(Y) **(c)** and xenotime-(Y)-II **(d)**; comparative evolution of some relevant structural parameters normalized to their ambient-conditions values (*i.e.*, REE-coordination polyhedron volume, TO_4 polyhedron volume [only for xenotime-(Y)] and unit-cell volume) for xenotime-(Y) **(e)** and xenotime-(Y)-II **(f)**.

The TO_4 structural units, on the other side, behave as quasi-rigid bodies and the overall comparison between the compressional behavior of the two coordination polyhedra and the unit-cell volume in

xenotime-(Y) is reported in the normalized volume *vs* pressure diagram in Figure 9.26e. Following the same criteria, in Figure 9.26f, is reported the compressional behavior of the unit-cell volume and of the YO_9 coordination polyhedron in the xenotime-(Y)-II polymorph. The volume of the TO_4 structural units *vs* pressure is too scattered for the xenotime-(Y)-II and, therefore, these data are not included in Figure 9.26f (see Table 8.14 and Table 8.15 for more details about). The refined bulk modulus of the YO_9 coordination polyhedron of xenotime-(Y)-II is K_{P_0,T_0}=87(26) GPa (V_0=30.4(12) Å^3). Therefore, independently from the structural type, the refined bulk moduli of the REE-coordination polyhedra are always smaller compared to those referred to the bulk volumes (Table 8.9). The compressional behavior of xenotime-(Y)-II, characterized by a lower symmetry with respect to the ambient-conditions polymorph, is much more complicated. Based on the Eulerian strain tensor analysis, it emerges that for xenotime-(Y)-II the direction of higher compressibility lies in the (010) plane, at a low angle with [100].

As shown in section 9.6.1 for gasparite-(Ce) (Figure 9.23), four possible independent lozenge-like units can be drawn in order to describe the relations between a REE-polyhedron and the adjacent ones, describing their distortion. Therefore, the same criteria applied to describe the compressional structural deformation of gasparite-(Ce) have been also applied to xenotime-(Y)-II. As for gasparite-(Ce), in xenotime-(Y)-II, the Y-O2-Y structural angle pertaining the lozenge-like unit I (Figure 9.23a) shows a rather clear opening (see Table 8.15 and section 9.9.2 below). Unfortunately, due to the scattering of the data, such a trend is not shown by the Y-O4-Y structural angle and, hence, it is not possible to unambiguously assess if xenotime-(Y)-II shows a closure of the lozenge-like unit I. The angle P-Y-P decreases with pressure, ranging from 175.9(5)° to 173.7(3)°, accommodating a slight shortening along [001], being the main deformation mechanism active along the *c* crystallographic axis in xenotime-(Y)-II.

9.7.2 High-temperature behavior of xenotime-(Y)

Thermoelastic properties in xenotime-(Y) under high temperature

The evolution of the unit-cell volume as a function of temperature is reported in Figure 9.27a,b, while the thermo-elastic behavior along the two crystallographic directions [100] and [001] is reported in the normalized diagram in Figure 9.27a. The structure is more expansible along the *c* crystallographic direction than in the (001) plane. In the first place, the thermal expansion of xenotime-(Y) has been modelled with the modified Holland-Powell EoS by means of the software *Eosfit_7c* (Gonzalez-Platas et al. 2016; Angel et al. 2014) as well as with a first and second-order polynomial equation with the *TEV* software (Langreiter and Kahlenberg 2015). The corresponding unit-cell volume thermal expansion parameters are reported in Table 8.23 and Table 8.24. Since xenotime-(Y) belongs

to the tetragonal crystal system, the direction of minimum and maximum thermal expansion run along the crystallographic axes [100]=[010] and [001]. A similar thermal evolution of the two crystallographic axes has been defined for several synthetic YPO_4 compounds (Bayer 1972; Subbarao 1968; Schopper 1972; Kahle 1970; Sallese 1986). The thermal expansion, as expected, increases with the temperature, from $\alpha^{HP}_{V_{30°C}}$=9.6(1.2)·10^{-6} K^{-1} at room temperature to $\alpha^{HP}_{V_{780°C}}$=22(2)·10^{-6} K^{-1} at 780°C. The synthetic phosphate counterparts of xenotime-(Y) (*i.e.*, $ScPO_4$, YPO_4, $TmPO_4$, $YbPO_4$ and $LuPO_4$) have been experimentally studied at high temperature by several authors (Schopper 1972; Subbaro et al. 1990; Bayer 1972; Subbarao 1968; Schopper 1972; Kahle 1970; Hikichi 1998; Taylor 1986; Sallese 1986), while theoretical studies on the whole zircon-type phosphate series has been carried out by Li et al. (2009). Conversely to chernovite-(Y), which LTEC determined in this study is significantly lower compared to its synthetic counterparts, the LTEC value refined for the xenotime-(Y) under study is comparable to those reported for other zircon-type YPO_4, characterized by an average LTEC of 5.9·10^{-6} K^{-1}.

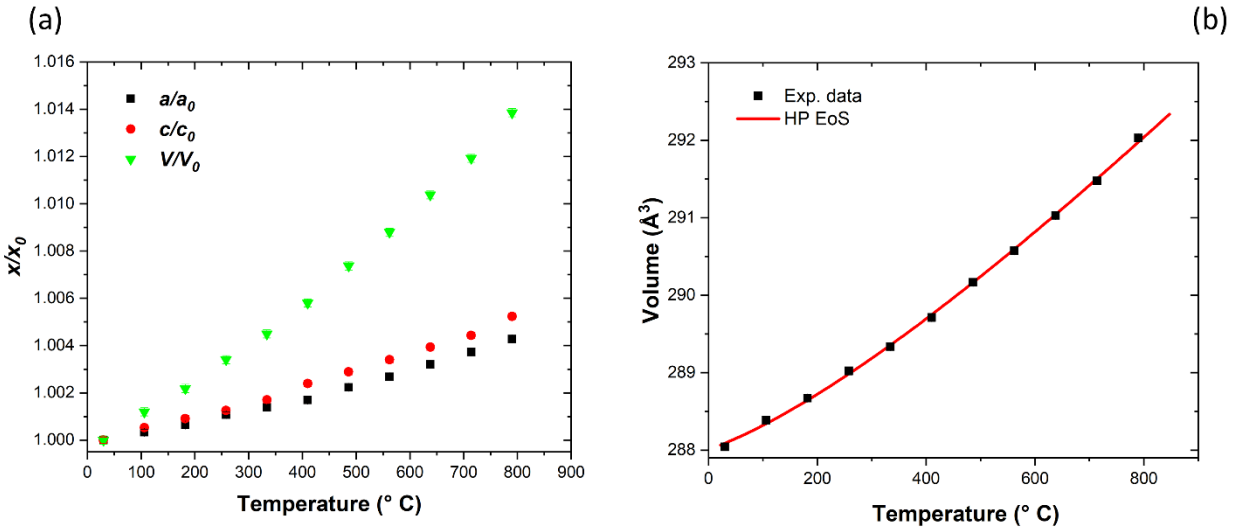

Figure 9.27: evolution as a function of temperature of the **(a)** normalized (to ambient-conditions values) unit-cell parameters of xenotime-(Y), showing that the *c*-axis is more expansible than the *a*-axis; **(b)** experimental unit-cell volume of xenotime-(Y) at high-temperature with the Holland-Powell (HP)-EoS.

Structural behavior of xenotime-(Y) under high temperature

Eventually, the thermal expansion of xenotime-(Y) is discussed from a structural point of view. The evolution of the two independent coordination polyhedral volumes (*i.e.*, TO_4 and AO_8 polyhedra) as a function of temperature has been analyzed and is reported in Table 8.26 and Figure 9.28. From the normalized diagram reported in Figure 9.28d the YO_8 coordination polyhedron appears significantly

more expansible compared to the phosphorus TO_4 polyhedron. The latter shows a rather small thermal expansion, behaving as an almost rigid unit through temperature. The thermal expansion of the YO_8 volume has been modelled with the Holland-Powell EoS. The calculated thermal expansion coefficient at ambient conditions ($\alpha_{YO_8}=18(2)\cdot10^{-6}$ K^{-1}) is higher compared to the one of the unit-cell volume. Finally, the two independent Y-O bond distances show an almost identical thermal expansion in the *T*-range under investigation.

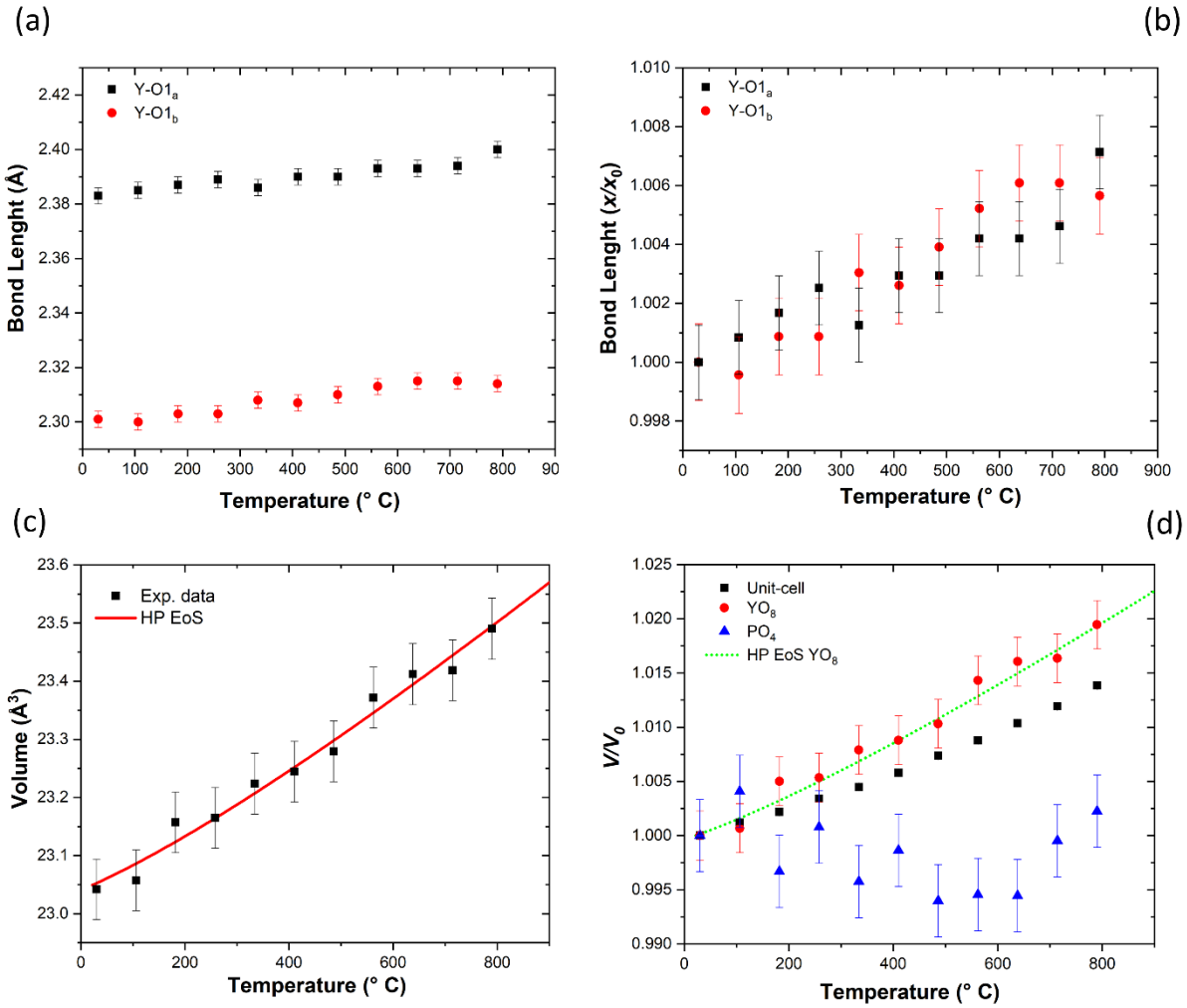

Figure 9.28: evolution, as a function of temperature, of the absolute **(a)** and normalized (to their values at room temperature) values of **(b)** two independent Y-O bond distances, showing the very similar thermal expansion behavior; **(c)** *T-V* diagram for the YO_8 polyedron, with the refined Holland-Powell (HP)-EoS in red; **(d)** comparative thermal expansion of the unit-cell volume, YO_8 and PO_4 polyhedron volumes.

9.8 Behavior of monazite-(Ce) at non-ambient conditions

9.8.1 High-pressure behavior of monazite-(Ce)

Elastic properties of monazite-(Ce) under compression

The H*P*-evolution of the unit-cell parameters of the monazite-(Ce) under study is reported in Table 8.8 and displayed in Figure 9.29. Monazite-(Ce) under H*P* is characterized by an anisotropic deformation, with the [100] and [001] being the most and least compressible directions, respectively, while [010] shows an intermediate compressional behavior. Monazite-(Ce) does not undergo any phase transition in the pressure range under investigation, but experiences a clear change in the compressional behavior, indicated by a deviation in the *P*-induced closure of the β angle at pressures exceeding ~18.4 GPa, which structural reasons are below discussed. Such a change in compressional behavior was already reported to occur in monazite-type compounds, like $LaPO_4$, $CePO_4$ (Huang et al. 2010) and gasparite-(Ce) (see section 9.6.1). On the other hand, as mentioned in section 9.6.1, Errandonea et al. (2018) do not report such a change of the compressional behavior for synthetic $CePO_4$.

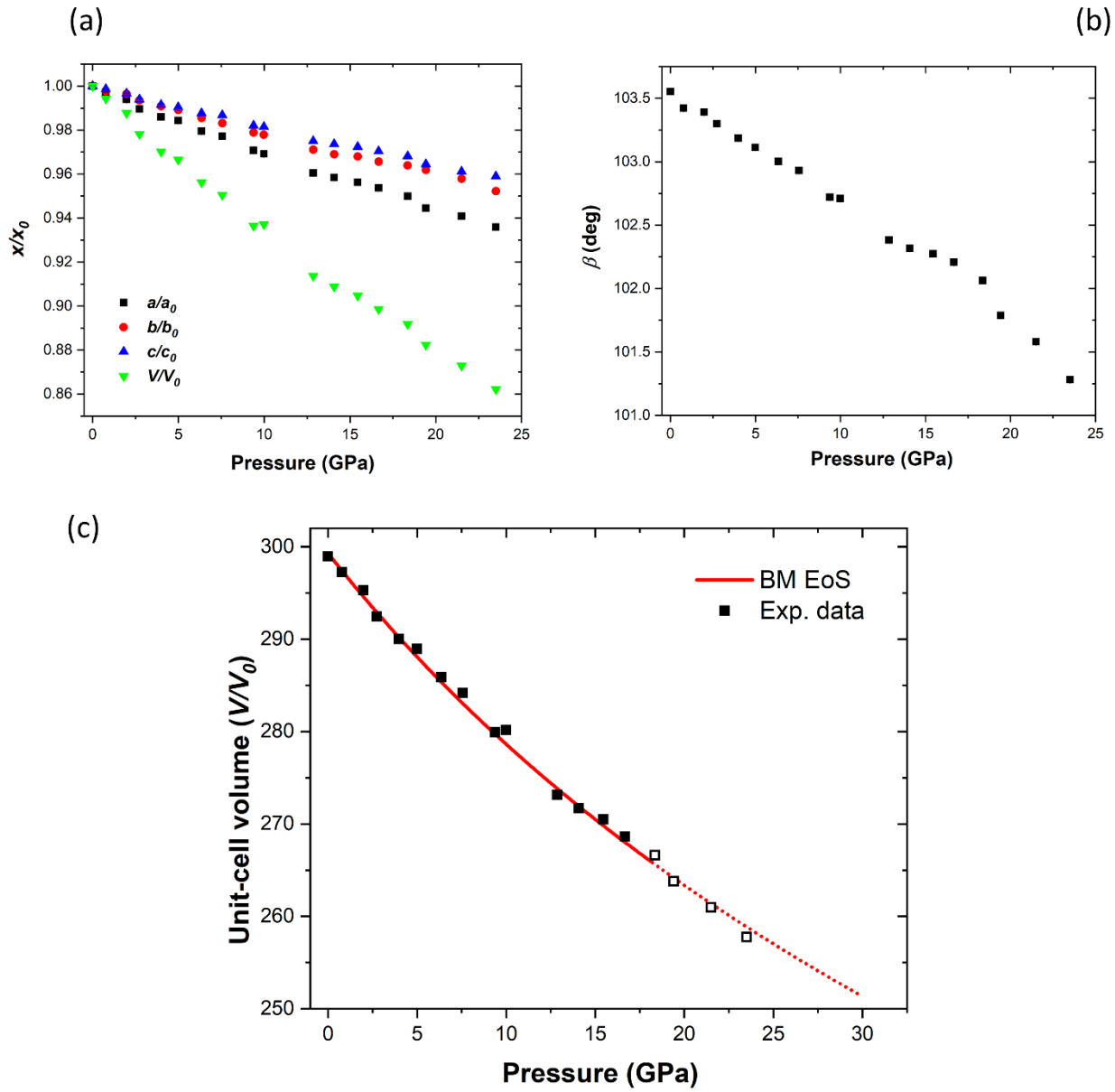

Figure 9.29: **(a)** high-pressure evolution of the experimental unit-cell parameters of monazite-(Ce)(normalized to ambient-conditions values); **(b)** high-pressure evolution of the β angle, showing the kinking at ~18 GPa; **(c)** high-pressure evolution of the experimental unit-cell volume of monazite-(Ce). The void dots represent the experimental data collected at pressure exceeding the change in compressional behavior, the red line represents the fitted BM2-EoS, while the dotted red line is an extension of the BM2-EoS at pressures exceeding the change in compressional behavior (see text for further details).

The bulk modulus at ambient-conditions of monazite-(Ce) has been refined by fitting the experimental *P*-*V* data (before the change in the compressional behavior previously described) with a BM2-EoS, yielding a value of K_{P_0,T_0}=121(3) GPa (β_V=0.0083(2) GPa^{-1}; V_0=299.3(4) Å^3). The bulk modulus is consistent with the experimental ones refined by Huang et al. (2010) and Errandonea et al. (2018). In addition, the compressibility refined in this study is also close to the ones obtained with theoretical models (Li et al. 2009). Moreover, between P_{atm} and 18.39 GPa, the finite Eulerian unit-

strain tensor analysis of monazite-(Ce) has been conducted using the software *Win_Strain* (Angel 2011) and a geometric setting with X//a^*, Y//b. The results show that the ellipsoid axes of maximum and minimum strain do not correspond with any of the crystallographic axes, as described in the following:

$$\begin{pmatrix}\varepsilon_1\\ \varepsilon_2\\ \varepsilon_3\end{pmatrix} \angle \begin{pmatrix}158.2(2)^\circ & 90^\circ & 56.2(2)^\circ\\ 90^\circ & 180^\circ & 90^\circ\\ 68.2(2)^\circ & 90^\circ & 33.8(2)^\circ\end{pmatrix} \cdot \begin{pmatrix}a\\ b\\ c\end{pmatrix}$$

The analysis of the finite Eulerian unit-strain tensor allowed to determine the mean compressibility values along the axes of the strain ellipsoid (with $\varepsilon_1>\varepsilon_2>\varepsilon_3$): ε_1=0.003030(11) GPa^{-1}, ε_2=0.00200(2) GPa^{-1}, ε_3=0.0014(12) GPa^{-1}. The direction of minimum compressibility lays in the (010) plane and the anisotropic scheme is ε_1:ε_2:ε_3=2.16:1.43:1.

Deformation mechanisms at the atomic scale in monazite-(Ce) under compression

The compressional behavior of the nine independent Ce-O bond distances has been described based on the structural models refined at different pressures. The two bond distances pertaining to the O3 atoms are the least compressible. On the other side, the two bonds pertaining to the O2 atoms and lying in the equatorial pentagon (*i.e.*, Ce-$O2_b$ and Ce-$O2_c$, according to Figure 9.30a,b) are the most compressible. Such a behavior of the Ce-O interatomic bonds yields to a slight rotation of the PO_4 tetrahedron that affects the geometry of the chain units, as it is discussed below in the present section.

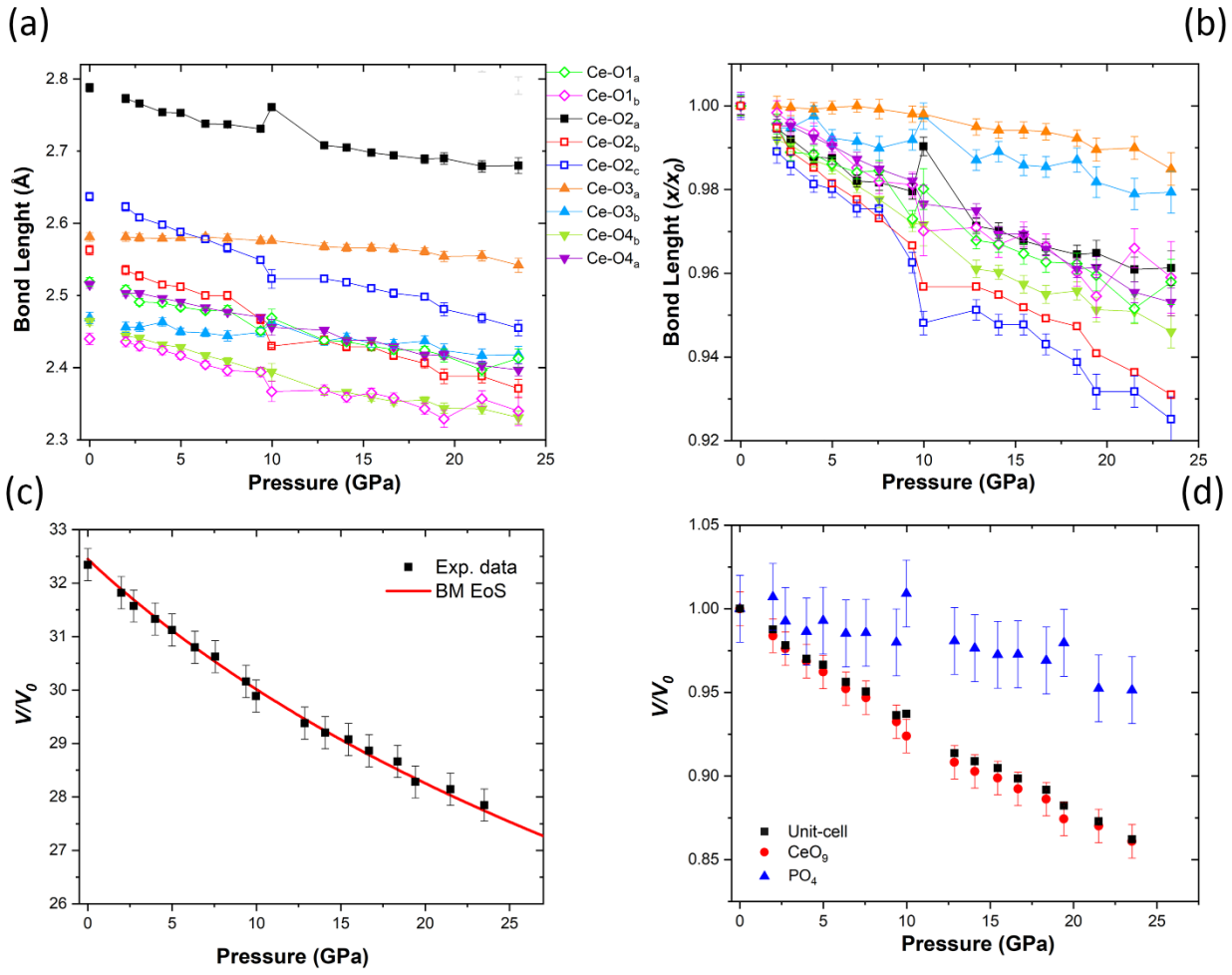

Figure 9.30: High-pressure evolution of the absolute **(a)** and normalized (to ambient conditions) values **(b)** of the nine independent Ce-O bond distances; **(c)** compressional behavior of the CeO_9 coordination polyhedron in monazite-(Ce); **(d)** *P*-*V* diagram (normalized to ambient-conditions values) showing the compressional evolution of the unit-cell, CeO_9 and PO_4 polyhedra volumes.

Moreover, the compressional behavior of the two coordination polyhedra (*i.e.*, TO_4 and CeO_9) has been modelled with a BM2-EoS. In Figure 9.30d, the evolution with pressure of the normalized volume of the polyhedra is compared to that of the unit-cell volume. The compressional behavior of the polyhedra has been modelled taking into account experimental data up to 18.36 GPa, in order to exclude the data following the change in the bulk compressional behavior. The refined bulk moduli are: K_{CeO_9}=110(4) GPa, V_0=32.45(8) Å^3 and K_{PO_4}=395(130) GPa, V_0=1.86(1) Å^3 for the CeO_9 and the TO_4 polyhedra, respectively. As also shown in Figure 9.30c,d, the compressibility of the CeO_9 coordination polyhedron is higher compared to that of the unit-cell volume (K_{P_0,T_0}=121(3) GPa), suggesting its paramount role in accommodating the bulk compression, while the TO_4 tetrahedra is

the less compressible unit. Among the authors who studied the monazite-type topology under high-pressure, the compressional behavior of the coordination polyhedra has been studied by Errandonea et al. (2018) for $LaPO_4$, $CePO_4$ and $PrPO_4$. Indeed, conversely to the results obtained in the present research, Errandonea et al. (2018) calculated a bulk modulus for the $REEO_9$ polyhedra that is slightly stiffer compared to the corresponding ones refined for the unit-cell volume (*i.e.*, K_{REEO_9} =114.2(5) GPa *vs* K_{cell} =120(1) GPa for $LaPO_4$; K_{REEO_9} =117.3(3) *vs* K_{cell} =122(1) GPa for $CePO_4$; K_{REEO_9} =120.2(6) *vs* K_{cell} =124(1) GPa for $PrPO_4$). On the other side, the bulk moduli refined for the PO_4 units are larger than 400 GPa and rather consistent with the one here obtained for monazite-(Ce).

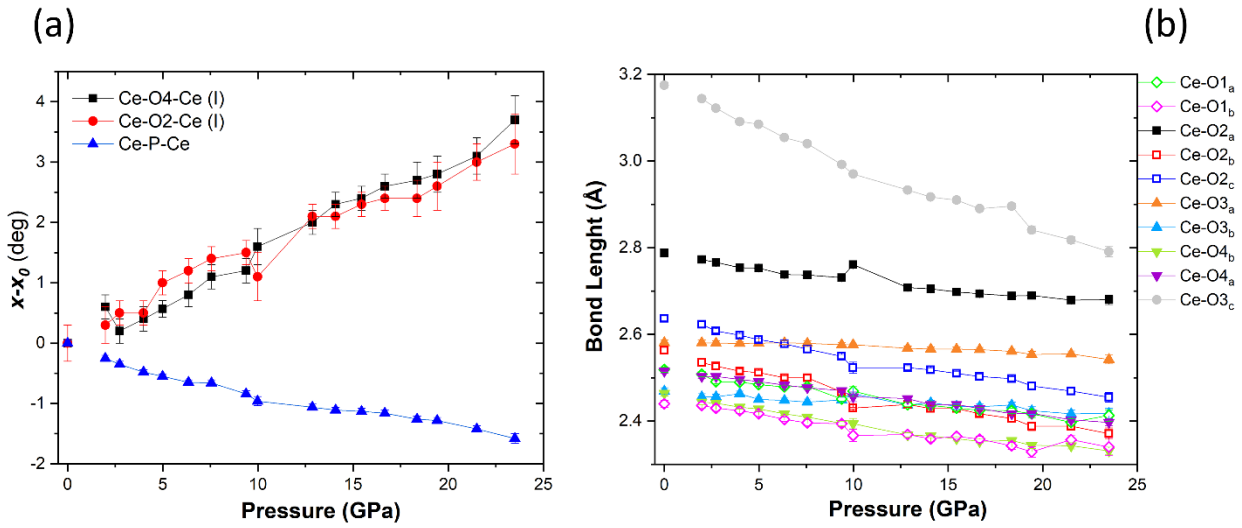

Figure 9.31: high-pressure evolution of **(a)** relevant interatomic angles and **(b)** of the ten Ce-O interatomic distances, showing that the Ce-$O3_c$ is rather more compressible than the others.

Figure 9.24 shows a comparison among the *A*-site coordination polyhedron in the monazite-type and in the postbarite-type (space group $P2_12_12_1$) structures, as it has been described by Ruiz-Fuertes et al. (2016). As described in chapter 3, the main atomic-scale structural difference among the two topologies is the coordination number of the *A*-site, which rises from nine in the monazite-type to eleven in the postbarite-type, respectively. In detail, two oxygen atoms (*i.e.*, $O3_c$ and $O4_c$) gain a new bond with the Ce atom leading to the new Ce-$O3_c$ and the Ce-$O4_c$ interatomic bonds. Therefore, in addition to the nine independent bond distances previously described, the compressional evolution of these two bonds has also been investigated. If no significant trend has been observed for the Ce-$O4_c$ bond, in Figure 9.31b it is reported the compressional evolution of the Ce-$O3_c$ bond as compared to the nine interatomic bonds of the monazite-type structure. The picture diagram (Figure 9.31b) clearly shows that the Ce-$O3_c$ bond is much more compressible than the others. In addition, as the pressure

increases, the Ce-$O3_c$ bond distance decreases from 3.175(6) Å at atmospheric pressure to a minimum of 2.791(12) Å at 23.50 GPa. At pressure exceeding 10 GPa, the Ce-$O3_c$ decreases with a slightly lower rate, reaching a local minimum at 18.36 GPa. Based on the described compressional behavior on the absolute values of the Ce-$O3_c$ interatomic bonds as a function of pressure, we can suggest that the $O3_c$ atom enters the coordination sphere of Ce at ~18 GPa, thus increasing the coordination number of the *A*- site from nine to ten. Consequently, based on these data, and on those previously described for gasparite-(Ce), it can be concluded that the monazite-to-postbarite phase transition is not the result of an abrupt change the in the coordination number of the *A*-site from nine to eleven, but at least an intermediate stage where the *A*-site is in a ten-fold coordination exists, due to a continuous shortening of the Ce-$O3_c$ bond. Apparently, the larger is the *T*-site ionic radius, the faster is the approach of the $O3_c$ atom to the coordination sphere of the *A*-site.

Eventually, following the same scheme used for gasparite-(Ce), the analysis of the interatomic bond angles has been performed: the evolution as a function of pressure of the P-Ce-P and several Ce-O-Ce angles, described as in Figure 9.23 is reported in Table 8.17. It is worth to mention that most of the structural angles here analyzed also show a change in the compressional behavior at ~18 GPa, suggesting that the angular kink of the β angle and the increase in the coordination number of the *A*-site are reflected by the overall crystal structure. The P-Ce-P angle decreases with pressure, yielding to a slight contraction along the [001] direction. Moreover, the 4 independent lozenge-like units connecting the adjacent chains have been considered (see Figure 9.23 and section 9.6.1 for a comprehensive description). The four independent units are defined as following: Ce-O4-Ce–Ce-O2-Ce (I); Ce-O1-Ce–Ce-O2-Ce (II), Ce-O2-Ce–Ce-O2-Ce (III); Ce-O3-Ce–Ce-O3-Ce (IV). Among the other angular deformation, only the unit I, defined by the angular bonds Ce-O2-Ce and Ce-O4-Ce, provides a significant contribution to describe the deformation mechanism in monazite-(Ce). As defined in section 9.6.1, such a unit defines a sinusoidal chain system running along the [101] direction: the expansion of the two Ce-O-Ce angles defining unit-I provides the structural reasons to understand the direction of lowest compressibility.

9.8.2 High-temperature behavior of monazite-(Ce)

Thermoelastic properties in monazite-(Ce) under high temperature

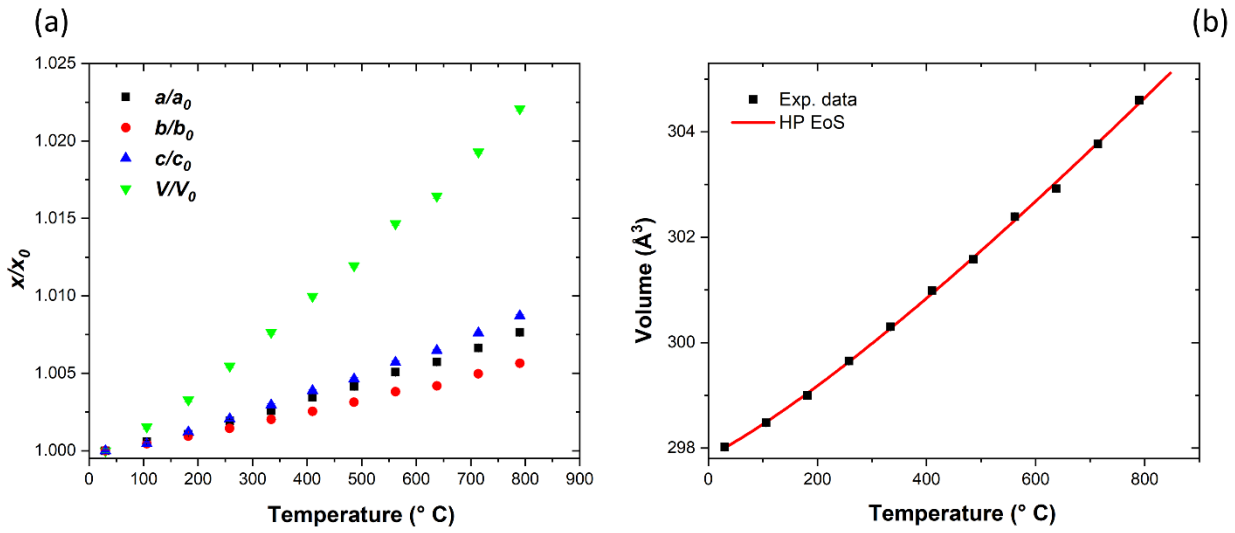

Figure 9.32: **(a)** thermal expansion behavior of the unit-cell parameters (normalized to ambient-conditions values) of monazite-(Ce) under high-temperature; **(b)** thermal expansion of the unit-cell volume of monazite-(Ce) and corresponding Holland-Powell (HP)-EoS.

The evolution of the unit-cell parameters of monazite-(Ce) with temperature is reported in Figure 9.32. The thermal expansion behavior of the unit-cell edges has been modelled with a linear equation, yielding to the following parameters: $\alpha_{[100]}=10.09\cdot10^{-6}$ K^{-1} (a_0=6.7754 Å), $\alpha_{[010]}=7.41\cdot10^{-6}$ K^{-1} (b_0=7.0031 Å) and $\alpha_{[001]}=11.61\cdot10^{-6}$ K^{-1} (c_0=6.4492 Å). In the monoclinic point group, the expansion along the three crystallographic axes does not provide a full description of the anisotropy of thermo-elastic behavior. Therefore, the thermal expansion has been modelled with the *TEV* (Thermal Expansion Visualizing) software (Langreiter and Kahlenberg 2015). The thermal expansion at 400°C is described through the following matrix:

$$\begin{pmatrix}\alpha_1\\ \alpha_2\\ \alpha_3\end{pmatrix} \measuredangle \begin{pmatrix}109.02° & 90° & 5.47°\\ 19.02° & 90° & 84.531°\\ 90° & 0° & 90°\end{pmatrix} \cdot \begin{pmatrix}a\\ b\\ c\end{pmatrix}$$

The mean thermal expansivity values along the axes of the unit-strain ellipsoid, determined between room temperature and 700°C, show a thermal anisotropy ($\alpha_1>\alpha_2>\alpha_3$) described by: $\alpha_1=11.56\cdot10^{-6}$ K^{-1}. $\alpha_2=9.93\cdot10^{-6}$ K^{-1}, $\alpha_3=7.39\cdot10^{-6}$ K^{-1}. Both the directions of minimum and maximum thermal expansion lie in the (010) plane. The anisotropic scheme of monazite-(Ce) upon heating is α_1:α_2:α_3=1.56:1.34:1. The direction of maximum thermal expansion lies at low angle with the [001] direction, the direction of minimum thermal expansion is parallel to [010], while the intermediate thermal expansibility lies at low angle with the [100] direction. In addition, the *TEV* software (Langreiter and Kahlenberg 2015) allows to investigate the Eulerian finite strain tensor as the

temperature increases. Thus, at room temperature and 700°C it is possible to define the following Eulerian finite strain tensors:

$$\begin{pmatrix}\alpha_1\\ \alpha_2\\ \alpha_3\end{pmatrix}_{30°C} \measuredangle \begin{pmatrix}108.93° & 90° & 5.39°\\ 18.93° & 90° & 84.61°\\ 90° & 0° & 90°\end{pmatrix}_{30°C} \cdot \begin{pmatrix}a\\ b\\ c\end{pmatrix}$$

$$\begin{pmatrix}\alpha_1\\ \alpha_2\\ \alpha_3\end{pmatrix}_{700°C} \measuredangle \begin{pmatrix}120.66° & 90° & 5.54°\\ 19.10° & 90° & 84.46°\\ 90° & 0° & 90°\end{pmatrix}_{700°C} \cdot \begin{pmatrix}a\\ b\\ c\end{pmatrix}$$

The direction of maximum thermal expansion turns ~10° clockwise around the rotation axis [010]. The bulk thermal expansion of the unit-cell volume has been modelled with a linear equation, a 2nd order polynomial and the Holland-Powell EoS. The α_V^{HP} ranges between 19.9(1.3)·10^{-6} K^{-1} at room temperature (as reported in Table 8.23) and 30(2)·10^{-6} K^{-1} at 780°C. The unit-cell volume thermal expansions modelled with both the linear and polynomial equations are rather consistent with α_V^{HP}. Indeed, the α_V^L, which describes the average thermal expansion in the range between room temperature and 780°C is close to the $\alpha_{V_{360°C}}^{HP}$=28(2)·10^{-6} K^{-1}, *i.e.* the thermal expansion coefficient calculated by the Holland-Powell EoS at 360°C.

Numerous studies have been dedicated to $CePO_4$ and other monazite-type phosphates under H*T*. The LTEC of the monazite-(Ce) from the current study is reported in Figure 9.33, along with several values reported by previous authors, carried out with different approaches, including *in situ* H*T* X-ray diffraction, dilatometry and theoretical models (see Table S13.18). The weighted ionic radius of the *A*-site in monazite-(Ce) lies between the ones of $^{IX}Ce^{3+}$ and $^{IX}Pr^{3+}$. Several authors (Hikichi 1997; Zhang et al. 2008; Li et al. 2008), in comparative studies, show that the LTEC increases along with the ionic radius of the *A*-site (see Figure 9.33). The thermal expansion coefficients are rather scattered and several LTEC have been defined for monazite-type compounds: for instance, the LTEC defined for $LaPO_4$ ranges from 7.5·10^{-6} K^{-1} to 10.5·10^{-6} K^{-1} (Morgan and Marshall 1995), while the one of $CePO_4$ lies between 7.71·10^{-6} K^{-1} to 9.9·10^{-6} K^{-1} (Li et al. 2009; Hikichi 1997). Therefore, the LTEC of the natural monazite-(Ce) of this study is consistent with the other values experimentally determined for $CePO_4$ (Asuvathraman and Kutty 2014; Hikichi et al. 1997) and $LaPO_4$ (Morgan and Marshall 1995; Hikichi 1998; and Perrière et al. 2007). In addition, the axial thermal expansions defined in the present study are consistent with those determined by Asuvathraman et al. (2014) and reported in Table S13.18. Eventually, the results of the present research confirm that the LTECs modelled by Li et al. (2009) by means of theoretical models are, in general, rather underestimated.

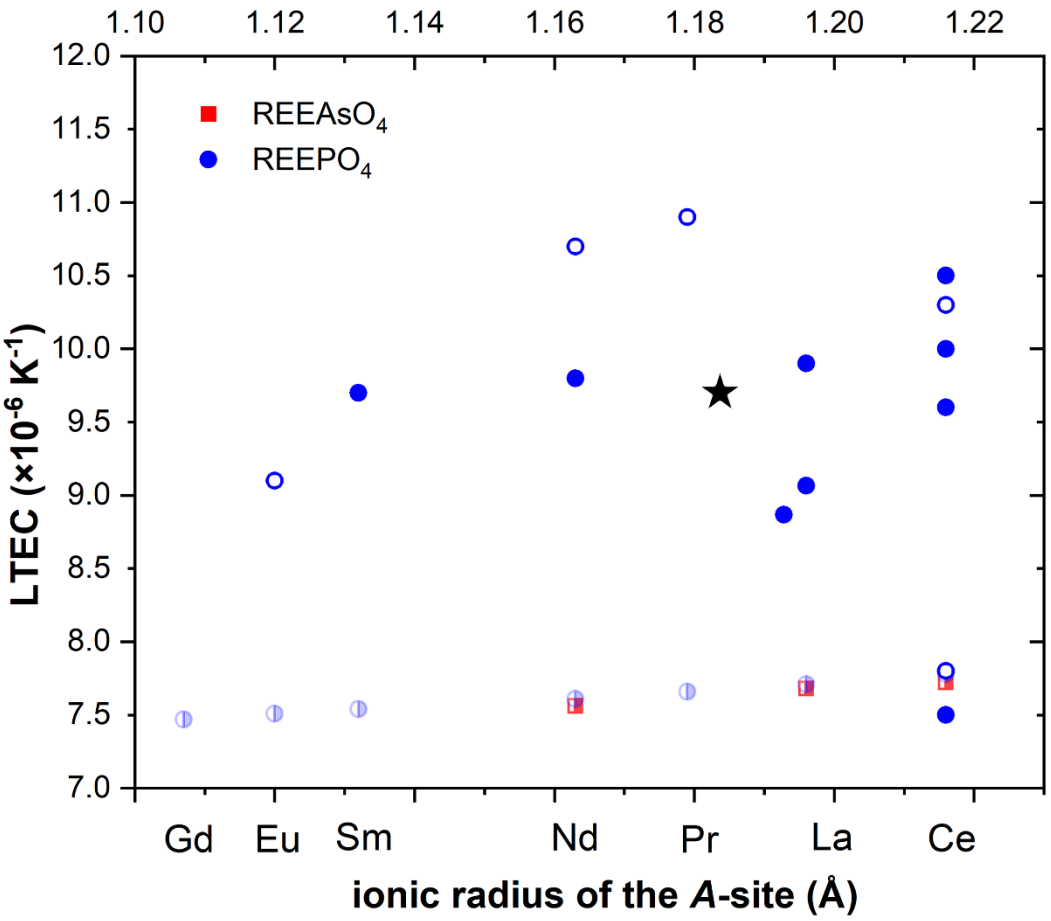

Figure 9.33: comparative linear thermal expansion coefficient of the studied monazite-(Ce) with those of other monazite-type compounds; the star symbol refers to the LTEC of monazite-(Ce) determined in the present study; filled symbols refer to LTEC based on X-ray diffraction experiments; void symbols refer to dilatometry data, while half-filled symbols pertain to theoretically-determined LTEC; the x-axis refers to the weighted atomic radii of the A-site: the value of the studied sample (star symbol) is based on the crystal chemical compositions of Mon14, according to Table S13.18. A complete list of the references is contained in Table S13.18.

Structural behavior of monazite-(Ce) at high temperature

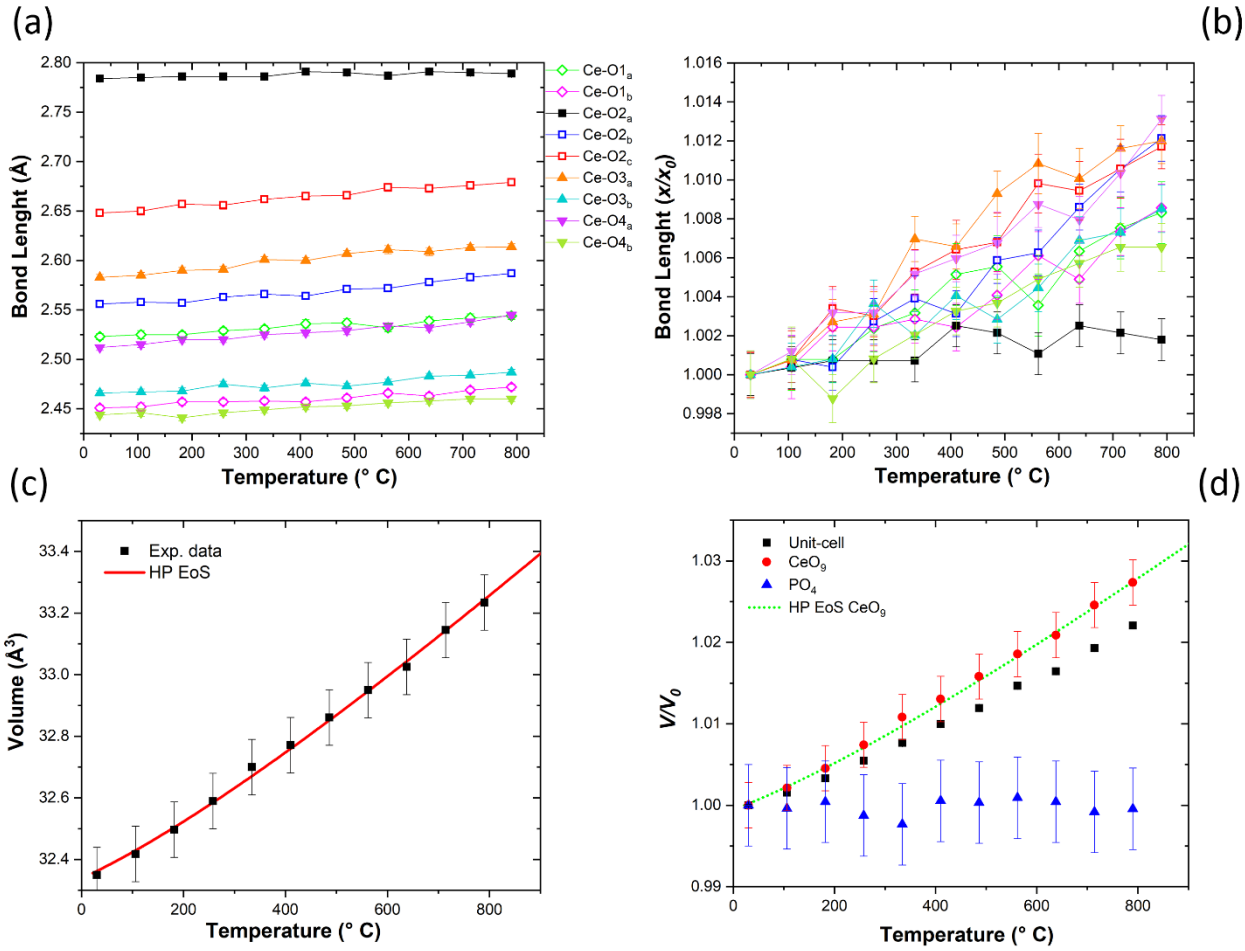

Figure 9.34: High-temperature evolution of the absolute **(a)** and normalized (to ambient conditions) values **(b)** of the nine independent Ce-O bond distances of monazite-(Ce); **(c)** behavior, upon high-temperature, of the CeO_9 coordination polyhedron volume in monazite-(Ce), where the red line refers to the fitted Holland-Powell (HP)-EoS; **(d)** *T-V* diagram (normalized to ambient-conditions values) showing the evolution, under heating, of the unit-cell, CeO_9 and PO_4 polyhedra volumes. The dotted green line refers to the Holland-Powell (HP)-EoS fitted to the V_{CeO_9} *vs. T* data.

The expansive behavior of the two coordination polyhedra in monazite-(Ce) is reported in Figure 9.34d and Table 8.28. In the first place, the CeO_9 polyhedron is more expansible compared to the TO_4 unit, which does not expand significantly in the whole *T*-range investigated. Moreover, as reported in Figure 9.34d, the unit-cell volume is slightly less expansible compared to the CeO_9 polyhedron, suggesting the important role of this unit in accommodating the bulk thermal expansion. Such a result is confirmed by the fitted equations of state of CeO_9 and unit-cell volume. The volume of the CeO_9 units, as a function of temperature, has been modelled with a Holland-Powell EoS using the *Eosfit_7c* software (Gonzalez-Platas et al. 2016; Angel et al. 2014). The thermal expansion coefficient of the

CeO_9 coordination polyhedron at ambient conditions is $\alpha_{CeO_9}^{HP}$=25(2)·10^{-6} K^{-1}, while the corresponding refined parameters are reported in Table 8.29.

Figure 9.34a,b shows the structural analysis conducted on the nine independent Ce-O bond distances in monazite-(Ce). From the temperature *vs* normalized bond distances (Figure 9.34b), three major trends can be drawn, as function of their thermal expansivity. Among the Ce-O bond distances, the Ce-$O2_a$ is significantly longer and the least expansible. On average, there are four more expansible bond distances (*i.e.*, Ce-$O2_c$, Ce-$O2_b$, Ce-$O3_a$ and Ce-$O4_a$) and four bond distances with a an "intermediate" thermal expansion (*i.e.*, Ce-$O1_a$, Ce-$O1_b$, Ce-$O3_b$ and Ce-$O4_b$). It is worth to mention that half of the bond distances with the "intermediate" thermal expansivity (apart from Ce-$O2_b$ and Ce-$O2_c$) are the ones that connect Ce with adjacent chain units, constituting the so-called equatorial pentagon in monazite-type structure (see Figure 3.6). The limited expansion of the Ce-$O2_a$ bond distance reasonably drives to the slight increase in the P-Ce-P angle along the [001] direction, as shown in Figure 9.35b.

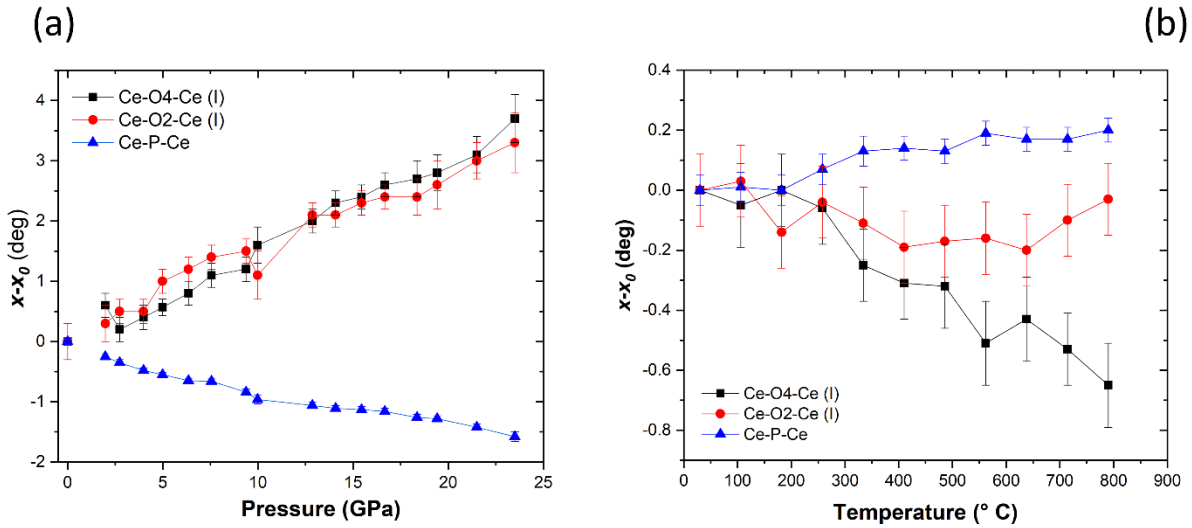

Figure 9.35: comparison among the compressional behavior **(a)** and the expansive behavior **(b)** of the Ce-O4-Ce–Ce-O2-Ce (I) angles of the lozenge-like structure and of the Ce-P-Ce structural angle. Note the opposite trends of the bond angles upon heating and compression.

As already discussed in section 9.6.1, the four set of lozenge-like units [Ce-O4-Ce–Ce-O2-Ce (I); Ce-O1-Ce–Ce-O2-Ce (II), Ce-O2-Ce–Ce-O2-Ce (III); Ce-O3-Ce–Ce-O3-Ce (IV)] can be successfully used to describe the thermal expansion deformation mechanisms of monazite-type phases here investigated (see Figure 9.23). The evolution with temperature of the four independent units, defined by the six independent Ce-O-Ce angles, is reported in Table 8.28. Among the lozenge-like structures, only the unit I (*i.e.*, Ce-O4-Ce–Ce-O2-Ce in Figure 9.23) shows a clear trend with temperature. In

Figure 9.35a, is reported the significant evolution with temperature of the Ce-O-Ce unit I, according to the structural deformation mechanism identified in monazite-(Ce). Indeed, the Ce-O4-Ce (I) bond angle undergoes a clear closure with increasing temperature, and, in a similar way, although rather slightly, the Ce-O2-Ce (I) also decreases with temperature. Among the other lozenge-like units, the Ce-O3-Ce–Ce-O3-Ce (IV) angles close with temperature (Table 8.28), although the geometric configuration of the two differently-oriented unit IV within the unit-cell (as reported in Figure 9.23) partially neutralize the potential impact of such deformation mechanism on the bulk volume variation.

9.8.3 Combined H*P*–H*T* behavior of monazite-(Ce)

Compressional behavior of monazite-(Ce) under combined H*T*–H*P* conditions

As reported in section 8.7, the *P*-*V*-*T* EoS has been fitted to the H*P* (at ambient-*T*), H*T* (at ambient-*P*) and combined H*T*–H*P* data, by using a 2nd order Birch-Murnaghan EoS and a modified Holland-Powell EoS and refining a constant $(dK/dT)_P$. The resulting parameters are reported in Table 8.23. The corresponding refined room-*T* α_V and *K* (see Table 8.32) are rather close to the elastic parameters refined in the individual H*P*- and H*T*-ramps of monazite-(Ce) (see Table 8.9 and Table 8.23). To the best of our knowledge, there are no studies about the elastic and structural behavior of monazite-type compounds under combined H*T*–H*P* conditions: therefore, there are no data to compare this study to. The structural behavior of monazite-(Ce) under H*T*–H*P* conditions is discussed below.

Structural behavior of monazite-(Ce) under combined H*T*–H*P* conditions

The same structural parameters used to describe the behavior of monazite-(Y) at high temperature (and ambient-*P*) and high pressure (and ambient-*T*) have been considered in the two combined ramps. The compressional behavior of the major structural units (*i.e.*, CeO_9 and PO_4 polyhedra) has been considered. The volume of the polyhedra has been determined with the tools implemented in the software *Vesta3* (Momma and Izumi 2011). The evolution with pressure of the CeO_9 has been modelled with a 2nd order Birch-Murnaghan EoS, yielding the following bulk moduli for the Mon14-*PT*$_{250}$ ramp and Mon14-*PT*$_{500}$ ramp respectively: $K_{CeO_9}^{250^\circ C}$=91(11) GPa (V_0=32.9(2) Å^3) and $K_{CeO_9}^{540^\circ C}$=108(9) GPa (V_0=32.9(2) Å^3).

As already discussed in section 9.6.1, 9.7.1, 9.8.1 and 9.8.2, the set of four lozenge-like units [Ce-O4-Ce–Ce-O2-Ce (I); Ce-O1-Ce–Ce-O2-Ce (II), Ce-O2-Ce–Ce-O2-Ce (III); Ce-O3-Ce–Ce-O3-Ce (IV)] can be successfully used to describe the compressional deformation mechanism of the monazite-type phases here investigated (see Figure 9.23). It is worth to mention that the *P*-dependent trends are comparable for all the analyzed bond angles. Eventually, the evolution of the P-Ce-P bond angle, in the two H*T*–H*P* ramps, shows a clear trend, analogous with the one drawn based on the data of the

Mon14-P_H ramp at ambient-T. It can therefore be concluded that the CeO_9 polyhedron deforms with the same mechanisms in the three independent ramps.

(a)

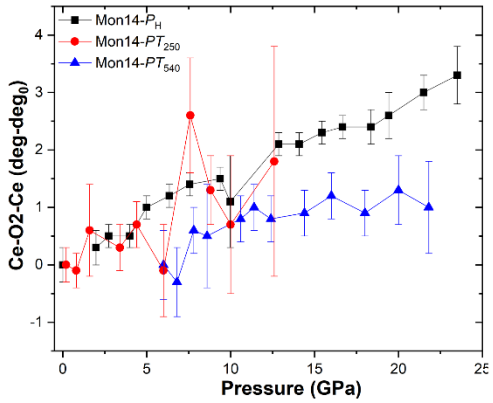
Mon14-P_H
Mon14-PT_{250}
Mon14-PT_{540}
Ce-O2-Ce (deg-deg$_0$)
Pressure (GPa)

(b)

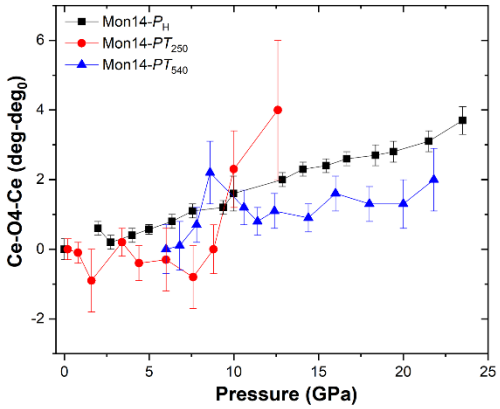
Mon14-P_H
Mon14-PT_{250}
Mon14-PT_{540}
Ce-O4-Ce (deg-deg$_0$)
Pressure (GPa)

(c)

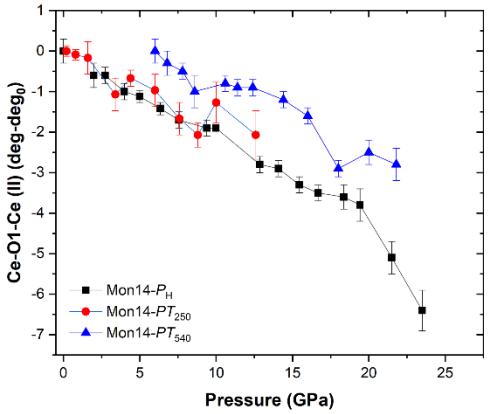
Mon14-P_H
Mon14-PT_{250}
Mon14-PT_{540}
Ce-O1-Ce (II) (deg-deg$_0$)
Pressure (GPa)

(d)

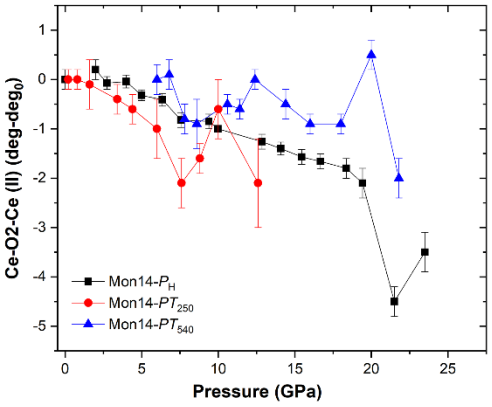
Mon14-P_H
Mon14-PT_{250}
Mon14-PT_{540}
Ce-O2-Ce (II) (deg-deg$_0$)
Pressure (GPa)

(e)

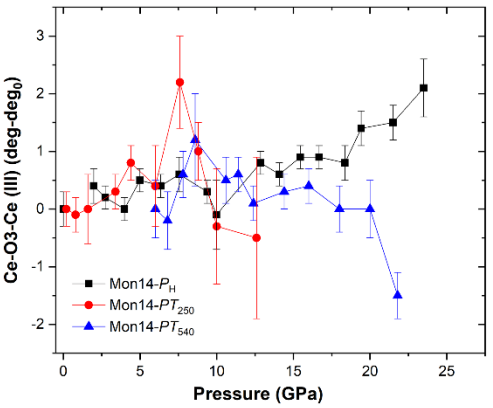
Mon14-P_H
Mon14-PT_{250}
Mon14-PT_{540}
Ce-O3-Ce (III) (deg-deg$_0$)
Pressure (GPa)

(f)

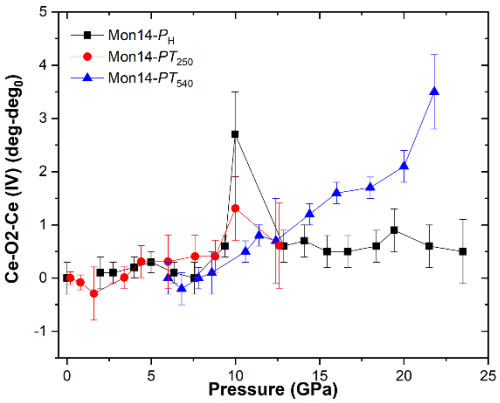
Mon14-P_H
Mon14-PT_{250}
Mon14-PT_{540}
Ce-O2-Ce (IV) (deg-deg$_0$)
Pressure (GPa)

(g)

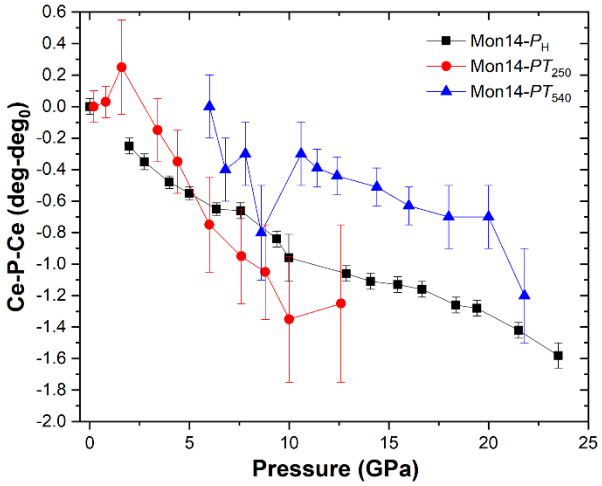
Mon14-P_H
Mon14-PT_{250}
Mon14-PT_{540}
Ce-P-Ce (deg-deg$_0$)
Pressure (GPa)

Figure 9.36: Comparison among the compressional behaviors of seven relevant bond angles of monazite-(Ce), from the refined models based on the data collected in three independent isothermal ramps (Mon-P_H, Mon14-PT_{250} and Mon14-PT_{500}).

9.9 Comparative analysis of the compressional behavior of the studied ATO_4 minerals

In this section, the compressional behaviors of the zircon-type and of the monazite-type minerals studied in this research are discussed and compared with literature data. First of all, the compressional behavior of the analyzed minerals suggests that, in general, the studied monazite-type compounds are more compressible compared to the zircon-type ones. On the other side, as Figure 9.37 shows, this conclusion may be biased by the role played by the ionic radius of the *A*-site. If, on one side, the bulk modulus decreases across the Ln series from the smaller Lu to the larger La for any group of compounds (*i.e.*, phosphates or arsenates), a discontinuity associated to a stiffening (i.e. increase in the bulk modulus value) occurs when the structure topology changes from the zircon- to monazite-type (Figure 9.37). Therefore, the lower bulk moduli shown by gasparite-(Ce) and monazite-(Ce), when compared to chernovite-(Y) and xenotime-(Y) respectively, can be mainly ascribed to the significant difference in the ionic radius of their *A*-sites, rather than to the structure topology. It can be concluded that the softening induced by the increase in the *A*-site ionic radius in gasparite-(Ce) and monazite-(Ce) is larger in magnitude than the stiffening induced by the shift from the zircon- to the monazite-type topology. In this respect, it is an anomaly the elastic behavior described in this study for xenotime-(Y) and its high-pressure polymorph xenotime-(Y)-II. Since the first shows a zircon topology and the latter a monazite one, a stiffening would be expected following the phase transition, but a quite similar bulk compressibility has been observed. In a similar way, such a result is confirmed by the compressional behavior of the two polymorphs of $LaVO_4$ (*i.e.*, the monazite- and the zircon-type, determined by Errandonea et al. (2014) and Yuan et al. (2015) respectively). The bulk modulus for the monazite-type $LaVO_4$ is K_{P_0,T_0}=95(5) GPa (Errandonea et al. 2016), while the one for the zircon-type $LaVO_4$ is K_{P_0,T_0}=93(2) GPa (Yuan et al. 2015). This aspect will be further discussed later.

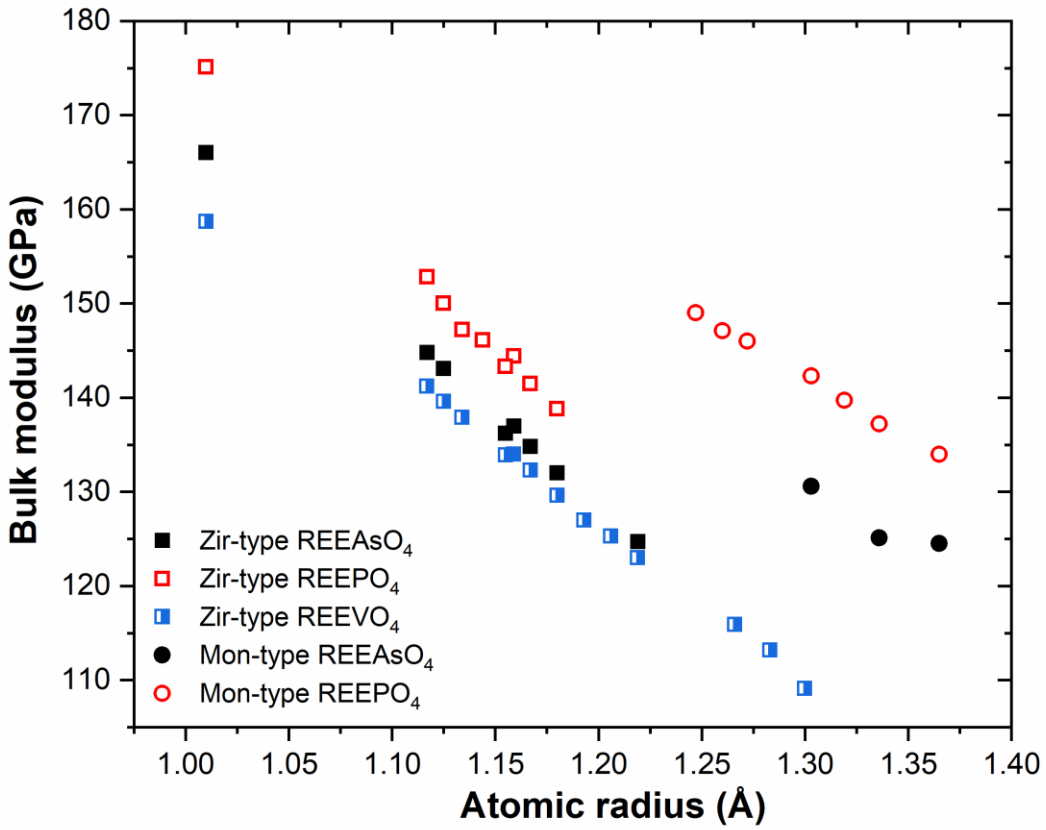

Figure 9.37: bulk moduli *vs A*-site atomic radii for several REE*T*O$_4$ (*T*=As,P,V) minerals after Li et al. (2009) and Zhang et al. (2008).

Moreover, it has been confirmed that, among each structural type, the arsenates are more compressible with respect the isostructural phosphates: indeed, gasparite-(Ce) is more compressible than monazite-(Ce), while chernovite-(Y) is more compressible than xenotime-(Y). The comparison among the compressional behaviors of the REEPO$_4$, REEAsO$_4$ and REEVO$_4$ based on literature data is reported in Figure 9.38. The modelled elastic behaviors of the minerals investigated in this study (Figure 9.38) confirm this conclusion.

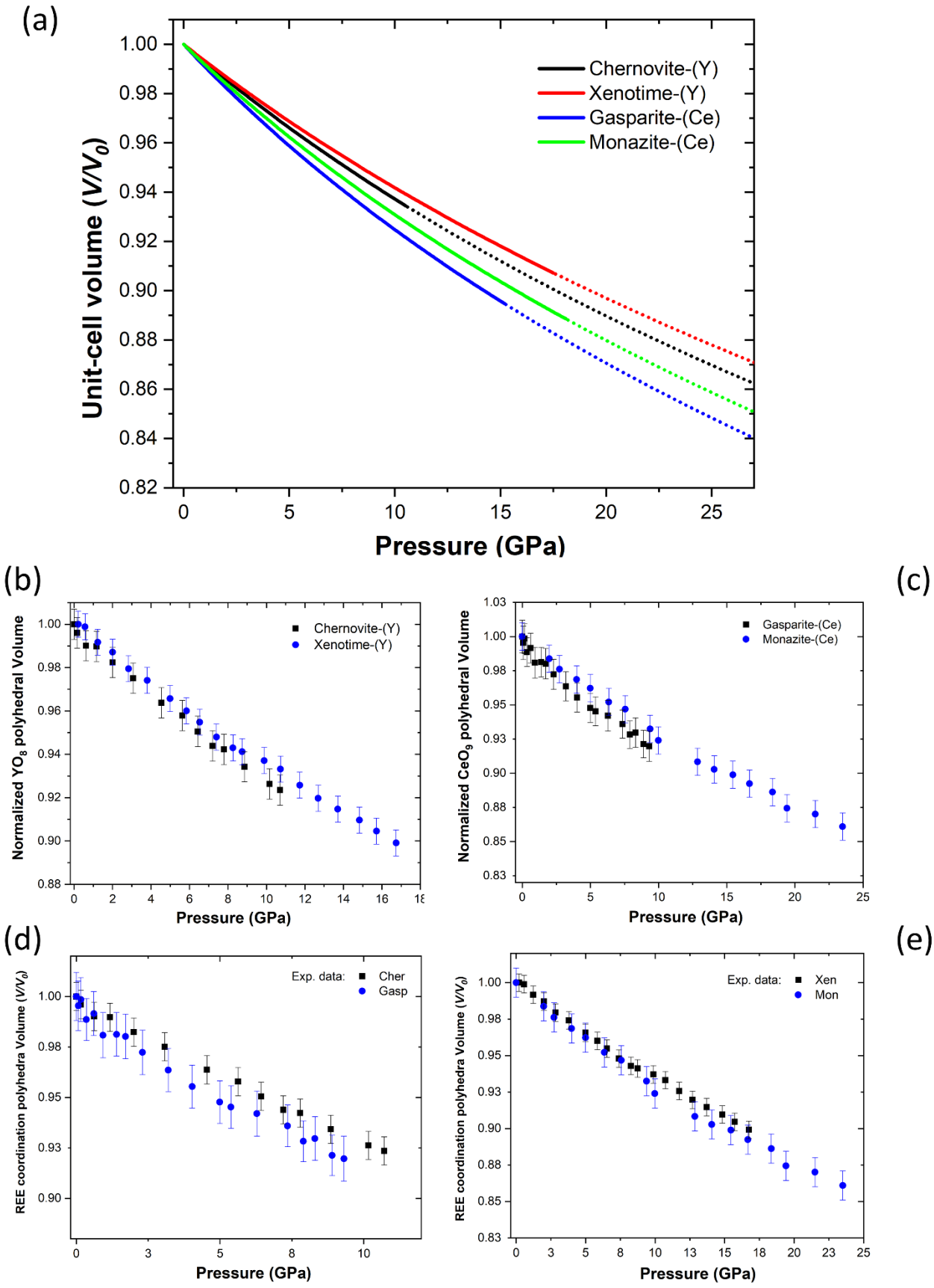

Figure 9.38: **(a)** comparison among the compressional behaviors of all the minerals under investigation; the continuous lines represent the BM-EoS of the studied minerals, while the dotted lines are the extrapolation of

the EoS after their stability fields. Comparison among the compressional behavior of the REE coordination polyhedra between zircon- **(b)** and monazite-type **(c)** minerals, showing that these structural units are less compressible in the phosphates compared to the isostructural arsenates. Comparison among the compressional behavior of the REE coordination polyhedra in arsenates **(d)** and phosphates **(e)**, showing that these units are always are less compressible in zircon-type compounds for both the arsenates and phosphates series.

The *A*-site coordination environment absorbs most of the compression, while the *T*-site behaves as a rather rigid unit (K_{TO_4}>300 GPa). Such a conclusion is confirmed by the results reported by Errandonea et al. (2018) and Gomis et al. (2017). In all the compounds investigated in the present research, the bulk moduli refined for the REE-coordination polyhedral volumes are always slightly smaller compared to the ones of the unit-cell volumes. The compressional behavior of the REE polyhedra is reported in Figure 9.38. The compressional evolution of the REE polyhedral volumes among the two structural topologies (Figure 9.38b,c) and the comparative ones among arsenates (Figure 9.38d) and phosphates (Figure 9.38e) shows that the compressional behavior of the REE polyhedron follows the same trends of the unit-cell volume: *i.e.*, it is significantly influenced by the chemical composition of the *T*-site (section 9.3), which apparently exerts the stronger control on the compressional behavior. The AsO_4 tetrahedron, indeed, is more compressible than the PO_4 one and this concurs to the higher compressibility of arsenates with respect to phosphates. However, as discussed earlier, the elemental nature of the *T*-site affects all the structural features of ATO_4 compounds, not only the size of the tetrahedral unit. How the influence of the crystal chemistry on the crystal structure affects the behavior at non-ambient conditions of temperature and pressure will be discussed more in detail in the following sections.

9.9.1 Zircon-type compounds at H*P*: chernovite-(Y) *vs* xenotime-(Y)

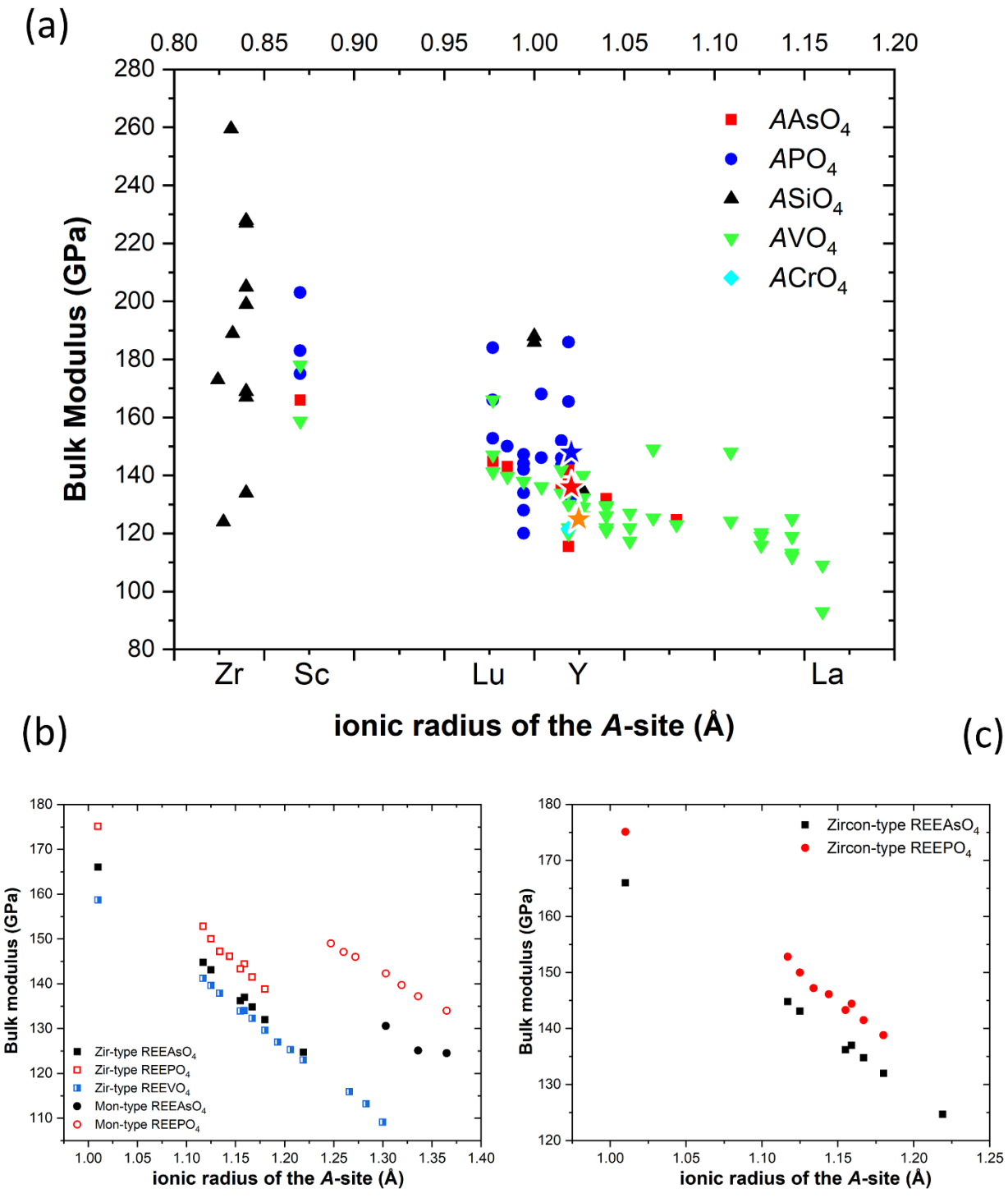

Figure 9.39: **(a)** comparative bulk moduli of zircon-type structure compounds studied in the present research with literature data (both experimental and theoretical data); the red, orange and blue stars represent the bulk moduli of Ch10-P_B, Ch13-P_C and Xen14-P_D ramps respectively; a complete list of the references is contained in Table S13.17; within the *x*-axis, the atomic species corresponding to some ionic radii is reported. **(b)** Bulk moduli of REE arsenates, phosphates and vanadates after Zhang et al. (2008) and Li et al. (2008), showing the theoretical relations among the bulk moduli and ionic radius of the *A*-site within the two structural topologies treated (*i.e.*, monazite- and zircon-type). **(c)** theoretical bulk moduli of the zircon-type arsenates and

phosphates after Li et al. (2009), showing the effect of the *A*- and the *T*-site in controlling the bulk moduli of ATO_4 compounds.

Both chernovite-(Y) and xenotime undergo a phase transition (with different high-pressure polymorphs) in the pressure-range studied, with the zircon-type phase - xenotime-(Y) - having a larger stability field. Figure 9.39 reports the refined bulk moduli of chernovite-(Y) (Ch10-P_{AB} and Ch13-P_C datasets) and xenotime-(Y) (Xen14-P_D dataset). As already mentioned, the compressional behavior of the ATO_4 minerals with zircon-type topology is described through the deformation of the *A*-site and the *T*-site coordination environments. Therefore, most of the present discussion is focused on these structural units.

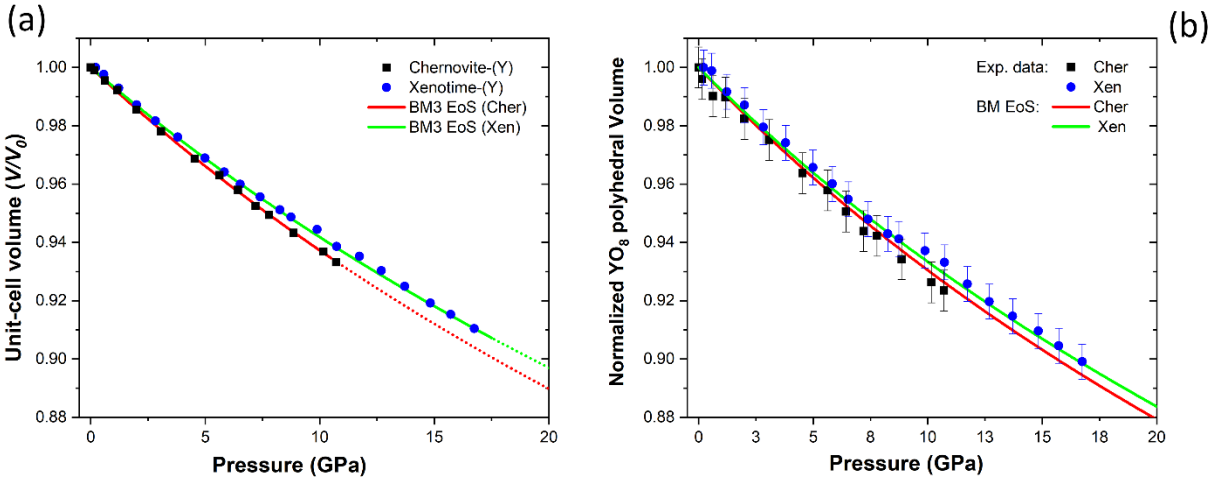

Figure 9.40: comparison among the compressional behavior of chernovite-(Y) (Ch10-P_B dataset) and xenotime-(Y) (Xen14-P_D dataset): **(a)** unit-cell volume and **(b)** YO_8 coordination polyhedron, both normalized to ambient-conditions values.

As discussed in section 9.1.1, no significant difference in the *A*-site composition among the Ch10 and the Xen14 samples exists. In addition, as already discussed above (section 9.3), the chemical composition of the *T*-site exerts a strong control on the structural features of ATO_4 minerals, especially on the *A*-site polyhedral volume and bond distances, whereas the crystal chemistry of the the *A*-site apparently exerts a milder control on the crystal structural features. Whether the *T*-site is mostly occupied by As or P affects the size of the *A*-site polyhedron: larger when the larger As prevails in the *T*-site, smaller when the smaller P is the prevailing tetrahedral cation. Consequently, the Y-O bond distances in chernovite-(Y) are longer, compared to the same structural features in xenotime-(Y). The experimental data of this study suggest that the larger *A*-site of arsenates is more compressible with respect to the smaller REE-hosting polyhedron of phosphates, at a similar chemical

composition in terms of Y and HREE (Figure 9.400b). The same behavior is reflected by the Y-O bond distances (Figure 9.41). In addition, as suggests Table 8.18, the AsO_4 tetrahedron is more compressible than the PO_4 one. Therefore, the observed different compressibility among chernovite-(Y) and xenotime-(Y) can be mainly ascribed to the different chemical composition of the *T*-site cations and its influence on the overall structural features.

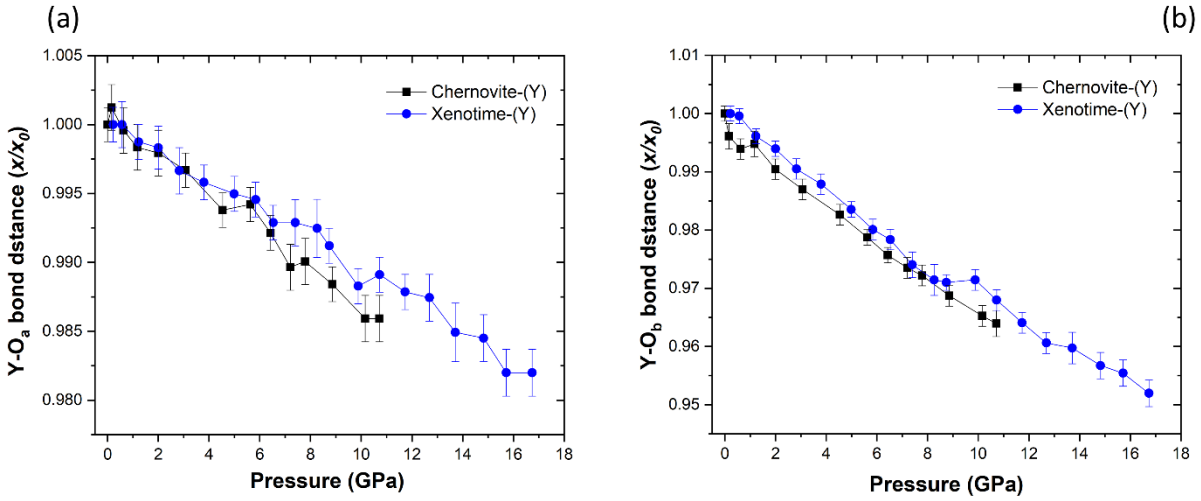

Figure 9.41: c comparison among the compressional behavior of the two independent Y-O bond distances in chernovite-(Y) (Ch10-P_B dataset) and xenotime-(Y) (Xen14-P_D dataset): **(a)** Y-O_a and **(b)** Y-O_b, showing that in both the cases the most compressible bonds are the ones of chernovite-(Y).

9.9.2 Monazite-type compounds at H*P*: gasparite-(Ce), monazite-(Ce) and xenotime-(Y)-II

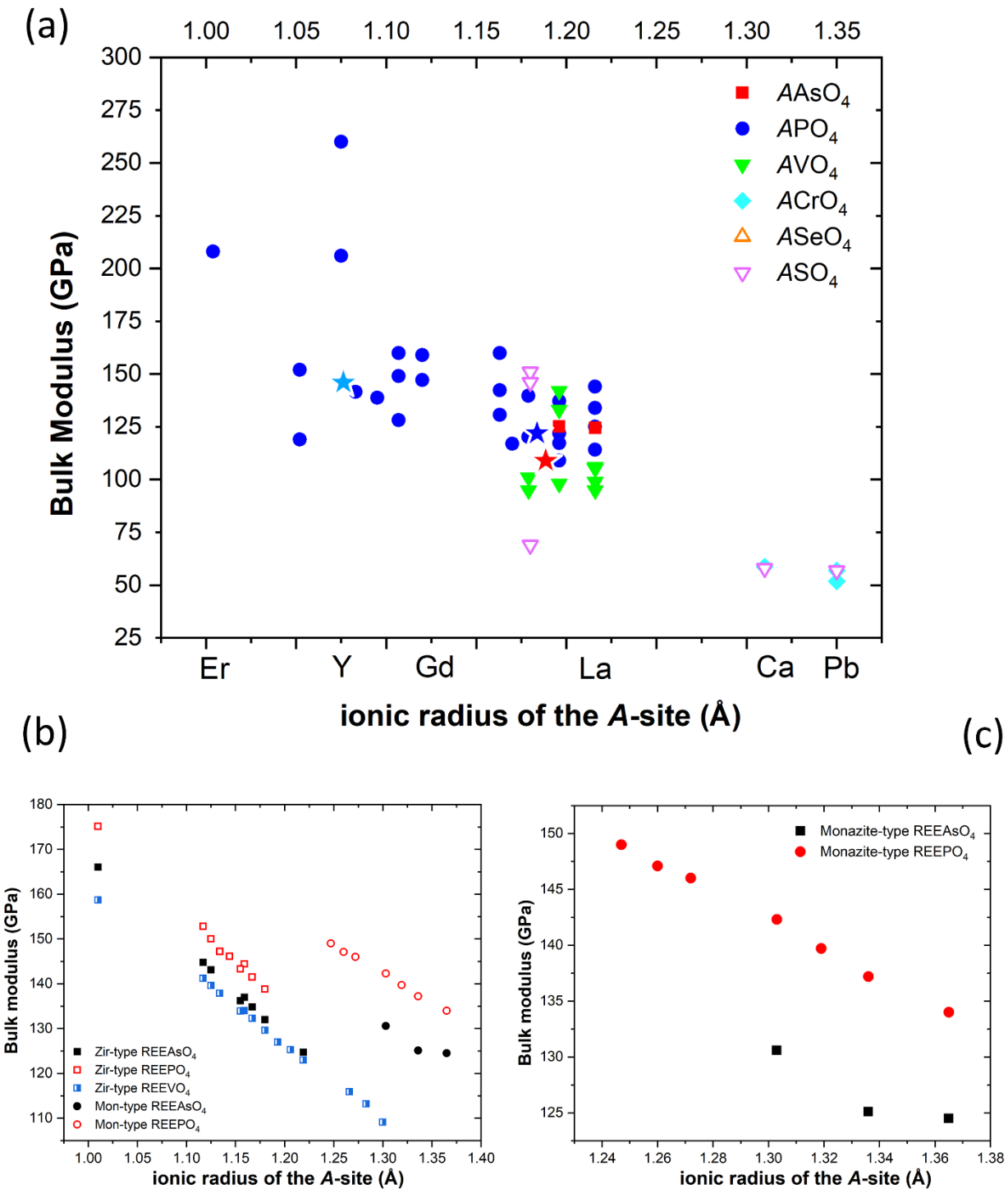

Figure 9.42: **(a)** bulk moduli of the monazite-type compounds determined in the present research compared with those reported in the literature (both experimental and theoretical data are considered); the red, blue and sky blue stars represent the bulk moduli of gasparite-(Ce), monazite-(Ce) and xenotime-(Y)-II respectively; a complete list of the references is contained in Table S13.17; on the *x*-axis, the elements corresponding to selected ionic radii are reported. **(b)** Bulk moduli of REE arsenates, phosphates and vanadates after Zhang et al. (2008) and Li et al. (2008), showing the theoretical relations among the bulk moduli and the the *A*-site ionic radius within the two structural topologies (*i.e.*, monazite- and zircon-type). **(c)** theoretical bulk moduli of the

monazite-type arsenates and phosphates after Li et al. (2009), showing the effect of the *A*- and the *T*-site size in controlling the bulk compressibility of ATO_4 compounds.

Despite its rather rigid behavior, the TO_4 polyhedron does not act as a passive unit in ATO_4 compounds. As discussed previously in section 9.3, the *T*-site exerts a strong influence on all the other structural features. Indeed, it has been demonstrated that the REE-O bond distances, and consequently the REE polyhedron volume, are affected by the chemical composition (*i.e.*, the ionic radius) of the *T*-site.

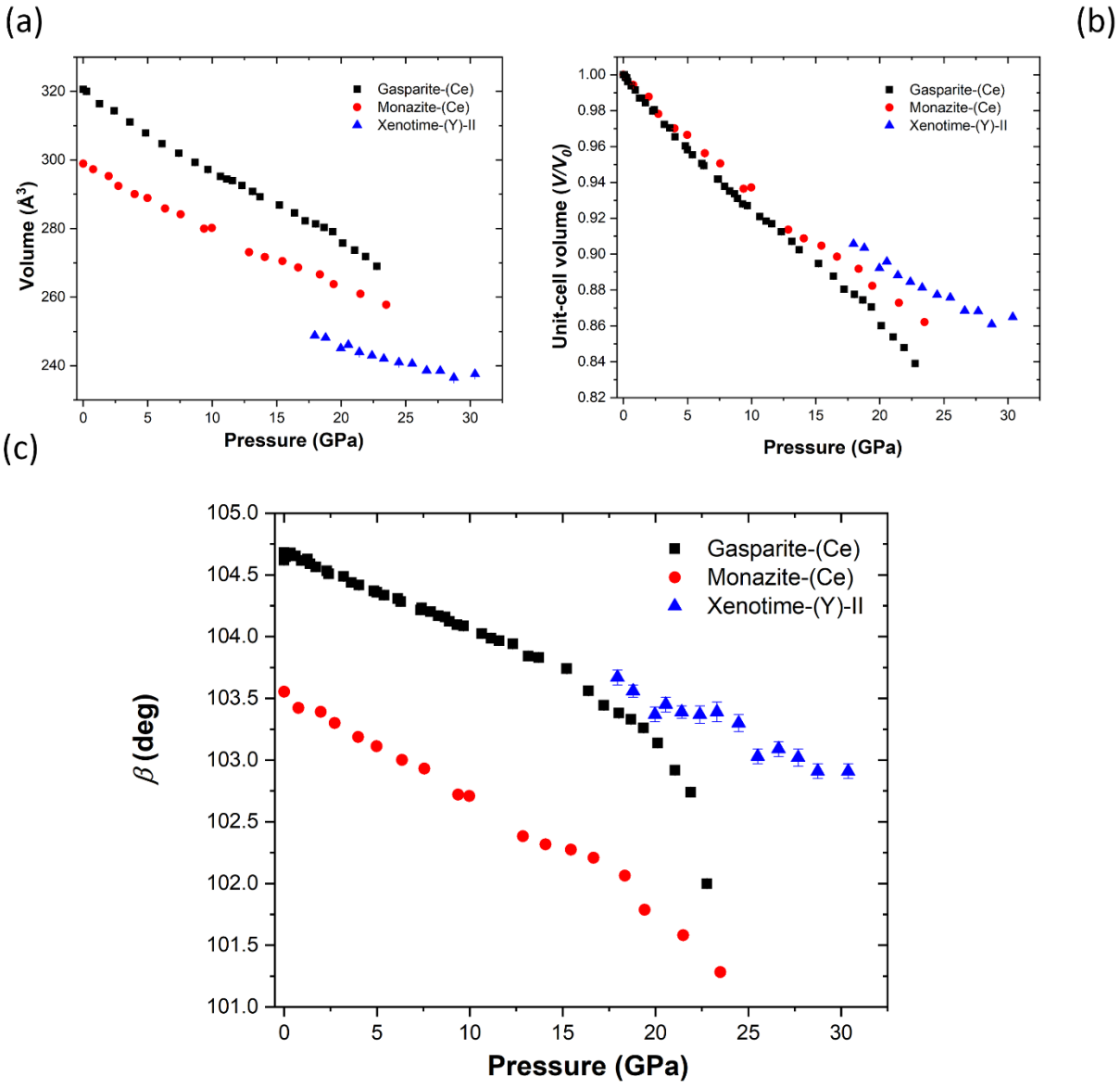

Figure 9.43: comparison among the absolute **(a)** and the normalized (to the atmospheric pressure) values **(b)** of the compressional behavior of gasparite-(Ce), monazite-(Ce) and xenotime-(Y)-II; **(c)** comparison among the compressional evolution of the β angle of the monazite-type minerals under study.

Figure 9.43 shows the high-pressure behavior of the unit-cell parameters of the monazite-type gasparite-(Ce), monazite-(Ce) and xenotime-(Y)-II. The three monazite-type compounds show a clear *P*-dependent behavior that reflects the *A*- or *T*-site composition. As reported in Figure 9.43, xenotime-(Y)-II is the least compressible, gasparite-(Ce) is the most compressible, while monazite-(Ce) shows the intermediate behavior. The relationship among the most and least compressible directions are rather consistent in all the compounds under investigation (see section9.6.1, 9.7.1 and 9.8.1). In agreement with the compressional behavior of any studied ATO_4 compound, the $REEO_9$ polyhedron is always more compressible than the bulk volume. A comparison of the compressional behavior of the $REEO_9$ polyhedra of the three minerals may suggest that this unit is more compressible in xenotime-(Y)-II, that would be surprising if we consider that this polymorph is the least-compressible among the three monazite-type compounds (see Figure 9.21, Figure 9.26 and Figure 9.30). However, these data should be considered very carefully, as it is rather difficult to compare the structural behavior of xenotime-(Y)-II, on one side, and that of gasparite-(Ce) and monazite-(Ce), on the other side. The lack of structural data at pressure below ~17 GPa in xenotime-(Y)-II leads to a limited accuracy of the YO_9 polyhedron fit of the *P*-*V* data. This is reflected by the fact that the uncertainties of the bulk moduli of the CeO_9 polyhedron in monazite-(Ce) and gasparite-(Ce) and that of the YO_9 polyhedron in xeotime-(Y)-II differ of an order of magnitude (Table 8.18). On the other hand, it is possible to unambiguously state that the CeO_9 polyhedron in gasparite-(Ce) is more compressible than in monazite-(Ce), as Figure 9.44b shows.

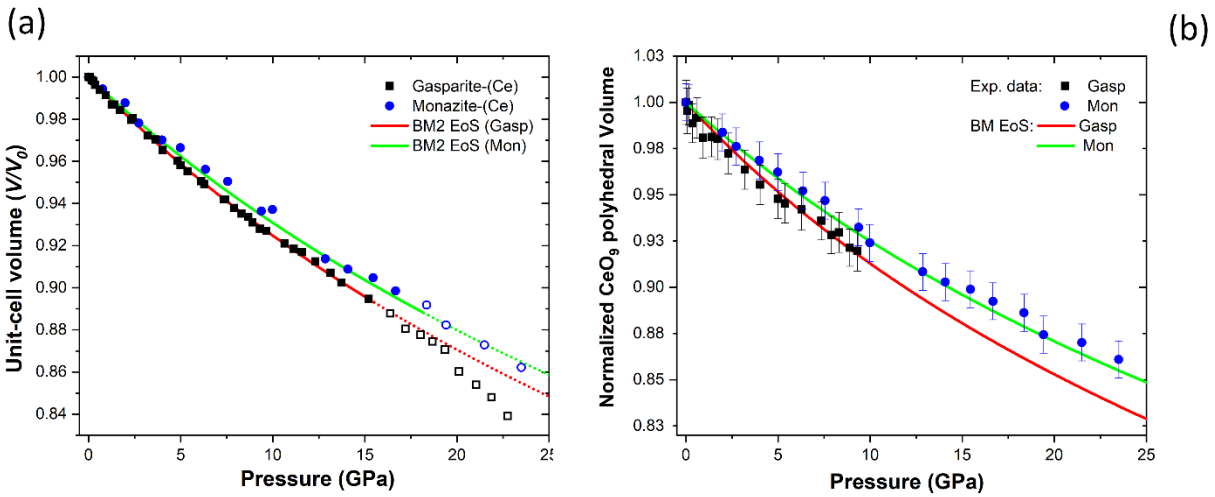

Figure 9.44: comparison among the compressional behavior of gasparite-(Ce) and monazite-(Ce): **(a)** unit-cell volume and **(b)** YO_8 coordination polyhedron.

The compressional behavior of the REE-*T*-REE chain units among the three compounds has also been examined (Figure 9.45). Xenotime-(Y)-II seems to experience the most dramatic deformation of the REE-*T*-REE bond (despite significant uncertainties), monazite-(Ce) shows am intermediate behavior, while gasparite-(Ce) is the one for which this angle deforms the less. Therefore, the compressibility of the REE-*T*-REE structural bonds seems inversely correlated with that of the unit-cell volume.

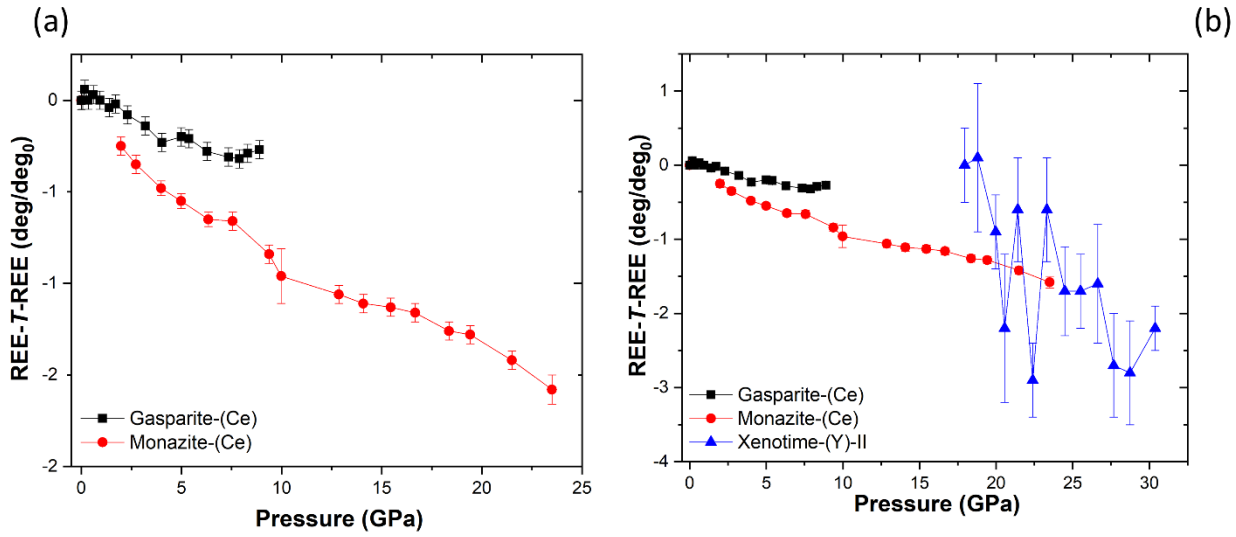

Figure 9.45: comparison among the compressional behavior of the REE-T-REE interatomic angle among gasparite-(Ce) and monazite-(Ce) **(a)** and among the three monazite-type compounds (*i.e.*, gasparite-(Ce), monazite-(Ce) and xenotime-(Y)-II **(b)**.

The compressional behavior of the bond distances has been considered among monazite-(Ce) and gasparite-(Ce) (6). Interestingly, the Ce-O_9 polyhedron in the arsenate and in the phosphates apparently behaves in a similar way. In addition, the evolution with pressure of the relevant bond angles in monazite-(Ce), gasparite-(Ce) and xenotime-(Y)-II (the six Ce-Ox-Ce defining the four lozenge-like connections and the REE-*T*-REE connections defined in Figure 9.47) show a rather consistent behavior in the three different compounds. The comparative behavior is shown in Figure 9.47. Both monazite-(Ce) and gasparite-(Ce) are characterized by the same deformation mechanisms accommodating the compressional behavior at the atomic scale and by the same change in the compressional behavior at the higher pressures (Figure 9.44). The change in compressional behavior, especially in gasparite-(Ce), seems strongly correlated with the shortening of the Ce-$O3_c$ length. In Figure 9.46h, the comparative H*P*-evolution of the "tenth" REE-O (*i.e.*, REE-$O3_c$ interatomic distance) is considered among monazite-(Ce) and gasparite-(Ce). In all the monazite-type compounds the REE-$O3_c$ is the most compressible interatomic distance considered. The "tenth" Y-$O3_c$

interatomic bond decreases also in xenotime-(Y)-II, reaching the minimum value of 2.83(6) Å at 30.18 GPa, but this shortening is not correlated to any clear change in the compressional behavior in xenotime-(Y)-II in the *P*-range investigated. Based on the obtained results, it is reasonable to conclude that the larger the size of the *A*- and *T*-sites coordination environments the earlier the change in the compressional behavior, linked to the increase in the coordination number of the *A*-site from nine to ten, occurs.

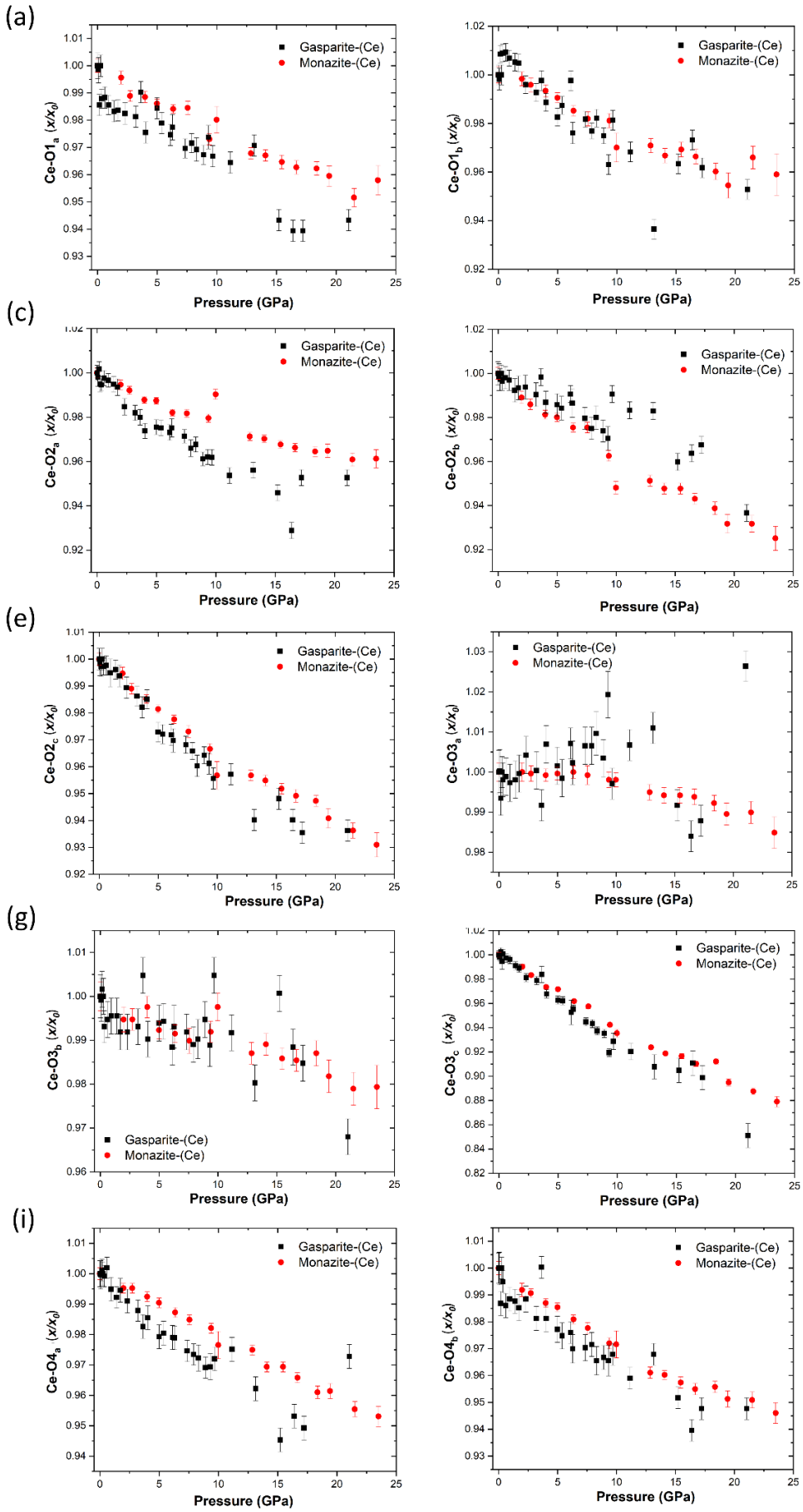
(a)
(b)
(c)
(d)
(e)
(f)
(g)
(h)
(i)
(l)
Gasparite-(Ce)
Monazite-(Ce)
Pressure (GPa)
Ce-O1a (x/x0)
Ce-O1b (x/x0)
Ce-O2a (x/x0)
Ce-O2b (x/x0)
Ce-O2c (x/x0)
Ce-O3a (x/x0)
Ce-O3b (x/x0)
Ce-O3c (x/x0)
Ce-O4a (x/x0)
Ce-O4b (x/x0)

Figure 9.46: compressional behavior of the nine independent bond distances (plus the "tenth" REE-$O3_c$ bond interatomic distance) of gasparite-(Ce) and monazite-(Ce), showing a rather similar compressional behavior of the CeO_9 polyhedron in both the monazite-type minerals under investigation.

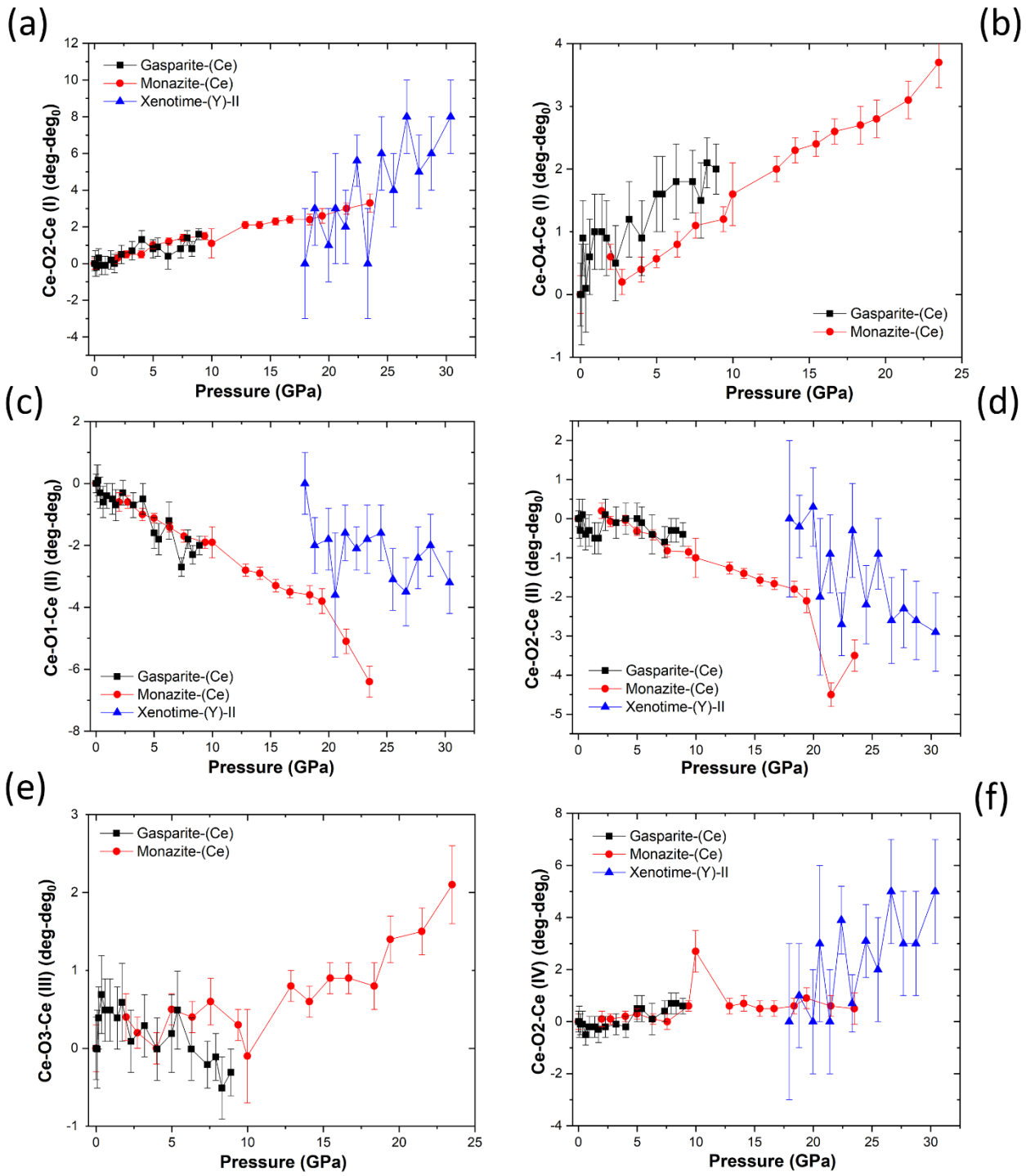

Figure 9.47: comparison among the normalized (to their atmospheric pressure value) compressional behaviors of the six bond angles of the four lozenge-like connections among gasparite-(Ce), monazite-(Y) and xenotime-(Y).

9.10 Comparative analysis of the thermal behavior of the studied *ATO*$_4$ minerals

9.10.1 Comparison among monazite and zircon-type compounds under *H*T conditions

It is worth to mention that, for all the zircon-type minerals investigated, the [001] is both the least compressible and most expansible crystallographic direction. Considering the atomic-scale structural deformation observed upon heating, based on the four single-crystal ramps (*i.e.*, Ch10-T_L, Xen14-T_N and Mon14-T_O), both common and different features can be described. In the first place, in all the cases, a similar behavior of the *A*-site polyhedron and of the *T*-site tetrahedron can be observed: in all the three minerals, the thermal expansion of the REE-polyhedron is higher compared to the bulk unit-cell, while the *T*-site tetrahedron is largely less expandable. Secondly, the behavior under heating of the monazite- and zircon-type structure is significantly different. Monazite-(Ce) is significantly more expansible compared to the zircon-type minerals studied in the present study. Such a behavior is clear in the normalized *T*-*V* diagram reported in Figure 9.48, where the four H*T* single crystal ramps of the three studied minerals are compared, and consistent with what predicted by theoretical studies (Figure 9.49b).

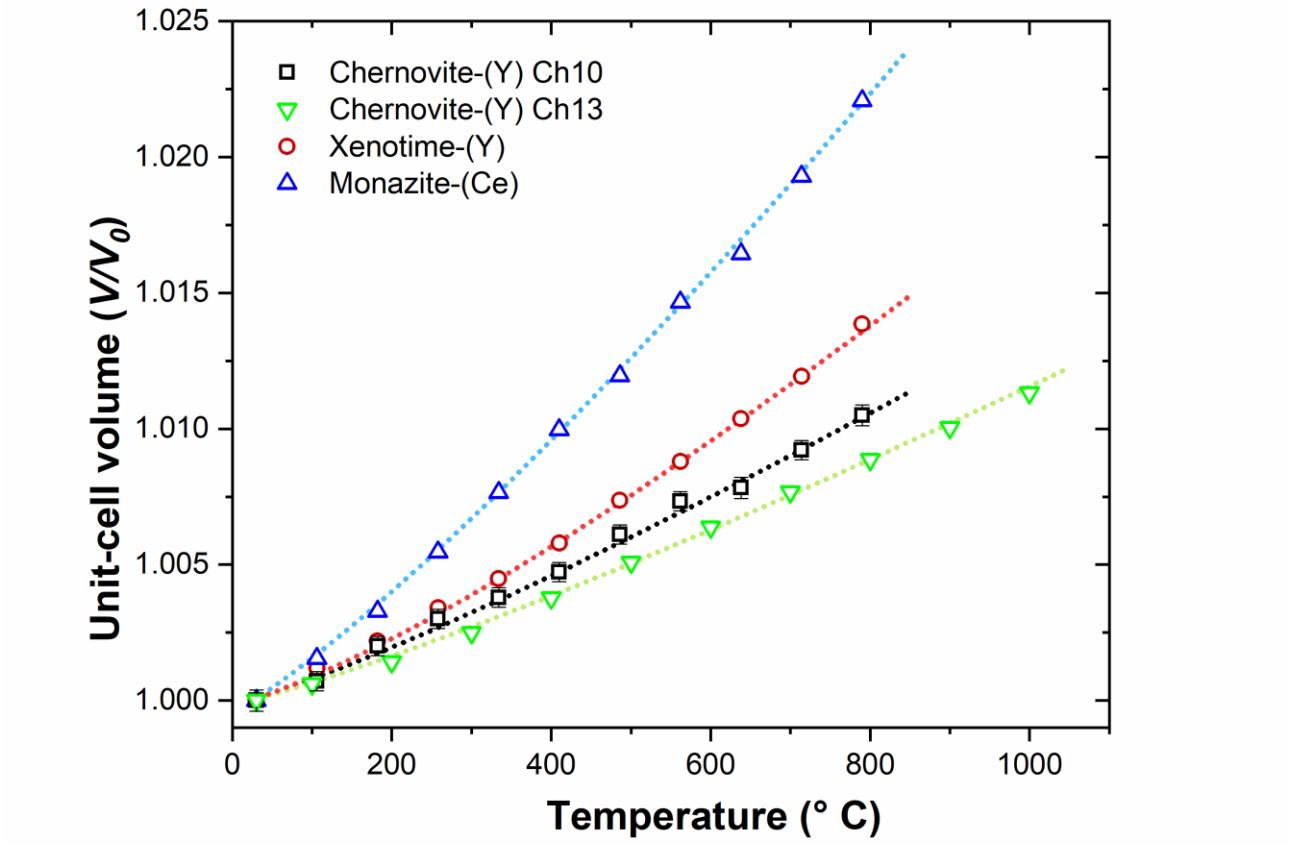

Figure 9.48: comparison among the thermal expansion behavior of normalized (to ambient-conditions values) unit-cell volumes of all the studied ATO_4 minerals, showing that monazite-(Ce) is significantly more expansible than the zircon-type minerals.

It is also reasonable to state that the phosphates are more expansible than the zircon-type arsenates studied in the present work. On the other hand, the lack of the H*T* ramp on gasparite-(Ce) does not allow a complete comparison among the zircon- and monazite-type phosphates and arsenates, although Li et al. (2007; 2009) state that monazite-type $REEAsO_4$ are less expansible compared to $REEPO_4$ (Figure 9.49b). The difference among isostructural phosphates and arsenates can relate to the role played by the TO_4 structural units, although the atomic structural behaviors, deduced on the basis of the data from the Ch10-T_L, Xen14-T_N and Mon14-T_O ramps, does not show any clear *T*-related trends of this unit. Therefore, following the discussion carried out in section 9.3, the expansive behavior of arsenates and phosphates may be correlated *indirectly* with the role played by the TO_4 units. The structure is affected by a chemical deformation, driven by the chemical composition of the *T*-site atom, as reported in section 9.3. Indeed, in the ATO_4 arsenates, the volume of the REE coordination polyhedron is larger compared to the one of the isostructural phosphates. As reported

by Zhang et al. (2008) and Li et al. (2007; 2009), the calculated bond distances thermal expansion of ATO_4 compounds is higher as the bond length decreases. In this light, the different behavior of phosphates and arsenates is bound to the different *A*-O bond lengths, in turn controlled by the chemical composition of the *T*-site, following the model previously described (section 9.3). This conclusion ifs further corroborated if we analyze the thermal expansion behavior of the Th-rich chernovite (Ch13-T_M ramp). In fact, the presence of Th and Ca in this sample further expands the average *A*-O bond distances (in that case independently from the *T*-site composition) and, as a result, the bulk thermal expansion is lower with respect to that of the Th-poor chernovite-(Y), as can be seen in Figure 9.48.

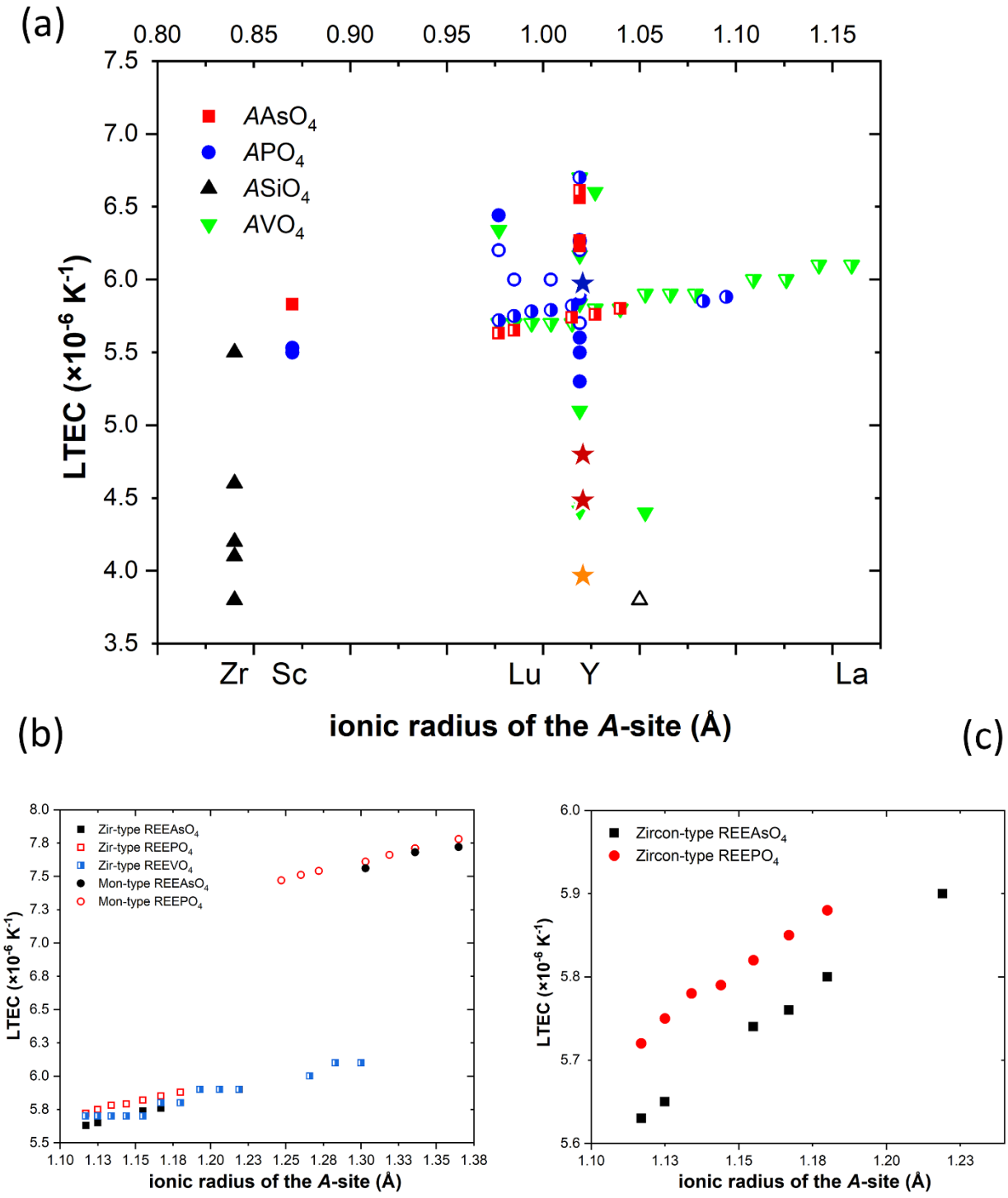

Figure 9.49: **(a)** LTEC of the zircon-type structure compounds studied in the present research compared with those reported by literature data [both experimental (filled dots for X-ray diffraction, void dots for dilatometry results) and theoretical (half-filled dots) data are considered]; the two red stars pertain to the results obtained from the Ch10 sample (Ch10-T_I and Ch10-T_L ramps), the orange one represents the LTEC based on the Ch13-T_M dataset, while the blue star represents the LTEC of xenotime-(Y) (Xen14-T_N ramp); a complete list of the references is contained in Table S13.18; on the x-axis, the atomic species corresponding to selected ionic radii are reported. **(b)** LTEC of REE arsenates, phosphates and vanadates after Zhang et al. (2008) and Li et al. (2008), showing the relations among the thermal expansivity and the ionic radius of the *A*-site within the two structural topologies (*i.e.*, monazite- and zircon-type). **(c)** theoretical LTEC of the monazite-type arsenates and

phosphates after Li et al. (2009), showing the effect of the *A*- and the *T*-site in controlling the thermal expansivity of ATO_4 compounds.

Eventually, the differences among the zircon-type compounds under H*T* is discussed. . Conversely to chernovite-(Y), a significant consistency among the results of this study and literature data for xenotime-(Y) and YPO_4 has been observed. Compared to $YAsO_4$, studied under high temperature, the zircon-type phosphates are supposed to be more expansive (Li et al. 2009), although such a relation is not confirmed by any experimental comparative study (Kahle 1970; Schopper 1972). Indeed, among literature data, the average LTEC defined for $YAsO_4$ is ~8% higher ($6.4 \cdot 10^{-6}$ K^{-1}) to the one defined for YPO_4 ($5.9 \cdot 10^{-6}$ K^{-1}) (Li et al. 2009; Bayer 1972; Subbarao 1968; Schopper 1972; Kahle 1970; Hikichi 1998; Taylor 1986; Sallese 1986; Reddy et al. 1988). It is interesting to highlight that in the present research, in comparing chernovite-(Y) and xenotime-(Y), a different relation has been observed. Indeed, based on all the three ramps on chernovite-(Y) samples, this arsenate was found to be significantly less expansible compared to xenotime-(Y) as reported in Figure 9.49 (see also Table S13.18). Therefore, our data confirm the relationship between the thermal expansion coefficients of xenotime-(Y) and chernovite-(Y) foreseen by Li et al. (2009), although the difference among the thermal expansion coefficients observed in the present study is much larger than what predicted by the theoretical studies (Li et al. 2009).

9.11 Relations among H*P* and H*T* behaviors in ATO_4 minerals

Eventually, an overall comparison among the compressional and thermal behaviors of the studied ATO_4 minerals has been carried out. It is important to remark that the combined H*T*–H*P* data should be treated very carefully, due the relatively large temperature uncertainty. The refined *P*-*V*-*T* EoS paameters are close to the ones refined in both the isothermal (H*P*) and isobaric (H*T*) ramps of chernovite-(Y) and monazite-(Ce). For both chernovite-(Y) and monazite-(Ce), the refined dK/dT_P confirm, as expected, that the bulk moduli decrease as the temperature increase. The refined dK/dT_P (Table 8.32) suggest that the bulk moduli of monazite-(Ce) is affected by temperature largely than chernovite-(Y), although their values are the same within 1σ value.

In addition, as claimed in section 9.3, the occurrence of As in place of P determine a chemical strain within the crystal structure of both zircon- and monazite-type compounds, determining a sort of expansion of the REE polyhedron, which follows the behaviour of the *T*-site. Therefore, the REE coordination polyhedron and the REE-O bond distances in the arsenates are more easily compressed, when compared to phosphates, due to their larger initial values at a similar composition of the *A*-site.

On the contrary, in phosphates, the volume of the $REEO_X$ polyhedron is rather smaller, due to the effect played by the smaller P within the *T*-site: therefore, the REE coordination polyhedron and bulk structure are much more hardly compressed. On the other side, upon heating, the same relations among the *T*-site chemical composition and the $REEO_X$ polyhedron strain are likely responsible for the observed opposite behavior: *i.e.*, the phosphates, characterized by smaller *T*- and *A*-sites coordination polyhedra and shorter T-O and A-O bond distances, are more expansible than arsenates. Consequently, the higher compressibility and smaller thermal expansion of the arsenates, compared to isostructural phosphates, is likely another indirect effect of the chemical composition of the *T*-site on the structural features and bulk elastic behaviour of ATO_4 compounds at ambient and non-ambient conditions.

In most cases (with the relevant exception of the results from the datasets of the Ch10-T_I, Ch10-T_L and Ch13-T_M ramps), the refined compressibilities and LTEC are consistent with the literature data. On the other hand, the relative compressibilities and LTEC determined in the present study are *always* comparable with literature comparative studies. In the previous sections, the paramount and somehow complementary role played by the *T*-site and the *A*-site polyhedra has been deeply discussed: the AO_X (*X*=8 for zircon-type and *X*=9 for monazite-type) polyhedron is either more compressible or expansible than the unit-cell, while the TO_4 is either much less compressible or expansible than the bulk unit-cell. As stated before, the chemical composition of the *T*-site *controls* the magnitude of the deformation mechanisms, while the AO_X has a mostly passive role, although it compresses or expands largely, with the relevant exception of Th-rich chernovite-(Y), where the larger *A*-O interatomic bond distances induce a larger compressibility and smaller expansivity, respectively, independently on the *T*-site composition. On the other hand, the behavior of these structural units only tells a part of the story about the compression and expansion of the structure of ATO_4 compounds with zircon- and monazite-type topologies. Therefore, in the next paragraphs, the deformation of some relevant structural units (*i.e.*, bond lengths and angles) upon compression and heating is discussed, in order to provide a complete description of the active deformation mechanisms.

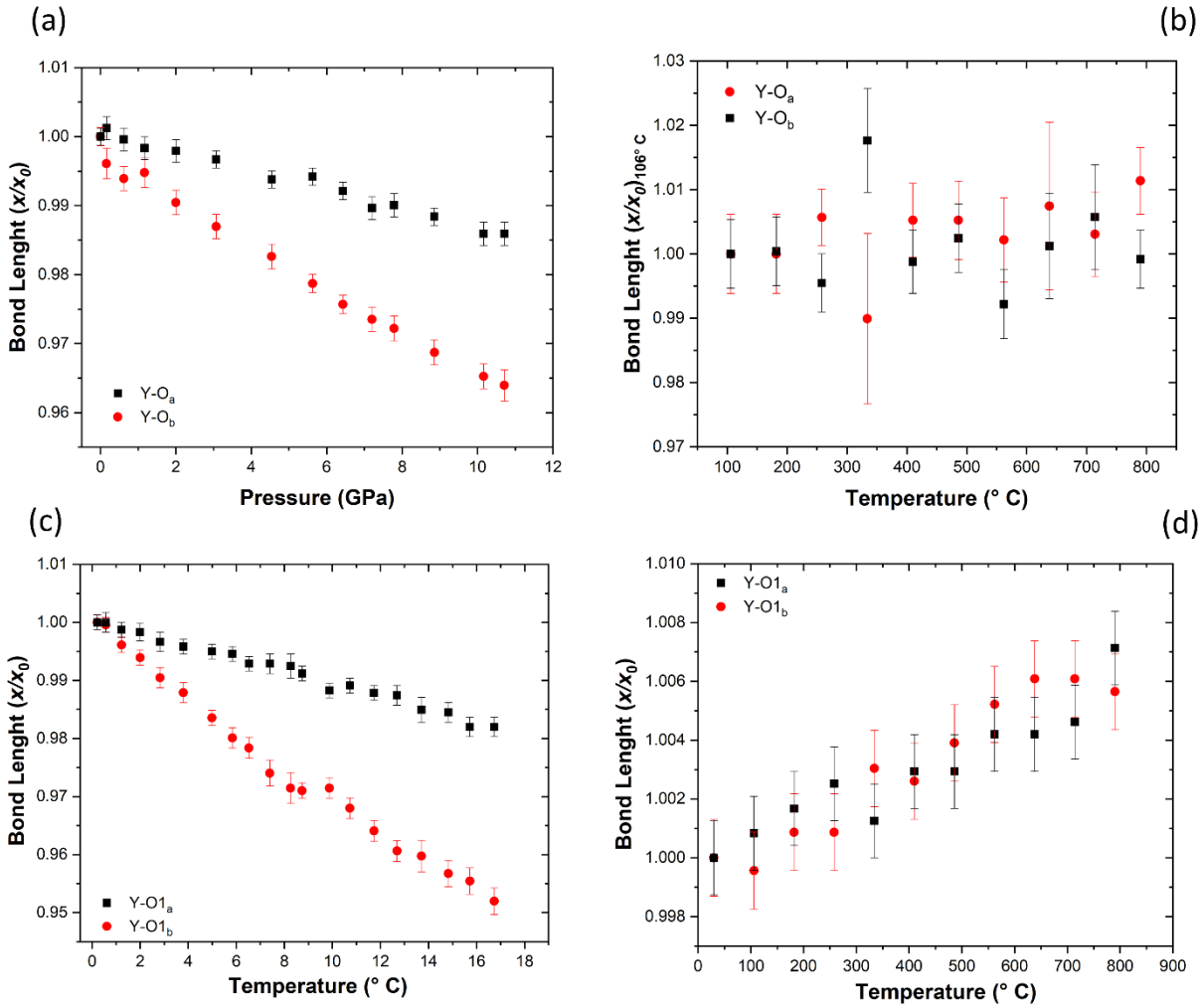

Figure 9.50: normalized [to their value at room conditions, or to its value at 106° C in **(b)**] behavior at non-ambient conditions of the Y-O bond distances of chernovite-(Y) and xenotime-(Y); **(a)** chernovite-(Y) under compression; **(b)** chernovite-(Y) under heating; **(c)** xenotime-(Y) under compression; **(d)** xenotime-(Y) under heating.

In general, concerning chernovite-(Y) and xenotime-(Y), a comparison among the H*T* and H*P* behavior of the main structural parameters is quite an easy task. Figure 9.50 shows the deformation of the two independent Y-O bonds (Y-O_a and Y-O_b) under compression and heating for chernovite-(Y) and xenotime-(Y). Interestingly, the Y-O_a and Y-O_b bonds are characterized by a significantly different compressional behavior under compression, but show a rather similar thermal expansion upon heating.

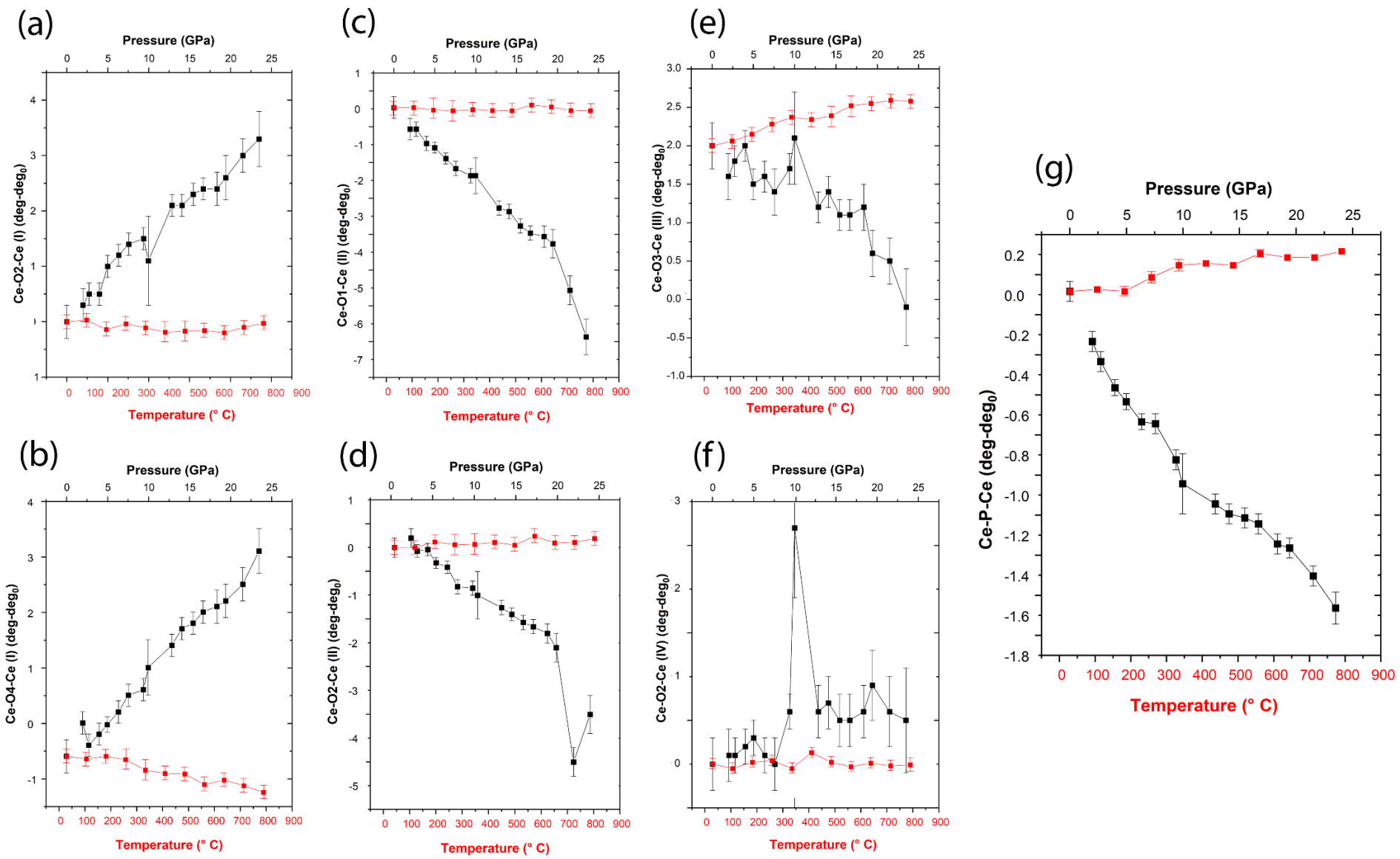
(a)
Pressure (GPa)
Ce-O2-Ce (I) (deg-deg0)
Temperature (° C)
(b)
Pressure (GPa)
Ce-O4-Ce (I) (deg-deg0)
Temperature (° C)
(c)
Pressure (GPa)
Ce-O1-Ce (II) (deg-deg0)
Temperature (° C)
(d)
Pressure (GPa)
Ce-O2-Ce (II) (deg-deg0)
Temperature (° C)
(e)
Pressure (GPa)
Ce-O3-Ce (III) (deg-deg0)
Temperature (° C)
(f)
Pressure (GPa)
Ce-O2-Ce (IV) (deg-deg0)
Temperature (° C)
(g)
Pressure (GPa)
Ce-P-Ce (deg-deg0)
Temperature (° C)

Figure 9.51: comparison among the compressional and thermal expansion behavior of significant bond angles, determined in Figure 9.23, for monazite-(Ce) upon heating (red dots) and compression (black dots). Due to the different magnitude of the deformation, only a comparison of the trends provides significant information on the difference among compression and heating.

Due to its lower symmetry, the monazite-type structure requires more structural parameters to describe its deformation upon compression or heating. The behavior of all the significant bond angles drawn in Figure 9.23 has been examined (Figure 9.51). Even though the magnitude of the deformation is rather different upon compression and heating, respectively, some clear trends can be drawn: the P-Ce-P angle, for example, tends to reduce under compression (as also happens in gasparite-(Ce) and xenotime-(Y)-II as reported in Figure 9.45) and to increase under heating. As reported in Figure 9.51 and discussed in section 9.8.1 and 9.8.2, the Ce-O4-Ce–Ce-O2-Ce (lozenge unit I) behaves in opposite ways under compression and heating. On the other hand, the lozenge unit II (Ce-O1-Ce–Ce-O2-Ce) (Figure 9.51c and Figure 9.51d) does not change its angular configuration upon heating.

Chapter 10

10 Conclusions and future prospects

The crystal chemical analyses of the studied REE*T*O_4 minerals suggest that a wide miscibility gap occurs among the two monazite-type species, while the zircon-type series shows a rather broad solid solution among the endmembers. A significant chemical heterogeneity has been observed for several investigated samples, especially related to the Th content, which is locally enriched in $ThSiO_4$ grains. In addition, the occurrence of Th and Si (*i.e.*, the most variable elements based on the chemical analysis) is accommodated by the crystal structure of the *AT*O_4 compounds according to three major charge compensating mechanisms: $(Th,U)^{4+}+Si^{4+}=REE^{3+}+(P,As)^{5+}$ (thorite substitution mechanism) is the most important for the zircon-type compounds and monazite-(Ce); $(Th,U)^{4+}+Ca^{2+}=2REE^{3+}$ (cheralite substitution mechanism) is relevant for monazite-(Ce) and the two most Th-enriched samples (*i.e.*, Ch13 and Ch16); $2(OH,F,Cl)^{-}+Ca^{2+}+Si^{4+}=2O^{2-}+REE^{3+}+(P,As)^{5+}$, relevant for gasparite-(Ce), characterized by an excess in Si with respect to Th. The results observed for gasparite-(Ce) are corroborated by the Raman spectroscopy data, which suggest the presence of O-H bonds. The structure refinements suggest that the crystal chemistry and the structural features are mutually correlated. In particular, among the Th-enriched Ch13 and Ch16, the high amount of the thorite component is reflected by the larger unit-cell volume. Moreover, it has been observed that the chemical composition of the *T*-site, whether occupied by P or As, affects any other structural parameter. Therefore, the REE-site polyhedron volume and the REE-O bond lengths are affected by the chemical composition of the *T*-site, as well as the structural features of the *T*O_4 tetrahedron (*i.e.*, its volume and the *T*-O bond distances), which are clearly dependent on the chemical composition of the *T*-site itself.

In the second part of the project, devoted to the understanding of the behavior at non-ambient (*P*,*T*) conditions of the REE*T*O_4 minerals under study, the elastic and thermoelastic parameters of the selected samples have been determined, along with the thermal and compressional evolution of some

relevant structural parameters. The bulk compressibilities of the investigated minerals are in general agreement with those reported in previous literature studies for the same compounds (see Table S13.17). The occurrence of different pressure-induced phase transitions has been determined for the two zircon-type minerals, in agreement with the literature data available for the $YAsO_4$ and YPO_4 compounds (Errandonea et al. 2011; Zhang et al. 2009; Lacomba-Perales et al. 2010). The compressional behaviour of the high-pressure polymorph xenotime-(Y)-II has been described, suggesting only a slight difference among the compressibilities of xenotime-(Y) and its H*P* polymorph. Gasparite-(Ce) and monazite-(Ce), do not show any phase transitions within the pressure-range investigated, but share a common feature under compression: the occurrence of a change in the compressional behaviour, highlighted by a discontinuity in the β angle and unit-cell volume evolution with pressure. The structural analysis suggests that such a change in the compressional behaviour is due to an increase in the coordination number of the *A*-site from nine to ten, determining a sort of intermediate structural configuration between the monazite and the postbarite polymorphs, the latter characterized by $P2_12_12_1$ space group and an elevenfold coordinated *A*-site (*e.g.*, Ruiz-Fuertes et al. 2016). The bulk moduli refined for the selected minerals suggest that the arsenates are more compressible compared to the isostructural phosphates, in agreement with the literature data. Moreover, from the obtained compressional data, the monazite-type structure appears more compressible than the zircon-type one, although this is likely to be ascribed not to the structural topology (which should induce a stiffening with respect to the zircon type), but to the significantly different *A*-site cations ionic radii of the monazite-type and zircon-type investigated minerals. The structural analysis, in addition, shows that, for all the studied minerals, independently from the chemical composition or the structural topology, the REE coordination polyhedron is always more compressible than the bulk volume, while the structural tetrahedron behaves as a quasi-rigid unit.

The thermal elastic parameters, determined for chernovite-(Y), xenotime-(Y) and monazite-(Ce), confirm that the monazite-type structure is characterized by a significantly higher thermal expansion coefficient compared to the zircon-type. The relationship among the thermal expansion parameters of zircon-type phosphate and arsenate suggests, as expected from comparative studies (*e.g.*, Li et al. 2009), that the arsenates are less expansible compared to isostructural phosphates. On the other side, the lack of thermal expansion data on gasparite-(Ce) makes not possible to draw the same conclusion for the monazite-type structure. The structural analysis conducted on H*T* data confirm that the REE coordination polyhedra are more expansible compared to the unit-cell volume. Interestingly, the analysis of the structural deformation (*i.e.*, bond distances and bond angles) upon heating and compression suggests that the same deformation mechanisms are responsible for compression and thermal expansion. In general, the thermo-elastic behavior of the selected minerals is always close to

that of their synthetic counterparts and confirm the literature data pertaining to the ATO_4 compounds, with the only incongruity having been observed for chernovite-(Y): the mineral investigated in this study is characterized by a significantly lower expansivity with respect to the behavior of synthetic compounds reported in previous studies (Table S13.18).

Another significant aspect highlighted by this study is the relationship between the thermal and compressional behavior of phosphates and arsenates: even in this case, the chemical composition of the *T*-site plays a dominant role, by influencing the REE-O bond distances and, in turn, the volume of the REE coordination polyhedron. The chemical strain induced by the enrichment of P or As, affects the compressibility and thermal expansion of the REE polyhedron and bulk structure: compared to the $REEPO_4$ minerals, the $REEAsO_4$ compounds are both the more compressible and the less expansible phases. Such a relation has been determined for the zircon series. The lack of H*T* data on gasparite-(Ce) does not allow a complete comparison for the monazite series, although the available data on monazite-type $REEAsO_4$ minerals (Li et al. 2009) suggests that tetragonal and monoclinic $REE*T*O_4$ behave similarly. Such a relationship can be briefly summarized as follows: the higher is the chemical strain induced by the *T*-site composition (*i.e.*, the higher is the structure expansion related to the *T*-site ionic radius), the higher is the bulk compressibility and the lower the thermal expansion.

Eventually, some significant issues are still open and need to be addressed by specific dedicated studies. Concerning the geology of the Cervandone area, a geological field mapping of the pegmatitic dykes and quartz fissures, as well as a complete petrographic study, need to be carried out. In addition, the crystal-chemical features of the solid solution among $REE*T*O_4$ phosphates and arsenates still require a full understanding that may be facilitated by dedicated syntheses at varying pressure, temperature and fluid composition, with the aim to draw a phase diagram of $REEAsO_4$ and $REEPO_4$ within the two series [*i.e.*, chernovite-(Y)–xenotime-(Y) and gasparite-(Ce)–monazite-(Ce)].

11 Acknowledgments

In the first place, Dr. Alessandro Guastoni is gratefully thanked for his role in defining the purpose of the project and his irreplaceable help in describing the crystal chemistry of the studied minerals, as well as providing the samples. Without his contribution, insights and knowledge about the topic of this study, the present work would not have been possible. The Italian Ministry of University and Research (MUR) is acknowledged for the funding of this doctoral fellowship through the project "Dipartimenti di Eccellenza 2018-2022 – Le Geoscienze per la società: Risorse e loro evoluzione" Paolo Lotti and G. Diego Gatta provided irreplaceable contribution and active sustain in the data collection, treatment and interpretation. Paolo Lotti and G. Diego Gatta also provided general organizational aid in many circumstances. Fernando Càmara supported both the organization of the project and help in treating both the chemical and XRD data. Davide Comboni provided active, strong support in collecting the high-pressure data, as well as organizing the ESRF beamtime. Volker Kahlenberg, Hannes Kruger, Clivia Hejny and Biljana Kruger provided fundamental help in collecting and analyzing the high temperature data at the Institute of Mineralogy and Petrology at the Innsbruck University. Hannes Kruger has been particularly helpful in explaining the data collection, treatment and interpretation of the XRD *HT* data. Volker Kahlenberg organized several key aspects pertaining the stay in Innsbruck. Tommaso Battiston, Sula Milani and Marco Merlini are acknowledged for their contribution in collecting the X-ray diffraction high-pressure data and support during the chemical analysis. Nicola Rotiroti provided help in describing the mineral association and collecting the room condition XRD data. Patrizia Fumagalli and Andrea Risplendente are acknowledged for their role in the data collection and data reduction of the Raman spectroscopic data and EPMA analysis, respectively. Enzo Sartori is gratefully thanked for providing the samples. Fabio Marchesini is gratefully acknowledged for the sample preparation. The synchrotron facilities of ESRF (Grenoble, France), Petra-III (Hamburg, Germany) and Elettra (Trieste, Italy) are acknowledged for the allocation of beamtime. Konstantin Glazyrin, Hanns-Peter Liermann and Huijeong Hwang (P02.2 beamline at Petra-III), Davide Comboni and Michael Hanfland (ID15B beamline at ESRF) and Lara Gigli (MCX beamline at Elettra) are acknowledged for their support as local contact at the synchrotron facilities. The research leading to this result has been supported by the project CALIPSOplus under the Grant Agreement 730872 from the EU Framework Programme for Research and Innovation HORIZON 2020 and by the University of Milano through the projects "Piano di sostegno alla Ricerca 2018, 2019 and 2020".

12 Bibliography

Akah A. (2017) Application of rare earths in fluid catalytic cracking: A review. Journal of Rare Earths, 35, 941-956.

Alam M.A., Zuga L. and Pecht M.G. (2012) Economics of rare earth elements in ceramic capacitors. Ceramics International, 38, 6091-6098.

Aldred A.T. (1984) Cell volumes of APO_4, AVO_4, and $ANbO_4$ compounds, where A=Sc, Y, La–Lu. Acta Crystallographica B 40, 569-574.

Alekseev V.I. and Marin Y.B. (2013) A Tribute to Nicolai Pavlovich Yushkin, one of the discoverers of chernovite. Chernovite-(Y) and other arsenic minerals in rare-metal granites and greisens of the Far East. Geology of Ore Deposits, 55, 601-606.

Ancsombe N. (2002) A new spin- Thin-disc Yb: YAG lasers. Photonics Spectra, 36, 54-56.

Anderson O.L. (1995) Equations of state of solids for geophysics and ceramic science. Oxford University Press on Demand.

Anderson O.L., Isaak D. G. and Yamamoto S. (1989) Anharmonicity and the equation of state for gold. Journal of Applied Physics, 65, 1534-1543.

Andersson S.S. (2019) Formation of hydrothermal REE-phosphate deposits. Department of Geosciences and Geography A76. Helsinky.

Andrehs G. and Heinrich W. (1998) Experimental determination of REE distributions between monazite and xenotime: potential for temperature-calibrated geochronology. [Doctoral dissertation, University of Helsinki, Faculty of Science, Department of Geosciences and Geography] Chemical Geology, 149, 83-96.

Angapova L.E. and Serebrennikov V.V. (1973) Thermal stability of rare earth arsenates. Zhurnal Neorganicheskoj Khimii, 18, 1706-1708.

Angel R.J. (2000) Equations of state. In: Hazen RM, Downs RT (ed) High-Temperature and High-Pressure Crystal Chemistry: review in mineralogy and geochemistry, vol 41. Mineralogical Society of America and Geochemical Society, Washington.

Angel R.J. (2002) Equations of state. In: Hazen RM, Downs RT (eds) High-Temperature and High-Pressure Crystal Chemistry. Rev Mineral Geochem, 41:35–60.

Angel R.J. (2011) Win_Strain. A program to calculate strain tensors from unit-cell parameters. http://www.rossangel.com/home.htm

Angel R.J., Alvaro M. and Gonzalez-Platas J. (2014) EosFit7c and a Fortran module (library) for equation of state calculations. Zeitschrift für Kristallographie-Crystalline Materials, 229, 405-419.

Angel R.J., Bujak M., Zhao J., Gatta G. D. and Jacobsen S. D. (2007) Effective hydrostatic limits of pressure media for high-pressure crystallographic studies. J Appl Crystallogr 40:26–32.

Anthony J.W., Bideaux R.A., Bladh K.W. and Nichols M.C. (2000) Handbook of Mineralogy, IV, Phosphates, Arsenates, Vanadates. Mineral Data Publishing, Tucson, Arizona. Geological Magazine, 138, 219-232.

Armbruster A. (1976) Infrared reflection studies on the phosphates, arsenates and vanadates of lutetium and yttrium. Journal of Physics and Chemistry of Solids, 37, 321-327.

Assefa Z., Haire R.G. and Raison P.E. (2004) Photoluminescence and Raman studies of Sm^{3+} and Nd^{3+} ions in zirconia matrices: example of energy transfer and host–guest interactions. Spectrochimica Acta Part A: Molecular and Biomolecular Spectroscopy, 60, 89-95.

Azzeddine H., Hanna A., Dakhouche A., Rabahi L., Scharnagl N., Dopita M., Brisset F., Helbert A. L. and Baudin T. (2020) Impact of rare-earth elements on the corrosion performance of binary magnesium alloys. Journal of Alloys and Compounds, 829, 154569.

Bagiński B., Macdonald R., Belkin H. E., Kotowski J., Jokubauskas P. and Marciniak Maliszewska B. (2020) The occurrence of wakefieldite, a rare earth element vanadate, in the rhyolitic Joe Lott Tuff, Utah, USA. Mineralogical Magazine, 84, 109-116.

Balaram V. (2019) Rare earth elements: A review of applications, occurrence, exploration, analysis, recycling, and environmental impact. Geoscience Frontiers, 10, 1285-1303.

Balewski K., Rohlsberger R., Franz H., Weckert E., Decking W. and Brefeld W. (2004) PETRA III: A low emittance synchrotron radiation source. Technical design report (No. DESY-2004-035).

Bandiello E., Errandonea D., Martinez-Garcia D., Santamaria-Perez D. and Manjón F.J. (2012) Effects of high-pressure on the structural, vibrational, and electronic properties of monazite-type $PbCrO_4$. Physical Review B, 85, 024108.

Baran E.J. and Aymonino P.J. (1971) Über Lanthanorthovanadat. Zeitschrift für anorganische und allgemeine Chemie, 383, 220-225.

Barnett J.D., Block S. and Piermarini G.J. (1973) An optical fluorescence system for quantitative pressure measurement in the diamond-anvil cell. Review of Scientific Instruments, 44, 1-9.

Barros G., Santos C.C., Ayala A.P., Guedes I., Boatner L.A. and Loong C.K. (2010) Raman investigations of rare-earth arsenate single crystals. Journal of Raman Spectroscopy, 41, 694-697.

Bashir J. and Khan M.N. (2006) X-ray powder diffraction analysis of crystal structure of lanthanum orthovanadate. Materials Letters, 60, 470-473.

Bassett W.A. (2009) Diamond anvil cell, 50th birthday. High Pressure Research, 29, 163-186.

Bastide J.P. (1987) Systématique simplifiée des composés ABX_4 ($X= O^{2-}, F^-$) et evolution possible de leurs structures cristallines sous pression. Journal of Solid State Chemistry, 71, 115-120.

Baur W.H. (1974) The geometry of polyhedral distortions. Predictive relationships for the phosphate group. Acta Crystallographica, B30, 1195-1215.

Bazuev G.V., Zhilyaev V.A. and Shvejkin G.P. (1974) Dimorphism of rare earth orthovanadates. Doklady Akademii Nauk SSSR, 218, 833-836.

Beall G.W., Boatner L.A., Mullica D.F. and Milligan W.O. (1981) The structure of cerium orthophosphate, a synthetic analogue of monazite. Journal of Inorganic and Nuclear Chemistry, 43, 101–105.

Bearth P. (1957) Die Umbiegung von Vanzone (Valle Anzasca). Verlag nicht ermittelbar.

Begun G.M., Beall G.W., Boatner L.A., and Gregor W.J. (1981) Raman spectra of the rare earth orthophosphates. Journal of Raman Spectroscopy, 11, 273-278.

Bergemann C.A., Gnos E., Berger A., Janots E. and Whitehouse M.J. (2020) Dating tectonic activity in the Lepontine Dome and Rhone-Simplon Fault regions through hydrothermal monazite-(Ce). Solid Earth, 11, 199-222.

Berger A., Mercolli I. and Engi M. (2005) The central Lepontine Alps: Notes accompanying the tectonic and petrographic map sheet Sopra Ceneri (1: 100’000). Schweizerische Mineralogische und Petrographische Mitteilungen, 85, 109-146.

Bianchi A. (1920) Augite diopside del Monte Cervandone in Val Devero (Ossola). Atti della Società italiana di scienze naturali, 59, 105-125.

Bigioggero B., Colombo A., Cavallo A., Aldighieri B. and Tunesi A.M. (2007) Geological-structural sketch-map of the Ossola-Simplon area (1: 50.000 map).

Binks W. (1926) The crystalline structure of zircon. Mineralogical magazine and journal of the Mineralogical Society, 21, 176-187.

Binnemans K., Jones P.T., Blanpain B., Van Gerven T., Yang Y., Walton A. and Buchert M. (2013) Recycling of rare earths: a critical review. Journal of cleaner production, 51, 1-22.

Birch F. (1947) Finite elastic strain of cubic crystals. Physical review, 71, 809.

Blengini G.A., Mathieux F., Mancini L., Nyberg M. and Viegas H.M. (2020) Study on the EU's list of Critical Raw Materials. Executive Summary. Publication Office of the European Commission, Luxembourg.

Boatner L.A. (2002) Synthesis, structure, and properties of monazite, pretulite, and xenotime. Reviews in mineralogy and geochemistry, 48, 87-121.

Bondar I.A., Domanskii A.I., Mezentseva, L.P. (1976) Physicochemical study of rare earth orthophosphates. Zhurnal Neorganicheskoi Khimii, 21, 2045-2050.256

Borst A.M., Smith M.P., Finch A.A., Estrade G., Villanova-de-Benavent C., Nason P., Marquis E., Horsburgh N.J., Goodenough K.M., Xu C., Kynický J. and Geraki K. (2020). Adsorption of rare earth elements in regolith-hosted clay deposits. *Nature communications*, *11*(1), 1-15.

Boston K.R., Rubatto D., Hermann J., Engi M. and Amelin Y. (2017) Geochronology of accessory allanite and monazite in the Barrovian metamorphic sequence of the Central Alps, Switzerland. Lithos, 286, 502-518.

Botto I.L. and Baran E.J. (1982) Characterization of the monoclinic rare earth orthoarsenates. Journal of the Less Common Metals, 83, 255-261.

Bouddouch A., Amaterz E., Bakiz B., Taoufyq A., Guinneton F., Villain S. and Benlhachemi A. (2021) Photocatalytic and photoluminescence properties of $CePO_4$ nanostructures prepared by coprecipitation method and thermal treatment. Optik, 238, 166683.

Bradbury S. E. and Williams Q. (2009) X-ray diffraction and infrared spectroscopy of monazite-structured $CaSO_4$ at high pressures: Implications for shocked anhydrite. Journal of Physics and Chemistry of Solids, 70, 134-141.

Bragg W. L. (1929) Atomic arrangement in the silicates. Transactions of the Faraday Society, 25, 291-314.

Brahim A., Mohamed Mongi F. and Amor H. (2002) Cerium arsenate, $CeAsO_4$. Acta Crystallographica Section E: Structure Reports Online, 58, i98-i99.

Brandt F., Neumeier S., Schuppik T., Arinicheva Y., Bukaemskiy A., Modolo G. and Bosbach D. (2014) Conditioning of minor actinides in lanthanum monazite ceramics: a surrogate study with europium. Progress in nuclear energy, 72, 140-143.

Breiter K. and Förster H. J. (2021) Compositional Variability of Monazite–Cheralite–Huttonite Solid Solutions, Xenotime, and Uraninite in Geochemically Distinct Granites with Special Emphasis to the Strongly Fractionated Peraluminous Li–F–P-Rich Podlesí Granite System (Erzgebirge/Krušné Hory Mts., Central Europe). Minerals, 11, 127.

Breiter K., Čopjaková R. and Škoda R. (2009) The involvement of F, CO_2, and As in the alteration of Zr–Th–REE-bearing accessory minerals in the Hora Svaté Kateriny A-type granite, Czech Republic. The Canadian Mineralogist, 47, 1375-1398.

Brik M.G., Bettinelli M. and Cavalli E. (2015) Modeling the lattice parameters of zircon-type MXO_4 (M= divalent, trivalent or tetravalent metal, X=V, P, As, Si) crystals. Journal of Solid State Chemistry, 230, 49-55.

Brown P.J., Fox A.G., Maslen E.N., O'keefe M.A. and Willis B.T.M. (2006) Intensity of diffracted intensities. In “International Tables for Crystallography, Vol. C” (E. Prince editor).

Burg J.P. and Gerya T.V. (2005) The role of viscous heating in Barrovian metamorphism of collisional orogens: thermomechanical models and application to the Lepontine Dome in the Central Alps. Journal of Metamorphic Geology, 23, 75-95.

Butterman W.C. and Foster W.R. (1967) Zircon stability and the ZrO_2-SiO_2 phase diagram. American Mineralogist: Journal of Earth and Planetary Materials, 52, 880-885.

Bykova E., Aprilis G., Bykov M., Glazyrin K., Wendt M., Wenz S. and Dubrovinsky L. (2019) Single-crystal diffractometer coupled with double-sided laser heating system at the Extreme Conditions Beamline P02.2 at PETRAIII. Review of Scientific Instruments, 90, 073907.

Cabella R., Lucchetti G. and Marescotti P. (1999) Occurrence of LREE-and Y-arsenates from a Fe-Mn deposit, Ligurian Briançonnais Domain, Maritime Alps, Italy. The Canadian Mineralogist, 37, 961-972.

Castiglioni G. (1958) Studio geologico e morfologico del territorio di Baceno e Premia (Val d'Ossola–Alpi Lepontine). Memorie degli Istituti di Geologia e Mineralogia dell'Università di Padova, XX, 2-82.

Černý P. (1991a) Rare-element granitic pegmatites. Part I: Anatomy and internal evolution of pegmatite deposits. Geoscience Canada, 18, 49-67.

Černý P. (1991b) Rare-element granitic pegmatites. Part II: Regional to global environments and petrogenesis. Geoscience Canada, 18, 68-81.

Černý P., and Ercit T. S. (2005) The classification of granitic pegmatites revisited. The Canadian Mineralogist, 43, 2005-2026.

Cesbron F.P. (1989) Mineralogy of the rare-earth elements. In "Lanthanoids, tantalum and niobium" (P. Möller, P. Černý, F. Saupé, editors).

Chakhmouradian A.R. and Zaitsev A.N. (2012) Rare earth mineralization in igneous rocks: sources and processes. Elements, 8, 347-353.

Chen Y. and Zheng B. (2019) What happens after the rare earth crisis: a systematic literature review. Sustainability, 11, 1288.

Chen Z. (2011) Global rare earth resources and scenarios of future rare earth industry. Journal of rare earths, 29, 1-6.

Cheng Z., Zhang Z., Aibai A., Kong W. and Holtz F. (2018) The role of magmatic and post-magmatic hydrothermal processes on rare-earth element mineralization: A study of the Bachu carbonatites from the Tarim Large Igneous Province, NW China. Lithos, 314, 71-87.

Cherniak D.J., Pyle J. and Rakovan J. (2004) Synthesis of REE and Y phosphates by Pb-free flux methods and their utilization as standards for electron microprobe analysis and in design of monazite chemical U-Th-Pb dating protocol. American Mineralogist, 89, 1533-1539.

Chervin J.C., Canny B. and Mancinelli M. (2001) Ruby-spheres as pressure gauge for optically transparent high pressure cells. International Journal of High Pressure Research, 21, 305-314.

Choudhary R.N.P. (1991) Structural and electrical properties of monoclinic $PrAsO_4$. Journal of materials science letters, 10, 432-434.

Choudhary R.N.P. and Choudhary B.K. (1990) Structural and dielectric studies of $GdAsO_4$. Journal of materials science letters, 9, 394-396.

Choudhary R.N.P. and Yadav K.L. (1992) Structural and dielectric properties of $DyAsO_4$. Journal of materials science letters, 11, 619-621.

Clavier N., Mesbah A., Szenknect S. and Dacheux N. (2018) Monazite, rhabdophane, xenotime and churchite: Vibrational spectroscopy of gadolinium phosphate polymorphs. Spectrochimica Acta Part A: Molecular and Biomolecular Spectroscopy, 205, 85-94.

Clavier N., Podor R. and Dacheux N. (2011) Crystal chemistry of the monazite structure. Journal of the European Ceramic Society, 31, 941–976.

Cleve P.T. (1879). Sur le scandium. Comptes Rendus, 89, 419-422.

Colombo A. and Cavallo A. (2007) Geological-structural sketch-map of the Ossola-Simplon area-Explanatory Notes. 1906-2006–100 anni Traforo del Sempione.

Connelly N G., Damhus T., Hartshorn R.M. and Hutton A.T. (2005) Nomenclature of inorganic chemistry: IUPAC recommendations 2005. Chemistry International.

Čopjaková R., Novák M. and Franců E. (2011) Formation of authigenic monazite-(Ce) to monazite-(Nd) from Upper Carboniferous graywackes of the Drahany Upland: Roles of the chemical composition of host rock and burial temperature. Lithos, 127, 373–385.

Crichton W.A., Merlini M., Müller H., Chantel J. and Hanfland M. (2012) The high-pressure monazite-to-scheelite transformation in $CaSeO_4$. Mineralogical Magazine, 76, 913-923.

Cullers R.L. and Graf J.L. (1984) Rare earth elements in igneous rocks of the continental crust: predominantly basic and ultrabasic rocks. In Developments in geochemistry, Vol. 2, pp. 237-274. Elsevier.

Dal Piaz G.V. (2010) The Italian Alps: a journey across two centuries of Alpine geology. Journal of the Virtual Explorer, 36, 77-106.

Dal Piaz G.V., Bistacchi A., and Massironi M. (2003) Geological outline of the Alps. Episodes, 26, 175-180.

Dal Piaz G. (1975) Angelo Bianchi. La val Devero ed i suoi minerali. Memorie Istituto Geologia Università Padova, allegato volume X. Società Cooperativa Tipografica, Padova.

Della Ventura G., Mottana A., Parodi G.C., Raudsepp M., Bellatreccia F., Caprilli E., Rossi P. and Fiori S. (1996) Monazite-huttonite solid-solutions from the Vico volcanic complex, Latium, Italy. Mineralogical Magazine, 60, 751-758.

Demartin F., Pilati T., Diella V., Donzelli S., Gentile P. and Gramaccioli C. M. (1991) The chemical composition of xenotime form fissures and pegmatites in the Alps. The Canadian Mineralogist, 29, 69-75.

Deming H.G. (1923) General Chemistry, An Elementary Approach. Wiley, New York.

Dent P. C. (2012) Rare earth elements and permanent magnets. Journal of applied physics, 111, 07A721.

Dimitrov D.T., Dushkin C. D., Petrova N.L., Todorovska R.V., Todorovsky D.S., Anastasova S.Y. and Oliver D. H. (2007) Oxygen detection using junctions based on thin films of yttria-stabilized zirconia doped with platinum nanoparticles and pure yttria-stabilized zirconia. Sensors and Actuators A: Physical, 137, 86-95.

Ding J.Y. and Deng G.Q. (2013) Main problems in the current ionic adsorption rare earth exploration specifications and their amendment proposals. Nonferrous Metals Science and Engineering, 4, 96-102.

Doronin V.P., Sorokina T.P., Lipin P.V., Potapenko O.V., Korotkova N.V. and Gordenko V.I. (2015) Development and introduction of zeolite containing catalysts for cracking with controlled contents of rare earth elements. Catalysis in Industry, 7, 12-16.

Dostal J. (2017) Rare earth element deposits of alkaline igneous rocks. Resources, 6, 34.

Dostal J., Kontak D.J. and Karl S.M. (2014. The Early Jurassic Bokan Mountain peralkaline granitic complex (southeastern Alaska): Geochemistry, petrogenesis and rare-metal mineralization. Lithos, 202, 395-412.

Du X. and Graedel T.E. (2013) Uncovering the end uses of the rare earth elements. Science of the Total Environment, 461, 781-784.

Dunstan D.J. and Spain I.L. (1989) Technology of diamond anvil high- pressure cells: I. Principles, design and construction. Journal of Physics E: Scientific Instruments, 22, 913.

Dushyantha N., Batapola N., Ilankoon I.M S.K., Rohitha S., Premasiri R., Abeysinghe B., Ratnayake N. and Dissanayake K. (2020) The story of rare earth elements (REEs): Occurrences, global distribution, genesis, geology, mineralogy and global production. Ore Geology Reviews, 122, 103521.

Dutta R. and Mandal N. (2012) Effects of pressure on the elasticity and stability of zircon ($ZrSiO_4$): First-principle investigations. Computational materials science, 54, 157-164.

Ehlers A.M., Zaffiro G., Angel R. J., Boffa-Ballaran T., Carpenter M.A., Alvaro M. and Ross N.L. (2022) Thermoelastic properties of zircon: Implications for geothermobarometry. American Mineralogist: Journal of Earth and Planetary Materials, 107, 74-81.

Ercit T.S., Linnen R.L. and Samson I.M. (2005) REE-enriched granitic pegmatites. Rare-element geochemistry and mineral deposits: Geological Association of Canada, GAC Short Course Notes, 17, 175-199.

Errandonea D. (2017) High-pressure phase transitions and properties of MTO_4 compounds with the monazite-type structure. Physica Status Solidi B, 254, 1700016.

Errandonea D., Achary S.N., Pellicer-Porres J. and Tyagi A.K. (2013) Pressure-induced transformations in $PrVO_4$ and $SmVO_4$ and isolation of high-pressure metastable phases. Inorganic Chemistry, 52, 5464-5469.

Errandonea D., Gomis O., Rodríguez-Hernández P., Muñoz A., Ruiz-Fuertes J., Gupta M., Achary S. N., Hirsch A., Manjon F.J., Peters L., Roth G., Tyagi A.K. and Bettinelli M. (2018) High-pressure structural and vibrational properties of monazite-type $BiPO_4$, $LaPO_4$, $CePO_4$, and $PrPO_4$. Journal of Physics: Condensed Matter, 30, 065401.

Errandonea D., Kumar R.S., Achary S.N. and Tyagi A.K. (2011) In situ high-pressure synchrotron x-ray diffraction study of $CeVO_4$ and $TbVO_4$ up to 50 GPa. Physical Review B, 84, 224121.

Errandonea D., Kumar R., Lopez-Solano J., Rodriguez-Hernandez P., Muñoz A., Rabie M.G. and Puche R.S. (2011) Experimental and theoretical study of structural properties and phase transitions in $YAsO_4$ and $YCrO_4$. Physical Review B, 83, 134109.

Errandonea D., Kumar R., Lopez-Solano J., Rodriguez-Hernandez P., Muñoz A., Rabie M.G. and Puche R.S. (2011) Experimental and theoretical study of structural properties and phase transitions in $YAsO_4$ and $YCrO_4$. Physical Review B, 83, 134109.

Errandonea D., Munoz A., Rodriguez-Hernandez P., Proctor J. E., Sapina F. and Bettinelli M. (2015) Theoretical and experimental study of the crystal structures, lattice vibrations, and band structures of monazite-type $PbCrO_4$, $PbSeO_4$, $SrCrO_4$, and $SrSeO_4$. Inorganic chemistry, 54, 7524-7535.

Errandonea D., Pellicer-Porres J., Martinez-Garcia D., Ruiz-Fuertes J., Friedrich A., Morgenroth W., Popescu C., Rodríguez-Hernandez P., Muñoz A. and Bettinelli M. (2016) Phase stability of lanthanum orthovanadate at high pressure. The Journal of Physical Chemistry C, 120, 13749-13762.

Feng J., Xiao B., Zhou R. and Pan W. (2013) Anisotropy in elasticity and thermal conductivity of monazite-type $REPO_4$ (RE= La, Ce, Nd, Sm, Eu and Gd) from first-principles calculations. Acta Materialia, 61, 7364-7383.

Finch R.J. and Hanchar J.M. (2003) Structure and chemistry of zircon and zircon-group minerals. Reviews in mineralogy and geochemistry, 53, 1-25.

Fiske P.S. (1999) Shock-induced phase transitions of $ZrSiO_4$, reversion kinetics, and implications for impact heating in terrestrial craters. In "APS Shock Compression of Condensed Matter Meeting Abstracts".

Fleischer M. and Altschuler Z.S. (1969) The relationship of the rare-earth composition of minerals to geological environment. Geochimica et Cosmochimica Acta, 33, 725-732.

Förster H.J. (1998) The chemical composition of REE-Y-Th-U-rich accessory minerals in peraluminous granites of the Erzgebirge-Fichtelgebirge region, Germany, Part I: The monazite-(Ce)-brabantite solid solution series. American Mineralogist, 83, 259-272.

Förster H.J. (2006) Composition and origin of intermediate solid solutions in the system thorite–xenotime–zircon–coffinite. Lithos, 88, 35-55.

Förster H.J., Ondrejka M. and Uher P. (2011) Mineralogical responses to subsolidus alteration of granitic rocks by oxidizing As-bearing fluids: REE arsenates and As-rich silicates from the Zinnwald granite, eastern Erzgebirge, Germany. The Canadian Mineralogist, 49, 913–930.

Freund J. and Ingalls R. (1989) Inverted isothermal equations of state and determination of B0, B'0 and B0. Journal of Physics and Chemistry of Solids, 50, 263-268.

Fukunga O. and Yamaoka S. (1979) Phase transformations in ABO_4 type compounds under high pressure. Physics and Chemistry of Minerals, 5, 167-177.

Gadolin J. (1794). Undersökning af en svart tung stenart ifrån Ytterby stenbrott i Roslagen.

Gambogi J. (2017) Rare Earths-Mineral Commodity Summaries. US Geological Survey.

Gatta G.D., Milani S., Corti L., Comboni D., Lotti P., Merlini M., and Liermann H.P. (2019) Allanite at high pressure: effect or REE on the elastic behaviour of epidote-group minerals. Physics and Chemistry of Minerals, 46, 783-793.

Gatta G.D., Pagliaro F., Lotti P., Guastoni A., Cañadillas-Delgado L., Fabelo O. and Gigli L. (2021) Allanite at high temperature: effect of REE on the thermal behaviour of epidote-group minerals. Physics and Chemistry of Minerals, 48, 1-16.

Gatta G D., Rotiroti N., Cámara F. and Meven M. (2018) On the labyrinthine world of arsenites: a single-crystal neutron and X-ray diffraction study of cafarsite. Physics and Chemistry of Minerals, 45, 819-829.

Gavrichev K.S., Ryumin M.A., Tyurin A.V., Gurevich V.M., Nikiforova G.E. and Komissarova L.N. (2013) Heat capacity and thermodynamic functions of $YbPO_4$ from 0 to 1800 K. Inorganic Materials, 49, 701-708.

Giarola M., Sanson A., Rahman A., Mariotto G., Bettinelli M., Speghini A. and Cazzanelli E. (2011) Vibrational dynamics of YPO_4 and $ScPO_4$ single crystals: an integrated study by polarized Raman spectroscopy and first-principles calculations. Physical Review B, 83, 224302.

Glass B.P., Liu S. and Leavens P.B. (2002) Reidite: An impact-produced high-pressure polymorph of zircon found in marine sediments. American Mineralogist, 87, 562-565.

Gleissner J., Errandonea D., Segura A., Pellicer-Porres J., Hakeem M.A., Proctor J.E. and Bettinelli M. (2016) Monazite-type $SrCrO_4$ under compression. Physical Review B, 94, 134108.

Glorieux B., Montel J.M. and Matecki M. (2009) Synthesis and sintering of a monazite–brabantite solid solution ceramics using metaphosphate. Journal of the European ceramic society, 29, 1679-1686.

Glushko V., Medvedev V., Bergman G., Vasilev B.P., Gurvich L.V., Alekseev V.I., Kolesov V.P., Yunga V.S., Ioffe N., Vorabev A.F., Reznitskii L.A., Khodakovskii I., Smirnova N.L., Galchenko G. and Baibuz V. F. (1972) Thermicheskie konstanti veshtestv. Academy of Science, Moscow, U.S.S.R.

Gnos E., Mullis J., Ricchi E., Bergemann C. A., Janots E. and Berger A. (2021) Episodes of fissure formation in the Alps: connecting quartz fluid inclusion, fissure monazite age, and fissure orientation data. Swiss journal of geosciences, 114, 1-25.

Golbs S., Cardoso-Gil R. and Schmidt M. (2009) Crystal structure of europium arsenate, $EuAsO_4$. Zeitschrift für Kristallographie-New Crystal Structures, 224, 179-180.

Goldin B.A., Yushkin N.P. and Fishman M.V. (1967) A new yttrium mineral, chernovite. Zap. Vses. Mineral. Obshchest, 96, 699-704.

Gomis O., Lavina B., Rodríguez-Hernández P., Muñoz A., Errandonea R., Errandonea D. and Bettinelli M. (2017) High-pressure structural, elastic, and thermodynamic properties of zircon-type $HoPO_4$ and $TmPO_4$. Journal of Physics: Condensed Matter, 29, 095401.

Gonzalez-Platas J., Alvaro M., Nestola F. and Angel R. (2016) EosFit7-GUI: a new graphical user interface for equation of state calculations, analyses and teaching. Journal of Applied Crystallography, 49, 1377-1382.

Goodenough K.M., Shaw R. A., Smith M., Estrade G., Marqu E., Bernard C. and Nex P. (2019) Economic mineralization in pegmatites: Comparing and contrasting NYF and LCT examples. The Canadian Mineralogist, 57, 753-755.

Goonan T.G. (2011) Rare earth elements: End use and recyclability. US Geological Survey.

Gracia L., Beltrán A., Errandonea D. and Andrés J. (2012) $CaSO_4$ and its pressure-induced phase transitions. A density functional theory study. Inorganic Chemistry, 51, 1751-1759.

Graeser S. (1998) Alpine minerals: a review of the most famous localities of the Central Swiss Alps. Rocks and Minerals, 73, 14-32.

Graeser S. and Albertini C. (1995) Wannigletscher und Conca Cervandone. Lapis, 20, 52-56.

Graeser S. and Roggiani A.G. (1976) Occurrence and genesis of rare arsenate and phosphate minerals around Pizzo Cervandone, Italy/Switzerland. Rendicontri della Societa Italiana di Mineralogia e Petrologia, 32, 279-288.

Graeser S. and Schwander H. (1987) Gasparite-(Ce) and monazite-(Nd): two new minerals to the monazite group from the Alps. Schweizerische Mineralogische und Petrographische Mitteilungen, 67, 103-113.

Graeser S., Schwander H. and Stalder H.A. (1973) A solid solution series between xenotime ($YtPO_4$) and chernovite ($YtAsO_4$). Mineralogical Magazine, 39, 145-151.

Gratz R. and Heinrich W. (1997) Monazite-xenotime thermobarometry: Experimental calibration of the miscibility gap in the binary system $CePO_4$-YPO_4. American Mineralogist, 82, 772-780.

Gratz R. and Heinrich W. (1998) Monazite-xenotime thermometry. III. Experimental calibration of the partitioning of gadolinium between monazite and xenotime. European Journal of Mineralogy, 579-588.

Greaser S. and Schwander H. (1987) Gasparite-(Ce) and monazite-(Nd): two new minerals to the monazite group from the Alps. Schweizerische Mineralogische und Petrographische Mitteilungen, 67, 103-113.

Guastoni A., Cámara F. and Nestola F. (2010) Arsenic-rich fergusonite-beta-(Y) from Mount Cervandone (Western Alps, Italy): Crystal structure and genetic implications. American Mineralogist, 95, 487-494.

Guastoni A., Nestola F., Ferraris C. and Parodi G. (2012) Xenotime-(Y) and Sn-rich thortveitite in miarolitic pegmatites from Baveno, Southern Alps, Italy. Mineralogical Magazine, 76, 761-767.

Guastoni A., Nestola F., Gentile P., Zorzi F., Alvaro M., Lanza A., Peruzzo L., Schiazza M. and Casati N. M. (2013) Deveroite-(Ce): a new REE-oxalate from Mount Cervandone, Devero Valley, Western-Central Alps, Italy. Mineralogical Magazine, 77, 3019-3026.

Guastoni A., Pezzotta F., and Vignola P. (2006) Characterization and genetic inferences of arsenates, sulfates and vanadates of Fe, Cu, Pb, Zn from Mt. Cervandone (Western Alps, Italy). Periodico di Mineralogia, 75, 141–150.

Guastoni A., Pozzi G., Secco L., Schiazza M., Pennacchioni G., Fioretti A. and Nestola F. (2016) Monazite-(Ce) and xenotime-(Y) from an LCT, NYF teritary pegmatite field: evidence from a regional study in the Central Alps (Italy and Switzerland). Canadian Mineralogist, 54, 4, 863-877.

Gupta CK, Krishnamurthy N (2005) Extractive metallurgy of the rare earths.

Gupta I., Singh S., Bhagwan S. and Singh D. (2021) Rare earth (RE) doped phosphors and their emerging applications: A review. Ceramics International, 47, 19282-19303.

Guyonnet D., Lefebvre G. and Menad N. (2018) Rare earth elements and high-tech products. Circular economy coalition for Europe, 1-11.

Haensel R. (1992) European synchrotron radiation facility (ESRF). Review of scientific instruments, 63, 1571-1572.

Haibel A., Beckmann F., Dose T., Herzen J., Utcke S., Lippmann T., Schell N. and Schreyer A. (2008) The GKSS beamlines at PETRA III and DORIS III. In “Developments in X-Ray Tomography VI”.

Han J., Wang Y., Liu R. and Wan F. (2020) Theoretical and experimental investigation of Xenotime-type rare earth phosphate $REPO_4$, (RE= Lu, Yb, Er, Y and Sc) for potential environmental barrier coating applications. Scientific Reports, 10, 1-13.

Harlov D. E. and Förster H.J. (2002) High-grade fluid metasomatism on both a local and regional scale: The Seward Peninsula, Alaska and the Val Strona di Omegna, Ivrea-Verbano zone, northern Italy. Part II: Phosphate mineral chemistry. Journal of Petrology, 43, 801-824.

Harlov D. E., Förster H. J. and Nijland T. G. (2002) Fluid induced nucleation of (Y + REE)-phosphate minerals in apatite: nature and experiment Part I. chlorapatite. American Mineralogist, 87, 245-261

Haskin L. A., Frey F. A., Schmitt R. A. and Smith R. H. (1966) Meteoritic, solar and terrestrial rare-earth distributions. Physics and Chemistry of the Earth, 7, 167-321.

Hay R. S., Mogilevsky P. and Boakye E. (2013) Phase transformations in xenotime rare-earth orthophosphates. Acta materialia, 61, 6933-6947.

Hayes-Labruto L., Schillebeeckx S. J., Workman M. and Shah N. (2013) Contrasting perspectives on China's rare earths policies: Reframing the debate through a stakeholder lens. Energy Policy, 63, 55-68.

Hedrick J.B. (2004). Rare earths in selected US defense applications. In 40th forum on the geology of industrial minerals.

Heffernan K.M., Ross N.L., Spencer E.C. and Boatner L.A. (2016) The structural response of gadolinium phosphate to pressure. Journal of Solid State Chemistry, 241, 180-186.

Heinrich W., Rehs G. and Franz G. (1997) Monazite–xenotime miscibility gap thermometry. I. An empirical calibration. Journal of Metamorphic Geology, 15, 3-16.

Helffrich G. and Connolly J.A.D. (2009) Physical contradictions and remedies using simple polythermal equations of state. American Mineralogist, 94, 1616-1619.

Herwartz D., Nagel T.J., Münker C., Scherer E.E. and Froitzheim N. (2011) Tracing two orogenic cycles in one eclogite sample by Lu–Hf garnet chronometry. Nature Geoscience, 4, 178-183.

Hessel O. (1926) Die Kristallstruktur einiger Verbindungen von der Zusammensetzung MRO_4-I Zirkon $ZrSiO_4$. Z. Krystallogr. 63, 247-254.

Hettmann K., Kreissig K., Rehkämper M., Wenzel T., Mertz-Kraus R. and Markl G. (2014) Thallium geochemistry in the metamorphic Lengenbach sulfide deposit, Switzerland: Thallium-isotope fractionation in a sulfide melt. American Mineralogist, 99, 793-803.

Heuser J.M., Palomares R.I., Bauer J.D., Rodriguez M.L., Cooper J., Lang M. and Deissmann G. (2018) Structural characterization of (Sm,Tb)PO_4 solid solutions and pressure-induced phase transitions. Journal of the European Ceramic Society, 38, 4070-4081.

Heuser J., Bukaemskiy A.A., Neumeier S., Neumann A. and Bosbach, D. (2014) Raman and infrared spectroscopy of monazite-type ceramics used for nuclear waste conditioning. Progress in nuclear energy, 72, 149-155.

Hikichi Y., Hukuo K. I. and Shiokawa J. (1978) Solid solutions in the systems monazite ($CePO_4$)-huttonite ($ThSiO_4$), and monazite-$Ca_{0.5}Th_{0.5}PO_4$. Nippon Kagaku Kaishi, 1978, 1635-1640.

Hikichi Y., Ota T. and Hattori T. (1997) Thermal, mechanical and chemical properties of sintered monazite-(La, Ce, Nd or Sm). Mineralogical journal, 19, 123-130.

Hikichi Y., Ota T., Daimon K., Hattori T. and Mizuno M. (1998) Thermal, Mechanical, and Chemical Properties of Sintered Xenotime-Type RPO_4 (R= Y, Er, Yb, or Lu). Journal of the American Ceramic Society, 81, 2216-2218.

Hinrichs R. and Da Jornada J.A.H. (1997) Piston–cylinder apparatus for high-pressure impedance spectroscopy. Review of scientific instruments, 68, 193-196.

Horchani-Naifer K. and Férid M. (2009) Crystal structure, energy band and optical characterizations of praseodymium monophosphate $PrPO_4$. Inorganica Chimica Acta, 362, 1793-1796.

Hoshino M., Sanematsu K. and Watanabe Y. (2016) REE mineralogy and resources. Handbook on the physics and chemistry of Rare Earths, 49, 129-291.

Huang T., Lee J.S., Kung J. and Lin C.M. (2010) Study of monazite under high pressure. Solid State Communications, 150, 1845-1850.

Hunziker J. C. (1966) Zur Geologie und Geochemie des Gebietes zwischen Valle Antigorio (Provincia di Novara) und Valle di Campo (Kt. Tessin). Schweizerische Mineralogische und Petrographische Mitteilungen, 46, 473-552.

Hunziker J.C., Desmons J. and Hurford A.J. (1992) Thirty-two years of geochronological work in the Central and Western Alps: a review on seven maps. Mémoires de la Géologie, (Lausanne), 13.

Hurford A.J. (1986) Cooling and uplift patterns in the Lepontine Alps, southcentral Switzerland, and an age of vertical movement on the Insubric fault line. Contributions to Mineralogy and Petrology, 93, 413-427.

Innocenzi V., Ippolito N.M., Pietrelli L., Centofanti M., Piga L. and Vegliò F. (2018) Application of solvent extraction operation to recover rare earths from fluorescent lamps. Journal of Cleaner Production, 172, 2840-2852.

Irving A.J. (1978) A review of experimental studies of crystal/liquid trace element partitioning. Geochimica et Cosmochimica Acta, 42, 743-770.

Izatt R.M., Izatt S.R., Bruening R.L., Izatt N.E. and Moyer B.A. (2014) Challenges to achievement of metal sustainability in our high-tech society. Chemical Society Reviews, 43, 2451-2475.

Janots E., Berger A., Gnos E., Whitehouse M., Lewin E. and Pettke T. (2012) Constraints on fluid evolution during metamorphism from U–Th–Pb systematics in Alpine hydrothermal monazite. Chemical Geology, 326, 61-71.

Jensen W.B. (2015) The positions of lanthanum (actinium) and lutetium (lawrencium) in the periodic table: an update. Foundations of Chemistry, 17, 23-31.

Jin G.B. and Soderholm L. (2015) Solid-state syntheses and single-crystal characterizations of three tetravalent thorium and uranium silicates. Journal of Solid State Chemistry, 221, 405-410.

Johan Z. and Johan V. (2005) Accessory minerals of the Cínovec (Zinnwald) granite cupola, Czech Republic: indicators of petrogenetic evolution. Mineralogy and Petrology, 83, 1131-50.

Jonsson E., Högdahl K., Sahlström F., Nysten P. and Sadeghi M. (2014) The Palaeoproterozoic skarn-hosted REE mineralisations of Bastnäs-type: overview and mineralogical-geological character. ERES Abstracts and Proceedings, 1, 382-389.

Jowitt S.M., Werner T.T., Weng Z. and Mudd G.M. (2018) Recycling of the rare earth elements. Current Opinion in Green and Sustainable Chemistry, 13, 1-7.

Kaiser A., Lobert M. and Telle R. (2008) Thermal stability of zircon ($ZrSiO_4$). Journal of the European Ceramic Society, 28, 2199-2211.

Kang D.H. and Schleid T. (2005) Single Crystals of La[AsO_4] with Monazite- and Sm[AsO_4] with Xenotime-Type Structure. ChemInform, 36, 1799–1802.

Kang D.H., Höss P. and Schleid, T. (2005) Xenotime-type Yb[AsO_4]. Acta Crystallographica Section E: Structure Reports Online, 61, i270–i272.

Keller L. M., Hess M., Fügenschuh B. and Schmid S.M. (2005) Structural and metamorphic evolution SW of the Simplon line. Eclogae Geologicae Helvetiae 98, 19-49.

Kennedy A.K., Lofgren G.E. and Wasserburg G.J. (1993) An experimental study of trace element partitioning between olivine, orthopyroxene and melt in chondrules: equilibrium values and kinetic effects. Earth and Planetary Science Letters, 115, 177-195.

Kerbey H.C. (2013) Chernovite-(Y) in reduction spots in Welsh Slate. Journal of the Russell Society, 16, 60-63.

Keskar M., Shelke G.P., Shafeeq M., Phatak R.A., Sali S.K. and Kannan S. (2019) Structural and thermal investigations of $CaU(PO_4)_2$; phase diagram study of $MO{-}UO_2{-}P_2O_5$ systems (M= Ca, Sr, Ba). Journal of Solid State Chemistry, 278, 120850.

Klotz S., Chervin J.C., Munsch P. and Le Marchand G. (2009) Hydrostatic limits of 11 pressure transmitting media. Journal of Physics D: Applied Physics, 42, 075413.

Klotz S., Paumier L., Le March G. and Munsch P. (2009) The effect of temperature on the hydrostatic limit of 4: 1 methanol–ethanol under pressure. High Pressure Research, 29, 649-652.

Knittle E. and Williams Q. (1993) High-pressure Raman spectroscopy of $ZrSiO_4$: Observation of the zircon to scheelite transition at 300 K. American Mineralogist, 78, 245-252.

Kolitsch U. and Holtstam D. (2004a) Crystal chemistry of $REEXO_4$ compounds (X= P, As, V). I. Paragenesis and crystal structure of phosphatian gasparite-(Ce) from the Kesebol Mn-Fe-Cu deposit, Västra Götaland, Sweden. European Journal of Mineralogy, 16, 111-116.

Kolitsch U. and Holtstam D. (2004b) Crystal chemistry of $REEXO_4$ compounds (X= P, As, V). II. Review of $REEXO_4$ compounds and their stability fields. European Journal of Mineralogy, 16, 117-126.

Konings R.J.M., Walter M. and Popa K. (2008) Excess properties of the $(Ln_2{-}2_xCa_xTh_x)(PO_4)_2$ (Ln= La, Ce) solid solutions. The Journal of Chemical Thermodynamics, 40, 1305-1308.

Krstanović I. (1965) Redetermination of oxygen parameters in xenotime, YPO_4. Zeitschrift für Kristallographie, 121, 315-316.

Kusaba K., Syono Y., Kikuchi M. and Fukuoka K. (1985) Shock behavior of zircon: Phase transition to scheelite structure and decomposition. Earth and Planetary Science Letters, 72, 433-439.

Lacomba-Perales R., Errandonea D., Meng Y. and Bettinelli M. (2010) High-pressure stability and compressibility of APO_4 (A= La, Nd, Eu, Gd, Er, and Y) orthophosphates: An x-ray diffraction study using synchrotron radiation. Physical Review B, 81, 064113.

Laing M. (2005) A revised periodic table: with the lanthanides repositioned. Foundations of Chemistry, 7, 203-233.

Laugsch J., Kahle H.G., Schwab M. and Wüchner W. (1975) Investigation of magnetic phase transitions in $HoPO_4$ and $HoAsO_4$. Physica B + C, 80, 269-286.

Lausi A., Polentarutti M., Onesti S., Plaisier J. R., Busetto E., Bais G., Barba L., Cassetta A., Campi G., Lamba D., Pifferi A., Mande S. C., Sarma D. D., Sharma S. M. and Paolucci, G. (2015). Status of the crystallography beamlines at Elettra. The European Physical Journal Plus, 130, 1-8.

Le Godec Y., Hamel G., Solozhenko V. L., Martinez-Garcia D., Philippe J., Hammouda T. and Klotz S. (2009) Portable multi-anvil device for in situ angle-dispersive synchrotron diffraction measurements at high pressure and temperature. Journal of synchrotron radiation, 16, 513-523.

Le Maitre R.W., Streckeisen A., Zanettin B., Le Bas M.J., Bonin B., Bateman P. and Schmid R. (2002) Igneous Rocks: A Classification and Glossary of Terms. Cambridge University Press, Cambridge, UK.

Ledderboge F., Nowak J., Massonne H.J., Förg K., Höppe H.A. and Schleid T. (2018) High-pressure investigations of yttrium (III) oxoarsenate (V): crystal structure and luminescence properties of Eu^{3+}-doped scheelite-type $Y[AsO_4]$ from xenotime-type precursors. Journal of Solid State Chemistry, 263, 65-71.

Lenz C., Nasdala L., Talla D., Hauzenberger C., Seitz R. and Kolitsch U. (2015) Laser-induced REE^{3+} photoluminescence of selected accessory minerals, an “advantageous artefact” in Raman spectroscopy. Chemical Geology, 415, 1-16.

Li H., Zhang S., Zhou S. and Cao X. (2009) Bonding characteristics, thermal expansibility, and compressibility of RXO_4 (R= Rare Earths, X= P, As) within monazite and zircon structures. Inorganic chemistry, 48, 4542-4548.

Li H., Zhou S. and Zhang S. (2007) The relationship between the thermal expansions and structures of ABO_4 oxides. Journal of Solid State Chemistry, 180, 589-595.

Li J., Peng K., Wang P., Zhang N., Feng K., Guan D. and Yang Q. (2020) Critical rare-earth elements mismatch global wind-power ambitions. One Earth, 3, 116-125.

Li M.Y.H., Zhou M.F. and Williams-Jones A.E. (2019) The genesis of regolith-hosted heavy rare earth element deposits: Insights from the world-class Zudong deposit in Jiangxi Province, South China. Economic Geology, 114, 541-568.

Li Y.H.M., Zhao W.W. and Zhou M.F. (2017) Nature of parent rocks, mineralization styles and ore genesis of regolith-hosted REE deposits in South China: an integrated genetic model. Journal of Asian Earth Sciences, 148, 65-95.

Liebermann R.C. (2011) Multi-anvil, high pressure apparatus: a half-century of development and progress. High Pressure Research, 31, 493-532.

Lipin B.R. and McKay G.A. (editors) (2018) Geochemistry and mineralogy of rare earth elements. Reviews in Mineralogy Vol. 21.

Lodders K. and Fegley B. (1998) The planetary scientist's companion. Oxford University Press on Demand.

Lohmüller V.G., Schmidt G., Deppisch B., Gramlich V. and Scheringer C. (1973) The crystal structures of yttrium vanadate, lutetium phosphate and lutetium arsenate. Acta Crystallographica Section B: Structural Crystallography and Crystal Chemistry, 29, 141-142.

Long F.G. and Stager, C.V. (1977) Low temperature crystal structure of $TbAsO_4$ and $DyAsO_4$. Canadian Journal of Physics, 55, 1633-1640.

Long K.R., Van Gosen B.S., Foley N.K. and Cordier D. (2012) The principal rare earth elements deposits of the United States: A summary of domestic deposits and a global perspective. In “Non-renewable resource issues” (Sinding-Larsen, R., and Wellmer F.W., editors).

López-Solano J., Rodríguez-Hernández P., Muñoz A., Gomis O., Santamaría-Perez D., Errandonea D. and Raptis C. (2010) Theoretical and experimental study of the structural stability of $TbPO_4$ at high pressures. Physical Review B, 81, 144126.

Loubet M., Bernat M., Javoy M. and Allegre C.J. (1972) Rare earth contents in carbonatites. Earth and Planetary Science Letters, 14, 226-232.

Lucas J. (1985) Rare earths in fluoride glasses. Journal of the Less Common Metals, 112, 27-40.

Lucas J. (2015) Introduction to Rare Earth Luminescent Materials. In "Rare Earths” (Lucas J., Lucas P., Le Mercier T., Rollat A. and Davenport W., editors).

Lyubetskaya T. and Korenaga J. (2007) Chemical composition of Earth's primitive mantle and its variance: 1. Method and results. J. Geophysical Research, 112, B03211.

Mancheri N.A. (2015) World trade in rare earths, Chinese export restrictions, and implications. Resources Policy, 46, 262-271.

Mancini S. (2000) Le mineralizzazioni a manganese delle Alpi Apuane. Doctoral dissertation, University of Pisa, Italy.

Mao H. K., Xu J.A. and Bell P.M. (1986) Calibration of the ruby pressure gauge to 800 kbar under quasi-hydrostatic conditions. Journal of Geophysical Research: Solid Earth, 91, 4673-4676.

Marignac J.C.G. (1878) Sur l'ytterbine, nouvelle terre contenue dans la gadolinite. Comptes Rendus, 81, 578-581.

Marinsky J.A., Glendenin L.E. and Coryell C.D. (1947) The Chemical Identification of Radioisotopes of Neodymium and of Element 611. Journal of the American chemical society, 69, 2781-2785.

Marqués M., Contreras-García J. Flórez M. and Recio J.M. (2008) On the mechanism of the zircon-reidite pressure induced transformation. Journal of Physics and Chemistry of Solids, 69, 2277-2280.

Marqués M., Florez M., Recio J.M., Gerward L. and Olsen J.S. (2006) Structure and stability of $ZrSiO_4$ under hydrostatic pressure. Physical Review B, 74, 014104.

Massari S. and Ruberti M. (2013) Rare earth elements as critical raw materials: Focus on international markets and future strategies. Resources Policy, 38, 36-43.

Maxelon M. and Mancktelow N.S. (2005) Three-dimensional geometry and tectonostratigraphy of the Pennine zone, Central Alps, Switzerland and Northern Italy. Earth-Science Reviews, 71, 171-227.

Mazeina L., Ushakov S.V., Navrotsky A. and Boatner, L.A. (2005) Formation enthalpy of $ThSiO_4$ and enthalpy of the thorite→huttonite phase transition. Geochimica et Cosmochimica Acta, 69, 4675-4683.

McCubbin F.M., Steele A., Nekvasil H., Schnieders A., Rose T., Fries M. and Jolliff B. L. (2010). Detection of structurally bound hydroxyl in fluorapatite from Apollo Mare basalt 15058, 128 using TOF-SIMS. American Mineralogist, 95, 1141-1150.

Merle O., Cobbold P.R. and Schmid S. (1989) Tertiary kinematics in the Lepontine dome. In "Alpine Tectonics. Geological Society Special Publication, 45" (Coward M. P., Dietrich D. and R.G. Park, editors).

Mesbah A., Clavier N., Lozano-Rodriguez M.J., Szenknect S. and Dacheux N. (2016) Incorporation of Thorium in the Zircon Structure Type through the $Th_{1-x}Er_x(SiO_4)_{1-x}(PO_4)_x$ Thorite–Xenotime Solid Solution. Inorganic Chemistry, 55, 11273-11282.

Metzger S.J., Ledderboge F., Heymann G., Huppertz H. and Schleid T. (2016) High-pressure investigations of lanthanoid oxoarsenates: I. Single crystals of scheelite-type $Ln[AsO_4]$ phases with Ln=La–Nd from monazite-type precursors. Zeitschrift für Naturforschung B, 71, 439-445.

Migdisov A.A. and Williams-Jones A.E. (2014) Hydrothermal transport and deposition of the rare earth elements by fluorine-bearing aqueous liquids. Mineralium Deposita, 49, 987-997.

Migdisov A., Guo X., Nisbet H., Xu H. and Williams-Jones A.E. (2019) Fractionation of REE, U, and Th in natural ore-forming hydrothermal systems: Thermodynamic modeling. The Journal of Chemical Thermodynamics, 128, 305-319.

Mihailova B., Waeselmann N., Stangarone C., Angel R.J., Prencipe M. and Alvaro M. (2019) The pressure-induced phase transition (s) of $ZrSiO_4$: revised: Experimental proof for the existence of a new high-pressure polymorph of zircon. Physics and Chemistry of Minerals, 46, 807-814.

Miletich R., Allan D.R. and Kuhs W.F. (2000) High-pressure single-crystal techniques. Reviews in Mineralogy and Geochemistry, 41, 445-519.

Miller S.A., Caspers H.H. and Rast H.E. (1968) Lattice vibrations of yttrium vanadate. Physical Review, 168, 964.

Mills S.J., Kartashov P.M., Kampf A.R., and Raudsepp M. (2010) Arsenoflorencite (La), a new mineral from the Komi Republic, Russian Federation: description and crystal structure. European Journal of Mineralogy, 22, 613–621.

Milnes A.G. (1973) Structural reinterpretation of the classic Simplon Tunnel Section of the Central Alps. Geological Society of America Bulletin, 84, 269-274.

Mobilio S., Boscherini F. and Meneghini C. (2016) Synchrotron Radiation. Springer-Verlag Berlin An.

Moëlo Y., Lulzac Y., Rouer O., Palvadeau P., Gloaguen É. and Léone P. (2002) Scandium mineralogy: pretulite with scandian zircon and xenotime-(Y) within an apatite-rich oolitic ironstone from Saint-Aubin-Des-Châteaux, Armorican Massif, France. The Canadian Mineralogist, 40, 1657-1673.

Mogilevsky P., Boakye E.E. and Hay R.S. (2007. Solid solubility and thermal expansion in a $LaPO_4$–YPO_4 system. Journal of the American Ceramic Society, 90, 1899-1907.

Mogilevsky P. (2007) On the miscibility gap in monazite–xenotime systems. *Physics and* Chemistry of Minerals, 34, 201-214.

Momma K. and Izumi F. (2011) VESTA 3 for three-dimensional visualization of crystal, volumetric and morphology data. Journal of Applied Crystallography, 44, 1272-1276.

Mondillo N., Balassone G., Boni M., Chelle-Michou C., Cretella S., Mormone A. and Tarallo M. (2019) Rare earth elements (REE) in Al- and Fe-(oxy)-hydroxides in bauxites of provence and languedoc (Southern France): implications for the potential recovery of rees as by-products of bauxite mining. Minerals, 9, 504.

Montel J.M., Glorieux B., Seydoux-Guillaume A.M. and Wirth R. (2006) Synthesis and sintering of a monazite–brabantite solid solution ceramic for nuclear waste storage. Journal of Physics and Chemistry of Solids, 67, 2489-2500.

Montel J.M., Devidal J.L., Gibert F., Cuney M., Brouand M. and Cuney M. (1999) Utilisation des phosphates comme matrices de stockage des déchets radioactifs. Programme INSU Matériaux.

Mooney R.C. (1948) Crystal structures of a series of rare earth phosphates. The Journal of Chemical Physics, 16, 1003-1003.

Mooney R.W. and Toma S.Z. (1967) Molecular Vibrations of the PO_4^{3-} Ion, Site Symmetry D 2 d, in YPO_4. The Journal of Chemical Physics, 46, 3364-3369.

Muller O., Roy R. and Wernick J.H. (1975) Crystal Chemistry of Non-Metallic Materials Vol. 4: The Major Ternary Structural Families. Physics Today, 28, 55.

Mullica D.F., Milligan W.O., Grossie D. A., Beall G. W. and Boatner L. A. (1984) Ninefold coordination $LaPO_4$: Pentagonal interpenetrating tetrahedral polyhedron. Inorganica Chimica Acta, 95, 231-236.

Mullis J. (1996) *PTt* path of quartz formation in extensional veins of the Central Alps. Schweizerische Mineralogische und Petrographische Mitteilungen, 76, 159-164.

Mullis J., Dubessy J., Poty B. and O'Neil J. (1994) Fluid regimes during late stages of a continental collision: Physical, chemical, and stable isotope measurements of fluid inclusions in fissure quartz from a geotraverse through the Central Alps, Switzerland. Geochimica et cosmochimica Acta, 58, 2239-2267.

Muñoz A. and Rodríguez-Hernández P. (2018) High-Pressure Elastic, Vibrational and Structural Study of Monazite-Type $GdPO_4$ from Ab Initio Simulations. Crystals, 8, 209.

Mursic Z., Vogt T., Boysen H. and Frey F. (1992) Single-crystal neutron diffraction study of metamict zircon up to 2000 K. Journal of Applied Crystallography, 25, 519-523.

Muthulakshmi V., Balaji M. and Sundrarajan M. (2020) Biomedical applications of ionic liquid mediated samarium oxide nanoparticles by Andrographis paniculata leaves extract. Materials Chemistry and Physics, 242, 122483.

Mysen B.O. and Virgo D. (1980) Trace element partitioning and melt structure: an experimental study at 1 atm pressure. Geochimica et Cosmochimica Acta, 44, 1917-1930.

Nandedkar R.H., Hürlimann N., Ulmer P. and Müntener O. (2016) Amphibole–melt trace element partitioning of fractionating calc-alkaline magmas in the lower crust: an experimental study. Contributions to Mineralogy and Petrology, 171, 1-25.

Nasdala L., Beran A., Libowitzky E. and Wolf D. (2001) The incorporation of hydroxyl groups and molecular water in natural zircon ($ZrSiO_4$). American Journal of Science, 301, 831-857.

Naslund H. R., Henrıquez F., Nystrom J. O., Vivallo W. and Dobbs F.M. (2002) Magmatic iron ores and associated mineralization: examples from the Chilean High Andes and Coastal cordillera. In "Hydrothermal Iron Oxide Copper-Gold and Related Deposits: A Global Perspective, Vol. 2" (Porter T. M., editor).

Nassar N.T., Du X. and Graedel T.E. (2015) Criticality of the rare earth elements. Journal of Industrial Ecology, 19, 1044-1054.

Naumov A.V. (2008) Review of the world market of rare-earth metals. Russian Journal of Non-Ferrous Metals, 49, 14-22.

Nemati Kharat A. and Zafari R. (2013). Application of zeolitic additives in the fluid catalytic cracking (FCC). Journal of Nanostructures, 3, 209-217.

Ni Y., Hughes J.M., and Mariano A.N. (1995) Crystal chemistry of the monazite and xenotime structures. American Mineralogist, 80, 21-26.

Nilson L.F. (1879a) Sur l'ytterbine, terre nouvelle de M. Marignac. Comptes rendus hebd séances acad sci, Paris 88, 642-647

Nilson L.F. (1879b) Über Scandium, ein neues Erdmetall. Berichte der Deutschen Chemischen Gesellschaft, 12, 554-557

Nipko J.C., Loong C.K., Loewenhaupt M., Braden M., Reichardt W. and Boatner L.A. (1997) Lattice dynamics of xenotime: the phonon dispersion relations and density of states of $LuPO_4$. Physical Review B, 56, 11584.

Nold J.L., Davidson P., Dudley M.A. (2013) The pilot knob magnetite deposit in the Proterozoic St. Francois Mountains Terrane, southeast Missouri, USA: a magmatic and hydrothermal replacement iron deposit. Ore Geology Review 53, 446-469.

Ondrejka M., Uher P., Pršek J. and Ozdín D. (2007) Arsenian monazite-(Ce) and xenotime-(Y), REE arsenates and carbonates from the Tisovec-Rejkovo rhyolite, Western Carpathians, Slovakia: Composition and substitutions in the (REE, Y)XO_4 system (X= P, As, Si, Nb, S). Lithos, 95, 116-129.

Ondrejka M. and Uher P. (2008) Accessory (REE+Y)XO_4 phases: substitutions of As, S, Nb, Zr, Th, Ca and Sr in endogenous systems. In "Goldschmidt Conference Abstracts. 18th Annual V.M. Goldschmidt Conference Vancouver, Canada July, 2008".

Ono S., Funakoshi K., Nakajima Y., Tange Y., and Katsura T. (2004b) Phase transition of zircon at high *PT* conditions. Contributions to Mineralogy and Petrology, 147, 505-509.

Ono S., Tange Y., Katayama I. and Kikegawa T. (2004a). Equations of state of $ZrSiO_4$ phases in the upper mantle. American Mineralogist, 89, 185-188.

Onuma N., Higuchi H., Wakita H. and Nagasawa H. (1968) Trace element partition between two pyroxenes and the host lava. Earth planet Scientific Letters, 5, 47-51.

OriginLab Corporation (2019). OriginPro, Northampton, MA, USA.

Özkan H. (1976). Effect of nuclear radiation on the elastic moduli of zircon. Journal of Applied Physics, 47, 4772-4779.

Özkan H., and Jamieson J. C. (1978) Pressure dependence of the elastic constants of nonmetamict zircon. Physics and Chemistry of Minerals, 2, 215-224.

Özkan H., Cartz L. and Jamieson J. C. (1974). Elastic constants of nonmetamict zirconium silicate. Journal of Applied Physics, 45, 556-562.

Pagliaro F., Lotti P., Guastoni A., Rotiroti N., Battiston T., Gatta G.D. (2022a) Crystal chemistry and miscibility of chernovite-(Y), xenotime-(Y), gasparite-(Ce) and monazite-(Ce) from Mt. Cervandone (Western Alps, Italy). Mineralogical Magazine, 86, 1-18.

Pagliaro F., Lotti P., Comboni D., Battiston T., Guastoni A., Fumagalli P., Rotiroti N. and Gatta G.D. (2022b) High-pressure behavior of gasparite-(Ce) (nominally $CeAsO_4$), a monazite-type arsenate. Physics and Chemistry of Minerals, 49, 1-11.

Panchal V., López-Moreno S., Santamaría-Pérez D., Errandonea D., Manjón F.J., Rodríguez-Hernandez P., Muñoz A., Achary S. N., Tyagi A. K. (2011) Zircon to monazite phase transition in $CeVO_4$: X-ray diffraction and Raman-scattering measurements. Physical Review B 84, 024111.

Papadopoulos A., Tzifas I.T. and Tsikos H. (2019). The potential for REE and associated critical metals in coastal sand (placer) deposits of Greece: A review. Minerals, 9, 469.

Papoutsa A. and Pe-Piper G. (2014) Variation of REE-hydrothermal circulation in complex shear zones: The Cobequid Highlands, Nova Scotia. The Canadian Mineralogist, **52**, 943-968.

Parrish W. (1939). Unit cell and space group of monazite, $(La,Ce,Y)PO_4$. American Mineralogist: Journal of Earth and Planetary Materials, 24, 651-652.

Paufler P. and Weber T. (1999) On the determination of linear expansion coefficients of triclinic crystals using X-ray diffraction. European journal of mineralogy, 11, 721-730.

Pavlik Jr R.S., Holland H.J., and Payzant E.A. (2001) Thermal decomposition of zircon refractories. Journal of the American Ceramic Society, 84, 2930-2936.

Peiffert C. and Cuney M. (1999) Hydrothermal synthesis and X-ray characteristics of compounds of the complete solid solution between monazite ($LaPO_4$) and huttonite ($ThSiO_4$) at 780° C and 200 MPa. In “Stabilisation des déchets et environnement: vers la définition d'objectifs de stabilisation des déchets industriels par la prise en compte de l'impact potentiel sur la santé et l'environnement”.

Pelletier L., Müntener O., Kalt A., Vennemann T.W. and Belgya T. (2008) Emplacement of ultramafic rocks into the continental crust monitored by light and other trace elements: An example from the Geisspfad body (Swiss-Italian Alps). Chemical Geology, 255, 143-159.

Perrière L., Bregiroux D., Naitali B., Audubert F., Champion E., Smith D. S. and Bernache-Assollant D. (2007). Microstructural dependence of the thermal and mechanical properties of monazite LnPO4 (Ln=La to Gd). Journal of the European Ceramic Society, 27, 3207-3213.

Petříček V., Dušek M. and Palatinus L. (2014) Crystallographic computing system JANA2006: general features, Zeitschrift für Kristallographie, 229, 345-352.

Piermarini G.J., Block S., Barnett J.D., Forman R.A. (1975). Calibration of the R1 ruby fluorescence line to 195 kbar. Journal of Applied Physics, 46, 2774-2780.

Plaisier J.R., Nodari L., Gigli L., San Miguel E.P.R., Bertoncello R. and Lausi A. (2017) The X-ray diffraction beamline MCX at Elettra: a case study of non-destructive analysis on stained glass. Acta Imeko, 6, 71-75.

Pradhan A.K. and Choudhary R.N.P. (1989). Raman and infrared effect of Sm^{3+} in $YAsO_4$ crystals. Physica Status Solidi B, 152, K69-K72.

Pradhan A.K., Choudhary R.N.P. and Wanklyn B.M. (1987) Raman and infrared spectra of $YAsO_4$. Physica status solidi B, 139, 337-345.

Prescher C. and Prakapenka V. B. (2015) DIOPTAS: a program for reduction of two-dimensional X-ray diffraction data and data exploration. High Pressure Research, 35, 223-230.

Randive K., Kumar J.V., Bhondwe A. and Lanjewar S. (2014) Understanding the behavior of rare earth elements in minerals and rocks. Gondwana Geological Magazine, 29, 1.

Rauchenstein-Martinek K., Wagner T., Wälle M., Heinrich C. A. and Arlt T. (2016) Chemical evolution of metamorphic fluids in the Central Alps, Switzerland: insight from LA-ICPMS analysis of fluid inclusions. Geofluids, 16, 877-908.

Rebuffi L., Plaisier J. R., Abdellatief M., Lausi A. and Scardi P. (2014) MCX: a Synchrotron Radiation Beamline for X-ray Diffraction Line Profile Analysis. Zeitschrift für anorganische und allgemeine Chemie, 640, 3100-3106.

Regis D., Rubatto D., Darling J., Cenki-Tok B., Zucali M., and Engi M. (2014) Multiple metamorphic stages within an eclogite-facies terrane (Sesia Zone, Western Alps) revealed by Th–U–Pb petrochronology. Journal of Petrology, 55, 1429-1456.

Reid A.F. and Ringwood A.E. (1969). Newly observed high pressure transformations in Mn_3O_4, $CaAl_2O_4$, and $ZrSiO_4$. Earth and Planetary Science Letters, 6, 205-208.

Rice C.E. Robinson W.R. (1976) Lanthanum orthophosphate. Acta Crystallographica B, 32, 2232-2233.

Richter L., Diamond L.W., Atanasova P., Banks D.A. and Gutzmer J. (2018) Hydrothermal formation of heavy rare earth element (HREE)–xenotime deposits at 100° C in a sedimentary basin. Geology, 46, 263-266.

Rigaku Oxford Diffraction (2019) CrysAlisPro Software system, version 1.171.40.67a. Rigaku Corporation, Wroclaw.

Ríos S. and Boffa-Ballaran T. (2003) Microstructure of radiation-damaged zircon under pressure. Journal of Applied Crystallography, 36, 1006-1012.

Rollinson H. and Pease V (1993) Using geochemical data. Evaluation, presentation, interpretation.

Ropp R.C. and Carroll B. (1973) Dimorphic lanthanum orthovanadate. Journal Inorganic Nuclei Chemistry, 35, 1153-1157

Rosenblum S. and Fleischer M. (1995) The distribution of rare-earth elements in minerals of the monazite family. US Geological Survey Bulletin 2140.

Rudnick R.L., Gao S., Holland H.D. and Turekian K.K. (2003) Composition of the continental crust. The crust, 3, 1-64.

Ruiz-Fuertes J., Hirsch A., Friedrich A., Winkler B., Bayarjargal L., Morgenroth W., Peters L., Roth G. and Milman V. (2016) High-pressure phase of $LaPO_4$ studied by x-ray diffraction and second harmonic generation. Physical Review B, 94, 134109.

Ryshkewitch E. (1951) Rigidity Modulus of Some Pure Oxide Bodies 8th Communication to Ceramography. Journal of the American Ceramic Society, 34, 322-326.

Salehuddin A.H.J.M., Ismail A.F., Aziman E.S., Mohamed N.A., Teridi M.A.M. and Idris W.M.R. (2021) Production of high-purity ThO_2 from monazite ores for thorium fuel-based reactor. Progress in Nuclear Energy, 136, 103728.

Samson I.M., Wood S.A. (2005) The rare earth elements: behavior in hydrothermal fluid and concentration in hydrothermal mineral deposits, exclusive of alkaline settings. In “Rare-Element Geochemistry and Mineral Deposits, Vol. 17” (Linnen R.L. and Samson I. M., editors).

Scerri E. (2021) Provisional report on discussions on group 3 of the periodic table. Chemistry International, 43, 31-34.

Schäfer W. and Will G. (1979) Neutron diffraction study of magnetically ordered $TbAsO_4$. Journal of Physics and Chemistry of Solids, 40, 239-245.

Schlenz H., Heuser J., Neumann A., Schmitz S. and Bosbach D. (2013) Monazite as a suitable actinide waste form. Zeitschrift für Kristallographie, 228, 1597.

Schmid S. M., Fügenschuh B., Kissling E. and Schuster R. (2004) Tectonic map and overall architecture of the Alpine orogen. Eclogae Geologicae Helvetiae, 97, 93-117.

Schmidt M., Müller U., Cardoso G.R., Milke E. and Binnewies M. (2005) Zum chemischen Transport und zur Kristallstruktur von Seltenerdarsenaten (V). Zeitschrift für anorganische und allgemeine Chemie, 631, 1154-1162.

Scott H.P., Williams Q. and Knittle E. (2001) Ultralow compressibility silicate without highly coordinated silicon. Physical Review Letters, 88, 015506.

Sengupta D. and Van Gosen B.S. (2016) Placer-type rare earth element deposits. In "Rare earth and critical elements in ore deposits, Reviews in Economic Geology, 18" (Verplanckand P. L. and Hitzman M.W., editors).

Servizio Geologico d'Italia: "Carta Geologica d'Italia alla scala 1:100.000, Foglio 5 (5A) (Val Formazza)". Poligrafico dello Stato.

Servizio Geologico d'Italia: "Carta Geologica d'Italia alla scala 1:100.000, Foglio 15 (Domodossola)". Poligrafico dello Stato.

Seydoux A.M. and Montel J.M. (1997) Experimental determination of the thorite-huttonite phase transition. Terra Nova, 9, 421.

Shannon R.D. (1976) Revised effective ionic radii and systematic studies of interatomic distances in halides and chalcogenides. Acta crystallographica, A32, 751-767.

Shchekina T.I., Rusak A.A., Alferyeva Y.O., Gramenitskiy E.N., Kotelnikov A.R., Zinovieva N.G. and Khvostikov V.A. (2020) REE, Y, Sc, and Li Partition between Aluminosilicate and Aluminofluoride Melts, Depending on Pressure and Water Content in the Model Granite System. Geochemistry International, 58, 391-407.

Shelyug A., Rafiuddin M.R., Mesbah A., Clavier N., Szenknect S., Dacheux N. and Navrotsky A. (2021) Effect of Annealing on Structural and Thermodynamic Properties of $ThSiO_4$-$ErPO_4$ Xenotime Solid Solution. Inorganic chemistry, 60, 12020-12028.

Simmons W.B.S. and Webber K.L. (2008). Pegmatite genesis: state of the art. European Journal of Mineralogy, 20, 421-438.

Sirdeshmukh D.B. and Subhadra K.G. (1975). Note on the elastic properties of zircon. Journal of Applied Physics, 46, 3681-3682.

Sjöberg S., Allard B., Rattray J.E., Callac N., Grawunder A., Ivarsson M. and Dupraz C. (2017) Rare earth element enriched birnessite in water-bearing fractures, the Ytterby mine, Sweden. Applied Geochemistry, 78, 158-171.

Sousa-Aguiar E.F., Trigueiro F.E. and Zotin F. M.Z. (2013) The role of rare earth elements in zeolites and cracking catalysts. Catalysis today, 218, 115-122.

Spear F.S. and Pyle J.M. (2002) Apatite, monazite, and xenotime in metamorphic rocks, Pp. 293-335. In "Phosphates: Geochemical, geobiological, and materials importance, Reviews in Mineralogy and Geochemistry" (Kohn M. J., Rakovan J., Hughes J. M., editors).

Speer J.A. and Cooper B.J. (1982) Crystal structure of synthetic hafnon, $HfSiO_4$, comparison with zircon and the actinide orthosilicates. American Mineralogist, **67**, 804-808.

Spring L., Reymond B., Masson H. and Steck A. (1992) La nappe du Lebendun entre Alte Kaserne et le Val Cairasca (massif du Simplon): nouvelles observations et interprétations. Eclogae geologicae Helvetiae, 85, 85-104

Stangarone C., Angel R.J., Prencipe M., Mihailova B. and Alvaro M. (2019) New insights into the zircon-reidite phase transition. American Mineralogist: Journal of Earth and Planetary Materials, 104, 830-837.

Staudigel H., Albarede F., Blichert-Toft J., Edmond J., McDonough B., Jacobsen S.B. and White W. (1998) Geochemical Earth Reference Model (GERM): description of the initiative. Chemical Geology, 145, 153-159.

Steck A. (2008) Tectonics of the Simplon massif and Lepontine gneiss dome: deformation structures due to collision between the underthrusting European plate and the Adriatic indenter. Swiss Journal of Geosciences, 101, 515-546.

Steck A., Della Torre F., Keller F., Pfeifer H.R., Hunziker J. and Masson H. (2013) Tectonics of the Lepontine Alps: ductile thrusting and folding in the deepest tectonic levels of the Central Alps. Swiss Journal of Geosciences, 106, 427-450.

Steck A., Epard J.L. and Masson H. (2019) The Maggia nappe: an extruding sheath fold basement nappe in the Lepontine gneiss dome of the Central Alps. International Journal of Earth Sciences, 108, 2429-2442.

Steck A., Masson H. and Robyr M. (2015) Tectonics of the Monte Rosa and surrounding nappes (Switzerland and Italy): Tertiary phases of subduction, thrusting and folding in the Pennine Alps. Swiss Journal of Geosciences, 108, 3-34.

Steck, A. and Hunziker (1994) The Tertiary structural and thermal evolution nof the Central Alps – compressional and extensional structures in an orogenic belt. Tectonophysics, 238, 229-254.

Stegen K. S. (2015). Heavy rare earths permanent magnets, and renewable energies: An imminent crisis. Energy Policy, 79, 1-8.

Strada M. and Schwendimann G. (1934) La struttura cristallina di alcuni fosfati ed arseniati di metalli trivalenti. II. Arseniato e fosfato di yttrio. Gazzetta Chimica Italiana, 64, 662-674.

Streckeisen A (1980) Classification and nomenclature of volcanic rocks, lamprophyres, carbonatites and melilitic rocks IUGS Subcommission on the Systematics of Igneous Rocks. Geologische Rundschau, 69, 194-207.

Strzelecki A.C., Barral T., Estevenon P., Mesbah A., Goncharov V., Baker J., Bai J., Clavier N., Szenknect S., Migdisov A., Xu H., Ewing R.C., Dacheux N. and Guo X. (2021) The Role of Water and Hydroxyl Groups in the Structures of Stetindite and Coffinite, $MSiO_4$ (M= Ce, U). Inorganic Chemistry, 60, 718-735.

Strzep A., Watras A., Zawisza K., Boutinaud P. and Wiglusz R.J. (2017) Forgotten and resurrected chernovite-(Y): $YAsO_4$ doped with Eu^{3+} ions as a potential nanosized luminophore. Inorganic Chemistry, 56, 10914-10925.

Swanson H.E., Morris M.C., Evans E. and Ulmer L. (1964) Standard X-ray Diffraction Powder Patterns; National Bureau of Standards; 25 section 3: Washington, DC, USA.

Swift T.K., Moore M.G., Rose-Glowacki H.R. and Sanchez E. (2014) The economic benefits of the North American rare earths industry. Rare Earth Technology Alliance, 1, 817-824.

Takemura K. (2001) Evaluation of the hydrostaticity of a helium-pressure medium with powder X-ray diffraction techniques. Journal of applied physics, 89, 662-668.

Tanabe S. (2015) Glass and rare-earth elements: A personal perspective. International Journal of Applied Glass Science, 6, 305-328.

Tatsi A., Stavrou E., Boulmetis Y. C., Kontos A. G., Raptis Y. S. and Raptis C. (2008) Raman study of tetragonal $TbPO_4$ and observation of a first-order phase transition at high pressure. Journal of Physics: Condensed Matter, 20, 425216.

Thust A., Arinicheva Y., Haussühl E., Ruiz-Fuertes J., Bayarjargal L., Vogel S.C. and Winkler B. (2015) Physical Properties of $La_{1-x}Eu_xPO_4$, $0 \leq x \leq 1$, Monazite-Type Ceramics. Journal of the American Ceramic Society, 98, 4016-4021.

Thust A., Hirsch A., Haussühl E., Schrodt N., Loison L., Schott P. and Winkler B. (2018) Physical properties and microstructures of $La_{1-x}Pr_xPO_4$, monazite-ceramics. Physics and Chemistry of Minerals, 45, 323-332.

Timms N.E., Erickson T.M., Pearce M.A., Cavosie A.J., Schmieder M., Tohver E. and Wittmann A. (2017) A pressure-temperature phase diagram for zircon at extreme conditions. Earth-Science Reviews, 165, 185-202.

Toby B.H. and Von Dreele R.B. (2013) GSAS-II: the genesis of a modern open-source all purpose crystallography software package. Journal of Applied Crystallography, 46, 544-549.

Tossell J.A. (1975) Electronic structures of silicon, aluminum, and magnesium in tetrahedral coordination with oxygen from SCF-X. alpha. MO calculations. Journal of the American Chemical Society, 97, 4840-4844.

Tripathi S., Tiwari R., Shrivastava A.K., Singh V.K., Dubey N. and Dubey V. (2018) A review reports on rare earth activated $AZrO_3$ (A= Ba, Ca, Sr) phosphors for display and sensing applications. Optik, 157, 365-381.

U.S. Geological Survey (2011) 2009 Rare Earth. Minerals yearbook 2009. U.S. Geological Survey, Reston.

U.S. Geological Survey (2021) Mineral commodity summaries 2021. U.S. Geological Survey, Reston.

Ueda T. (1953) The Crystal Structure of Monazite ($CePO_4$) Memoirs of the College of Science, University of Kyoto. Series B 20, 227-246.

Ueda T. (1967) Reexamination of the crystal structure of monazite. Journal of the Japanese Association of Mineralogy, Petroleum and Econimic Geology 58, 170-179.

Ushakov S.V., Helean K.B., Navrotsky A. and Boatner L.A. (2001) Thermochemistry of rare-earth orthophosphates. Journal of Materials Research, 16, 2623-2633.

Van Gosen B.S., Verplanck P.L., Seal R.R., Long K.R. and Gambogi J. (2017) Rare-earth elements, Chap. 0. In “Critical mineral resources of the United States, Economic and environmental geology and prospects for future supply” (Schulz K. J., DeYoung J. H., Seal R. R. and Bradley D.C., editors).

Van Middlesworth P.E. and Wood S.A. (1998) The aqueous geochemistry of the rare earth elements and yttrium. Part 7. REE, Th and U contents in thermal springs associated with the Idaho batholith. Applied Geochemistry, 13, 861-884.

Van Westrenen W., Frank M.R., Hanchar J.M., Fei Y., Finch R. J. and Zha C.S. (2004) In situ determination of the compressibility of synthetic pure zircon ($ZrSiO_4$) and the onset of the zircon-reidite phase transition. American Mineralogist, 89, 197-203.

Vegard L. (1916) VI. Results of crystal analysis. The London, Edinburgh, and Dublin Philosophical Magazine and Journal of Science, 32, 65-96.

Vegard L. (1926) CIV. Results of crystal analysis. The London, Edinburgh, and Dublin Philosophical Magazine and Journal of Science, 1, 1151-1193.

Vegard L. (1927) XLVII. The structure of xenotime and the relation between chemical constitution and crystal structure. The London, Edinburgh, and Dublin Philosophical Magazine and Journal of Science, 4, 511-525.

Vereshchagin O.S., Britvin S.N., Perova, E.N., Brusnitsyn A.I., Polekhovsky Y.S., Shilovskikh V.V., Bocharov V.N., van der Burgt A., Cuchet S. and Meisser N. (2019) Gasparite-(La), La(AsO_4), a new mineral from Mn ores of the Ushkatyn-III deposit, Central Kazakhstan, and metamorphic rocks of the Wanni glacier, Switzerland. American Mineralogist, 104, 1469-1480.

Voncken J. H.L. (2016) The rare earth elements: an introduction. Cham, Switzerland: Springer Intern.

Vorres K.S. (1962) Correlating ABO_4 compound structures. Journal of Chemical Education, 39, 566.

Wall F. (2014) Rare earth elements. Critical metals handbook, 312-339.

Wang L., Yu X., Wei Y., Liu J. and Zhao Z. (2021) Research advances of rare earth catalysts for catalytic purification of vehicle exhausts−Commemorating the 100th anniversary of the birth of Academician Guangxian Xu. Journal of Rare Earths, 39, 1151-1180.

Wang X., Wang B., Tan D., Xiao W. and Song M. (2021) Phase transformations of zircon-type $DyVO_4$ at high pressures up to 36.4 GPa: X-ray diffraction measurements. Journal of Alloys and Compounds, 875, 159926.

Wang Z.Y., Fan H.R., Zhou L., Yang K.F. and She H.D. (2020) Carbonatite-related REE deposits: An overview. Minerals, 10, 965.

Warr L.N. (2021) IMA–CNMNC approved mineral symbols. Mineralogical Magazine, 85, 291-320.

Washburn E.W. and Libman E. E. (1920) An Approximate Determination of the Melting Point Diagram of the System Zirconia-Silica. Journal of the American Ceramic Society, 3, 634-640.

Wasson J.T. and Kallemeyn G. W. (1988) Compositions of chondrites. Philosophical Transactions of the Royal Society of London. Series A, Mathematical and Physical Sciences, 325, 535-544.

Weber T., Harz M., Wehner B., Zahn G. and Paufler P. (1998). Thermal expansion of $CuMoO_4$ below room temperature. Zeitschrift für Kristallographie-Crystalline Materials, 213, 210-216.

Weeks M. E. (1932) The discovery of the elements. XVI. The rare earth elements. Journal of Chemical Education, 9, 1751.

Weisenberger T.B., Rahn M., Van Der Lelij R., Spikings R.A. and Bucher K. (2012) Timing of low-temperature mineral formation during exhumation and cooling in the Central Alps, Switzerland. Earth and Planetary Science Letters, 327, 1-8.

Weng Z., Jowitt S.M., Mudd G.M. and Haque N. (2015) A detailed assessment of global rare earth element resources: opportunities and challenges. Economic Geology, 110, 1925-1952.

White W.M. and Klein E.M. (2013) The oceanic crust. Treatise of Geochemistry, second ed.

Williams-Jones A.E., Migdisov A.A. and Samson I.M. (2012) Hydrothermal mobilisation of the rare earth elements–a tale of "ceria" and "yttria". Elements, 8, 355-360.

Worlton T.G., Cartz L., Niravath A., Ozkan H. (1972) Anisotropic thermal expansion and compressibility of $ZrSiO_4$. High Temperatures-High Pressures, 4, 463-469.

Wu Y., Song M., Zhang Q. and Wang W. (2021) Review of rare-earths recovery from polishing powder waste. Resources, Conservation and Recycling, 171, 105660.

Wyckoff R. W. G. and Hendricks S. B. (1928) Die Kristallstruktur von Zirkon und die Kriterien für spezielle Lagen in tetragonalen Raurngruppen. Zeitschrift für Kristallographie, 66, 73-102.

Yan S. and Liu W. (2022) Rare earth elements in the iron-oxide apatite (IOA) deposit: insights from apatite. International Geology Review, 1-18.

Yang Z. and Woolley A. (2006) Carbonatites in China: A review. Journal of Asian Earth Sciences, 27, 559-575.

Zaman M.M. and Antao S.M. (2020) Crystal structure refinements of four monazite samples from different localities. Minerals, 10, 1028.

Zepf V. (2013) Rare Earth Elements: What and where they are. In "Rare Earth Elements, A New Approach to the Nexus of Supply, Demand and Use: Exemplified along the Use of Neodymium in Permanent Magnets".

Zhang F.X., Wang J.W., Lang M., Zhang J.M., Ewing R.C. and Boatner L.A. (2009) High-pressure phase transitions of $ScPO_4$ and YPO_4. Physical Review B, 80, 18411.

Zhang S., Zhou S., Li H. and Li L. (2008) Investigation of thermal expansion and compressibility of rare-earth orthovanadates using a dielectric chemical bond method. Inorganic chemistry, 47, 7863-7867.

Zhang X., Wei W., Cheng L., Liu J., Wu K. and Liu M. (2019) Effects of niobium and rare earth elements on microstructure and initial marine corrosion behavior of low-alloy steels. Applied Surface Science, 475, 83-93.

Zhao H., Xia J., Yin D., Luo M., Yan C. and Du Y. (2019) Rare earth incorporated electrode materials for advanced energy storage. Coordination Chemistry Reviews, 390, 32-49.

13 Appendix

Table S 13.1: Chemical composition (expressed in oxide wt % and in atoms per formula unit calculated on the basis of 4 oxygen atoms) of all the EPMA-WDS data points of the Mon1 sample.

	Mon1-1	Mon1-2	Mon1-3	Mon1-4	Mon1-5	Mon1-6	Mon1-7	Mon1-8	Mon1-9	Mon1-10
As_2O_5	0.20	0.22	0.12	0.12	0.1	0.18	0.13	0.1	0.23	0.11
P_2O_5	29.00	28.33	28.39	28.94	28.81	28.55	28.47	28.69	28.40	28.83
SiO_2	0.15	0.09	0.05	0.09	0.11	0.37	0.35	0.34	0.31	0.26
V_2O_5	b.d.l.	b.d.l.	b.d.l.	b.d.l.	b.d.l.	b.d.l.	b.d.l.	b.d.l.	b.d.l.	b.d.l.
CaO	1.16	1.65	1.59	1.61	1.23	1.52	1.55	1.38	1.44	0.88
Y_2O_3	1.00	0.76	0.75	0.65	0.70	1.08	1.00	1.12	0.99	0.96
La_2O_3	12.35	13.98	14.59	14.19	14.76	12.12	12.44	12.40	12.77	12.77
Ce_2O_3	29.82	30.88	30.00	30.37	31.23	28.97	29.07	29.22	28.77	30.52
Pr_2O_3	3.26	2.79	3.44	3.28	3.45	3.39	3.35	3.31	3.11	3.36
Nd_2O_3	14.36	12.79	12.31	12.15	12.46	13.06	12.55	13.23	12.98	13.39
Sm_2O_3	3.21	2.18	2.07	2.15	2.16	2.56	2.67	2.70	2.68	2.63
Eu_2O_3	b.d.l.	b.d.l.	b.d.l.	b.d.l.	b.d.l.	b.d.l.	b.d.l.	b.d.l.	b.d.l.	b.d.l.
Gd_2O_3	2.33	1.69	1.33	1.74	1.51	2.24	1.89	2.18	1.97	1.86
Tb_2O_3	b.d.l.	b.d.l.	b.d.l.	b.d.l.	b.d.l.	b.d.l.	b.d.l.	b.d.l.	b.d.l.	b.d.l.
Dy_2O_3	0.19	0.26	0.28	0.18	0.19	0.47	0.66	0.41	0.70	0.54
Ho_2O_3	0.75	0.26	0.40	0.36	0.21	0.63	0.41	0.49	0.49	0.54
Er_2O_3	b.d.l.	0.03	b.d.l.	0.06	0.10	b.d.l.	b.d.l.	b.d.l.	b.d.l.	b.d.l.
Tm_2O_3	b.d.l.	0.03	b.d.l.	0.17	0.05	0.13	0.10	0.06	b.d.l.	0.30
Yb_2O_3	0.02	b.d.l.	b.d.l.	0.01	b.d.l.	b.d.l.	b.d.l.	b.d.l.	b.d.l.	0.08
Lu_2O_3	0.14	0.12	0.05	0.46	0.13	0.02	0.18	0.19	0.14	0.03
PbO	0.03	b.d.l.	b.d.l.	b.d.l.	b.d.l.	0.12	0.10	b.d.l.	0.01	b.d.l.
ThO_2	1.47	2.51	2.76	2.57	2.11	4.45	4.52	4.26	4.03	2.31
UO_2	0.20	b.d.l.	0.07	0.07	b.d.l.	0.04	b.d.l.	b.d.l.	0.01	0.18
Tot.	99.74	98.67	98.29	99.27	99.41	99.99	99.54	100.17	99.13	99.64

	Mon1-1	Mon1-2	Mon1-3	Mon1-4	Mon1-5	Mon1-6	Mon1-7	Mon1-8	Mon1-9	Mon1-10
As	0.004	0.004	0.002	0.002	0.002	0.003	0.002	0.002	0.004	0.002
P	0.974	0.965	0.970	0.975	0.972	0.961	0.963	0.964	0.963	0.972

Si	0.006	0.003	0.002	0.003	0.004	0.014	0.014	0.013	0.012	0.010
V	/	/	/	/	/	/	/	/	/	/
Ca	0.049	0.071	0.069	0.069	0.052	0.065	0.066	0.058	0.062	0.037
Y	0.021	0.016	0.016	0.013	0.014	0.022	0.021	0.023	0.021	0.020
La	0.180	0.207	0.217	0.208	0.217	0.177	0.183	0.181	0.188	0.187
Ce	0.433	0.455	0.443	0.442	0.455	0.421	0.425	0.424	0.422	0.445
Pr	0.047	0.041	0.050	0.047	0.050	0.049	0.048	0.048	0.045	0.048
Nd	0.203	0.183	0.177	0.172	0.177	0.185	0.179	0.187	0.185	0.190
Sm	0.044	0.030	0.028	0.029	0.029	0.035	0.036	0.037	0.037	0.036
Eu	/	/	/	/	/	/	/	/	/	/
Gd	0.030	0.022	0.017	0.023	0.020	0.029	0.025	0.028	0.026	0.024
Tb	/	/	/	/	/	/	/	/	/	/
Dy	0.002	0.003	0.003	0.002	0.002	0.006	0.008	0.005	0.009	0.007
Ho	0.009	0.003	0.005	0.004	0.002	0.008	0.005	0.006	0.006	0.006
Er	/	/	/	/	0.001	/	/	/	/	/
Tm	/	/	/	0.002	/	0.001	0.001	/	/	0.003
Yb	/	/	/	/	/	/	/	/	/	/
Lu	0.001	0.001	/	0.005	0.001	/	0.002	0.002	0.001	/
Pb	/	/	/	/	/	0.001	0.001	/	/	/
Th	0.013	0.023	0.025	0.023	0.019	0.040	0.041	0.038	0.036	0.021
U	0.001	/	/	/	/	/	/	/	/	0.001

Table S 13.2: Chemical composition (expressed in oxide wt % and in atoms per formula unit calculated on the basis of 4 oxygen atoms) of all the EPMA-WDS data points of the Mon2 sample.

	Mon2-1	Mon2-2	Mon2-3	Mon2-4	Mon2-5	Mon2-6	Mon2-7	Mon2-8
As_2O_5	2.04	2.17	3.12	3.15	1.63	2.18	1.40	2.44
P_2O_5	28.33	28.50	26.85	26.69	28.30	27.30	28.62	27.55
SiO_2	0.09	0.13	0.39	0.59	0.12	0.22	0.14	0.20
V_2O_5	b.d.l.	b.d.l.	b.d.l.	b.d.l.	b.d.l.	b.d.l.	b.d.l.	b.d.l.
CaO	0.36	0.20	0.85	1.19	0.68	1.22	0.26	0.71
Y_2O_3	0.50	0.43	0.49	0.54	0.56	0.67	0.52	0.49
La_2O_3	13.55	12.86	12.40	12.39	14.53	13.11	12.40	13.44
Ce_2O_3	32.61	32.10	30.64	29.13	31.78	30.80	31.55	31.91
Pr_2O_3	3.90	3.74	3.10	3.33	3.86	3.69	4.03	3.93
Nd_2O_3	13.96	14.99	13.44	12.72	13.42	12.86	15.03	13.21
Sm_2O_3	2.73	2.64	2.50	2.38	2.42	2.28	2.81	2.30
Eu_2O_3	b.d.l.	b.d.l.	b.d.l.	b.d.l.	b.d.l.	b.d.l.	b.d.l.	b.d.l.
Gd_2O_3	1.36	1.35	1.21	1.63	1.93	1.59	1.62	1.17
Tb_2O_3	b.d.l.	b.d.l.	b.d.l.	b.d.l.	b.d.l.	b.d.l.	b.d.l.	b.d.l.
Dy_2O_3	0.12	0.11	0.46	0.49	0.37	0.26	0.15	0.43
Ho_2O_3	0.01	0.23	0.41	0.45	0.22	0.54	0.29	0.41
Er_2O_3	0.02	b.d.l.	b.d.l.	b.d.l.	b.d.l.	b.d.l.	b.d.l.	b.d.l.
Tm_2O_3	0.01	0.01	b.d.l.	b.d.l.	b.d.l.	0.32	b.d.l.	b.d.l.
Yb_2O_3	b.d.l.	0.06	b.d.l.	b.d.l.	0.06	b.d.l.	b.d.l.	0.01
Lu_2O_3	b.d.l.	0.11	0.14	0.03	b.d.l.	0.23	b.d.l.	0.34
PbO	b.d.l.	0.05	b.d.l.	b.d.l.	0.03	b.d.l.	b.d.l.	b.d.l.
ThO_2	0.90	1.36	4.35	5.30	0.94	2.41	1.28	2.01
UO_2	0.18	b.d.l.	0.23	0.11	0.23	0.13	0.13	0.06
Tot.	100.74	101.12	100.65	100.19	101.16	99.88	100.30	100.69

	Mon2-1	Mon2-2	Mon2-3	Mon2-4	Mon2-5	Mon2-6	Mon2-7	Mon2-8
As	0.042	0.044	0.065	0.065	0.033	0.045	0.029	0.050
P	0.947	0.948	0.908	0.903	0.945	0.926	0.959	0.927

Si	0.003	0.005	0.015	0.023	0.004	0.009	0.005	0.008
V	/	/	/	/	/	/	/	/
Ca	0.015	0.008	0.036	0.051	0.028	0.052	0.011	0.030
Y	0.010	0.009	0.010	0.011	0.011	0.014	0.011	0.010
La	0.197	0.186	0.182	0.182	0.211	0.193	0.181	0.197
Ce	0.471	0.461	0.448	0.426	0.459	0.451	0.457	0.464
Pr	0.056	0.053	0.045	0.048	0.055	0.054	0.058	0.057
Nd	0.196	0.210	0.191	0.181	0.189	0.184	0.212	0.187
Sm	0.037	0.035	0.034	0.032	0.032	0.031	0.038	0.031
Eu	/	/	/	/	/	/	/	/
Gd	0.017	0.017	0.016	0.021	0.025	0.021	0.021	0.015
Tb	/	/	/	/	/	/	/	/
Dy	0.001	0.001	0.005	0.006	0.004	0.003	0.001	0.005
Ho	/	0.002	0.005	0.005	0.002	0.006	0.003	0.005
Er	/	/	/	/	/	/	9.562	/
Tm	/	/	/	/	/	0.004	/	/
Yb	/	/	/	/	/	/	/	/
Lu	/	0.001	0.001	/	/	0.002	/	0.004
Pb	/	/	/	/	/	/	/	/
Th	0.008	0.012	0.039	0.048	0.008	0.022	0.011	0.018
U	0.001	/	0.002	0.001	0.002	0.001	0.001	/

Table S 13.3: Chemical composition (expressed in oxide wt % and in atoms per formula unit calculated on the basis of 4 oxygen atoms) of all the EPMA-WDS data points of the Gasp3 sample.

	Gasp3-1	Gasp3-2	Gasp3-3	Gasp3-4	Gasp3-5	Gasp3-6	Gasp3-	Gasp3-8
As_2O_5	40.59	39.90	38.79	39.13	36.38	38.81	38.67	36.60
P_2O_5	0.36	0.25	0.82	0.27	3.01	0.55	0.48	0.87
SiO_2	1.43	1.64	1.36	2.39	1.21	1.90	2.29	1.56
V_2O_5	b.d.l.	b.d.l.	b.d.l.	b.d.l.	b.d.l.	b.d.l.	b.d.l.	b.d.l.
CaO	1.22	1.34	1.79	1.44	1.56	1.41	1.44	1.50
Y_2O_3	b.d.l.	b.d.l.	b.d.l.	b.d.l.	b.d.l.	b.d.l.	b.d.l.	b.d.l.
La_2O_3	12.16	11.30	10.89	11.18	11.79	11.92	10.74	11.07
Ce_2O_3	29.09	27.38	28.96	27.08	31.19	27.40	27.47	27.84
Pr_2O_3	3.38	3.08	3.03	2.98	2.95	2.94	2.68	2.83
Nd_2O_3	11.54	12.75	10.86	12.27	10.26	11.72	12.15	11.48
Sm_2O_3	1.26	1.66	1.33	1.73	0.90	1.58	1.84	1.16
Eu_2O_3	b.d.l.	b.d.l.	b.d.l.	b.d.l.	b.d.l.	b.d.l.	b.d.l.	b.d.l.
Gd_2O_3	0.20	0.56	0.53	0.58	0.19	0.62	0.30	0.04
Tb_2O_3	b.d.l.	b.d.l.	b.d.l.	b.d.l.	b.d.l.	b.d.l.	b.d.l.	b.d.l.
Dy_2O_3	0.05	b.d.l.	0.13	b.d.l.	b.d.l.	b.d.l.	b.d.l.	0.06
Ho_2O_3	b.d.l.	b.d.l.	b.d.l.	b.d.l.	b.d.l.	b.d.l.	b.d.l.	0.06
Er_2O_3	0.03	0.05	0.01	0.13	b.d.l.	b.d.l.	b.d.l.	b.d.l.
Tm_2O_3	b.d.l.	0.07	b.d.l.	0.15	b.d.l.	b.d.l.	0.02	b.d.l.
Yb_2O_3	0.16	b.d.l.	0.11	b.d.l.	b.d.l.	0.06	b.d.l.	0.04
Lu_2O_3	b.d.l.	0.09	b.d.l.	b.d.l.	0.08	b.d.l.	0.14	b.d.l.
PbO	b.d.l.	b.d.l.	b.d.l.	b.d.l.	0.09	b.d.l.	0.07	b.d.l.
ThO_2	0.32	0.14	0.65	1.74	0.95	1.03	2.23	0.13
UO_2	0.01	b.d.l.	b.d.l.	b.d.l.	b.d.l.	b.d.l.	b.d.l.	b.d.l.
Tot.	101.88	100.27	99.33	101.12	100.63	100.05	100.57	95.38

	Gasp3-1	Gasp3-2	Gasp3-3	Gasp3-4	Gasp3-5	Gasp3-6	Gasp3-	Gasp3-8
As	0.945	0.942	0.922	0.914	0.846	0.917	0.909	0.907
P	0.013	0.009	0.031	0.010	0.113	0.021	0.018	0.035
Si	0.063	0.074	0.062	0.107	0.054	0.086	0.103	0.074
V	b.d.l.	b.d.l.	b.d.l.	b.d.l.	b.d.l.	b.d.l.	b.d.l.	b.d.l.
Ca	0.058	0.064	0.087	0.069	0.074	0.068	0.069	0.076

Y	/	/	/	/	/	0.001	/	0.001
La	0.199	0.188	0.182	0.184	0.193	0.198	0.178	0.193
Ce	0.474	0.452	0.482	0.443	0.508	0.453	0.452	0.483
Pr	0.054	0.050	0.050	0.048	0.047	0.048	0.044	0.049
Nd	0.183	0.205	0.176	0.195	0.163	0.189	0.195	0.194
Sm	0.019	0.025	0.020	0.026	0.013	0.024	0.028	0.019
Eu	/	/	/	/	/	/	/	/
Gd	0.003	0.008	0.008	0.008	0.002	0.009	0.004	/
Tb	/	/	/	/	/	/	/	/
Dy	/	/	0.001	/	/	/	/	0.001
Ho	/	/	/	/	/	/	/	/
Er	/	/	/	0.001	/	/	/	/
Tm	/	0.001	/	0.002	/	/	/	/
Yb	0.002	/	0.001	/	/	/	/	/
Lu	/	0.001	/	/	0.001	/	0.001	/
Pb	/	/	/	/	0.001	/	/	/
Th	0.003	0.001	0.006	0.017	0.009	0.010	0.022	0.001
U	/	/	/	/	/	/	/	/

Table S 13.4: Chemical composition (expressed in oxide wt % and in atoms per formula unit calculated on the basis of 4 oxygen atoms) of all the EPMA-WDS data points of the Gasp4 sample.

	Gasp4-1	Gasp4-2	Gasp4-3	Gasp4-4	Gasp4-5	Gasp4-6	Gasp4-7	Gasp4-8	Gasp4-9	Gasp4-10	Gasp4-11	Gasp4-12	Gasp4-13	Gasp4-14	Gasp4-15	Gasp4-16	Gasp4-17
As_2O_5	40.22	38.45	39.92	40.15	40.99	42.06	41.43	42.63	42.52	42.97	42.52	42.69	40.90	41.23	41.09	41.33	40.96
P_2O_5	0.35	0.06	0.04	0.61	0.11	b.d.l.	0.05	0.02	0.24	0.26	0.04	0.23	0.02	0.13	0.07	0.16	0.12
SiO_2	2.03	3.11	1.97	1.70	1.99	1.28	0.60	1.17	0.58	0.67	1.01	0.70	1.61	1.58	1.42	1.68	1.77
V_2O_5	b.d.l.	b.d.l.	b.d.l.	b.d.l.	b.d.l.	b.d.l.	b.d.l.	b.d.l.	b.d.l.	b.d.l.	b.d.l.	b.d.l.	b.d.l.	b.d.l.	b.d.l.	b.d.l.	b.d.l.
CaO	1.80	1.69	1.71	1.88	2.03	1.90	2.15	2.05	1.73	1.86	1.64	1.74	2.25	2.00	1.64	1.98	2.26
Y_2O_3	0.13	0.04	0.04	0.05	0.11	0.03	b.d.l.	0.02	b.d.l.	b.d.l.	0.01	b.d.l.	0.01	0.09	0.05	0.09	0.11
La_2O_3	12.14	10.89	11.97	13.24	12.01	13.42	14.43	13.43	13.30	13.39	13.94	13.84	12.51	12.50	12.84	12.97	12.00
Ce_2O_3	27.11	24.56	25.29	25.97	26.25	27.24	26.01	26.96	27.15	27.76	26.99	27.59	26.84	27.41	27.95	27.11	27.32
Pr_2O_3	2.76	2.52	2.69	1.92	2.72	2.67	2.60	2.64	2.62	2.27	2.43	2.82	2.47	2.60	2.53	2.58	2.58
Nd_2O_3	9.58	8.23	8.03	8.04	9.40	9.43	9.22	9.46	9.46	8.90	9.01	9.24	10.20	9.89	10.11	10.06	10.03
Sm_2O_3	1.32	1.33	1.06	0.91	1.35	1.18	1.04	1.05	1.10	0.96	1.08	1.29	1.48	1.24	1.47	1.37	1.33
Eu_2O_3	b.d.l.	b.d.l.	b.d.l.	b.d.l.	0.02	b.d.l.	b.d.l.	b.d.l.	b.d.l.	b.d.l.	b.d.l.	b.d.l.	b.d.l.	b.d.l.	b.d.l.	b.d.l.	b.d.l.
Gd_2O_3	0.72	0.80	0.56	0.56	0.55	0.50	0.41	0.72	0.47	0.31	0.49	0.50	0.81	0.55	0.97	0.71	0.81
Tb_2O_3	b.d.l.	b.d.l.	b.d.l.	b.d.l.	b.d.l.	b.d.l.	b.d.l.	b.d.l.	b.d.l.	b.d.l.	b.d.l.	b.d.l.	b.d.l.	b.d.l.	b.d.l.	b.d.l.	b.d.l.
Dy_2O_3	b.d.l.	0.12	0.04	0.17	0.04	b.d.l.	b.d.l.	b.d.l.	b.d.l.	0.02	b.d.l.	b.d.l.	0.19	b.d.l.	b.d.l.	0.22	b.d.l.
Ho_2O_3	0.13	b.d.l.	b.d.l.	b.d.l.	0.16	0.05	b.d.l.	0.14	b.d.l.	0.12	b.d.l.	0.01	0.05	b.d.l.	b.d.l.	b.d.l.	b.d.l.
Er_2O_3	0.13	b.d.l.	b.d.l.	b.d.l.	b.d.l.	0.06	0.23	b.d.l.	b.d.l.	b.d.l.	b.d.l.	0.22	b.d.l.	b.d.l.	b.d.l.	b.d.l.	b.d.l.
Tm_2O_3	b.d.l.	b.d.l.	b.d.l.	0.03	0.09	b.d.l.	0.06	b.d.l.	0.01	b.d.l.	b.d.l.	b.d.l.	b.d.l.	b.d.l.	b.d.l.	b.d.l.	0.13
Yb_2O_3	b.d.l.	0.12	0.17	b.d.l.	b.d.l.	b.d.l.	b.d.l.	0.12	b.d.l.	0.08	b.d.l.	b.d.l.	0.06	0.22	b.d.l.	0.01	0.04
Lu_2O_3	b.d.l.	0.11	0.16	0.08	0.06	b.d.l.	0.09	0.05	0.12	b.d.l.	0.15	b.d.l.	b.d.l.	0.02	0.07	0.02	0.07
PbO	0.21	b.d.l.	0.02	0.14	0.06	b.d.l.	0.12	0.04	0.07	0.04	b.d.l.	0.12	0.01	b.d.l.	0.06	b.d.l.	0.10
ThO_2	3.93	9.13	6.52	5.05	3.14	0.96	0.46	0.83	1.08	1.20	0.63	0.90	0.53	1.06	0.49	0.93	0.92
UO_2	0.15	0.26	0.19	0.12	0.08	b.d.l.	0.17	b.d.l.	0.05	b.d.l.	b.d.l.	b.d.l.	b.d.l.	b.d.l.	b.d.l.	b.d.l.	0.06
Tot.	102.77	101.49	100.46	100.69	101.22	100.87	99.15	101.40	100.57	100.87	99.99	101.96	100.02	100.58	100.83	101.29	100.69

	Gasp4-1	Gasp4-2	Gasp4-3	Gasp4-4	Gasp4-5	Gasp4-6	Gasp4-7	Gasp4-8	Gasp4-9	Gasp4-10	Gasp4-11	Gasp4-12	Gasp4-13	Gasp4-14	Gasp4-15	Gasp4-16	Gasp4-17
As	0.926	0.900	0.943	0.938	0.949	0.978	0.988	0.984	0.995	0.997	0.995	0.987	0.958	0.960	0.962	0.955	0.951
P	0.013	0.002	0.001	0.023	0.004	/	0.002	/	0.009	0.009	0.001	0.008	0	0.005	0.002	0.006	0.004
Si	0.089	0.139	0.089	0.076	0.088	0.057	0.027	0.051	0.026	0.029	0.045	0.031	0.072	0.070	0.063	0.074	0.078
V	/	/	/	/	/	/	/	/	/	/	/	/	/	/	/	/	/
Ca	0.085	0.081	0.083	0.090	0.096	0.090	0.105	0.097	0.083	0.088	0.078	0.082	0.108	0.095	0.078	0.093	0.107

Y	0.003	/	0.001	0.001	0.002	/	/	/	/	/	/	/	/	0.002	0.001	0.002	0.002
La	0.197	0.179	0.199	0.218	0.196	0.220	0.242	0.218	0.219	0.219	0.230	0.225	0.206	0.205	0.212	0.211	0.196
Ce	0.437	0.402	0.418	0.424	0.425	0.443	0.434	0.436	0.445	0.451	0.442	0.446	0.440	0.447	0.458	0.439	0.444
Pr	0.044	0.041	0.044	0.031	0.044	0.043	0.043	0.042	0.042	0.036	0.039	0.045	0.040	0.042	0.041	0.041	0.041
Nd	0.150	0.131	0.129	0.128	0.148	0.149	0.150	0.149	0.151	0.141	0.144	0.146	0.163	0.157	0.161	0.158	0.159
Sm	0.020	0.020	0.016	0.014	0.020	0.018	0.016	0.016	0.016	0.014	0.016	0.019	0.022	0.019	0.022	0.020	0.020
Eu	/	/	/	/	/	/	/	/	/	/	/	/	/	/	/	/	/
Gd	0.010	0.011	0.008	0.008	0.008	0.007	0.006	0.010	0.007	0.004	0.007	0.007	0.012	0.008	0.014	0.010	0.011
Tb	/	/	/	/	/	/	/	/	/	/	/	/	/	/	/	/	/
Dy	/	0.001	/	0.002	/	/	/	/	/	/	/	/	0.002	/	/	0.003	/
Ho	0.001	/	/	/	0.002	/	/	0.002	/	0.001	/	/	/	/	/	/	/
Er	0.001	/	/	/	/	/	0.003	/	/	/	/	0.003	/	/	/	/	/
Tm	/	/	/	/	0.001	/	/	/	/	/	/	/	/	/	/	/	0.001
Yb	/	0.001	0.002	/	/	/	/	0.001	/	0.001	/	/	/	0.003	/	/	/
Lu	/	0.001	0.002	0.001	/	/	0.001	/	0.001	/	0.002	/	/	/	/	/	/
Pb	0.002	/	/	0.001	/	/	0.001	/	/	/	/	0.001	/	/	/	/	0.001
Th	0.039	0.093	0.067	0.051	0.031	0.009	0.004	0.008	0.011	0.012	0.006	0.009	0.005	0.010	0.005	0.009	0.009
U	0.001	0.002	0.001	0.001	/	/	0.001	/	/	/	/	/	/	/	/	/	/

Table S 13.5: Chemical composition (expressed in oxide wt % and in atoms per formula unit calculated on the basis of 4 oxygen atoms) of all the EPMA-WDS data points of the Ch6 sample.

	Ch6-1	Ch6-2	Ch6-3	Ch6-4	Ch6-5	Ch6-6	Ch6-7	Ch6-8	Ch6-9	Ch6-10	Ch6-11	Ch6-12	Ch6-13	Ch6-14	Ch6-15	Ch6-16
As_2O_5	34.40	34.77	35.57	35.07	30.14	34.46	32.16	30.56	34.40	32.17	34.44	35.07	31.92	35.61	33.06	33.01
P_2O_5	7.38	7.01	6.48	6.41	10.1	6.87	8.82	10.0	6.66	8.29	7.12	6.62	9.36	2.17	7.99	8.02
SiO_2	0.57	0.59	0.62	0.66	0.49	0.75	0.39	0.50	1.02	0.77	0.62	0.67	0.61	3.17	0.72	0.71
V_2O_5	b.d.l.	0.07	b.d.l.	b.d.l.	0.04	0.01	b.d.l.	b.d.l.	b.d.l.	b.d.l.	0.02	b.d.l.	b.d.l.	b.d.l.	b.d.l.	0.01
CaO	b.d.l.	0.03	0.03	0.01	b.d.l.	0.03	0.06	0.04	0.01	0.02	0.03	0.04	0.02	0.01	b.d.l.	b.d.l.
Y_2O_3	34.57	34.01	33.80	33.47	35.05	33.35	34.47	34.89	33.01	33.36	33.61	34.21	34.35	25.38	33.81	33.65
La_2O_3	b.d.l.	0.03	b.d.l.	b.d.l.	b.d.l.	0.01	0.22	0.13	b.d.l.	0.13	0.02	b.d.l.	b.d.l.	0.01	b.d.l.	0.05
Ce_2O_3	0.36	0.04	0.16	0.19	0.15	0.18	0.33	0.13	0.04	0.01	0.08	0.01	0.11	0.37	0.10	0.06
Pr_2O_3	b.d.l.	b.d.l.	b.d.l.	0.02	b.d.l.	b.d.l.	b.d.l.	b.d.l.	b.d.l.	0.10	0.09	0.11	0.17	0.04	0.09	0.07
Nd_2O_3	0.64	0.61	0.56	0.59	0.38	0.58	0.57	0.40	0.65	0.52	0.45	0.58	0.71	2.20	0.85	0.62
Sm_2O_3	0.99	0.92	0.92	0.87	0.73	0.87	0.95	1.02	0.97	1.00	0.85	1.11	0.96	2.36	1.30	0.91
Eu_2O_3	b.d.l.	0.10	0.02	0.10	b.d.l.	0.05	0.07	b.d.l.	0.04	0.03	b.d.l.	0.09	0.25	0.02	0.20	b.d.l.
Gd_2O_3	2.46	2.50	2.40	2.60	2.10	2.49	2.71	2.61	2.90	2.81	2.35	2.40	2.69	4.52	3.18	2.58
Tb_2O_3	0.57	0.77	0.71	0.31	0.67	0.68	0.59	0.55	0.61	0.37	0.63	0.62	0.57	0.76	0.60	0.58
Dy_2O_3	4.89	4.89	5.36	5.11	5.07	4.58	5.21	4.45	4.70	4.70	4.72	4.98	4.72	4.58	4.67	4.90
Ho_2O_3	2.24	2.38	2.24	2.40	2.15	2.46	2.27	2.57	2.54	2.39	2.40	2.59	2.43	3.05	2.66	2.11
Er_2O_3	3.29	3.53	3.39	3.39	3.85	3.47	3.37	3.12	3.51	2.95	3.32	3.45	3.26	2.23	3.19	3.56
Tm_2O_3	0.48	0.61	0.33	0.47	0.49	0.62	0.38	0.29	0.37	0.30	0.35	0.52	0.51	0.52	0.47	0.11
Yb_2O_3	3.20	2.90	3.04	2.65	2.92	3.14	3.10	2.77	2.97	2.96	2.92	2.81	2.85	1.73	2.46	3.01
Lu_2O_3	1.15	1.19	1.10	1.27	1.26	1.32	0.82	1.18	1.16	1.54	1.28	1.35	1.35	1.13	1.20	0.99
PbO	0.08	0.12	0.32	0.29	0.19	0.18	0.20	0.26	0.06	0.29	0.15	0	0.37	0.31	0.13	0.21
ThO_2	2.06	2.55	2.31	2.66	1.72	2.81	1.87	2.10	4.27	2.68	2.38	2.41	2.17	10.8	2.87	2.79
UO_2	0.82	1.17	1.02	1.12	0.71	1.11	0.70	0.62	1.17	0.82	1.33	1.04	0.65	1.96	0.60	0.81
Tot.	100.22	100.89	100.49	99.75	98.31	100.13	99.38	98.32	101.17	98.32	99.25	100.79	100.13	103.07	100.27	98.85

	Ch6-1	Ch6-2	Ch6-3	Ch6-4	Ch6-5	Ch6-6	Ch6-7	Ch6-8	Ch6-9	Ch6-10	Ch6-11	Ch6-12	Ch6-13	Ch6-14	Ch6-15	Ch6-16
As	0.716	0.724	0.745	0.741	0.627	0.724	0.670	0.635	0.720	0.679	0.725	0.732	0.657	0.782	0.689	0.693
P	0.248	0.236	0.220	0.219	0.340	0.234	0.297	0.337	0.226	0.283	0.242	0.224	0.312	0.077	0.269	0.273
Si	0.022	0.023	0.025	0.026	0.019	0.030	0.015	0.019	0.041	0.031	0.025	0.027	0.024	0.133	0.028	0.028
V	0	0.002	0	0	0.001	0	0	0	0	0	0	0	0	0	0	0
Ca	0	0.001	0.001	0	0	0.001	0.002	0.002	0	0	0.001	0.001	0	0	0	0
Y	0.732	0.721	0.720	0.720	0.742	0.713	0.731	0.737	0.703	0.717	0.720	0.727	0.720	0.567	0.717	0.719

La	0	0	0	0	0	0	0.003	0.001	0	0.002	0	0	0	0	0	0
Ce	0.005	0	0.002	0.002	0.002	0.002	0.004	0.001	0	0	0.001	0	0.001	0.005	0.001	0.001
Pr	0	0	0	0	0	0	0	0	0	0.001	0.001	0.001	0.002	0	0.001	0.001
Nd	0.009	0.008	0.008	0.008	0.005	0.008	0.008	0.005	0.009	0.007	0.006	0.008	0.010	0.033	0.012	0.008
Sm	0.013	0.012	0.012	0.012	0.010	0.012	0.013	0.014	0.013	0.014	0.011	0.015	0.013	0.034	0.017	0.012
Eu	0	0	0	0	0	0	0	0	0	0	0	0	0	0	0	0
Gd	0.032	0.033	0.031	0.034	0.027	0.033	0.035	0.034	0.038	0.037	0.031	0.031	0.035	0.063	0.042	0.034
Tb	0.007	0.010	0.009	0.004	0.008	0.009	0.007	0.007	0.008	0.005	0.008	0.008	0.007	0.010	0.007	0.007
Dy	0.062	0.062	0.069	0.066	0.065	0.059	0.067	0.056	0.060	0.061	0.061	0.064	0.059	0.061	0.060	0.063
Ho	0.028	0.030	0.028	0.030	0.027	0.031	0.028	0.032	0.032	0.030	0.030	0.032	0.030	0.040	0.033	0.026
Er	0.041	0.044	0.042	0.043	0.048	0.043	0.042	0.039	0.044	0.037	0.042	0.043	0.040	0.029	0.039	0.045
Tm	0.005	0.007	0.004	0.006	0.006	0.007	0.004	0.003	0.004	0.003	0.004	0.006	0.006	0.006	0.005	0.001
Yb	0.038	0.035	0.037	0.032	0.035	0.038	0.037	0.033	0.036	0.036	0.035	0.034	0.034	0.022	0.029	0.036
Lu	0.013	0.014	0.013	0.015	0.015	0.016	0.009	0.014	0.014	0.018	0.015	0.016	0.016	0.014	0.014	0.012
Pb	0	0.001	0.003	0.003	0.002	0.002	0.002	0.002	0	0.003	0.001	0	0.003	0.003	0.001	0.002
Th	0.018	0.023	0.021	0.024	0.015	0.025	0.017	0.018	0.038	0.024	0.021	0.021	0.019	0.103	0.026	0.025
U	0.007	0.010	0.009	0.010	0.006	0.009	0.006	0.005	0.010	0.007	0.011	0.009	0.005	0.018	0.005	0.007

Table S 13.6: Chemical composition (expressed in oxide wt % and in atoms per formula unit calculated on the basis of 4 oxygen atoms) of all the EPMA-WDS data points of the Ch7 sample.

	Ch7-1	Ch7-2	Ch7-3	Ch7-4	Ch7-5	Ch7-6	Ch7-7	Ch7-8	Ch7-9	Ch7-10
As_2O_5	39.44	36.83	37.77	37.76	32.82	37.23	35.65	35.75	35.25	38.26
P_2O_5	4.01	4.84	4.63	4.77	8.87	6.12	6.13	6.37	6.53	4.24
SiO_2	0.82	1.08	0.95	0.83	0.29	0.34	0.80	0.65	0.65	0.71
V_2O_5	0.03	b.d.l.	b.d.l.	0.10	b.d.l.	b.d.l.	0.02	b.d.l.	b.d.l.	0.01
CaO	b.d.l.	0.03	0.03	b.d.l.	b.d.l.	0.03	b.d.l.	0.03	0.01	b.d.l.
Y_2O_3	35.50	35.11	35.30	35.46	37.17	36.21	36.01	36.51	36.67	36.03
La_2O_3	0.07	0.02	0.04	0.08	0.02	0.16	b.d.l.	0.08	b.d.l.	b.d.l.
Ce_2O_3	0.18	0.20	0.05	0.08	0.01	0.19	0.16	0.19	0.02	b.d.l.
Pr_2O_3	b.d.l.	b.d.l.	b.d.l.	b.d.l.	b.d.l.	b.d.l.	b.d.l.	b.d.l.	b.d.l.	0.05
Nd_2O_3	0.25	0.21	0.23	0.22	0.07	0.32	0.35	0.24	0.18	0.21
Sm_2O_3	0.34	0.61	0.60	0.22	0.30	0.53	0.34	0.37	0.37	0.45
Eu_2O_3	b.d.l.	b.d.l.	b.d.l.	b.d.l.	b.d.l.	b.d.l.	b.d.l.	b.d.l.	0.09	b.d.l.
Gd_2O_3	1.85	1.51	1.77	1.38	1.39	1.72	1.43	1.44	1.59	1.53
Tb_2O_3	0.52	0.29	0.33	0.50	0.47	0.62	0.47	0.43	0.57	0.37
Dy_2O_3	4.30	4.07	4.41	4.06	4.14	4.38	3.84	3.98	3.68	3.93
Ho_2O_3	2.28	1.77	1.94	1.73	1.70	2.02	1.81	1.84	1.57	1.84
Er_2O_3	3.26	3.24	3.26	3.58	3.72	3.20	3.27	3.50	3.47	3.42
Tm_2O_3	0.53	0.35	0.31	0.33	0.39	0.38	0.32	0.18	0.48	0.38
Yb_2O_3	2.56	2.85	2.77	3.12	2.98	3.14	3.25	3.19	2.97	2.59
Lu_2O_3	0.89	1.05	1.15	0.74	1.33	1.08	0.98	1.15	0.96	0.94
PbO	0.27	0.13	0.29	0.24	0.20	0.31	0.40	0.33	0.26	0.39
ThO_2	0.90	0.95	0.89	0.99	0.33	0.52	0.71	0.55	0.67	0.84
UO_2	3.85	4.01	4.04	3.68	2.08	2.15	3.78	2.83	3.24	2.97
Tot.	101.95	99.26	100.85	99.94	98.37	100.73	99.79	99.72	99.32	99.29

	Ch7-1	Ch7-2	Ch7-3	Ch7-4	Ch7-5	Ch7-6	Ch7-7	Ch7-8	Ch7-9	Ch7-10
As	0.821	0.780	0.792	0.794	0.679	0.770	0.746	0.745	0.737	0.811
P	0.135	0.166	0.157	0.162	0.297	0.205	0.207	0.215	0.221	0.145
Si	0.032	0.043	0.038	0.033	0.011	0.013	0.032	0.026	0.026	0.029
V	0.001	0	0	0.003	0	0	0	0	0	0
Ca	0	0.001	0.001	0	0	0.001	0	0.001	0	0
Y	0.752	0.757	0.753	0.759	0.783	0.762	0.767	0.775	0.781	0.778

La	0.001	0	0	0.001	0	0.002	0	0.001	0	0
Ce	0.002	0.003	0	0.001	0	0.002	0.002	0.002	0	0
Pr	0	0	0	0	0	0	0	0	0	0
Nd	0.003	0.003	0.003	0.003	0.001	0.004	0.005	0.003	0.002	0.003
Sm	0.004	0.008	0.008	0.003	0.004	0.007	0.004	0.005	0.005	0.006
Eu	0	0	0	0	0	0	0	0	0	0
Gd	0.024	0.020	0.023	0.018	0.018	0.022	0.019	0.019	0.021	0.020
Tb	0.006	0.003	0.004	0.006	0.006	0.008	0.006	0.005	0.007	0.005
Dy	0.055	0.053	0.057	0.052	0.052	0.055	0.049	0.051	0.047	0.051
Ho	0.028	0.022	0.024	0.022	0.021	0.025	0.023	0.023	0.019	0.023
Er	0.040	0.041	0.041	0.045	0.046	0.039	0.041	0.043	0.043	0.043
Tm	0.006	0.004	0.003	0.004	0.004	0.004	0.004	0.002	0.005	0.004
Yb	0.031	0.035	0.033	0.038	0.036	0.037	0.039	0.038	0.036	0.032
Lu	0.010	0.012	0.013	0.009	0.015	0.012	0.011	0.013	0.011	0.011
Pb	0.002	0.001	0.003	0.002	0.002	0.003	0.004	0.003	0.002	0.004
Th	0.008	0.008	0.008	0.009	0.002	0.004	0.006	0.005	0.006	0.007
U	0.034	0.036	0.036	0.032	0.018	0.018	0.033	0.025	0.028	0.026

Table S 13.7: Chemical composition (expressed in oxide wt % and in atoms per formula unit calculated on the basis of 4 oxygen atoms) of all the EPMA-WDS data points of the Ch8 sample.

	Ch8-1	Ch8-2	Ch8-3	Ch8-4	Ch8-5	Ch8-6	Ch8-7	Ch8-8
As_2O_5	37.14	35.64	35.73	34.22	36.45	34.72	36.70	36.97
P_2O_5	5.25	6.21	5.23	6.47	4.73	7.14	5.36	4.63
SiO_2	0.61	0.62	0.69	0.76	0.60	0.43	0.67	0.76
V_2O_5	b.d.l.	b.d.l.	0.01	0.04	0.01	b.d.l.	b.d.l.	b.d.l.
CaO	0.01	0.01	b.d.l.	b.d.l.	b.d.l.	0.04	b.d.l.	0.02
Y_2O_3	33.67	34.71	34.38	35.04	34.39	35.22	34.17	33.78
La_2O_3	0.04	0.01	0.07	b.d.l.	b.d.l.	0.09	0.10	b.d.l.
Ce_2O_3	0.10	0.18	b.d.l.	b.d.l.	0.19	0.10	0.16	0.03
Pr_2O_3	b.d.l.	0.12	b.d.l.	b.d.l.	0.03	0.03	0.03	b.d.l.
Nd_2O_3	0.41	0.22	0.49	0.09	0.42	0.32	0.54	0.40
Sm_2O_3	0.89	0.92	0.86	0.65	0.97	0.78	0.82	0.92
Eu_2O_3	b d.l	b d.l	b d.l	b d.l	b d.l	b d.l	b d.l	b d.l
Gd_2O_3	2.84	2.66	3.13	2.64	3.35	3.02	3.20	3.08
Tb_2O_3	0.49	0.52	0.56	0.68	0.67	0.65	0.50	0.64
Dy_2O_3	4.79	5.34	5.12	5.25	5.59	5.58	5.58	5.21
Ho_2O_3	2.76	2.55	2.60	2.58	2.70	2.60	2.69	2.91
Er_2O_3	3.06	3.19	3.03	3.02	3.01	2.72	2.88	3.11
Tm_2O_3	0.40	0.65	0.40	0.46	0.24	0.48	0.72	0.35
Yb_2O_3	2.84	3.22	2.52	2.08	1.69	2.00	1.88	2.34
Lu_2O_3	1.33	1.27	1.21	1.50	1.33	1.22	1.11	1.05
PbO	0.26	0.31	0.20	0.21	0.18	0.25	0.25	0.24
ThO_2	3.08	3.04	3.31	3.39	3.05	2.07	2.91	3.09
UO_2	0.34	0.36	0.28	0.58	0.32	0.49	0.43	0.30
Tot.	100.41	102.04	99.92	99.81	100.00	100.16	100.80	99.90

	Ch8-1	Ch8-2	Ch8-3	Ch8-4	Ch8-5	Ch8-6	Ch8-7	Ch8-8
As	0.784	0.741	0.762	0.723	0.780	0.724	0.772	0.789
P	0.179	0.209	0.180	0.221	0.164	0.241	0.182	0.160
Si	0.025	0.024	0.028	0.030	0.024	0.017	0.027	0.031
V	0	0	0	0.001	0	0	0	0
Ca	0	0	0	0	0	0.001	0	0.001
Y	0.723	0.735	0.747	0.753	0.749	0.747	0.732	0.734

La	0	0	0.001	0	0	0.001	0.001	0
Ce	0.001	0.002	0	0	0.002	0.001	0.002	0
Pr	0	0.001	0	0	0	0	0	0
Nd	0.005	0.003	0.007	0.001	0.006	0.004	0.007	0.005
Sm	0.012	0.012	0.012	0.009	0.013	0.010	0.011	0.013
Eu	0	0	0	0	0	0	0	0
Gd	0.038	0.035	0.042	0.035	0.045	0.040	0.042	0.041
Tb	0.006	0.006	0.007	0.009	0.009	0.008	0.006	0.008
Dy	0.062	0.068	0.067	0.068	0.073	0.071	0.072	0.068
Ho	0.035	0.032	0.033	0.033	0.035	0.033	0.034	0.037
Er	0.038	0.039	0.038	0.038	0.038	0.034	0.036	0.039
Tm	0.005	0.008	0.005	0.005	0.003	0.006	0.009	0.004
Yb	0.035	0.039	0.031	0.025	0.021	0.024	0.023	0.029
Lu	0.016	0.015	0.014	0.018	0.016	0.014	0.013	0.012
Pb	0.002	0.003	0.002	0.002	0.002	0.002	0.002	0.002
Th	0.028	0.027	0.030	0.031	0.028	0.018	0.026	0.028
U	0.003	0.003	0.002	0.005	0.002	0.004	0.003	0.002

Table S 13.8: Chemical composition (expressed in oxide wt % and in atoms per formula unit calculated on the basis of 4 oxygen atoms) of all the EPMA-WDS data points of the Ch9 sample.

	Ch9-1	Ch9-2	Ch9-3	Ch9-4	Ch9-5	Ch9-6	Ch9-7	Ch9-8	Ch9-9	Ch9-10
As_2O_5	38.83	37.71	35.99	34.75	36.14	34.80	36.16	34.38	36.80	37.09
P_2O_5	3.94	4.44	5.57	7.27	5.81	6.69	5.89	6.53	5.24	5.06
SiO_2	0.81	0.65	0.81	0.16	0.59	0.57	0.68	0.59	0.85	0.52
V_2O_5	0.03	0.02	b.d.l.	b.d.l.	b.d.l.	b.d.l.	b.d.l.	b.d.l.	0.04	b.d.l.
CaO	b.d.l.	b.d.l.	0.02	b.d.l.	b.d.l.	0.02	b.d.l.	0.05	0.01	0.03
Y_2O_3	34.95	34.09	34.37	35.01	33.70	34.58	34.06	33.94	34.45	33.91
La_2O_3	0.07	0.04	0.07	b.d.l.	0.14	0.04	0.07	0.07	0.07	0.02
Ce_2O_3	0.17	0.14	0.17	0.12	0.19	b.d.l.	0.28	0.16	0.10	0.04
Pr_2O_3	b.d.l.	b.d.l.	b.d.l.	0.04	0.08	0.14	0.11	0.08	b.d.l.	0.05
Nd_2O_3	0.25	0.40	0.25	0.19	0.53	0.47	0.48	0.32	0.39	0.47
Sm_2O_3	0.34	0.83	0.55	0.62	0.80	0.75	0.93	0.71	0.94	0.69
Eu_2O_3	b.d.l.	b.d.l.	b.d.l.	b.d.l.	b.d.l.	b.d.l.	b.d.l.	b.d.l.	b.d.l.	b.d.l.
Gd_2O_3	1.82	3.25	2.62	2.66	3.35	3.45	3.27	3.15	2.85	2.79
Tb_2O_3	0.52	0.71	0.52	0.60	0.68	0.64	0.76	0.85	0.52	0.81
Dy_2O_3	4.23	5.13	4.65	4.77	5.27	5.18	5.25	5.10	4.96	5.05
Ho_2O_3	2.24	2.66	2.66	2.45	2.77	2.77	2.77	2.61	2.74	2.75
Er_2O_3	3.21	3.15	3.31	3.42	3.01	3.04	2.92	2.89	2.77	3.39
Tm_2O_3	0.52	0.50	0.49	0.48	0.61	0.45	0.39	0.38	0.32	0.29
Yb_2O_3	2.52	2.31	2.38	3.31	1.76	1.86	1.96	2.31	2.22	3.33
Lu_2O_3	0.87	1.08	0.88	1.01	1.39	1.22	0.98	1.17	1.47	1.37
PbO	0.26	0.20	0.20	0.47	0.19	0.06	0.22	0.38	0	0.21
ThO_2	0.89	3.60	4.23	1.50	2.31	2.48	3.09	2.36	3.77	2.94
UO_2	3.79	0.21	0.51	0.11	0.44	0.71	0.76	0.64	0.32	0.15
Tot.	100.38	101.35	100.35	99.07	99.87	100.06	101.11	98.78	100.91	101.11

	Ch9-1	Ch9-2	Ch9-3	Ch9-4	Ch9-5	Ch9-6	Ch9-7	Ch9-8	Ch9-9	Ch9-10
As	0.821	0.797	0.759	0.730	0.764	0.730	0.757	0.732	0.772	0.783
P	0.135	0.152	0.190	0.247	0.199	0.227	0.199	0.225	0.178	0.173
Si	0.032	0.026	0.032	0.006	0.024	0.023	0.027	0.024	0.034	0.021
V	0.001	0	0	0	0	0	0	0	0.001	0
Ca	0	0	0	0	0	0.001	0	0.002	0	0.001
Y	0.752	0.733	0.738	0.749	0.725	0.739	0.726	0.736	0.735	0.729

La	0.001	0	0.001	0	0.002	0	0.001	0.001	0.001	0
Ce	0.002	0.002	0.002	0.001	0.002	0	0.004	0.002	0.001	0
Pr	0	0	0	0	0.001	0.002	0.001	0.001	0	0
Nd	0.003	0.005	0.003	0.002	0.007	0.006	0.006	0.004	0.005	0.006
Sm	0.004	0.011	0.007	0.008	0.011	0.010	0.012	0.010	0.013	0.009
Eu	0	0	0	0	0	0	0	0	0	0
Gd	0.024	0.043	0.035	0.035	0.045	0.045	0.043	0.042	0.037	0.037
Tb	0.006	0.009	0.006	0.008	0.009	0.008	0.010	0.011	0.006	0.010
Dy	0.055	0.066	0.060	0.061	0.068	0.067	0.067	0.066	0.064	0.065
Ho	0.028	0.034	0.034	0.031	0.035	0.035	0.035	0.033	0.035	0.035
Er	0.040	0.040	0.041	0.043	0.038	0.038	0.036	0.037	0.034	0.043
Tm	0.006	0.006	0.006	0.006	0.007	0.005	0.004	0.004	0.004	0.003
Yb	0.031	0.028	0.029	0.040	0.021	0.022	0.024	0.028	0.027	0.041
Lu	0.010	0.013	0.010	0.012	0.016	0.014	0.011	0.014	0.017	0.016
Pb	0.002	0.002	0.002	0.005	0.002	0	0.002	0.004	0	0.002
Th	0.008	0.033	0.038	0.013	0.021	0.022	0.028	0.021	0.034	0.027
U	0.034	0.001	0.004	0.001	0.003	0.006	0.006	0.005	0.002	0.001

Table S 13.9: Chemical composition (expressed in oxide wt % and in atoms per formula unit calculated on the basis of 4 oxygen atoms) of all the EPMA-WDS data points of the Ch10 sample.

	Ch10-1	Ch10-2	Ch10-3	Ch10-4	Ch10-5	Ch10-6	Ch10-7	Ch10-8	Ch10-9	Ch10-10	Ch10-11	Ch10-12	Ch10-13
As_2O_5	36.94	36.87	38.02	34.77	36.91	35.12	35.20	36.53	36.00	35.66	35.95	35.50	36.00
P_2O_5	5.35	5.23	4.81	6.72	5.32	5.78	6.86	3.93	4.47	5.59	5.39	5.50	5.32
SiO_2	0.69	0.67	0.62	0.55	0.67	0.78	0.45	1.49	1.59	0.70	0.82	0.84	0.78
V_2O_5	b.d.l.	b.d.l.	0.05	b.d.l.	b.d.l.	0.02	0.01	0.05	b.d.l.	b.d.l.	b.d.l.	0.05	0.02
CaO	b.d.l.	0.02	0.03	b.d.l.	0.02	b.d.l.	0.01	b.d.l.	0.03	b.d.l.	0.01	0.03	b.d.l.
Y_2O_3	34.80	35.19	34.44	35.38	34.30	34.78	35.06	29.91	30.06	31.93	30.84	31.77	31.83
La_2O_3	b.d.l.	b.d.l.	0.03	b.d.l.	b.d.l.	b.d.l.	b.d.l.	0.05	b.d.l.	b.d.l.	0.01	0.03	b.d.l.
Ce_2O_3	0.12	0.23	0.10	0.01	0.14	0.03	0.20	0.02	0.01	0.25	0.18	0.20	0.14
Pr_2O_3	0.25	b.d.l.	b.d.l.	b.d.l.	b.d.l.	0.01	b.d.l.	b.d.l.	0.09	0.03	0.05	0.06	b.d.l.
Nd_2O_3	0.48	0.40	0.48	0.03	0.65	0.16	0.42	0.23	0.39	0.50	0.53	0.21	0.34
Sm_2O_3	0.67	0.70	0.93	0.55	1.06	0.75	0.56	0.70	0.64	0.73	0.76	0.48	0.99
Eu_2O_3	b.d.l.	b.d.l.	b.d.l.	b.d.l.	b.d.l.	b.d.l.	b.d.l.	b.d.l.	b.d.l.	b.d.l.	b.d.l.	b.d.l.	b.d.l.
Gd_2O_3	2.64	2.81	3.00	2.09	3.07	2.50	2.28	2.21	2.08	1.99	1.73	1.65	1.90
Tb_2O_3	0.70	0.65	0.74	0.48	0.55	0.52	0.59	0.46	0.39	0.58	0.60	0.36	0.50
Dy_2O_3	5.36	5.33	5.43	5.41	5.58	5.26	5.38	4.96	4.85	4.82	4.39	4.75	4.73
Ho_2O_3	2.47	2.72	2.69	2.33	2.78	2.57	2.46	2.45	2.09	2.25	2.17	2.07	2.03
Er_2O_3	2.80	3.07	2.90	3.05	2.98	3.16	3.13	3.73	4.13	4.24	4.13	4.20	4.12
Tm_2O_3	0.49	0.18	0.33	0.32	0.35	0.27	0.36	0.60	0.64	0.69	0.83	0.63	0.53
Yb_2O_3	2.21	1.91	2.05	2.14	2.05	1.87	1.99	4.49	4.71	4.84	5.07	5.15	5.47
Lu_2O_3	1.03	1.24	1.02	1.06	1.25	1.21	1.01	1.73	1.52	1.45	1.36	1.59	1.32
PbO	0.24	0.27	0.45	0.27	0.25	0.23	0.25	0.29	0.31	0.20	0.19	0.33	0.13
ThO_2	2.52	2.22	1.95	1.16	1.72	1.72	0.78	4.41	4.94	2.24	2.29	2.50	2.74
UO_2	1.73	1.72	1.90	2.06	2.13	2.31	2.32	2.14	2.14	1.41	1.26	2.00	1.58
Tot.	101.69	101.52	102.05	98.49	101.88	99.17	99.41	100.48	101.17	100.26	98.67	100.04	100.59

	Ch10-1	Ch10-2	Ch10-3	Ch10-4	Ch10-5	Ch10-6	Ch10-7	Ch10-8	Ch10-9	Ch10-10	Ch10-11	Ch10-12	Ch10-13
As	0.771	0.771	0.794	0.734	0.772	0.747	0.737	0.792	0.773	0.762	0.776	0.761	0.769
P	0.181	0.177	0.162	0.230	0.180	0.199	0.232	0.138	0.155	0.193	0.188	0.190	0.184
Si	0.027	0.026	0.024	0.022	0.027	0.032	0.018	0.061	0.065	0.028	0.034	0.034	0.031
V	0	0	0.001	0	0	0	0	0.001	0	0	0	0.001	0
Ca	0	0.001	0.001	0	0	0	0	0	0.001	0	0	0.001	0
Y	0.739	0.749	0.732	0.761	0.730	0.753	0.747	0.660	0.657	0.694	0.678	0.693	0.692

La	0	0	0	0	0	0	0	0	0	0	0	0	0
Ce	0.001	0.003	0.001	0	0.002	0	0.003	0	0	0.003	0.002	0.003	0.002
Pr	0.003	0	0	0	0	0	0	0	0.001	0	0	0.001	0
Nd	0.006	0.005	0.006	0	0.009	0.002	0.006	0.003	0.005	0.007	0.007	0.003	0.005
Sm	0.009	0.009	0.012	0.007	0.014	0.010	0.007	0.010	0.009	0.010	0.010	0.006	0.014
Eu	0	0	0	0	0	0	0	0	0	0	0	0	0
Gd	0.034	0.037	0.039	0.028	0.040	0.033	0.030	0.030	0.028	0.027	0.023	0.022	0.025
Tb	0.009	0.008	0.009	0.006	0.007	0.007	0.007	0.006	0.005	0.007	0.008	0.004	0.006
Dy	0.069	0.068	0.069	0.070	0.072	0.069	0.069	0.066	0.064	0.063	0.058	0.062	0.062
Ho	0.031	0.034	0.034	0.030	0.035	0.033	0.031	0.032	0.027	0.029	0.028	0.027	0.026
Er	0.035	0.038	0.036	0.038	0.037	0.040	0.039	0.048	0.053	0.054	0.053	0.054	0.053
Tm	0.006	0.002	0.004	0.004	0.004	0.003	0.004	0.007	0.008	0.008	0.010	0.008	0.006
Yb	0.026	0.023	0.025	0.026	0.025	0.023	0.024	0.056	0.059	0.060	0.064	0.064	0.068
Lu	0.012	0.015	0.012	0.012	0.015	0.014	0.012	0.021	0.018	0.018	0.017	0.019	0.016
Pb	0.002	0.003	0.004	0.002	0.002	0.002	0.002	0.003	0.003	0.002	0.002	0.003	0.001
Th	0.022	0.020	0.017	0.010	0.015	0.015	0.007	0.041	0.046	0.020	0.021	0.023	0.025
U	0.015	0.015	0.016	0.018	0.019	0.020	0.020	0.019	0.019	0.012	0.011	0.018	0.014

Table S 13.10: chemical composition (expressed in oxide wt % and in atoms per formula unit calculated on the basis of 4 oxygen atoms) of all the EPMA-WDS data points of the Ch11 sample (*: data point referring to $ThSiO_4$ iclusions)

	Ch11-1	Ch11-2	Ch11-3	Ch11-4	Ch11-5	Ch11-6*	Ch11-7	Ch11-8	Ch11-9	Ch11-10
As_2O_5	22.21	19.55	23.39	41.63	45.10	4.429	43.35	36.51	21.75	38.14
P_2O_5	17.24	19.10	14.62	1.17	0.27	1.51	0.25	4.45	16.05	2.74
SiO_2	0.04	0.17	0.86	0.43	0.04	14.52	0.02	1.10	0.83	1.50
V_2O_5	0.04	b.d.l.	b.d.l.	b.d.l.	b.d.l.	0.02	b.d.l.	b.d.l.	b.d.l.	b.d.l.
CaO	b.d.l.	0.04	b.d.l.	0.12	0.11	b.d.l.	0.10	0.02	0.02	0.04
Y_2O_3	38.10	38.03	35.59	26.55	22.82	5.083	20.04	31.37	36.07	27.97
La_2O_3	0.02	b.d.l.	b.d.l.	0.24	0.51	b.d.l.	0.73	0.07	b.d.l.	0.04
Ce_2O_3	b.d.l.	0.07	0.10	2.34	3.47	0.02	3.87	0.75	0.10	0.64
Pr_2O_3	b.d.l.	0.06	b.d.l.	0.63	0.84	b.d.l.	1.23	b.d.l.	0.06	0.20
Nd_2O_3	0.39	0.30	0.42	4.13	8.99	0.05	10.8	1.38	0.35	2.73
Sm_2O_3	0.68	0.75	0.68	2.14	4.84	0.16	5.18	1.37	0.41	1.86
Eu_2O_3	b.d.l.	b.d.l.	b.d.l.	b.d.l.	b.d.l.	b.d.l.	b.d.l.	b.d.l.	b.d.l.	b.d.l.
Gd_2O_3	1.99	2.11	1.89	3.57	5.09	0.56	5.63	2.82	1.94	3.33
Tb_2O_3	0.62	0.35	0.52	0.51	0.56	0.14	0.59	0.60	0.38	0.47
Dy_2O_3	5.13	4.92	5.11	4.19	3.13	0.88	2.96	4.85	5.19	4.35
Ho_2O_3	2.43	2.09	2.19	2.63	2.70	0.67	2.80	2.61	2.29	2.55
Er_2O_3	4.01	4.18	3.69	2.71	1.11	0.54	0.81	3.40	3.75	2.63
Tm_2O_3	0.78	0.52	0.30	0.57	0.43	0.21	0.50	0.50	0.34	0.42
Yb_2O_3	4.16	4.26	3.87	2.62	0.82	0.71	0.90	3.20	3.48	2.34
Lu_2O_3	1.36	1.38	1.28	0.78	0.52	0.19	0.48	1.18	1.49	0.93
PbO	0.25	0.28	0.24	0.22	b.d.l.	0.01	b.d.l.	0.18	0.29	0.23
ThO_2	0.53	0.79	2.85	1.10	b.d.l.	59.41	0.06	3.01	2.58	4.23
UO_2	b.d.l.	0.04	1.45	1.04	0.07	5.41	b.d.l.	1.56	0.95	2.07
Tot.	100.07	99.09	99.17	99.42	101.52	94.59	100.41	101.06	98.45	99.53

	Ch11-1	Ch11-2	Ch11-3	Ch11-4	Ch11-5	Ch11-6	Ch11-7	Ch11-8	Ch11-9	Ch11-10
As	0.435	0.381	0.473	0.929	0.993	0.125	0.983	0.782	0.436	0.839
P	0.547	0.603	0.479	0.042	0.009	0.069	0.009	0.154	0.522	0.097
Si	0.001	0.006	0.033	0.018	0.002	0.789	0	0.045	0.032	0.063
V	0.001	0	0	0	0	0.001	0	0	0	0
Ca	0	0.001	0	0.005	0.005	0	0.004	0.001	0.001	0.001
Y	0.760	0.755	0.733	0.603	0.511	0.147	0.462	0.684	0.737	0.626

La	0	0	0	0.003	0.008	0	0.011	0.001	0	0
Ce	0	0.001	0.001	0.036	0.053	0	0.061	0.011	0.001	0.009
Pr	0	0	0	0.009	0.012	0	0.019	0	0	0.003
Nd	0.005	0.004	0.005	0.063	0.135	0.001	0.167	0.020	0.004	0.041
Sm	0.008	0.009	0.009	0.031	0.070	0.003	0.077	0.019	0.005	0.027
Eu	0	0	0	0	0	0	0	0	0	0
Gd	0.024	0.026	0.024	0.050	0.071	0.010	0.081	0.038	0.024	0.046
Tb	0.007	0.004	0.006	0.007	0.007	0.002	0.008	0.008	0.004	0.006
Dy	0.062	0.059	0.063	0.057	0.042	0.015	0.041	0.064	0.064	0.059
Ho	0.029	0.024	0.027	0.035	0.036	0.011	0.038	0.034	0.028	0.034
Er	0.047	0.049	0.044	0.036	0.014	0.009	0.011	0.043	0.045	0.034
Tm	0.009	0.006	0.003	0.007	0.005	0.003	0.006	0.006	0.004	0.005
Yb	0.047	0.048	0.045	0.034	0.010	0.011	0.012	0.040	0.040	0.030
Lu	0.015	0.015	0.015	0.010	0.006	0.003	0.006	0.014	0.017	0.011
Pb	0.002	0.002	0.002	0.002	0	0	0	0.002	0.003	0.002
Th	0.004	0.006	0.025	0.010	0	0.734	0	0.028	0.022	0.040
U	0	0	0.012	0.009	0	0.065	0	0.014	0.008	0.019

Table S 13.11: Chemical composition (expressed in oxide wt % and in atoms per formula unit calculated on the basis of 4 oxygen atoms) of all the EPMA-WDS data points of the Ch12 sample.

	Ch12-1	Ch12-2	Ch12-3	Ch12-4	Ch12-5
As_2O_5	39.13	38.08	38.16	40.50	37.68
P_2O_5	4.32	5.25	5.02	3.55	5.49
SiO_2	0.10	0.15	0.16	0.14	0.02
V_2O_5	b.d.l.	0.06	b.d.l.	b.d.l.	0.05
CaO	b.d.l.	0.01	0.04	b.d.l.	0.03
Y_2O_3	34.23	35.51	34.25	34.73	35.47
La_2O_3	b.d.l.	b.d.l.	b.d.l.	0.13	0.13
Ce_2O_3	0.21	0.11	0.16	0.08	0.01
Pr_2O_3	0.09	b.d.l.	0.03	b.d.l.	b.d.l.
Nd_2O_3	0.68	0.26	0.78	0.42	0.42
Sm_2O_3	0.94	0.57	1.23	0.69	0.52
Eu_2O_3	b.d.l.	b.d.l.	b.d.l.	b.d.l.	b.d.l.
Gd_2O_3	2.76	2.98	3.31	3.02	2.52
Tb_2O_3	0.73	0.65	0.97	0.89	0.68
Dy_2O_3	5.10	5.60	5.62	6.18	5.62
Ho_2O_3	2.73	2.69	2.88	2.95	2.25
Er_2O_3	2.59	3.38	2.58	3.06	3.23
Tm_2O_3	0.54	0.30	0.30	0.31	0.27
Yb_2O_3	2.03	2.09	1.74	2.25	2.43
Lu_2O_3	1.01	1.31	1.54	0.99	1.31
PbO	0.21	0.18	0.26	0.29	0.23
ThO_2	0.66	0.39	0.36	0.27	0.21
UO_2	0.77	0.99	0.60	0.78	0.78
Tot.	98.93	100.63	100.08	101.32	99.43

	Ch12-1	Ch12-2	Ch12-3	Ch12-4	Ch12-5
As	0.835	0.797	0.806	0.854	0.794
P	0.149	0.178	0.171	0.121	0.187
Si	0.004	0.006	0.006	0.005	0
V	0	0.002	0	0	0.001
Ca	0	0	0.001	0	0.001
Y	0.743	0.756	0.736	0.745	0.761

La	0	0	0	0.002	0.001
Ce	0.003	0.001	0.002	0.001	0
Pr	0.001	0	0	0	0
Nd	0.009	0.003	0.011	0.006	0.006
Sm	0.013	0.007	0.017	0.009	0.007
Eu	0	0	0	0	0
Gd	0.037	0.039	0.044	0.040	0.033
Tb	0.009	0.008	0.012	0.011	0.009
Dy	0.067	0.072	0.073	0.080	0.073
Ho	0.035	0.034	0.037	0.037	0.028
Er	0.033	0.042	0.032	0.038	0.041
Tm	0.006	0.003	0.003	0.004	0.003
Yb	0.025	0.025	0.021	0.027	0.029
Lu	0.012	0.015	0.018	0.012	0.015
Pb	0.002	0.002	0.002	0.003	0.002
Th	0.006	0.003	0.003	0.002	0.001
U	0.007	0.008	0.005	0.007	0.007

Table S 13.12: Chemical composition (expressed in oxide wt % and in atoms per formula unit calculated on the basis of 4 oxygen atoms) of all the EPMA-WDS data points of the Ch13 sample.

	Ch13-1	Ch13-2	Ch13-3	Ch13-4	Ch13-5	Ch13-6	Ch13-7	Ch13-8	Ch13-9
As_2O_5	30.95	32.11	38.24	42.80	35.82	34.31	40.42	35.84	36.79
P_2O_5	4.52	3.37	1.51	1.51	2.49	2.36	1.46	1.38	2.06
SiO_2	3.61	2.93	2.93	1.30	2.20	2.54	1.10	2.92	2.07
V_2O_5	0.02	b.d.l.	b.d.l.	b.d.l.	b.d.l.	b d.l	b.d.l.	b.d.l.	b.d.l.
CaO	1.15	1.26	0.09	0.03	0.88	0.63	0.03	0.06	0.55
Y_2O_3	30.00	26.30	27.19	31.94	32.00	28.53	30.60	25.94	30.26
La_2O_3	b.d.l.	0.20	b.d.l.	b.d.l.	0.08	b.d.l.	0.10	0.03	0.02
Ce_2O_3	0.21	0.14	0.13	0.10	0.24	0.07	0.20	0.26	0.08
Pr_2O_3	b d.l	0.01	0.11	0.13	b.d.l.	0.03	0.03	0.10	b.d.l.
Nd_2O_3	0.07	0.57	0.94	0.77	0.28	0.50	0.77	0.89	0.34
Sm_2O_3	0.27	1.05	1.60	0.73	0.26	0.93	0.84	1.40	0.51
Eu_2O_3	b.d.l.	b.d.l.	b.d.l.	b.d.l.	b.d.l.	b.d.l.	b.d.l.	b.d.l.	b.d.l.
Gd_2O_3	1.83	4.19	5.44	1.72	1.72	3.67	1.70	4.33	2.54
Tb_2O_3	0.53	0.86	0.84	0.47	0.48	0.76	0.40	0.68	0.63
Dy_2O_3	4.16	4.85	5.05	3.81	4.12	4.77	3.95	5.12	4.80
Ho_2O_3	1.90	2.94	3.44	1.87	1.88	2.68	2.00	2.94	1.99
Er_2O_3	2.34	2.06	1.76	3.73	2.52	2.26	3.76	2.49	2.33
Tm_2O_3	b.d.l.	0.21	0.48	0.68	0.40	0.45	0.71	0.41	b.d.l.
Yb_2O_3	1.85	1.39	1.24	4.58	1.93	1.99	4.55	1.42	1.64
Lu_2O_3	1.00	1.14	1.04	0.94	1.09	0.95	1.49	0.92	1.01
PbO	0.10	b.d.l.	0.18	0.07	0.14	0.39	0.01	0.23	0.30
ThO_2	10.1	12.7	8.75	1.70	7.14	8.99	1.40	8.47	6.64
UO_2	4.37	3.25	3.29	4.60	4.97	4.14	3.72	3.24	3.78
Tot.	99.15	101.67	104.35	103.59	100.74	101.05	99.36	99.18	98.43

	Ch13-1	Ch13-3	Ch13-4	Ch13-5	Ch13-6	Ch13-7	Ch13-8	Ch13-9	Ch13-
As	0.674	0.713	0.822	0.899	0.782	0.765	0.892	0.814	0.820
P	0.159	0.121	0.052	0.051	0.088	0.085	0.052	0.050	0.074
Si	0.150	0.124	0.120	0.052	0.092	0.108	0.046	0.126	0.088
V	0	0	0	0	0	0	0	0	0
Ca	0.051	0.057	0.004	0.001	0.039	0.029	0.001	0.003	0.025
Y	0.665	0.594	0.595	0.683	0.711	0.648	0.687	0.599	0.686

La	0	0.003	0	0	0.001	0	0.001	0	0
Ce	0.003	0.002	0.002	0.001	0.003	0.001	0.003	0.004	0.001
Pr	0	0	0.001	0.001	0	0	0	0.001	0
Nd	0.001	0.008	0.013	0.011	0.004	0.007	0.011	0.013	0.005
Sm	0.003	0.015	0.022	0.010	0.003	0.013	0.012	0.021	0.007
Eu	0	0	0	0	0	0	0	0	0
Gd	0.025	0.059	0.074	0.022	0.023	0.052	0.023	0.062	0.035
Tb	0.007	0.012	0.011	0.006	0.006	0.010	0.005	0.009	0.008
Dy	0.055	0.066	0.066	0.049	0.055	0.065	0.053	0.071	0.066
Ho	0.025	0.039	0.045	0.023	0.025	0.036	0.026	0.040	0.027
Er	0.030	0.027	0.022	0.047	0.033	0.030	0.049	0.034	0.031
Tm	0	0.002	0.006	0.008	0.005	0.006	0.009	0.005	0
Yb	0.023	0.018	0.015	0.056	0.024	0.025	0.058	0.018	0.021
Lu	0.012	0.014	0.012	0.011	0.013	0.012	0.019	0.012	0.013
Pb	0.001	0	0.002	0	0.001	0.004	0	0.002	0.003
Th	0.096	0.123	0.081	0.015	0.067	0.087	0.013	0.083	0.064
U	0.040	0.030	0.030	0.041	0.046	0.039	0.035	0.031	0.035

Table S 13.13: Chemical composition (expressed in oxide wt % and in atoms per formula unit calculated on the basis of 4 oxygen atoms) of all the EPMA-WDS data points of the Xen14 sample (*: data point referring to $ThSiO_4$ inclusions).

	Xen14-1	Xen14-2	Xen14-3	Xen14-4	Xen14-5	Xen14-6	Xen14-7	Xen14-8	Xen14-9	Xen14-10	Xen14-11	Xen14-12	Xen14-13	Xen14-14	Xen14-15	Xen14-16
As_2O_5	6.37	5.63	4.25	3.75	5.52	5.57	5.92	3.45	3.92	5.18	6.81	6.01	5.88	6.20	5.94	5.81	6.33
P_2O_5	27.56	27.83	30.33	30.38	28.59	28.33	28.77	31.00	29.94	28.53	28.23	28.98	27.77	28.55	27.93	25.99	28.57
SiO_2	0.75	0.72	0.06	b.d.l.	0.39	0.59	0.27	0.03	0.06	0.32	0.18	0.19	0.81	0.16	0.66	0.74	0.28
V_2O_5	b.d.l.	b.d.l.	b.d.l.	0.02	b.d.l.	b.d.l.	0.08	0.03	b.d.l.	b.d.l.	0.01	0.02	b.d.l.	b.d.l.	b.d.l.	0.02	b.d.l.
CaO	b.d.l.	b.d.l.	0.01	0.01	0.04	0.02	b.d.l.	0.01	0.01	0.03	b.d.l.	b.d.l.	0.07	b.d.l.	b.d.l.	0.07	0.05
Y_2O_3	38.76	38.86	40.71	40.61	39.23	38.91	38.82	40.35	40.39	39.14	40.26	39.32	38.75	39.81	38.81	37.11	39.21
La_2O_3	0.04	0.02	b.d.l.	0.06	0.04	0.12	0.03	b.d.l.	0.05	0.01	0.03	b.d.l.	b.d.l.	b.d.l.	0.10	b.d.l.	b.d.l.
Ce_2O_3	0.03	0.04	0.07	0.04	0.02	0.02	0.11	0.05	b.d.l.	0.17	b.d.l.	b.d.l.	b.d.l.	0.05	0.17	b.d.l.	0.13
Pr_2O_3	b.d.l.	0.08	b.d.l.	b.d.l.	0.10	b.d.l.	0.09	0.00	b.d.l.	0.03	0.18	0.15	b.d.l.	b d.l	b.d.l.	b.d.l.	b.d.l.
Nd_2O_3	0.32	0.20	0.11	0.19	0.28	0.24	0.32	0.27	0.29	0.23	0.25	0.23	0.39	0.08	0.24	0.33	0.18
Sm_2O_3	0.74	0.43	0.62	0.55	0.72	0.69	1.03	0.81	0.78	0.72	0.43	0.78	0.69	0.55	0.86	0.60	0.86
Eu_2O_3	b.d.l.	b.d.l.	b.d.l.	b.d.l.	b.d.l.	b.d.l.	b.d.l.	b.d.l.	b.d.l.	b.d.l.	b.d.l.	b.d.l.	b.d.l.	b.d.l.	b.d.l.	b.d.l.	b.d.l.
Gd_2O_3	3.63	3.33	3.86	3.66	4.01	3.02	4.95	4.15	4.39	3.81	3.27	4.39	2.95	3.63	3.10	3.05	4.64
Tb_2O_3	0.86	0.89	0.76	0.78	1.01	0.81	0.97	0.90	0.85	0.96	0.73	1.05	0.77	0.89	0.84	0.71	1.07
Dy_2O_3	6.27	5.93	6.53	6.22	6.69	5.98	6.40	6.31	6.13	6.27	5.79	6.48	5.84	6.34	6.33	5.36	6.22
Ho_2O_3	3.05	2.83	3.58	3.43	3.32	2.82	3.86	3.57	3.44	3.28	2.81	3.41	2.65	3.29	3.05	2.70	3.64
Er_2O_3	3.68	3.13	3.92	3.60	3.38	3.68	3.20	3.75	3.57	3.37	4.13	3.73	3.34	3.82	3.50	3.23	3.24
Tm_2O_3	0.59	0.53	0.41	b.d.l.	0.28	0.61	0.53	0.51	0.45	0.30	0.55	0.55	0.42	0.37	0.47	0.42	0.60
Yb_2O_3	3.38	3.30	3.42	3.49	2.72	3.24	2.51	3.71	3.10	2.34	3.31	2.99	3.58	3.42	3.05	3.17	2.74
Lu_2O_3	1.55	1.61	1.48	1.41	1.55	1.95	1.88	1.07	1.34	1.50	1.45	1.39	1.55	1.51	1.71	1.51	1.47
PbO	0.26	0.31	0.13	0.21	0.05	0.26	0.36	0.10	0.39	0.12	0.35	0.29	0.28	0.34	0.23	0.47	0.26
ThO_2	3.67	3.31	0.86	0.59	2.39	3.10	1.55	0.59	0.75	1.65	1.50	1.37	3.87	1.18	2.98	3.49	1.34
UO_2	0.24	0.63	0.39	0.19	0.62	0.74	0.42	0.35	0.27	0.70	0.18	0.56	0.49	0.44	0.46	0.31	0.37
Tot.	101.85	99.73	101.58	99.27	101.04	100.79	102.18	101.11	100.24	98.75	100.52	101.98	100.18	100.70	100.50	95.16	101.28

	Xen14-1	Xen14-2	Xen14-3	Xen14-4	Xen14-5	Xen14-6	Xen14-7	Xen14-8	Xen14-9	Xen14-10	Xen14-11	Xen14-12	Xen14-13	Xen14-14	Xen14-15	Xen14-16
As	0.118	0.105	0.077	0.069	0.102	0.103	0.108	0.062	0.072	0.097	0.110	0.114	0.116	0.121	0.119	0.115	0.107
P	0.829	0.846	0.894	0.907	0.857	0.853	0.856	0.912	0.895	0.868	0.843	0.831	0.852	0.850	0.845	0.848	0.870
Si	0.026	0.026	0.002	0	0.013	0.021	0.009	0.001	0.002	0.011	0.023	0.028	0.010	0.005	0.005	0.013	0
V	0	0	0	0	0	0	0.002	0	0	0	0	0	0	0	0	0	0
Ca	0	0	0	0	0.001	0	0	0	0	0.001	0	0.002	0.001	0.001	0	0	0.001
Y	0.732	0.742	0.754	0.762	0.739	0.736	0.726	0.746	0.759	0.748	0.737	0.746	0.735	0.744	0.742	0.730	0.774

La	0	0	0	0	0	0.001	0	0	0	0	0.001	0	0	0	0.001	0.001	0
Ce	0	0	0	0	0	0	0.001	0	0	0.002	0.002	0	0.001	0.002	0.002	0	0
Pr	0	0.001	0	0	0.001	0	0.001	0	0	0	0	0	0	6.958	0	0	0.001
Nd	0.004	0.002	0.001	0.002	0.003	0.003	0.004	0.003	0.003	0.003	0.003	0.004	0.002	0.002	0.003	0.004	0.002
Sm	0.009	0.005	0.007	0.006	0.008	0.008	0.012	0.009	0.009	0.008	0.010	0.007	0.010	0.008	0.010	0.012	0.006
Eu	0	0	0	0	0	0	0	0	0	0	0	0	0	0	0	0	0
Gd	0.042	0.039	0.044	0.042	0.047	0.035	0.057	0.047	0.051	0.045	0.036	0.038	0.054	0.050	0.050	0.050	0.036
Tb	0.010	0.010	0.008	0.009	0.011	0.009	0.011	0.010	0.009	0.011	0.009	0.008	0.012	0.010	0.010	0.010	0.009
Dy	0.071	0.068	0.073	0.070	0.076	0.068	0.072	0.070	0.069	0.072	0.072	0.065	0.070	0.069	0.070	0.075	0.071
Ho	0.034	0.032	0.039	0.038	0.037	0.032	0.043	0.039	0.038	0.037	0.034	0.032	0.040	0.039	0.039	0.036	0.034
Er	0.041	0.035	0.042	0.039	0.037	0.041	0.035	0.040	0.039	0.038	0.039	0.038	0.035	0.037	0.041	0.038	0.038
Tm	0.006	0.005	0.004	0	0.003	0.006	0.005	0.005	0.005	0.003	0.005	0.004	0.006	0.005	0.003	0.005	0.002
Yb	0.036	0.036	0.036	0.037	0.029	0.035	0.027	0.039	0.033	0.025	0.033	0.036	0.029	0.028	0.033	0.029	0.032
Lu	0.016	0.017	0.015	0.015	0.016	0.021	0.019	0.011	0.014	0.016	0.018	0.017	0.015	0.018	0.018	0.013	0.018
Pb	0.002	0.003	0.001	0.002	0	0.002	0.003	0	0.003	0.001	0.002	0.004	0.002	0.002	0.001	0.002	0.002
Th	0.029	0.027	0.006	0.004	0.019	0.025	0.012	0.004	0.006	0.013	0.024	0.030	0.010	0.010	0.010	0.015	0.002
U	0.001	0.005	0.003	0.001	0.004	0.005	0.003	0.002	0.002	0.005	0.003	0.002	0.002	0.001	0.004	0.004	0

	Xen14-	Xen14-	Xen14-	Xen14-	Xen14-	Xen14-	Xen14-	Xen14-	Xen14-	Xen14-
As_2O_5	6.60	6.50	6.19	5.87	6.18	6.20	3.73	3.53	1.66	1.30
P_2O_5	28.54	28.33	28.06	29.35	27.49	27.60	30.25	30.52	6.76	1.92
SiO_2	0.16	0.14	0.38	b.d.l.	0.73	0.70	0.22	0.06	13.89	17.23
V_2O_5	0.01	b.d.l.	0.02	b.d.l.	b.d.l.	b.d.l.	b.d.l.	0.011	0.09	0.13
CaO	0.03	0.02	0.01	0.05	b.d.l.	0.03	0.03	b.d.l.	0.02	b.d.l.
Y_2O_3	39.72	39.57	38.43	41.55	38.55	38.48	40.58	40.11	9.45	3.27
La_2O_3	b.d.l.	0.09	0.12	b.d.l.	0.05	b.d.l.	b.d.l.	0.04	b.d.l.	b.d.l.
Ce_2O_3	0.19	0.20	0.04	0.07	b.d.l.	0.09	0.17	0.13	b.d.l.	0.14
Pr_2O_3	b.d.l.	b.d.l.	b.d.l.	0.12	b.d.l.	b.d.l.	0.09	0.03	b.d.l.	0.02
Nd_2O_3	0.17	0.24	0.37	0.23	0.25	0.48	0.43	0.26	0.34	0.15
Sm_2O_3	0.74	0.84	1.01	0.50	0.81	0.61	1.04	0.86	0.21	0.26
Eu_2O_3	b.d.l.	b.d.l.	b.d.l.	b.d.l.	b.d.l.	b.d.l.	b.d.l.	b.d.l.	b.d.l.	b.d.l.
Gd_2O_3	4.35	4.27	4.23	3.15	3.39	3.44	4.19	5.03	1.16	0.70
Tb_2O_3	0.92	0.94	0.87	0.81	0.68	0.80	0.92	0.91	0.16	0.24
Dy_2O_3	6.15	6.21	6.56	6.31	6.23	6.21	6.17	6.70	2.18	1.16
Ho_2O_3	3.53	3.51	3.18	3.06	3.10	3.12	3.32	4.14	1.07	0.55

Er_2O_3	3.36	3.77	3.46	3.45	3.39	3.70	3.83	3.55	1.04	0.53
Tm_2O_3	0.47	0.32	0.53	0.26	0.68	0.48	0.57	0.53	0.44	0.01
Yb_2O_3	2.69	3.07	2.67	3.03	3.19	3.21	2.97	2.64	1.13	0.33
Lu_2O_3	1.69	1.74	1.26	1.73	1.83	1.63	1.57	1.62	0.44	0.08
PbO	0.26	0.17	0.28	0.31	0.19	0.04	0.45	0.30	0.08	b.d.l.
ThO_2	1.26	1.32	1.87	0.31	3.41	3.19	1.06	0.64	51.62	65.50
UO_2	0.22	0.56	0.56	0.01	0.48	0.41	0.17	0.32	3.63	5.12
Tot.	101.15	101.96	100.30	100.26	100.73	100.52	101.86	102.03	95.45	98.72

	Xen14-	Xen14-	Xen14-	Xen14-	Xen14-	Xen14-	Xen14-	Xen14-	Xen14-	Xen14-27
As	0.115	0.126	0.110	0.110	0.114	0.116	0.068	0.064	0.042	0.035
P	0.833	0.845	0.860	0.841	0.855	0.835	0.893	0.900	0.282	0.084
Si	0.026	0.006	0.006	0.029	0.005	0.025	0.007	0.002	0.685	0.892
V	0	0	0	0	0	0	0	0	0.003	0.005
Ca	0	0	0	0.002	0	0	0.001	0	0.001	0
Y	0.735	0.758	0.733	0.737	0.749	0.732	0.753	0.743	0.248	0.090
La	0	0	0	0	0	0	0	0	0	0
Ce	0	0	0	0	0	0.001	0.002	0.001	0	0.002
Pr	0	0.002	0.002	0	0	0	0.001	0	0	0
Nd	0.003	0.003	0.002	0.005	0.001	0.006	0.005	0.003	0.006	0.002
Sm	0.010	0.005	0.009	0.008	0.006	0.007	0.012	0.010	0.003	0.004
Eu	0	0	0	0	0	0	0	0	0	0
Gd	0.040	0.038	0.051	0.035	0.042	0.040	0.048	0.058	0.019	0.012
Tb	0.008	0.008	0.012	0.009	0.010	0.009	0.010	0.010	0.002	0.004
Dy	0.071	0.066	0.073	0.067	0.072	0.071	0.069	0.075	0.034	0.019
Ho	0.035	0.031	0.038	0.030	0.037	0.035	0.036	0.045	0.016	0.009
Er	0.038	0.045	0.041	0.037	0.042	0.041	0.042	0.038	0.016	0.008
Tm	0.007	0.006	0.006	0.004	0.004	0.005	0.006	0.005	0.006	0
Yb	0.034	0.035	0.031	0.039	0.036	0.035	0.031	0.028	0.017	0.005
Lu	0.019	0.015	0.014	0.016	0.016	0.017	0.016	0.017	0.006	0.001
Pb	0.001	0.003	0.002	0.002	0.003	0	0.004	0.002	0.001	0
Th	0.027	0.012	0.010	0.031	0.009	0.025	0.008	0.005	0.579	0.771
U	0.003	0.001	0.004	0.003	0.003	0.003	0.001	0.002	0.039	0.059

Table S 13.14: Chemical composition (expressed in oxide wt % and in atoms per formula unit calculated on the basis of 4 oxygen atoms) of all the EPMA-WDS data points of the Mon14 sample.

	Mon14-1	Mon14-2	Mon14-3	Mon14-4	Mon14-5	Mon14-6	Mon14-7	Mon14-8	Mon14-9	Mon14-10	Mon14-11	Mon14-12
As_2O_5	2.8	2.85	1.53	1.42	2.05	1.4	1.61	1.97	1.47	1.37	2.47	2.58
P_2O_5	27.11	26.60	28.21	28.10	28.32	28.55	28.09	27.64	27.93	28.24	26.93	26.76
SiO_2	0.69	0.65	0.10	0.06	0.11	0.02	0.06	0.06	0.05	0.08	0.53	0.48
V_2O_5	b.d.l.	b.d.l.	b.d.l.	b.d.l.	b.d.l.	b.d.l.	b.d.l.	b.d.l.	b.d.l.	b.d.l.	b.d.l.	b.d.l.
CaO	1.11	1.09	1.33	1.43	0.55	0.54	1.47	1.16	1.40	1.43	1.59	1.17
Y_2O_3	0.58	0.62	0.53	0.59	0.60	0.43	0.39	0.49	0.60	0.47	0.62	0.60
La_2O_3	12.31	12.47	14.70	15.00	13.35	15.61	15.82	15.15	15.10	15.67	12.47	12.48
Ce_2O_3	29.74	28.82	31.87	31.22	31.40	32.95	32.07	32.12	30.10	31.15	28.41	30.19
Pr_2O_3	3.25	3.09	3.48	3.50	3.93	3.56	3.44	3.45	3.55	3.48	3.43	3.42
Nd_2O_3	13.02	13.52	12.43	12.47	14.46	12.70	12.21	12.99	12.78	12.49	12.75	12.70
Sm_2O_3	2.39	2.45	1.97	2.22	2.39	2.23	2.18	2.28	2.11	1.86	2.24	2.07
Eu_2O_3	b.d.l.	b.d.l.	b.d.l.	b.d.l.	b.d.l.	b.d.l.	b.d.l.	b.d.l.	b.d.l.	b.d.l.	b.d.l.	b.d.l.
Gd_2O_3	1.55	1.43	1.36	1.46	2.06	1.23	1.04	1.31	1.47	1.06	1.64	1.31
Tb_2O_3	b.d.l.	b.d.l.	b.d.l.	b.d.l.	b.d.l.	b.d.l.	b.d.l.	b.d.l.	b.d.l.	b.d.l.	b.d.l.	b.d.l.
Dy_2O_3	0.40	0.25	0.18	0.13	0.32	0.41	0.18	0.15	0.21	0.27	0.43	0.27
Ho_2O_3	0.13	0.42	0.13	0.36	0.44	0.24	0.20	0.26	0.15	0.36	0.25	0.10
Er_2O_3	0.22	0.02	b.d.l.	b.d.l.	0.03	b.d.l.	0.03	b.d.l.	b.d.l.	b.d.l.	b.d.l.	0.05
Tm_2O_3	b.d.l.	b.d.l.	b.d.l.	b.d.l.	0.17	b.d.l.	b.d.l.	b.d.l.	0.15	0.14	0.17	0.21
Yb_2O_3	b.d.l.	b.d.l.	b.d.l.	b.d.l.	b.d.l.	b.d.l.	b.d.l.	b.d.l.	0.09	0.39	b.d.l.	0.02
Lu_2O_3	0.14	0.24	b.d.l.	0.04	0.18	b.d.l.	0.07	b.d.l.	0.05	0.03	b.d.l.	0.18
PbO	b.d.l.	b.d.l.	b.d.l.	0.01	0.20	b.d.l.	b.d.l.	b.d.l.	b.d.l.	0.07	0.08	b.d.l.
ThO_2	5.38	5.39	1.32	1.60	1.20	0.57	1.33	0.68	1.64	1.06	5.70	4.73
UO_2	0.09	0.17	b.d.l.	b.d.l.	b.d.l.	b.d.l.	b.d.l.	0.05	0.06	0.01	0.08	0.15
Tot.	100.98	100.14	99.20	99.70	101.84	100.52	100.26	99.83	98.97	99.70	99.86	99.56

	Mon14-1	Mon14-2	Mon14-3	Mon14-4	Mon14-5	Mon14-6	Mon14-7	Mon14-8	Mon14-9	Mon14-10	Mon14-11	Mon14-12
As	0.058	0.059	0.031	0.029	0.042	0.028	0.033	0.041	0.030	0.028	0.051	0.054
P	0.909	0.904	0.951	0.947	0.941	0.956	0.943	0.935	0.948	0.950	0.914	0.913
Si	0.027	0.026	0.004	0.002	0.004	0.001	0.002	0.002	0.002	0.003	0.021	0.019
V	0	0	0	0	0	0	0	0	0	0	0	0
Ca	0.047	0.047	0.057	0.061	0.023	0.023	0.062	0.050	0.060	0.061	0.068	0.050
Y	0.012	0.013	0.011	0.012	0.012	0.009	0.008	0.010	0.012	0.010	0.013	0.013

La	0.179	0.184	0.216	0.220	0.193	0.227	0.231	0.223	0.223	0.229	0.184	0.185
Ce	0.431	0.423	0.464	0.455	0.451	0.477	0.465	0.469	0.442	0.453	0.416	0.445
Pr	0.047	0.045	0.050	0.050	0.056	0.051	0.049	0.050	0.051	0.050	0.050	0.050
Nd	0.184	0.193	0.176	0.177	0.202	0.179	0.172	0.185	0.183	0.177	0.182	0.182
Sm	0.032	0.033	0.027	0.030	0.032	0.030	0.029	0.031	0.029	0.025	0.030	0.028
Eu	0	0	0	0	0	0	0	0	0	0	0	0
Gd	0.020	0.019	0.018	0.019	0.026	0.016	0.013	0.017	0.019	0.014	0.021	0.017
Tb	0	0	0	0	0	0	0	0	0	0	0	0
Dy	0.005	0.003	0.002	0.001	0.004	0.005	0.002	0.001	0.002	0.003	0.005	0.003
Ho	0.001	0.005	0.001	0.004	0.005	0.003	0.002	0.003	0.001	0.004	0.003	0.001
Er	0.002	0	0	0	0	0	0	0	0	0	0	0
Tm	0	0	0	0	0.002	0	0	0	0.001	0.001	0.002	0.002
Yb	0	0	0	0	0	0	0	0	0.001	0.004	0	
Lu	0.001	0.002	0	0	0.002	0	0	0	0	0	0	0.002
Pb	0	0	0	0	0.002	0	0	0	0	0	0	0
Th	0.048	0.049	0.012	0.014	0.010	0.005	0.012	0.006	0.015	0.009	0.051	0.043
U	0	0.001	0	0	0	0	0	0	0	0	0	0.001

Table S 13.15: Chemical composition (expressed in oxide wt % and in atoms per formula unit calculated on the basis of 4 oxygen atoms) of all the EPMA-WDS data points of the Ch16 sample.

	Ch16-1	Ch16-2	Ch16-3	Ch16-4	Ch16-5	Ch16-6	Ch16-7	Ch16-8	Ch16-9	Ch16-10	Ch16-11	Ch16-12	Ch16-13
As_2O_5	31.99	39.91	39.61	37.71	23.63	38.16	38.91	18.40	24.11	36.45	38.88	38.85	36.31
P_2O_5	3.24	1.91	3.04	6.53	7.27	4.05	2.43	11.88	7.68	2.43	2.78	2.45	3.02
SiO_2	2.73	1.98	1.68	0.32	2.83	1.31	2.16	2.64	3.03	2.66	2.16	2.58	2.20
V_2O_5	0.04	b.d.l.	b.d.l.	b.d.l.	0.02	b.d.l.	0.03	0.03	b.d.l.	0.05	b.d.l.	0.05	b.d.l.
CaO	0.83	b.d.l.	0.05	b.d.l.	1.71	0.11	b.d.l.	1.93	1.82	0.19	0.02	0.05	0.59
Y_2O_3	28.94	30.52	30.53	34.68	27.48	31.50	30.69	30.28	29.29	32.26	35.04	32.53	32.22
La_2O_3	0.07	0.06	b.d.l.	b.d.l.	b.d.l.	0.03	0.05	0.23	0.06	0.07	0.01	0.14	b.d.l.
Ce_2O_3	0.13	0.19	0.28	0.29	0.16	0.22	0.10	0.55	0.35	b.d.l.	b.d.l.	0.03	0.20
Pr_2O_3	0.05	b.d.l.	0.01	0.06	0.03	b.d.l.	b.d.l.	0.02	b.d.l.	0.12	0.04	b.d.l.	b.d.l.
Nd_2O_3	0.49	0.99	1.43	1.29	0.66	1.20	0.79	0.43	0.32	0.10	0.06	0.27	0.33
Sm_2O_3	0.78	0.98	1.56	1.22	0.73	1.41	0.71	0.33	0.22	0.67	0.10	0.65	0.33
Eu_2O_3	b.d.l.	b.d.l.	b.d.l.	b.d.l.	b.d.l.	b.d.l.	b.d.l.	b.d.l.	b.d.l.	b.d.l.	b.d.l.	b.d.l.	b.d.l.
Gd_2O_3	2.15	1.99	2.83	2.84	1.95	2.98	2.01	2.36	2.09	2.82	1.55	2.58	1.86
Tb_2O_3	0.55	0.40	0.68	0.72	0.45	0.59	0.52	0.49	0.41	0.61	0.65	0.79	0.66
Dy_2O_3	4.29	4.35	4.59	4.81	4.21	4.77	4.48	4.39	4.22	4.94	4.10	5.16	3.71
Ho_2O_3	1.82	1.83	2.40	1.97	1.85	2.19	1.89	1.76	1.94	2.39	1.72	2.48	1.96
Er_2O_3	3.07	3.27	2.86	3.69	2.53	3.18	3.30	2.27	2.11	2.49	2.80	2.50	2.76
Tm_2O_3	0.50	0.64	0.51	0.56	0.11	0.63	0.37	0.04	0.18	0.15	0.19	0.33	0.33
Yb_2O_3	3.26	3.51	3.31	3.62	2.64	2.93	3.66	1.62	1.47	1.42	1.86	1.47	1.68
Lu_2O_3	1.17	0.99	1.29	1.49	0.96	1.12	1.74	1.26	1.17	1.27	0.64	0.95	1.01
PbO	0.24	0.10	0.22	0.27	0.25	0.29	0.20	0.29	0.24	0.23	0.03	0.29	0.29
ThO_2	5.82	3.42	4.24	0.44	11.52	2.97	3.17	11.81	10.96	7.26	4.21	6.75	6.76
UO_2	5.82	5.86	3.19	1.20	4.37	3.02	6.06	3.18	4.48	4.14	4.17	4.33	3.43
Tot.	98.10	102.97	104.41	103.93	95.47	102.76	103.38	96.30	96.19	102.81	101.11	105.32	99.75

	Ch16-1	Ch16-2	Ch16-3	Ch16-4	Ch16-5	Ch16-6	Ch16-7	Ch16-8	Ch16-9	Ch16-10	Ch16-11	Ch16-12	Ch16-13
As	0.724	0.851	0.828	0.763	0.543	0.802	0.826	0.403	0.540	0.780	0.818	0.806	0.786
P	0.118	0.066	0.103	0.214	0.271	0.138	0.083	0.422	0.279	0.084	0.094	0.082	0.106
Si	0.118	0.080	0.067	0.012	0.124	0.052	0.087	0.110	0.130	0.109	0.087	0.102	0.091
V	0.001	0	0	0	0	0	0.001	0.001	0	0.001	0	0.001	0
Ca	0.038	0	0.002	0	0.080	0.005	0	0.086	0.083	0.008	0	0.002	0.026
Y	0.667	0.662	0.649	0.714	0.643	0.674	0.663	0.676	0.668	0.703	0.750	0.687	0.710

La	0.001	0	0	0	0	0	0	0.003	0	0.001	0	0.002	0
Ce	0.002	0.002	0.004	0.004	0.002	0.003	0.001	0.008	0.005	0	0	0	0.003
Pr	0	0	0	0	0	0	0	0	0	0.001	0	0	0
Nd	0.007	0.014	0.020	0.017	0.010	0.017	0.011	0.006	0.004	0.001	0	0.003	0.004
Sm	0.011	0.013	0.021	0.016	0.011	0.019	0.010	0.004	0.003	0.009	0.001	0.008	0.004
Eu	0	0	0	0	0	0	0	0	0	0	0	0	0
Gd	0.030	0.027	0.037	0.036	0.028	0.039	0.027	0.032	0.029	0.038	0.020	0.034	0.025
Tb	0.007	0.005	0.008	0.009	0.006	0.007	0.007	0.006	0.005	0.008	0.008	0.010	0.009
Dy	0.059	0.057	0.059	0.060	0.059	0.061	0.058	0.059	0.058	0.065	0.053	0.066	0.049
Ho	0.025	0.023	0.030	0.024	0.026	0.028	0.024	0.023	0.026	0.031	0.022	0.031	0.025
Er	0.041	0.041	0.035	0.045	0.034	0.040	0.042	0.029	0.028	0.032	0.035	0.031	0.036
Tm	0.006	0.008	0.006	0.006	0.001	0.007	0.004	0	0.002	0.001	0.002	0.004	0.004
Yb	0.043	0.043	0.040	0.042	0.035	0.035	0.045	0.020	0.019	0.017	0.022	0.017	0.021
Lu	0.015	0.012	0.015	0.017	0.012	0.013	0.021	0.016	0.015	0.015	0.007	0.011	0.012
Pb	0.002	0.001	0.002	0.002	0.003	0.003	0.002	0.003	0.002	0.002	0	0.003	0.003
Th	0.057	0.031	0.038	0.003	0.115	0.027	0.029	0.112	0.106	0.067	0.038	0.061	0.063
U	0.056	0.053	0.028	0.010	0.042	0.027	0.054	0.029	0.042	0.037	0.037	0.038	0.031

Table S 13.16: Unit-cell, *A*-site polyhedron and *T*-site tetrahedron volumes of selected synthetic REE*T*O_4 compounds.

Compound	Structure type	Unit-cell Volume (Å^3)	*A*-site polyhedron (Å^3)	*T*-site tetrahedron (Å^3)	Reference
YPO_4	zircon	286.53(5)	23.15(6)	1.86(1)	Ni et al. 1995
$LaPO_4$	monazite	305.73(6)	33.31(8)	1.858(8)	Ni et al. 1995
$CePO_4$	monazite	299.93(7)	32.56(8)	1.837(7)	Ni et al. 1995
$NdPO_4$	monazite	291.31(7)	31.27(8)	1.851(7)	Ni et al. 1995
$TbPO_4$	zircon	291.14(8)	23.73(7)	1.84(1)	Ni et al. 1995
$HoPO_4$	zircon	287.92(7)	23.34(8)	1.85(1)	Ni et al. 1995
$DyPO_4$	zircon	284.62(6)	23.08(7)	1.83(1)	Ni et al. 1995
$YbPO_4$	zircon	287.92(7)	22.20(7)	1.83(1)	Ni et al. 1995
$LuPO_4$	zircon	273.58(8)	21.84(7)	1.83(1)	Ni et al. 1995
$YAsO_4$	zircon	312.27(4)	23.46(4)	2.377(9)	Ledderboge et al. 2018
$LaAsO_4$	monazite	330.65(3)	33.84(5)	2.400(5)	Kang and Schleid 2005
$CeAsO_4$	monazite	327.29(11)	38.34(14)	2.43(2)	Brahim et al. 2002
$NdAsO_4$	monazite	315.67(3)	31.75(8)	2.399(9)	Schmidt et al. 2005
$TbAsO_4$	zircon	319.9(2)	24.14(13)	2.42(3)	Long and Stager 1977
$HoAsO_4$	zircon	314.5(3)	23.73(5)	2.377(9)	Schmidt et al. 2005
$DyAsO_4$	zircon	312.8(2)	23.51(10)	2.39(2)	Long and Stager 1977
$YbAsO_4$	zircon	303.40(3)	22.52(4)	2.38(1)	Kang et al. 2005
$LuAsO_4$	zircon	300.69(15)	22.28(6)	2.37(1)	Lohmüller et al. 1973

Table S 13.17: bulk moduli of several ATO_4 compounds from literature. Information about the ionic radii (Shannon et al. 1970) is also reported.

	A-site ionic radii (Å)	Zircon (GPa)	Monazite (GPa)	Scheelite (GPa)	$BaWO_4$-II (GPa)	Postbarite (GPa)	Reference
$ScPO_4$	0.87	175.1					Li et al. (2009)§
$ScPO_4$	0.87	203					Zhang et al. (2009)
$ScPO_4$	0.87	183					Zhang et al. (2009)§
$ScPO_4$-II	0.87			376			Zhang et al. (2009)
$ScPO_4$-II	0.87			334			Zhang et al. (2009)§
$ScAsO_4$	0.87	166					Li et al. (2009)§
$ScVO_4$	0.87	178					Errandonea et al. (2009)
$ScVO_4$	0.87	158.7					Zhang et al. (2008)§
$ScVO_4$-II	0.87			210			Errandonea et al. (2009)
xenotime-(Y)	1.021	148					Mogilewsky et al. (2006)
xenotime-(Y)-II	1.076		146				This study
xenotime-(Y)	1.020	132					This study
YPO_4	1.019	144.4					Li et al. (2009)§
YPO_4	1.019	145.2					Errandonea et al. (2005)
YPO_4	1.019	165.5					Zhang et al. (2009)§
YPO_4	1.019	186					Zhang et al. (2009)
YPO_4	1.019	149					Lacomba-Perales et al. (2010)
YPO_4-II	1.075		260				Zhang et al. (2009)
YPO_4-II	1.075		206				Lacomba-Perales et al. (2010)
YPO_4-III	1.019			213			Zhang et al. (2009)§
chernovite-(Y)	1.023	136					This study
chernovite-(Y)	1.053	125					This study
$YAsO_4$	1.019	137					Li et al. (2009)§
$YAsO_4$	1.019	135					Errandonea et al. (2005)§
$YAsO_4$	1.019	142					Errandonea et al. (2011)
$YAsO_4$	1.019	115.5					Errandonea et al. (2011)§
$YAsO_4$-II	1.019			149			Errandonea et al. (2011)
$YCrO_4$	1.019	136					Errandonea et al. (2011)
$YCrO_4$	1.019	121.61					Li et al. (2006)§
$YCrO_4$-II	1.019			151			Errandonea et al. (2011)
$YCrO_4$-II	1.019			141.2			Li et al. (2006)§
YVO_4	1.019	130					Wang et al. (2004)
YVO_4	1.019	122					Zhang et al. (2007)§
YVO_4	1.019	120					Huang et al. (2012)§
YVO_4	1.019	134					Zhang et al. (2008)§
YVO_4-II	1.019			138			Wang et al. (2004)
YVO_4-II	1.019			155.4			Huang et al. (2013)§
YVO_4-II	1.019			126.8			Huang et al. (2013)§
$LaPO_4$	1.216		134				Li et al. (2009)§
$LaPO_4$	1.216		114.2				Errandonea et al. (2018)
$LaPO_4$	1.216		125				Ruitz-Fuertes et al. (2016)
$LaPO_4$	1.216		144				Lacomba-Perales et al. (2010)
$LaPO_4$-II	1.31					143	Lacomba-Perales et al. (2010)
$LaAsO_4$	1.216		124.5				Li et al. (2009)§
$LaVO_4$	1.216		95				Errandonea et al. (2016)
$LaVO_4$	1.216		105.2				Errandonea et al. (2016)§
$LaVO_4$	1.16	109.1					Zhang et al. (2008)§

$LaVO_4$	1.16	93				Yuan et al. (2015)
$LaVO_4$	1.216		106			Errandonea et al. (2014)
$LaVO_4$	1.216		99			Errandonea et al. (2014)
$LaVO_4$	0.99				154	Erradnonea et al. (2016)§
monazite-(Ce)	1.184		122			This study
$CePO_4$	1.196		137.2			Li et al. (2009)§
$CePO_4$	1.196		117.3			Errandonea et al. (2018)
$CePO_4$	1.196		122			Huang et al. (2010) (up to 11 Gpa)
$CePO_4$	1.196		109			Huang et al. (2010) (up to 20 Gpa)
gasparite-(Ce)	1.189		109			This study
$CeAsO_4$	1.196		125.1			Li et al. (2009)§
$CeVO_4$	1.143	125				Errandonea et al. (2011)
$CeVO_4$	1.143	118.9				Panchal et al. (2011)
$CeVO_4$	1.143	112				Garg et al. (2013)
$CeVO_4$	1.143	113.2				Zhang et al. (2008)§
$CeVO_4$-II	1.196		133			Errandonea et al. (2011)
$CeVO_4$-II	1.196		142			Panchal et al. (2011)
$CeVO_4$-II	1.196		98			Errandonea et al. (2013)
$PrPO_4$	1.179		139.7			Li et al. (2009)§
$PrPO_4$	1.179		120.2			Errandonea et al. (2018)
$PrVO_4$	1.126	115.9				Zhang et al. (2008)§
$PrVO_4$	1.126	120.3				Bandiello et al. (2020)
$PrVO_4$	1.126	119				Bandiello et al. (2020)§
$PrVO_4$-II	1.179		95			Bandiello et al. (2020)
$PrVO_4$-II	1.179		101			Bandiello et al. (2020)§
$PrVO_4$-III	0.99				147	Bandiello et al. (2020)
$PrVO_4$-III	0.99				125	Bandiello et al. (2020)§
$NdPO_4$	1.163		142.3			Li et al. (2009)§
$NdPO_4$	1.163		160			Lacomba-Perales et al. (2010)
$NdAsO_4$	1.163		130.6			Li et al. (2009)§
$NdVO_4$	1.109	148				Errandonea et al. (2014)
$NdVO_4$	1.109	124.2				Panchal et al. (2017)§
$SmPO_4$	1.132			146		Li et al. (2009)§
$SmAsO_4$	1.079	124.7				Li et al. (2009)§
$SmVO_4$	1.079	123				Zhang et al. (2008)§
$EuPO_4$	1.12		147.1			Li et al. (2009)§
$EuPO_4$	1.12		159			lacomba-Peralez et al. (2010)
$EuVO_4$	1.066	149				Errandonea et al. (2009)
$EuVO_4$	1.066	125.3				Zhang et al. (2008)§
$EuVO_4$-II	1.066			199		Errandonea et al. (2009)
$GdPO_4$	1.107		149			Li et al. (2009)§
$GdPO_4$	1.107		160			lacomba-Peralez et al. (2010)
$GdPO_4$	1.107		128.1			Heffernan et al. 2016
$GdVO_4$	1.053	122				Marqueño et al. (2019)
$GdVO_4$	1.053	117.3				Marqueño et al. (2019)§
$GdVO_4$	1.053	127				Zhang et al. (2008)§
$GdVO_4$-II	1.053			137		Marqueño et al. (2019)
$GdVO_4$-II	1.053			138.03		Marqueño et al. (2019)§
$TbPO_4$	1.095		138.8			Li et al. (2009)§
$TbAsO_4$	1.04	132				Li et al. (2009)§

$TbVO_4$	1.04	129				Hirano et al. (2002) in Errandonea et al. (2009)
$TbVO_4$	1.04	122				Errandonea et al. (2011)
$TbVO_4$	1.04	121				Minykayev et al. (2010)
$TbVO_4$	1.04	126				Marques (1980)§
$TbVO_4$	1.04	129.6				Zhang et al. (2008)§
$TbVO_4$-II	1.04			163		Errandonea et al. (2011)
$DyPO_4$	1.083		141.5			Li et al. (2009)§
$DyAsO_4$	1.027	134.8				Li et al. (2009)§
$DyVO_4$	1.027	140				Hirano et al. (2002) in Errandonea et al. (2009)
$DyVO_4$	1.027	126				Marques (1980)§
$DyVO_4$	1.027	132.3				Zhang et al. (2008)§
$DyVO_4$	1.027	129				Wang et al. 2021
$DyVO_4$-II	1.027			184		Wang et al. 2022
$HoPO_4$	1.015	143.3				Li et al. (2009)§
$HoPO_4$	1.015	152				Gomis et al. (2017)
$HoPO_4$	1.015	146				Gomis et al. (2017)§
$HoAsO_4$	1.015	136.2				Li et al. (2009)§
$HoVO_4$	1.015	133.9				Zhang et al. (2008)§
$HoVO_4$	1.015	142				Hirano et al. (2002) in Errandonea et al. (2009)
$ErPO_4$	1.004	146.1				Li et al. (2009)§
$ErPO_4$	1.004	168				lacomba-Peralez et al. (2010)
$ErPO_4$-II	1.004		208			Lacomba-Peralez et al. (2010)
$ErVO_4$	1.004	136.1				Zhang et al. (2008)§
$ErVO_4$	1.004	136				Hirano et al (2002)
$TmPO_4$	0.994	147.2				Li et al. (2009)§
$TmPO_4$	0.994	144				Gomis et al. (2017)
$TmPO_4$	0.994	142				Gomis et al. (2017)§
$TmPO_4$	0.994	120				Bandiello et al. (2020)
$TbPO_4$	0.994	128				López-Solano et al. (2010)
$TbPO_4$	0.994	144				López-Solano et al. (2011)§
$TbPO_4$	0.994	134				López-Solano et al. (2012)§
$TbPO_4$-II	1.052		119			López-Solano et al. (2010)
$TbPO_4$-II	1.052		152			López-Solano et al. (2011)§
$TbPO_4$-III	0.994			152		López-Solano et al. (2011)§
$TbPO_4$-IIII	0.99				196	López-Solano et al. (2011)§
$TmVO_4$	0.994	137.9				Zhang et al. (2008)§
$YbPO_4$	0.985	150				Li et al. (2009)§
$YbPO_4$	0.985	150				Zhang et al. (2008)
$YbPO_4$-II	0.985			218		Zhang et al. (2008)
$YbAsO_4$	0.985	143.1				Li et al. (2009)§
$YbVO_4$	0.985	139.6				Zhang et al. (2008)§
$LuPO_4$	0.977	152.8				Li et al. (2009)§
$LuPO_4$	0.977	166				Armbruster (1976) in Lacomba-Perales et al. (2010)
$LuPO_4$	0.977	184				Zhang et al. (2008)
$LuPO_4$-II	0.977			226		Zhang et al. (2008)
$LuAsO_4$	0.977	144.8				Li et al. (2009)§
$LuVO_4$	0.977	166				Errandonea et al. (2009)

$LuVO_4$	0.977	147				Mittal et al. (2008)
$LuVO_4$	0.977	141.2				Zhang et al. (2008)[§]
$LuVO_4$-II	0.977			195		Errandonea et al. (2009)
$LuVO_4$-II	0.977			195		Mittal et al. (2008)
$ZrSiO_4$	0.83242	189				van Westrenen et al. (2005)
$ZrSiO_4$	0.84	169				Ríos and Boffa-Ballaran (2003)
$ZrSiO_4$	0.84	134				Özkan (1976)
$ZrSiO_4$	0.8316	259.5				Binvignat et al. (2018)
$ZrSiO_4$	0.82425	173				Binvignat et al. (2018)
$ZrSiO_4$	0.82737	124				Binvignat et al. (2018)
$ZrSiO_4$	0.84	167				Crocombette and Ghaleb (1998)
$ZrSiO_4$	0.84	199				van Westrenen et al. (2004)
$ZrSiO_4$	0.84	205				Ono et al. (2004)
$ZrSiO_4$	0.84	227.9				Özkan and Jamieson (1979)
$ZrSiO_4$	0.84	227				Hazen and Finger (1979)
$ZrSiO_4$-II	0.84			301		Scottet al. (2001)
$ZrSiO_4$-II	0.84			392		Ono et al. (2004)
$ZrSiO_4$-II	0.84			259		Marques et al. (2006)
$USiO_4$	1	188				Zhang et al. (2009)
$USiO_4$	1	186				Bauer et al. (2014)
$USiO_4$-II	1			204		Bauer et al. (2015)
$USiO_4$-II	1			274		Zhang et al. (2009)
$PbCrO_4$	1.35		57			Bandiello et al. (2012)
$PbCrO_4$	1.35		51.89			Errandonea et al. (2015)
$PbSeO_4$	1.35		56.75			Errandonea et al. (2015)
$SrCrO_4$	1.31		58.7			Errandonea et al. (2015)
$SrSeO_4$	1.31		57.83			Errandonea et al. (2015)
$BiPO_4$	1.17		111.9(4)			Errandonea et al. (2018)
$CaSO_4$	1.18		151			Bradbury and Williams (2009)
$CaSO_4$	1.18		146			Gracia et al. (2012)[§]

[§]: theoretical data.

Table S 13.18: LTEC of several monazite- and zircon-type compounds.

Compound	ionic radii *A*-site (Å)	Zircon LTEC (10^{-6} K^{-1})	Monazite LTEC (10^{-6} K^{-1})	reference
$ScPO_4$	0.87	7		Li et al. (2009)[§]
$ScPO_4$	0.87	5.5		Schopper (1972)
$ScPO_4$	0.87	5.5		Subbaro et al. (1990)
$ScAsO_4$	0.87	6.9		Li et al. (2009)[§]
$ScAsO_4$	0.87	5.8		Schopper (1972)
$ScVO_4$	0.87	6.9		Zhang et al. (2008)[§]
$ScVO_4$	0.87	7.3		kahle (1970)
$ScVO_4$	0.87	7		Schopper (1972)
xenotime-(Y)	1.021	6.0		This work
YPO_4	1.019	6.7		Li et al. (2009)[§]
YPO_4	1.019	5.3		Bayer (1972)
YPO_4	1.019	5.6		Bayer (1972)
YPO_4	1.019	5.5		Subbarao (1968)
YPO_4	1.019	6.3		Schopper (1972)
YPO_4	1.019	5.9		Schopper (1972)
YPO_4	1.019	6.3		kahle (1970)
YPO_4	1.019	5.9		kahle (1970)
YPO_4	1.019	6.2		Hikichi (1998)[*]
YPO_4	1.019	5.7		Taylor (1986)[*]
YPO_4	1.019	5.5		Sallese (1986)
YPO_4	1.019	5.9		Sallese (1986)[*]
chernovite-(Y)	1.023	4.8		this study
chernovite-(Y)	1.023	4.6		this study
chernovite-(Y)	1.053	4.0		this study
$YAsO_4$	1.019	6.6		Li et al. (2009)[§]
$YAsO_4$	1.019	6.3		Schopper (1972)
$YAsO_4$	1.019	6.6		Schopper (1972)
$YAsO_4$	1.019	6.2		kahle (1970)
$YAsO_4$	1.019	6.3		reddy et al. (1988)
$YAsO_4$	1.019	6.6		kahle (1970)
YVO_4	1.019	6.7		Zhang et al. (2008)[§]
YVO_4	1.019	5.8		Bayer (1972)
YVO_4	1.019	5.8		Bayer (1972)
YVO_4	1.019	6.2		Bayer (1972)
YVO_4	1.019	6.7		kahle (1970)
YVO_4	1.019	5.1		Sallese (1986)
YVO_4	1.019	4.8		Sallese (1986)[*]
YVO_4	1.019	4.5		reddy et al. (1988)
YVO_4	1.019	4.4		reddy et al. 1985
YVO_4	1.019	4.5		Reddy and Murthy (1983)
$LaPO_4$	1.216		7.8	Li et al. (2009)[§]
$LaPO_4$	1.216		10.3(5)	Perrière et al. (2007)[*]
$LaPO_4$	1.216		7.8(3)	Thust et al. (2015)[*]
$LaPO_4$	1.216		10	Hikichi (1998)
$LaPO_4$	1.216		7.5	Morgan and marshall (1995)
$LaPO_4$	1.216		10.5	Morgan and marshall (1995)
$LaPO_4$	1.216		9.6	Morgan and marshall (1995)
$LaAsO_4$	1.216		7.7	Li et al. (2009)[§]
$LaVO_4$	1.160	6.1		Zhang et al. (2008)[§]
monazite-(Ce)	1.184		9.7	this study

$CePO_4$	1.196		7.7	Li et al. (2009)[§]
$CePO_4$	1.196		9.9	Hikichi 1997
$CePO_4$	1.196		9.1	Asuvathraman et al. (2014)
$CePO_4$	1.193		8.9	Asuvathraman et al. (2014)
$CeAsO_4$	1.196		7.7	Li et al. (2009)[§]
$CeVO_4$	1.143	6.1		Zhang et al. (2008)
$PrPO_4$	1.179		7.7	Li et al. (2009)[§]
$PrPO_4$	1.179		10.9(5)	Perrière et al. (2007)[*]
$PrVO_4$	1.126	6		Zhang et al. (2008)[§]
$NdPO_4$	1.163		7.6	Li et al. (2009)[§]
$NdPO_4$	1.163		10.7(5)	Perrière et al. (2007)[*]
$NdPO_4$	1.163		9.8	Hikichi 1997
$NdAsO_4$	1.163		7.6	Li et al. (2009)[§]
$NdVO_4$	1.109	6		Zhang et al. (2008)[§]
$NdVO_4$	1.109	6		reddy et al (1995)
$SmPO_4$	1.132		7.5	Li et al. (2009)[§]
$SmPO_4$	1.132		11(0.5)	Perrière et al. (2007)[*]
$SmPO_4$	1.132		9.7	Hikichi 1997
$SmAsO_4$	1.079	5.9		Li et al. (2009)[§]
$SmVO_4$	1.079	5.9		Zhang et al. (2008)[§]
$EuPO_4$	1.12		7.5	Li et al. (2009)[§]
$EuPO_4$	1.12		11.1(5)	Perrière et al. (2007)[*]
$EuPO_4$	1.12		9.1(3)	Thust et al. (2015)[*]
$EuVO_4$	1.066	5.9		Zhang et al. (2008)[§]
$EuVO_4$	1.066	6.9		Reddy and Murthy (1983)
$GdPO_4$	1.107		7.5	Li et al. (2009)[§]
$GdPO_4$	1.107		11.4(5)	Perrière et al. (2007)[*]
$GdVO_4$	1.053	5.9		Zhang et al. (2008)[§]
$GdVO_4$	1.053	4.4		Reddy et al 1985
$GdVO_4$	1.053	6		Anitha et al. (pers comm) In Patwe et al. (2009)
$GdVO_4$	1.053	5.3		Anitha et al. (pers comm) In Patwe et al. (2009)
$TbPO_4$	1.04	5.9		Li et al. (2009)[§]
$TbAsO_4$	1.04	5.8		Li et al. (2009)[§]
$TbVO_4$	1.04	5.8		Zhang et al. (2008)[§]
$DyPO_4$	1.027	5.9		Li et al. (2009)[§]
$DyAsO_4$	1.027	5.8		Li et al. (2009)[§]
$DyVO_4$	1.027	5.8		Zhang et al. (2008)[§]
$DyVO_4$	1.027	6.6		Reddy and Murthy 1981
$HoPO_4$	1.015	5.8		Li et al. (2009)[§]
$HoAsO_4$	1.015	5.7		Li et al. (2009)[§]
$HoVO_4$	1.015	5.7		Zhang et al. (2008)[§]
$ErPO_4$	1.004	5.8		Li et al. (2009)[§]
$ErPO_4$	1.004	6		Hikichi et al. (1998)[*]
$ErVO_4$	1.004	5.7		Zhang et al. (2008)[§]
$TmPO_4$	0.994	5.8		Li et al. (2009)[§]
$TmVO_4$	0.994	5.7		Zhang et al. (2008)[§]
$YbPO_4$	0.985	5.8		Li et al. (2009)[§]
$YbPO_4$	0.985	6		Hikichi et al. (1998)[*]
$YbAsO_4$	0.985	5.7		Li et al. (2009)[§]
$YbVO_4$	0.985	5.7		Zhang et al. (2008)[§]
$LuPO_4$	0.977	5.7		Li et al. (2009)
$LuPO_4$	0.977	6.2		Hikichi et al. (1998)[*]
$LuPO_4$	0.977	6.4		Patwe et al. (2009)

$LuAsO_4$	0.977	5.6	Li et al. (2009)[§]
$LuVO_4$	0.986	4.1	Zhao et al (2004)
$LuVO_4$	0.977	5.7	Zhang et al. (2008)[§]
$LuVO_4$	0.977	2.3	Skanthakumar et al. (1995)
$LuVO_4$	0.977	6.3	Patwe et al. (2009)
$ThSiO_4$	1.05	3.4	Sallese (1986)
$ThSiO_4$	1.05	3.8	Sallese (1986)[*]
$ZrSiO_4$	0.84	4.1	Bayer (1972)
$ZrSiO_4$	0.84	4.6	Sallese (1986)
$ZrSiO_4$	0.84	2.6	Sallese (1986)[*]
$ZrSiO_4$	0.84	4.2	Austin (1931)
$ZrSiO_4$	0.84	5.5	Subbarao (1968)
$ZrSiO_4$	0.84	4.2	Subbarao (1968)
$ZrSiO_4$	0.84	3.8	Worlton et al. (1972)

[§]: theoretical data; [*]: experimental data obtained with dilatometry.